Women in cancer metabolism: 2021/2022
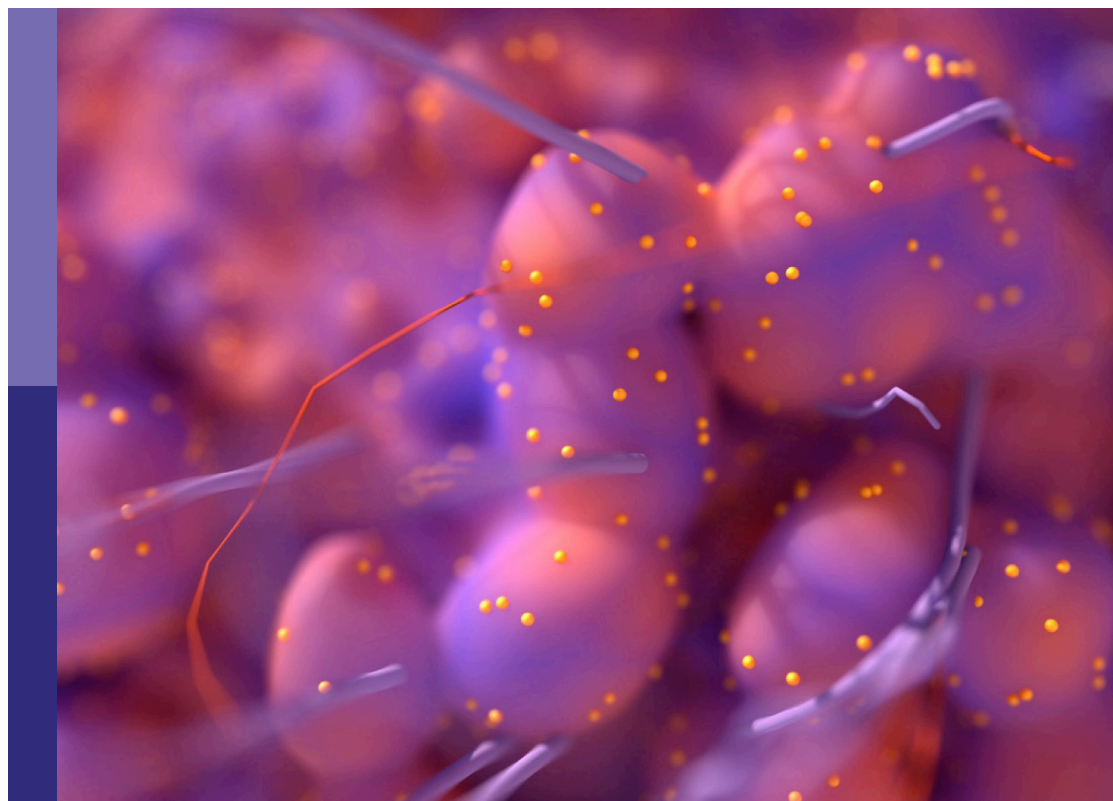
Edited by
Tuuli Käämbre and Atrayee Basu Mallick

Published in
Frontiers in Oncology

About Frontiers

Frontiers is more than just an open access publisher of scholarly articles: it is a pioneering approach to the world of academia, radically improving the way scholarly research is managed. The grand vision of Frontiers is a world where all people have an equal opportunity to seek, share and generate knowledge. Frontiers provides immediate and permanent online open access to all its publications, but this alone is not enough to realize our grand goals.

Frontiers journal series

The Frontiers journal series is a multi-tier and interdisciplinary set of open-access, online journals, promising a paradigm shift from the current review, selection and dissemination processes in academic publishing. All Frontiers journals are driven by researchers for researchers; therefore, they constitute a service to the scholarly community. At the same time, the *Frontiers journal series* operates on a revolutionary invention, the tiered publishing system, initially addressing specific communities of scholars, and gradually climbing up to broader public understanding, thus serving the interests of the lay society, too.

Dedication to quality

Each Frontiers article is a landmark of the highest quality, thanks to genuinely collaborative interactions between authors and review editors, who include some of the world's best academicians. Research must be certified by peers before entering a stream of knowledge that may eventually reach the public – and shape society; therefore, Frontiers only applies the most rigorous and unbiased reviews. Frontiers revolutionizes research publishing by freely delivering the most outstanding research, evaluated with no bias from both the academic and social point of view. By applying the most advanced information technologies, Frontiers is catapulting scholarly publishing into a new generation.

What are Frontiers Research Topics?

Frontiers Research Topics are very popular trademarks of the *Frontiers journals series*: they are collections of at least ten articles, all centered on a particular subject. With their unique mix of varied contributions from Original Research to Review Articles, Frontiers Research Topics unify the most influential researchers, the latest key findings and historical advances in a hot research area.

Find out more on how to host your own Frontiers Research Topic or contribute to one as an author by contacting the Frontiers editorial office: frontiersin.org/about/contact

Women in cancer metabolism: 2021/2022

Topic editors

Tuuli Käämbre — National Institute of Chemical Physics and Biophysics, Estonia
Atrayee Basu Mallick — Thomas Jefferson University, United States

Table of contents

Editorial: Women in cancer metabolism: 2021/2022

Tuuli Kaambre*

Laboratory of Chemical Biology, National Institute of Chemical Physics and Biophysics, Tallinn, Estonia

Editorial on the Research Topic
Women in cancer metabolism: 2021/2022

Women have participated in research and made important contributions to it since the beginning of the history of science. On the other hand, women's participation has often been hindered by the prevalent patriarchal worldview; higher positions are mostly held by men, while women are predominantly in teaching positions. In recent years, the role of women in science has begun to increase, including in cancer research. This collection of articles supports women scientists to make their work more visible in the scientific community.

Cancer cells need energy for survival, proliferation, and the formation of metastases. Several mechanisms are involved in these processes. Today's research is focused on how essential nutrients such as glucose, lactate, fatty acids, and glutamine are utilized by the cells, cellular metabolomics, and also on the regulation and communication of metabolic pathways. The need to find new tumor drug targets and biomarkers has become very important and these studies allow getting closer to that goal.

Breast and ovarian cancer studies – from woman to woman

In this issue, three female scientists have contributed to the study of tumors that directly attack women like breast and ovarian cancer.

The article by Ruggiero et. al., where they studied the lifetime of the intracellular water as the tumor biomarker, is dedicated to breast cancer described relaxometric measurements using FFC-NMR on tumor specimens *in vivo* using 4T1 and doxorubicin-resistant 4T1R cell lines and by using a model of Balb/c Mice Bearing 4T1 tumors *in vitro*. These experiments resulted in a decrease in kio (cellular water efflux rate constant) during the doxorubicin treatment which decreased the activity of Na+/K+-ATPase (validated in the control experiments on the cellular uptake of Rb ions). The results reported show that kio can be considered a non-invasive, early, and predictive biomarker

for the identification of responsive patients immediately after the first doxorubicin treatment.

Penkert with colleagues described systemic metabolic alterations that exist in BRCA1+ individuals independent of cancer incidence. This group detected one single metabolite, pyruvate, and two metabolite ratios involving pyruvate, lactate, and a metabolite of yet unknown structure (RI1984, MS studies showing this a sugar acid), significantly altered between the cohorts of BRCA1+ women and 72 age-matched female controls. The results allow us to assume that constitutional alterations in energy metabolism may be involved in the etiology of BRCA1-associated breast cancer.

Ovarian cancer is one of the most aggressive malignancies worldwide and He et al. studied the aberrant cholesterol metabolism of this tumor. The authors give a systematic overview of the key proteins involved in cholesterol and oxysterol metabolism in ovarian cancer, including the rate-limiting enzymes in cholesterol biosynthesis, and the proteins involved in cholesterol uptake, storage, and trafficking. Both cholesterol and oxysterol reprogram the cellular microenvironment, high levels of these sterols may be immunosuppressive.

Energy metabolism of glioblastoma

Glioblastoma (GMB) is still a tumor with a very poor prognosis and complicated treatment; this tumor is also rather radioresistant and therefore understanding the metabolism type of this tumor is essential. One very important metabolite for tumor cells is lactate; its effect on glioblastoma has been described by McKelvey et al. They showed, that glucose and FAO metabolic pathways are similar among two glioblastoma cell culture subtypes, and enzymes of the glycolytic and FAO pathways are upregulated in GBM tumors compared to normal brain tissues. These cellular energetic pathways are closed down by the inhibitor of glycolysis - dichloroacetate, and the partial fatty acid oxidation inhibitor ranolazine (Rano). Based on the work, it became clear that dual targeting of glycolytic and FAO metabolic pathways (or/and adjuvant to standard chemoradiation) provides new avenues in treatment principles of cancer.

The importance of lactate in tumors is also evident in the following work Longhitano et al. described the role of monocarboxylate transporter-1 and hydroxycarboxylic acid receptor 1 role of tumor growth and progression in glioblastoma *in vitro* and *in vivo* models of zebrafish. They showed that lactate increased MCT1 and HCAR1 expression; lactate modulated epithelial-mesenchymal transition protein markers E-Cadherin and β-Catenin and therefore proliferation, migration, and colony formation ability.

Harland and her colleagues described the metabolic models of characteristics of glioma stem-like cells. They showed three possible models: 1) the cancer stem cell hierarchical model; 2) rthe stochastic/clonal evolution model and 3) the plasticity model which looks to be a more veracious description of the development and behavior of these cells. This article is a very comprehensive review of almost all metabolic aspects of glioblastoma interaction between metabolism and GSCs which may create an opportunity for future strategies for overcoming GSC resistance.

Metabolic aspects of the lung cancer

Another example of tumors with a very poor prognosis is lung cancer. Daks et al. showed, that the knockdown of Set7/9 methyltransferase (lysine-specific methyltransferase) in human NSCLC cell models upregulates several important glycolytic enzymes like hexokinase, aldolase, and lactate dehydrogenase together with their key activators—oncogenes c-Myc and HIF1A - at both transcriptional and protein levels. Both activators are well-known coordinators of glycolysis, oxygen consumption, one-carbon metabolism, and the metabolism of glutamine and lipids upon tumorigenesis. Set7/9 methylates the p53 protein, which leads to p53 stabilization *via* inactivation of SIRT1 by its methylation.

Another article by Evers et al. sheds light on metabolic changes in lung cancer describes the epithelial-mesenchymal transition in relationship with extracellular ATP (eATP) and TGF-beta. eATP induced several EMT-related changes in metabolic pathways including the rearrangement of the cytoskeletal architecture, glycolysis, glutaminolysis, ROS, and individual metabolic changes similar to those induced by TGF-β. The extracellular ATP-induced gene expression is not identical to the TGF-β-initiated expression, but they are similar. The same phenomenon is shown also in downregulated genes, primarily epithelial genes. As the cancer cells can use either TGF-β or eATP or both, this may be the reason for metabolic flexibility. This paper is a new and interesting direction to open novel targets to inhibit EMT in cancer.

Advances in other tumors

Colorectal cancer (CRC) is one of the three most common cancers worldwide; it is the fourth reason for cancer deaths on average and the most frequent cause for non-smokers. The ideal screening biomarkers would be detectable by a non-invasive technique that allows rapid determination of specific metabolites in blood or urine. Mika et al. described rearrangements of blood and tissue fatty acid profiles in this cancer. Their study confirms significant changes in the fatty acid profiles in serum and tumor tissue of CRC patients, the clearest change in patients with CRC

is the presence of very long chain fatty acids, which increased 5-10 times. The study about fatty acid profiles is providing a new diagnostic approach for use in the clinic.

One serious challenge for oncologists is the high-grade metastatic chondrosarcomas which are very often not amenable to surgery and are resistant to chemotherapy and radiation therapy. Micaily et al. with her colleagues described profoundly metabolic pathways and targets in chondrosarcoma like the relationship between signaling *via* isocitrate dehydrogenase 1 and 2, hedgehog, PI3K-mTOR-AKT, and SRC, as well as histone acetylation and angiogenesis. As a result of their research, they summarized potential metabolic and therapeutic targets in chondrosarcoma.

Pita-Grisanti et al. described the potential and risk of bacterial siderophores in cancer. Siderophores are iron-chelating small molecules (MW ~ 500–1500 Daltons) essential to mammalian iron homeostasis. Siderophores is a previously almost unexplored field of cancer studies. Cancer cells need increased iron concentration for proliferation. During exogenous siderophore treatment, siderophores bind iron and decrease the levels of free iron available for bacteria. These molecules can interact with the immune system, are linked to pathogen virulence, are signaling molecules, can bind other metals, could be iron chelating anticancer agents, and mediators of drug delivery. However, this topic needs a lot of further research.

We can only hope that the rapid progress in tumor research will continue and that interesting times with fascinating results are ahead.

Author contributions

The author confirms being the sole contributor of this work and has approved it for publication.

Conflict of interest

The author declares that the research was conducted in the absence of any commercial or financial relationships that could be construed as a potential conflict of interest.

Publisher's note

All claims expressed in this article are solely those of the authors and do not necessarily represent those of their affiliated organizations, or those of the publisher, the editors and the reviewers. Any product that may be evaluated in this article, or claim that may be made by its manufacturer, is not guaranteed or endorsed by the publisher.

Glycolysis and Fatty Acid Oxidation Inhibition Improves Survival in Glioblastoma

Kelly J. McKelvey[1]*, Erica B. Wilson[2], Susan Short[2], Alan A. Melcher[3], Michael Biggs[4], Connie I. Diakos[1,5,6] and Viive M. Howell[1]

[1] Bill Walsh Translational Cancer Research Laboratory, Faculty of Medicine and Health, The University of Sydney, St Leonards, NSW, Australia, [2] Translational Neuro-Oncology, Leeds Institute of Medical Research at St James's, University of Leeds, Leeds, United Kingdom, [3] Translational Immunotherapy, Division of Radiotherapy and Imaging, Institute for Cancer Research, London, United Kingdom, [4] Department of Neurosurgery, North Shore Private Hospital, St Leonards, NSW, Australia, [5] Department of Medical Oncology, Northern Sydney Cancer Centre, Royal North Shore Hospital, St Leonards, NSW, Australia, [6] Northern Clinical School, Faculty of Medicine and Health, The University of Sydney, St Leonards, NSW, Australia

Glioblastoma (GBM) is the most aggressive adult glioma with a median survival of 14 months. While standard treatments (safe maximal resection, radiation, and temozolomide chemotherapy) have increased the median survival in favorable O(6)-methylguanine-DNA methyltransferase (MGMT)-methylated GBM ($\sim$21 months), a large proportion of patients experience a highly debilitating and rapidly fatal disease. This study examined GBM cellular energetic pathways and blockade using repurposed drugs: the glycolytic inhibitor, namely dicholoroacetate (DCA), and the partial fatty acid oxidation (FAO) inhibitor, namely ranolazine (Rano). Gene expression data show that GBM subtypes have similar glucose and FAO pathways, and GBM tumors have significant upregulation of enzymes in both pathways, compared to normal brain tissue ($p < 0.01$). DCA and the DCA/Rano combination showed reduced colony-forming activity of GBM and increased oxidative stress, DNA damage, autophagy, and apoptosis *in vitro*. In the orthotopic Gl261 and CT2A syngeneic murine models of GBM, DCA, Rano, and DCA/Rano increased median survival and induced focal tumor necrosis and hemorrhage. In conclusion, dual targeting of glycolytic and FAO metabolic pathways provides a viable treatment that warrants further investigation concurrently or as an adjuvant to standard chemoradiation for GBM.

Keywords: glioblastoma, cancer metabolism, ranolazine, dichloroacetate, radiation, temozolomide

INTRODUCTION

Glioblastoma (GBM) is a biologically heterogeneous and uniformly fatal disease. Verhaak et al. (1) describe classical, mesenchymal, neural, and proneural subtypes of GBM based on an 840 gene signature. These have been adopted as clinically relevant molecular subtypes with different disease progression and prognosis. While brain cancer makes up 1.3% of all new cancer diagnoses in Australia, it accounts for 3.2% of cancer-related deaths (2). GBM accounts for 54% of brain cancer cases and has a 5-year survival rate <5% (3). Despite the recognized heterogeneity in GBM epigenetics, genetics, and transcription (4); histological patterns (5); immune infiltration

(6); and metabolism (7), the current treatment for GBM remains maximal safe surgical resection, followed by external beam radiation therapy (RT) with concurrent and adjuvant temozolomide (TMZ) (8). This increases median overall survival from 14 months for TMZ-resistant O(6)-methylguanine-DNA methyltransferase (MGMT) promoter unmethylated GBMs to 21.2 months for TMZ-sensitive MGMT promoter methylated GBMs (9).

In addition to a uniform reliance of cancer cells on aerobic glycolysis, recent studies have demonstrated the dependence of GBM cells on fatty acid oxidation (FAO) (7). Human gliomas express the FAO enzymes medium-chain acyl-CoA dehydrogenase (MCAD), short-chain L-3-hydroxyacyl-CoA dehydrogenase (SCHAD), very-long-chain acyl-CoA dehydrogenase (VLCAD), hydroxyacyl-CoA dehydrogenase (HADH)/3-ketoacyl-CoA thiolase/enoyl-CoA hydratase (ECH), and carnitine palmitoyltransferase 1a (CPT1a) and demonstrate decreased oxygen consumption in the presence of an FAO inhibitor, etomoxir (10). Genomic, metabolomic, and functional analyses by Prabhu et al. (7) show that FAO is a key driver of progression from low-grade gliomas into GBM. In a syngeneic glioma model (oncogenic neural stem cells), etomoxir increased survival (10), whereas, the combination of etomoxir, glucose analog, and glycolytic inhibitor 2-deoxy-D-glucose (2-DG) led to metabolic lethality *in vitro* and increased median survival in MES93 mesenchymal GBM tumor-bearing mice (11). Ranolazine (Rano), a partial FAO inhibitor, has shown neuroprotective effects on healthy astrocytes and neurons in rodent cell cultures (12). Targeting FAO in GBM also shows promise in alleviating the immunosuppressive tumor microenvironment as FAO ameliorates the tolerogenic and immunosuppressive mechanisms of tumor myeloid-derived suppressor cells (MDSC) and reduces tumor growth in the syngeneic murine models of lung (3LL) and colon (MCA-38) cancer (13).

Glycolytic inhibitor dichloroacetate (DCA) induces apoptosis in GBM and putative GBM stem cells *in vitro* and *in vivo* (14) and has demonstrated clinical efficacy in a small cohort of patients with GBM (15). In addition, DCA sensitizes GBM to radiation (16) and has synergistic effects on GBM growth and survival induced by mitochondrial oxidative stress, when combined with mitochondrial inhibitor 4-[N-(S-penicillaminylacetyl)amino] phenylarsonous acid (17) and when inhibiting stem cell self-renewal in combination with metformin (18).

Glucose metabolism and reactive oxygen species (ROS) are bidirectionally linked, and cancer cells are metabolically adaptive to the changing oxygen and nutrient microenvironment (19). Therein, it was hypothesized that dual blockade of the glycolysis and FAO pathways would inhibit GBM tumor growth by increasing oxidative phosphorylation and enhancing chemoradiation-induced ROS. In the present study, we investigative the novel combination of the glycolytic inhibitor, DCA, and the partial FAO inhibitor, Rano, in two syngeneic immune-competent models of GBM, against "standard of care" chemoradiation.

MATERIALS AND METHODS

Human Gene Expression Data

Gene lists for human glucose (#RAH49R3) and FAO metabolism (#RPKA3DE) were obtained from Taqman® Arrays (https://www.thermofisher.com). Gene expression and GBM subtype data from 48 primary GBM cell lines were acquired from the human glioblastoma cell culture (HGCC) Affymetrix Human Exon 1.0 ST Array (NCBI Gene Omnibus GSE72217; https://www.ncbi.nlm.nih.gov/geo/) (20). Classical, mesenchymal, proneural, and neural GBM subtyping was performed by HGCC (20) using the gene signatures described by Verhaak et al. (1). Data were analyzed using Gene Cluster 3.0 for Windows, Department of Genetics, Stanford University, CA, USA (21) and TreeView 3.0 beta1 for Windows, Department of Genetics, Stanford University, CA, USA (22) with the Pearson's correlation proximity-based hierarchical clustering. The Cancer Genome Atlas (TCGA; https://www.cancer.gov/tcga) GBM, TCGA normal, and the Genotype-Tissue Expression (GTEx; https://www.gtexportal.org/home/) data box plots were acquired through the Gene Expression Profiling Interactive Analysis (23) (GEPIA; available at http://gepia.cancer-pku.cn/). Data are expressed as the $\log_2$ fold change (FC) [defined as median (tumor) – median (normal)].

Cells

Murine glioma Gl261 cells were donated by Géza Safrany (Frederic Joliot-Curie National Research Institute for Radiology and Radiohygiene, Budapest, Hungary) and CT2A by Tomas Seyfried (Boston College, Boston, MA, USA). U-87 MG, U-251 MG, and T98G from the CellBank Australia, Westmead, NSW, Australia. Cell lines were authenticated by the Satellite Tandem Repeat profiling (Garvan Institute of Medical Research, Sydney, NSW, Australia) and mycoplasma negative by the MycoProbe® Mycoplasma Detection Kit (R&D Systems, Inc., Minneapolis, MN, USA). Cells were cultured in Dulbecco's modified Eagle's medium (DMEM) containing 10% v/v fetal bovine serum (FBS) in a humidified incubator with 5% CO_2 at 37°C with 60% relative humidity.

Treatments

Drugs used in this study were DCA (sodium DCA #347795; Sigma-Aldrich, St. Louis, MO, USA), TMZ (#T2577; Sigma-Aldrich St. Louis, MO, USA), and Rano (Rano dihydrochloride #R6152; Sigma-Aldrich St. Louis, MO, USA) dissolved in complete media for *in vitro* studies and in sterile water for *in vivo* studies at stock concentrations of 40, 5, and 10 mg/ml, respectively. X-ray radiation was delivered using the Small Animal Radiation Research Platform (SARRP; Xstrahl Inc., Suwanee, GA, USA) at a dose rate of 2.97 Gy/min as described earlier (24). In all experiments, the drug treatment preceded irradiation by 1 h to enable the drugs to act on their respective cellular targets. The cells were detached with 0.5% v/v and trypsin/0.2% v/v ethylenediaminetetraacetic acid in phosphate-buffered saline (PBS) and counted by MUSE® cell count and viability assay (Luminex Corp., Austin, TX, USA) according to the instructions of the manufacturer.

FIGURE 1 | Human gene expression of glucose and fatty acid oxidation (FAO) pathways. **(A)** Heat map and hierarchical clustering of genes associated with the glucose and FAO metabolic pathways. **(B)** Human glioblastoma cell culture (HGCC) glioblastoma (GBM) subtype gene expression of selected targetable enzymes involved in glycolytic and β-oxidation pathways. **(C)** The Cancer Genome Atlas (TCGA) GBM vs. normal gene expression. Data are expressed as median ± interquartile range of log₂ fold change [median (tumor) − median (normal)]. *$p < 0.01$ by the Kruskal–Wallis test with the Dunn's multiple comparison test.

FIGURE 2 | Sensitivity and survival of murine glioma cell lines to drug and radiation therapy (RT) treatment combinations. **(A)** Drug IC50s for temozolomide (TMZ), dicholoroacetate (DCA), and ranolazine (Rano) were determined from confluency at 72 h and for RT by clonogenic assay at 10 days post-treatment using a four-parameter logistic model. Symbols show mean survival (%) ± SEM for six replicates per experiment (N = 3). **(B)** Heat maps of the cell survival for TMZ/RT and DCA/Rano combinations. Black boxes represent the best synergy combination indices as calculated using the CompuSyn Software (Paramus, NJ, USA).
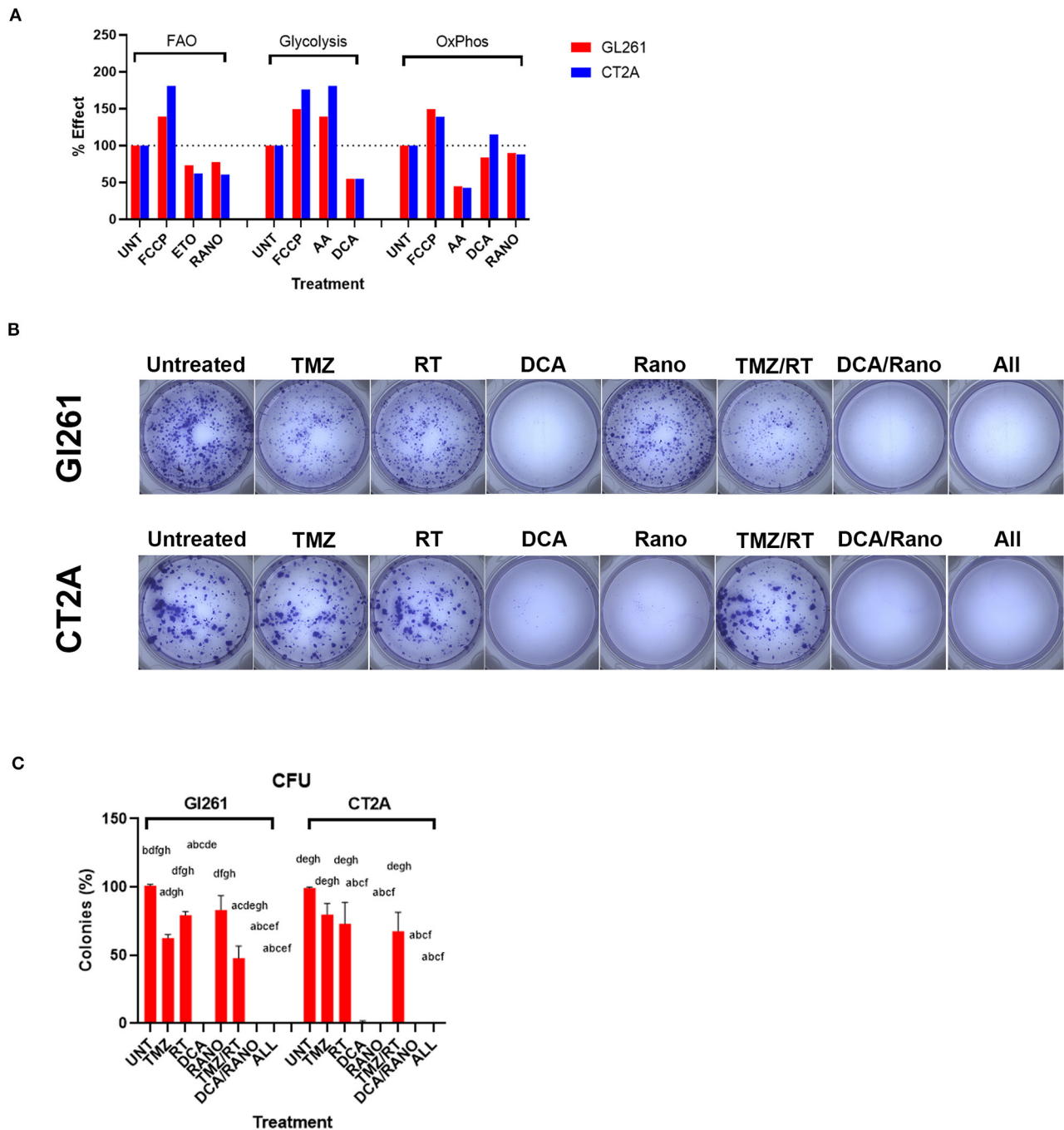
FIGURE 3 | Temozolomide (TMZ), RT, DCA, and their combination reduce GBM cell proliferation. **(A)** Percentage effect of dual-read time-resolved fluorescent lifetime at 60-min post-treatment relative to untreated control (Unt) for fatty acid oxidation (FAO) and glycolytic and oxidative phosphorylation (OxPhos) metabolism. Carbonyl cyanide-4-(trifluoromethoxy)phenylhydrazone (FCCP; 2.5 μm), etomoxir (Eto; 40 μm), and antimycin A (AA; 1 μm) were used as positive and negative controls where appropriate. Data are expressed as mean of triplicates. **(B)** Micrographs of colonies (>50 cells) 10-day post-treatment. **(C)** Column graphs show mean ± SEM of triplicates from three independent experiments. Column graphs show the mean ± SEM from three independent experiments [a]$p < 0.05$ vs. Unt; [b]$p < 0.05$ vs. TMZ; [c]$p < 0.05$ vs. RT; [d]$p < 0.05$ vs. DCA; [e]$p < 0.05$ vs. ranolazine (Rano); [f]$p < 0.05$ vs. TMZ/RT; [g]$p < 0.05$ vs. DCA/Rano; and [h]$p < 0.05$ vs. All-combined treatments were determined by Kruskal–Wallis test alongwith the Dunn's multiple comparison test.
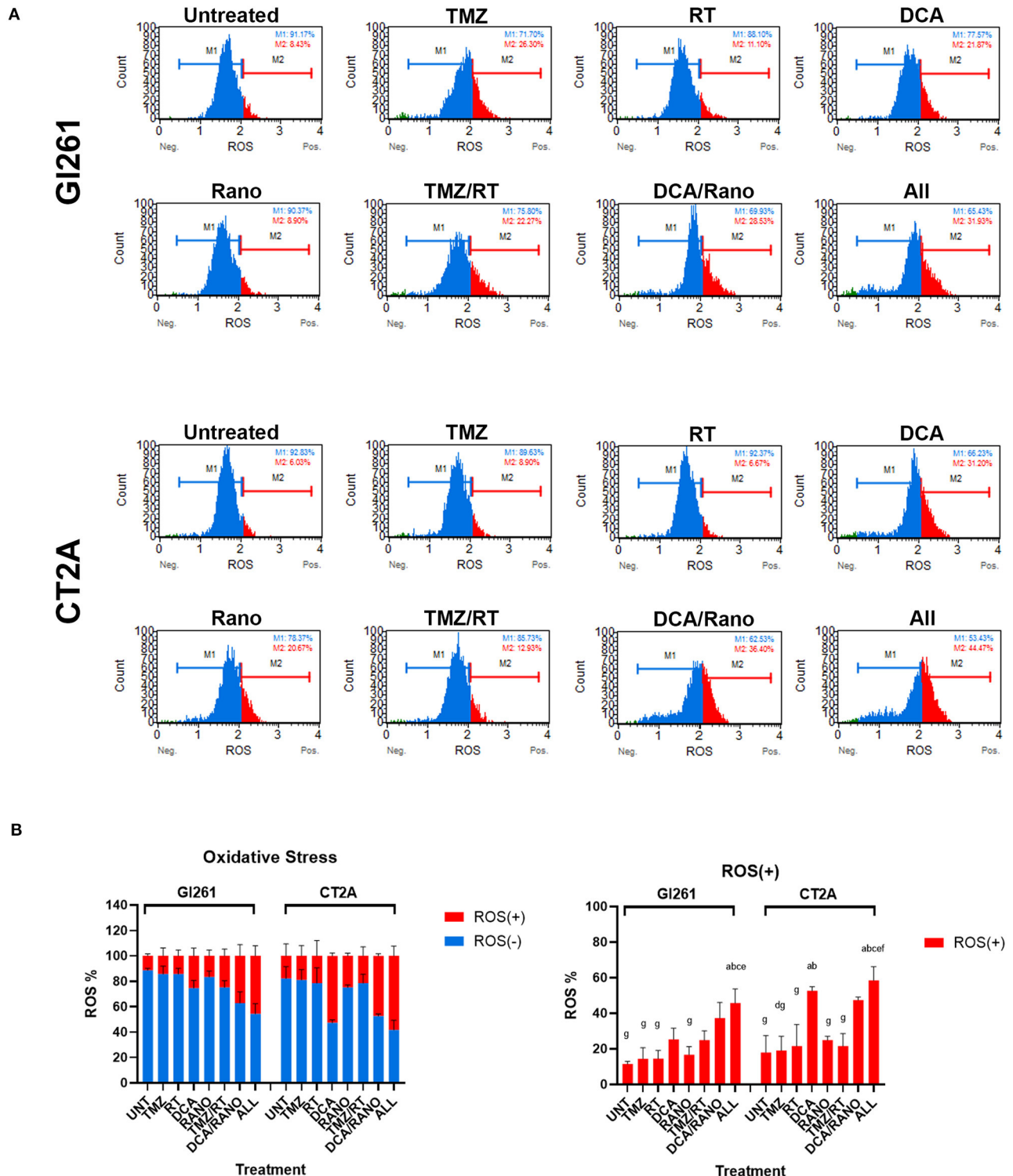
FIGURE 4 | DCA/ranolazine (Rano) increases reactive oxygen species (ROS) levels in murine GBM cells. **(A)** Representative Luminex® histograms (Luminex Corp., Austin, TX, USA) show the ROS fluorescent intensity as ROS⁻ (M1; blue) and ROS⁺ (M2; red) in GI261 and CT2A GBM lines. **(B)** Column graphs showing the mean ± SEM from three independent experiments as in **(A)**. [a]$p < 0.05$ vs. Unt; [b]$p < 0.05$ vs. temozolomide (TMZ); [c]$p < 0.05$ vs. radiation therapy (RT); [d]$p < 0.05$ vs. DCA; [e]$p < 0.05$ vs. Rano; [f]$p < 0.05$ vs. TMZ/RT; and [g]$p < 0.05$ vs. All-combined treatments were determined by the two-way ANOVA test along with the Tukey's multiple comparison test.
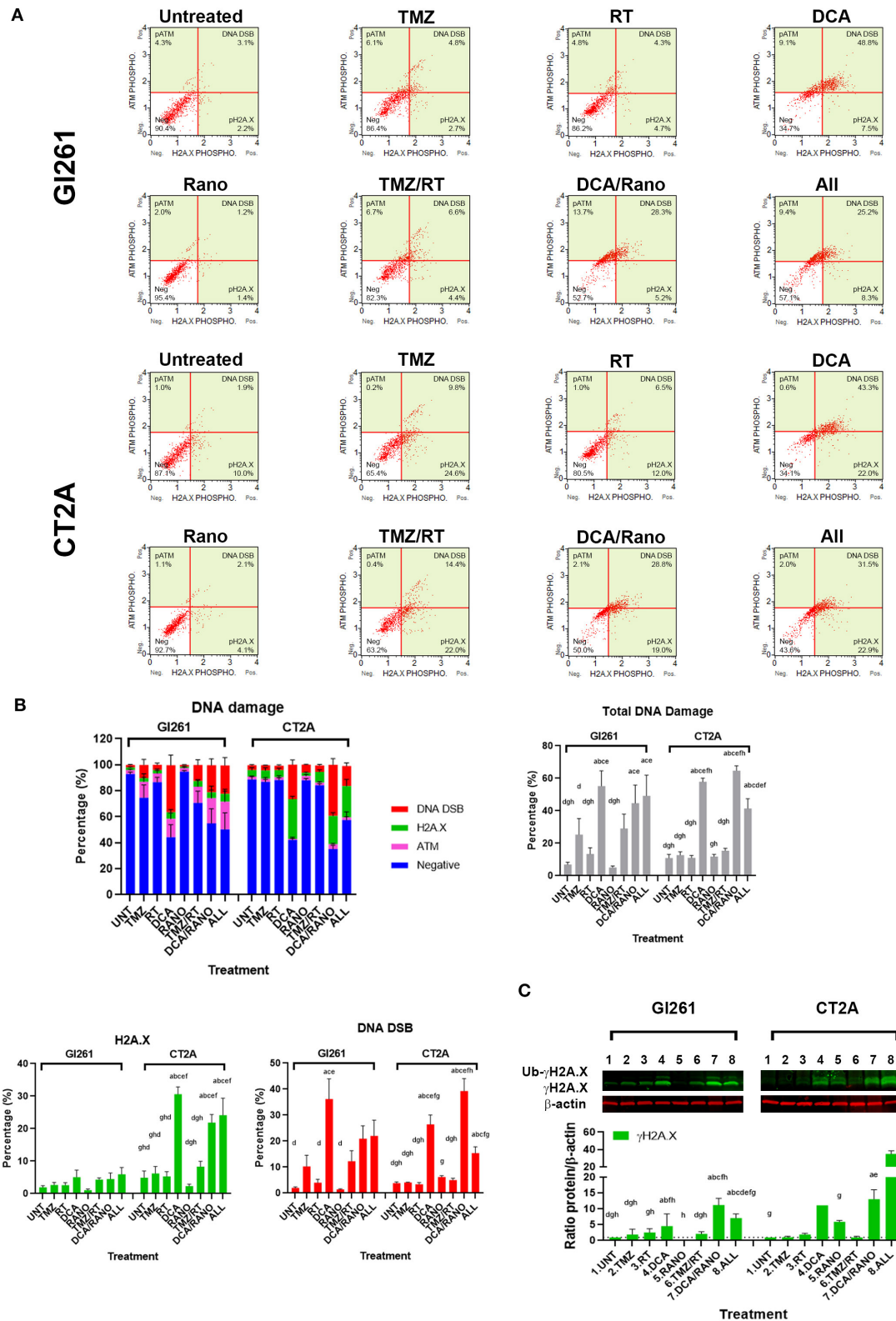
FIGURE 5 | TMZ and DCA increase DNA damage in GBM cell lines. **(A)** Representative Luminex® dot plots (Luminex Corp., Austin, TX, USA) depict increased phosphoryated ataxia telangiectasia mutated (ATM) (upper left), phosphoryated H2A.X (lower right), or both (DSB; upper right). **(B)** Column graphs show mean ± SEM from three independent experiments as in **(A)**. [a]$p < 0.05$ vs. Unt; [b]$p < 0.05$ vs. TMZ; [c]$p < 0.05$ vs. RT; [d]$p < 0.05$ vs. DCA; [e]$p < 0.05$ vs. Rano; [f]$p < 0.05$ vs.

(Continued)

Cell Survival

Cells were plated at 8,000 cells per well in a 96-well plate with 100 μl of medium per well, which were left overnight to equilibrate, and assessed for confluency (%) after 72 h following the drug treatments. Five images per 96 wells (×10 objective) were acquired using the IncuCyte® Live Imaging System (IncuCyte® Software (v2019B), Sartorius, Gottingen, Germany) and analyzed using the imaging analysis software. Six wells were used per treatment per experimental replicate.

Energy Metabolism Assays

Cells were plated at 40,000 cells per well in a 96-well plate with 200 μl of medium per well and left overnight to equilibrate. The Glycolysis (extracellular acidification; ab197244; Abcam, Cambridge, UK), FAO Complete (ab222944; Abcam, Cambridge, UK), and Extracellular Oxygen Consumption (ab197243; Abcam, Cambridge, UK) assays were performed as per the instructions of the manufacturer and detected using the dual-read time-resolved fluorescence (FLUOstar Omega; BMG LABTECH, Ortenberg, Germany). For FAO metabolism, cells were glucose deprived overnight. Carbonyl cyanide 4-(trifluoromethoxy) phenylhydrazone (FCCP; 2.5 μm), etomoxir (40 μm), and antimycin A (1 μm) were used as positive and negative controls where appropriate. Data are expressed as percentage effect of Lifetime (μs; **Equation (1)**) for the treatment relative to the untreated control.

$$Lifetime\ (\mu s)\ [T] = (D2 - D1) / \ln\left(\frac{W1}{W2}\right) \quad (1)$$

where, W1 and W2 are the times for the dual measurement windows and D1 and D2 are the delay times prior to W1 and W2, respectively.

Clonogenic/Colony Forming Unit Assay

Cells were seeded at 1,500 cells per well in 6-well plates with 2 ml of DMEM/10% v/v FBS. After 10 days, colonies were stained with crystal violet (0.5% w/v, 1:1 methanol:distilled water) and then imaged and quantitated using a vSpot® Spectrum ELISpot/FluoroSpot Reader System (Autoimmun Diagnostika Gmbh, Straßberg, Germany). Three wells were used per treatment per experimental replicate.

Functional Assays

Cells were plated at 500,000 cells per T25 flask, equilibrated overnight, and then treated for 72 h. The Luminex® Oxidative Stress (ROS; Luminex Corp., Austin, TX, USA), DNA Damage [ataxia telangiectasia mutated (ATM)/histone 2A family member × (H2A.X)], Cell Cycle, Annexin-V, and Dead Cell, and Autophagy LC3 assays were carried out according to the instructions of the manufacturer. Cell events (1,000–5,000 assay dependent) were acquired and analyzed using the Guava® Muse® Cell Analyser (Luminex Corp., Austin, TX, USA).

Western Blot

About 50 μg protein was loaded on Any kDa™ Mini-PROTEAN® TGX™ Precast protein gels and transferred to low-autofluorescence polyvinylidene fluoride (PVDF) membranes (Bio-Rad, Hercules, CA, USA). For autophagy Western blots, cells were treated with a 100 nM Bafilomycin A1 (B1793; Sigma-Aldrich St. Louis, MO, USA) 4 h before collection to accumulate LC3B in the cytoplasm. Primary antibodies were γH2A.X (1:1,000; ab11174; Abcam, Cambridge, UK), cyclin-dependent kinase 2 (Cdc2) (1:1,000; 28439S; Cell Signaling Technology, Danvers, MA, USA), cyclin B1 (1:1,000; 4138S; Cell Signaling Technology, Danvers, MA, USA), p21 (1:1,000; ab188224; Abcam, Cambridge, UK), Bax (1:1,000; ab3191; Abcam, Cambridge, UK), Bcl-2 (1:1,000; ab16904; Abcam, Cambridge, UK), caspase 3 (1:1,000; ab188224; Abcam, Cambridge, UK), SQSTM1/p62 (1:1,000; ab56416; Abcam, Cambridge, UK), LC3B (1:1,000; PM036; MBL International Corp., Woburn, MA, USA), and β-actin (1:10,000; A1978; Sigma-Aldrich St. Louis, MO, USA). Immunoblots were detected with 1:10,000 goat-anti-mouse DyLight™ 680 conjugated or donkey-anti-rabbit DyLight™ 800 conjugated using an Odyssey CLx Near-Infrared Fluorescence Imaging System (LI-COR Biosciences, Lincoln, NE, USA).

In vivo Glioma Models

The murine survival study was reviewed, approved, and performed in accordance with the guidelines of the Northern Sydney Local Health District Animal Ethics Committee, Royal North Shore Hospital, St Leonards, NSW, Australia (Approval #RESP/17/205), which enforces the New South Wales Animal Research Act 1985.

Eight-week-old male C57Bl/6 mice (20–26 g) were provided by the Kearn's Animal Facility, Australia. Mice were housed in Allentown individually ventilated cages (3–5 per cage) with cellulose bedding under specific pathogen-free conditions. Enrichment was provided in the form of autoclaved ice block sticks or straws. Rooms were temperature-controlled (22°C) and were kept on a 12-h light/dark cycle (7:00/19:00 h) with a standard chow and water *ad libitum*.

Mice were inoculated with $1 \times 10^5/2$ μl murine glioma Gl261 or CT2A cells using a stereotactic frame, a microinjection unit (David Kopf Instruments, Tujunga, CA, USA), and a 5 μl syringe with custom 32-G needle (Hamilton Company, Reno, NV, USA) into the right caudoputamen (striatum) at 2 mm in mediolateral, 0.1 mm in anteroposterior, 2.6 mm in dorsoventral bregma under isoflurane anesthesia (2% v/v per 1 L oxygen i.h.) as described earlier (6). Mice were randomly assigned into one of the eight treatment groups (six mice per group). Treatments were administered five times a week for 2 weeks commencing at day 7 postinoculation: TMZ (50 mg/kg/day i.p.), DCA (200 mg/kg/day i.p.), and Rano (50 mg/kg/day i.p.). External beam irradiation of
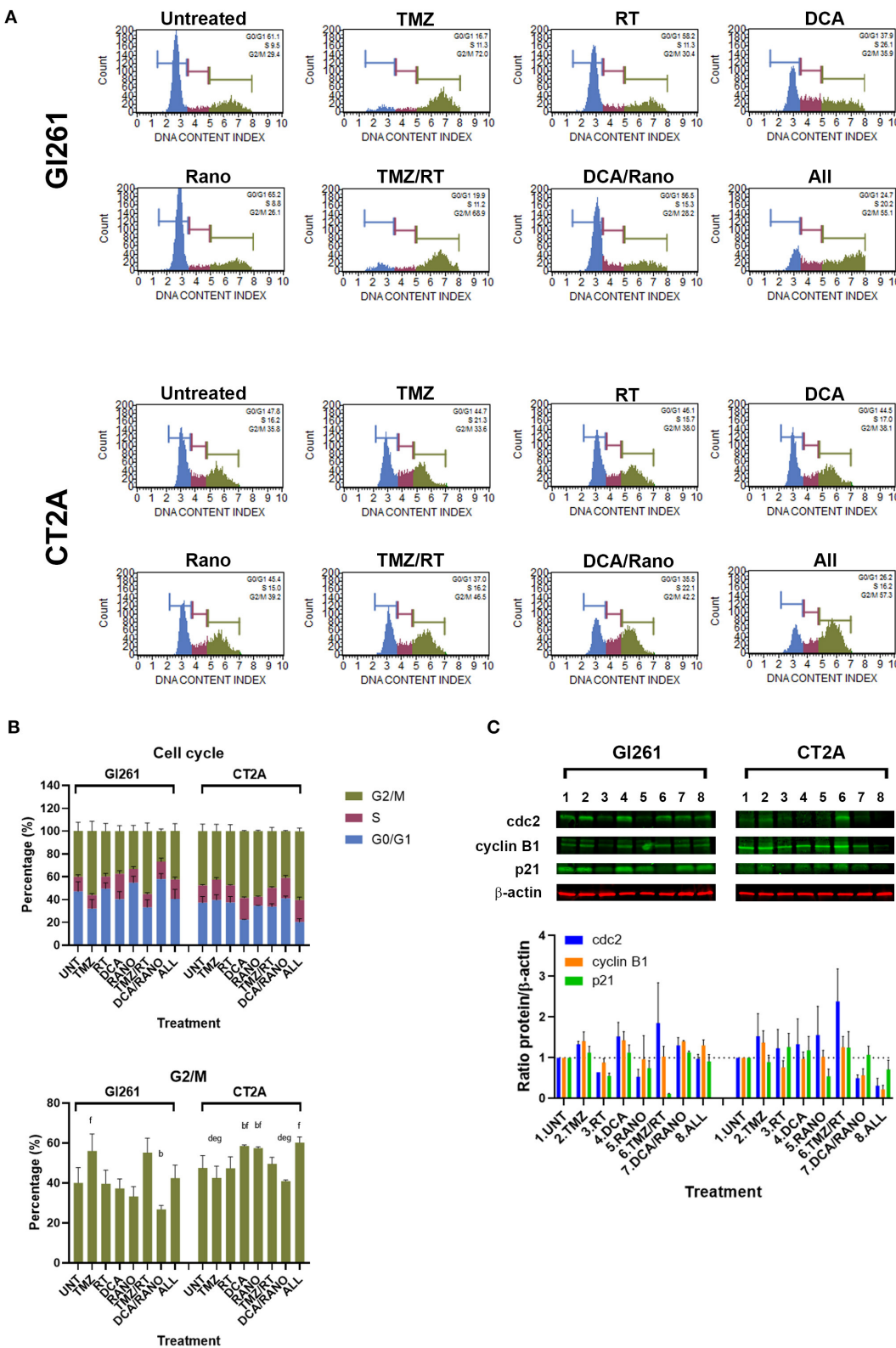
FIGURE 6 | TMZ alone or combined with RT arrests GI261 cells in the G2/M phase. **(A)** Representative Luminex® cell cycle histograms (Luminex Corp., Austin, TX, USA) show fluorescent intensity as the G0/G1 phase in blue, the S phase in purple, and the G2/M phase in green. **(B)** Column graphs show mean ± SEM from three independent experiments as in **(A)**. [a]$p < 0.05$ vs. Unt; [b]$p < 0.05$ vs. TMZ; [c]$p < 0.05$ vs. RT; [d]$p < 0.05$ vs. DCA; [e]$p < 0.05$ vs. Rano; [f]$p < 0.05$ vs. DCA/Rano;

(Continued)

20 Gy/10 (i.e., 2 Gy per dose; RT) was performed using the Image-Guided SARRP (Xstrahl Inc., Suwanee, GA, USA) using a 5 × 5 mm collimator and 60° (30° to –30°) Arc beam at a dose rate of 3.71 Gy/min (24). For combination treatment groups, radiation was delivered 1-h post-drug administration.

Animal weight and well-being were assessed two times every week and euthanized by cardiac puncture under isoflurane anesthesia (2% v/v per 1 L oxygen i.h.) followed by cervical dislocation at the humane endpoint or a long-term survival (100 days postinoculation). No adverse events were encountered.

Histopathological Analyses

Four-micron sections of paraffin-embedded tissues were stained with Mayer's H&E Y/erythrosine B staining, Ki67 (0.084 µg/ml; 12202S; Cell Signaling Technologies, Danvers, MA, USA), and γH2A.X (0.06 µg/ml; ab11174; Abcam, Cambridge, UK) as described earlier (6, 24) and terminal deoxynucleotidyl transferase dUTP nick end labeling (TUNEL) apoptosis by immunohistochemical staining [ab206386; Abcam, Cambridge, UK) with Mayer's hematoxylin nuclear stain. Slides were imaged using an Aperio XT slide scanner and captured using Aperio ImageScope (Leica Biosystems, Wetzlar, Germany), and five high-power images were assessed per sample ($N = 4$–6 brains per treatment group] using ImmunoRatio (Seinajoki, Finland) as described earlier (24).

Statistical Analyses

Drug IC50 concentrations were calculated using a four-parameter response vs. drug concentration non-linear regression, and synergistic doses were calculated using the CompuSyn Software (Paramus, NJ, USA) (25, 26). To determine the statistical difference between treatments, the two-way ANOVA test along with the Tukey's multiple comparison test were performed for Annexin-V, DNA Damage, Oxidative Stress, and Cell Cycle MUSE® assays (Luminex Corp., Austin, TX, USA); and the one-way ANOVA test was performed with the Dunn's multiple comparison test for Autophagy LC3, Western blot fluorescent intensity, and CFU assays. Murine survival studies are expressed as Kaplan–Meier curves. All statistics were performed using the Prism version 8 for Windows (GraphPad Software Inc., San Diego, CA, USA), considering a significant p-value <0.05.

RESULTS

Glucose and FAO Metabolism in GBM

Using the publicly available HGCC gene expression dataset, we investigated the glucose and FAO metabolic pathways in 48 GBM primary cell lines. Hierarchical clustering demonstrated that glucose and FAO metabolic pathways did not differ between the classical, mesenchymal, and proneural/neural GBM subtypes, offering a potentially wide-ranging therapeutic avenue (**Figure 1A**), compared to therapies targeting specific

genetic mutations (e.g., EGFR and IDH1). This contrasts a recent report of 498 GBM IDH wildtype tumours which demonstrated increased glycolytic activity in the mesenchymal subtype (27).

Further examination showed that the expression of selected targetable enzymes in the glycolytic pathway, pyruvate dehydrogenase kinase (PDK) 1–4, and the FAO pathways, acetyl CoA dehydrogenase (ACAD), thiolase [acetyl-coenzyme A acetyltransferase (ACAT)], cronotase (ECH), and HADH, were similarly expressed across the GBM subtypes, except ECH was significantly higher in proneural/neural compared to classical tumors ($p = 0.0022$; **Figure 1B**). To confirm the role of PDKs and FAO enzymes in GBM, we compared the gene expression using the TCGA GBM and normal brain. The expression of PDK1, PDK3, ECH, and HADH were ~1.5-fold higher in the GBM tumors compared to the normal tissue (all $p < 0.01$; **Figure 1C**). These data confirm that targetable metabolic pathways exist within GBM.

From these results, we sought to investigate whether the combination of PDK inhibitor, DCA, and FAO enzyme inhibitor, Rano, can inhibit GBM cellular metabolism and cell growth and can increase survival in the syngeneic Gl261 and CT2A models of GBM.

Gl261 and CT2A Demonstrate Different Sensitivities to Treatment

To determine the IC50 for drug and RT treatment, murine GBM cell lines were treated with a 2-fold increase in drug concentrations, and cell survival was assessed as either % confluency at 72 h for drug treatment or colony-forming units (CFUs) at 10 days for RT.

Gl261 was more TMZ-sensitive compared to CT2A (IC50; 2,526 vs. >10,000 µM) but less sensitive to DCA (25.9 vs. 16.0 mM), Rano (766.2 vs. 423.9 µM), and RT (4.0 vs. 2.2 Gy; **Figure 2A**). Comparative IC50 for human immortalized GBM cell lines U87-MG, U251-MG, and T98G is provided in **Supplementary Figure 1**. Synergistic drug concentrations for TMZ/RT and DCA/Rano were determined using the CompuSyn Software (Paramus, NJ, USA) (25, 26). Combination indices <1 indicate synergy, where 0 is additive and >1 antagonistic. The combination indices indicated that the synergistic doses for Gl261 were 39 µM TMZ/2 Gy RT and 37.5 mM DCA/156 µM Rano and for CT2A were 19.5 µM TMZ/1 Gy RT and 37.5 mM DCA/39.06 µM Rano (**Figure 2B**).

DCA and Rano Energy Metabolism Assays Confirm Inhibition at Syngeneic Doses

To confirm that DCA and Rano synergistic drug doses were sufficient to (partially) inhibit glycolytic and FAO metabolism, respectively, we performed dual-read time-resolved fluorescent assays. These assays measure the rate of fluorescent decay by

FIGURE 7 | TMZ/RT and DCA/Rano induce autophagy in GBM cell lines. **(A)** Representative Luminex® histograms (Luminex Corp., Austin, TX, USA) of LC3 fluorescent intensity in Unt (blue) and treatment (red). **(B)** Column graphs show mean ± SEM from four independent experiments as in **(A)**. [a]$p < 0.05$ vs. Unt; [b]$p < 0.05$ vs. TMZ; [c]$p < 0.05$ vs. DCA; [d]$p < 0.05$ vs. Rano; [e]$p < 0.05$ vs. TMZ/RT; and [f]$p < 0.05$ vs. All-combined treatments were determined by the Kruskal–Wallis test

(Continued)

FIGURE 7 | along with the Dunn's multiple comparison test. **(C)** Western blot immunoblot (top) and densitometric analysis (bottom) of the expression of p62, LC3-II, and β-actin in GBM cell lines following treatment as indicated ($N = 5$). The protein expression was normalized to reference protein β-actin expression.

providing a more stable and greater dynamic range than the traditional signal intensity measurements. Fluorescence lifetime was calculated as described in "Energy Metabolism Assays" section, and data were expressed relative to untreated controls (Unt). Each drug decreased its respective metabolic pathway by 23–45% at 60 min post-treatment (**Figure 3A**).

To assess the delayed impact on cell growth/survival, CFU assays were performed (**Figure 3B**). Using the synergistic doses identified in **Figure 2B**, DCA, Rano, and their combination significantly reduced colony formation compared to Unt (all $p < 0.0001$; **Figure 3C**), indicating no escape from the treatment control or emergence of resistance. In contrast, TMZ and RT alone and in combination with reduced CFU ~50% showed incomplete lethality. This suggests that DCA/Rano metabolic targeting is a viable strategy that did not induce a resistant population. We next sought to investigate potential chemo-radio-enhancement in oxidative stress, DNA damage, cell cycle, autophagy, and apoptotic mechanisms.

DCA/Rano Increases ROS Levels in Murine GBM Cells

The ability of RT to induce DNA damage is dependent on the generation of ROS (*via* radiolysis of water in cells). Inhibition of glycolysis and FAO by DCA and Rano, respectively, should increase the dependency of GBM cells on oxygen, thus increasing the ROS levels. In both cell lines, DCA and DCA/Rano induced an increase in ROS levels at 72-h post-treatment (**Figure 4A**). However, this was not significantly greater than TMZ/RT (**Figure 4B**). While all-combined treatments induced ROS generation, DCA was the primary single-treatment contributor, indicating that it may lead to increased DNA damage.

DCA and TMZ Increase DNA Damage in Murine GBM Cells

To determine whether the increased ROS levels led to increased DNA damage, phosphorylation of ATM (pATM) and H2A.X (pH2A.X) were assessed as early indicators of DNA double-strand breaks (DSB; **Figure 5A**). In both cell lines, DCA alone and DCA/Rano significantly increased total DNA damage to ~6-fold compared to Unt ($p = 0.0059$) and above that for TMZ/RT (CT2A; $p < 0.0001$). In Gl261, this was reflected in increased H2A.X phosphorylation and ATM activation (DNA DSB) at 72 h, whereas CT2A cells showed predominantly increased H2A.X phosphorylation (**Figure 5B**). Western blot of γH2A.X protein expression confirmed upregulation at 72-h post-treatment (**Figure 5C**).

DCA and Rano Do Not Significantly Alter Cell Cycle Progression

The cell cycle contains several checkpoints to prevent the proliferation of cells with DNA damage. To determine the effect of DCA and Rano on cell cycle, the percentage of

cells in non/early-dividing (G0/G1), synthesis (S), and late-dividing/mitosis (G2/M) were assessed (**Figure 6A**). Treatment of Gl261 with TMZ or TMZ/RT led to an increase of 40% of cells in the G2/M phase, whereas the same treatment in CT2A had no effect (**Figures 6A,B**). This is consistent with an observed reduction in the size of individual TMZ and RT-treated colonies for Gl261 but not CT2A colonies in **Figure 3B**. TMZ/RT also showed a trend toward upregulated Cdc2, which is necessary for S/G2 and G2/M transition, but not cyclin B1 or p21 (**Figure 6C**). However, in both cell lines, the DCA/Rano reduced G2/M arrest, with a trend toward greater S-phase arrest, but did not reach significance.

DCA and DCA/Rano Induce Autophagy in GBM Cells Lines

DNA damage-induced autophagy can delay apoptotic cell death by mediating the degradation of specific cell cycle proteins, regulation of cell division, and promotion of DNA damage repair. To determine whether DCA and Rano induce autophagy, the expression of markers of the autophagosomal membrane, microtubule-associated protein light chain 3-II (LC3), was assessed by Luminex® assay (Luminex Corp., Austin, TX, USA), and Western blotting. In Gl261 cells, DCA/Rano, and all-combined treatments induced the expression of LC3 (**Figure 7A**) and 2.5-fold greater that LC3 induction of autophagy compared to Unt ($p < 0.0001$) (**Figure 7B**). This was accompanied by a decrease in the autophagy substrate p62 at 72-h post-treatment (**Figure 7C**), though it did not reach significance. Similarly, in CT2A cells, DCA, DCA/Rano, and all-combined treatments showed a trend toward a 2-fold increase in LC3-autophagic induction ($p = 0.0211$; **Figure 7B**). In CT2A cells, DCA, and DCA/Rano showed increased p62 levels (**Figure 7C**). Although p62 is recognized for its role in autophagic flux, it also has roles in the anti-oxidative stress response, nutrient sensing, and apoptosis (28), consistent with the increased ROS (**Figure 4B**) and the Bax:Bcl-2 ratio (**Figure 8C**) noted in CT2A cells. These results suggest that DCA induces autophagy in GBM cells but may be more effective when combined with Rano in Gl261 cells, as observed in the Gl261 DCA/Rano and all-combined groups.

DCA Alone or Combined Increases Apoptosis in GBM Cell Lines

If GBM cells fail to overcome the increased ROS, DNA damage, cell cycle arrest, and autophagy, they will finally undergo apoptotic cell death. To assess the levels of apoptosis in Unt Gl261 and CT2A, the membrane-impermeable DNA dye 7-aminoactinomycin (7-AAD) and Annexin-V were assessed by Luminex® assay (Luminex Corp., Austin, TX, USA; **Figure 8A**). In DCA, DCA/Rano, and all-combined treatments, the total number of apoptotic cells increased 2- to 3-fold compared to Unt ($p = 0.0273$; **Figure 8B**). In both cell lines, the total apoptosis was
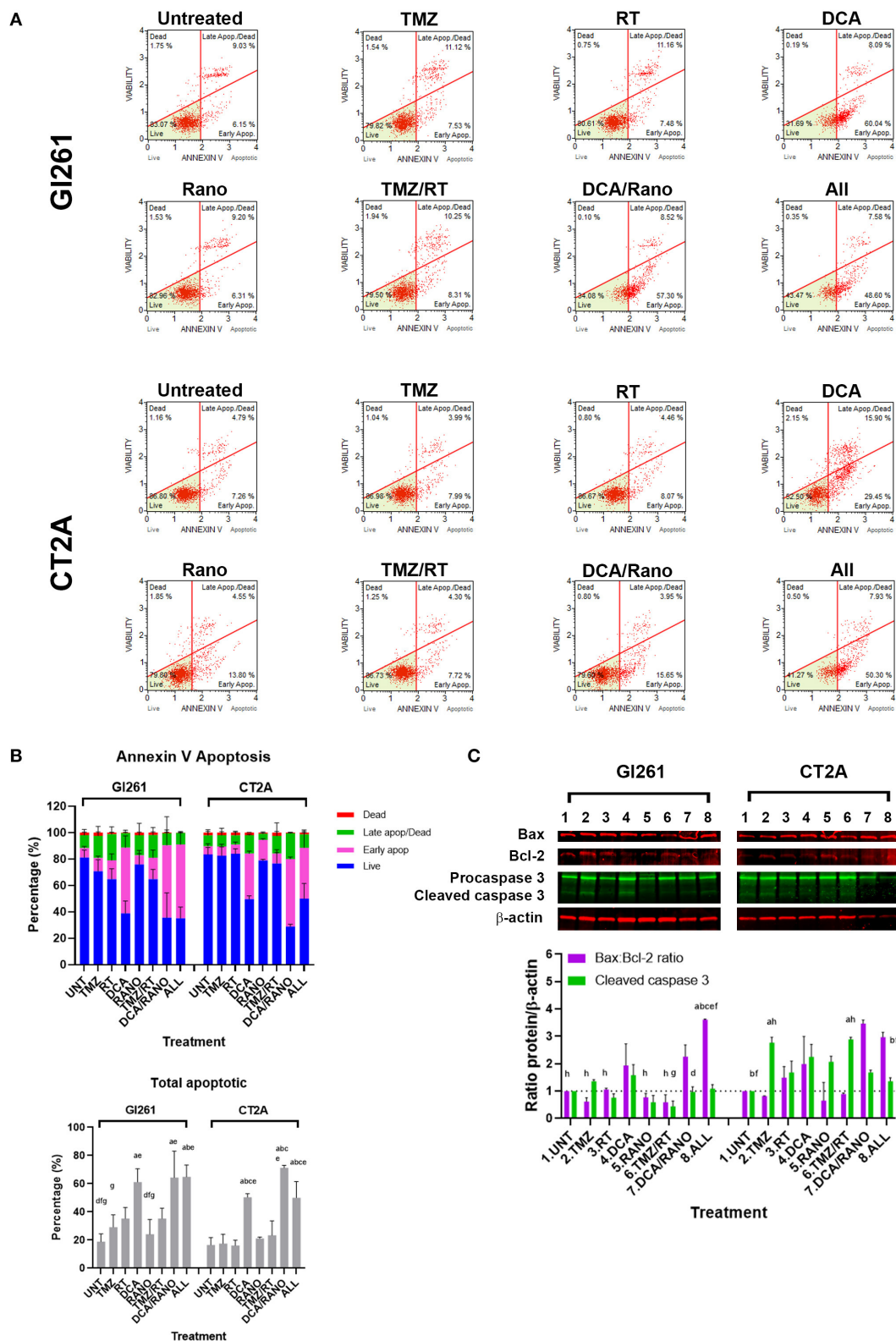
FIGURE 8 | DCA alone or in combination increases early apoptosis in GBM cell lines. **(A)** Representative Luminex® dot plots (Luminex Corp., Austin, TX, USA) show live (lower left) annexin V(AV−)/7AAD(−) cells, early apoptotic (lower right) AV(+)/7AAD(−) cells, late apoptotic (upper right) AV(+)/7AAD(+) cells, and dead cells (upper left) AV(−)/7AAD(+) cells. **(B)** Column graphs show mean ± SEM from three independent experiments as in **(A)**. [a]$p < 0.05$ vs. Unt; [b]$p < 0.05$ vs. TMZ;

(Continued)

mostly manifested in increased early apoptotic events [annexin-$V^+/7$-AAD^- (viability); **Figure 8B**]. Consistent with the CFU data (**Figure 3B**), TMZ/RT did not significantly induce apoptosis (**Figure 8B**). To assess the nature of the apoptotic signal, we determined the expression of early proapoptotic protein Bax and anti-apoptotic protein Bcl-2 and late apoptotic cleaved caspase 3 (**Figure 3C**) by immunoblotting. In both cell lines, the Bax:Bcl-2 ratio, and caspase 3 in CT2A were increased by DCA, DCA/Rano, and all-combined treatments (**Figure 8C**), suggesting that DCA induces the mitochondrial (intrinsic) apoptotic pathway in GBM cell lines. In CT2A cells, TMZ, and TMZ/RT increased caspase 3 in the absence of increased annexin V and Bax:Bcl-2 (**Figure 8C**). For explanation, see "Discussion" section.

DCA/Rano Increases *in vivo* Murine GBM Survival

Our *in vitro* data shows that DCA induces ROS generation, DNA damage, autophagy, and apoptosis, whereas, the effects of Rano were minimal. Some of the effects of Rano treatment have been shown to affect the immune and tumor microenvironment and the function of normal astrocytes and neurons (12, 13). To determine the clinical effect of Rano and combination treatments, we use two orthotopic syngeneic murine models (**Supplementary Figure 2**). Mice were injected intracranially with $1 \times 10^5/2$ µl Gl261 or CT2A cells on day 0 and TMZ (50 mg/kg/day i.p.), DCA (200 mg/kg/day i.p.), Rano (50 mg/kg/day i.p.), and/or RT (20 Gy/10) treatment were administered daily from day 7 to 18. For both Gl261 and CT2A tumor models, DCA, Rano, and DCA/Rano significantly increased survival; up to 20% in Gl261 tumor-bearing mice (median survival; 21 vs. 17.5 days; $p < 0.0001$) and 40% in CT2A tumor-bearing mice compared to Unt tumor-bearing controls (29.5 vs. 21 days; $p < 0.0001$; **Figure 9A**). No significant differences in toxicity (as assessed by weight of animals) between treatments were observed (data not shown). Consistent with our *in vitro* IC50 data (**Figure 2A**), the median survival for CT2A tumor-bearing mice demonstrated greater TMZ resistance and RT sensitivity than Gl261 tumor-bearing mice (**Figure 9A**). The TMZ/RT combination in both models was superior to DCA/Rano with 50% median survival, thus not reaching the 100-day period (indicating long-term survival).

The histopathological analysis of the tumor morphology revealed that DCA and DCA/Rano induced focal regions of necrosis and hemorrhage with increased Ki67 proliferation indices and DNA fragmentation (cell death; TUNEL staining) in Gl261 tumors (**Figure 9B**); Rano significantly decreased Ki67 in Gl261 tumors but increased TUNEL in CT2A tumors. Tumors treated with TMZ and/or RT and all-combined treatment showed increased DNA damage (γH2A.X; $p < 0.001$; **Figure 9C**). We have previously observed this phenomenon of prolonged γH2A.X at 28 days after RT treatment in noncancerous

brain, lung, and colon tissues (24). As the patterning is not observed in unirradiated (untreated) brains, we believe that it indicates radiotoxicity to the "healthy" cells, including radiosensitive oligodendrocytes, which have shown limited regenerative capacity out to 18-month postirradiations (29). In brain tissue where tumors resolved, TUNEL staining was limited to immune cells present along the wound tract (**Figure 9B**) and therein not quantitated.

DISCUSSION

Contrary to a recent report by Duraj and colleagues (27), we show that glucose and FAO metabolic pathways are similar among GBM subtypes, and enzymes of the glycolytic and FAO pathways are upregulated in GBM tumors compared to normal brain tissues. While many therapies aim to target the genetic differences in GBM tumors (e.g., EGFR, IDH, FGFR, and TACC), the inhibition of GBM cellular energetics is a potentially wide ranging approach with impact irrespective of GBM subtype.

Chemoradiation forms part of the "standard of care" for patients with GBMs; therefore, we compared the effects of DCA, Rano, and DCA/Rano in relation to chemoradiation and their known mechanism of action; ROS > DNA damage > cell cycle > apoptosis/autophagy, as well as *in vivo* efficacy. DCA and Rano induced oxidative stress, DNA damage, autophagy, and apoptosis (summarized in **Supplementary Figure 3**). At 72 h, the CT2A cells had lower ROS levels and less ATM activation compared to Gl261 cells. The subtle disparity in the response of Gl261 and CT2A cells may be partially attributable to differences in TP53 with Gl261 ($P53^{MUT}$) and CT2A ($P53^{WT}$) (30). TP53 is one of the most commonly dysregulated genes in GBM, with up to 54% of patients with $TP53^{MUT}$ depending on the GBM subtype (1). However, it is reported that $P53^{WT}$ inhibits lipid synthesis and glycolysis in normal and tumor cells, whereas $T53^{MUT}$ promotes lipid synthesis and glycolysis (31). In tumor cells, it is not that simple. Not all P53 mutants increase glycolysis (32) and wild-type P53 can promote the metabolic switch from oxidative phosphorylation to glycolysis by inducing p53 upregulated modulator of apoptosis (PUMA)-mediated disruption of mitochondrial pyruvate uptake in cancer cells (33). Therein where we would have expected Gl261 ($P53^{MUT}$) to be more sensitive to DCA, we instead observed higher IC50s for both DCA and Rano in the Gl261 line due to its precedence. In normal cells, wild-type P53 positively regulates ferroptosis, yet in tumor cells, $TP53^{MUT}$ sensitizes tumor cells to ferroptosis, a process noted to have a role in TMZ resistance and is associated with GBM autophagy and apoptotic mechanisms (31). Further, examination of the P53 mutant and wild-type regulation of glycolytic and FAO pathways in GBM is needed.

One point of difference in our study was that in both cell lines, DCA increased annexin V, Bax:Bcl-2 ratio, and CT2A caspase
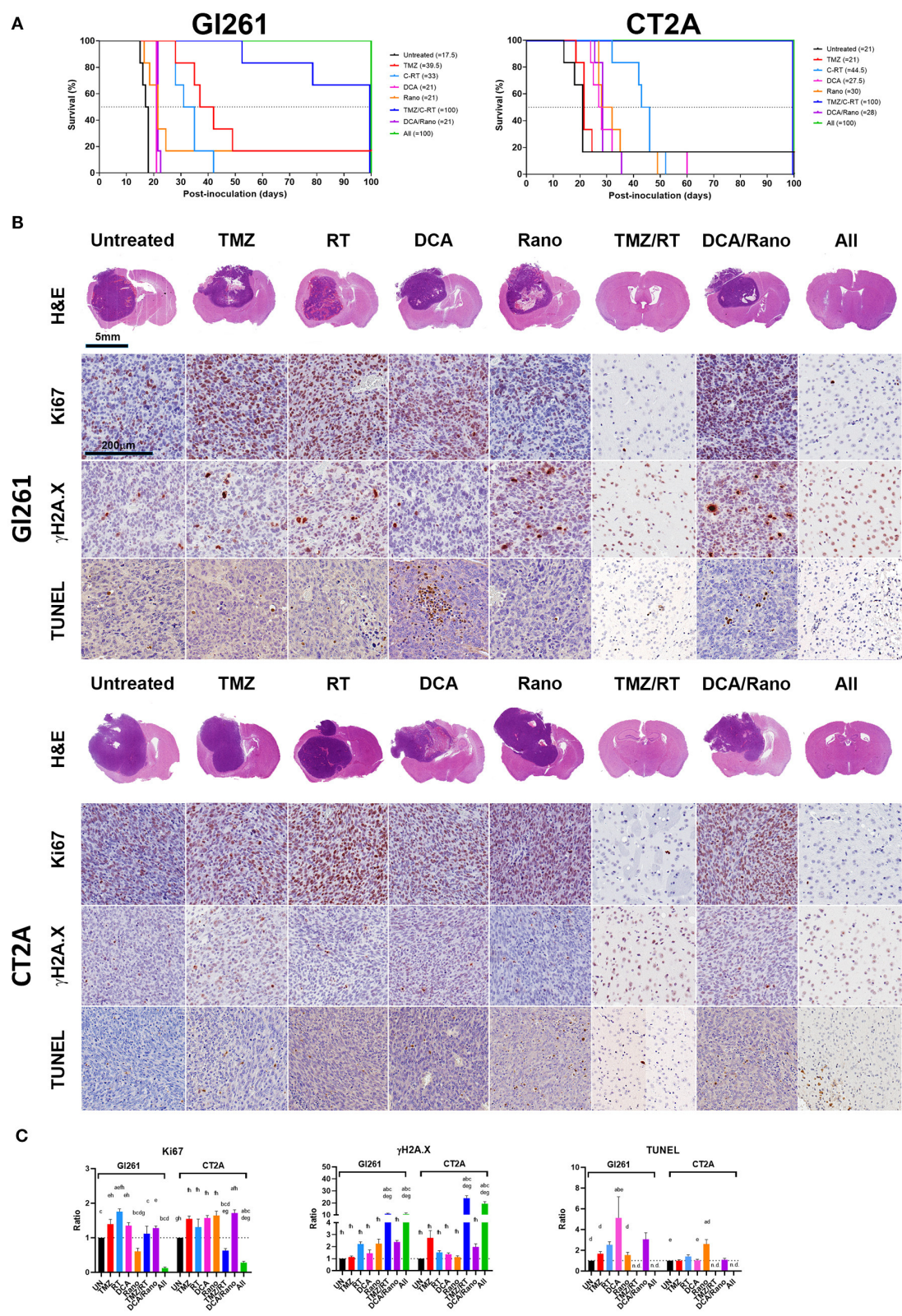
FIGURE 9 | DCA and Rano increased median survival but were not more efficacious than chemoradiation. Mice were injected intracranially with $1 \times 10^5/2\,\mu l$ murine GBM cells on day 0 and TMZ (50 mg/kg/day i.p.), DCA (200 mg/kg/day i.p.), Rano; 50 mg/kg/day i.p.), and/or RT (20 Gy/10) treatment administered daily from day 7 to day 21. **(A)** The Kaplan–Meier plots show median survival per treatment and are indicated in the graph legend. Six mice per treatment were monitored for 100-day

(Continued)

FIGURE 9 | postinoculation or until humane endpoint. **(B)** Endpoint Gl261 (top) and CT2A (bottom) tumors were immunohistochemically stained for cell proliferation marker, Ki67, DNA damage marker, γH2A.X (S139), and apoptotic marker, terminal deoxynucleotidyl transferase dUTP nick end labeling (TUNEL) stain. **(C)** Column graphs of the quantitation of positively stained cells in treated mice compared to controls. Data are expressed as mean ± SEM for five high-power fields ($N = 6$ tumors per treatment group). [a]$p < 0.05$ vs. Unt; [b]$p < 0.05$ vs. TMZ; [c]$p < 0.05$ vs. RT; [d]$p < 0.05$ vs. DCA; [e]$p < 0.05$ vs. Rano; [f]$p < 0.05$ vs. TMZ/RT; [g]$p < 0.05$ vs. DCA/Rano; and [h]$p < 0.05$ vs. All-combined treatments were determined by the two-way ANOVA test along with the Tukey's multiple comparison test. n.d., not determined.

3, indicating that DCA induces the mitochondrial (intrinsic) apoptotic pathway in GBM cell lines. Yet, in CT2A, but not Gl261 cells, TMZ increased caspase 3 without increased annexin V or Bax:Bcl-2. A study by Roos et al. (34) proposed that, in glioma cells, O^6-methylating agents, such as TMZ, induce the accumulation of DNA DSBs. In P53[WT] cells (e.g., CT2A), this induction activates the extrinsic apoptotic pathway *via* FasR and caspase 8, whereas in P53[MUT] cells (e.g., Gl261) the same response triggers the intrinsic apoptotic pathway *via* Bax:Bcl-2 and caspase 9. Both apoptotic pathways led to increased caspase 3 cleavage. Therein in our study, DCA and TMZ may trigger the intrinsic and extrinsic apoptotic pathways in CT2A, respectively, which was not observed in Gl261 cells due to differences in P53 status; however, we cannot account for the absence of membrane translocation for TMZ-treated CT2A cells in this study.

In line with other murine models examining glycolytic inhibitors, 2-DG, and/or FAO inhibitors, etomoxir or Rano, in GBM, lung and colon cancers, median survival, or tumor growth were minimally affected (11, 13). However, the combination strategy showed an enhanced antitumor effect (13). The observed 20–40% increase in median survival in syngeneic murine models using DCA/Rano (Gl261: 17.5 vs. 21 days, $p < 0.0001$ and CT2A: 21 vs. 28 days, $p < 0.0001$) was comparable to an immunocompromised model of GBM (MES93) using 2-DG/etomoxir, which increased median survival from 17 to 24 days ($p < 0.001$) (11). It is noted that the effects of Rano on the cell may not be limited to FAO inhibition. Although, noted as a partial FAO inhibitor, Rano was found to lack the FAO-interfering activity in complete media with or without serum (35), despite showing FAO-inhibiting ability in our FAO assay utilizing glucose-deprivation and a single FAO source (18C unsaturated fatty acid oleate).

In GBM, DCA has shown promising results across a range of preclinical studies, yet these data have not translated into pronounced improvements in the few clinic trials undertaken thus far. Although, we demonstrated *in vitro* that DCA and Rano induced ROS, DNA damage, autophagy, and apoptosis, our *in vivo* survival data did not reflect this. *In vivo* dose, regimen, and sequencing of drugs may have limited therapeutic efficacy. In the present study, we administered DCA and Rano concurrently with chemoradiation. As most DNA damage from RT is due to indirect ionization of oxygen and increased ROS (peaking at ∼30–120 min post-RT) and FDA clinical pharmacokinetic data available for TMZ, DCA, and Rano indicating that they reach peak plasma concentrations (C_{max}) at 1–2 h, we elected to deliver RT at ∼1-h post-drug administration. This contrasts phase I clinical trials in recurrent GBM, wherein, patients received DCA monotherapy two times daily for 30 days, without chemoradiation (36), and Rano monotherapy is FDA approved for administration two times daily for the treatment of angina.

Further, elucidation of the best dose regimen and sequencing of the novel or repurposed therapeutics to target cancer cell metabolism will improve efficacy.

In GBM, the peripheral neuropathy of the patient from DCA has been noted, albeit transient and dose-dependent (15). The computational modeling reveals that the docking binding energy values of DCA are PDK2 > PDK1 > PDK4 > PDK3 (37), suggesting that DCA has greatest binding affinity for PDK2, for which we showed no significant difference in PDK2 gene expression between GBM tumors and normal brain tissue in the TCGA dataset. Of equal concern is the fact that *in vitro* concentrations of DCA are in the millimolar range, raising the notion that DCA derivatives, novel or repurposed drugs with selective PDK1/3 binding affinity, and micromolar or nanomolar IC50s may be better therapeutic avenues to explore.

In conclusion, the present study shows that dual glycolytic and FAO targeting with and without concomitant chemoradiation warrants further investigation in immunocompetent syngeneic models for GBM.

DATA AVAILABILITY STATEMENT

The datasets presented in this study can be found in online repositories. The names of the repository/repositories and accession number(s) can be found below: https://www.ncbi.nlm.nih.gov/geo/, GSE72217; https://www.ncbi.nlm.nih.gov/gap/, phs000178.

ETHICS STATEMENT

The animal study was reviewed and approved by Northern Sydney Local Heath District Animal Ethics Committee, Royal North Shore Hospital, St Leonards, Australia.

AUTHOR CONTRIBUTIONS

KM, EW, MB, SS, AM, CD, and VH contributed to the conception and design of the study. KM performed the *in vitro* and *in vivo* experimentation and statistical analyses and wrote the first draft of the manuscript. All authors contributed to the manuscript revision and read and approved the submitted version.

FUNDING

ACKNOWLEDGMENTS

SUPPLEMENTARY MATERIAL

The Supplementary Material for this article can be found online at: https://www.frontiersin.org/articles/10.3389/fonc.2021.633210/full#supplementary-material

Supplementary Figure 1 | Sensitivity and survival of murine and human glioma cell lines to drug and RT treatment combinations. Drug IC50s for TMZ, DCA, and Rano were determined from confluency (%) at 72 h, and RT by clonogenic assay at 10-day post-treatment using the four-parameter logistic model. Symbols show mean survival (%) $\pm$ SEM for six replicates per experiment ($N = 3$). U-87 MG did not form colonies in the RT assessment.

Supplementary Figure 2 | Experimental timeline for Gl261 and CT2A tumor-bearing mice. Drugs and radiation therapy (RT) were assessed individually and in combination; RT 2 Gy/10, 50 mg/kg i.p. TMZ, 200 mg/kg i.p. DCA, and/or 50 mg/kg i.p. Rano five times per week for 2 weeks commencing at day 7 post-intracranial injection of $1 \times 10^5/2$ µl Gl261 or CT2A cells. Mice were euthanized at humane endpoints or at day 100 postinoculation (considered long-term survival).

Supplementary Figure 3 | Schematic representation of DCA and Rano inhibition on murine GBM cell lines. Drugs and chemoradiation were assessed individually and in combination. PS, phosphatidylserine.

REFERENCES

1. Verhaak RG, Hoadley KA, Purdom E, Wang V, Qi Y, Wilkerson MD, et al. Integrated genomic analysis identifies clinically relevant subtypes of glioblastoma characterized by abnormalities in PDGFRA, IDH1, EGFR, and NF1. *Cancer Cell.* (2010) 17:98–110. doi: 10.1016/j.ccr.2009.12.020

2. Health AIo, Welfare. *Cancer Data in Australia.* Canberra: AIHW (2020).

3. Dolecek TA, Propp JM, Stroup NE, Kruchko C. CBTRUS statistical report: primary brain and central nervous system tumors diagnosed in the United States in 2005-2009. *Neuro Oncol.* (2012) 14(Suppl. 5):v1–49. doi: 10.1093/neuonc/nos218

4. Parker NR, Hudson AL, Khong P, Parkinson JF, Dwight T, Ikin RJ, et al. Intratumoral heterogeneity identified at the epigenetic, genetic and transcriptional level in glioblastoma. *Sci Rep.* (2016) 6:22477. doi: 10.1038/srep22477

5. Olar A, Aldape KD. Using the molecular classification of glioblastoma to inform personalized treatment. *J Pathol.* (2014) 232:165–77. doi: 10.1002/path.4282

6. McKelvey KJ, Hudson AL, Prasanna Kumar R, Wilmott JS, Attrill GH, Long GV, et al. Temporal and spatial modulation of the tumor and systemic immune response in the murine Gl261 glioma model. *PLoS ONE.* (2020) 15:e0226444. doi: 10.1371/journal.pone.0226444

7. Prabhu AH, Kant S, Kesarwani P, Ahmed K, Forsyth P, Nakano I, et al. Integrative cross-platform analyses identify enhanced heterotrophy as a metabolic hallmark in glioblastoma. *Neuro Oncol.* (2019) 21:337–47. doi: 10.1093/neuonc/noy185

8. Stupp R, Mason WP, van den Bent MJ, Weller M, Fisher B, Taphoorn MJ, et al. Radiotherapy plus concomitant and adjuvant temozolomide for glioblastoma. *N Engl J Med.* (2005) 352:987–96. doi: 10.1056/NEJMoa043330

9. Gilbert MR, Wang M, Aldape KD, Stupp R, Hegi ME, Jaeckle KA, et al. Dose-dense temozolomide for newly diagnosed glioblastoma: a randomized phase III clinical trial. *J Clin Oncol.* (2013) 31:4085–91. doi: 10.1200/JCO.2013.49.6968

10. Lin H, Patel S, Affleck VS, Wilson I, Turnbull DM, Joshi AR, et al. Fatty acid oxidation is required for the respiration and proliferation of malignant glioma cells. *Neuro Oncol.* (2017) 19:43–54. doi: 10.1093/neuonc/now128

11. Kant S, Kesarwani P, Prabhu A, Graham SF, Buelow KL, Nakano I, et al. Enhanced fatty acid oxidation provides glioblastoma cells metabolic plasticity to accommodate to its dynamic nutrient microenvironment. *Cell Death Dis.* (2020) 11:253. doi: 10.1038/s41419-020-2449-5

12. Aldasoro M, Guerra-Ojeda S, Aguirre-Rueda D, Mauricio MD, Vila JM, Marchio P, et al. Effects of ranolazine on astrocytes and neurons in primary culture. *PLoS ONE.* (2016) 11:e0150619. doi: 10.1371/journal.pone.0150619

13. Hossain F, Al-Khami AA, Wyczechowska D, Hernandez C, Zheng L, Reiss K, et al. Inhibition of fatty acid oxidation modulates immunosuppressive functions of myeloid-derived suppressor cells and enhances cancer therapies. *Cancer Immunol Res.* (2015) 3:1236–47. doi: 10.1158/2326-6066.CIR-15-0036

14. Moher D, Liberati A, Tetzlaff J, Altman DG. Preferred reporting items for systematic reviews and meta-analyses: the PRISMA statement. *PLoS Med.* (2009) 6:1–6. doi: 10.1371/journal.pmed.1000097

15. Michelakis ED, Sutendra G, Dromparis P, Webster L, Haromy A, Niven E, et al. Metabolic modulation of glioblastoma with dichloroacetate. *Sci Transl Med.* (2010) 2:31–4. doi: 10.1126/scitranslmed.3000677

16. Shen H, Hau E, Joshi S, Dilda PJ, McDonald KL. Sensitization of glioblastoma cells to irradiation by modulating the glucose metabolism. *Mol Cancer Ther.* (2015) 14:1794. doi: 10.1158/1535-7163.MCT-15-0247

17. Shen H, Decollogne S, Dilda PJ, Hau E, Chung SA, Luk PP, et al. Dual-targeting of aberrant glucose metabolism in glioblastoma. *J Exp Clin Cancer Res.* (2015) 34:14. doi: 10.1186/s13046-015-0130-0

18. Jiang W, Finniss S, Cazacu S, Xiang C, Brodie Z, Mikkelsen T, et al. Repurposing phenformin for the targeting of glioma stem cells and the treatment of glioblastoma. *Oncotarget.* (2016) 7:56456–70. doi: 10.18632/oncotarget.10919

19. Goetzman ES, Prochownik EV. The role for Myc in coordinating glycolysis, oxidative phosphorylation, glutaminolysis, and fatty acid metabolism in normal and neoplastic tissues. *Front Endocrinol.* (2018) 9:129. doi: 10.3389/fendo.2018.00129

20. Xie Y, Bergström T, Jiang Y, Johansson P, Marinescu VD, Lindberg N, et al. The human glioblastoma cell culture resource: validated cell models representing all molecular subtypes. *EBioMedicine.* (2015) 2:1351–63. doi: 10.1016/j.ebiom.2015.08.026

21. de Hoon MJ, Imoto S, Nolan J, Miyano S. Open source clustering software. *Bioinformatics.* (2004) 20:1453–4. doi: 10.1093/bioinformatics/bth078

22. Keil CLR, Faizaan SM, Bezawada S, Parsons L, Baryshnikova A. *Treeview 3 (beta 1) - Visualization and Analysis of Large Data Matrices.* Meyrin: Zenodo (2016).

23. Tang Z, Li C, Kang B, Gao G, Li C, Zhang Z. GEPIA: a web server for cancer and normal gene expression profiling and interactive analyses. *Nucleic Acids Res.* (2017) 45:W98–102. doi: 10.1093/nar/gkx247

24. McKelvey KJ, Hudson AL, Prasanna Kumar R, Eade T, Clarke SJ, Wheeler HR, et al. Sub-acute toxicity in non-cancerous tissue and immune-related adverse events of a novel combination therapy for cancer. *Front Oncol.* (2020) 9:1504. doi: 10.3389/fonc.2019.01504

25. Chou T-C, Talalay P. Quantitative analysis of dose-effect relationships: the combined effects of multiple drugs or enzyme inhibitors. *Adv Enzyme Regul.* (1984) 22:27–55. doi: 10.1016/0065-2571(84)90007-4

26. Chou TC. Theoretical basis, experimental design, and computerized simulation of synergism and antagonism in drug combination studies. *Pharmacol Rev.* (2006) 58:621–81. doi: 10.1124/pr.58.3.10

27. Duraj T, Garcia-Romero N, Carrión-Navarro J, Madurga R, de Mendivil AO, Prat-Acin R, et al. Beyond the warburg effect: oxidative and glycolytic phenotypes coexist within the metabolic heterogeneity of glioblastoma. *Cells.* 10:202. doi: 10.3390/cells10020202

28. Sánchez-Martín P, Komatsu M. p62/SQSTM1 – steering the cell through health and disease. *J Cell Sci.* (2018) 131:jcs222836. doi: 10.1242/jcs.222836

29. Begolly S, Olschowka JA, Love T, Williams JP, O'Banion MK. Fractionation enhances acute oligodendrocyte progenitor cell radiation sensitivity and leads to long term depletion. *Glia.* (2018) 66:846–61. doi: 10.1002/glia.23288

30. Oh T, Fakurnejad S, Sayegh ET, Clark AJ, Ivan ME, Sun MZ, et al. Immunocompetent murine models for the study of glioblastoma immunotherapy. *J Transl Med.* (2014) 12:107. doi: 10.1186/1479-5876-12-107

31. Gnanapradeepan K, Basu S, Barnoud T, Budina-Kolomets A, Kung C-P, Murphy ME. The p53 tumor suppressor in the control of metabolism and ferroptosis. *Front Endocrinol.* (2018) 9:124. doi: 10.3389/fendo.2018.00124

32. Eriksson M, Ambroise G, Ouchida AT, Lima Queiroz A, Smith D, Gimenez-Cassina A, et al. Effect of mutant p53 proteins on glycolysis and mitochondrial metabolism. *Mol Cell Biol.* (2017) 37:e00328-17. doi: 10.1128/MCB.00328-17

33. Kim J, Yu L, Chen W, Xu Y, Wu M, Todorova D, et al. Wild-Type p53 promotes cancer metabolic switch by inducing PUMA-dependent suppression of oxidative phosphorylation. *Cancer Cell.* (2019) 35:191–203.e8. doi: 10.1016/j.ccell.2018.12.012

34. Roos WP, Batista LF, Naumann SC, Wick W, Weller M, Menck CF, et al. Apoptosis in malignant glioma cells triggered by the temozolomide-induced DNA lesion O6-methylguanine. *Oncogene.* (2007) 26:186–97. doi: 10.1038/sj.onc.1209785

35. Ma Y, Wang W, Devarakonda T, Zhou H, Wang X-Y, Salloum FN, et al. Functional analysis of molecular and pharmacological modulators of mitochondrial fatty acid oxidation. *Sci Rep.* (2020) 10:1450. doi: 10.1038/s41598-020-58334-7

36. Dunbar EM, Coats BS, Shroads AL, Langaee T, Lew A, Forder JR, et al. Phase 1 trial of dichloroacetate (DCA) in adults with recurrent malignant brain tumors. *Invest New Drugs.* (2014) 32:452–64. doi: 10.1007/s10637-013-0047-4

37. Fereidoonnezhad M, Faghih Z, Mojaddami A, Sakhteman A, Rezaei Z. A comparative docking studies of dichloroacetate analogues on four isozymes of pyruvate dehydrogenase kinase in humans. *Indian J Pharm Educ Res.* (2016) 50:S32–8. doi: 10.5530ijper.50.2.15

Plasma Metabolome Signature Indicative of *BRCA1* Germline Status Independent of Cancer Incidence

Judith Penkert[1]*[†], Andre Märtens[2†], Martin Seifert[3], Bernd Auber[1], Katja Derlin[4], Ursula Hille-Betz[5], Philipp Hörmann[2], Norman Klopp[6], Jana Prokein[7], Lisa Schlicker[8], Frank Wacker[4], Hannah Wallaschek[1], Brigitte Schlegelberger[1], Karsten Hiller[2,9‡], Tim Ripperger[1‡] and Thomas Illig[1,6‡]

[1] Department of Human Genetics, Hannover Medical School, Hannover, Germany, [2] Department of Bioinformatics and Biochemistry, Braunschweig Integrated Center of Systems Biology (BRICS), Technische Universität Braunschweig, Braunschweig, Germany, [3] Connexome Consulting, Fischen, Germany, [4] Department of Diagnostic and Interventional Radiology, Hannover Medical School, Hannover, Germany, [5] Department of Obstetrics and Gynecology, Hannover Medical School, Hannover, Germany, [6] Hannover Unified Biobank (HUB), Hannover, Germany, [7] Center for Information Management, Hannover Medical School, Hannover, Germany, [8] Division of Tumour Metabolism and Microenvironment, German Cancer Research Center (DKFZ), Heidelberg, Germany, [9] Computational Biology of Infection Research, Helmholtz Centre for Infection Research, Braunschweig, Germany

Individuals carrying a pathogenic germline variant in the breast cancer predisposition gene *BRCA1* (g*BRCA1*+) are prone to developing breast cancer. Apart from its well-known role in DNA repair, BRCA1 has been shown to powerfully impact cellular metabolism. While, in general, metabolic reprogramming was named a hallmark of cancer, disrupted metabolism has also been suggested to drive cancer cell evolution and malignant transformation by critically altering microenvironmental tissue integrity. Systemic metabolic effects induced by germline variants in cancer predisposition genes have been demonstrated before. Whether or not systemic metabolic alterations exist in g*BRCA1*+ individuals independent of cancer incidence has not been investigated yet. We therefore profiled the plasma metabolome of 72 g*BRCA1*+ women and 72 age-matched female controls, none of whom (carriers and non-carriers) had a prior cancer diagnosis and all of whom were cancer-free during the follow-up period. We detected one single metabolite, pyruvate, and two metabolite ratios involving pyruvate, lactate, and a metabolite of yet unknown structure, significantly altered between the two cohorts. A machine learning signature of metabolite ratios was able to correctly distinguish between g*BRCA1*+ and controls in ~82%. The results of this study point to innate systemic metabolic differences in g*BRCA1*+ women independent of cancer incidence and raise the question as to whether or not constitutional alterations in energy metabolism may be involved in the etiology of *BRCA1*-associated breast cancer.

Keywords: breast cancer, plasma metabolome, *BRCA1* germline mutation, energy metabolism, NAD⁺ balance, HIF1 alpha, lactate, aerobic glycolysis

INTRODUCTION

During recent years, the idea of the tumor suppressor and breast cancer predisposition gene *BRCA1* and its protein product exclusively serving as a critical DNA repair agent maintaining genomic stability has been challenged, as it has become increasingly apparent that BRCA1's pleiotropic functions comprise mechanisms as widespread as epigenetic regulation (1), chromatin remodeling and gene transcription (2, 3), differentiation of mammary stem/progenitor cells to mature luminal epithelial cells (4), control of cancer stem cell-like characteristics (5), and the powerful regulation of cellular metabolism (6–13).

At the same time, the emerging concept of cancer initiation and progression being an evolutionary process in which not only the accumulation of mutational burden in tumor cells but also tissue integrity and alterations in stem cell niche microenvironments play a fundamental role (14) gains stronger interest. In this context, progressively degrading tissues, e.g. due to aging processes, chronic pro-inflammatory status, or external insults such as radiation, represent a challenge for resident stem cells poorly adapted to such niche changes and provide a competitive advantage to those that improve their fitness through specific oncogenic mutations (a process termed "adaptive oncogenesis"). For the emergence of altered microenvironment conditions, metabolic cellular reprogramming of stromal cells such as cancer-associated fibroblasts (CAFs) plays an integral role [reviewed in (15)]. Therefore, it seems conceivable that germline alterations that constitutionally push the organism towards a metabolic state resembling aging conditions or chronic inflammation amount to a microenvironment that—in advance of natural aging—supports adaptive oncogenesis and, thus, contributes to cancer predisposition.

As has previously been shown for recognized "Inborn Errors of Metabolism", metabolic alterations such as succinate dehydrogenase (SDH) or fumarate hydratase (FH) deficiency are capable of fostering malignant transformation efficiently and reliably, and heterozygous germline alterations in the respective genes are associated with cancer predisposition syndromes [reviewed in (16)]. Not only has metabolic cellular reprogramming been named a hallmark of cancer (17), but emerging evidence seems to also raise the question if disrupted metabolism may in fact be a prerequisite for cancer evolution. BRCA1, specifically, has been shown to strongly impact energy metabolism, fatty acid metabolism, and antioxidative pathways in breast epithelial cells and breast cancer cell lines (11–13). A reversion of the Warburg effect has been postulated upon transfection of a *BRCA1*-mutated breast cancer cell line by wildtype *BRCA1* (11). In CAFs, BRCA1 has been shown to influence proliferation rates, response to hypoxia, autophagy, and SDH complex efficiency (18). Many of these effects seem to involve the transcription factor and master regulator of metabolism hypoxia-inducible factor 1 (HIF1) (11, 12, 18), the overexpression of which has been demonstrated in *BRCA1*-related invasive breast cancer as well as ductal carcinoma

in situ (DCIS), suggesting hypoxia to already play a role in early stages of *BRCA1*-related breast carcinogenesis (19, 20).

While little is known about systemic effects of heterozygous pathogenic germline *BRCA1* variants (g*BRCA1*+), luteal phase sex hormones—in particular progesterone (P4)—were observed to be elevated and osteoprotegerin (OPG) levels were decreased in serum of g*BRCA1*+ carriers (21, 22). In women without known genetic predisposition, high receptor activator of NFκB ligand (RANKL)/OPG ratios were suggested indicative of breast cancer manifestation, and elevated RANKL and P4 serum levels stratified a subgroup of women at high risk of developing breast cancer 1–2 years before diagnosis (23), though recently a report rebutted plasma RANKL levels correlating with breast cancer risk in germline *BRCA1/2* mutation carriers (24). In patients with triple-negative breast cancer (TNBC), a plasma metabolomics signature has been described, which distinguishes diseased g*BRCA1*+ patients from diseased germline *BRCA1* wildtype patients (25). Whether or not systemic effects of globally altered metabolism exist in non-cancer-diseased g*BRCA1*+ individuals and whether these can be detected *via* metabolome analyses has, to our knowledge, not yet been investigated.

The purpose of the present study was to evaluate if plasma metabolome signatures of non-cancer-diseased g*BRCA1*+ carriers and healthy age-matched controls mirror genotype, as has previously been shown for carriers of pathogenic germline *PTEN* variants (26). We intentionally selected for non-diseased, treatment-naïve females seeking to confine confounding factors such as tumor burden, radio-chemotherapy, or anti-hormonal treatment to a minimum to allow primary focus on genotype-related metabolic differences. Findings of distinct systemic metabolic alterations preceding tumor formation could not only have vast consequences in terms of diagnostic procedures, predictive measures, and prognostic assessment, but also could they provide clues to etiologically critical drivers of cancer evolution in g*BRCA1*+ carriers and potentially uncover preventive as well as therapeutic options.

MATERIALS AND METHODS

Study Cohort
Patient Selection
Plasma samples of 72 women carrying a heterozygous (likely) pathogenic germline variant in *BRCA1* (ACMG criteria class 4/5)—but not previously diagnosed with any type of malignancy—were recruited from the Departments of Human Genetics, Radiology, or Obstetrics and Gynecology, Hannover Medical School, during 2015 to 2018. All of the study subjects' pedigrees of at least three generations had been established during genetic counseling. Subjects who knowingly carried an additional (likely) pathogenic variant (PV) in any other established cancer predisposition gene were dismissed from study inclusion.

In order to diminish the possibility of metabolomics effects arising from potentially pre-existing breast cancer disease in g*BRCA1*+ individuals at the time of blood draw, patients who developed invasive or *in situ* breast cancer during the follow-up

period were excluded from the cohort. The follow-up period comprised a minimum of 19 months and a maximum of 56 months. For 14 g*BRCA1*+ women (19%), no clinical follow-up data was available.

Female relatives of patients in whom a PV in an established predisposition gene associated with Mendelian disease had previously been detected and who tested negative for this familial variant were included as age-matched control subjects (i.e., +/- 5 years, in one pair 6 years, at time of sample collection; 42/72 (~60%) of pairs being age-matched ≤2 years). As these individuals had also been seen in the outpatient clinic of the Department of Human Genetics, their personal medical and family histories were available, which enabled us to specifically exclude any sporadic cancer patients or any whose family history was suggestive of cancer predisposition in the other family branch according to currently available genetic testing criteria.

Known carriers of variants of uncertain significance (ACMG class 3) or PVs in other genes were excluded. Among the included control subjects, there were 33, 24, 3, 2, and two in which a familial PV in *BRCA1*, *BRCA2*, *MSH2*, *MSH6*, and *TP53*, was excluded, respectively, and eight with exclusion of a familial PV in either *APC*, *CFTR*, *FBN1*, *GLI3*, *MLH1*, *PALB2*, *PTEN*, or of a duplication of 22q11. No clinical follow-up data were available for control subjects.

Cohort Characteristics

The final cohort (**Figures 1A, B**) consisted of 144 individuals from 130 different families, including three families out of which cases and controls were integrated. The age range of cases and controls was 24–65 years (median 35 years), and 19–67 years (median 39 years), respectively. For age-stratified analyses, the cohort was split into three distinct age groups: G1: 19–34 years,
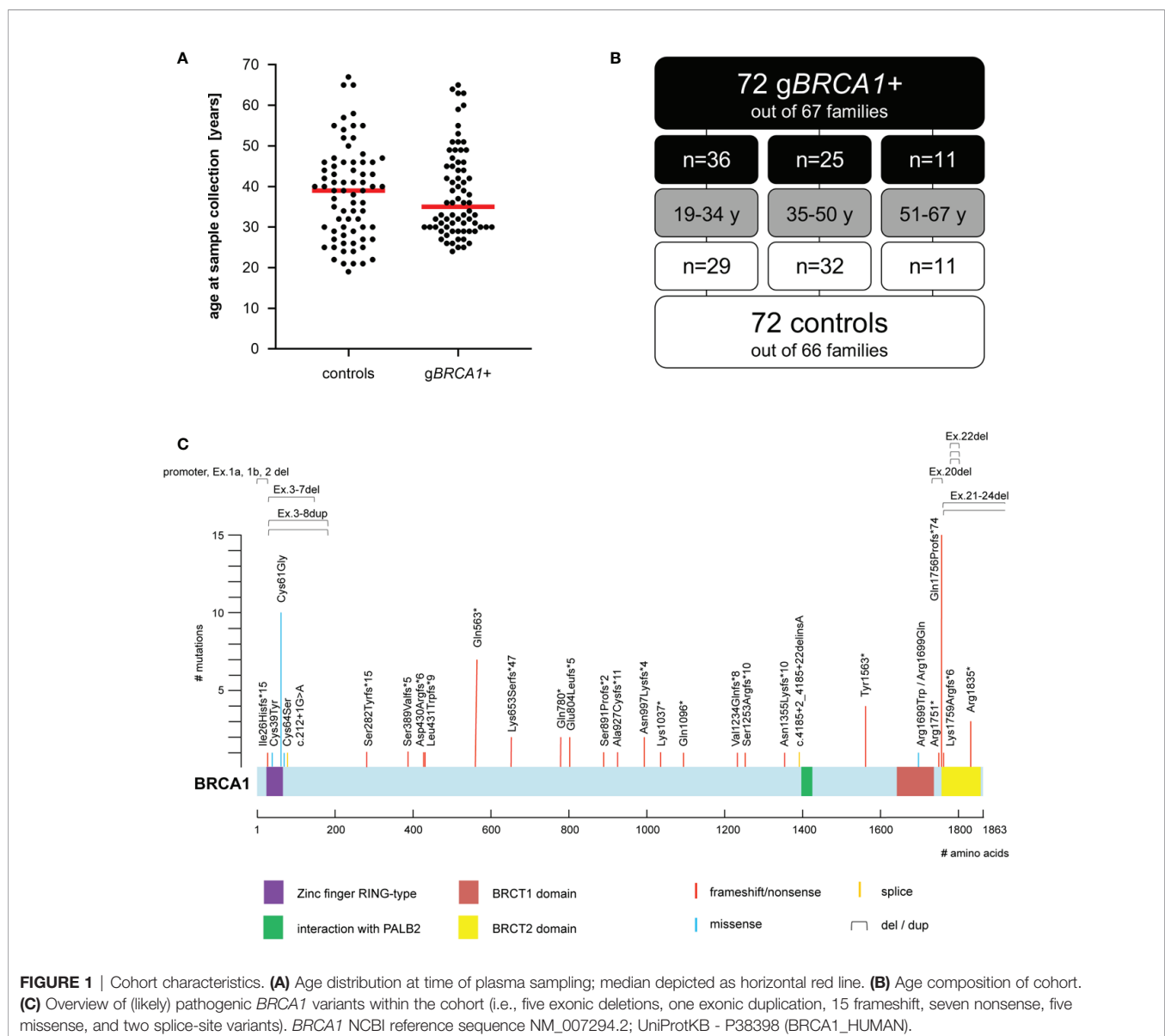
FIGURE 1 | Cohort characteristics. **(A)** Age distribution at time of plasma sampling; median depicted as horizontal red line. **(B)** Age composition of cohort. **(C)** Overview of (likely) pathogenic *BRCA1* variants within the cohort (i.e., five exonic deletions, one exonic duplication, 15 frameshift, seven nonsense, five missense, and two splice-site variants). *BRCA1* NCBI reference sequence NM_007294.2; UniProtKB - P38398 (BRCA1_HUMAN).

G2: 35–50 years, and G3: 51–67 years. The gBRCA1+ cohort contained 35 distinct variants in the *BRCA1* gene (for details, see **Figure 1C**).

The majority of patients and controls were assumed to be of European-Caucasian ancestry. The present study was performed in accordance with the Declaration of Helsinki and was approved by the institutional ethics review board of Hannover Medical School. Written informed consent was obtained from all participants.

Sample Processing and Gas Chromatography-Mass Spectrometry Measurement

Sample Collection

Peripheral blood EDTA samples were transferred to Hannover Unified Biobank (HUB) in a cool box immediately after blood draw. For plasma separation, samples were centrifuged at 2.000 x g for 10 min at 4°C and aliquoted within 2 h from blood collection. Plasma aliquots were immediately stored at −192°C. Samples were stored and tracked according to standard operating procedures at HUB and sent to Technical University, Braunschweig, on dry ice for further analyses.

Metabolite Extraction

All blood plasma samples were processed in technical duplicates. For each replicate, 20 µl of plasma were mixed with 180 µl methanol/water mixture (4 + 1; v/v) and vortexed on a thermomixer (Eppendorf) for 5 min at 1.400 rpm at 4°C. The mix was then directly centrifuged at 17.000 x g for 5 min at 4°C (Eppendorf 5415R), and 140 µl of the supernatant were transferred into GC glass vials. Samples were completely dried in a refrigerated rotary vacuum evaporator (Labconco) at 4°C for at least 40 min. In order to avoid condensation of water on the glass surface of the vials, the refrigerated rotary vacuum evaporator was heated up to room temperature for 25 min prior to taking out the vials. In addition, plasma metabolite pools (quality controls) were produced during the metabolite extraction procedure by mixing an equal amount of each sample. The GC glass vials were stored at −80°C until GC-MS measurements.

Metabolite Derivatization and GC-MS Analysis

Derivatization of the samples was performed by an autosampler (Axel Semrau) directly before GC-MS measurement. The dried samples were dissolved in 15 µl methoxyamine hydrochloride (Sigma-Aldrich) in pyridine (20 mg/ml) at 40°C for 60 min under shaking, followed by addition of 15 µl N-Methyl-N-(trimethylsilyl)trifluoroacetamide (Macherey-Nagel) and subsequent incubation for 30 min at 40°C.

GC-MS measurements were performed on a 7890B GC coupled to a 5977B MSD (both Agilent Technologies). The gas chromatograph was equipped with a 30 m DB-35ms capillary column (I.D. 250 µm, film 0.25 µm) + 5 m DuraGuard capillary in front of the analytical column (Agilent J&W GC Column). A sample volume of 1 µl was injected into a split/splitless inlet, operating in splitless mode at 270°C. Helium was used as carrier gas with a constant flow rate of 1 ml/min. The GC oven temperature was held at 80°C for 6 min, ramped with 6°C/min to 300°C and was held for 10 min. Then, the temperature was increased to 325°C at 10°C/min and held for additional 4 min. The total run time was 59.167 min. The transfer line temperature was set to 280°C. The MSD was operating under electron ionization at 70 eV. The MS source was held at 230°C and the quadrupole at 150°C. Full scan mass spectra were acquired from m/z 70 to m/z 800. Pool samples have been measured after 8 GC-MS measurements for quality control and data correction.

Data Processing, Statistical Analysis, and Machine Learning

All GC-MS chromatograms were processed using MetaboliteDetector, v3.320200313 (27). The software package supports automatic deconvolution of all mass spectra. Compounds were annotated by retention time and mass spectrum using an in-house mass spectral library. Data normalization was performed by dividing each metabolite intensity by the median intensity of the three chronologically nearest pool samples of the corresponding metabolite. After pool normalization, a total of 262 metabolites have been selected for further analysis after filtering of GC-MS measurement artefacts, such as siloxanes.

Normalized data were subject to statistical analysis using Python (version 3.7.6). To diminish potential deteriorating effects of outliers, mal-assigned signals, and artefacts on statistical analysis, we excluded all metabolites featuring a relative standard deviation (RSD) of ≥20%. We performed a two-tailed Welch's t-test (scipy version 1.4.1) as well as correction for multiple testing by Benjamini & Hochberg p-value adjustment (statsmodels version 0.11.0), the designed level of significance being p<.05. Metabolite ratios were determined per patient and replicate, means for both replicate-ratios were generated for each patient, and subsequently the two cohorts were compared.

For machine learning approaches we used the Waikato Environment for Knowledge Analysis (Weka) (https://www.cs.waikato.ac.nz/ml/weka/). Weka is a workbench for machine learning that is intended to aid in the application of machine learning techniques to a variety of data mining problems in bioinformatics research (28). Different machine learning algorithms including random forest, J48 simple logistic, and SMO (Sequential Minimal Optimization) – a training algorithm of support vector machines – were evaluated. Each classification method was used with Weka's default settings. We mainly performed Simple Logistic Regression analyses, which are frequently applied for cancer classification issues. Simple Logistic in Weka fits a multinomial logistic regression model using the LogitBoost algorithm (29). The number of LogitBoost iterations was manually selected based on an optimization of cross validation results. To build a classifier *via* stratified cross validation (training), we used 1) raw data, 2) averaged data (mean from both replicates per metabolite and patient), 3) averaged data of metabolites with RSD <20%, 4) metabolite ratios (see above), and 5) metabolite ratios plus metabolites

with RSD <20% for different sub-analyses. The resulting classifiers were subsequently applied to a) the whole dataset, and b) the separate age-subgroups (re-evaluation on test set).

RESULTS

Differentially Expressed Metabolites Between g*BRCA1*+ Carriers and Controls

We profiled the plasma metabolome of 72 g*BRCA1*+ and 72 healthy controls in technical duplicates. The analysis yielded 262 metabolites with unique retention time and mass spectrum detectable across all subjects (**Supplementary Material 1**). After excluding all metabolites featuring an RSD of ≥20%, 78 out of 262 identifiable metabolites remained within the analysis (**Supplementary Material 2**). From these, we identified three metabolites with significantly differing concentrations between g*BRCA1*+ and control subjects. After applying multiple testing correction *via* Benjamini-Hochberg adjustment, pyruvic acid was left as the sole significantly different metabolite, elevated in g*BRCA1*+ (**Figure 2A**).

Differentially Expressed Metabolite Ratios Between g*BRCA1*+ Carriers and Controls

Alterations of pairwise metabolite ratios are often more informative about specific metabolic pathways and disease mechanisms. Including all 78 metabolites with an RSD <20%, the resulting matrix consisted of 3.003 possible pairwise ratios. Of these, 208 metabolite ratios significantly differed between g*BRCA1*+ and control subjects. After Benjamini-Hochberg adjustment, two metabolite ratios remained significant, specifically RI1984:pyruvic acid and lactic acid: pyruvic acid, both reduced in g*BRCA1*+ carriers (**Figure 2B**). Although we have not been able to elucidate the structure of RI1984, its mass spectrum suggests a sugar acid. Based on a

reference measurement, we excluded gluconic acid as candidate metabolite.

Machine-Learning Signature

Additionally, we applied a machine learning approach in order to disclose complex interrelations between metabolites and metabolite ratios for genotype prediction. A 10-fold cross validation strategy was applied. Best results were obtained for the classifier based on pairwise metabolite ratios. After training of the Simple Logistic Model with this data set, we obtained 63.9% correct classification of samples per genotype. Using this classifier to evaluate the entire dataset, 81.9% of subjects (specificity: 0.79, sensitivity: 0.85) were assigned the correct genotype (**Figure 3**). Evaluation of the three age-subgroups separately yielded 80.0%, 84.2%, and 81.8% correct classification of G1, G2, and G3, respectively.

The classifier resulting from training on ratios plus averaged data of metabolites with RSD <20% exclusively contained metabolite ratios, indicating that metabolite ratios are more informative and perform better than single metabolite data. All classifiers generated contained the elements pyruvic acid, lactic acid, and RI1984, except for the classifier based on averaged data, which did not include lactic acid. In all sub-analyses, the classifiers consistently performed best on the middle age group G2, which included subjects aged 35–50 years at time of plasma sampling. Given the 10-fold cross validation strategy, we tried to avoid over-fitting. For an overview of all classifiers produced by sub-analyses, see **Supplementary Material 3**. For complete raw data, see **Supplementary Material 4**.

DISCUSSION

Inquiring an organism's plasma metabolome represents a unique challenge distinct from investigating primary tissue of interest.

FIGURE 2 | Results of statistical analyses after multiple testing correction. Box plots of **(A)** pyruvic acid as single plasma metabolite, and **(B)** two metabolite ratios significantly differing between g*BRCA1*+ individuals and controls.

FIGURE 3 | Receiver operating characteristic (ROC) curve of metabolite ratios classifier for the prediction of *BRCA1* genotype, obtained by machine learning. Area under ROC is a performance metric used to evaluate classification models that classify subjects into one of two categories. The ROC curve is created by plotting the true positive rate (i.e., sensitivity) against the false positive rate (i.e., 1-specificity). Smaller values on the x-axis of the plot indicate lower false positives and higher true negatives. Larger values on the y-axis of the plot indicate higher true positives and lower false negatives. Area under ROC equals 0.5 when the ROC curve corresponds to random chance and the model allows no classification. An area under ROC of 1.0 means perfect accuracy (i.e., sensitivity and specificity being 100%). Generally, an area under ROC greater than 0.8 indicates very good classification performance. All metabolite ratios included in the machine learning classifier are listed in the light gray box below the curve. This classifier correctly classifies ~82% of the cohort per genotype (specificity: 0.79, sensitivity: 0.85).

As such, the plasma metabolome can be seen as a dynamic equilibrium between total tissue consumption of specific metabolites, total flux from tissue into bloodstream (including endogenous production rates of metabolites), intestinal absorption of metabolites, and excretion *via* elimination mechanisms such as bile acid secretion or kidney filtration.

In comparison with age-matched controls, we detected two metabolite ratios significantly reduced in plasma of g*BRCA1*+ carriers after multiple testing correction, i.e., lactic acid:pyruvic acid and RI1984:pyruvic acid. Of the involved metabolites, pyruvate showed the most significant deviation as a single metabolite. Although the differences were not highly statistically significant, we believe that even discreet metabolic plasma effects justify appropriate notice in a study cohort fully consisting of healthy individuals lacking a personal history of cancer. As effect sizes were not particularly strong, we additionally applied a machine learning approach as a second method, which resulted in the correct discrimination between g*BRCA1*+ and controls in ~82% *via* a metabolite ratios signature that included both ratios previously identified as significantly different. Since no breast cancer was observed in g*BRCA1*+ subjects within a minimum follow-up period of 19 months, it seems unlikely that metabolic effects depicted in this cohort are attributable to preclinical undiagnosed breast cancer incidence in g*BRCA1*+ women. Because clinical follow-up data were not available for control subjects, breast cancer incidence during follow-up of g*BRCA1*+ cases cannot be ruled out for the control cohort. However, as we had excluded all subjects whose family pedigree suggested another cancer predisposition or who had previously been diseased, our control cohort was extremely carefully composed and potentially co-occurring malignancies should constitute rare events. The results of this study therefore point to innate systemic metabolic differences in g*BRCA1*+ individuals independent of and preceding cancer incidence, raising the disputable question as to whether or not metabolic alterations may pave the way for cancer evolution in g*BRCA1*+ individuals.

The observed metabolic changes can be interpreted within the scope of a network of alterations already known to correlate with BRCA1-low conditions (**Figure 4**): NFkB signaling is induced in precancerous breast tissue of g*BRCA1*+ carriers *via* paracrine signaling mechanisms involving P4-RANKL (30–32) (**Figure 4**, key factor 1), leading to pro-inflammatory stromal conditions that augment hypoxia-inducible factor 1 alpha (HIF1A) transcription (33)—one of two subunits constituting the transcription factor HIF1. Upregulation of HIF1A in BRCA1-deficient fibroblasts has previously been shown to drive breast cancer growth (18). In addition to upregulated transcription, HIF1A is stabilized in BRCA1-low conditions *via* impairment of two of four subunits of the mitochondrial SDH complex and subsequent accumulation of the oncometabolite succinate (11, 18), and *via* suppressed sirtuin 1 (SIRT1) levels (34) mimicking a pseudohypoxic state that results in loss of mitochondrial homeostasis (35). HIF1 (**Figure 4**, key factor 2) acts as a master transcriptional regulator of metabolism mediating i) massively increased glycolytic flux *via* transcriptional activation of glycolytic enzymes and glucose transporter 1 (GLUT1), ii) a reduction in mitochondrial-encoded gene expression, resulting in reduced mitochondrial function and impaired OXPHOS (35), iii) activation of pro-inflammatory genes and growth factors such as TNFα, interleukin 6 (IL-6), and VEGF (36), and iv) strong activation of pyruvate dehydrogenase kinase 1 (PDK1) (37), which regulates pyruvate dehydrogenase complex (PDC), resulting in reduced conversion of pyruvate to acetyl-CoA and, thus, pyruvate accumulation. The lack of glycolytic acetyl-CoA as the major substrate for the TCA cycle results in its decrement and further suppression of mitochondrial respiration. In summary, HIF1 regulates multiple genes contributing to the "Warburg effect"—a metabolic switch towards glycolytic over oxidative metabolism under normoxic conditions, i.e., "aerobic glycolysis" [reviewed in (38)].

Moreover, NAD+ levels are known to be elevated in BRCA1-low conditions, partly due to upregulated nicotinamide phosphoribosyltransferase (NAMPT)-mediated NAD+ synthesis (**Figure 4**, key factor 3), and increased NAD+ levels as well as elevated NAD+/NADH ratios have been shown to activate *BRCA1* transcription in turn (39, 40). The equilibrium between pyruvate and lactate is governed by cellular NAD+/NADH ratios, as are multiple other reversible enzymatic reactions, and it has been suggested that redox buffering of
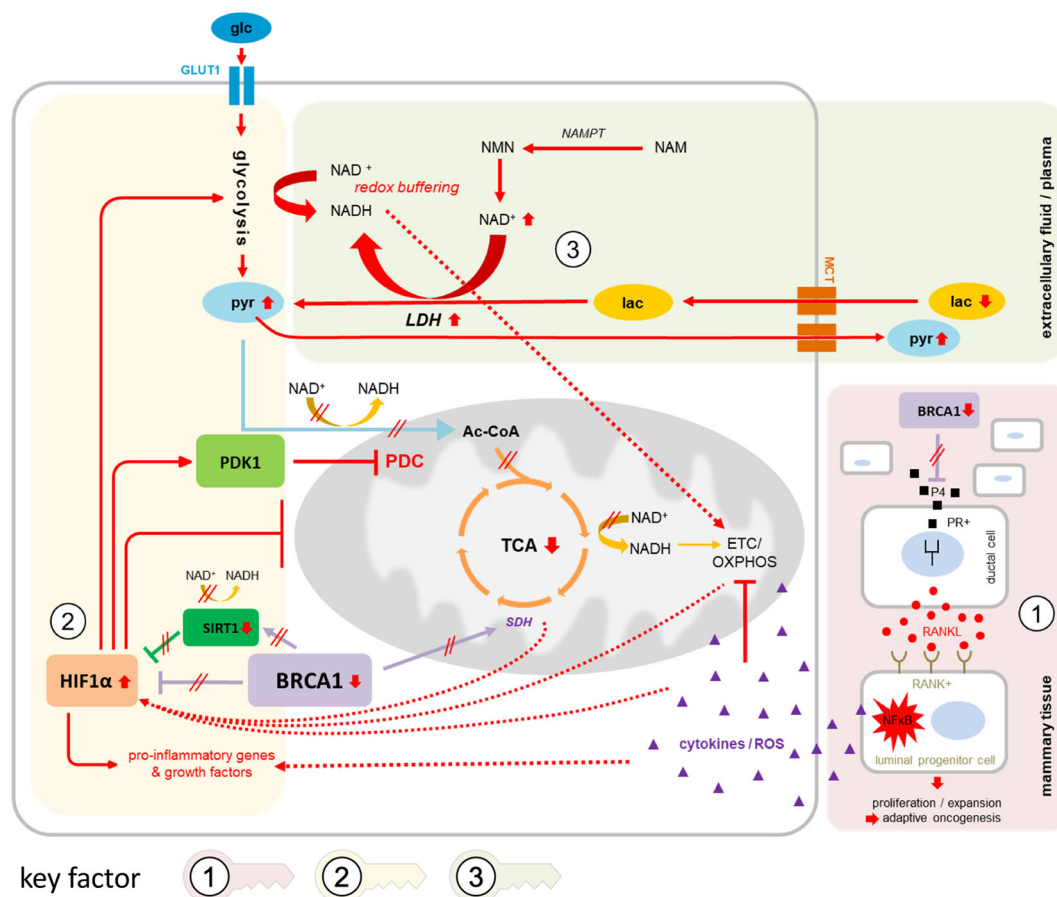
FIGURE 4 | Suggested network of contributing factors in g*BRCA1*+ oncogenesis. Circled numbers/shaded areas = key factors. In g*BRCA1*+ precancerous mammary tissue (key factor 1, red shading), amplification of the progesterone signaling axis due to elevated P4 levels and heightened PR activity in BRCA1-low conditions mediate RANKL secretion in PR+ ductal cells and subsequent paracrine binding to corresponding RANK on RANK+ luminal progenitor cells (LPC). In these cells, NFκB signaling is strongly activated, leading—in parallel—to i) chronic pro-inflammatory, ROS-enriched microenvironmental conditions, which contribute to OXPHOS impairment and mitochondrial dysfunction, eventually resulting in declined tissue integrity supportive of cancer evolution, and ii) a strong pro-proliferative signal specifically in RANK+ LPCs, increasing the chances of eruption of malignant phenotypes that are properly adjusted to challenging environmental conditions (the process of adaptive oncogenesis). Hypoxic as well as pseudohypoxic triggers mediate the stabilization and activation of HIF1A (key factor 2, yellow shading), amplified through direct and indirect interactions *via* BRCA1 as well as BRCA1-mediated alterations in SIRT1 and SDH activities. Downstream effects of HIF1A activation cause i) a massive increase in glycolytic flux *via* transcriptional activation of glycolytic enzymes and GLUT1, ii) further reinforcement of mitochondrial dysfunction and impaired OXPHOS, e.g. *via* TFAM iii) induction of pro-inflammatory genes and growth factors, and iv) strong activation of PDK1 resulting in impaired conversion of pyruvate to acetyl-CoA and, thus, diminished fuel for TCA cycling and energy generation from three-carbon compounds. The equilibrium between pyruvate and lactate *via* LDH, i.e., the direction of net LDH flux, is governed by cellular NAD+/NADH ratios (key factor 3, green shading); as NAD+ levels are elevated in BRCA1-low conditions due to upregulated NAMPT-mediated synthesis, lactate may be more readily converted into pyruvate than vice versa. Lactate influx and pyruvate efflux through MCTs would therefore mediate redox buffering of intracellular NAD+/NADH ratios while affecting net pyruvate and lactate levels in systemic circulation. NADH generated from glycolysis and from conversion of lactate into pyruvate may immediately be transported into mitochondria *via* malate-aspartate or glycerol phosphate shuttles to feed the otherwise neglected ETC for energy generation. 3PG, 3-phosphoglycerate; Ac-CoA, acetyl coenzyme A; αKG, alpha-ketoglutarate; ETC, electron transport chain; F1,6BP, fructose 1,6-bisphosphate; F6P, fructose 6-phosphate; fum, fumarate; G6P, glucose 6-phosphate; glc, glucose; GLUT1, glucose transporter 1; HIF1A, hypoxia-inducible factor 1 alpha; HK2, hexokinase 2; IL-6, interleukin 6; lac, lactate; LDH, lactate dehydrogenase; MCT, monocarboxylate transporter; NAD+, nicotinamide adenine dinucleotide (oxidized form); NADH, nicotinamide adenine dinucleotide (reduced form); NAM, nicotinamid; NFκB, nuclear factor "kappa-light-chain-enhancer" of activated B-cells; NMN, nicotinamide mononucleotide; OAA, oxaloacetate; OXPHOS, oxidative phosphorylation; P4, progesterone; PDC, pyruvate dehydrogenase complex; PDK1, pyruvate dehydrogenase kinase 1; PEP, phosphoenolpyruvate; PFK2, phosphofructokinase 2; PKM2, pyruvate kinase isozyme M2; PR+, progesterone receptor positive; pyr, pyruvate; RANK+, Receptor Activator of NFκB positive; RANKL, Receptor Activator of NFκB ligand; ROS, reactive oxygen species; SDH, succinate dehydrogenase; SIRT1, sirtuin 1; succ, succinate; TCA, tricarboxylic acid cycle; TFAM, mitochondrial transcription factor A; TNFα, tumor necrosis factor alpha; VEGF, vascular endothelial growth factor.

intracellular NAD+/NADH ratios across cells and tissues could take place *via* uptake regulation of lactate or pyruvate through nearly universally expressed MCT transporters from systemic circulation (41). Thus, in such a setting of excessive NAD+ over

NADH, cellular net uptake of lactate and simultaneous excretion of pyruvate would help alleviate intracellular redox imbalance. Notably, this scenario would require high lactate dehydrogenase (LDH) activity, the expression of which was indeed shown to be

upregulated in a BRCA1-mutated cell line (11). The generated NADH, in turn—both scarce and valuable due to low NADH output through TCA cycling—would likely be instantly shuttled into mitochondria *via* malate-aspartate or glycerol-3-phosphate shuttles in an attempt to produce energy *via* OXPHOS, further perpetuating increased cellular $NAD^+/NADH$ ratios. The significantly elevated pyruvate levels and reduced lactate:pyruvate ratios in plasma of g*BRCA1*+ individuals observed in our study may reflect on these alterations in co-factor balance and equilibrium adjustment.

In line with previously published data on *BRCA1*-driven metabolic rewiring, our results support a bioenergetic shift in g*BRCA1*+ individuals towards aerobic glycolysis, traceable even in the plasma metabolome of healthy g*BRCA1*+ carriers. Within the context of "adaptive oncogenesis," in which stromal tissue degradation sets the stage for cancer cell evolution *via* selection for adaptive phenotypes in heterogeneous populations of stem or progenitor cells (14), an excessively anabolic, pro-inflammatory, and pro-proliferative environment producing massive amounts of macromolecules from glycolysis and shuttling them to surrounding cells could provide the necessary growth advantage to adjacent (pre)-malignant cells that acquired the ability to import and thrive on these nutrients [a phenomenon known as the "reverse Warburg effect," reviewed in (15)].

The strengths of this study include a well-characterized cohort of g*BRCA1*+ and age-matched control subjects, comprising established family pedigrees as well as individual clinical information. We have collected standardized and documented high-quality biosamples, which were frozen within 2 h of blood draw. We were able to carefully select control subjects pursuant to their bland familial backgrounds, which contrasts conventional practice and is a privilege of this particular study. To avoid confounding factors, none of the study subjects had previously been diagnosed with malignant disease, nor were any diagnosed during the follow-up period.

Limitations include the following:

- Only two technical replicates per sample and no biological replicates were analyzed.
- Due to relatively small study size, the method is susceptible to errors, overfitting can occur, and study power is limited.
- Many metabolites lack a clear identity.
- Samples were not collected during identical menstrual cycle phases, e.g. luteal phase in which P4 levels are physiologically elevated and effects might be stronger.
- No clinical follow-up data were available for control subjects.
- Results were not validated in an independent validation cohort.

Future validation in an independent cohort and proteomics/transcriptomics analyses on plasma as well as metabolomics and other -omics analyses on breast tissue of g*BRCA1*+ carriers (preferably single cell analyses) are instrumental in further addressing currently hypothetic pathogenic mechanisms. Importantly, if proven correct, these complex disease mechanisms would yield multiple options for therapeutic targets and preventative measures in g*BRCA1*+ carriers. Moreover, the classifier prediction model of *BRCA1*+ status, if validated and enhanced, could have great implications for diagnostic genotype prediction independent of genetic testing or complementation of genetic testing in case of non-conclusive results, for personalized risk assessment, and for individual clinical measures.

DATA AVAILABILITY STATEMENT

The datasets presented in this study can be found in online repositories. The names of the repository/repositories and accession number(s) can be found in the article/**Supplementary Material**.

ETHICS STATEMENT

The studies involving human participants were reviewed and approved by the institutional ethics review board of Hannover Medical School. The patients/participants provided their written informed consent to participate in this study.

AUTHOR CONTRIBUTIONS

JPe, TR, and TI contributed to conception and design of the study. BS, BA, HW, KD, FW, and UH-B were involved in resource acquisition. NK and JPr organized the database. LS, PH, AM, and KH contributed to the acquisition of data. AM, MS, and KH performed the statistical analysis. JPe wrote the original draft of the manuscript. All authors contributed to the article and approved the submitted version.

SUPPLEMENTARY MATERIAL

The Supplementary Material for this article can be found online at: https://www.frontiersin.org/articles/10.3389/fonc.2021.627217/full#supplementary-material

REFERENCES

1. Shukla V, Coumoul X, Lahusen T, Wang RH, Xu X, Vassilopoulos A, et al. BRCA1 affects global DNA methylation through regulation of DNMT1. *Cell Res* (2010) 20(11):1201–15. doi: 10.1038/cr.2010.128

2. Bochar DA, Wang L, Beniya H, Kinev A, Xue Y, Lane WS, et al. BRCA1 is associated with a human SWI/SNF-related complex: linking chromatin remodeling to breast cancer. *Cell* (2000) 102(2):257–65. doi: 10.1016/s0092-8674(00)00030-1

3. Mullan PB, Quinn JE, Harkin DP. The role of BRCA1 in transcriptional regulation and cell cycle control. *Oncogene* (2006) 25(43):5854–63. doi: 10.1038/sj.onc.1209872

4. Liu S, Ginestier C, Charafe-Jauffret E, Foco H, Kleer CG, Merajver SD, et al. BRCA1 regulates human mammary stem/progenitor cell fate. *Proc Natl Acad Sci United States America* (2008) 105(5):1680–5. doi: 10.1073/pnas.0711613105

5. Kim H, Lin Q, Yun Z. BRCA1 regulates the cancer stem cell fate of breast cancer cells in the context of hypoxia and histone deacetylase inhibitors. *Sci Rep* (2019) 9(1):9702. doi: 10.1038/s41598-019-46210-y

6. Martinez-Outschoorn UE, Balliet R, Lin Z, Whitaker-Menezes D, Birbe RC, Bombonati A, et al. BRCA1 mutations drive oxidative stress and glycolysis in the tumor microenvironment: implications for breast cancer prevention with antioxidant therapies. *Cell Cycle* (2012) 11(23):4402–13. doi: 10.4161/cc.22776

7. Jackson KC, Gidlund EK, Norrbom J, Valencia AP, Thomson DM, Schuh RA, et al. BRCA1 is a novel regulator of metabolic function in skeletal muscle. *J Lipid Res* (2014) 55(4):668–80. doi: 10.1194/jlr.M043851

8. Tang X, Lin CC, Spasojevic I, Iversen ES, Chi JT, Marks JR. A joint analysis of metabolomics and genetics of breast cancer. *Breast Cancer Res BCR* (2014) 16(4):415. doi: 10.1186/s13058-014-0415-9

9. Vazquez-Arreguin K, Maddox J, Kang J, Park D, Cano RR, Factor RE, et al. BRCA1 through Its E3 Ligase Activity Regulates the Transcription Factor Oct1 and Carbohydrate Metabolism. *Mol Cancer Res MCR* (2018) 16(3):439–52. doi: 10.1158/1541-7786.MCR-17-0364

10. Chiyoda T, Hart PC, Eckert MA, McGregor SM, Lastra RR, Hamamoto R, et al. Loss of BRCA1 in the Cells of Origin of Ovarian Cancer Induces Glycolysis: A Window of Opportunity for Ovarian Cancer Chemoprevention. *Cancer Prev Res* (2017) 10(4):255–66. doi: 10.1158/1940-6207.CAPR-16-0281

11. Privat M, Radosevic-Robin N, Aubel C, Cayre A, Penault-Llorca F, Marceau G, et al. BRCA1 induces major energetic metabolism reprogramming in breast cancer cells. *PloS One* (2014) 9(7):e102438. doi: 10.1371/journal.pone.0102438

12. Concolino A, Olivo E, Tamme L, Fiumara CV, De Angelis MT, Quaresima B, et al. Proteomics Analysis to Assess the Role of Mitochondria in BRCA1-Mediated Breast Tumorigenesis. *Proteomes* (2018) 6(2):16 doi: 10.3390/proteomes6020016

13. Cuyas E, Fernandez-Arroyo S, Alarcon T, Lupu R, Joven J, Menendez JA. Germline BRCA1 mutation reprograms breast epithelial cell metabolism towards mitochondrial-dependent biosynthesis: evidence for metformin-based "starvation" strategies in BRCA1 carriers. *Oncotarget* (2016) 7(33):52974–92. doi: 10.18632/oncotarget.9732

14. Liggett LA, DeGregori J. Changing mutational and adaptive landscapes and the genesis of cancer. *Biochim Biophys Acta Rev Cancer* (2017) 1867(2):84–94. doi: 10.1016/j.bbcan.2017.01.005

15. Penkert J, Ripperger T, Schieck M, Schlegelberger B, Steinemann D, Illig T. On metabolic reprogramming and tumor biology: A comprehensive survey of metabolism in breast cancer. *Oncotarget* (2016) 7(41):67626–49. doi: 10.18632/oncotarget.11759

16. Erez A, DeBerardinis RJ. Metabolic dysregulation in monogenic disorders and cancer - finding method in madness. *Nat Rev Cancer* (2015) 15(7):440–8. doi: 10.1038/nrc3949

17. Hanahan D, Weinberg RA. Hallmarks of cancer: the next generation. *Cell* (2011) 144(5):646–74. doi: 10.1016/j.cell.2011.02.013

18. Salem AF, Howell A, Sartini M, Sotgia F, Lisanti MP. Downregulation of stromal BRCA1 drives breast cancer tumor growth via upregulation of HIF-1alpha, autophagy and ketone body production. *Cell Cycle* (2012) 11(22):4167–73. doi: 10.4161/cc.22316

19. van der Groep P, Bouter A, Menko FH, van der Wall E, van Diest PJ. High frequency of HIF-1alpha overexpression in BRCA1 related breast cancer. *Breast Cancer Res Treat* (2008) 111(3):475–80. doi: 10.1007/s10549-007-9817-z

20. van der Groep P, van Diest PJ, Smolders YH, Ausems MG, van der Luijt RB, Menko FH, et al. HIF-1alpha overexpression in ductal carcinoma in situ of the

21. Widschwendter M, Burnell M, Fraser L, Rosenthal AN, Philpott S, Reisel D, et al. Osteoprotegerin (OPG), The Endogenous Inhibitor of Receptor Activator of NF-kappaB Ligand (RANKL), is Dysregulated in BRCA Mutation Carriers. *EBioMedicine* (2015) 2(10):1331–9. doi: 10.1016/j.ebiom.2015.08.037

22. Widschwendter M, Rosenthal AN, Philpott S, Rizzuto I, Fraser L, Hayward J, et al. The sex hormone system in carriers of BRCA1/2 mutations: a case-control study. *Lancet Oncol* (2013) 14(12):1226–32. doi: 10.1016/S1470-2045(13)70448-0

23. Kiechl S, Schramek D, Widschwendter M, Fourkala EO, Zaikin A, Jones A, et al. Aberrant regulation of RANKL/OPG in women at high risk of developing breast cancer. *Oncotarget* (2017) 8(3):3811–25. doi: 10.18632/oncotarget.14013

24. Zaman T, Sun P, Narod SA, Salmena L, Kotsopoulos J. Plasma RANKL levels are not associated with breast cancer risk in BRCA1 and BRCA2 mutation carriers. *Oncotarget* (2019) 10(25):2475–83. doi: 10.18632/oncotarget.26810

25. Roig B, Rodriguez-Balada M, Samino S, Lam EW, Guaita-Esteruelas S, Gomes AR, et al. Metabolomics reveals novel blood plasma biomarkers associated to the BRCA1-mutated phenotype of human breast cancer. *Sci Rep* (2017) 7(1):17831. doi: 10.1038/s41598-017-17897-8

26. Yehia L, Ni Y, Feng F, Seyfi M, Sadler T, Frazier TW, et al. Distinct Alterations in Tricarboxylic Acid Cycle Metabolites Associate with Cancer and Autism Phenotypes in Cowden Syndrome and Bannayan-Riley-Ruvalcaba Syndrome. *Am J Hum Genet* (2019) 105(4):813–21. doi: 10.1016/j.ajhg.2019.09.004

27. Hiller K, Hangebrauk J, Jager C, Spura J, Schreiber K, Schomburg D. MetaboliteDetector: comprehensive analysis tool for targeted and nontargeted GC/MS based metabolome analysis. *Anal Chem* (2009) 81(9):3429–39. doi: 10.1021/ac802689c

28. Frank E, Hall M, Trigg L, Holmes G, Witten IH. Data mining in bioinformatics using Weka. *Bioinformatics* (2004) 20(15):2479–81. doi: 10.1093/bioinformatics/bth261

29. Sumner M, Frank E, Hall M. Speeding up logistic model tree induction. *Lect Notes Artif Int* (2005) 3721:675–83. doi: 10.1007/11564126_72

30. Nolan E, Vaillant F, Branstetter D, Pal B, Giner G, Whitehead L, et al. RANK ligand as a potential target for breast cancer prevention in BRCA1-mutation carriers. *Nat Med* (2016) 22(8):933–9. doi: 10.1038/nm.4118

31. Nolan E, Lindeman GJ, Visvader JE. Out-RANKing BRCA1 in Mutation Carriers. *Cancer Res* (2017) 77(3):595–600. doi: 10.1158/0008-5472.CAN-16-2025

32. Rao S, Cronin SJF, Sigl V, Penninger JM. RANKL and RANK: From Mammalian Physiology to Cancer Treatment. *Trends Cell Biol* (2018) 28(3):213–23. doi: 10.1016/j.tcb.2017.11.001

33. van Uden P, Kenneth NS, Rocha S. Regulation of hypoxia-inducible factor-1alpha by NF-kappaB. *Biochem J* (2008) 412(3):477–84. doi: 10.1042/BJ20080476

34. Wang RH, Zheng Y, Kim HS, Xu X, Cao L, Luhasen T, et al. Interplay among BRCA1, SIRT1, and Survivin during BRCA1-associated tumorigenesis. *Mol Cell* (2008) 32(1):11–20. doi: 10.1016/j.molcel.2008.09.011

35. Gomes AP, Price NL, Ling AJ, Moslehi JJ, Montgomery MK, Rajman L, et al. Declining NAD(+) induces a pseudohypoxic state disrupting nuclear-mitochondrial communication during aging. *Cell* (2013) 155(7):1624–38. doi: 10.1016/j.cell.2013.11.037

36. Palazon A, Goldrath AW, Nizet V, Johnson RS. HIF transcription factors, inflammation, and immunity. *Immunity* (2014) 41(4):518–28. doi: 10.1016/j.immuni.2014.09.008

37. Kim JW, Tchernyshyov I, Semenza GL, Dang CV. HIF-1-mediated expression of pyruvate dehydrogenase kinase: a metabolic switch required for cellular adaptation to hypoxia. *Cell Metab* (2006) 3(3):177–85. doi: 10.1016/j.cmet.2006.02.002

38. Nagao A, Kobayashi M, Koyasu S, Chow CCT, Harada H. HIF-1-Dependent Reprogramming of Glucose Metabolic Pathway of Cancer Cells and Its Therapeutic Significance. *Int J Mol Sci* (2019) 20(2):238. doi: 10.3390/ijms20020238

39. Li D, Chen NN, Cao JM, Sun WP, Zhou YM, Li CY, et al. BRCA1 as a nicotinamide adenine dinucleotide (NAD)-dependent metabolic switch in ovarian cancer. *Cell Cycle* (2014) 13(16):2564–71. doi: 10.4161/15384101.2015.942208

40. Di LJ, Fernandez AG, De Siervi A, Longo DL, Gardner K. Transcriptional regulation of BRCA1 expression by a metabolic switch. *Nat Struct Mol Biol* (2010) 17(12):1406–13. doi: 10.1038/nsmb.1941

41. Rabinowitz JD, Enerback S. Lactate: the ugly duckling of energy metabolism. *Nat Metab* (2020) 2(7):566–71. doi: 10.1038/s42255-020-0243-4

Conflict of Interest: MS was employed by the company Connexome Consulting.

The remaining authors declare that the research was conducted in the absence of any commercial or financial relationships that could be construed as a potential conflict of interest.

Rearrangements of Blood and Tissue Fatty Acid Profile in Colorectal Cancer - Molecular Mechanism and Diagnostic Potential

Adriana Mika[1,2], Katarzyna Duzowska[1], Lukasz P. Halinski[2], Alicja Pakiet[2], Aleksandra Czumaj[1], Olga Rostkowska[3], Malgorzata Dobrzycka[3], Jaroslaw Kobiela[3] and Tomasz Sledzinski[1*]

[1] Department of Pharmaceutical Biochemistry, Faculty of Pharmacy, Medical University of Gdansk, Gdansk, Poland, [2] Department of Environmental Analysis, Faculty of Chemistry, University of Gdansk, Gdansk, Poland, [3] Department of General, Endocrine and Transplant Surgery, Faculty of Medicine, Medical University of Gdansk, Gdansk, Poland

Colorectal cancer (CRC) is often diagnosed at an advanced stage due to the invasiveness of colonoscopy; thus, non-invasive CRC diagnostics are desirable. CRC is associated with lipid alterations. We aimed to verify whether fatty acid (FA) profiles in CRC patients may serve as a potential diagnostic tool for CRC diagnosis. FA profiles were assayed by GC-MS in cancer tissue, paired normal mucosa and serum from CRC patients and healthy controls. The levels of very long FAs – VLCFAs (26:0, 28:0 and 26:1) were the most highly increased FAs in cancer tissue compared to normal colon mucosa. Moreover, these FA were present in serum of CRC patients, they were absent in the serum of healthy subjects, or present in only trace amounts. To verify if cancer cells are the source of small amounts of these VLCFAs in the serum of patients we performed experiment in HT-29 CRC cells, which proved that CRC cells can produce and release VLCFAs into the blood. Most importantly, we defined a panel of FAs that may be assayed in a single analysis that definitely distinguishes CRC patients and healthy subjects, which was confirmed by PLS-DA and multivariate ROC analysis (AUC = 0.985). This study shows that selected FA panel may serve as a diagnostic marker for CRC.

Keywords: colorectal cancer, gas chromatography-mass spectrometry, fatty acid, lipids, PCA, PLS-DA

INTRODUCTION

Colorectal cancer (CRC) is among the most common cancers occurring worldwide. Despite the well-known benefits of early detection, CRC is often diagnosed at an advanced stage (1). CRC screening is commonly performed; however, the invasiveness and discomfort of the most effective diagnostic method – colonoscopy – are high. This results in unsatisfactory screening compliance, and only one-third of eligible patients are diagnosed at an early stage (2). To obtain higher screening compliance and, consequently, a higher survival rate and lower cost of treatment, a minimally invasive serum-based test for risk stratification, detection and staging of CRC is needed (2).

Biochemically, the cancer tissue of CRC patients is characterized by alterations in lipid metabolism including alterations in fatty acid profiles (3, 4).

Fatty acids (FAs) display different metabolic effects (5). Recently, studies have shown that certain FAs or their metabolites could serve as diagnostic tools for CRC (6–8), but more research needs to be conducted to confirm these results. Some studies indicate that certain FA levels change depending on the stage of disease (5). Recently, our study confirmed these observations and showed other alterations in the FA profile in colorectal cancer tissue (9). Fatty acid profile alterations, such as the presence of cerotic acid (6) and decrease in the concentration of hydroxylated, polyunsaturated ultra-long-chain fatty acids (10), can also be found in the sera of CRC patients.

To the best of our knowledge, few studies have analyzed the correlation between CRC stages and whole FA profiles (5, 11, 12). In this study, we performed an analysis of the whole FA profile obtained from the sera of CRC patients as well as CRC tissue using gas chromatography paired with mass spectrometry and analyzed the results to examine whether the whole FA profile may serve as a diagnostic tool for the detection of CRC. Moreover, to verify the hypothesis that CRC cells are a source of very long-chain FAs - VLCFAs (26:0, 26:1, and 28:0) that are found exclusively in patient sera, an experiment using HT-29 CRC cell cultures was performed. Advanced statistical methods, including principal component analysis (PCA), were used to analyze the data set (13).

MATERIALS AND METHODS

Patients

In this study, tissue samples from 92 CRC patients were included. Among them, we selected a subgroup of 44 CRC patients who were similar in terms of age to 35 healthy controls for the comparison of serum FA profiles in these two groups. The patients with stage I to IV CRC were treated with surgical resection of the large bowel segment. None of the patients received preoperative neoadjuvant treatment. The biochemical and clinical characteristics of the study subjects are presented in **Tables 1** and **2**. Tissue samples were collected from the tumor

and normal large intestinal mucosa within the resection margin that were at least 5 cm from the tumor interface. Normal and cancer tissue samples were obtained from the same patient. Each sample was divided into two parts. The part used for the FA analysis was frozen in liquid nitrogen immediately after collection and stored in aliquots at -80°C until analysis. The other part was used for histopathological examination with H&E staining that was performed to confirm the presence of cancer and normal mucosa. The protocol of the study was compliant with the Declaration of Helsinki of the World Medical Association and with approval from the Local Bioethics Committee at the Medical University of Gdansk (decision no. NKBN/487/2015). Written informed consent was obtained from all the patients prior to the study.

CRC Cell Supplementation With ^{13}C-18:0
The HT-29 cell line (human colon adenocarcinoma cells) was obtained from the American Tissue Culture Collection (ATCC) and cultured as described previously (14). An equal number of cells were seeded in 100 mm plates with standard medium or with medium + ^{13}C-18:0 (75 μM) for 24 and 72 h. ^{13}C-18:0 was dissolved in dimethyl sulfoxide (DMSO) and mixed with the standard medium 24 h before the experiment. Neither DMSO nor ^{13}C-18:0 had any effect on cell viability. After incubation, the culture medium was collected. Cells were washed with phosphate-buffered saline (PBS), detached from the plates by a trypsin/EDTA solution (0.05%/0.02%), and centrifuged at 700 × g for 5 min at 8°C. After discarding the supernatant, the cell pellet was resolved in PBS. Cells and culture media were frozen in liquid nitrogen immediately after collection and stored at −20°C for further analysis.

Fatty Acid Profile Analysis
Extraction of total lipids from tissue and serum samples was performed according to the method of Folch et al. (15). After lipid hydrolysis with KOH in methanol, washing with water/n-hexane, the n-hexane phase was evaporated to dryness under a stream of nitrogen. Free FAs were then methylated with 10% boron trifluoride. The FA methyl esters (FAMEs) were analyzed with GC-EI-MS QP-2010 SE (Shimadzu, Japan), as described by Mika et al. (14).

TABLE 1 | Biochemical characteristics of the study subjects.

Parameter	HC	CRC1	CRC2	p (HC vs CRC1)	p (HC vs CRC2)
Sex	17m/18f	50m/42f	24m/20f	–	–
Age (years)	53.3 ± 1.60	68.6 ± 1.26	57.3 ± 1.17	<0.001	0.057
BMI (kg/m^2)	26.6 ± 0.69	26.7 ± 0.59	26.8 ± 0.64	0.835	0.789
CRP-hs (mg/L)	1.90 ± 0.22	4.43 ± 0.64	3.58 ± 0.77	<0.001	<0.001
Total serum cholesterol (mg/dL)	204 ± 7.69	171 ± 6.02	189 ± 8.72	<0.001	0.008
Triacylglycerols (mg/dL)	129 ± 10.5	126 ± 75.1	140 ± 14.8	0.154	0.077
HDL (mg/dL)	54.9 ± 2.29	41.9 ± 1.27	42.5 ± 1.88	<0.001	<0.001
LDL (mg/dL)	123 ± 6.90	111 ± 4.61	126 ± 7.32	<0.001	<0.001
Glucose (mg/dL)	99.8 ± 3.98	112 ± 3.79	110 ± 4.16	0.028	0.065
Albumin (g/dL)	3.98 ± 0.44	3.34 ± 0.72	3.43 ± 1.11	<0.001	<0.001
Total protein (g/dL)	7.43 ± 0.083	6.51 ± 0.14	6.59 ± 0.21	<0.001	0.001

HC, healthy controls; CRC1, whole group of CRC patients; CRC2, subgroup of CRC patients, that do not differ in terms of age from HC group, from whom serum was analyzed. BMI, body mass index; CRP-hs – high-sensitivity C-reactive protein; HDL, high density lipoprotein; LDL, low density lipoprotein; SEM, standard error of the mean. Values are mean ± SEM.

TABLE 2 | Clinical characteristics of the CRC patients.

Parameter	CRC1	CRC2
Location of primary tumor		
Cecum	19	11
Ascending colon	10	2
Transverse colon	11	3
Descending/proximal sigmoid colon	20	13
Cecum AND Descending/proximal sigmoid colon	1	0
Rectosigmoid	15	5
Rectum	16	10
T stage		
T1	5	3
T2	18	10
T3	57	25
T4	12	6
UICC stage		
I	18	10
II	27	14
III	33	12
IV	14	8
Lymph node status		
N0	48	26
N1/N2	44	18
Degree of differentiation		
Well differentiated	7	6
Moderately differentiated	75	34
Poorly differentiated	10	4

CRC1, whole group of CRC patients; CRC2 – subgroup of CRC patients, that do not differ in terms of age from healthy control group, from whom serum was analyzed. T stage, tumor stage; UICC stage, Union for International Cancer Control stage.

SIM Analysis of the Products of the Conversion of ^{13}C-Labelled Stearic Acid in HT-29 Cells

The extraction and hydrolysis of lipids from HT-29 CRC cells treated with ^{13}C-18:0 and media and the derivatization of FAs into FAMEs were performed as mentioned above. Characteristic fragment ions were selected to identify product elongation and the desaturation or shortening of ^{13}C-labelled stearate, including saturated FA (SFA) and monounsaturated FA (MUFA) from 14:0 to 32:0. We did not analyze the characteristic fragment ions of polyunsaturated FA (PUFA), since in human cells, PUFA cannot be produced from SFA or MUFA (16). The fragment ions were analyzed by GC-MS with selective ion monitoring (SIM). The overall run time of the analysis was 67.5 min, and the column temperature was set between 60-310°C. The chromatographic and mass conditions of GC-MS analysis remained the same. Least squares regression analysis was implemented by comparing the peak area ratios to the increasing standard concentrations to obtain calibration linearity.

Statistical/Chemometric Analysis

The statistical significance of the differences in the study parameters was verified with a paired Student's t-test (cancer tissue vs. normal colorectal mucosa) for data with a normal distribution, and a Wilcoxon signed-rank test was used for data with a non-normal distribution. The differences were considered significant at $p < 0.05$. The results are presented as the means ± standard error of the mean (SEM). All statistical calculations were carried out with SigmaPlot software (Systat, Software Inc., San Jose, CA, USA).

The chemometric data analysis was carried out using the computing environment R (17) (R Core Team). Two-way hierarchical cluster analysis (HCA) was carried out using the mixOmics package (18). Cluster analysis was performed using the Ward method, with the squared Euclidean distance used as the measure of similarity. Principal component analysis (PCA) was performed using the FactoMineR package (19) with the factoextra package for data visualization. All data matrices were autoscaled before the analysis. The PCA results were statistically processed using an unpaired t-test, and differences were accepted as statistically significant at $p < 0.01$. The PLS-DA models and ROC analysis were generated with the application MetaboAnalyst 4.0 (20).

RESULTS

Serum Fatty Acid Profile

The results of the basic lipidogram analysis revealed dyslipidaemia in CRC patients, in contrast to healthy controls (HC) (**Table 1**). Due to the limited information obtained based on the lipoprotein fractions, we used another method to determine the lipidome of CRC patients. The more advanced analysis of the FA profile by mass spectrometry showed that the content of some individual FAs in the serum of HC and CRC patients was very different (**Table 3**). The total monounsaturated fatty acids (MUFAs) were increased in the serum of CRC patients, mostly due to the increased amount of 18:1. However, it should be noted that despite the strong significance of the difference in serum 18:1 between HC and CRC patients, this difference was not large – it was only approximately 8%.

Among the polyunsaturated fatty acids (PUFA) group, we observed significantly decreased alpha-linolenic acid (ALA) in the serum of CRC patients, and in the case of linoleic acid (LA), a downward trend was observed (**Table 3**). Among saturated fatty acids (SFAs) cerotic acid (26:0) was detected only in trace amounts in the HC group, unlike the CRC group, whereas montanic acid (28:0) was not observed in the HC group at the LOD or LOQ level of the analytical instrument used for GC-MS analysis and was detected in trace amounts in the serum of CRC patients (**Table 3**). Furthermore, the representative of VLCFA from the MUFA group – hexacodenoic acid (26:1) – was not detected in serum from HCs and was present in small amounts in CRC patients. In turn, FAs with shorter chains (11:0, 12:0, 13:0, and 14:0) were detected at levels in the serum of CRC patients that were several-fold lower than those in HCs, which is similar to the results for several representatives of branched chain FA (BCFAs) (**Table 3**).

Fatty Acid Profile in Cancer Tissue and Normal Colon Mucosa

Then, we analyzed the FA profiles in the tumor tissue and paired normal colon mucosa of every CRC patient. We found significant differences between the normal mucosa and cancer tissue (**Table 4**). The levels of MUFA were significantly

TABLE 3 | Fatty acids profile (%) in serum of healthy controls (HC) and CRC patients.

	HC n=35	CRC n=44	p
10:0	0.021 ± 0.001	0.019 ± 0.006	0.804
12:0	0.25 ± 0.019	0.14 ± 0.016	<0.001
14:0	1.20 ± 0.051	0.88 ± 0.059	<0.001
16:0	23.3 ± 0.29	23.3 ± 0.33	0.966
18:0	7.25 ± 0.12	6.88 ± 0.16	0.073
20:0	0.078 ± 0.004	0.088 ± 0.005	0.113
22:0	0.15 ± 0.008	0.17 ± 0.009	0.151
24:0	0.14 ± 0.006	0.14 ± 0.009	0.906
26:0	traces	0.020 ± 0.007	–
28:0	ND	traces	–
Total ECFA	**32.4 ± 0.31**	**31.7 ± 0.32**	**0.103**
11:0	0.013 ± 0.001	0.005 ± 0.001	<0.001
13:0	0.027 ± 0.002	0.012 ± 0.002	<0.001
15:0	0.23 ± 0.009	0.23 ± 0.010	0.768
17:0	0.25 ± 0.007	0.25 ± 0.008	0.954
19:0	0.031 ± 0.002	0.019 ± 0.002	<0.001
21:0	0.014 ± 0.001	0.013 ± 0.001	0.395
23:0	0.056 ± 0.003	0.050 ± 0.004	0.190
Total OCFA	**0.63 ± 0.017**	**0.58 ± 0.021**	**0.093**
13-methyl-14:0	0.031 ± 0.002	0.020 ± 0.002	<0.001
14-methyl-15:0	0.073 ± 0.003	0.054 ± 0.007	0.014
other iso-BCFA	0.13 ± 0.007	0.13 ± 0.008	0.717
Total iso BCFA	**0.24 ± 0.011**	**0.20 ± 0.014**	**0.063**
12-methyl-14:0	0.046 ± 0.002	0.032 ± 0.004	0.002
14-methyl-16:0	0.12 ± 0.007	0.067 ± 0.004	<0.001
20-methyl-22:0	0.003 ± 0.000	0.005 ± 0.001	0.061
Total anteiso BCFA	**0.17 ± 0.008**	**0.10 ± 0.008**	**<0.001**
Total SFA	**33.5 ± 0.30**	**32.6 ± 0.34**	**0.054**
14:1	0.075 ± 0.005	0.039 ± 0.004	<0.001
16:1	3.11 ± 0.16	3.02 ± 0.13	0.669
18:1	27.0 ± 0.50	29.2 ± 0.43	0.001
19:1	0.027 ± 0.002	0.021 ± 0.003	0.059
20:1	0.17 ± 0.007	0.16 ± 0.008	0.145
22:1	0.034 ± 0.004	0.021 ± 0.003	0.006
24:1	0.23 ± 0.017	0.24 ± 0.015	0.689
26:1	ND	0.001 ± 0.000	–
Total MUFA	**30.6 ± 0.57**	**32.7 ± 0.49**	**0.007**
CPOA2H	0.17 ± 0.005	0.11 ± 0.006	<0.001
ALA	0.34 ± 0.018	0.23 ± 0.017	<0.001
EPA	1.08 ± 0.13	0.87 ± 0.060	0.153
DHA	1.14 ± 0.076	1.43 ± 0.077	0.011
other PUFAn-3	0.39 ± 0.010	0.41 ± 0.016	0.301
Total PUFAn-3	**2.95 ± 0.20**	**2.94 ± 0.14**	**0.963**
LA	25.7 ± 0.61	24.2 ± 0.55	0.077
DGLA	1.16 ± 0.039	1.15 ± 0.056	0.821
ARA	5.60 ± 0.20	6.00 ± 0.211	0.175
AdA	0.10 ± 0.005	0.12 ± 0.014	0.134
other PUFAn-6	0.23 ± 0.008	0.19 ± 0.008	<0.001
Total PUFAn-6	**32.8 ± 0.63**	**31.7 ± 0.63**	**0.217**

Values are mean ± SEM. ND, not detected. AdA, adrenic acid (22:4 n-6); ALA, linolenic acid (18:3 n-3); ARA, arachidonic acid (20:4 n-6); BCFA, branched chain fatty acids; CPOA2H, cyclopropaneoctanoic acid 2-hexyl; DGLA, dihomo–linolenic acid (20:3 n-6); DHA, docosahexaenoic acid (22:6 n-3); DPA, docosapentaenoic acid (22:5 n-3); ECFA, even chain fatty acids; EPA, eicosapentaenoic acid (20:5 n-3); LA, linoleic acid (18:2 n-6); MUFA, monounsaturated fatty acids, OCFA, odd chain fatty acids; PUFA, polyunsaturated fatty acids; SFA, saturated fatty acids. Bold represents main groups of fatty acids.

decreased; however, very long n-6 PUFAs were found at higher levels in cancer tissues than in normal mucosa. In turn, the levels of n-3 PUFAs were almost two-fold higher in cancer tissues (**Table 4**). BCFAs, regardless of the tissue, were at the same levels, whereas the levels of odd chain fatty acids (OCFAs) were elevated in cancer tissues (**Table 4**). In cancer tissue, we observed a large accumulation of both saturated and monounsaturated VLCFAs compared to that in normal mucosal tissue. The

differences between the content of these VLCFAs in tumor comparing to normal tissue were the greatest and were up to 10-fold in the case of 26:1, so if cancer cells could release these VLCFAs outside the cell, one can expect that cancer cells are the source of small amounts of this VLCFA in the serum of patients. To verify this hypothesis, we performed an *in vitro* experiment using HT-29 CRC cells, which were treated with ^{13}C-labelled stearate (^{13}C-18:0).

TABLE 4 | Profile of fatty acids (%) in normal mucosa and CRC tissues.

	NORMAL tissue n=92	CANCER tissue n=92	p
16:0	21.6 ± 0.20	20.7 ± 0.22	<0.001
18:0	7.78 ± 0.27	11.9 ± 0.35	<0.001
20:0	0.17 ± 0.008	0.28 ± 0.014	<0.001
22:0	0.15 ± 0.011	0.27 ± 0.015	<0.001
24:0	0.14 ± 0.012	0.38 ± 0.026	<0.001
26:0	0.010 ± 0.001	0.051 ± 0.006	<0.001
28:0	0.002 ± 0.000	0.009 ± 0.001	<0.001
other ECFA	2.57 ± 0.09	1.92 ± 0.09	<0.001
Total ECFA	**32.4 ± 0.33**	**35.4 ± 0.36**	**<0.001**
15:0	0.32 ± 0.010	0.33 ± 0.012	0.497
17:0	0.34 ± 0.013	0.40 ± 0.014	<0.001
19:0	0.023 ± 0.001	0.041 ± 0.002	<0.001
21:0	0.014 ± 0.001	0.022 ± 0.002	<0.001
23:0	0.033 ± 0.003	0.069 ± 0.005	<0.001
Other OCFA	0.022 ± 0.001	0.022 ± 0.001	0.618
Total OCFA	**0.75 ± 0.023**	**0.88 ± 0.026**	**<0.001**
iso BCFA	0.24 ± 0.008	0.24 ± 0.008	0.753
anteiso BCFA	0.15 ± 0.007	0.15 ± 0.007	0.785
Total SFA	**33.6 ± 0.35**	**36.7 ± 0.37**	**<0.001**
16:1	4.57 ± 0.17	3.70 ± 0.12	<0.001
18:1	42.9 ± 0.57	36.0 ± 0.65	<0.001
20:1	0.63 ± 0.022	0.72 ± 0.032	0.011
22:1	0.054 ± 0.004	0.113 ± 0.007	<0.001
24:1	0.15 ± 0.01	0.43 ± 0.032	<0.001
26:1	0.002 ± 0.000	0.020 ± 0.002	<0.001
other MUFA	0.22 ± 0.014	0.13 ± 0.009	<0.001
Total MUFA	**48.5 ± 0.68**	**41.1 ± 0.72**	**<0.001**
CPOA2H	0.19 ± 0.007	0.20 ± 0.010	<0.001
ALA	0.037 ± 0.002	0.049 ± 0.004	0.003
EPA	0.26 ± 0.020	0.45 ± 0.028	<0.001
DHA	0.60 ± 0.03	1.07 ± 0.05	<0.001
other PUFAn-3	0.37 ± 0.014	0.63 ± 0.028	<0.001
Total PUFAn-3	**1.27 ± 0.06**	**2.20 ± 0.10**	**<0.001**
LA	11.6 ± 0.21	10.9 ± 0.23	0.012
DGLA	0.34 ± 0.03	1.19 ± 0.058	<0.001
ARA	3.55 ± 0.24	6.40 ± 0.32	<0.001
AdA	0.40 ± 0.02	0.84 ± 0.056	<0.001
other PUFAn-6	0.39 ± 0.027	0.40 ± 0.02	0.564
Total PUFAn-6	**16.4 ± 0.43**	**19.8 ± 0.48**	**<0.001**

Values are mean ± SEM. AdA, adrenic acid (22:4 n-6); ALA, α-linolenic acid (18:3 n-3); ARA, arachidonic acid (20:4 n-6); BCFA, branched chain fatty acids; CPOA2H, cyclopropaneoctanoic acid 2-hexyl; DGLA, dihomo-γ-linolenic acid (20:3 n-6); DHA, docosahexaenoic acid (22:6 n-3); ECFA, even chain fatty acids; EPA, eicosapentaenoic acid (20:5 n-3); LA, linoleic acid (18:2 n-6); MUFA, monounsaturated fatty acids, OCFA, odd chain fatty acids; PUFA, polyunsaturated fatty acids; SFA, saturated fatty acids. Boldface - major groups of fatty acids.

The Treatment of HT-29 CRC Cells With ^{13}C-Labelled Stearate

The characteristic fragment ions of the labelled products were identified by single ion monitoring (SIM) analysis, and their content was determined based on internal standards.

As presented in **Table 5**, the level of ^{13}C-labelled stearate in the medium during incubation decreased, which suggests that this FA is transported into cancer cells. This supposition is supported by the fact that [13]C-18:0 appears inside HT-29 cells during incubation (**Table 5**). Moreover, after 24 h and 72 h of incubation, we were able to detect other ^{13}C-FAs inside the cells, which means that [13]C-18:0 is metabolized into other FAs. The major product of ^{13}C-labelled stearate is 18:1, but we also found saturated VLCFAs with 20-30 carbons in their chains (**Table 5**), which suggests that the abovementioned FAs are the main products of 18:0 metabolism in CRC cells. Most importantly,

we found most of these FAs in the culture medium, and their levels increased during incubation (**Table 5**). These results revealed that CRC cells used [13]C-18:0 to produce VLCFAs and oleate, which were then released outside the cells into the medium. The other fatty acids mentioned in section *SIM Analysis of the Products of the Conversion of ^{13}C-Labelled Stearic Acid in HT-29 Cells* were not identified, which indicates that [13]C-18:0 is not metabolized into shorter SFAs (12:0, 14:0) and MUFAs (14:1, 16:1). The pathways of 18:0 conversion in CRC cells are summarized in **Figure 1**.

Examination of Diagnostic Potential of Fatty Acid Profile by Chemometric Methods

To examine whether the whole FA profile may potentially serve as a diagnostic tool for the detection of CRC, we performed

TABLE 5 | The amounts of ^{13}C labelled fatty acids (ng) in the media and HT29 CRC cells after culture.

		Fragment ions m/z	0h	24h	72h
MEDIUM	[13]C-18:0	76; 316	8210	456 ± 23.6	158 ± 14.4
	[13]C-20:0	76; 344	0	3.22 ± 0.37	6.68 ± 1.01
	[13]C-22:0	76; 372	0	2.26 ± 0.43	6.62 ± 1.89
	[13]C-24:0	76; 400	0	2.11 ± 0.33	17.9 ± 2.60
	[13]C-26:0	76; 428	0	1.47 ± 0.37	7.94 ± 2.16
	[13]C-28:0	76; 456	0	0.21 ± 0.04	0.41 ± 0.12
	[13]C-18:1	76; 314	0	13.5 ± 1.48	49.1 ± 6.98
HT-29 CELLS	[13]C-16:0	76; 288	0	0.92 ± 0.58	1.25 ± 0.08
	[13]C-18:0	76; 316	0	1433 ± 62.7	531 ± 13.9
	[13]C-20:0	76; 344	0	54.8 ± 3.65	28.6 ± 1.07
	[13]C-22:0	76; 372	0	28.2 ± 3.22	22.2 ± 1.27
	[13]C-24:0	76; 400	0	76.6 ± 11.71	70.5 ± 2.62
	[13]C-26:0	76; 428	0	30.2 ± 5.52	29.7 ± 1.49
	[13]C-28:0	76; 456	0	1.63 ± 0.30	1.57 ± 0.12
	[13]C-30:0	76; 484	0	traces	–
	[13]C-18:1	76; 314	0	336 ± 16.1	484 ± 5.07

Values are mean ± SEM.

multivariate analysis. The selection of the most appropriate principal components was based on differences in average PC values between patient groups (**Supplementary Table S1**). However, PCA showed that the whole FA profile in the serum of CRC patients was only partially different compared to that in the serum of healthy subjects (**Figure 2**). Therefore, the whole serum FA profile cannot serve as a standalone diagnostic tool.

The most promising FA, that were significantly different between HC and CRC patient serum, were selected on the basis of the results in **Table 3**. These 15 FAs were visualized by a heatmap using two-way hierarchical cluster analysis (**Figure 3**). The serum samples of CRC patients and HCs are clustered separately. This separation suggests that the profiles of selected FA are quite different between the two research groups.

FIGURE 1 | Pathways of conversions of labelled ^{13}C stearic acid in HT-29 CRC cell. The labelled ^{13}C stearic acid was added into HT-29 CRC cell culture, and during the incubation its level in medium was decreasing, whereas inside the cells was increasing. This indicate, that ^{13}C stearate has been absorbed by cancer cells. At the same time the labeled products of the metabolism of this FA (including VLCFA and oleic acid) appeared in the cells. Moreover, they appeared also in the medium, and their levels in medium was increasing. This experiment proved that CRC cells can synthesize oleic acid and VLCFA from stearic acid and release them outside the cell.

To examine whether multivariate analysis of the group of 15 selected FAs may potentially be used in diagnostics, a PLS-DA model was built (**Figure 4**). The VLCFAs 26:0, 28:0 and 26:1 were not included in this analysis because they were absent or present in only trace amounts in the sera of subjects from the HC group. An evident separation between these two groups can be easily observed for the first and second latent variables (LVs). The model was statistically significant at p < 0.05. Tridecanoic acid was identified as the FA with the highest coefficient score.

We also used ROC curves to evaluate the performance of the potential biomarkers among selected 15 FAs using univariate and multivariate analyses. **Supplementary Figure S1** presents the ROC curves of the 15 selected FAs for cancer patients. The accuracy and other parameters of the ROC analysis of each FA are shown in **Table S2**. The results of this analysis showed that among the serum FAs, 11:0, 13:0, 14:0, 19:0, 14:1, CPOA2H, 12-M-14:0, 14-M-15:0 and 14-M-16:0 were the best predictors of CRC (AUC > 0.8). The multivariate ROC analysis using a panel consisting of the same FAs as those used in the univariate ROC analyses showed the best predictive ability with a ROC area of 0.985 for the tested dataset (**Figure 5**).

We also performed PCA of the whole FA profile in the tissues of CRC patients. The analysis also showed only slight differentiation between normal and cancer tissue (**Supplementary Figure S2**), but we can see a group of cancer tissue samples that differ significantly from normal tissue samples in terms of the FA profile, which was mostly due to the elevations of the levels of some of the long-chain saturated, monounsaturated and polyunsaturated FAs. On the other hand, short-chain FAs and some of the branched compounds were present in larger amounts in normal tissues.
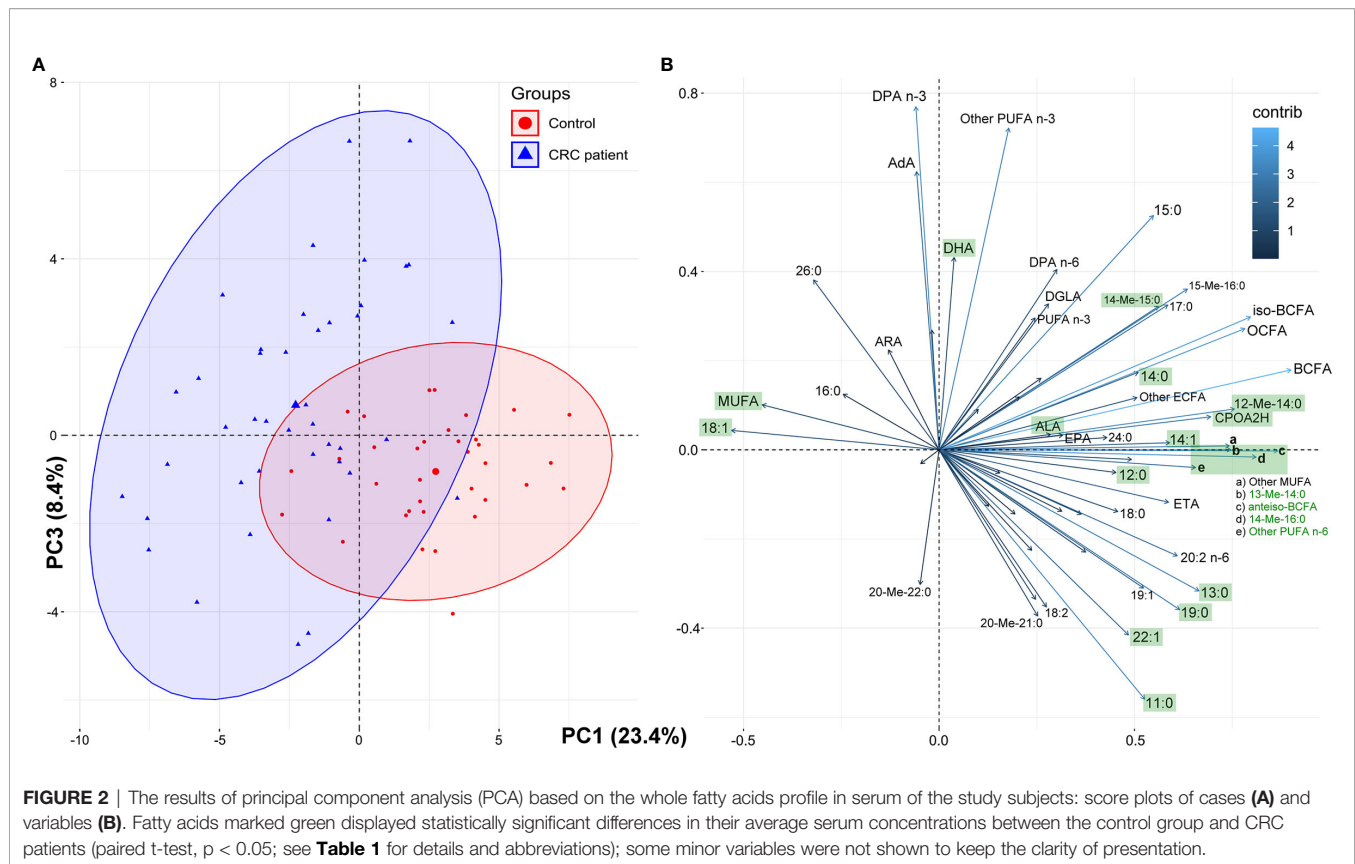
Upon analyzing the FA profiles in different stages of CRC development, the changes observed in the whole group of studied CRC subjects (**Table 2**) were also observed in particular stages of CRC (**Supplementary Table S3**). However, when comparing the FA profiles in cancer tissue from patients at each stage of CRC by analysis of variance (ANOVA), no statistically significant differences were found. Additionally, we did not find any differences between the FA profiles in cancer tissue samples from patients in different stages of CRC development *via* PCA (**Supplementary Figure S3**).

DISCUSSION

Our study has shown significant changes in the FA profiles in both the serum and tumor tissue of CRC patients. The different FA profiles in the serum of CRC patients compared to those in the serum of healthy subjects may constitute a potential diagnostic tool, whereas the differences in FA profiles between CRC tumor tissue and normal colon mucosa may enable the identification of the molecular mechanisms underlying the changes seen in the serum. The most notable modification in the serum FA profile of patients with CRC is the presence of the VLCFAs 26:0, 28:0 and 26:1, which are absent in the serum of healthy subjects (28:0 and 26:1) or present in only trace amounts

(26:0). This finding partially overlaps with that of our earlier study (6), which concerned the presence of 26:0 in the serum of CRC patients, but in this study, it was confirmed in a larger group of patients, and additional FAs (28:0 and 26:1) that are specifically found in the serum of CRC patients were identified. Moreover, in the present work, we attempted to discover the molecular mechanism underlying the occurrence of these specific VLCFAs in the blood of CRC patients. First, on the basis of the analysis of the FA profile in the cancer tissue of CRC patients and their normal colon mucosa, we found that the VLCFAs 26:0, 28:0 and 26:1 were the most highly increased FAs in cancer tissue compared to normal colon mucosa and were increased by 5-, 4.5- and 10-fold, respectively. We must bear in mind that the tumor constitutes a very small part of the CRC patient body. However, such a great increase in the content of the abovementioned VLCFAs may lead to an increase in their content in the blood, but this will only be the case if CRC cells are able to release these FAs into the bloodstream. The hypothesis of the CRC tumor origin of 26:0, 28:0 and 26:1 VLCFAs in the serum of CRC patients is also supported by our earlier study that showed the high overexpression of elongases ELOVL1 and ELOVL6 (elongation of very long chain fatty acids protein 1 and 6) in CRC tumors, which are responsible for the elongation of SFAs and MUFAs (6). However, these data allow us to speculate only on the mechanism of the occurrence of these VLCFAs in the serum of CRC patients. Thus, to experimentally verify our hypothesis, we used an *in vitro* model of HT-29 CRC cells. This experiment with ^{13}C-labelled stearate allowed us to track its conversion in CRC cells. The results of this experiment are summarized in **Figure 1**, and they proved that a) ^{13}C-18:0 enters CRC cells, b) ^{13}C-18:0 in CRC cells is transformed into ^{13}C-18:1 and ^{13}C VLCFAs and c) VLCFAs produced from ^{13}C-18:0 are released outside the cells. Thus, this *in vitro* experiment supports the hypothesis that CRC cells can produce and release VLCFAs into the blood and suggests that the VLCFAs 26:0, 28:0 and 26:1 in serum may be biomarkers of CRC. The question arises as to why CRC cells overproduce VLCFAs. A few studies have shown that elevated VLCFA in the cell membrane of cancer tissue compared to that of matched normal tissue is a common feature in various cancers (21). VLCFAs included in phospholipids and sphingolipids affect cell membrane structure and dynamics, which have an impact on cell size, division and differentiation as well as the membrane curvature (22). The long chain length of VLCFAs allows them to be simultaneously present in both leaflets of the lipid bilayer in the cell membrane, which stabilizes its curved shape (23). Moreover, the longer aliphatic chain of FA causes cell membranes to become more impervious (24). Knockdown of ELOVL1 increased apoptosis induced by anticancer drugs or UV (25). Thus, increased VLCFA synthesis in cancer cells may be a kind of protection against environmental factors that may cause cells to become "armored".

Other FAs that are significantly changed in the serum of CRC patients are those from the BCFA group. These FAs originate from food and intestinal bacteria and can probably be produced in human adipose tissue (26). According to Vlaeminck et al. (27)

FIGURE 2 | The results of principal component analysis (PCA) based on the whole fatty acids profile in serum of the study subjects: score plots of cases **(A)** and variables **(B)**. Fatty acids marked green displayed statistically significant differences in their average serum concentrations between the control group and CRC patients (paired t-test, p < 0.05; see **Table 1** for details and abbreviations); some minor variables were not shown to keep the clarity of presentation.

BCFAs display anticancer properties, so the decrease in their levels may promote cancer development. We also found increase in 18:1 in serum of CRC patients. Since 18:1 is the major component of TAG (28), this change may be related to the increased TAG concentration in CRC patients. However, based on the results of our *in vitro* experiment (see **Figure 1**) and the increased expression of stearoyl-CoA desaturase-1 (SCD1) in CRC tissue (29), the release of 18:1 from CRC cells may also contribute to its elevated level in serum. In contrast, in cancer tissue, 18:1 was observed in smaller amounts than those in normal mucosa. Our recent study suggests that this may be due to the high energy requirement of cancer cells during their rapid proliferation; 18:1, which is found in TAG, undergoes intensive β-oxidation as an energy source in CRC cells (9). We also found lower levels of ALA and a trend toward a decrease in LA. As we reported in our earlier paper (14), decreased levels of these essential FAs may result from preferential uptake by cancer cells. The increased expression of the enzymes involved in PUFA elongation (ELOVL2, -4, and -5) and desaturation (fatty acid desaturases FADS-1 and -2) in cancer tissue compared to those in normal mucosa suggests that ALA and LA are further metabolized into longer and more highly unsaturated PUFAs in cancer tissue (14). PUFAs are essential for the formation of cell membrane phospholipids during the rapid proliferation of cancer cells (29). The rapid proliferation of cells is responsible for their smaller size and the higher percentage of cell membrane content compared to cytosol content (30). Lipids are responsible

for at least 50% of the total membrane mass (31). This explains why in the present study, we found much higher SFA and PUFA levels (FAs that form cell membranes) in cancer tissue than in normal colon mucosa (**Table 4**).

As described above, our study suggests that 26:0, 28:0 and 26:1 may constitute potential tools for the non-invasive diagnosis of CRC. However, a good diagnostic tool should comprise as many parameters as possible. The method of FA profile analysis allows for the detection of over 40 different FAs in one analysis of human serum. Despite that multivariate PCA analysis of the whole FA profile in serum revealed that CRC patients and control subjects were not fully separated, a few statistical analyses using only the 15 FAs that were significantly different in serum between CRC patients and control subjects showed that these 15 FA may be considered as potential CRC biomarker. First, two-way hierarchical cluster analysis showed that this set of 15 FAs allowed us to separately cluster the controls and CRC patients. Second, both groups were well differentiated using advanced discrimination analysis (PLS-DA). Finally, the multivariate ROC curve analysis confirmed that this set of 15 FAs met the criteria of a very good diagnostic marker (AUC = 0.985). Moreover, our method allows us to combine this set of 15 FAs with 26:0, 28:0 and 26:1 in one GC-MS analysis. This indicates the particular value of our research; the good performance of the discriminant model presented here implies that CRC patients and healthy subjects may present with different lipidomic fingerprints. We discerned that these
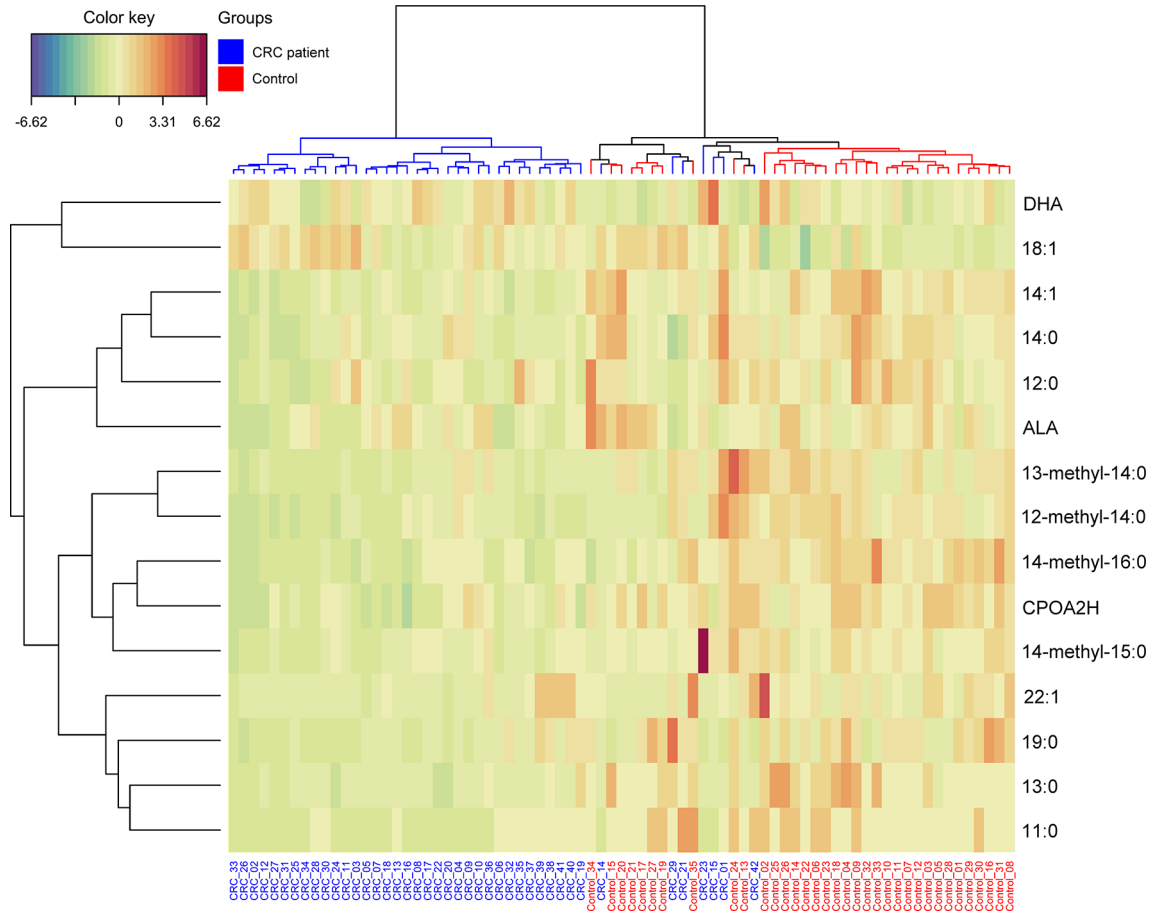
FIGURE 3 | Heatmap representing the relative levels of fatty acids among two tested groups. Warm colors on the heatmap indicate high content of a given FA in relation to the mean value in the whole dataset, while cold colors represent its low content when compared to the average. The serum samples of CRC patients and HCs are represented by blue and red, respectively.
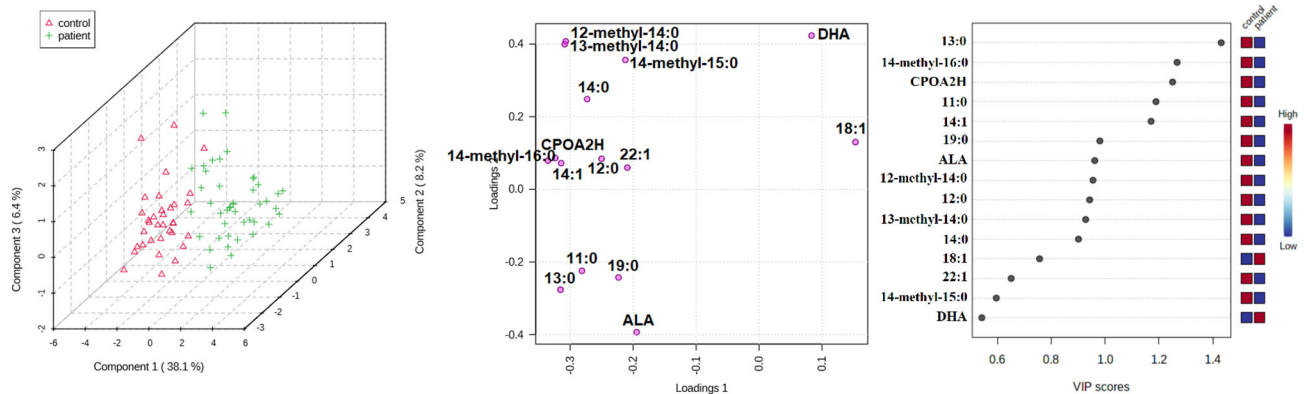
FIGURE 4 | Partial least squares regression (PLS-DA) model, biplot and VIP score for comparison of selected FA in serum of CRC patients and healthy controls.
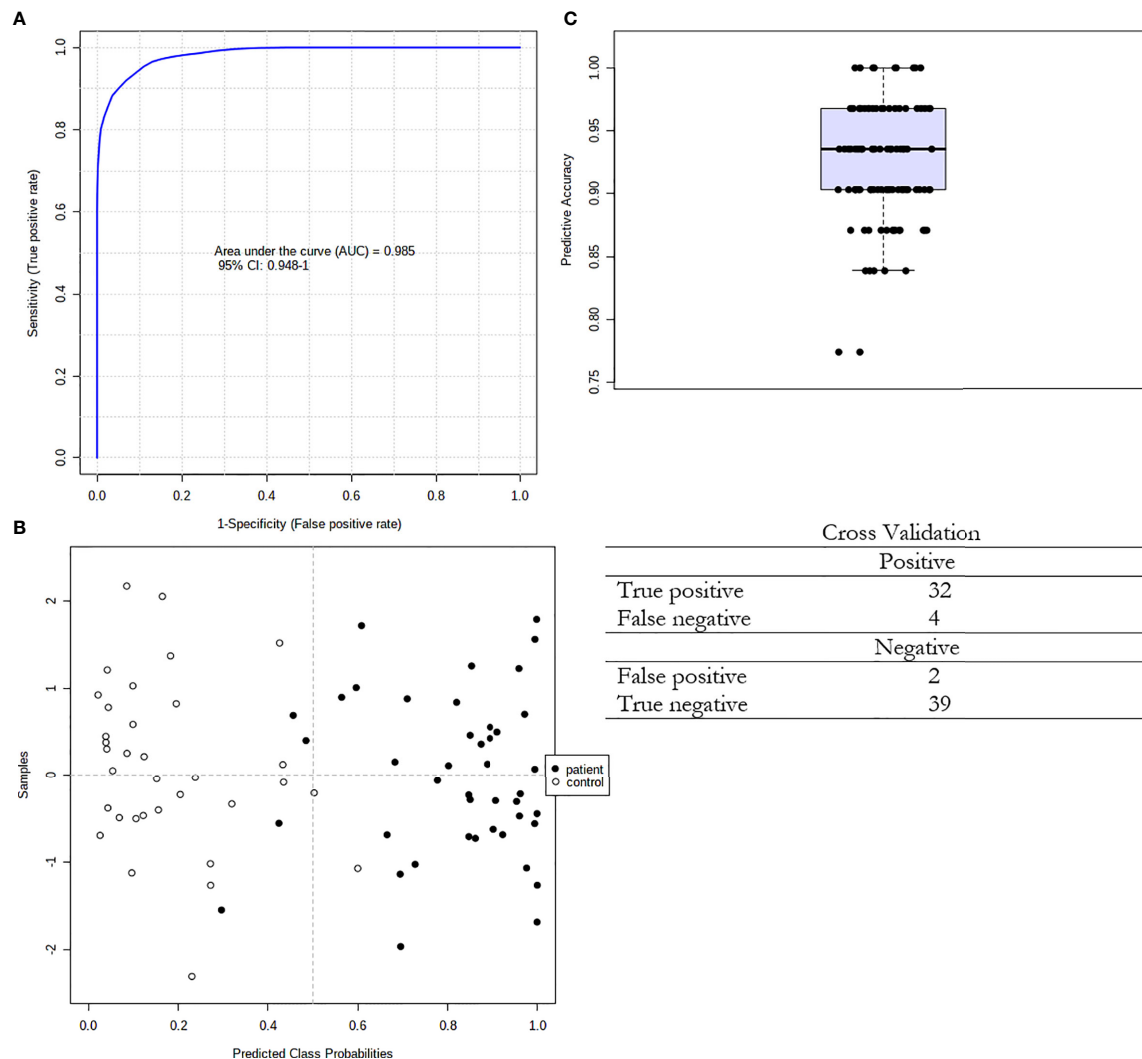
FIGURE 5 | Multivariate ROC curve exploration. **(A)** Plot of the ROC curve for the created biomarker model based upon its average performance across all Monte Carlo cross-validation runs. The 95 percent confidence interval can be computed; **(B)** Plot of the predicted class probabilities for all samples using the created biomarker model. Due to balanced subsampling, the classification boundary is at the centre (x=0.5, dotted line); **(C)** Box plot of the predictive accuracy of the created biomarker model. The average accuracy based on 100 cross validations is 0.924.

alterations in the evaluated FAs are due to the development of colorectal cancer.

The comparison of the FA profiles in cancer tissue and normal mucosa revealed that the contents of almost all FAs were different. These results indicate the complete alteration of the cancer tissue FA profile compared to that in normal mucosa. Unexpectedly, PCA of the FA profile in cancer tissue and normal mucosa did not show an unequivocal separation between the FA profiles in these two types of tissue. The possible reason for this apparent discrepancy is the high heterogeneity of the tumors and individual diversity. Most importantly, the results presented in **Table 4** were analyzed using a paired t-test, which means that the normal mucosa of every one of our 92 patients served as a control for his/her cancer tissue. PCA, as an unsupervised technique,

does not allow us to take into account that each sample of cancer tissue and normal mucosa was obtained from the same subject, so perhaps this type of analysis is not very good for paired samples. Indeed, some authors did not find significant differences in the lipidome composition in cancer tissue and normal colonic mucosa using PCA (32). However, different lipid profiles in patients with locally advanced, unrespectable or metastatic colorectal cancer compared with those in healthy volunteers were found by PCA by de Figueiredo Junior et al. (31). We also did not find significant differences between individual FAs (analyzed by ANOVA – **Supplementary Table S3**) and the whole FA profile (analyzed by PCA) in cancer tissue from patients in successive stages of CRC, which was possibly due to the reasons discussed above.

In conclusion our study revealed the partial alteration of the FA profile in the serum of CRC patients and the complete alteration of the cancer tissue FA profile compared to that in normal mucosa. We have confirmed in *in vitro* experiment that CRC cells are able to synthesize and release VLCFAs, that may serve as potential noninvasive CRC biomarker. These results indicate that neoplastic transformation of intestinal cells causes significant changes in FA metabolism. Moreover, these disorders can also affect the composition of FA in the blood. We have also defined of a panel of FAs that may be assayed in a single analysis together with abovementioned VLCFAs and can serve as a potential reliable diagnostic marker indicating the presence of CRC and the need for a colonoscopy. However, our results need to be confirmed in a larger group of CRC patients and healthy controls prior to introducing this new diagnostic approach for use in the clinic.

DATA AVAILABILITY STATEMENT

The datasets presented in this study can be found in the article and in the **Supplementary Material**.

ETHICS STATEMENT

The studies involving human participants were reviewed and approved by Local Bioethics Committee at the Medical University of Gdansk (decision no. NKBN/487/2015). The patients/participants provided their written informed consent to participate in this study.

AUTHOR CONTRIBUTIONS

FUNDING

SUPPLEMENTARY MATERIAL

The Supplementary Material for this article can be found online at: https://www.frontiersin.org/articles/10.3389/fonc.2021.689701/full#supplementary-material

REFERENCES

1. Henley SJ, Ward EM, Scott S, Ma J, Anderson RN, Firth AU, et al. Annual Report to the Nation on the Status of Cancer, Part I: National Cancer Statistics. *Cancer* (2020) 126:2225–49. doi: 10.1002/cncr.32802

2. Roy HK, Backman V, Goldberg MJ. Colon Cancer Screening: The Good, the Bad, and the Ugly. *Arch Intern Med* (2006) 166:2177–9. doi: 10.1001/archinte.166.20.2177

3. Yan G, Li L, Zhu B, Li Y. Lipidome in Colorectal Cancer. *Oncotarget* (2016) 7:33429–39. doi: 10.18632/oncotarget.7960

4. Cottet V, Vaysse C, Scherrer ML, Ortega-Deballon P, Lakkis Z, Delhorme JB, et al. Fatty Acid Composition of Adipose Tissue and Colorectal Cancer: A Case-Control Study. *Am J Clin Nutr* (2015) 101:192–201. doi: 10.3945/ajcn.114.088948

5. Zhang J, Zhang L, Ye X, Chen L, Zhang L, Gao Y, et al. Characteristics of Fatty Acid Distribution is Associated With Colorectal Cancer Prognosis. *Prostaglandins Leukot Essent Fat Acids* (2013) 88:355–60. doi: 10.1016/j.plefa.2013.02.005

6. Mika A, Kobiela J, Czumaj A, Chmielewski M, Stepnowski P, Sledzinski T. Hyper-Elongation in Colorectal Cancer Tissue – Cerotic Acid is a Potential Novel Serum Metabolic Marker of Colorectal Malignancies. *Cell Physiol Biochem* (2017) 41:722–30. doi: 10.1159/000458431

7. Kondo Y, Nishiumi S, Shinohara M, Hatano N, Ikeda A, Yoshie T, et al. Serum Fatty Acid Profiling of Colorectal Cancer by Gas Chromatography/ Mass Spectrometry. *Biomark Med* (2011) 5:451–60. doi: 10.2217/bmm.11.41

8. Zhang L, Chen B, Zhang J, Li J, Yang Q, Zhong Q, et al. Serum Polyunsaturated Fatty Acid Metabolites as Useful Tool for Screening Potential Biomarker of Colorectal Cancer. *Prostaglandins Leukot Essent Fat Acids* (2017) 120:25–31. doi: 10.1016/j.plefa.2017.04.003

9. Mika A, Pakiet A, Czumaj A, Kaczynski Z, Liakh I. Decreased Triacylglycerol Content and Elevated Contents of Cell Membrane Lipids in Colorectal Cancer Tissue: A Lipidomic Study. *J Clin Med* (2020) 9:1–11. doi: 10.3390/jcm9041095

10. Ritchie SA, Heath D, Yamazaki Y, Grimmalt B, Kavianpour A, Krenitsky K, et al. Reduction of Novel Circulating Long-Chain Fatty Acids in Colorectal Cancer Patients is Independent of Tumor Burden and Correlates With Age. *BMC Gastroenterol* (2010) 10:140. doi: 10.1186/1471-230X-10-140

11. Notarnicola M, Lorusso D, Tutino V, De Nunzio V, De Leonardis G, Marangelli G, et al. Differential Tissue Fatty Acids Profiling Between Colorectal Cancer Patients With and Without Synchronous Metastasis. *Int J Mol Sci* (2018) 19:962. doi: 10.3390/ijms19040962

12. Farshidfar F, Weljie AM, Kopciuk K, Buie WD, MacLean A, Dixon E, et al. Serum Metabolomic Profile as a Means to Distinguish Stage of Colorectal Cancer. *Genome Med* (2012) 4:1–13. doi: 10.1186/gm341

13. Abdi H, Williams LJ. Principal Component Analysis. *Wiley Interdiscip Rev Comput Stat* (2010) 2:433–59. doi: 10.1002/wics.101

14. Mika A, Kobiela J, Pakiet A, Czumaj A, Sokołowska E, Makarewicz W, et al. Preferential Uptake of Polyunsaturated Fatty Acids by Colorectal Cancer Cells. *Sci Rep* (2020) 10:1954. doi: 10.1038/s41598-020-58895-7

15. Folch J, Lees M, Sloane Stanley GH. A Simple Method for the Isolation and Purification of Total Lipides From Animal Tissues. *J Biol Chem* (1957) 226:497–509. doi: 10.1016/S0021-9258(18)64849-5

16. Czumaj A, Śledziński T. Biological Role of Unsaturated Fatty Acid Desaturases in Health and Disease. *Nutrients* (2020) 12:356. doi: 10.3390/nu12020356

17. R Core Team. *R: The R Project for Statistical Computing* (2019). Available at: https://www.r-project.org/ (Accessed July 5, 2019).

18. González I, Cao K-AL, Davis MJ, Déjean S. Visualising Associations Between Paired 'Omics' Data Sets. *BioData Min* (2012) 5:19. doi: 10.1186/1756-0381-5-19

19. Lê S, Josse J, Husson F. FactoMineR: An *R* Package for Multivariate Analysis. *J Stat Softw* (2008) 25:1–18. doi: 10.18637/jss.v025.i01

20. Xia J, Wishart DS. Web-Based Inference of Biological Patterns, Functions and Pathways From Metabolomic Data Using Metaboanalyst. *Nat Protoc* (2011) 6:743–60. doi: 10.1038/nprot.2011.319

21. Butler LM, Perone Y, Dehairs J, Lupien LE, de Laat V, Talebi A, et al. Lipids and Cancer: Emerging Roles in Pathogenesis, Diagnosis and Therapeutic Intervention. *Adv Drug Delivery Rev* (2020) 159:245–93. doi: 10.1016/j.addr.2020.07.013

22. Bach L, Faure JD. Role of Very-Long-Chain Fatty Acids in Plant Development, When Chain Length Does Matter. *Comptes Rendus - Biol* (2010) 333:361–70. doi: 10.1016/j.crvi.2010.01.014

23. Denic V. Weissman Js. A Molecular Caliper Mechanism for Determining Very Long-Chain Fatty Acid Length. *Cell* (2007) 130:663–77. doi: 10.1016/j.cell.2007.06.031

24. Uchida Y. The Role of Fatty Acid Elongation in Epidermal Structure and Function. *Dermatoendocrinol* (2011) 3:65–9. doi: 10.4161/derm.3.2.14662

25. Sassa T, Kihara A. Metabolism of Very Long-Chain Fatty Acids: Genes and Pathophysiology. *Biomol Ther (Seoul)* (2014) 22:83–92. doi: 10.4062/biomolther.2014.017

26. Pakiet A, Wilczynski M, Rostkowska O, Korczynska J, Jabłonska P, Kaska L, et al. The Effect of One Anastomosis Gastric Bypass on Branched-Chain Fatty Acid and Branched-Chain Amino Acid Metabolism in Subjects With Morbid Obesity. *Obes Surg* (2020) 30:304–12. doi: 10.1007/s11695-019-04157-z

27. Vlaeminck B, Fievez V, Cabrita ARJ, Fonseca AJM, Dewhurst RJ. Factors Affecting Odd- and Branched-Chain Fatty Acids in Milk: A Review. *Anim Feed Sci Technol* (2006) 131:389–417. doi: 10.1016/j.anifeedsci.2006.06.017

28. Matthan NR, Ip B, Resteghini N, Ausman LM, Lichtenstein AH. Long-Term Fatty Acid Stability in Human Serum Cholesteryl Ester, Triglyceride, and Phospholipid Fractions. *J Lipid Res* (2010) 51:2826–32. doi: 10.1194/jlr.D007534

29. Pakiet A, Kobiela J, Stepnowski P, Sledzinski T, Mika A. Changes in Lipids Composition and Metabolism in Colorectal Cancer: A Review. *Lipids Health Dis* (2019) 18:29. doi: 10.1186/s12944-019-0977-8

30. Akutsu N, Ooguri M, Onodera T, Kobayashi Y, Katsuyama M, Kunizawa N, et al. Functional Characteristics of the Skin Surface of Children Approaching Puberty:Age and Seasonal Influences. *Acta Derm Venereol* (2009) 89:21–7. doi: 10.2340/00015555-0548

31. de Figueiredo Junior AG, Serafim PVP, de Melo AA, Felipe AV, Lo Turco EG, da Silva IDCG, et al. Analysis of the Lipid Profile in Patients With Colorectal Cancer in Advanced Stages. *Asian Pac J Cancer Prev* (2018) 19:1287–93. doi: 10.22034/APJCP.2018.19.5.1287

32. Wang Y, Hinz S, Uckermann O, Hönscheid P, von Schönfels W, Burmeister G, et al. Shotgun Lipidomics-Based Characterization of the Landscape of Lipid Metabolism in Colorectal Cancer. *Biochim Biophys Acta - Mol Cell Biol Lipids* (2020) 1865:158579. doi: 10.1016/j.bbalip.2019.158579

Glioma Stem-Like Cells and Metabolism: Potential for Novel Therapeutic Strategies

Abigail Harland[1]*, Xia Liu[1], Mattia Ghirardello[2], M. Carmen Galan[2], Claire M. Perks[3†] and Kathreena M. Kurian[1*†]

[1] Brain Tumour Research Centre, Bristol Medical School, University of Bristol, Bristol, United Kingdom, [2] Galan Research Group, School of Chemistry, University of Bristol, Bristol, United Kingdom, [3] IGFs and Metabolic Endocrinology Group, Bristol Medical School, Translational Health Sciences, Southmead Hospital, University of Bristol, Bristol, United Kingdom

Glioma stem-like cells (GSCs) were first described as a population which may in part be resistant to traditional chemotherapeutic therapies and responsible for tumour regrowth. Knowledge of the underlying metabolic complexity governing GSC growth and function may point to potential differences between GSCs and the tumour bulk which could be harnessed clinically. There is an increasing interest in the direct/indirect targeting or reprogramming of GSC metabolism as a potential novel therapeutic approach in the adjuvant or recurrent setting to help overcome resistance which may be mediated by GSCs. In this review we will discuss stem-like models, interaction between metabolism and GSCs, and potential current and future strategies for overcoming GSC resistance.

Keywords: cancer stem cell (CSC), therapeutic strategies, cancer metabolism, glioma stem-like cell, metabolic reprogramming

INTRODUCTION

Innovative treatment approaches to Glioblastoma (GBM) have thus far been unsuccessful in part due to therapeutic resistance, resulting in disease recurrence (1). GBM is the most common intrinsic brain tumour in adults and is classed as the highest grade (IV) astrocytoma by the World Health Organisation (WHO) (2). Characteristic infiltration into surrounding structures of the brain as well as central necrotic regions can be identified using histopathological studies (2). Post diagnosis, GBM has a survival time of just 12-18 months in response to current chemoradiation protocols following surgical resection as outlined in the Stupp protocol (3–5). In addition, only around 5% of patients survive longer than 5 years post-diagnosis (5). Previously, GBMs have been categorised based on whether they derive from lower grade lesions, first defined by Scherer in the 1940s (2). The rapid and *de novo* development of aggressive lesions is defined as primary GBM, accounting for approximately 95% of cases and thought to develop in part from a defined set of oncogenic mutations (6). In contrast, secondary GBM cases have been identified as evolving from lower grade astrocytoma precursors, often distinguished by the presence of the isocitrate dehydrogenase 1 (*IDH1*) mutation and given a more favourable prognosis due to more frequent diagnosis in younger patients (6, 7).

To gain insight into the molecular drivers of GBM, studies have extensively profiled tumours, reporting both genetic and epigenetic mutations believed to play a part in tumour initiation and progression including loss of heterozygosity (LOH) 10q, amplification of epidermal growth factor

receptor (EGFR), deletion of *p16INK4a* and mutations in tumour protein 53 (*TP53*) and phosphatase and tensin homolog (*PTEN*) (6). Reports from The Cancer Genome Atlas (TCGA) have also provided insight for grade IV tumours, providing a comprehensive understanding of genetic, expression and epigenetic aberrations (8). Clustering GBM data for gene expression, survival and treatment response has identified distinct neoplasm subtypes. The classification of these phenotypic profiles varies between research groups but include: proneural (PN), proliferative, sometimes split into neural (N) and classical (C) and mesenchymal (MES) (9, 10). Complicating matters further, data inclusive of intratumoural heterogeneity through genomic multisampling, has revealed the presence of multiple co-existing subtypes within the same patient tumour (11).

In addition, the recognition that many cancers are defined by common hallmarks such as abnormal metabolic function, pioneered by Hanahan and Weinberg (2011), has provided the possibility that the differences between tumour and normal cells could be defined as therapeutic targets (12). Experimentally observed metabolic differences in GBM studies are thought to be a combined result of oncogenic drivers, the tumour microenvironment (TME) and the presence of distinct cell populations such as GSCs (13, 14). Despite controversial beginnings, the acceptance of a cell type with characteristics distinct from the tumour bulk conferring resistance to standard treatment has led to a widespread belief that the eradication of GSCs would hinder tumour initiation, reestablishment and greatly improve patient outcome (15, 16). Therefore, there is an increasing aim to understand the apparent intrinsic metabolic plasticity of these cells and their ability to adapt and compensate for extreme environmental stressors such as toxic chemotherapeutics (17). Furthermore, it is becoming increasingly clear from the field of cancer research that the combination of multiple therapies may be the most promising approach to overcome heterogenic treatment responses of different cells (18, 19).

The objective of this review is to investigate experimental evidence for GSC metabolic flexibility and particularly bioenergetic capacity in comparison with normal and tumour bulk cells. Due to the pressing need for increasing GBM survival beyond such dismal figures, this review also aims to give an overview of the rationale behind new metabolic strategies (both experimental and clinical) for GBM treatment, with a focus on the GSC population.

GSCs AND CANCER STEM-LIKE CELL MODELS

Cancer Stem Cells (CSCs), (see **Figure 1**- stem cell/hierarchical model) in some cases are thought to derive from the mutation of non-neoplastic stem cells, recapitulating certain stem cell properties and the potential to reconstitute a tumour through

unidirectional symmetric self-renewal of the CSC pool and asymmetric divisions to generate the differentiated tumour bulk (13, 20–22). However, contradictory experimental evidence has led to a contrasting model (see **Figure 1**- stochastic/clonal evolution model) in which the selective oncogenic mutation of any somatic cell could progressively accumulate mutations that produce a stem-like phenotype, forming several CSCs clones which have selective growth and evolutionary advantages over others (23–25). These linear models have since been hybridised (see **Figure 1**-plasticity model) with the suggestion that all the cells forming the tumour bulk have the potential to become CSCs through a dedifferentiation process (26, 27).

Singh et al. first described the concept of brain tumour initiating cells based on experimental data suggesting that only the Prominin 1/CD133+ population within GBM had the ability to initiate brain tumours in non-obese, diabetic/severe combined immunodeficiency (NOD/SCID) mice, compared with the CD133- negative population (13). Their group proposed that this glioma stem-like population may follow the unidirectional stem cell/hierarchical model of cell division described above, also reviewed by Singh et al. (13, 28). More recent evidence for this finding includes studies by Lan et al. in which lineage tracing and lentiviral DNA barcoding of NOD/SCID/IL2rγ^{null} mice implanted with GSC clones revealed the retention of a proliferative hierarchy (20). By contrast, subsequent studies have shown that the CD133-population also have brain tumour initiating properties, suggestive of potential non-hierarchical phenotypic alterations (29–32). Although the field recognises the challenge of identifying a single specific glioma stem marker (originally thought to be CD133) or combination of markers to define a specific developmental duration, it's possible that stochastic marker expression such as CD133, CD15 and CD44 could confer a survival advantage (33, 34). In this way, the plasticity model looks to be a more accurate description of the development and behaviour of these cells, giving rise to the vast heterogeneity observed within a GBM tumour (33). Suva et al. demonstrated that neurodevelopmental transcription factors: sex determining region Y box 2 (SOX2), oligodendrocyte transcription factor (OLIG2), POU domain class 3 transcription factor 2 (POU3F2) and spalt like transcription factor 2 (SALL2) can be used to artificially reprogramme single cell primary glioblastoma cultures to a stem-like state, provides evidence for central nervous system (CNS) cell susceptibility to hierarchical reversal (35, 36). Furthermore, other groups have used mathematical modelling to predict stem cell marker combinations which may reflect plasticity during glioblastoma growth and dictate phenotypic heterogeneity within the stem cell population (14). Collectively, this evidence has led to novel interpretations of the GBM energetic landscape consisting of intrinsic diverse transcriptional and epigenetic microstates as well as plasticity in response to extrinsic cues as one of the most challenging concepts to overcome for treatment success (represented in **Figure 2**) (14).
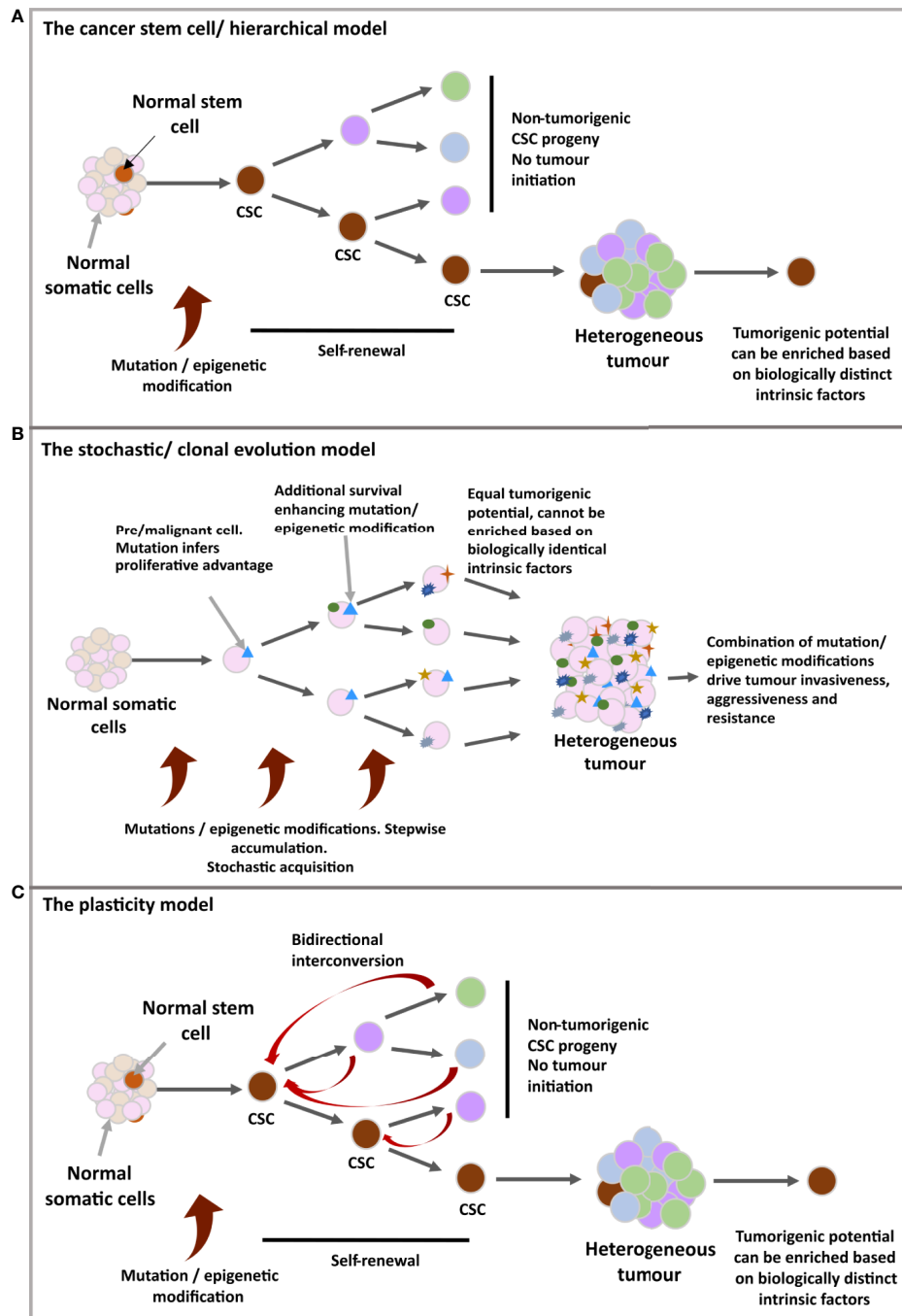
FIGURE 1 | (A) The cancer stem cell/hierarchical model: The CSC benefits from inherent stem cell features to support malignancy; unlimited clonal expansion and self-renewal. The self-maintaining CSC population(s) are believed to differentiate in a reversible manner, producing different tumoral populations of faster proliferating cells with limited lifespan. A hierarchy is set up in which CSCs define a biologically distinct subdivision of a tumour, giving rise to further behaviourally and functionally heterogenous, non-tumorigenic cells of the tumour bulk. **(B)** The stochastic/clonal evolution model: Following neoplastic induction *via* oncogenic mutation, rapid proliferation, in combination with cumulative mutation acquisition would give rise to variants with additional selective advantages. In this model, any malignant cell is assumed as having an equal probability for tumour initiation due to identical biological features and the stochastic nature of mutation acquisition, as well as the unpredictable influence of external cues on behavioural shifts. Therefore, tumour initiating ability cannot be isolated or enriched for. **(C)** The plasticity model: A more flexible model, 'merging' the two previous models. Possible incorporation for bidirectional interconversion between cellular potencies, including the retrodifferentiation of non-cancer stem cells to reacquire stem characteristics.
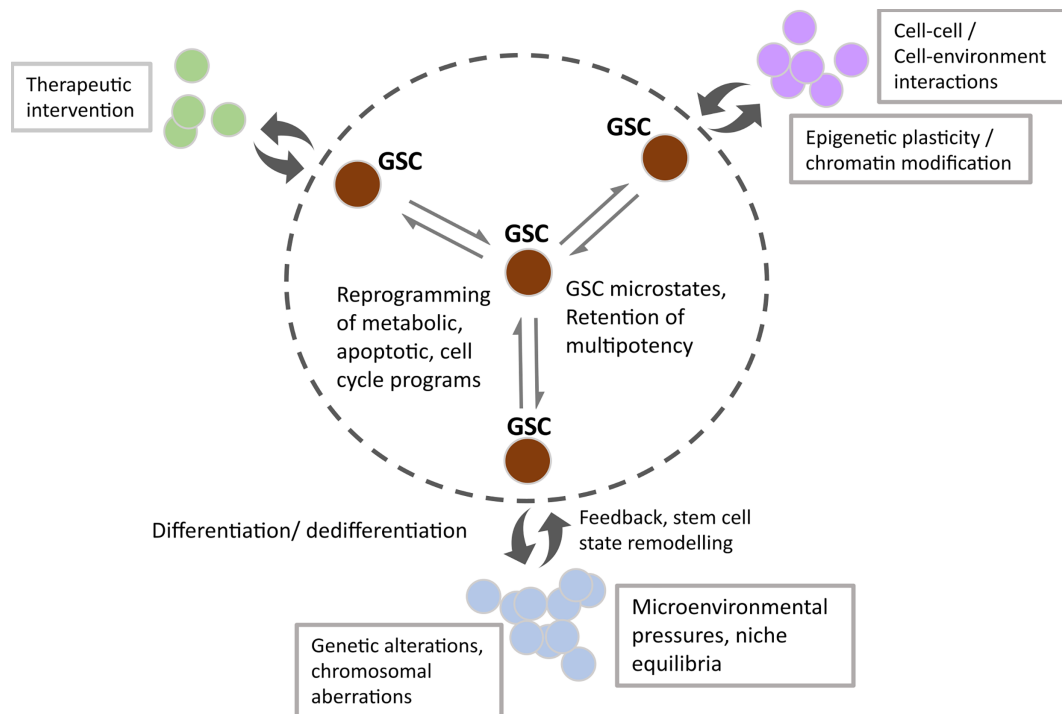
FIGURE 2 | Schematic showing the microstate transitions within the GSC population (within the circled dotted line) due to enhanced transcriptional and epigenetic potential, underpinned by extrinsic cues. Double headed arrows represent dynamic transitioning between GSC states, resulting in cellular reprogramming of metabolic, apoptotic and cell cycle programs. Non-tumorigenic subpopulations emerge due to the reversible differentiation and feedback of GSC states (double-headed curly arrows). Factors affecting transition state, subpopulation size and dynamic fluxing between states include external cues such as therapeutic intervention, cell-cell/cell-environmental interactions and spatial tissue characteristics. Intrinsic changes manifest as subpopulations with distinct genetic/chromosomal aberrations and epigenetic programmes.

ALTERED METABOLISM IN GSCs

Cellular metabolic reprogramming is considered a novel emerging hallmark of cancer as evidenced by Hanahan and Weinberg's 'Hallmarks of Cancer: The Next Generation' (2011) (12). The identification of malignant metabolic alterations conferring advantages for cellular growth and resistance has now become a major research aim, as reviewed by Tennant et al. (37). Experimental studies evidencing GSC superior resistance against current therapeutics have led to the suggestion that inherent metabolic plasticity allows these cells to adapt and compensate, and in some cases initiate the conversion of tumour bulk cells towards a stem-like phenotype to adopt this resistance (38, 39) (See **Figure 3** for a schematic representation of GSC metabolism). Therefore, it is important to consider that GSCs may be metabolically diverse from both normal somatic cells as well as cells of the tumour bulk, that have been well studied for malignant transformation of these processes.

In normal cells when oxygen is abundant, differentiated mammalian cells fully oxidise extracellularly imported glucose in a highly efficient series of reactions. Glucose uptake is regulated through glucose transporters (GLUTs) into the cellular cytoplasm where it can then be processed to pyruvate through multiple enzyme-catalysed reactions. Pyruvate can be

shuttled into the mitochondrial matrix for entrance into the tricarboxylic acid cycle (TCA) and oxidative phosphorylation (OXPHOS), yielding approximately 30/32 adenosine triphosphate (ATP) molecules for every molecule of glucose imported (40).

However, the early investigations into metabolic energy alterations in tumours by Otto Warburg and Carl and Gerty Cori in the 1920s revealed the paradoxical observation that cancer cells preferentially respire using glycolytic lactate production despite the presence of oxygen; later known as 'The Warburg effect' (41). This phenomenon, also referred to as the process of 'aerobic glycolysis' *i.e.* using anaerobic glycolysis in an oxidative environment, only yields approximately two molecules of (ATP) per glucose molecule. The finding has since precipitated widespread acceptance that increased glucose uptake is a shared cancer trait and can be exploited by positron emission tomography (PET) to inform clinical diagnosis of malignancy (42). PET measurements of glucose and oxygen processing in 14 patients with high grade tumours reported by Vlassenko et al. showed increased aerobic glycolysis that was associated with significant tumour proliferation and aggression, correlating with poor patient survival (43).

Since rapid cell division requires large concentrations of cytoplasmic macromolecular precursors for building new cells, it is believed that reducing glucose processing at pyruvate as

FIGURE 3 | Schematic showing some of the major metabolic pathways for GSC bioenergetic function and potential adaptability. The import of both glucose and glutamine are emphasised as the major nutrients available for cellular uptake though their respective transporters. Glucose is imported through the cellularly expressed glucose transporter, in this case either GLUT1 or GLUT3 and is enzymatically processed in the cytoplasm to pyruvate. Glycolytic processing can yield intermediate precursors largely subject to processing *via* the PPP – a majo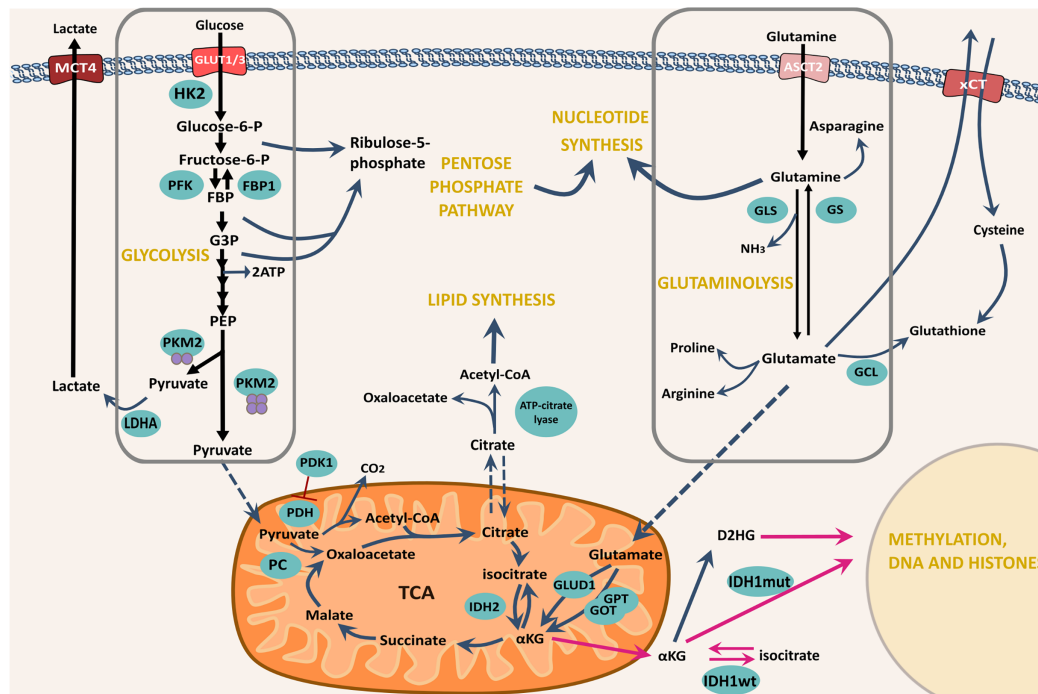r nucleotide synthesis pathway. Complete glycolytic processing to pyruvate is determined by the final enzymatic step - conversion of PEP by PKM2, yielding either lactate for export through MCT4 or pyruvate for mitochondrial entrance and processing *via* TCA and OXPHOS. In addition, Glutamine is imported *via* the ASCT2 transporter and enzymatically converted to glutamate *via* GLS. The reverse reaction is catalysed by GS. Direct conversion of Glutamate to cytoplasmic glutathione can take place *via* GCL, however, indirect conversion can also take place *via* xCT export, coupled to cystine import. Glutamate can be processed further to synthesise amino acids and lipids but can similarly be used for TCA anaplerosis *via* mitochondrial import and conversion to αKG by the transaminases *GPT* and *GOT* or GLUD. Black arrows represent glycolysis and glutaminolysis. Blue curly arrows represent the shuttling of intermediates from glycolysis and glutaminolysis and their processing by subsequent enzyme-catalysed reactions. Blue dashed arrows represent mitochondrial import/export. Magenta arrows represent the reactions that take place as a result of IDH1/2 mutations. αKG, α-ketoglutarate; ECT, Electron transport chain; FBP1, Fructose-1,6 bisphosphatase 1; G3P, Glyceraldehyde-3-phosphate; GCL, Glutamate-cysteine ligase; GLS, Glutaminase; GLUD1, Glutamate dehydrogenase; GLUT1/3, Glucose transporters 1/3; GOT, Glutamic oxaloacetic transaminase; GPT, Glutamate pyruvic transaminase; GS, Glutamine synthetase; HK2, hexokinase 2; IDH, Isocitrate dehydrogenase; LDHA, lactate dehydrogenase A; MCT4, Monocarboxylate transporter 2; OXPHOS, Oxidative phosphorylation; P, Phosphate; PC, Pyruvate carboxylase; PDH, Pyruvate dehydrogenase; PDK1- Pyruvate dehydrogenase kinase 1 PEP- Phophoenolpyruvate; PFK, Phosphofructokinase; PKM2, Pyruvate kinase M2, TCA, The citric acid cycle.

described by Warburg, facilitates the diversion of carbon through alternative biosynthetic processes (44). The pentose phosphate pathway (PPP) is mainly responsible for nucleotide biosynthesis and rapid flux has been described as a major driver of proliferation for the 'Warburg phenotype' (45). In fact, PPP functioning was shown by De Preter et al. to be instrumental in a range of malignancies such as SiHa human cervix squamous cell carcinoma using pharmacological inhibition and enzymatic siRNA knock down of the pathway, resulting in a dramatic decrease in proliferation (45). A combination of studies has also been instrumental in understanding that fine tuning between glycolytic and PPP flux can lead to phenotypic balancing in GSCs, with a hypoxia driven metabolic switch to non-oxidative glucose processing causing an initial reduction in PPP enzyme expression, provoking cell migration (46, 47). Moreover, investigations of cells exposed to long-term hypoxia showed that PPP enzymes vital for proliferation can become

upregulated, mirroring the phenotype of oxygenated GSCs from hypoxic culture, carried out by Kathagen et al. (46, 48). In addition to the PPP, ^{13}C nuclear magnetic resonance (NMR) spectroscopic analysis of patient high grade glioma samples obtained by Maher et al. revealed additional glucose shuttling into other enzymatic reactions for cellular glutamate, glutamine and glycine pool replenishment (49).

Key regulators of the Warburg phenotype have been investigated. Pyruvate kinase (PK) - the final control point in the glycolysis pathway, exhibits pivotal roles in sensing cellular metabolic state and functioning as a rate-limiting enzyme (50). In addition, the unequal expression of isoforms (PK-M1 and PK-M2) has been described for cancers including GBM, imperative for dictating the energetic fate of glucose (51, 52). Isoform expression analysis by Mukherjee et al. revealed a much greater PK-M1 expression in the normal brain, contrasting with PK-M2 in grade I-IV astrocytoma specimens. In addition

to this disparity, PK-M2 mRNA showed 3-5 times higher expression in GBM compared to grade I-III gliomas, indicating that dramatic increases in expression could enhance tumour severity (52). Constitutively active PK-M2 exists as a tetramer, favouring the production of pyruvate and TCA cycle processing for the production of ATP through OXPHOS (53). However, this enzyme is also susceptible to post-translational modification and allosteric regulation by fructose 1,6-bisphosphate (FBP) making it unstable and likely to exist as a dimer with lower affinity for phosphoenolpyruvate (PEP), promoting glycolytic intermediate accumulation (53). In fact, PKM2 has been used as a biomarker for GBM malignant growth in studies by both Witney et al. and Beinat et al. in which PET imaging with the experimental radiotracer 1-((2-fluoro- 6-[^{18}F]fluorophenyl)sulfonyl)-4-((4-methoxyphenyl)sulfonyl)piperazine ([^{18}F]DASA- 23) was used to assess the glycolytic response of cells to a range of current treatments (54, 55). The effectiveness of this radiotracer for diagnosis of suspected GBM cases is currently being investigated in a phase I clinical trial (trial identifier: NCT03539731).

ONCOGENIC DRIVERS OF AEROBIC GLYCOLYSIS IN GBM

Classically, oncogenic events have been examined for their role in the dynamic alteration of cellular metabolism and due to the ground-breaking description of the Warburg effect, the focus of many studies has been key drivers of this malignant process. There is an abundance of studies that illustrate a correlation between malignancy and increasing concentrations of glycolytic biosynthetic machinery such as GLUT1/3 and glycolytic enzymes for accelerated pathway flux (56, 57).

For GBM, common driver and tumour-suppressor genetic alterations include phosphoinisitide 3-kinase (PI3K) mutations for uncontrolled signalling, driving the continual activation of protein kinase B/Akt and leading to high rates of glucose import (58). Characteristic to GBM, upstream activation of PI3K often takes place through epidermal growth factor receptor (EGFR) via amplification or mutation as well as loss of PTEN antagonism (59). Crucially, PI3K/Akt signalling can be activated downstream of a wide array of growth factor receptors including platelet-derived growth factor receptor (PDGFR) – normally implicated in the mediation of tumoral proliferation predominantly in the PN GBM subtype (60). In contrast, the PDGFR has also been shown to regulate glycolysis in GSCs independently of proliferation (60). Constitutive Akt activation has been repeatedly implicated in tumoral glucose 'addiction', often being termed the main instigator of the aerobic switch, involved in elevated GLUT expression, membrane translocation and the regulation of carbon biosynthetic shuttling (58, 60).

In addition, changes in hexokinase (HK) expression have been reported in GBM studies such as those by Wolf et al., showing that higher GBM grades express higher levels of HK2 leading to the promotion of cell survival and growth (61). Moreover, siRNA knockdown of HK2 using intracranial xenografts conferred increased tumour invasion but less ability

to proliferate and carry out angiogenesis (61). Furthermore, transcription and growth factor studies in hepatocellular carcinoma cell lines have helped delineate signalling events that can give rise to HK2 expression, including cyclic adenosine monophosphate (cAMP), glucagon, mutant p53, insulin growth factor (IGF), hypoxia inducible factor-1α (HIF-1α) during hypoxia and Myc signalling (62, 63). PI3K/Akt signalling has also been shown to stimulate HK2-mediated cell survival via mitochondrial translocation and interaction with voltage-dependent anion channels in HeLa cells, preventing the binding of bcl-2-like protein 4 (BAX), and increasing the release of cytochrome C (64). A depleted level of HK2 antagonism by downregulation of miR-143 in GSCs has been established to increase the self-renewal potential of these cells in studies by Zhao et al. Lentiviral miR-143 transfection of GSCs by the group showed decreased tumorigenicity even under hypoxic culture, suggesting that loss of miR-143 is instrumental for GSC progression, favourably implicating miR-134 upregulation as a therapeutic target (65).

c-Myc has also been frequently described as another major driver of aerobic glycolysis, with overexpression causing the downstream upregulation of HK2, PKM2 and lactate dehydrogenase A (LDHA) in studies by Tateishi et al. (66). The mechanistic target of rapamycin complex 2 (mTORC2), a downstream nutrient sensor of Akt involved in the control of lipid and protein synthesis has also been shown to activate Myc in the absence of upstream Akt (67). Furthermore, the retrospective analysis of patients with brain metastases by Neider et al. showed elevated LDH levels, with additional studies in GBM showing that tumour derived LDH5 can confer immune escape by impeding the recognition of the tumour by natural killer cells (68, 69). Additionally, higher LDH-A expression in studies by Kim et al. using U87 GBM cells was shown to be associated with faster tumour growth kinetics, mirroring that of astrocytes (70). Moreover, the small molecule inhibition of LDH-A by Daniele et al. promoted cellular apoptosis in U87 cells as well as an induction of GSC differentiation of neurospheres (71).

Lastly, inherently characteristic to GBM categorisation, mutant IDH1/2 has a significant impact on tumoural prognosis (72). Wild type IDH catalyses the recognised TCA conversion of isocitrate to α-ketoglutarate (α-KG) and is predominantly associated with primary/de novo cases of GBM (73). α-KG can function as a co-factor for enzymes such as dioxygenases and histone demethylases involved in epigenetic modification (74). However, mutant IDH has been observed in more than 90% of secondary GBM cases, catalysing the conversion of isocitrate to the clinically recognised oncometabolite D-2-hydroxyglutarate (D-2-HG) (73, 75). D-2-HG is involved in the competitive inhibition of the α-KG dependent dioxygenases, leading to alterations in global deoxyribonucleic acid (DNA) hypermethylation [including O^6-methylguanine-DNA methyltransferase (MGMT) promoter methylation] and differentiation suppression (74, 76). In addition, IDH1 mutant glioma is associated with the CpG island methylator phenotype (CIMP) first described for colorectal cancer, and in GBM (G-CIMP) is associated with the PN molecular subtype (77–79). This mutation

is clinically associated with a higher frequency of occurrence in younger patients and largely correlates with longer overall survival time (7, 78, 80).

GSC METABOLIC RESILIENCE

Glucose Oxidation

In one of the first assessments of CSC metabolic states, Vlashi et al. studied the oxygen consumption rate and external acidification rate of GSC neurospheres derived from three independent GBM samples, compared with differentiated progenies cultured as monolayers (81). The group found that GSCs exhibited lower glucose uptake rates, lower lactate production, higher ATP levels and were therefore less glycolytic. Moreover, the group proposed that differentiation could induce a switch from a dominant use of OXPHOS for ATP production to glycolytic dependency (81). By contrast, GSCs derived in the same way from U87 tumours by Zhou et al. showed no significant difference in ATP levels in hypoxic versus normoxic conditions (82). When assessed under exclusive normoxia, elevated GSC lactate production was observed as well as a 4-fold increase in glucose uptake, suggestive of predominant glycolysis (82). Rationalisation of this result with findings from other GSC studies include the increased expression of neuronal GLUT3 by these cells for higher affinity glucose uptake, with GLUT3 knockdown in studies by Flavahan et al. conferring a significant decrease in the growth of GSCs (83). In addition, Zhou et al. showed that GSCs derived from two GBM surgical specimens expressed lower levels of voltage-dependent anion channel 2 (VDAC2) than the differentiated phenotype, believed to be essential for preservation of stem cell features, tumorigenicity and phosphofructokinase (PFKP) mediated glycolysis (84).

By collectively interpreting contrasting results from the GSC studies discussed, more detailed analysis reveals additional complexity, suggestive of heterogenous metabolic phenotypes within a single tumour (85). For example, Hoang-Minh et al.'s separation using CellTrace dyes and metabolic characterisation of GBM cell cycling speeds relative to bioenergetic strategy indicated that slow cycling cell (SCC) tumour populations, believed to be enriched in GSCs, were shown to survive predominantly using OXPHOS and lipid metabolism (86). SCCs derived from primary human GBM cell lines also displayed elevated chemoresistance and invasive capacity (86). Furthermore, a multitude of studies have recorded GSC metabolic subtype disparity, in which Gene Set Variation Analysis (GSVA) of TCGA GBM subtypes reveal that MES GBMs predominantly correlate with glycolytic pathways (87). Moreover, the metabolic enzyme analyses of MES GBM have revealed preferential glycolytic enzyme expression such as aldehyde dehydrogenase 1A3 (ALDH1A3) (87). This metabolic heterogeneity has been further highlighted by Duraj et al.'s application of 4 different metabolic drugs (metformin (MF), dichloroacetate, sodium oxamate and diazo-5-oxo-L-norleucine) to three GSC types, shown to exhibit different drug

sensitivities due to initial cellular glycolytic/oxidative tendencies (88).

The employment of updated techniques to directly quantify metabolites for metabolic flux analysis in vitro and in vivo has also catalysed an increased acceptance for metabolic plasticity, challenging the categorisation of discrete malignant metabolic phenotypes pioneered by Warburg (89). In more contemporary studies, Shibao et al. derived isogenic glioma initiating cells (GICs) from neural stem cells (NSCs) expressing the H-Ras^{V12} oncoprotein and showed that orthotopic primary tumour initiation was independent of initial cellular metabolic state and glycolytic enzyme expression (90). Furthermore, clonally derived GSCs from the same GIC 14 days post in vivo initiation showed tumour sustenance of metabolic diversity, thought to demonstrate the possibility for coexistence of GSCs with different bioenergetic strategies within the same tumour, relative to their environmental niche (90). Transcriptional up/downregulation of the glycolytic enzymes HK2, PKM2, LDHA and PDK1 were also recorded following the observation that cells were able to glycolytically compensate on exposure to hypoxia, and vice versa using OXPHOS after glycolytic inhibition, indicative of cellular metabolic coping mechanisms for continued biosynthesis (90).

Glutamate Metabolism

Regardless of the potential that the Warburg hypothesis brought for glycolytic inhibitor targeting, cancer cell survival and resistance remains a barrier to therapeutic success. As time has passed, the elucidation of a tangled cellular metabolic network has precipitated increasing futility of unimodal targeting strategies excluding tumoral heterogeneity and TME remodelling. Therefore, it is important to consider how the glycolytic pathway fits into a larger picture of cellular metabolism (**Figure 3**) and thus, isolated targeting of this pathway may be increasingly misjudging the tangled network of cell coping mechanisms. DeBerardinis et al. noted that simply observing a heavy cellular reliance on aerobic glycolysis may be accessory to a temporary metabolic strategy, facilitating the production of proliferative precursors as opposed to a complete impairment of the oxidative pathway (91). The group also illustrated that the catabolism of glutamine in addition to other carbon sources such as acetate shown by Mashimo et al. may be an imperative feature of Warburg's observed cancer cell phenotype, 'picking up' the burden of TCA anaplerosis and nicotinamide adenine dinucleotide phosphate (NADPH) synthesis for continued cell maintenance (91, 92).

Glutamine is an abundant plasma nutrient essential for cellular catabolic regulation, flux and processing of carbon, nitrogen and reducing equivalents (91). Integrating results from the study of GBM, other cancers and neurodegenerative disorders, a crucial balance between glutamine synthesis and catabolism has been recognised (93). Glutamine uptake by the alanine/serine/cysteine transporter 2 (ASCT2) transporter is followed by cytoplasmic glutaminase (GLS) conversion to glutamate and subsequent fate processing dependent upon cell requirements. Glutamate can be directly processed to the antioxidant glutathione via glutamate-cysteine ligase (GCL)

enzymatic combination with intracellular cysteine or exported though through xCT (cysteine/glutamate transporter) subject to cysteine import (94). The GBM xCT mediated export of glutamate has been shown to confer tumoural invasive expansion of rat striata implanted glioma cell clones with staining showing neuronal degeneration and inflammation of the surrounding TME (95). Moreover, immunoprecipitation analysis of three glioma cell lines and two primary human GBM cells by Tsuchihashi et al., revealed the control of xCT surface expression was subject to direct interaction with the EGFR intracellular domain, a mechanism which has since been further delineated by the group (96, 97). Glutamate is also instrumental for non-essential amino acid synthesis as well as purine and pyrimidine nucleotide precursors (94). Furthermore, glutaminolysis for the continued TCA flux and maintenance of biosynthetic intermediates has been a prominent feature in the study of cancer transformation.

In the healthy brain glutamine production *via* the glutamine synthetase (GS) catalytic condensation of glutamate and ammonia exclusively by astrocytes can be cooperatively utilised by neuronal GLS for glutamate hydrolysis and subsequent neurotransmission; termed 'the glutamine-glutamate cycle' (98). The ammonia utilised by GS is a product of amino acid breakdown and this enzyme is therefore essential for detoxification as well as uncontrolled neurotransmission through clearing glutamate from the synaptic cleft. However, importantly astrocytic *de novo* glutamate synthesis for neurotransmitter pool maintenance is dependent upon the enzyme pyruvate carboxylase (PC) and has been used as a specific marker of astrocytes. PC shuttling of glucose-derived pyruvate into the TCA for glutamate synthesis is subsequently converted to glutamine through GS.

An unmistakable metabolic adaptation drawn from glioma studies including GBM is an 'addiction' to glutamine for survival and growth, particularly in hostile conditions. *In vitro* experiments by Wise et al. using the paediatric GBM cell line SF188 revealed glutamine growth dependence, such that removal of glutamine from the culture medium inhibited cell survival despite the presence of glucose (99). This finding is well established for other cells including cancer with many early studies reporting cell survival in glutamine and nucleoside supplemented culture media in the absence of any sugar (100–102). Furthermore, inhibition of the established oncogenic drivers of glucose addiction PI3K and Akt by Wise et al. showed no effect on glutaminolysis mediation, precipitating the finding that elevated *MYC* expression resulted in upregulation of glutamine dependence genes (99). Myc was shown to stimulate increased *SLC1A5* (ASCT2) transcription for higher rates of uptake and glutamine mediated TCA anaplerosis, essential for the replenishment of precursors for growth limiting macromolecule synthesis (99). This data implied the possibility that anaplerotic nutrient use was driven by discrete oncogenic systems. Other studies to further analyse high *MYC* expression and nutrient dependence in a range of human cell lines including human lung fibroblasts and human lymphoblastoid cells have found that Myc dependent miR-23a and miR-23b transcriptional

repression upregulates GLS expression as well as sensitising cells to apoptosis during glutamine deprivation (103, 104).

Anaplerotic Balancing
Besides studies implicating glutamine as an extremely important molecule for TCA anaplerosis and cell survival, it is important to recognise that a balance exists between glucose, glutamine, and other cellular respiratory substrates. As mentioned for astrocytic systems, glucose can be catabolised to pyruvate and diverted away from PDH mediated entrance into the TCA, instead being carboxylated to oxaloacetate by PC. Nonetheless, observations consistent with the Warburg effect have rarely implicated glucose as the predominant precursor for neoplasm anaplerosis, supported by findings from metabolic flux experiments in well established "glutamine addicted" SF188 paediatric GBM cells with negligible PC activity (91). In fact, *in vitro* SF188 metabolic flux analysis has shown near exclusive nutrient favouring, with DeBerardinis et al. stating that cells derive up to 90% of anaplerotic oxaloacetate production from glutamine (91). Nonetheless, studies in human lung cancer tissue and hepatocellular carcinoma cell lines *in vivo* and *in vitro* respectively have evidenced preferential PC anaplerosis mediation, resulting in different sensitivities to experimental nutrient withdrawal (105, 106). As a result, some GBM experimental designs have since focussed on delineating neoplasm anaplerotic carbon source flexibility during nutrient deprivation. This is of clinical importance due to the potential for therapeutic confounding resulting from cellular complementation and survival mechanisms using alternative pathways (105). Accordingly, further analysis using GLS suppression in SF188 and adult LN229 GBM cell lines by Cheng et al. have since revealed that despite limited growth, cells are able to compensate using other GLS independent amidotransferase-catalysed glutamate generating pathways as well as glucose-derived carbon incorporation into TCA intermediates through PC (105). The additionally observed upregulation of PC after glutamine deprivation led the group to conclude: "PC is dispensable for growth of glutamine-replete glioblastoma cells, but required when glutamine supply is limited" (105).

Further to studies using single cell lines, the use of patient derived primary GBM samples has since been imperative for the delineation of tumoural metabolic heterogeneity. Metabolic analysis of 14 patient GBMs by Oizel et al. revealed phenotypic disparity and clustering as two distinct groups (107). One group exhibited substrate flexibility including glutamine utilisation for TCA directed nicotinamide adenine dinucleotide (NADH) formation, as well as higher expression of *SLC1A5*, *GLS* and Glutamic-Oxaloacetic Transaminase 1 (*GOT*) (107). The other exhibited glucose dependency for survival and growth. Substrate removal and substitution experiments revealed that the metabolically flexible phenotype was essential for maintaining cell proliferation when glucose was removed (107). In addition, the long-term inhibition of glutamine metabolism using the inhibitor, epigallocatechin gallate allowed cells to use glucose mediated TCA flux (107). Data such as these have been essential

for recognising the concurrent existence of cells with different substrate sensitivities within a whole tumour. Later, the group combined metabolic analysis with molecular subtyping data, revealing that cells with higher substrate flexibility and metabolic adaptation potential could be categorised as MES, whilst glucose dependent cells represented one of the other subtypes. Further extension of experiments to the U87 cell line associated with GSC features, conformed to the MES subtype and thus, exhibited glutamine-mediated anaplerotic shuttling (107). The MES subtype has been heavily implicated for hypoxic survival and represents a subset of GBM (9, 10). These findings correlate with experimental data from Flavahan et al. using patient derived GSCs confirmed by assessing self-renewal, proliferation and expression of stem cell markers to show the association of high GLUT3 expression with GSCs in the PN subtype (83). However, earlier isotopic analysis studies using ^{13}C mass spectrometry of isolated GSCs in neurospheres cultured from GBM orthotopic mouse models by Marin-Valencia et al. displayed rapid consumption of glucose for PC mediated anaplerosis and mitochondrial oxidation in addition to *de novo* glutamate production (108). Corresponding transcription data revealed the low expression of GLS in contrast to PC and GS levels, accessory to the observation that glucose-derived glutamate was used to maintain a large intracellular pool of glutamine, mediated by GS (108). Corroborating data from other studies have shown that GBM cells with high GS expression showed little to no reliance on extracellular glutamine uptake for growth preservation *via* glutaminolysis, but instead a dependence on *de novo* glutamine synthesis for intracellular pool replenishment (109). Assumptions based on this data have since exclusively defined GSCs as displaying high GS levels, contrary to data from Oizel at al. in which molecular subtyping is believed to be the more dominant driver of metabolic phenotype, with both GS-positive and GS-negative GSCs described (107, 109) Molecular subtyping of the GSCs studied by Marian-Valencia et al. would have revealed whether this data correlated with finding by Oizel et al., such that these cells showed subtyping distinct from the MES phenotype.

Nonetheless, combining these study outcomes, a distinction has been made between GBM cells displaying low GS levels as being mainly reliant on glutamine for TCA anaplerosis, with the ability to switch to largely glucose as a main substrate under glutamine repression (107). In contrast, GBM cells with high GS levels frequently defined as GSCs are believed to rely upon PC-mediated anaplerosis as a major source of glutamate GS mediated glutamine pool replenishment. In this way, these cells show major similarities to untransformed astrocytic systems in which PC and GS activities are required for glucose-derived glutamine pool maintenance, with little reliance on external glutamine uptake for cell proliferation. In studies by Tardito et al. proportionate protein levels were recorded for astrocytes and GS-positive GBM cells (109). The heavy reliance on *de novo* glutamate production as observed in GSCs with high GS expression, is believed to be an abundant source of nucleotide precursors for sustained purine biosynthesis (49, 108, 109).

GSCs as Astrocytic 'Parasites'/Metabolic Adaptability and the TME

Metabolic crosstalk between GBM cells and the stroma in the context of plastic substrate utilisation is essential for transformed cell survival during chaotic TME dynamics. In addition, studies evidencing the ability of subpopulations of tumour cells to adapt during nutrient restriction has led to investigations of cancer-stromal alliances in a range of cancers for survival (110–112). Tardito et al. reported low kinetic uptake of glutamine from the blood by GS-negative GBM cells and the healthy brain (109). Since GS-negative GBM cells have shown high glutamine uptake for anaplerotic pathways, orthotopic mouse models of GS-negative GBM revealed that other GS expressing tumour cells as well as astrocytes were a major source of the amino acid. Moreover, co-culture of astrocytes and GS negative LN18 GBM cells revealed growth sustenance based on astrocytic glutamine production in the absence of media supplementation (109). This data shows that subject to transformation, glutamine excreted into the TME for endogenous neuronal transmission, can instead support the growth of malignant cells that require a supply of metabolic nutrients. Furthermore, Kallenberg et al.'s magnetic resonance spectroscopy data illustrated a higher concentration of glutamine in the hemispheres of GBM patients relative to healthy controls, reported as a marker for early tumour infiltration (113). In addition, cross section staining for astrocytes and GS level of human derived GBM xenografts display a symbiotic positioning of astrocytes surrounding GS-negative GBM cells (109).

CLINICAL RELEVANCE – METABOLIC TARGETING

Glycolysis Inhibition – Targeting the Warburg Phenotype

The widespread acceptance of the Warburg effect as well as experimental evidence supporting this metabolic shift in GBM tumours has been instrumental for the emergence of glycolytic targeting strategies. Glucose uptake inhibition has been dominated by the use of GLUT1 antagonists such as indinavir and ritonavir, shown *in vitro* to reduce GBM cell proliferation including in GSC cell lines (114). However, despite the synergistic effect of ritonavir when combined with chemotherapeutics *in vitro*, both compounds are unable to effectively cross the blood brain barrier (BBB), and therefore not able to reach effective concentrations in the brain (114). Alternatives have included compounds such as 2-fluoro-6-(*m*-hydroxybenzoyloxy) phenyl *m*-hydroxybenzoate (WZB117), displaying successful *in vitro* inhibition of GSC self-renewal ability (115). However, despite the beneficial effects observed for the inhibition of this transporter, the robustness of the targeting strategy has been challenged due to widespread GLUT1 expression in the human brain and therefore potential for off target effects (116). Consequently, GLUT3 has since emerged as a more promising target with protein expression analysis by Flavahan et al. showing elevated levels of the

transporter in GSCs (83). Moreover, studies by Cosset et al. have interrogated GLUT3 expression further, showing that targeting with therapeutics may specifically inhibit classical/proneural cells within GBM tumours (117).

Other glycolytic inhibition strategies have included the suppression of HK2 with antifungals, as well as use of the glucose analogue 2-deoxy-D-glucose (2-DG) for competitive inhibition of cellular glucose uptake, and overall reduction in glycolysis (118, 119). The depletion in ATP production resulting from 2-DG treatment has been shown to promote cellular endoplasmic reticulum (ER) stress, followed by the unfolded protein response (UPR), similarly observed as an effect post radiotherapy (119). It is believed that GSCs have a greater ability to escape this stress with superior autophagic pathway promotion and reestablishment of ER homeostasis (120). Therefore, currently, there are efforts to promote tumour apoptosis by preventing autophagic and UPR mediated ER homeostasis reestablishment, with some groups finding that blocking ER stress altogether and the downstream protective mechanisms could enhance the cytotoxic effects of small therapeutic compounds such as shikonin (121). An increasingly established downstream effector of the UPR is 78-kDa glucose-regulated protein (GRP78) - a member of the heat shock protein family, instrumental for downstream activation of ER homeostasis regulators as well as observed cell surface translocation, characteristic of invasive cancers (119, 122). Whilst the translocation of GRP78 from the ER to the cell surface is not well understood, it is believed that GRP78 may also regulate cellular interactions with the surrounding TME (123).

The Ketogenic Diet

Further to treatment strategies requiring administration of small molecule inhibitors, the modification of patient dietary nutrient intake has become a potentially effective approach for diverting tumour metabolism, such as short-term starvation shown by *in vitro* colon cancer studies for apoptosis induction (124). The dietary reduction of serum glucose concentrations involves restricting carbohydrate consumption, traditionally implemented by following a 4:1 fat to protein and carbohydrate ratio (commercially available as KetoCal®) that is well tolerated in patient studies for targeting GBM energy metabolism (125–127). As a result, multiple clinical trials are either complete or ongoing evaluating the safety/tolerance and effectiveness of the ketogenic diet (KD) as an adjuvant to current treatment in GBM: NCT01865162, NCT023939378, NCT 04691960, NCT02302235, NCT00575146, NCT03451799, NCT01754350, NCT03075514, NCT03278249, NCT01535911, NCT04730869, NCT02286167. This dietary limitation forces the liver to metabolically adapt, using fats to produce ketone bodies which can be used as an alternative fuel source for cellular energy metabolism; originally pioneered for the beneficial reduction in seizures in epileptic children (128). Furthermore, Otto Warburg's description of tumoural exploitation of aerobic glycolysis provided initial rationale for the approach in GBM, suggested as an effective strategy to slow tumour growth and reduce ability of cells to exhibit a Warburg phenotype (129). As such, the efficacy of this treatment has been shown by Abdelwahab et al's. use of a bioluminescent mouse model of malignant glioma to confer increased survival (127). Moreover, the retrospective statistical analysis of patient data suggests that postoperative hyperglycaemia is associated with poor survival; an effect that could be suppressed by lowering glucose levels during treatment (130–132).

Despite studies demonstrating efficacy of the KD for increased GBM survival, Sperry et al. have explored GBM intratumoural heterogeneity to reveal that populations of tumour cells could in fact thrive using ketone bodies and upregulated fatty acid oxidation for survival, therefore mitigating the effectiveness of the KD (133). However, the authors highlight that the KD in combination with additional metabolic inhibition of enzymes such as carnitine palmitoyltransferase 1A (CPT1A) – the rate-limiting enzyme for fatty acid oxidation, or implementation of additional calorie restriction to exacerbate the effect of serum glucose reduction could increase the efficacy of the KD, as evidenced by Shelton et al. in GBM (133, 134). Tumour survival *via* the exploitation of pathways that circumvent low glucose concentrations such as glutaminolysis have also become a concern for implementation of the KD as an effective treatment (135). Moreover, despite the maintenance of low glutamine levels in the healthy brain *via* the glutamine-glutamate cycle, studies by Takano et al. have shown that glioma glutamate secretion into the surrounding brain could be readily recycled by tumours for sustained energy metabolism and growth (95). Therefore, strategies implementing the calorie restricted KD in combination with 6-diazo-5-oxo-L-norleucine (DON) – a gluatminolysis antagonist has been tested *in vivo* GBM mouse models by Mukherjee et al. conferring increased survival and tumour cell apoptosis (135).

Besides a reduction in glycolytic flux resulting from the KD, other downstream cellular responses have been investigated by Ji et al. using GSCs derived from both patients and cell lines (136). Culture medium high in β-hydroxybutyrate for mimicking the effects of the KD resulted in reduced GSC proliferation and tumorigenicity as well as revealing the possibility for the induction of damaging morphological and functional mitochondrial alterations (136). In addition, studies by Seyfried et al. using *in vivo* astrocytoma models exposed to restricted standard and KDs showed alterations in metabolic modulators such as a reduction of IGF-I (137). Both IGF-I, the IGF1 receptor (IGF-1R) and associated signalling network have been linked with tumour survival in a range of cancers, with experimental data showing the presence of the receptor providing protection from apoptosis following cytotoxic treatment (138, 139). Moreover, the IGFR1 exhibits elevated expression in GBM cells when compared with normal brain cells and is therefore believed to be a marker of reduced patient survival and inhibition of tumour cell apoptosis (140, 141). In fact, Zhang et al. carried out *in vitro* culture studies comparing control U87 GBM cells to those overexpressing the IGF-R1, revealing that in response to hydrogen peroxide exposure, the cells with higher IGF-R1 could inhibit apoptosis. In addition, increasing concentrations of IGF1 or overexpression of the IGF-1R resulted in Akt phosphorylation, believed to increase

PI3K/Akt pathway activation and subsequent apoptosis suppression (140).

Peroxisome Proliferator-Activated Receptors and Differentiation Induction

The 2010 retrospective review of high-grade glioma patients by Grommes et al. exposed that diabetic patients receiving treatment with PPARγ agonists (Thiazolidinediones) had a median survival increase of 13 months in comparison to those not taking this medication (142). Despite analysis of the data defining this result as not significant due to small sample size, expression data showing elevated levels of PPARγ in malignancies such as colon, duodenal, lung, prostate, thyroid, primary and metastatic breast cancer has provoked an increased interest in the clinical relevance of this receptor family, of which there are 3 mammalian members: PPARα, PPARβ/δ and PPARγ (143–148). The PPARs are part of the nuclear receptor superfamily and function as ligand-inducible transcription factors which under normal conditions bind dietary fats as well as regulating both adipocyte and macrophage biology (149).

PPAR agonists have therefore gained traction with studies by Keshamouni et al. demonstrated that treatment of non-small cell lung cancer (NSCLC) patient tumours with the PPARγ ligand troglitazone conferred anti-proliferative effects due to G0/G1 cell cycle arrest and reduction in cyclin D/E expression (145). The same cell cycle arrest has also been recorded in GBM tissue samples using the PPARγ ligand pioglitazone by Zang et al., with other research groups showing that this ligand could additionally stimulate β-catenin mediated apoptosis of GBM cell lines (150, 151). Interestingly, Chearwae and Bright (152) treated neurospheres generated from commercial GBM cell lines with the PPARγ agonists 15-deoxy-$\Delta^{12,14}$-prostaglandin J$_2$ (15d-PGJ2) or all-*trans* retinoic acid to induce apoptosis and inhibit neurosphere formation and expansion through Tyk2-Stat3 inhibition (152). The notion that these ligands exert effects though the Janus kinase-signal transducer and activator of transcription (JAK-STAT) pathway has been complemented by studies by Mo et al. using PPARγ ligands in mouse embryonic stem cells (153). Since STAT3 is crucial for the self-renewal of GSCs, the potential downstream inhibition of this pathway could be important for sensitisation to chemotherapeutics such as temozolomide (TMZ), as shown by Villalva et al. (154).

Further to the delineation of different populations of GBM cells with distinct cycling kinetics by Hoang-Minh et al., enhanced cytotoxic resistance of slow-cycling populations have been described by studies performed in colon and breast tumour cells by Moore et al. despite being successful against the more proliferative tumour bulk (86, 155). Therefore, the induction of differentiation in stem populations has become a promising therapeutic strategy for cellular sensitisation to standard chemo and radiotherapy for GBM (Stupp protocol) (4). Pestereva et al. used imatinib to inhibit the PDGFR and stem cell factor receptor (c-Kit), with encouraging reductions of stem cells markers and tumorigenicity of tissue derived GSCs (156). There is also

promise that PPARγ agonists could be useful for inducing differentiation of GSCs within tumours due to indications that ciglitazone and 15d-PGJ2 caused altered expression of stemness genes such as *SOX2* and *NANOG* (157). This was again tested in mouse derived NSCs cultured as neurospheres by Kanakasabai et al. with stem cell gene expression analysis before and after treatment with iglitazone or 15d-PGJ2 revealing a downregulation of stem and differentiation associated genes (158). However, despite the potential benefits of this approach, studies by Caren et al. have highlighted the importance of ensuring terminal GSC differentiation in a stable manner, due to the variable responses of cells to bone morphogenic protein (BMP) therapies. Therefore, studies are required to investigate the mechanisms used by cells to evade patterns of commitment, making them vulnerable to dedifferentiation (159).

In addition to the potential beneficial effect of PPARγ agonists on GBM, the elevated expression of PPARα recorded in GBM tissue by Haynes et al. has been complemented by data demonstrating tumour growth suppression following the use of agonists such as gemfibrozil (160, 161). This beneficial effect has also been observed in NSCLC cells, where induction of PPARα inhibited growth and angiogenesis, as well as leading to apoptosis in ovarian cancer cells when combined with PPARγ induction (162, 163). However, a compelling aspect of PPARα is that it is imperative for ketogenesis due to transcriptionally regulating 3-hydroxy-3-methylglutaryl-CoA (HMGCS) – the rate-limiting enzyme for the conversion of acetyl-CoA to β-hydroxybutyrate and acetoacetate (164, 165). Therefore, PPARα can also downregulate IGF/Akt signalling discussed for the KD as well as GLUT1 and 4 receptors, essential for supressing the Warburg phenotype (166–168).

Mitochondrial Targeting

Further to studies revealing that GBMs undergo glucose oxidation, the discovery of mitochondrial aberrations including electron transport chain (ETC) components and mitochondrial reserve capacity have provided insight into additional GBM survival mechanisms (169). Mitochondrial DNA (mtDNA) profiling has revealed mutations in complex I, III and IV of the ETC, affecting the balance between OXPHOS and aerobic glycolysis (170, 171). GBM patient tumour tissue analysis by Lloyd et al. revealed that at least one mitochondrial DNA (mtDNA) mutation is present in 43% of patients (171). Further to this, large scale mtDNA alterations, ETC remodelling, and enzyme activity modulation has been shown to be critical for TMZ resistance in both cell lines and human GBM specimens, with chemoresistance largely driven by cytochrome C oxidase (COX) (172). Moreover, subject to research by Oliva et al., COX subunit-IV (COX-IV) was shown mainly to be associated with COX isoform I (COX-IV-I) for cellular nutrient sensing and modulation of energy production in TMZ resistant cells (172). This finding was later extended to GSCs, with COX-IV-I displaying cooperation with downstream targets to enhance tumorigenicity and self-renewal (173). Consequently, ETC pharmacological and genomic intervention

has been further investigated, with results suggesting TMZ sensitisation following COX-IV-I targeting (174, 175).

Furthermore, the anti-diabetic biguanide drug, MF, has been analysed as a promising therapeutic strategy for decreasing cancer proliferation and inducing apoptosis subject to nutrient availability. Investigations in colon cancer cells have revealed that MF reversibly inhibits the function of ETC complex I subject to the presence of membrane potential and glucose (176, 177). Other studies have revealed that in the absence of glucose, MF can induce cellular apoptosis as well as a possible selective effect on CSCs (177–181). Further to this, phenformin - a MF analogue with elevated potency, was used by Jiang et al. *in vitro* and for *in vivo* tumour mouse models, revealing multiple beneficial effects including a reduction in GSC self-renewal and overall prolonged mouse survival (182). However, since biguanide use is associated with lactic acidosis induction, combining MF with the inhibition of PDK by dichloroacetate (DCA) by Haugrud et al. conferred a cell survival advantage, both reducing lactate production and inhibition of oxidative metabolism in breast cancer cells (182, 183). GBM oxidative stress induction has also been described for other compounds such as the anthelmintic drug Ivermectin, similarly shown to induce apoptosis *via* ETC complex I inhibition as well as targeting angiogenesis and the Akt/mTOR pathway in GSC cell lines (184). Interestingly, this drug also induces apoptosis in human microvascular endothelial cells (HBMEC), thus breaking an important protective and synergistic relationship believed to be critical for GBM niche maintenance (184).

Combination Strategies

Further to the identification of isolated metabolic targets, the combination of existing GBM chemoradiation protocols with agonists/antagonists of multiple signalling pathways such as sonic hedgehog (Shh), murine double minute 2 (MDM2), p53, PI3K/mTOR, EGFRvIII, poly(ADP-ribose) polymerase 1 (*PARP1*), cyclin-dependent kinase 4/6 (CDK4/6) have exhibited cytotoxic sensitisation efficacy of GBM models (185–191). Further experimental combinatorial strategies include the use of impridone compounds for inhibiting both glycolysis and OXPHOS *via* Akt/ERK dual inhibition, c-Myc degradation and apoptosis in GSCs (192). In addition, Yuan et al. effectively used the glycolytic inhibitor 3-bromo-2-oxopropionate-1-propyl ester (3-BrOP) and the alkylating chemotherapeutic carmustine/BCNU in GSCs that were initially highly glycolytic, causing major ATP depletion and abrogation of DNA repair capacity (193). Furthermore, the development of the arsenic-based mitochondrial toxin, 4-(N-(S-penicillaminylacetyl)amino) phenylarsonous acid (PENAO) by Shen et al. to trigger mitochondrial apoptosis had better efficacy when used with DCA for dual targeting of glucose metabolism (194). Other combinations of drugs undergoing clinical development for GBM have also been tested with existing compounds such as Navitoclax/ABT-263 (a Bcl-2/Bcl-xL inhibitor) with encouraging *in vivo* low toxicity and suppression of tumour growth (195). Moreover, studies using chemotherapeutics with both MF and phenformin have shown beneficial effects tumour growth inhibition, with Jiang et al.

using phenformin and TMZ *in vivo* for prolonged mouse survival (182).

However, the epidemiological identification of existing drugs with anti-tumour effects is not restricted to the biguanides, many repurposed compounds are currently under scrutiny in clinical trials in combination with existing chemoradiation protocols (see **Table 1**). Moreover, clinical trials to test the coordinated blocking of multiple different cell survival pathways has become an attractive strategy, with efforts to use multiple repurposed compounds that will work synergistically for the greatest therapeutic benefit. In 2016, the CUSP9v3 trial (identifier: NCT027703780) started, combining TMZ with Aprepitant, Minocycline, Disulfiram, Celecoxib, Sertraline, Captopril, Itraconazole, Ritonavir and Auranofin in additive treatment cycles for the treatment of recurrent GBM cases; a strategy originally proposed in 2013 by Kast et al. (216, 217). Although the results have not been released at the time of writing this review, experimental studies to test the robustness of the CUSP9 strategy have been published, including Skaga et al.'s investigations using 15 GSC cultures, derived from 15 patient GBMs including relapsed tumours (18). The group found that the combination of drugs was significantly more effective than when used alone, as well as increasing the therapeutic benefit of TMZ for sphere eradication in most of the cell lines, with the highest resistance in a proneural population (18). In addition to testing compound efficacy with conventional therapy, it has come to light that patient tumour profiling prior to therapeutic application may give a greater therapeutic benefit. Recently, the antiproliferative effects of four different compounds: MF, dichloroacetate (DCA), sodium oxamate (SOD) and diazo-5-oxo-L-norleucine (DON) were tested on 4 GSC subpopulations with different initial oxidative/glycolytic metabolism tendencies by Duraj et al. (88). The group found that GSC inhibitor sensitivity differed relative to Warburg-like/OXPHOS phenotype, and Seahorse XF to determine glycolytic/mitochondrial ATP production shifts following treatment. The authors suggest that predictive metabolic shifts despite initial bioenergetic plasticity following treatment, could be used as "metabolic priming" (88). In this way, the malignant cells could be pushed towards exhibiting a phenotype with enhanced sensitivity to subsequent small molecular inhibitors, chemo- or radiotherapy.

CONCLUSION

Mechanisms for conferring resistance to current GBM treatments have been described for GSCs including quiescence, slow cell cycling, upregulated expression of drug efflux proteins, enhanced DNA repair capacity, drug resistance and advanced plasticity. Attempting to overcome these molecular blockades has heightened the importance of delineating the metabolic phenotypes that are adopted by these cells; with shifts before, during and after standard treatment believed to be imperative for tumour reestablishment. metabolic inhibition strategies have recently gained traction, requiring a detailed knowledge of the

TABLE 1 | Repurposed drugs currently in clinical trials for the assessment of efficacy against GBM.

Repurposed drug	Mechanism of action	Indication of therapeutic benefit for GSCs	References	Trial identifier	Therapeutic combination	Tumour inclusion criteria	Reported results
Metformin (antidiabetic)	-↓ mitochondrial ATP production, ↓ oxygen consumption, ↑ lactate and glycolytic ATP production -↑AMPK, ↓ STAT3 & Akt/PKB -↓ SOX2 expression in TMZ-resistant glioma cells. (yang) -mTOR pathway inhibition -Inhibition of complex I of the ETC. -↓ superoxide dismutase (SOD) activity ↑ caspase 3 activity.	-Inhibition of STAT3 phosphorylation -↓ neurosphere formation. -↓ proliferation via chloride intracellular channel-1 (CLIC1) inhibition. G1 arrest. ↑AMPK, ↑FOXO3 – promotion of differentiation.	Leidgens et al. (196); Yang et al. (197); Gritti et al. (198); Owen et al. (199); Xiong et al. (200); Sato et al. (201)	NCT02780024	Metformin + radiation + TMZ.	Newly diagnosed GBM.	Estimated completion date December 2021.
				NCT03243851	Metformin + low dose TMZ.	Progressive or recurrent Glioblastoma.	No published results.
Chloroquine (antimalarial)	-Inhibition of autophagy. -Induction of p53-dependent apoptosis. Experimental indication of mitochondrial cristae damage and DNA break repair prevention (triple negative breast cancer stem cells).	-Inhibition of the PI3K/Akt pathway for sensitisation to radiation-induced apoptosis. -Inhibition of autophagy and promotion of apoptosis. -↑ radio sensitisation. Induction of p63-dependent G1 arrest.	Firat et al. (202); Kim et al. (203); Lee et al. (204); Ye et al. (205); Liang et al. (206)	NCT00224978	Chloroquine + conventional chemotherapy: caumustine and radiotherapy.	Tumour restricted to one brain hemisphere. First or second recurrence or relapse.	Median survival after surgery = 24 months for chloroquine-treated patients & 11 months for controls.
				NCT02432417	Chloroquine + chemoradiation	de novo GBM.	N/A. Estimated completion date January 2024.
				NCT02378532	Chloroquine + radiation +TMZ.	Newly diagnosed GBM, histopathological conformation of MGMT and EGFRvIII status.	44 adverse events recorded possibly/likely due to chloroquine including seizure and vomiting. Median overall survival = 8.1 months (EGFRvIII negative) & 13.4 months (EGFRvIII positive. 7 patients alive a median 9 month follow up. Maximum tolerated dose was established as 200mg daily chloroquine combined with RT and concurrent TMZ for newly diagnosed GBM.
Mefloquine (antimalarial)	Proposed cytotoxicity by inhibition of autophagy in glioma cells.		Golden et al. (207)	NCT01430351	Mefloquine + TMZ (arm 2 of study) + metformin	Histologically proven supratentorial glioblastoma.	Mefloquine induction of Abnormal ECG (2 patients) & QTc interval prolongation (1 patient).

(Continued)

TABLE 1 | Continued

Repurposed drug	Mechanism of action	Indication of therapeutic benefit for GSCs	References	Trial identifier	Therapeutic combination	Tumour inclusion criteria	Reported results
					(arm 6) + memantine (arm 4) + metformin & memantine (arm 7).		Possible induction of grade 1 sinus bradycardia (1 patient). Established final mefloquine dose - 250 mg 3 times weekly. Median OS = 21 months (95% CI, 16.2-29.7 months), 2-year survival rate = 43% (95% CI, 34%-56%).
Atorvastatin (statin)	-Mevalonate pathway inhibition (leukaemia). -Inhibition of protein prenylation *via* upstream HMG-CoA reductase inhibition. -Suppression of Ras and downstream signalling pathways including Erk enhancement of TMZ efficacy.	-Apoptotic induction, ↓ migration and invasion of spheroids (U87).	Bayat et al. (208); Peng et al. (209)	NCT02029573	Atorvastatin + TMZ + radiation.	Histologically proven newly diagnosed GBM malignant GBM or variants. No prior chemotherapy or radiotherapy.	Interim analysis reported treatment safety, PFS-6 rate was 67% with median 9.1 months PFS. No published results from completed trial.
Celecoxib (NSAID)	-P53 dependent Induction of DNA damage and inhibition of DNA synthesis. Indications of G1 cell cycle arrest and autophagy.	-Regulation of chemokine axes (CCL2/CCR2 and CXCL10/CXCR3). Decrease of mRNA expression to viability of GSCs. -↓ of PD-L1 *via* FKBP5.	Kang et al. (210); Shono et al. (211); Yamaguchi et al. (212)	NCT00112502	Randomisation of 8 treatment arms. Combination of TMZ + thalidomide and/ or celecoxib.	Histologically confirmed supratentorial GBM. Must have undergone biopsy, subtotal, or gross total tumour resection. Must have undergone radiotherapy within 5 weeks prior.	PFS for treatment arms combined was 11.6 months. Overall, 6-month PFS rate = 73%. Arms containing celecoxib showed a median PFS of 8.3 months compared with 7.4.
				NCT00068770	Two treatment arms: 1.p450 inhibitor + celecoxib + radiotherapy. 2.No p450 inhibitor + Celecoxib + radiotherapy.	Histologically confirmed GBM. No prior chemotherapy, radiotherapy, endocrine therapy, immunotherapy, or biological agents for malignancy. Recovered from surgery.	Study ended early, unethical to continue due to other trial data indicating the therapeutic benefit of including TMZ in treatment plan.
Disulfiram (alcohol addiction)	-Inhibition of ALDH. -Suppression of proteasomal activity. -↑ROS, activation of JNK & p38, inhibition of NF-κB in GBM cells. -Proposed modulation of apoptosis *via* Bcl2 family mediation. -Inhibition of PLK1 expression. -Inhibition of MGMT, ↑ alkylating DNA damage.	-Inhibition of chymotrypsin-like proteasomal activity, elevated effect with copper addition. -Inhibition of the ubiquitin-proteasome pathway. -Inhibition of self-renewal. -Enhancement of TMZ treatment activity in stem-cell like populations of GBM.	Hothi et al. (213); Triscott et al. (214); Paranjpe et al. (215)	NCT02678975	Disulfiram + copper + chemotherapy.	Previous diagnosis of glioblastoma (histologically verified) and presenting with a first progression/ recurrence documented by MRI.	No published results.

(Continued)

TABLE 1 | Continued

Repurposed drug	Mechanism of action	Indication of therapeutic benefit for GSCs	References	Trial identifier	Therapeutic combination	Tumour inclusion criteria	Reported results
				NCT01907165	Disulfiram + copper + TMZ.	Histologically confirmed GBM. Received or in the process of completing definitive radiotherapy with concurrent TMZ.	1-year PFS = 57%, & 1-year OS = 69%. No significant difference in PFS/OS according to Disulfiram dose, surgical extent, or MGMT methylation status. Better PFS & OS in GBMs with IDH1 (n = 6), BRAF (n = 2), or NF1 (n = 1) mutations than without: 1-year PFS: 100% *vs* 22%, respectively, p = 0.001; 1-year OS: 100% *vs* 42%, respectively, p = 0.006>
				NCT02715609	Preoperative treatment: Disulfiram + copper gluconate. Post-surgery: standard radiation + TMZ + concurrent Disulfiram/ copper gluconate.	Dose escalation cohort: Diagnosis of GBM or its histological variants Dose expansion cohort: diagnosis of GBM (or its histological variants) with IDH, BRAF, or NF1 mutations. Confirmation of these mutations may be either by immunohistochemistry or next generation sequencing.	N/A. Estimated completion date December 15, 2023.
				NCT03034135	Disulfiram/ copper gluconate + TMZ, 6-month course.	Histologically confirmed GBM, Radiotherapy completed with concurrent TMZ at least 12 weeks prior to start of study treatment. Or pathological verification of recurrent tumour at least 4 weeks after radiotherapy with concurrent TMZ. Exclusion of IDH mutants or secondary GBMs.	OOR = 0%, but 14% had clinical benefit. Median PFS = 1.7 months & median OS = 7.1 months. 1patient displayed dose limiting toxicity. Disulfiram concluded to have limited activity and was unable to recapitulate TMZ sensitivity in patients tested.

The potential mechanisms of these inhibitors against GSCs based on experimental studies are also included. The clinical trial identifiers are given as well as any published results from these studies.

metabolome and adaptability potential of cells following targeted pathway inhibition. However, it's important to highlight that a metabolic treatment regimen designed to solely target GSCs may not improve GBM prognosis. For example, GSC differentiation induction strategies must ensure stable and terminal GSC differentiation as well as coordinated blocking of the reverse process. As highlighted by **Figure 1**, dedifferentiation of differentiated tumour bulk cells could result in the formation of new GSCs. Therefore, even if complete clearance of the GSC population could be achieved through metabolic targeting, this outcome may only be temporary, highlighting the limitations of this singular approach. In this way, metabolic regimens to target GSCs can be explored as an effective supplement for combinatorial use with current and emerging treatment

strategies to ensure complete therapeutic coverage of heterogenic GBM tumours.

AUTHOR CONTRIBUTIONS

AH was responsible for article structure, figure design and building, drafting the introduction and main body of text. XL, MG, and MCG provided critical revision of the article and figures. CP provided critical revision of the article and figures, joint supervising author. KK was responsible for the article

conception, drafting the article abstract and providing critical revision of the article and figures, joint supervising author. All authors contributed to the article and approved the submitted version.

FUNDING

REFERENCES

1. Milano MT, Okunieff P, Donatello RS, Mohile NA, Sul J, Walter KA, et al. Patterns and Timing of Recurrence After Temozolomide-Based Chemoradiation for Glioblastoma. *Int J Radiat Oncol Biol Phys* (2010) 78 (4):1147–55. doi: 10.1016/j.ijrobp.2009.09.018

2. Louis DN, Ohgaki H, Wiestler OD, Cavenee WK, Burger PC, Jouvet A, et al. The 2007 WHO Classification of Tumours of the Central Nervous System. *Acta Neuropathol* (2007) 114(2):97–109. doi: 10.1007/s00401-007-0243-4

3. Stupp R, Dietrich PY, Ostermann Kraljevic S, Pica A, Maillard I, Maeder P, et al. Promising Survival for Patients With Newly Diagnosed Glioblastoma Multiforme Treated With Concomitant Radiation Plus Temozolomide Followed by Adjuvant Temozolomide. *J Clin Oncol* (2002) 20(5):1375–82. doi: 10.1200/JCO.2002.20.5.1375

4. Stupp R, Mason WP, van den Bent MJ, Weller M, Fisher B, Taphoorn MJ, et al. Radiotherapy Plus Concomitant and Adjuvant Temozolomide for Glioblastoma. *N Engl J Med* (2005) 352(10):987–96. doi: 10.1056/NEJMoa043330

5. Marenco-Hillembrand L, Wijesekera O, Suarez-Meade P, Mampre D, Jackson C, Peterson J, et al. Trends in Glioblastoma: Outcomes Over Time and Type of Intervention: A Systematic Evidence Based Analysis. *J Neurooncol* (2020) 147(2):297–307. doi: 10.1007/s11060-020-03451-6

6. Ohgaki H, Dessen P, Jourde B, Horstmann S, Nishikawa T, Di Patre PL, et al. Genetic Pathways to Glioblastoma: A Population-Based Study. *Cancer Res* (2004) 64(19):6892–9. doi: 10.1158/0008-5472.CAN-04-1337

7. Parsons DW, Jones S, Zhang X, Lin JC, Leary RJ, Angenendt P, et al. An Integrated Genomic Analysis of Human Glioblastoma Multiforme. *Science* (2008) 321(5897):1807–12. doi: 10.1126/science.1164382

8. Network CGAR. Comprehensive Genomic Characterization Defines Human Glioblastoma Genes and Core Pathways. *Nature* (2008) 455 (7216):1061–8. doi: 10.1038/nature07385

9. Verhaak RG, Hoadley KA, Purdom E, Wang V, Qi Y, Wilkerson MD, et al. Integrated Genomic Analysis Identifies Clinically Relevant Subtypes of Glioblastoma Characterized by Abnormalities in PDGFRA, IDH1, EGFR, and NF1. *Cancer Cell* (2010) 17(1):98–110. doi: 10.1016/j.ccr.2009.12.020

10. Phillips HS, Kharbanda S, Chen R, Forrest WF, Soriano RH, Wu TD, et al. Molecular Subclasses of High-Grade Glioma Predict Prognosis, Delineate a Pattern of Disease Progression, and Resemble Stages in Neurogenesis. *Cancer Cell* (2006) 9(3):157–73. doi: 10.1016/j.ccr.2006.02.019

11. Sottoriva A, Spiteri I, Piccirillo SG, Touloumis A, Collins VP, Marioni JC, et al. Intratumor Heterogeneity in Human Glioblastoma Reflects Cancer Evolutionary Dynamics. *Proc Natl Acad Sci USA* (2013) 110(10):4009–14. doi: 10.1073/pnas.1219747110

12. Hanahan D, Weinberg RA. Hallmarks of Cancer: The Next Generation. *Cell* (2011) 144(5):646–74. doi: 10.1016/j.cell.2011.02.013

13. Singh SK, Hawkins C, Clarke ID, Squire JA, Bayani J, Hide T, et al. Identification of Human Brain Tumour Initiating Cells. *Nature* (2004) 432 (7015):396–401. doi: 10.1038/nature03128

14. Dirkse A, Golebiewska A, Buder T, Nazarov PV, Muller A, Poovathingal S, et al. Stem Cell-Associated Heterogeneity in Glioblastoma Results From Intrinsic Tumor Plasticity Shaped by the Microenvironment. *Nat Commun* (2019) 10(1):1787. doi: 10.1038/s41467-019-09853-z

15. Wei J, Barr J, Kong LY, Wang Y, Wu A, Sharma AK, et al. Glioblastoma Cancer-Initiating Cells Inhibit T-Cell Proliferation and Effector Responses by the Signal Transducers and Activators of Transcription 3 Pathway. *Mol Cancer Ther* (2010) 9(1):67–78. doi: 10.1158/1535-7163.MCT-09-0734

16. Bao S, Wu Q, McLendon RE, Hao Y, Shi Q, Hjelmeland AB, et al. Glioma Stem Cells Promote Radioresistance by Preferential Activation of the DNA Damage Response. *Nature* (2006) 444(7120):756–60. doi: 10.1038/nature05236

17. Ye F, Zhang Y, Liu Y, Yamada K, Tso JL, Menjivar JC, et al. Protective Properties of Radio-Chemoresistant Glioblastoma Stem Cell Clones Are Associated With Metabolic Adaptation to Reduced Glucose Dependence. *PloS One* (2013) 8(11):e80397. doi: 10.1371/journal.pone.0080397

18. Skaga E, Skaga I, Grieg Z, Sandberg CJ, Langmoen IA, Vik-Mo EO. The Efficacy of a Coordinated Pharmacological Blockade in Glioblastoma Stem Cells With Nine Repurposed Drugs Using the CUSP9 Strategy. *J Cancer Res Clin Oncol* (2019) 145(6):1495–507. doi: 10.1007/s00432-019-02920-4

19. Bayat Mokhtari R, Homayouni TS, Baluch N, Morgatskaya E, Kumar S, Das B, et al. Combination Therapy in Combating Cancer. *Oncotarget* (2017) 8 (23):38022–43. doi: 10.18632/oncotarget.16723

20. Lan X, Jörg DJ, Cavalli FMG, Richards LM, Nguyen LV, Vanner RJ, et al. Fate Mapping of Human Glioblastoma Reveals an Invariant Stem Cell Hierarchy. *Nature* (2017) 549(7671):227–32. doi: 10.1038/nature23666

21. Deleyrolle LP, Harding A, Cato K, Siebzehnrubl FA, Rahman M, Azari H, et al. Evidence for Label-Retaining Tumour-Initiating Cells in Human Glioblastoma. *Brain* (2011) 134(Pt 5):1331–43. doi: 10.1093/brain/awr081

22. Yuan X, Curtin J, Xiong Y, Liu G, Waschsmann-Hogiu S, Farkas DL, et al. Isolation of Cancer Stem Cells From Adult Glioblastoma Multiforme. *Oncogene* (2004) 23(58):9392–400. doi: 10.1038/sj.onc.1208311

23. Chaffer CL, Brueckmann I, Scheel C, Kaestli AJ, Wiggins PA, Rodrigues LO, et al. Normal and Neoplastic Nonstem Cells can Spontaneously Convert to a Stem-Like State. *Proc Natl Acad Sci USA* (2011) 108(19):7950–5. doi: 10.1073/pnas.1102454108

24. Nowell PC. The Clonal Evolution of Tumor Cell Populations. *Science* (1976) 194(4260):23–8. doi: 10.1126/science.959840

25. Dick JE. Looking Ahead in Cancer Stem Cell Research. *Nat Biotechnol* (2009) 27(1):44–6. doi: 10.1038/nbt0109-44

26. Olmez I, Shen W, McDonald H, Ozpolat B. Dedifferentiation of Patient-Derived Glioblastoma Multiforme Cell Lines Results in a Cancer Stem Cell-Like State With Mitogen-Independent Growth. *J Cell Mol Med* (2015) 19 (6):1262–72. doi: 10.1111/jcmm.12479

27. Zhang QB, Ji XY, Huang Q, Dong J, Zhu YD, Lan Q. Differentiation Profile of Brain Tumor Stem Cells: A Comparative Study With Neural Stem Cells. *Cell Res* (2006) 16(12):909–15. doi: 10.1038/sj.cr.7310104

28. Singh SK, Clarke ID, Hide T, Dirks PB. Cancer Stem Cells in Nervous System Tumors. *Oncogene* (2004) 23(43):7267–73. doi: 10.1038/sj.onc.1207946

29. Ogden AT, Waziri AE, Lochhead RA, Fusco D, Lopez K, Ellis JA, et al. Identification of A2B5+CD133- Tumor-Initiating Cells in Adult Human Gliomas. *Neurosurgery* (2008) 62(2):505–14; discussion 14-5. doi: 10.1227/01.neu.0000316019.28421.95

30. Chen R, Nishimura MC, Bumbaca SM, Kharbanda S, Forrest WF, Kasman IM, et al. A Hierarchy of Self-Renewing Tumor-Initiating Cell Types in

Glioblastoma. *Cancer Cell* (2010) 17(4):362–75. doi: 10.1016/j.ccr. 2009.12.049

31. Beier D, Hau P, Proescholdt M, Lohmeier A, Wischhusen J, Oefner PJ, et al. CD133(+) and CD133(-) Glioblastoma-Derived Cancer Stem Cells Show Differential Growth Characteristics and Molecular Profiles. *Cancer Res* (2007) 67(9):4010–5. doi: 10.1158/0008-5472.CAN-06-4180

32. Zheng X, Shen G, Yang X, Liu W. Most C6 Cells Are Cancer Stem Cells: Evidence From Clonal and Population Analyses. *Cancer Res* (2007) 67 (8):3691–7. doi: 10.1158/0008-5472.CAN-06-3912

33. Brown DV, Filiz G, Daniel PM, Hollande F, Dworkin S, Amiridis S, et al. Expression of CD133 and CD44 in Glioblastoma Stem Cells Correlates With Cell Proliferation, Phenotype Stability and Intra-Tumor Heterogeneity. *PloS One* (2017) 12(2):e0172791. doi: 10.1371/journal.pone.0172791

34. Kenney-Herbert E, Al-Mayhani T, Piccirillo SG, Fowler J, Spiteri I, Jones P, et al. CD15 Expression Does Not Identify a Phenotypically or Genetically Distinct Glioblastoma Population. *Stem Cells Transl Med* (2015) 4(7):822–31. doi: 10.5966/sctm.2014-0047

35. Suvà ML, Rheinbay E, Gillespie SM, Patel AP, Wakimoto H, Rabkin SD, et al. Reconstructing and Reprogramming the Tumor-Propagating Potential of Glioblastoma Stem-Like Cells. *Cell* (2014) 157(3):580–94. doi: 10.1016/j.cell.2014.02.030

36. Kondo T, Raff M. Oligodendrocyte Precursor Cells Reprogrammed to Become Multipotential CNS Stem Cells. *Science* (2000) 289(5485):1754–7. doi: 10.1126/science.289.5485.1754

37. Tennant DA, Durán RV, Gottlieb E. Targeting Metabolic Transformation for Cancer Therapy. *Nat Rev Cancer* (2010) 10(4):267–77. doi: 10.1038/nrc2817

38. Kumar S, Visvanathan A, Arivazhagan A, Santhosh V, Somasundaram K, Umapathy S. Assessment of Radiation Resistance and Therapeutic Targeting of Cancer Stem Cells: A Raman Spectroscopic Study of Glioblastoma. *Anal Chem* (2018) 90(20):12067–74. doi: 10.1021/acs.analchem.8b02879

39. Auffinger B, Tobias AL, Han Y, Lee G, Guo D, Dey M, et al. Conversion of Differentiated Cancer Cells Into Cancer Stem-Like Cells in a Glioblastoma Model After Primary Chemotherapy. *Cell Death Differ* (2014) 21(7):1119–31. doi: 10.1038/cdd.2014.31

40. Ivanov AI, Malkov AE, Waseem T, Mukhtarov M, Buldakova S, Gubkina O, et al. Glycolysis and Oxidative Phosphorylation in Neurons and Astrocytes During Network Activity in Hippocampal Slices. *J Cereb Blood Flow Metab* (2014) 34(3):397–407. doi: 10.1038/jcbfm.2013.222

41. Warburg O, Wind F, Negelein E. THE METABOLISM OF TUMORS IN THE BODY. *J Gen Physiol* (1927) 8(6):519–30. doi: 10.1085/jgp.8.6.519

42. van der Hiel B, Pauwels EK, Stokkel MP. Positron Emission Tomography With 2-[18F]-Fluoro-2-Deoxy-D-Glucose in Oncology. Part IIIa: Therapy Response Monitoring in Breast Cancer, Lymphoma and Gliomas. *J Cancer Res Clin Oncol* (2001) 127(5):269–77. doi: 10.1007/s004320000191

43. Vlassenko AG, McConathy J, Couture LE, Su Y, Massoumzadeh P, Leeds HS, et al. Aerobic Glycolysis as a Marker of Tumor Aggressiveness: Preliminary Data in High Grade Human Brain Tumors. *Dis Markers* (2015) 2015:874904. doi: 10.1155/2015/874904

44. Ganapathy-Kanniappan S. Molecular Intricacies of Aerobic Glycolysis in Cancer: Current Insights Into the Classic Metabolic Phenotype. *Crit Rev Biochem Mol Biol* (2018) 53(6):667–82. doi: 10.1080/10409238.2018.1556578

45. De Preter G, Neveu MA, Danhier P, Brisson L, Payen VL, Porporato PE, et al. Inhibition of the Pentose Phosphate Pathway by Dichloroacetate Unravels a Missing Link Between Aerobic Glycolysis and Cancer Cell Proliferation. *Oncotarget* (2016) 7(3):2910–20. doi: 10.18632/oncotarget.6272

46. Kathagen A, Schulte A, Balcke G, Phillips HS, Martens T, Matschke J, et al. Hypoxia and Oxygenation Induce a Metabolic Switch Between Pentose Phosphate Pathway and Glycolysis in Glioma Stem-Like Cells. *Acta Neuropathol* (2013) 126(5):763–80. doi: 10.1007/s00401-013-1173-y

47. Kathagen-Buhmann A, Schulte A, Weller J, Holz M, Herold-Mende C, Glass R, et al. Glycolysis and the Pentose Phosphate Pathway Are Differentially Associated With the Dichotomous Regulation of Glioblastoma Cell Migration Versus Proliferation. *Neuro Oncol* (2016) 18(9):1219–29. doi: 10.1093/neuonc/now024

48. Sanzey M, Abdul Rahim SA, Oudin A, Dirkse A, Kaoma T, Vallar L, et al. Comprehensive Analysis of Glycolytic Enzymes as Therapeutic Targets in the Treatment of Glioblastoma. *PloS One* (2015) 10(5):e0123544. doi: 10.1371/journal.pone.0123544

49. Maher EA, Marin-Valencia I, Bachoo RM, Mashimo T, Raisanen J, Hatanpaa KJ, et al. Metabolism of [U-13 C]glucose in Human Brain Tumors *In Vivo*. *NMR BioMed* (2012) 25(11):1234–44. doi: 10.1002/nbm.2794

50. Christofk HR, Vander Heiden MG, Wu N, Asara JM, Cantley LC. Pyruvate Kinase M2 Is a Phosphotyrosine-Binding Protein. *Nature* (2008) 452 (7184):181–6. doi: 10.1038/nature06667

51. Desai S, Ding M, Wang B, Lu Z, Zhao Q, Shaw K, et al. Tissue-Specific Isoform Switch and DNA Hypomethylation of the Pyruvate Kinase PKM Gene in Human Cancers. *Oncotarget* (2014) 5(18):8202–10. doi: 10.18632/oncotarget.1159

52. Mukherjee J, Phillips JJ, Zheng S, Wiencke J, Ronen SM, Pieper RO. Pyruvate Kinase M2 Expression, But Not Pyruvate Kinase Activity, Is Up-Regulated in a Grade-Specific Manner in Human Glioma. *PloS One* (2013) 8(2):e57610. doi: 10.1371/journal.pone.0057610

53. Yang W. Structural Basis of PKM2 Regulation. *Protein Cell* (2015) 6(4):238–40. doi: 10.1007/s13238-015-0146-4

54. Witney TH, James ML, Shen B, Chang E, Pohling C, Arksey N, et al. PET Imaging of Tumor Glycolysis Downstream of Hexokinase Through Noninvasive Measurement of Pyruvate Kinase M2. *Sci Transl Med* (2015) 7(310):310ra169. doi: 10.1126/scitranslmed.aac6117

55. Beinat C, Patel CB, Xie Y, Gambhir SS. Evaluation of Glycolytic Response to Multiple Classes of Anti-Glioblastoma Drugs by Noninvasive Measurement of Pyruvate Kinase M2 Using. *Mol Imaging Biol* (2020) 22(1):124–33. doi: 10.1007/s11307-019-01353-2

56. Davis-Yadley AH, Abbott AM, Pimiento JM, Chen DT, Malafa MP. Increased Expression of the Glucose Transporter Type 1 Gene Is Associated With Worse Overall Survival in Resected Pancreatic Adenocarcinoma. *Pancreas* (2016) 45(7):974–9. doi: 10.1097/MPA.0000000000000580

57. Wun T, McKnight H, Tuscano JM. Increased Cyclooxygenase-2 (COX-2): A Potential Role in the Pathogenesis of Lymphoma. *Leuk Res* (2004) 28 (2):179–90. doi: 10.1016/s0145-2126(03)00183-8

58. Elstrom RL, Bauer DE, Buzzai M, Karnauskas R, Harris MH, Plas DR, et al. Akt Stimulates Aerobic Glycolysis in Cancer Cells. *Cancer Res* (2004) 64 (11):3892–9. doi: 10.1158/0008-5472.CAN-03-2904

59. Zhu H, Acquaviva J, Ramachandran P, Boskovitz A, Woolfenden S, Pfannl R, et al. Oncogenic EGFR Signaling Cooperates With Loss of Tumor Suppressor Gene Functions in Gliomagenesis. *Proc Natl Acad Sci USA* (2009) 106(8):2712–6. doi: 10.1073/pnas.0813314106

60. Ran C, Liu H, Hitoshi Y, Israel MA. Proliferation-Independent Control of Tumor Glycolysis by PDGFR-Mediated AKT Activation. *Cancer Res* (2013) 73(6):1831–43. doi: 10.1158/0008-5472.CAN-12-2460

61. Wolf A, Agnihotri S, Micallef J, Mukherjee J, Sabha N, Cairns R, et al. Hexokinase 2 is a Key Mediator of Aerobic Glycolysis and Promotes Tumor Growth in Human Glioblastoma Multiforme. *J Exp Med* (2011) 208(2):313–26. doi: 10.1084/jem.20101470

62. Mathupala SP, Rempel A, Pedersen PL. Glucose Catabolism in Cancer Cells: Identification and Characterization of a Marked Activation Response of the Type II Hexokinase Gene to Hypoxic Conditions. *J Biol Chem* (2001) 276 (46):43407–12. doi: 10.1074/jbc.M108181200

63. Mathupala SP, Rempel A, Pedersen PL. Glucose Catabolism in Cancer Cells. Isolation, Sequence, and Activity of the Promoter for Type II Hexokinase. *J Biol Chem* (1995) 270(28):16918–25. doi: 10.1074/jbc.270.28.16918

64. Pastorino JG, Shulga N, Hoek JB. Mitochondrial Binding of Hexokinase II Inhibits Bax-Induced Cytochrome C Release and Apoptosis. *J Biol Chem* (2002) 277(9):7610–8. doi: 10.1074/jbc.M109950200

65. Zhao S, Liu H, Liu Y, Wu J, Wang C, Hou X, et al. miR-143 Inhibits Glycolysis and Depletes Stemness of Glioblastoma Stem-Like Cells. *Cancer Lett* (2013) 333(2):253–60. doi: 10.1016/j.canlet.2013.01.039

66. Tateishi K, Iafrate AJ, Ho Q, Curry WT, Batchelor TT, Flaherty KT, et al. Myc-Driven Glycolysis Is a Therapeutic Target in Glioblastoma. *Clin Cancer Res* (2016) 22(17):4452–65. doi: 10.1158/1078-0432.CCR-15-2274

67. Masui K, Tanaka K, Akhavan D, Babic I, Gini B, Matsutani T, et al. mTOR Complex 2 Controls Glycolytic Metabolism in Glioblastoma Through FoxO Acetylation and Upregulation of C-Myc. *Cell Metab* (2013) 18(5):726–39. doi: 10.1016/j.cmet.2013.09.013

68. Crane CA, Austgen K, Haberthur K, Hofmann C, Moyes KW, Avanesyan L, et al. Immune Evasion Mediated by Tumor-Derived Lactate Dehydrogenase Induction of NKG2D Ligands on Myeloid Cells in Glioblastoma Patients. *Proc Natl Acad Sci USA* (2014) 111(35):12823–8. doi: 10.1073/pnas.1413933111

69. Nieder C, Marienhagen K, Dalhaug A, Aandahl G, Haukland E, Pawinski A. Prognostic Models Predicting Survival of Patients With Brain Metastases: Integration of Lactate Dehydrogenase, Albumin and Extracranial Organ Involvement. *Clin Oncol (R Coll Radiol)* (2014) 26(8):447–52. doi: 10.1016/j.clon.2014.03.006

70. Kim J, Han J, Jang Y, Kim SJ, Lee MJ, Ryu MJ, et al. High-Capacity Glycolytic and Mitochondrial Oxidative Metabolisms Mediate the Growth Ability of Glioblastoma. *Int J Oncol* (2015) 47(3):1009–16. doi: 10.3892/ijo.2015.3101

71. Daniele S, Giacomelli C, Zappelli E, Granchi C, Trincavelli ML, Minutolo F, et al. Lactate Dehydrogenase-A Inhibition Induces Human Glioblastoma Multiforme Stem Cell Differentiation and Death. *Sci Rep* (2015) 5:15556. doi: 10.1038/srep15556

72. Ohno M, Narita Y, Miyakita Y, Matsushita Y, Yoshida A, Fukushima S, et al. Secondary Glioblastomas With IDH1/2 Mutations Have Longer Glioma History From Preceding Lower-Grade Gliomas. *Brain Tumor Pathol* (2013) 30(4):224–32. doi: 10.1007/s10014-013-0140-6

73. Andronesi OC, Kim GS, Gerstner E, Batchelor T, Tzika AA, Fantin VR, et al. Detection of 2-Hydroxyglutarate in IDH-Mutated Glioma Patients by *In Vivo* Spectral-Editing and 2D Correlation Magnetic Resonance Spectroscopy. *Sci Transl Med* (2012) 4(116):116ra4. doi: 10.1126/scitranslmed.3002693

74. Xu W, Yang H, Liu Y, Yang Y, Wang P, Kim SH, et al. Oncometabolite 2-Hydroxyglutarate is a Competitive Inhibitor of α-Ketoglutarate-Dependent Dioxygenases. *Cancer Cell* (2011) 19(1):17–30. doi: 10.1016/j.ccr.2010.12.014

75. Salamanca-Cardona L, Shah H, Poot AJ, Correa FM, Di Gialleonardo V, Lui H, et al. *In Vivo* Imaging of Glutamine Metabolism to the Oncometabolite 2-Hydroxyglutarate in IDH1/2 Mutant Tumors. *Cell Metab* (2017) 26(6):830–41.e3. doi: 10.1016/j.cmet.2017.10.001

76. Lu C, Ward PS, Kapoor GS, Rohle D, Turcan S, Abdel-Wahab O, et al. IDH Mutation Impairs Histone Demethylation and Results in a Block to Cell Differentiation. *Nature* (2012) 483(7390):474–8. doi: 10.1038/nature10860

77. Turcan S, Rohle D, Goenka A, Walsh LA, Fang F, Yilmaz E, et al. IDH1 Mutation Is Sufficient to Establish the Glioma Hypermethylator Phenotype. *Nature* (2012) 483(7390):479–83. doi: 10.1038/nature10866

78. Noushmehr H, Weisenberger DJ, Diefes K, Phillips HS, Pujara K, Berman BP, et al. Identification of a CpG Island Methylator Phenotype That Defines a Distinct Subgroup of Glioma. *Cancer Cell* (2010) 17(5):510–22. doi: 10.1016/j.ccr.2010.03.017

79. Toyota M, Ahuja N, Ohe-Toyota M, Herman JG, Baylin SB, Issa JP. CpG Island Methylator Phenotype in Colorectal Cancer. *Proc Natl Acad Sci USA* (1999) 96(15):8681–6. doi: 10.1073/pnas.96.15.8681

80. Ohno M, Narita Y, Miyakita Y, Matsushita Y, Arita H, Yonezawa M, et al. Glioblastomas With IDH1/2 Mutations Have a Short Clinical History and Have a Favorable Clinical Outcome. *Jpn J Clin Oncol* (2016) 46(1):31–9. doi: 10.1093/jjco/hyv170

81. Vlashi E, Lagadec C, Vergnes L, Matsutani T, Masui K, Poulou M, et al. Metabolic State of Glioma Stem Cells and Nontumorigenic Cells. *Proc Natl Acad Sci USA* (2011) 108(38):16062–7. doi: 10.1073/pnas.1106704108

82. Zhou Y, Shingu T, Feng L, Chen Z, Ogasawara M, Keating MJ, et al. Metabolic Alterations in Highly Tumorigenic Glioblastoma Cells: Preference for Hypoxia and High Dependency on Glycolysis. *J Biol Chem* (2011) 286(37):32843–53. doi: 10.1074/jbc.M111.260935

83. Flavahan WA, Wu Q, Hitomi M, Rahim N, Kim Y, Sloan AE, et al. Brain Tumor Initiating Cells Adapt to Restricted Nutrition Through Preferential Glucose Uptake. *Nat Neurosci* (2013) 16(10):1373–82. doi: 10.1038/nn.3510

84. Zhou K, Yao YL, He ZC, Chen C, Zhang XN, Yang KD, et al. VDAC2 Interacts With PFKP to Regulate Glucose Metabolism and Phenotypic Reprogramming of Glioma Stem Cells. *Cell Death Dis* (2018) 9(10):988. doi: 10.1038/s41419-018-1015-x

85. Saga I, Shibao S, Okubo J, Osuka S, Kobayashi Y, Yamada S, et al. Integrated Analysis Identifies Different Metabolic Signatures for Tumor-Initiating Cells in a Murine Glioblastoma Model. *Neuro Oncol* (2014) 16(8):1048–56. doi: 10.1093/neuonc/nou096

86. Hoang-Minh LB, Siebzehnrubl FA, Yang C, Suzuki-Hatano S, Dajac K, Loche T, et al. Infiltrative and Drug-Resistant Slow-Cycling Cells Support Metabolic Heterogeneity in Glioblastoma. *EMBO J* (2018) 37(23). doi: 10.15252/embj.201798772

87. Mao P, Joshi K, Li J, Kim SH, Li P, Santana-Santos L, et al. Mesenchymal Glioma Stem Cells Are Maintained by Activated Glycolytic Metabolism Involving Aldehyde Dehydrogenase 1A3. *Proc Natl Acad Sci USA* (2013) 110(21):8644–9. doi: 10.1073/pnas.1221478110

88. Duraj T, García-Romero N, Carrión-Navarro J, Madurga R, Mendivil AO, Prat-Acin R, et al. Beyond the Warburg Effect: Oxidative and Glycolytic Phenotypes Coexist Within the Metabolic Heterogeneity of Glioblastoma. *Cells* (2021) 10(2):202. doi: 10.3390/cells10020202

89. Özcan E, Çakır T. Reconstructed Metabolic Network Models Predict Flux-Level Metabolic Reprogramming in Glioblastoma. *Front Neurosci* (2016) 10:156. doi: 10.3389/fnins.2016.00156

90. Shibao S, Minami N, Koike N, Fukui N, Yoshida K, Saya H, et al. Metabolic Heterogeneity and Plasticity of Glioma Stem Cells in a Mouse Glioblastoma Model. *Neuro Oncol* (2018) 20(3):343–54. doi: 10.1093/neuonc/nox170

91. DeBerardinis RJ, Mancuso A, Daikhin E, Nissim I, Yudkoff M, Wehrli S, et al. Beyond Aerobic Glycolysis: Transformed Cells Can Engage in Glutamine Metabolism That Exceeds the Requirement for Protein and Nucleotide Synthesis. *Proc Natl Acad Sci USA* (2007) 104(49):19345–50. doi: 10.1073/pnas.0709747104

92. Mashimo T, Pichumani K, Vemireddy V, Hatanpaa KJ, Singh DK, Sirasanagandla S, et al. Acetate is a Bioenergetic Substrate for Human Glioblastoma and Brain Metastases. *Cell* (2014) 159(7):1603–14. doi: 10.1016/j.cell.2014.11.025

93. Castegna A, Menga A. Glutamine Synthetase: Localization Dictates Outcome. *Genes (Basel)* (2018) 9(2):108. doi: 10.3390/genes9020108

94. Jin L, Alesi GN, Kang S. Glutaminolysis as a Target for Cancer Therapy. *Oncogene* (2016) 35(28):3619–25. doi: 10.1038/onc.2015.447

95. Takano T, Lin JH, Arcuino G, Gao Q, Yang J, Nedergaard M. Glutamate Release Promotes Growth of Malignant Gliomas. *Nat Med* (2001) 7 (9):1010–5. doi: 10.1038/nm0901-1010

96. Suina K, Tsuchihashi K, Yamasaki J, Kamenori S, Shintani S, Hirata Y, et al. Epidermal Growth Factor Receptor Promotes Glioma Progression by Regulating xCT and GluN2B-Containing N-Methyl-D-Aspartate-Sensitive Glutamate Receptor Signaling. *Cancer Sci* (2018) 109(12):3874–82. doi: 10.1111/cas.13826

97. Tsuchihashi K, Okazaki S, Ohmura M, Ishikawa M, Sampetrean O, Onishi N, et al. The EGF Receptor Promotes the Malignant Potential of Glioma by Regulating Amino Acid Transport System Xc(-). *Cancer Res* (2016) 76 (10):2954–63. doi: 10.1158/0008-5472.can-15-2121

98. Walls AB, Waagepetersen HS, Bak LK, Schousboe A, Sonnewald U. The Glutamine-Glutamate/GABA Cycle: Function, Regional Differences in Glutamate and GABA Production and Effects of Interference With GABA Metabolism. *Neurochem Res* (2015) 40(2):402–9. doi: 10.1007/s11064-014-1473-1

99. Wise DR, DeBerardinis RJ, Mancuso A, Sayed N, Zhang XY, Pfeiffer HK, et al. Myc Regulates a Transcriptional Program That Stimulates Mitochondrial Glutaminolysis and Leads to Glutamine Addiction. *Proc Natl Acad Sci USA* (2008) 105(48):18782–7. doi: 10.1073/pnas.0810199105

100. Wice BM, Reitzer LJ, Kennell D. The Continuous Growth of Vertebrate Cells in the Absence of Sugar. *J Biol Chem* (1981) 256(15):7812–9. doi: 10.1016/S0021-9258(18)43351-0

101. Reitzer LJ, Wice BM, Kennell D. Evidence That Glutamine, Not Sugar, is the Major Energy Source for Cultured HeLa Cells. *J Biol Chem* (1979) 254 (8):2669–76. doi: 10.1016/S0021-9258(17)30124-2

102. Linker W, Löffler M, Schneider F. Uridine, But Not Cytidine can Sustain Growth of Ehrlich Ascites Tumor Cells in Glucose-Deprived Medium With Altered Proliferation Kinetics. *Eur J Cell Biol* (1985) 36(2):176–81.

103. Yuneva M, Zamboni N, Oefner P, Sachidanandam R, Lazebnik Y. Deficiency in Glutamine But Not Glucose Induces MYC-Dependent Apoptosis in Human Cells. *J Cell Biol* (2007) 178(1):93–105. doi: 10.1083/jcb.200703099

104. Gao P, Tchernyshyov I, Chang TC, Lee YS, Kita K, Ochi T, et al. C-Myc Suppression of miR-23a/B Enhances Mitochondrial Glutaminase Expression and Glutamine Metabolism. *Nature* (2009) 458(7239):762–5. doi: 10.1038/nature07823

105. Cheng T, Sudderth J, Yang C, Mullen AR, Jin ES, Matés JM, et al. Pyruvate Carboxylase Is Required for Glutamine-Independent Growth of Tumor Cells. *Proc Natl Acad Sci USA* (2011) 108(21):8674–9. doi: 10.1073/pnas.1016627108

106. Fan TW, Lane AN, Higashi RM, Farag MA, Gao H, Bousamra M, et al. Altered Regulation of Metabolic Pathways in Human Lung Cancer Discerned by (13)C Stable Isotope-Resolved Metabolomics (SIRM). *Mol Cancer* (2009) 8:41. doi: 10.1186/1476-4598-8-41

107. Oizel K, Chauvin C, Oliver L, Gratas C, Geraldo F, Jarry U, et al. Efficient Mitochondrial Glutamine Targeting Prevails Over Glioblastoma Metabolic Plasticity. *Clin Cancer Res* (2017) 23(20):6292–304. doi: 10.1158/1078-0432.CCR-16-3102

108. Marin-Valencia I, Yang C, Mashimo T, Cho S, Baek H, Yang XL, et al. Analysis of Tumor Metabolism Reveals Mitochondrial Glucose Oxidation in Genetically Diverse Human Glioblastomas in the Mouse Brain *In Vivo*. *Cell Metab* (2012) 15(6):827–37. doi: 10.1016/j.cmet.2012.05.001

109. Tardito S, Oudin A, Ahmed SU, Fack F, Keunen O, Zheng L, et al. Glutamine Synthetase Activity Fuels Nucleotide Biosynthesis and Supports Growth of Glutamine-Restricted Glioblastoma. *Nat Cell Biol* (2015) 17(12):1556–68. doi: 10.1038/ncb3272

110. Semba S, Kodama Y, Ohnuma K, Mizuuchi E, Masuda R, Yashiro M, et al. Direct Cancer-Stromal Interaction Increases Fibroblast Proliferation and Enhances Invasive Properties of Scirrhous-Type Gastric Carcinoma Cells. *Br J Cancer* (2009) 101(8):1365–73. doi: 10.1038/sj.bjc.6605309

111. Yoriki K, Mori T, Kokabu T, Matsushima H, Umemura S, Tarumi Y, et al. Estrogen-Related Receptor Alpha Induces Epithelial-Mesenchymal Transition Through Cancer-Stromal Interactions in Endometrial Cancer. *Sci Rep* (2019) 9(1):6697. doi: 10.1038/s41598-019-43261-z

112. Biasoli D, Sobrinho MF, da Fonseca AC, de Matos DG, Romão L, de Moraes Maciel R, et al. Glioblastoma Cells Inhibit Astrocytic P53-Expression Favoring Cancer Malignancy. *Oncogenesis* (2014) 3:e123. doi: 10.1038/oncsis.2014.36

113. Kallenberg K, Bock HC, Helms G, Jung K, Wrede A, Buhk JH, et al. Untreated Glioblastoma Multiforme: Increased Myo-Inositol and Glutamine Levels in the Contralateral Cerebral Hemisphere at Proton MR Spectroscopy. *Radiology* (2009) 253(3):805–12. doi: 10.1148/radiol.2533071654

114. Azzalin A, Nato G, Parmigiani E, Garello F, Buffo A, Magrassi L. Inhibitors of GLUT/SLC2A Enhance the Action of BCNU and Temozolomide Against High-Grade Gliomas. *Neoplasia* (2017) 19(4):364–73. doi: 10.1016/j.neo.2017.02.009

115. Shibuya K, Okada M, Suzuki S, Seino M, Seino S, Takeda H, et al. Targeting the Facilitative Glucose Transporter GLUT1 Inhibits the Self-Renewal and Tumor-Initiating Capacity of Cancer Stem Cells. *Oncotarget* (2015) 6(2):651–61. doi: 10.18632/oncotarget.2892

116. Veys K, Fan Z, Ghobrial M, Bouché A, García-Caballero M, Vriens K, et al. Role of the GLUT1 Glucose Transporter in Postnatal CNS Angiogenesis and Blood-Brain Barrier Integrity. *Circ Res* (2020) 127(4):466–82. doi: 10.1161/CIRCRESAHA.119.316463

117. Cosset É, Ilmjärv S, Dutoit V, Elliott K, von Schalscha T, Camargo MF, et al. Glut3 Addiction Is a Druggable Vulnerability for a Molecularly Defined Subpopulation of Glioblastoma. *Cancer Cell* (2017) 32(6):856–68. doi: 10.1016/j.ccell.2017.10.016

118. Agnihotri S, Mansouri S, Burrell K, Li M, Mamatjan Y, Liu J, et al. Ketoconazole and Posaconazole Selectively Target HK2-Expressing Glioblastoma Cells. *Clin Cancer Res* (2019) 25(2):844–55. doi: 10.1158/1078-0432.CCR-18-1854

119. Shah SS, Rodriguez GA, Musick A, Walters WM, de Cordoba N, Barbarite E, et al. Targeting Glioblastoma Stem Cells With 2-Deoxy-D-Glucose (2-DG) Potentiates Radiation-Induced Unfolded Protein Response (UPR). *Cancers (Basel)* (2019) 11(2):159. doi: 10.3390/cancers11020159

120. Abbas S, Singh SK, Saxena AK, Tiwari S, Sharma LK, Tiwari M. Role of Autophagy in Regulation of Glioma Stem Cells Population During Therapeutic Stress. *J Stem Cells Regener Med* (2020) 16(2):80–9. doi: 10.46582/jsrm.1602012

121. Liu J, Wang P, Xue YX, Li Z, Qu CB, Liu YH. Enhanced Antitumor Effect of Shikonin by Inhibiting Endoplasmic Reticulum Stress *via* JNK/c-Jun Pathway in Human Glioblastoma Stem Cells. *Biochem Biophys Res Commun* (2015) 466(1):103–10. doi: 10.1016/j.bbrc.2015.08.115

122. Kang BR, Yang SH, Chung BR, Kim W, Kim Y. Cell Surface GRP78 as a Biomarker and Target for Suppressing Glioma Cells. *Sci Rep* (2016) 6:34922. doi: 10.1038/srep34922

123. Zhang Y, Liu R, Ni M, Gill P, Lee AS. Cell Surface Relocalization of the Endoplasmic Reticulum Chaperone and Unfolded Protein Response Regulator GRP78/BiP. *J Biol Chem* (2010) 285(20):15065–75. doi: 10.1074/jbc.M109.087445

124. Bianchi G, Martella R, Ravera S, Marini C, Capitanio S, Orengo A, et al. Fasting Induces Anti-Warburg Effect That Increases Respiration But Reduces ATP-Synthesis to Promote Apoptosis in Colon Cancer Models. *Oncotarget* (2015) 6(14):11806–19. doi: 10.18632/oncotarget.3688

125. Zuccoli G, Marcello N, Pisanello A, Servadei F, Vaccaro S, Mukherjee P, et al. Metabolic Management of Glioblastoma Multiforme Using Standard Therapy Together With a Restricted Ketogenic Diet: Case Report. *Nutr Metab (Lond)* (2010) 7:33. doi: 10.1186/1743-7075-7-33

126. Klein P, Tyrlikova I, Zuccoli G, Tyrlik A, Maroon JC. Treatment of Glioblastoma Multiforme With "Classic" 4:1 Ketogenic Diet Total Meal Replacement. *Cancer Metab* (2020) 8(1):24. doi: 10.1186/s40170-020-00230-9

127. Abdelwahab MG, Fenton KE, Preul MC, Rho JM, Lynch A, Stafford P, et al. The Ketogenic Diet is an Effective Adjuvant to Radiation Therapy for the Treatment of Malignant Glioma. *PloS One* (2012) 7(5):e36197. doi: 10.1371/journal.pone.0036197

128. Henderson CB, Filloux FM, Alder SC, Lyon JL, Caplin DA. Efficacy of the Ketogenic Diet as a Treatment Option for Epilepsy: Meta-Analysis. *J Child Neurol* (2006) 21(3):193–8. doi: 10.2310/7010.2006.00044

129. Seyfried TN, Kiebish M, Mukherjee P, Marsh J. Targeting Energy Metabolism in Brain Cancer With Calorically Restricted Ketogenic Diets. *Epilepsia* (2008) 49 Suppl 8:114–6. doi: 10.1111/j.1528-1167.2008.01853.x

130. McGirt MJ, Chaichana KL, Gathinji M, Attenello F, Than K, Jimenez Ruiz A, et al. Persistent Outpatient Hyperglycemia is Independently Associated With Decreased Survival After Primary Resection of Malignant Brain Astrocytomas. *Neurosurgery* (2008) 63(2):286–91; discussion 91. doi: 10.1227/01.NEU.0000315282.61035.48

131. Derr RL, Ye X, Islas MU, Desideri S, Saudek CD, Grossman SA. Association Between Hyperglycemia and Survival in Patients With Newly Diagnosed Glioblastoma. *J Clin Oncol* (2009) 27(7):1082–6. doi: 10.1200/JCO.2008.19.1098

132. Tieu MT, Lovblom LE, McNamara MG, Mason W, Laperriere N, Millar BA, et al. Impact of Glycemia on Survival of Glioblastoma Patients Treated With Radiation and Temozolomide. *J Neurooncol* (2015) 124(1):119–26. doi: 10.1007/s11060-015-1815-0

133. Sperry J, Condro MC, Guo L, Braas D, Vanderveer-Harris N, Kim KKO, et al. Glioblastoma Utilizes Fatty Acids and Ketone Bodies for Growth Allowing Progression During Ketogenic Diet Therapy. *iScience* (2020) 23(9):101453. doi: 10.1016/j.isci.2020.101453

134. Shelton LM, Huysentruyt LC, Mukherjee P, Seyfried TN. Calorie Restriction as an Anti-Invasive Therapy for Malignant Brain Cancer in the VM Mouse. *ASN Neuro* (2010) 2(3):e00038. doi: 10.1042/AN20100002

135. Mukherjee P, Augur ZM, Li M, Hill C, Greenwood B, Domin MA, et al. Therapeutic Benefit of Combining Calorie-Restricted Ketogenic Diet and Glutamine Targeting in Late-Stage Experimental Glioblastoma. *Commun Biol* (2019) 2:200. doi: 10.1038/s42003-019-0455-x

136. Ji CC, Hu YY, Cheng G, Liang L, Gao B, Ren YP, et al. A Ketogenic Diet Attenuates Proliferation and Stemness of Glioma Stem–Like Cells by Altering Metabolism Resulting in Increased ROS Production. *Int J Oncol* (2020) 56(2):606–17. doi: 10.3892/ijo.2019.4942

137. Seyfried TN, Sanderson TM, El-Abbadi MM, McGowan R, Mukherjee P. Role of Glucose and Ketone Bodies in the Metabolic Control of Experimental Brain Cancer. *Br J Cancer* (2003) 89(7):1375–82. doi: 10.1038/sj.bjc.6601269

138. Perer ES, Madan AK, Shurin A, Zakris E, Romeguera K, Pang Y, et al. Insulin-Like Growth Factor I Receptor Antagonism Augments Response to Chemoradiation Therapy in Colon Cancer Cells. *J Surg Res* (2000) 94(1):1–5. doi: 10.1006/jsre.2000.5923

139. Resnicoff M, Abraham D, Yutanawiboonchai W, Rotman HL, Kajstura J, Rubin R, et al. The Insulin-Like Growth Factor I Receptor Protects Tumor Cells From Apoptosis. *Vivo Cancer Res* (1995) 55(11):2463–9.

140. Zhang M, Liu J, Li M, Zhang S, Lu Y, Liang Y, et al. Insulin-Like Growth Factor 1/Insulin-Like Growth Factor 1 Receptor Signaling Protects Against Cell Apoptosis Through the PI3K/AKT Pathway in Glioblastoma Cells. *Exp Ther Med* (2018) 16(2):1477–82. doi: 10.3892/etm.2018.6336

141. Maris C, D'Haene N, Trépant AL, Le Mercier M, Sauvage S, Allard J, et al. IGF-IR: A New Prognostic Biomarker for Human Glioblastoma. *Br J Cancer* (2015) 113(5):729–37. doi: 10.1038/bjc.2015.242

142. Grommes C, Conway DS, Alshekhlee A, Barnholtz-Sloan JS. Inverse Association of Pparγ Agonists Use and High Grade Glioma Development. *J Neurooncol* (2010) 100(2):233–9. doi: 10.1007/s11060-010-0185-x

143. Sarraf P, Mueller E, Smith WM, Wright HM, Kum JB, Aaltonen LA, et al. Loss-Of-Function Mutations in PPAR Gamma Associated With Human Colon Cancer. *Mol Cell* (1999) 3(6):799–804. doi: 10.1016/s1097-2765(01)80012-5

144. Tsubouchi Y, Sano H, Kawahito Y, Mukai S, Yamada R, Kohno M, et al. Inhibition of Human Lung Cancer Cell Growth by the Peroxisome Proliferator-Activated Receptor-Gamma Agonists Through Induction of Apoptosis. *Biochem Biophys Res Commun* (2000) 270(2):400–5. doi: 10.1006/bbrc.2000.2436

145. Keshamouni VG, Reddy RC, Arenberg DA, Joel B, Thannickal VJ, Kalemkerian GP, et al. Peroxisome Proliferator-Activated Receptor-Gamma Activation Inhibits Tumor Progression in Non-Small-Cell Lung Cancer. *Oncogene* (2004) 23(1):100–8. doi: 10.1038/sj.onc.1206885

146. Mueller E, Smith M, Sarraf P, Kroll T, Aiyer A, Kaufman DS, et al. Effects of Ligand Activation of Peroxisome Proliferator-Activated Receptor Gamma in Human Prostate Cancer. *Proc Natl Acad Sci USA* (2000) 97(20):10990–5. doi: 10.1073/pnas.180329197

147. Nagata D, Yoshihiro H, Nakanishi M, Naruyama H, Okada S, Ando R, et al. Peroxisome Proliferator-Activated Receptor-Gamma and Growth Inhibition by Its Ligands in Prostate Cancer. *Cancer Detect Prev* (2008) 32(3):259–66. doi: 10.1016/j.cdp.2008.05.008

148. Kroll TG, Sarraf P, Pecciarini L, Chen CJ, Mueller E, Spiegelman BM, et al. PAX8-PPARgamma1 Fusion Oncogene in Human Thyroid Carcinoma [Corrected]. *Science* (2000) 289(5483):1357–60. doi: 10.1126/science.289.5483.1357

149. Lefterova MI, Steger DJ, Zhuo D, Qatanani M, Mullican SE, Tuteja G, et al. Cell-Specific Determinants of Peroxisome Proliferator-Activated Receptor Gamma Function in Adipocytes and Macrophages. *Mol Cell Biol* (2010) 30(9):2078–89. doi: 10.1128/mcb.01651-09

150. Zang C, Wächter M, Liu H, Posch MG, Fenner MH, Stadelmann C, et al. Ligands for PPARgamma and RAR Cause Induction of Growth Inhibition and Apoptosis in Human Glioblastomas. *J Neurooncol* (2003) 65(2):107–18. doi: 10.1023/b:neon.0000003728.80052.a8

151. Wan Z, Shi W, Shao B, Shi J, Shen A, Ma Y, et al. Peroxisome Proliferator-Activated Receptor γ Agonist Pioglitazone Inhibits β-Catenin-Mediated Glioma Cell Growth and Invasion. *Mol Cell Biochem* (2011) 349(1-2):1–10. doi: 10.1007/s11010-010-0637-9

152. Chearwae W, Bright JJ. PPARgamma Agonists Inhibit Growth and Expansion of CD133+ Brain Tumour Stem Cells. *Br J Cancer* (2008) 99(12):2044–53. doi: 10.1038/sj.bjc.6604786

153. Mo C, Chearwae W, Bright JJ. PPARgamma Regulates LIF-Induced Growth and Self-Renewal of Mouse ES Cells Through Tyk2-Stat3 Pathway. *Cell Signal* (2010) 22(3):495–500. doi: 10.1016/j.cellsig.2009.11.003

154. Villalva C, Martin-Lannerée S, Cortes U, Dkhissi F, Wager M, Le Corf A, et al. STAT3 Is Essential for the Maintenance of Neurosphere-Initiating Tumor Cells in Patients With Glioblastomas: A Potential for Targeted Therapy? *Int J Cancer* (2011) 128(4):826–38. doi: 10.1002/ijc.25416

155. Moore N, Houghton J, Lyle S. Slow-Cycling Therapy-Resistant Cancer Cells. *Stem Cells Dev* (2012) 21(10):1822–30. doi: 10.1089/scd.2011.0477

156. Dong Y, Han Q, Zou Y, Deng Z, Lu X, Wang X, et al. Long-Term Exposure to Imatinib Reduced Cancer Stem Cell Ability Through Induction of Cell Differentiation *via* Activation of MAPK Signaling in Glioblastoma Cells. *Mol Cell Biochem* (2012) 370(1-2):89–102. doi: 10.1007/s11010-012-1401-0

157. Pestereva E, Kanakasabai S, Bright JJ. Pparγ Agonists Regulate the Expression of Stemness and Differentiation Genes in Brain Tumour Stem Cells. *Br J Cancer* (2012) 106(10):1702–12. doi: 10.1038/bjc.2012.161

158. Kanakasabai S, Pestereva E, Chearwae W, Gupta SK, Ansari S, Bright JJ. Pparγ Agonists Promote Oligodendrocyte Differentiation of Neural Stem Cells by Modulating Stemness and Differentiation Genes. *PloS One* (2012) 7(11):e50500. doi: 10.1371/journal.pone.0050500

159. Carén H, Beck S, Pollard SM. Differentiation Therapy for Glioblastoma - Too Many Obstacles? *Mol Cell Oncol* (2016) 3(2):e1124174. doi: 10.1080/23723556.2015.1124174

160. Strakova N, Ehrmann J, Bartos J, Malikova J, Dolezel J, Kolar Z. Peroxisome Proliferator-Activated Receptors (PPAR) Agonists Affect Cell Viability, Apoptosis and Expression of Cell Cycle Related Proteins in Cell Lines of Glial Brain Tumors. *Neoplasma* (2005) 52(2):126–36.

161. Haynes HR, White P, Hares KM, Redondo J, Kemp KC, Singleton WGB, et al. The Transcription Factor Pparα is Overexpressed and is Associated With a Favourable Prognosis in IDH-Wildtype Primary Glioblastoma. *Histopathology* (2017) 70(7):1030–43. doi: 10.1111/his.13142

162. Hann SS, Zheng F, Zhao S. Targeting 3-Phosphoinositide-Dependent Protein Kinase 1 by N-Acetyl-Cysteine Through Activation of Peroxisome Proliferators Activated Receptor Alpha in Human Lung Cancer Cells, the Role of P53 and P65. *J Exp Clin Cancer Res* (2013) 32:43. doi: 10.1186/1756-9966-32-43

163. Skrypnyk N, Chen X, Hu W, Su Y, Mont S, Yang S, et al. Pparα Activation can Help Prevent and Treat Non-Small Cell Lung Cancer. *Cancer Res* (2014) 74(2):621–31. doi: 10.1158/0008-5472.CAN-13-1928

164. Grabacka MM, Wilk A, Antonczyk A, Banks P, Walczyk-Tytko E, Dean M, et al. Fenofibrate Induces Ketone Body Production in Melanoma and Glioblastoma Cells. *Front Endocrinol (Lausanne)* (2016) 7:5. doi: 10.3389/fendo.2016.00005

165. Kostiuk MA, Keller BO, Berthiaume LG. Palmitoylation of Ketogenic Enzyme HMGCS2 Enhances Its Interaction With PPARalpha and Transcription at the Hmgcs2 PPRE. *FASEB J* (2010) 24(6):1914–24. doi: 10.1096/fj.09-149765

166. Urbanska K, Pannizzo P, Grabacka M, Croul S, Del Valle L, Khalili K, et al. Activation of PPARalpha Inhibits IGF-I-Mediated Growth and Survival Responses in Medulloblastoma Cell Lines. *Int J Cancer* (2008) 123(5):1015–24. doi: 10.1002/ijc.23588

167. Ribet C, Montastier E, Valle C, Bezaire V, Mazzucotelli A, Mairal A, et al. Peroxisome Proliferator-Activated Receptor-Alpha Control of Lipid and Glucose Metabolism in Human White Adipocytes. *Endocrinology* (2010) 151(1):123–33. doi: 10.1210/en.2009-0726

168. You M, Jin J, Liu Q, Xu Q, Shi J, Hou Y. Pparα Promotes Cancer Cell Glut1 Transcription Repression. *J Cell Biochem* (2017) 118(6):1556–62. doi: 10.1002/jcb.25817

169. Vidone M, Clima R, Santorsola M, Calabrese C, Girolimetti G, Kurelac I, et al. A Comprehensive Characterization of Mitochondrial DNA Mutations in Glioblastoma Multiforme. *Int J Biochem Cell Biol* (2015) 63:46–54. doi: 10.1016/j.biocel.2015.01.027

170. Yeung KY, Dickinson A, Donoghue JF, Polekhina G, White SJ, Grammatopoulos DK, et al. The Identification of Mitochondrial DNA Variants in Glioblastoma Multiforme. *Acta Neuropathol Commun* (2014) 2:1. doi: 10.1186/2051-5960-2-1

171. Lloyd RE, Keatley K, Littlewood DT, Meunier B, Holt WV, An Q, et al. Identification and Functional Prediction of Mitochondrial Complex III and IV Mutations Associated With Glioblastoma. *Neuro Oncol* (2015) 17(7):942–52. doi: 10.1093/neuonc/nov020

172. Oliva CR, Nozell SE, Diers A, McClugage SG, Sarkaria JN, Markert JM, et al. Acquisition of Temozolomide Chemoresistance in Gliomas Leads to Remodeling of Mitochondrial Electron Transport Chain. *J Biol Chem* (2010) 285(51):39759–67. doi: 10.1074/jbc.M110.147504

173. Oliva CR, Markert T, Gillespie GY, Griguer CE. Nuclear-Encoded Cytochrome C Oxidase Subunit 4 Regulates BMI1 Expression and Determines Proliferative Capacity of High-Grade Gliomas. *Oncotarget* (2015) 6(6):4330–44. doi: 10.18632/oncotarget.3015

174. Oliva CR, Markert T, Ross LJ, White EL, Rasmussen L, Zhang W, et al. Identification of Small Molecule Inhibitors of Human Cytochrome C Oxidase That Target Chemoresistant Glioma Cells. *J Biol Chem* (2016) 291 (46):24188–99. doi: 10.1074/jbc.M116.749978

175. Oliva CR, Zhang W, Langford C, Suto MJ, Griguer CE. Repositioning Chlorpromazine for Treating Chemoresistant Glioma Through the Inhibition of Cytochrome C Oxidase Bearing the COX4-1 Regulatory Subunit. *Oncotarget* (2017) 8(23):37568–83. doi: 10.18632/oncotarget.17247

176. Birsoy K, Possemato R, Lorbeer FK, Bayraktar EC, Thiru P, Yucel B, et al. Metabolic Determinants of Cancer Cell Sensitivity to Glucose Limitation and Biguanides. *Nature* (2014) 508(7494):108–12. doi: 10.1038/nature13110

177. Wheaton WW, Weinberg SE, Hamanaka RB, Soberanes S, Sullivan LB, Anso E, et al. Metformin Inhibits Mitochondrial Complex I of Cancer Cells to Reduce Tumorigenesis. *Elife* (2014) 3:e02242. doi: 10.7554/eLife.02242

178. Sikka A, Kaur M, Agarwal C, Deep G, Agarwal R. Metformin Suppresses Growth of Human Head and Neck Squamous Cell Carcinoma *via* Global Inhibition of Protein Translation. *Cell Cycle* (2012) 11(7):1374–82. doi: 10.4161/cc.19798

179. Würth R, Pattarozzi A, Gatti M, Bajetto A, Corsaro A, Parodi A, et al. Metformin Selectively Affects Human Glioblastoma Tumor-Initiating Cell Viability: A Role for Metformin-Induced Inhibition of Akt. *Cell Cycle* (2013) 12(1):145–56. doi: 10.4161/cc.23050

180. Yu Z, Zhao G, Xie G, Zhao L, Chen Y, Yu H, et al. Metformin and Temozolomide Act Synergistically to Inhibit Growth of Glioma Cells and Glioma Stem Cells *In Vitro* and *In Vivo*. *Oncotarget* (2015) 6(32):32930–43. doi: 10.18632/oncotarget.5405

181. Hirsch HA, Iliopoulos D, Tsichlis PN, Struhl K. Metformin Selectively Targets Cancer Stem Cells, and Acts Together With Chemotherapy to Block Tumor Growth and Prolong Remission. *Cancer Res* (2009) 69 (19):7507–11. doi: 10.1158/0008-5472.CAN-09-2994

182. Jiang W, Finniss S, Cazacu S, Xiang C, Brodie Z, Mikkelsen T, et al. Repurposing Phenformin for the Targeting of Glioma Stem Cells and the Treatment of Glioblastoma. *Oncotarget* (2016) 7(35):56456–70. doi: 10.18632/oncotarget.10919

183. Haugrud AB, Zhuang Y, Coppock JD, Miskimins WK. Dichloroacetate Enhances Apoptotic Cell Death *via* Oxidative Damage and Attenuates Lactate Production in Metformin-Treated Breast Cancer Cells. *Breast Cancer Res Treat* (2014) 147(3):539–50. doi: 10.1007/s10549-014-3128-y

184. Liu Y, Fang S, Sun Q, Liu B. Anthelmintic Drug Ivermectin Inhibits Angiogenesis, Growth and Survival of Glioblastoma Through Inducing Mitochondrial Dysfunction and Oxidative Stress. *Biochem Biophys Res Commun* (2016) 480(3):415–21. doi: 10.1016/j.bbrc.2016.10.064

185. Liu YJ, Ma YC, Zhang WJ, Yang ZZ, Liang DS, Wu ZF, et al. Combination Therapy With Micellarized Cyclopamine and Temozolomide Attenuate Glioblastoma Growth Through Gli1 Down-Regulation. *Oncotarget* (2017) 8(26):42495–509. doi: 10.18632/oncotarget.17205

186. Wang H, Cai S, Bailey BJ, Reza Saadatzadeh M, Ding J, Tonsing-Carter E, et al. Combination Therapy in a Xenograft Model of Glioblastoma: Enhancement of the Antitumor Activity of Temozolomide by an MDM2 Antagonist. *J Neurosurg* (2017) 126(2):446–59. doi: 10.3171/2016.1.JNS152513

187. Kim SS, Rait A, Kim E, Pirollo KF, Chang EH. A Tumor-Targeting P53 Nanodelivery System Limits Chemoresistance to Temozolomide Prolonging Survival in a Mouse Model of Glioblastoma Multiforme. *Nanomedicine* (2015) 11(2):301–11. doi: 10.1016/j.nano.2014.09.005

188. Prasad G, Sottero T, Yang X, Mueller S, James CD, Weiss WA, et al. Inhibition of PI3K/mTOR Pathways in Glioblastoma and Implications for Combination Therapy With Temozolomide. *Neuro Oncol* (2011) 13(4):384–92. doi: 10.1093/neuonc/noq193

189. Nitta Y, Shimizu S, Shishido-Hara Y, Suzuki K, Shiokawa Y, Nagane M. Nimotuzumab Enhances Temozolomide-Induced Growth Suppression of Glioma Cells Expressing Mutant EGFR *In Vivo*. *Cancer Med* (2016) 5 (3):486–99. doi: 10.1002/cam4.614

190. Lesueur P, Chevalier F, El-Habr EA, Junier MP, Chneiweiss H, Castera L, et al. Radiosensitization Effect of Talazoparib, a Parp Inhibitor, on Glioblastoma Stem Cells Exposed to Low and High Linear Energy Transfer Radiation. *Sci Rep* (2018) 8(1):3664. doi: 10.1038/s41598-018-22022-4

191. Whittaker S, Madani D, Joshi S, Chung SA, Johns T, Day B, et al. Combination of Palbociclib and Radiotherapy for Glioblastoma. *Cell Death Discovery* (2017) 3:17033. doi: 10.1038/cddiscovery.2017.33

192. Ishida CT, Zhang Y, Bianchetti E, Shu C, Nguyen TTT, Kleiner G, et al. Metabolic Reprogramming by Dual AKT/ERK Inhibition Through Imipridones Elicits Unique Vulnerabilities in Glioblastoma. *Clin Cancer Res* (2018) 24(21):5392–406. doi: 10.1158/1078-0432.CCR-18-1040

193. Yuan S, Wang F, Chen G, Zhang H, Feng L, Wang L, et al. Effective Elimination of Cancer Stem Cells by a Novel Drug Combination Strategy. *Stem Cells* (2013) 31(1):23–34. doi: 10.1002/stem.1273

194. Shen H, Decollogne S, Dilda PJ, Hau E, Chung SA, Luk PP, et al. Dual-Targeting of Aberrant Glucose Metabolism in Glioblastoma. *J Exp Clin Cancer Res* (2015) 34:14. doi: 10.1186/s13046-015-0130-0

195. Karpel-Massler G, Bâ M, Shu C, Halatsch ME, Westhoff MA, Bruce JN, et al. TIC10/ONC201 Synergizes With Bcl-2/Bcl-xL Inhibition in Glioblastoma by Suppression of Mcl-1 and Its Binding Partners *In Vitro* and *In Vivo*. *Oncotarget* (2015) 6(34):36456–71. doi: 10.18632/oncotarget.5505

196. Leidgens V, Proske J, Rauer L, Moeckel S, Renner K, Bogdahn U, et al. Stattic and Metformin Inhibit Brain Tumor Initiating Cells by Reducing STAT3-Phosphorylation. *Oncotarget* (2017) 8(5):8250–63. doi: 10.18632/oncotarget.14159

197. Yang SH, Li S, Lu G, Xue H, Kim DH, Zhu JJ, et al. Metformin Treatment Reduces Temozolomide Resistance of Glioblastoma Cells. *Oncotarget* (2016) 7(48):78787–803. doi: 10.18632/oncotarget.12859

198. Gritti M, Würth R, Angelini M, Barbieri F, Peretti M, Pizzi E, et al. Metformin Repositioning as Antitumoral Agent: Selective Antiproliferative Effects in Human Glioblastoma Stem Cells, *via* Inhibition of CLIC1-Mediated Ion Current. *Oncotarget* (2014) 5(22):11252–68. doi: 10.18632/oncotarget.2617

199. Owen MR, Doran E, Halestrap AP. Evidence That Metformin Exerts Its Anti-Diabetic Effects Through Inhibition of Complex 1 of the Mitochondrial Respiratory Chain. *Biochem J* (2000) 348 Pt 3:607–14. doi: 10.1042/bj3480607

200. Xiong ZS, Gong SF, Si W, Jiang T, Li QL, Wang TJ, et al. Effect of Metformin on Cell Proliferation, Apoptosis, Migration and Invasion in A172 Glioma Cells and Its Mechanisms. *Mol Med Rep* (2019) 20(2):887–94. doi: 10.3892/mmr.2019.10369

201. Sato A, Sunayama J, Okada M, Watanabe E, Seino S, Shibuya K, et al. Glioma-Initiating Cell Elimination by Metformin Activation of FOXO3 *via* AMPK. *Stem Cells Transl Med* (2012) 1(11):811–24. doi: 10.5966/sctm.2012-0058

202. Firat E, Weyerbrock A, Gaedicke S, Grosu AL, Niedermann G. Chloroquine or Chloroquine-PI3K/Akt Pathway Inhibitor Combinations Strongly Promote γ-Irradiation-Induced Cell Death in Primary Stem-Like Glioma Cells. *PloS One* (2012) 7(10):e47357. doi: 10.1371/journal.pone.0047357

203. Kim EL, Wüstenberg R, Rübsam A, Schmitz-Salue C, Warnecke G, Bücker EM, et al. Chloroquine Activates the P53 Pathway and Induces Apoptosis in Human Glioma Cells. *Neuro Oncol* (2010) 12(4):389–400. doi: 10.1093/neuonc/nop046

204. Lee SW, Kim HK, Lee NH, Yi HY, Kim HS, Hong SH, et al. The Synergistic Effect of Combination Temozolomide and Chloroquine Treatment is Dependent on Autophagy Formation and P53 Status in Glioma Cells. *Cancer Lett* (2015) 360(2):195–204. doi: 10.1016/j.canlet.2015.02.012

205. Ye H, Chen M, Cao F, Huang H, Zhan R, Zheng X. Chloroquine, an Autophagy Inhibitor, Potentiates the Radiosensitivity of Glioma Initiating Cells by Inhibiting Autophagy and Activating Apoptosis. *BMC Neurol* (2016) 16(1):178. doi: 10.1186/s12883-016-0700-6

206. Liang DH, Choi DS, Ensor JE, Kaipparettu BA, Bass BL, Chang JC. The Autophagy Inhibitor Chloroquine Targets Cancer Stem Cells in Triple Negative Breast Cancer by Inducing Mitochondrial Damage and Impairing DNA Break Repair. *Cancer Lett* (2016) 376(2):249–58. doi: 10.1016/j.canlet.2016.04.002

207. Golden EB, Cho HY, Jahanian A, Hofman FM, Louie SG, Schönthal AH, et al. Chloroquine Enhances Temozolomide Cytotoxicity in Malignant Gliomas by Blocking Autophagy. *Neurosurg Focus* (2014) 37(6):E12. doi: 10.3171/2014.9.FOCUS14504

208. Bayat N, Ebrahimi-Barough S, Norouzi-Javidan A, Saberi H, Tajerian R, Ardakan MMM, et al. Apoptotic Effect of Atorvastatin in Glioblastoma

Spheroids Tumor Cultured in Fibrin Gel. *BioMed Pharmacother* (2016) 84:1959–66. doi: 10.1016/j.biopha.2016.11.003

209. Peng P, Wei W, Long C, Li J. Atorvastatin Augments Temozolomide's Efficacy in Glioblastoma *via* Prenylation-Dependent Inhibition of Ras Signaling. *Biochem Biophys Res Commun* (2017) 489(3):293–8. doi: 10.1016/j.bbrc.2017.05.147

210. Kang KB, Zhu C, Yong SK, Gao Q, Wong MC. Enhanced Sensitivity of Celecoxib in Human Glioblastoma Cells: Induction of DNA Damage Leading to P53-Dependent G1 Cell Cycle Arrest and Autophagy. *Mol Cancer* (2009) 8:66. doi: 10.1186/1476-4598-8-66

211. Shono K, Yamaguchi I, Mizobuchi Y, Kagusa H, Sumi A, Fujihara T, et al. Downregulation of the CCL2/CCR2 and CXCL10/CXCR3 Axes Contributes to Antitumor Effects in a Mouse Model of Malignant Glioma. *Sci Rep* (2020) 10(1):15286. doi: 10.1038/s41598-020-71857-3

212. Yamaguchi I, Nakajima K, Shono K, Mizobuchi Y, Fujihara T, Shikata E, et al. Downregulation of PD-L1 *via* FKBP5 by Celecoxib Augments Antitumor Effects of PD-1 Blockade in a Malignant Glioma Model. *Neurooncol Adv* (2020) 2(1):vdz058. doi: 10.1093/noajnl/vdz058

213. Hothi P, Martins TJ, Chen L, Deleyrolle L, Yoon JG, Reynolds B, et al. High-Throughput Chemical Screens Identify Disulfiram as an Inhibitor of Human Glioblastoma Stem Cells. *Oncotarget* (2012) 3(10):1124–36. doi: 10.18632/oncotarget.707

214. Triscott J, Lee C, Hu K, Fotovati A, Berns R, Pambid M, et al. Disulfiram, a Drug Widely Used to Control Alcoholism, Suppresses the Self-Renewal of Glioblastoma and Over-Rides Resistance to Temozolomide. *Oncotarget* (2012) 3(10):1112–23. doi: 10.18632/oncotarget.604

215. Paranjpe A, Zhang R, Ali-Osman F, Bobustuc GC, Srivenugopal KS. Disulfiram is a Direct and Potent Inhibitor of Human O6-Methylguanine-DNA Methyltransferase (MGMT) in Brain Tumor Cells and Mouse Brain and Markedly Increases the Alkylating DNA Damage. *Carcinogenesis* (2014) 35(3):692–702. doi: 10.1093/carcin/bgt366

216. Kast RE, Boockvar JA, Brüning A, Cappello F, Chang WW, Cvek B, et al. A Conceptually New Treatment Approach for Relapsed Glioblastoma: Coordinated Undermining of Survival Paths With Nine Repurposed Drugs (CUSP9) by the International Initiative for Accelerated Improvement of Glioblastoma Care. *Oncotarget* (2013) 4(4):502–30. doi: 10.18632/oncotarget.969

217. Kast RE, Karpel-Massler G, Halatsch ME. CUSP9* Treatment Protocol for Recurrent Glioblastoma: Aprepitant, Artesunate, Auranofin, Captopril, Celecoxib, Disulfiram, Itraconazole, Ritonavir, Sertraline Augmenting Continuous Low Dose Temozolomide. *Oncotarget* (2014) 5(18):8052–82. doi: 10.18632/oncotarget.2408

p53-Independent Effects of Set7/9 Lysine Methyltransferase on Metabolism of Non-Small Cell Lung Cancer Cells

Alexandra Daks[1†], Oleg Shuvalov[1†], Olga Fedorova[1], Alexey Petukhov[1,2], Larissa Lezina[3], Arsenia Zharova[1], Ekaterina Baidyuk[1], Alexander Khudiakov[2] and Nickolai A. Barlev[1,3*]

[1] Institute of Cytology, Russian Academy of Sciences, St Petersburg, Russia, [2] Institute of Molecular Biology and Genetics, Almazov National Medical Research Centre, St Petersburg, Russia, [3] Regulation of Cell Signaling Laboratory, Moscow Institute of Physics and Technology, Dolgoprudny, Russia

Set7/9 is a lysine-specific methyltransferase, which regulates the functioning of both the histone and non-histone substrates, thereby significantly affecting the global gene expression landscape. Using microarray expression profiling, we have identified several key master regulators of metabolic networks, including c-Myc, that were affected by Set7/9 status. Consistent with this observation, c-Myc transcriptional targets—genes encoding the glycolytic enzymes hexokinase (HK2), aldolase (ALDOB), and lactate dehydrogenase (LDHA)—were upregulated upon Set7/9 knockdown (Set7/9KD). Importantly, we showed the short hairpin RNA (shRNA)-mediated attenuation of Set7/9 augmented c-Myc, GLUT1, HK2, ALDOA, and LDHA expression in non-small cell lung cancer (NSCLC) cell lines, not only at the transcriptional but also at the protein level. In line with this observation, Set7/9KD significantly augmented the membrane mitochondrial potential (MMP), glycolysis, respiration, and the proliferation rate of NSCLC cells. Importantly, all these effects of Set7/9 on cell metabolism were p53-independent. Bioinformatic analysis has shown a synergistic impact of Set7/9 together with either GLUT1, HIF1A, HK2, or LDHA on the survival of lung cancer patients. Based on these evidence, we hypothesize that Set7/9 can be an important regulator of energy metabolism in NSCLC.

Keywords: Set7/9, SETD7, non-small cell lung cancer (NSCLC), glycolysis, metabolism

INTRODUCTION

Lysine methylation plays an important role in global transcription regulation. Depending on the location of the target lysine in histone tails, this post-translational modification can either promote or repress transcription by affecting the architecture of chromatin. In addition, lysine methylation, by competing with other lysine-specific modifications (e.g., acetylation, ubiquitinylation, and SUMOylation), can affect the protein stability and hence its functioning (1). Set7/9 (alternative

---

Abbreviations: MMP, mitochondrial membrane potential; NSCLC, non-small cell lung cancer; TMRE, tetramethylrhodamine, ethyl ester; ECAR, extracellular acidification rate; OCR, oxygen consumption rate.

name SETD7) is a SET [Su(var)-3–9, Enhancer-of-Zeste, Trithorax] domain-containing protein that utilizes both histone and non-histone proteins as substrates. Initially, Set7/9 was shown to specifically monomethylate lysine 4 of histone 3 (H3K4me1), which is a positive mark for transcriptional activation (2, 3).

For instance, Set7/9-mediated methylation of histone H3 at lysine 4 enhances the transcriptional activation of myogenic differentiation genes (MYOD, MYOGENIN, MHC, and MCK) (4), the inflammatory gene RelA/NFκB (5), nitric oxide synthase (NOS2) (6), SREK1IP1, and PGC (7). Later, in addition to histone H3, Set7/9 was shown to methylate histones H2A, H2B, and H1.4 (8–10).

Several examples of non-histone substrates of Set7/9 include the tumor suppressor p53 (11), estrogen receptor alpha (ERa) (12), PCAF (P300/CBP-associated factor) (13), RelA (NFκB) (14), β-catenin (15), and E2F1 (16). By methylating these substrates, Set7/9 regulates their activity, stability, and subcellular localization (8).

Set7/9 is shown to be involved in various signaling pathways associated with several diseases, including cancer (8). We and other researchers have demonstrated the involvement of this lysine methyltransferase in the progression of various malignancies, including lung cancer (16–19). Lung cancer is one of the most frequent and dangerous groups of malignancies. It tops the list of cancer-related deaths in men and ranks second in women worldwide (20). The 5-year survival rate with all types of lung cancer ranges between only 17% and 21%. Importantly, the role of Set7/9 in lung cancer is rather contradictive, since it was shown to have both oncogenic (16, 18) and tumor-suppressive properties (21).

Using RNA-seq analysis, Keating with co-authors (22) have revealed a correlation between the gene expression profile in Set7/9 knocked down cells and the status of several transcription factors known to be the targets of Set7/9, including p53, NFκB, c-Jun, c-Fos, GATA2, ERa, and STAT3. This study linked the cellular status of Set7/9 with global changes in gene expression profiles of various cell lines.

To further elucidate the role of Set7/9 in tumorigenesis, we assessed the effect of Set7/9 ablation on global gene expression in various cancer cell lines. We have identified c-Myc and HIF1A as Set7/9-dependent genes. Moreover, we have shown that NSCLC cells with an attenuated expression of Set7/9 displayed increased mitochondrial membrane potential (MMP), glycolysis, and respiration rates. In line with these observations, Set7/9-deficient cells possessed elevated proliferation rates. Bioinformatic analysis revealed the synergistic effect between the Set7/9 and either HIF1A, HK2, GLUT1, or LDHA expression levels on the survival outcome of lung cancer patients.

MATERIALS AND METHODS

Cell Cultures and Stable Cell Lines Establishment

All cell lines were purchased from American Type Culture Collection (ATCC) (USA) and genotyped by the shared research facility "Vertebrate cell culture collection," Institute of Cytology, Russian Academy of Science, St Petersburg, Russia. Cells were incubated in either Dulbecco's modified Eagle's medium (DMEM) (U2OS osteosarcoma cells) or Roswell Park Memorial Institute (RPMI) (H1299, A549, and H1975) media, supplemented with 10% fetal bovine serum (FBS) (Gibco, USA), and 50 µg/ml gentamicin.

U2OS cells with tetracycline-inducible (Tet-on) expression of short hairpin RNA (shRNA) against Set7/9 (pSuperior-shRNA-Set7/9 or U2OS Set7/9 KD) and the reference cell line (U2OS pSuperior) were generated as described previously (16).

To establish lung cancer cell lines (H1299 and H1975) with stable Set7/9 knockdown, the lentiviral transduction by pLKO1.puro shRNA Set7/9 or scramble was carried out as described (23). The following specific shRNA oligonucleotides were annealed prior to cloning into the pLKO.1-TRC vector digested with AgeI and EcoR1 enzymes: top, 5′-CCGGGATCTATGCACTACGTTTAT CCTCGAGGATAAACGTAGTGCATAGATCTTTTT-3′ and bottom, 5′-AATTAAAAAGATCTATGCACTACGTTTATCCTC GAGGATAAACGTAGTGCATAGATC-3′.

H1299 cell lines with tetracycline-inducible (Tet-on) expression of wild-type p53 (p53wt) and mutant p53 R273H mutation (p53mut) and a control cell line (ctrl) (a kind gift of Dr P. Muller, University of Leicester, UK) were used to knockdown Set7/9.

Set7/9 knockout in A549 cells was generated using CRISPR/Cas9 technology. Guide RNA (5′-TAGCGACGACGAGAT GGTGGAGG-3′) specific to Set7/9 was cloned into lenti_V2.0 vector (Addgene) according to the manufacturer's instructions. A549 cells were transfected by Lipofectamin 2000 (Invitrogen, USA) with either a vehicle (lenti_V2.0 vector) or a vector encoding for Set7/9-specific gRNA, followed by 3 days selection with puromycin (5 µM).

Western Blotting

For Western blot analysis, whole-cell extracts were prepared using radioimmunoprecipitation assay (RIPA) buffer. The primary antibodies used against the analyzed proteins were as follows: Set7/9 (1:1,000, 2813, Cell Signaling), β-actin (1:5,000, A3854, Sigma-Aldrich, USA), HK2 (1:1,000, B-8, Santa Cruz Biotechnologies, USA), c-Myc (1:500, 9402S, Cell Signaling, USA), HIF1A (1:1,000, ab16066, Abcam, USA), ALDOA (1:1,000, sc-377058, Santa Cruz Biotechnologies, USA), and LDHA 1:1,000, 2012S, Cell Signaling, USA). The secondary antibodies used were antimouse and anti-rabbit (1:10,000; Sigma-Aldrich, USA). Normalization of Western blot signals was performed based on the ratio between pixel intensities of the bands corresponding to target proteins and loading controls (β-actin), respectively. Densitometry was carried out using the application of Bio-Rad Image Lab software.

Real-Time PCR

Total RNA was extracted from cells using TRIzol Reagent (Invitrogen, USA) according to the manufacturer's instructions. Two micrograms of total RNA were reverse transcribed to complementary DNA (cDNA) with oligo d(T) primer using a RevertAid First-Strand cDNA Synthesis Kit (Evrogen, Russia). cDNAs were amplified by real-time PCR on a CFX 1000 PCR machine (BioRad, USA) using SYBR green mix (Evrogen, Russia) in

triplicate. Data were analyzed by CFX Manager software. Relative amounts of SLC19A1, Hk2, ALDOA, LDHA, c-Myc, and HIF1A messenger RNAs (mRNAs) were normalized to β-actin mRNA. The following primers were used: SLC2A (GLUT1), forward 5′-AAGGTGATCGAGGAGTTCTACA-3′ and reverse 5′-ATGCCC CCAACAGAAAAGATG-3′; HK2, forward 5′-AAGGCTTCAAG GCATCTG-3′ and reverse 5′-GCCAGGTCCTTCACTGTCTC-3′; ALDOA, forward 5′-CGGGAAGAAGGAGAACCTG-3′ and reverse 5′-CCACAGGTCATCATAGTTCC-3′; LDHA, forward 5′- AGCCCGATTCCGTTACCT-3′ and reverse 5′-AGCCCG ATTCCGTTACCT-3′; HIF1A, forward 5′-CATAAAGTC TGCAACATGGAAGGT-3′ and reverse 5′-ATTTGATGG GTGAGGAATGGGTT-3′; Myc (c-Myc), forward 5′-CTCCTC CTCGTCGCAGTAGA-3′ and reverse 5′-GCTGCTTAGACGCT GGATTT-3′; SETD7 (Set7/9), forward 5′-TCATTGATGTG CCTGAGCCCTA-3′ and reverse 5′-TCAGGGTGCGGAT GCATTTGAT-3′; β-actin, forward 5′-GCACCACACCTTC TACAATGAGC-3′ and reverse 5′-TAGCACAGCCTGGAT AGCAACG-3′.

Assessment of Mitochondrial Membrane Potential

A day after seeding, cells were treated with 200 nM TMRE (Thermo Fisher Scientific, USA) for 30 min at 37°C in a CO_2 incubator. Then, cells were washed in phosphate-buffered saline (PBS), detached with trypsin, and analyzed by flow cytometry (CytoFlex, Beckman Coulter, USA). Values of the median were used for calculations. Results were represented as the mean ± SEM of three experiments.

Reactive Oxygen Species Detection Assay

The total reactive oxygen species (ROS) production was analyzed using the 2′,7′-dichlorodihydrofluorescein diacetate (H2DCFDA) substrate (Thermo Fisher Scientific, USA) in a final concentration of 50 μM. For detection, superoxide anions (O_2^-) dihydroethidium (DHE) (Thermo Fisher Scientific, USA) in a final concentration of 5 μM was used. The next day after seeding, cells were treated with H2DCFDA or dihydroethidium (DHE) for 30 min at 37°C in a CO_2 incubator. Following the incubation, cells were washed in PBS, detached with trypsin, and analyzed by flow cytometry (FC) (CytoFlex, Beckman Coulter, USA). Values of the median were used for calculation. Results were represented as the mean ± SD of three experiments.

Proliferation Assay

The proliferation analysis was performed using the xCELLigence technology (ACEA Biosciences, USA) according to the manufacturer's instructions. A total of 20,000 cells were planted into each well of an ACEA E-plate 16 in triplicate. The cell index was registered every 10 min for 10–40 h. Results were represented as the mean ± SEM of three experiments.

Cell Cycle Analysis

Flow cytometry analysis of the cell cycle was carried out. A total of 50,000 H1299 and H1975 cells, with Set7/9 KD or scramble, and A549 control and Set7/9 KO, were planted in triplicates. Two days after seeding, cells were harvested, washed once with

PBS, and fixed in 70% ethanol at −20°C for 1 h. Then, 30 min staining of DNA content was carried out by using 50 μg/ml of PI (Invitrogen, USA) and 1 μg/ml RNase A (Thermo Fisher Scientific, USA). Samples were analyzed by a CytoFLEX (Beckman Coulter, USA) flow cytometer. Results were processed by CytoExpert software (Beckman Coulter, USA).

Analysis of Glycolysis and Respiration

The SeaHorse energy profiling of lung cancer cell lines with either Set7/9 KD or scramble was carried out as described in (24) with small modifications. Briefly, 17,000 cells were seeded in SeaHorse 24-well plates a day prior to analysis. The SeaHorse Energy Phenotype test was used in accordance with the manufacturer's recommendations. Stressor mix consisted of carbonyl cyanide p-(trifluoromethoxy)-phenyl-hydrazone (FCCP) and oligomycin (Agilent Technologies, USA) to achieve the final concentrations of 2 and 4 μM, respectively. Results are represented as the mean ± SEM. For further analysis of the impact of Set7/9 on glycolysis in detail, GlycoStress kit (Agilent Technologies, USA) was used according to the manufacturer's instructions. The following concentrations were used in the glycolysis stress experiments: 10 mM of glucose, 4 μM of oligomycin, and 50 mM of 2-DG. Results are represented as the mean ± SEM.

Microarray

The microarray gene expression study was carried out using Human Gene Expression 4x44K Microarrays and a Low Input Quick Amp Labeling Kit (Agilent Technologies, USA) according to the manufacturer's instructions. RNA quality was assessed using a 2100 Bioanalyzer (Agilent Technologies, USA). One hundred nanograms of each RNA sample were used for cDNA synthesis and were simultaneously labeled with Cy-3. After purification, cDNA samples were hybridized with oligonucleotide probes on microarray slides for 18 h. The next day, the slides were washed and scanned. Data were analyzed by GeneSpring GX11.5 software.

Bioinformatic Analysis of Lung Cancer Patients' Survival Rates

The single and synergistic effect of SETD7 (Set7/9), SLC2A1 (GLUT1), HIF1A, HK2, and LDHA expression levels on the survival rate of lung cancer patients was determined by using Syntarget software as described in (25).

Statistical Analysis

Data are represented as mean ± standard deviation (SD) or standard error of the mean (SEM) of at least three replicates. Statistical significance was analyzed using Student's t-test. $p < 0.05$ was considered significant. $p < 0.05$ was denoted as * and $p < 0.01$ as **.

RESULTS

Set7/9 Knockdown Upregulates c-Myc, HIF1A, and Genes of Glycolytic Enzymes in U2OS Human Osteosarcoma Cells

Set7/9 lysine methyltransferase is a well-known regulator of transcription (8, 10). Previously, we have shown that Tet-

inducible Set7/9 knockdown in U2OS human osteosarcoma cells augmented the sensitivity of cells to genotoxic stress by upregulating the transcription of MDM2 (26).

To expand our observations on the role of Set7/9 in transcriptional regulation and to obtain the knowledge on global gene expression affected by Set7/9, we have carried out a microarray gene expression analysis of the same U2OS cells with Tet-inducible Set7/9 knockdown. We have treated U2OS with tetracycline for 2 days, followed by mRNA extraction, cDNA synthesis, labeling, and hybridization with oligonucleotide probes on microarray slides of the Illumina Human Gene Expression 4x44K Microarray Kit. The list of genes affected by Set7/9 KD is given in the **Supplementary Table 1**. The gene ontology analysis of differentially regulated genes in Set7/9 KD *versus* Set7/9 wt (U2OS pSuperior) cells revealed several functional pathways, among which the metabolic one was significantly represented. We focused on this pathway, since cancer metabolism is considered to be one of the hallmarks of cancer (27).

Intriguingly, a number of genes encoding for the regulators of energy metabolism, e.g., glucose transporter [GLUT1 (SLC2A1)], glycolytic enzymes—hexokinase 2 (HK2) and aldolase (ALDOB)—and their key transcription regulators c-Myc and HIF1 were found among genes being significantly upregulated in Set7/9KD cells compared to control cells (U2OS pSuperior cells) (**Figures 1A, B**).

We have verified the microarray data by independent analysis using gene-specific real-time PCR. Indeed, Set7/9 knockdown augmented the mRNA levels of both c-Myc and HIF1A and their transcriptional targets—GLUT1, HK2, ALDOA, and LDHA (**Figure 1C**).

Set7/9 Knockdown Upregulates c-Myc, HIF1A, and Glycolytic Genes in NSCLC Cells at Both Transcriptional and Protein Levels

We next asked if Set7/9 also affected the expression of c-Myc, HIF1A, GLUT1, and glycolytic enzymes in non-small cell lung cancer cell lines (NSCLCs). To this end, we stably suppressed Set7/9 expression [knock-down (KD) or knock-out (KO)] in three NSCLC cell lines with different p53 status [H1299 (p53-null), A549 (wild-type p53), and H1975 (mutant R273H p53)] (**Figure 2A** and **Supplementary Figure S1**). The mRNA level of c-Myc, HIF1A, GLUT1, HK2, ALDOA, and LDHA were assessed by real-time PCR (**Figure 2B** and **Supplementary**
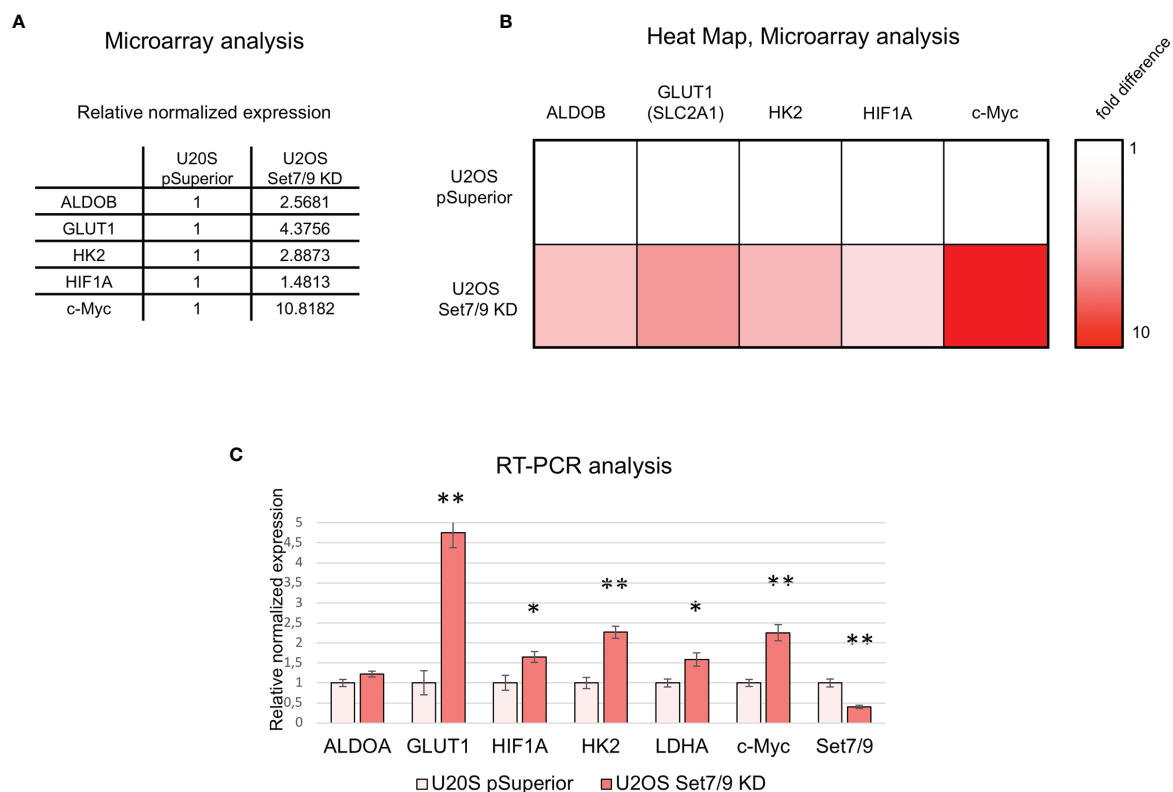
FIGURE 1 | Microarray data analysis of U2OS Set7/9KD cells. **(A)** Relative expression of ALDOB, GLUT1, HK2, HIF1A, and c-Myc mRNAs in U2OS cells with tetracyclin-induced Set7/9 knockdown (tet-on system) compared to control U2OS pSuperior cells. Both cell lines were treated with doxycycline for 48 h prior to microarray analysis. **(B)** Heat map demonstrating ALDOB, GLUT1, HK2, HIF1A, and c-Myc mRNAs expression changes in Set7/9 KD U2OS cells compared to control U2OS pSuperior cells. **(C)** Validation of microarray data using quantitative RT-PCR: analysis of ALDOA, GLUT1, LDHA, HK2, HIF1A, c-Myc, and Set7/9 mRNAs expression in U2OS cells with tetracyclin-induced Set7/9 knock-down (Tet-on system) compared to control U2OS pSuperior cells. *p < 0.05; **p < 0.01.

Figure S1). The results shown in **Figure 2A** demonstrate that, in general, the suppression of Set7/9 in NSCLC cells augmented the expression of energy metabolism factors similar to that observed in USOS osteosarcoma cells. Western blots were also consistent with RT-PCR results, i.e., attenuated levels of Set7/9 resulted in the increased production of the respective proteins, albeit to a different extent. Notably, the effect of Set7/9 was more pronounced in p53-negative cells (H1299) compared to A549 (p53-positive cells) or H1975 cell (p53 mut) (**Figure 2A** and **Supplementary Figure S1**). Furthermore, we found that the protein level of HIF1A was not significantly affected by Set7/9 in H1299 and A549 cells but was altered in H1975 cells with mutant p53 (**Figure 2** and **Supplementary Figure S1**, respectively).

Set7/9 Knockdown Upregulates Mitochondrial Membrane Potential, Glycolysis, and Respiration

c-Myc and HIF1A are the two well-known master regulators of metabolic networks including energy metabolism, deregulations of which are recognized now as one of the "hallmarks of cancer." Enhanced glycolysis in malignant cells is associated with tumor progression, migration, invasion, and resistance against chemo- and radiotherapy. Since our results suggested that ablation of Set7/9 caused an increase in c-Myc, GLUT1, and several glycolytic enzymes both at the mRNA and protein levels, we decided to examine whether Set7/9 affected the MMP, glycolysis, and respiration.

First, we stained H1299 and A549 cell lines with Set7/9 KD or Set7/9 KO, respectively, with the TMRE agent to measure the levels of MMP intensity. The respective parental control cell lines with wild-type Set7/9 were also used in the experiment. Cell lines with Set7/9 KD or KO increased the MMP level in the range of 10–60% depending on NSCLC cell line (**Figures 3A, B** and **Supplementary Figure S2A**). Importantly, the most pronounced effect was observed in p53-negative H1299 cells.

To confirm that the effect of Set7/9 ablation on MMP was not dependent on the p53 status, we used H1299 cell lines with Tet-inducible expression of wild-type p53 (p53wt) or mutant p53 R273H (p53mut) proteins, and control cells with knocked down Set7/9. We showed that in all three H1299-derived cell lines (control, p53wt, and p53mut), suppression of Set7/9 led to an increase in MMP levels (**Supplementary Figure S3**).
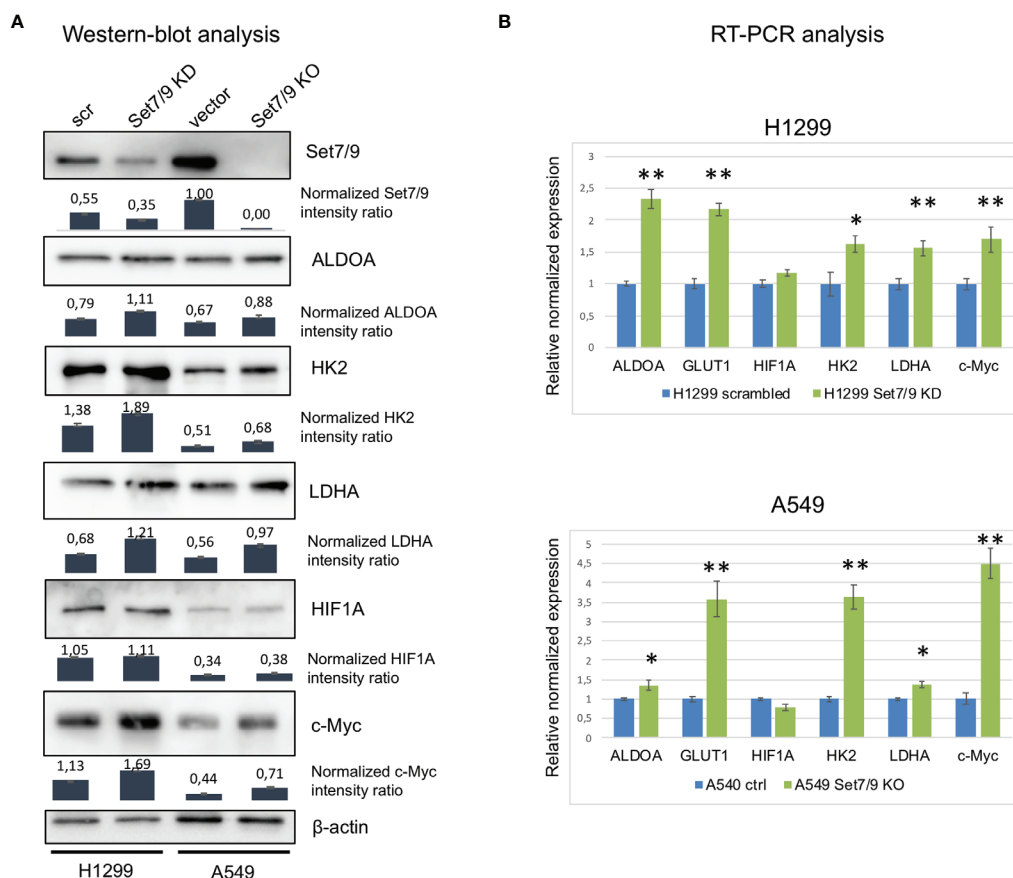
FIGURE 2 | The effect of Set7/9 decrease on ALDOA, GLUT1, LDHA, HK2, HIF1A, and c-Myc levels. **(A)** Western blot analysis of ALDOA, LDHA, HK2, HIF1A, and c-Myc levels in NSCLC cell lines H1299 knockdown (Set7/9 KD) and A549 with Set7/9 knockout (Set7/9 KO) compared to control (scrambled or vector) cells. Densitometry analysis was performed on the basis of three measurements. Error bars indicate ± SD; **(B)** Quantitative RT-PCR: analysis of ALDOA, GLUT1, LDHA, HK2, HIF1A, and c-Myc mRNAs in the above cells. *p < 0.05; **p < 0.01.

FIGURE 3 | The effect of Set7/9 decrease on mitochondrial membrane potential (MMP) of NSCLC cell lines H1299, A549 and H1975. FC analysis of TMRE staining of NSCLC cell lines **(A)** H1299 and **(B)** A549 with Set7/9 knockdown (Set7/9 KD) and knockout (Set7/9 KO) compared to control (scrambled or vector) cells. $*p < 0.01$.

In general, malignant cells have 1.5–2 times higher MMP levels than their non-malignant counterparts, which is the consequence of an elevated energy metabolism. The level o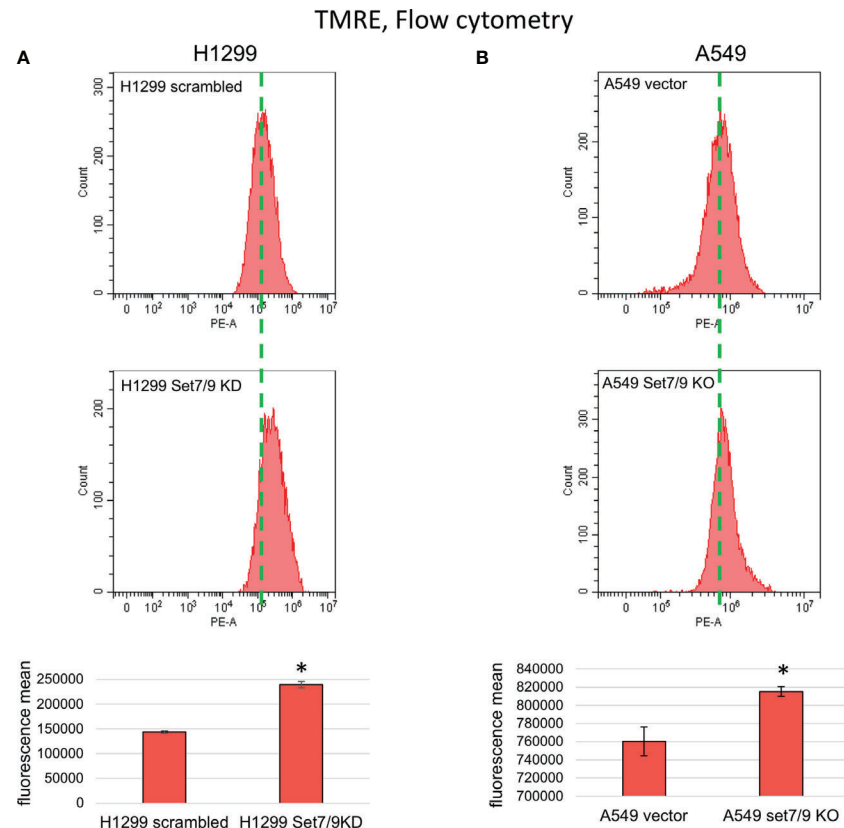f MMP enhancement is associated with the degree of malignancy of neoplastic cells, including enhanced resistance to aggressive conditions and elevation of their metastatic potential (28).
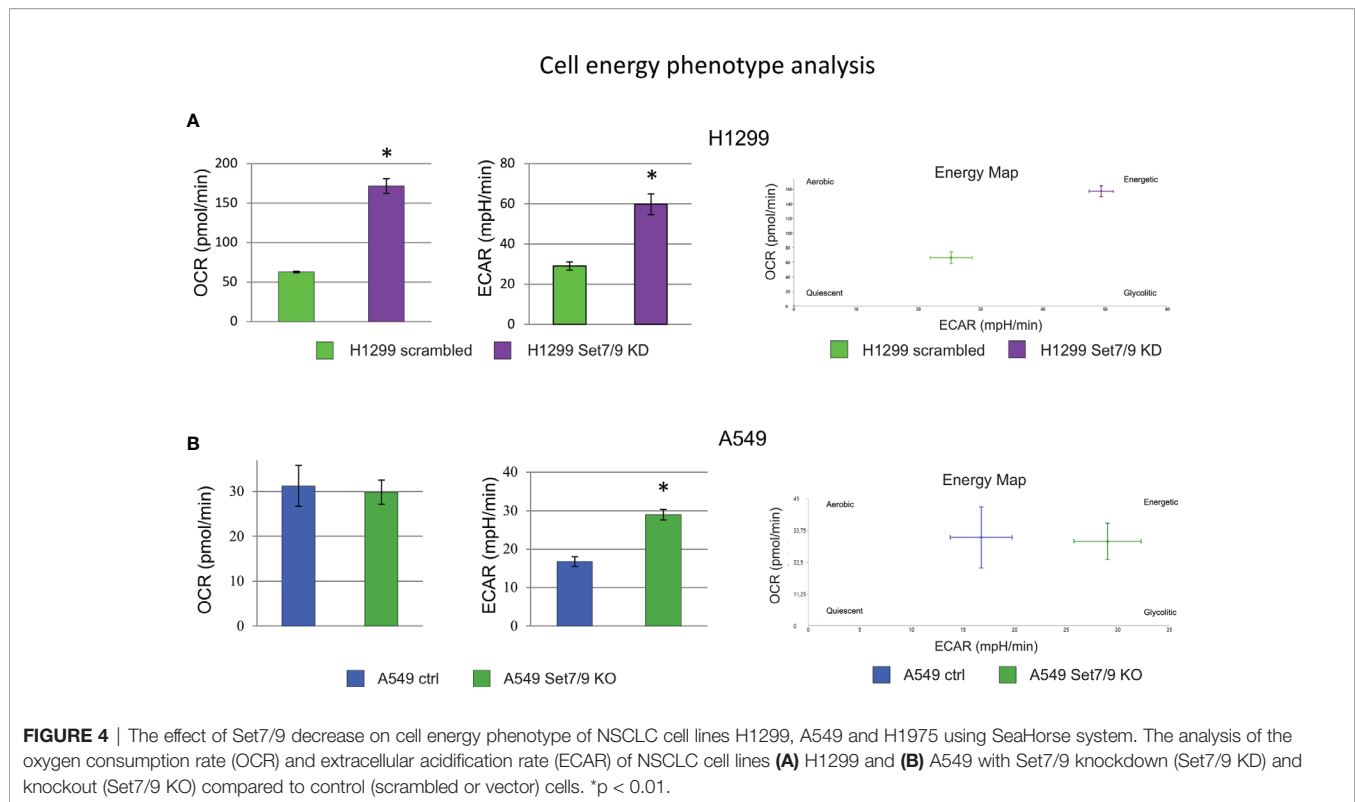
Next, we used the SeaHorse energy profiling technology to study the impact of Set7/9 KD on glycolysis and respiration. Using the SeaHorse Energy Phenotype kit, we showed that Set7/9 KO upregulated only ECAR (glycolysis) in p53-positive A549 cells, whereas p53-negative H1299 cells and p53-mutant H1975 cells with Set7/9 knockdown displayed elevated levels of both glycolysis and respiration compared to control cells (**Figures 4A, B** and **Supplementary Figure S2C**).

Using the SeaHorse GlycoStress kit, we have further analyzed the impact of Set7/9 on several parameters of glycolysis (**Supplementary Figures S4–S6**). The attenuation of Set7/9 expression upregulated both glycolysis and respiration in H1299 and H1975 cell lines (**Supplementary Figures S4, S5**). On the contrary, only glycolysis was augmented in A549 cells upon Set7/9 attenuation, while respiration did not change significantly (**Supplementary Figure S6**). These results

correlate with the data obtained using the SeaHorse Energy Phenotype kit (**Figure 4B**).

A previous study by Shen et al. showed that Set7/9 acts as a negative regulator of β-catenin in response to ROS (15). Importantly, β-catenin affects c-Myc expression, which in turn regulates the expression of glycolytic genes. Thus, it was plausible that Set7/9 mediated its effects on these genes through the β-catenin/c-Myc axis. To test this hypothesis, we assessed the effect of Set7/9 suppression on β-catenin levels in the NSCLC cell lines and observed no correlation between β-catenin levels and the status of Set7/9 (**Supplementary Figure S7A**).

Furthermore, we have tested the intracellular concentration of ROS in these cell lines. Using DHE staining, we have shown that the level of superoxide anions (O2−) was higher in all three Set7/9-deficient cell lines compared to control lines (**Supplementary Figure S7B**). However, the total amount of ROS species was either the same or lower in Set7/9 KD or Set7/9KO cells (**Supplementary Figure S7C**) compared to control cells. Since the intracellular superoxide anions content correlates with the activity of mitochondria (29, 30), this result further confirms the effect of Set7/9 suppression on mitochondrial activity.

FIGURE 4 | The effect of Set7/9 decrease on cell energy phenotype of NSCLC cell lines H1299, A549 and H1975 using SeaHorse system. The analysis of the oxygen consumption rate (OCR) and extracellular acidification rate (ECAR) of NSCLC cell lines **(A)** H1299 and **(B)** A549 with Set7/9 knockdown (Set7/9 KD) and knockout (Set7/9 KO) compared to control (scrambled or vector) cells. *$p < 0.01$.

Set7/9 KD Enhances the Proliferation of NSCLC Cell Lines

The increased glycolysis is usually associated with the enhanced proliferation (31) and aggressiveness of tumors. Thus, we decided to study the effect of Set7/9 attenuation on the proliferation of the NSCLC cell lines. To address this question, we used the xCelligence platform. As shown in **Figures 5A, B** and **Supplementary Figure S8A**, all three NSCLC cell lines with Set7/9 KD/KO displayed augmented proliferation rates from 1.2- to 2-fold, compared to their respective controls. These results are in agreement with our data on the stimulatory effect of Set7/9 KD on glycolysis and respiration.

These results prompted us to assess the effect of Set7/9 on the cell cycle. To this end, we analyzed the cell cycle distribution of H1299, A549, and H1975 with different Set7/9 status. We observed a significant increase in S-phase in Set7/9 KD/KO cells in all three cell lines investigated in comparison to control cells (**Figures 5C, D** and **Supplementary Figure S8B**). These results, taken together with the results on proliferation obtained by xCelligence, strongly suggest that either the attenuation or ablation of Set7/9 upregulates proliferation rates of H1299, A549, and H1975 cells.

Expression Levels of Set7/9, HIF1A, GLUT1, HK2, and LDHA Correlate With Survival Rates of Lung Cancer Patients

Increased rates of glycolysis in tumor cells are inversely associated with patient survival (32). We sought to investigate whether there are correlations between the expression levels of glycolytic genes

HIF1A, GLUT1, HK2, and LDHA, in lung cancer patients and the rates of the patients' survival. We carried out a bioinformatic analysis of several cancer samples databases using an algorithm previously described in SynTarget software (25).

Kaplan–Meier plots (**Figure 6A**) demonstrate that the high levels of HK2, SLC2A1 (GLUT1), LDHA, and HIF1a expression were associated with poor survival of lung cancer patients. Moreover, low expression of Set7/9 together with high expression of each of aforementioned genes is also associated with poor outcome. On the contrary, high levels of Set7/9 expression in conjunction with low expression of HK2, SLC2A1 (GLUT1), LDHA, and HIF1A are associated with increased survival of patients (**Figure 6B**).

These observations reinforce our hypothesis that Set7/9 may have an impact on survival of cancer patients *via* regulating the energy metabolism of NSCLC.

DISCUSSION

A number of Set7/9 non-histone substrates, including p53 (33), MDM2 (34), E2F1 (16), STAT3 (21), affect proliferation, apoptosis, and resistance of NSCLC cells against chemotherapeutics.

In the present manuscript, we have provided evidence that the knockdown of Set7/9 methyltransferase in human NSCLC cell models upregulates a number of glycolytic enzymes (hexokinase, aldolase, and lactate dehydrogenase) and their key transcriptional activators—oncogenes c-Myc and HIF1A—at both transcriptional and protein levels.
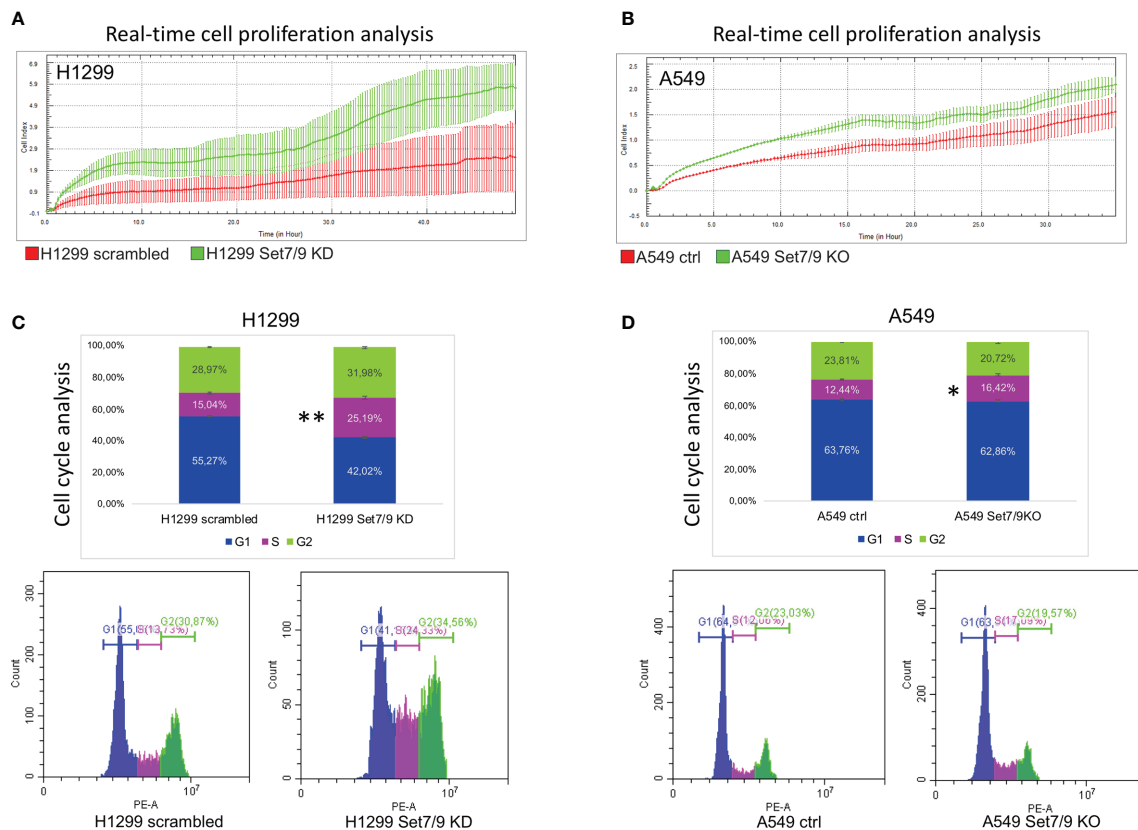
FIGURE 5 | The effect of Set7/9 downregulation on the proliferation and cell cycle of NSCLC cell lines H1299 and A549. **(A, B)** The analysis of cell proliferation in real time, using the xCelligence system, of NSCLC cell lines **(A)** H1299 and **(B)** A549 with Set7/9 knockdown (Set7/9 KD) and knockout (Set7/9 KO), compared to control (scrambled or vector) cells. **(C, D)** The analysis of the cell cycle phases' distribution of NSCLC cell lines **(C)** H1299 and **(D)** A549 with Set7/9 knockdown (Set7/9 KD) and knockout (Set7/9 KO) compared to control (scrambled or vector) cells. *$p < 0.05$; **$p < 0.01$.

Enhanced glycolysis has been a well-known feature of malignant cells since Otto Warburg's pioneering works were published in 1925 (35). The so-called "Warburg effect" is part of metabolic reprogramming, which is considered now as one of the "hallmarks of cancer" (36). There are at least three main reasons why malignant cells benefit from glycolysis (37–39). First of all, glycolysis fuels biosynthetic anabolic pathways of rapidly proliferating cells by diverting glucose flux towards pentose-phosphate pathways and one-carbon metabolism. The latter are highly required for the synthesis of DNA, lipids, S-adenosyl methionine (the main donor of methyl groups), glutathione (an important factor of red-ox homeostasis), etc. Second, glycolysis helps neoplastic cells to fine-tune their interaction with the microenvironment by manipulating cancer-associated fibroblasts (CAFs). Finally, glycolysis provides extracellular acidification that protects malignant cells from the attack of immune cells, which are not effective at low pH.

c-Myc and HIF1A are master regulators of metabolic networks. They upregulate and coordinate glycolysis, respiration, one-carbon metabolism, and the metabolism of glutamine and lipids upon tumorigenesis (28, 40, 41). It is important to note that HIF1A and c-Myc are both known to regulate the expression of tumor-specific isoforms of glycolytic proteins such as GLUT1, HK2, PKM, and LDHA, thereby diminishing the Warburg effect in cancer cells (42–44). Moreover, both c-Myc and HIF1A play known roles in the upregulation of metabolic networks and the proliferation of NSCLC (23, 39, 45, 46).

Previously, two research groups have shown that Set7/9-mediated methylation of HIF1A and HIF2A leads to their destabilization and negatively regulates their transcriptional activity (47). In contrast, our present results suggest that Set7/9 affects HIF1A expression only at the level of mRNA in H1299 and A549 cells and only modestly on the protein level in H1975. Given that these three cell lines have different p53 statuses, it is unlikely that the effect of Set7/9, or lack thereof, was a p53-dependent effect. It is possible that the upregulation of HIF1A observed on the level of mRNA in the absence of Set7/9 could also be detected on the protein level should those cells be treated with hypoxia. Future experiments under hypoxic conditions should clarify this possibility. Nevertheless, in the present study, we have directly shown that the ablation of Set7/9 in several NSCLC cell lines upregulated glycolysis and respiration even in the absence of hypoxia (i.e., in normoxic conditions)
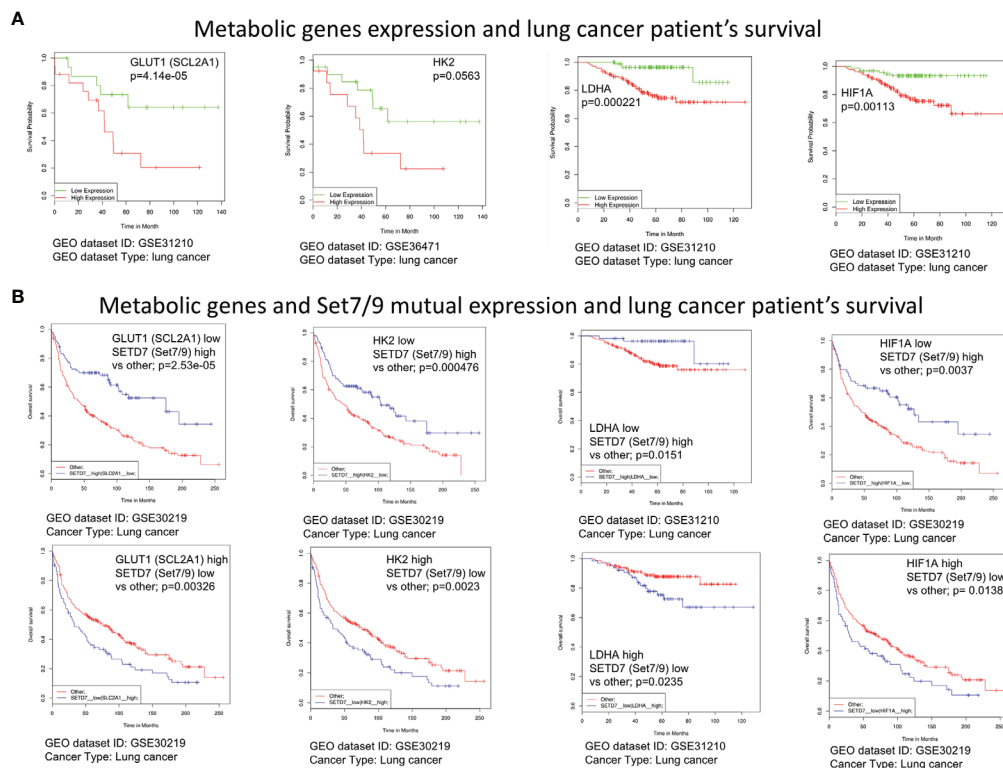
FIGURE 6 | The expression level of Set7/9, HIF1A, GLUT1, HK2, and LDHA affects survival rate of lung cancer patients. **(A)** The bioinformatic analysis of the association of GLUT1 (SCL2A1), LDHA, HK2, and HIF1A expression levels with NSCLC patients' survival. **(B)** The bioinformatic analysis of the GLUT1 (SCL2A1), LDHA, HK2, and HIF1A and Set7/9 (SETD7) mutual expression effect on NSCLC patients' survival.

(**Figure 4** and **Supplementary Figure S2**). These effects were likely due to the increased expression of the key glycolytic genes.

Importantly, HIF1A and c-Myc share common target genes such as HK2, ENO1, and LDHA, whose products are involved in glycolysis. In fact, most genes coding for glycolytic enzymes have in their promoter regions consensus binding sequences for both HIF1A and c-Myc (48). Thus, it is plausible that Set7/9 controls glycolysis indirectly, by affecting c-Myc expression. In support of this assumption is the fact that A549 and H1299 cells with suppressed Set7/9 displayed an increased expression of c-Myc both at the transcriptional and protein levels.

Among various malignancies, elevated glycolysis is associated with increased proliferation (49), metastasis (50–52), increased resistance to chemotherapy (53–55), and a poor survival prognosis (32).

In the present study, we demonstrated that the ablation of Set7/9 augmented the levels of HIF1A, c-Myc, and several genes coding for glycolytic enzymes. This points to Set7/9 as a potential tumor suppressor. Along with this notion, studies from several groups including ours also suggest that Set7/9 plays antiproliferative and tumor-protective roles in various cancers (7, 15, 56, 57), including NSCLC (21, 58).

In a number of works, Set7/9-mediated tumor suppressive effects have been achieved through p53 stabilization and

activation. Indeed, we and others showed that Set7/9 is able to directly methylate the p53 protein, which leads to p53 stabilization and nuclear translocation and enhances the expression of p53 target genes (11, 59). Additionally, it was demonstrated that Set7/9 contributes to p53 stability *via* inactivation of SIRT1 by its methylation. Thus, the Set7/9-mediated methylation of SIRT1 prevented p53 deacetylation and hence increased p53 transactivation under genotoxic stress (60). Here, we demonstrate that Set7/9 acts as a regulator of glycolysis in NSCLC cells regardless of the p53 status. These results contribute to a better understanding of the p53-independent role of Set7/9 in tumorigenesis.

However, several papers on the role of Set7/9 in intestinal regeneration argue against the tumor-suppressive role of Set7/9. Apparently, being part of a YAP/AXIN1/β-catenin complex Set7/9 facilitates Wnt-induced nuclear accumulation of β-catenin, a known oncogenic protein (61).

Thus, the role of Set7/9 in tumorigenesis is likely to be cell tissue dependent. Future studies should discern the molecular mechanisms involving Set7/9 that affect tumor growth and metastases. Our results presented in this study indicate that Set7/9 is a potentially important regulator of metabolic networking in NSCLC.

DATA AVAILABILITY STATEMENT

All datasets presented in this study are included in the article/**Supplementary Material**. The proceeded microarray data was published in the Mendeley Datasets Repository (doi: 10.17632/hkgfsz9yhn.1 https://data.mendeley.com/datasets/hkgfsz9yhn/1).

AUTHOR CONTRIBUTIONS

AD, OS, and NB designed experiments and wrote the manuscript. AD and OS carried out majority of the experiments. OF and AZ participated in MMP assays. AP and EB participated in the establishment of cell lines and performed ROS analysis. AK participated in experiments using SeaHorse. LL performed microarray analysis. All authors contributed to the article and approved the submitted version.

FUNDING

ACKNOWLEDGMENTS

SUPPLEMENTARY MATERIAL

The Supplementary Material for this article can be found online at: https://www.frontiersin.org/articles/10.3389/fonc.2021.706668/full#supplementary-material

REFERENCES

1. Morgunkova A, Barlev NA. Lysine Methylation Goes Global. *Cell Cycle* (2006) 5(12):1308–12. doi: 10.4161/cc.5.12.2820

2. Nishioka K, Rice JC, Sarma K, Erdjument-Bromage H, Werner J, Wang Y, et al. PR-Set7 Is a Nucleosome-Specific Methyltransferase That Modifies Lysine 20 of Histone H4 and Is Associated With Silent Chromatin. *Mol Cell* (2002) 9(6):1201–13. doi: 10.1016/S1097-2765(02)00548-8

3. Wang H, Cao R, Xia L, Erdjument-Bromage H, Borchers C, Tempst P, et al. Purification and Functional Characterization of a Histone H3-Lysine 4-Specific Methyltransferase. *Mol Cell* (2001) 8(6):1207–17. doi: 10.1016/S1097-2765(01)00405-1

4. Tao Y, Neppl RL, Huang Z-P, Chen J, Tang R-H, Cao R, et al. The Histone Methyltransferase Set7/9 Promotes Myoblast Differentiation and Myofibril Assembly. *J Cell Biol* (2011) 194(4):551–65. doi: 10.1083/jcb.201010090

5. He S, Owen DR, Jelinsky SA, Lin L-L. Lysine Methyltransferase SETD7 (SET7/9) Regulates ROS Signaling Through Mitochondria and NFE2L2/ARE Pathway. *Sci Rep* (2015) 5(1):1–14. doi: 10.1038/srep14368

6. Fujimaki K, Ogihara T, Morris DL, Oda H, Iida H, Fujitani Y, et al. SET7/9 Enzyme Regulates Cytokine-Induced Expression of Inducible Nitric-Oxide Synthase Through Methylation of Lysine 4 at Histone 3 in the Islet β Cell. *J Biol Chem* (2015) 290(27):16607–18. doi: 10.1074/jbc.M115.661777

7. Akiyama Y, Koda Y, Byeon S-J, Shimada S, Nishikawaji T, Sakamoto A, et al. Reduced Expression of SET7/9, A Histone Mono-Methyltransferase, Is Associated With Gastric Cancer Progression. *Oncotarget* (2016) 7(4):3966. doi: 10.18632/oncotarget.6681

8. Batista I, Helguero LA. Biological Processes and Signal Transduction Pathways Regulated by the Protein Methyltransferase SETD7 and Their Significance in Cancer. *Signal Transduction Targeted Ther* (2018) 3(1):1–14. doi: 10.1038/s41392-018-0017-6

9. Dhayalan A, Kudithipudi S, Rathert P, Jeltsch A. Specificity Analysis-Based Identification of New Methylation Targets of the SET7/9 Protein Lysine Methyltransferase. *Chem Biol* (2011) 18(1):111–20. doi: 10.1016/j.chembiol.2010.11.014

10. Keating S, El-Osta A. Transcriptional Regulation by the Set7 Lysine Methyltransferase. *Epigenetics* (2013) 8(4):361–72. doi: 10.4161/epi.24234

11. Chuikov S, Kurash JK, Wilson JR, Xiao B, Justin N, Ivanov GS, et al. Regulation of P53 Activity Through Lysine Methylation. *Nature* (2004) 432(7015):353–60. doi: 10.1038/nature03117

12. Subramanian K, Jia D, Kapoor-Vazirani P, Powell DR, Collins RE, Sharma D, et al. Regulation of Estrogen Receptor α by the SET7 Lysine Methyltransferase. *Mol Cell* (2008) 30(3):336–47. doi: 10.1016/j.molcel.2008.03.022

13. Masatsugu T, Yamamoto K. Multiple Lysine Methylation of PCAF by Set9 Methyltransferase. *Biochem Biophys Res Commun* (2009) 381(1):22–6. doi: 10.1016/j.bbrc.2009.01.185

14. Ea C-K, Baltimore D. Regulation of NF-κb Activity Through Lysine Monomethylation of P65. *Proc Natl Acad Sci* (2009) 106(45):18972–7. doi: 10.1073/pnas.0910439106

15. Shen C, Wang D, Liu X, Gu B, Du Y, Wei FZ, et al. SET7/9 Regulates Cancer Cell Proliferation by Influencing β-Catenin Stability. *FASEB J* (2015) 29(10):4313–23. doi: 10.1096/fj.15-273540

16. Lezina L, Aksenova V, Ivanova T, Purmessur N, Antonov A, Tentler D, et al. KMTase Set7/9 Is a Critical Regulator of E2F1 Activity Upon Genotoxic Stress. *Cell Death DifFer* (2014) 21(12):1889–99. doi: 10.1038/cdd.2014.108

17. Fu L, Wu H, Cheng SY, Gao D, Zhang L, Zhao Y. Set7 Mediated Gli3 Methylation Plays a Positive Role in the Activation of Sonic Hedgehog Pathway in Mammals. *Elife* (2016) 5:e15690. doi: 10.7554/eLife.15690.001

18. Gu Y, Wang X, Liu H, Li G, Yu W, Ma Q. SET7/9 Promotes Hepatocellular Carcinoma Progression Through Regulation of E2F1. *Oncol Rep* (2018) 40(4):1863–74. doi: 10.3892/or.2018.6621

19. Si W, Zhou J, Zhao Y, Zheng J, Cui L. SET7/9 Promotes Multiple Malignant Processes in Breast Cancer Development *via* RUNX2 Activation and Is Negatively Regulated by TRIM21. *Cell Death Dis* (2020) 11(2):1–15. doi: 10.1038/s41419-020-2350-2

20. Barta JA, Powell CA, Wisnivesky JP. Global Epidemiology of Lung Cancer. *Ann Global Health* (2019) 85(1):1–16. doi: 10.5334/aogh.2419

21. Cao L, Ren Y, Guo X, Wang L, Zhang Q, Li X, et al. Downregulation of SETD7 Promotes Migration and Invasion of Lung Cancer Cells *via* JAK2/STAT3 Pathway. *Int J Mol Med* (2020) 45(5):1616–26. doi: 10.3892/ijmm.2020.4523

22. Keating ST, Ziemann M, Okabe J, Khan AW, Balcerczyk A, El-Osta A. Deep Sequencing Reveals Novel Set7 Networks. *Cell Mol Life Sci* (2014) 71(22):4471–86. doi: 10.1007/s00018-014-1651-y

23. Daks A, Petukhov A, Fedorova O, Shuvalov O, Merkulov V, Vasileva E, et al. E3 Ubiquitin Ligase Pirh2 Enhances Tumorigenic Properties of Human Non-Small Cell Lung Carcinoma Cells. *Genes Cancer* (2016) 7(11-12):383. doi: 10.18632/genesandcancer.123

24. Shuvalov O, Kizenko A, Petukhov A, Fedorova O, Daks A, Bottrill A, et al. SEMG1/2 Augment Energy Metabolism of Tumor Cells. *Cell Death Dis* (2020) 11(12):1–14. doi: 10.17632/24nng467bp.1

25. Amelio I, Tsvetkov P, Knight R, Lisitsa A, Melino G, Antonov A. SynTarget: An Online Tool to Test the Synergetic Effect of Genes on Survival Outcome in Cancer. *Cell Death Differ* (2016) 23(5):912. doi: 10.1038/cdd.2016.12

26. Lezina L, Aksenova V, Fedorova O, Malikova D, Shuvalov O, Antonov AV, et al. KMT Set7/9 Affects Genotoxic Stress Response *via* the Mdm2 Axis. *Oncotarget* (2015) 6(28):25843. doi: 10.18632/oncotarget.4584

27. Hanahan D, Weinberg RA. Hallmarks of Cancer: The Next Generation. *Cell* (2011) 144(5):646–74. doi: 10.1016/j.cell.2011.02.013

28. Shuvalov O, Daks A, Fedorova O, Petukhov A, Barlev N. Linking Metabolic Reprogramming, Plasticity and Tumor Progression. *Cancers* (2021) 13(4):762. doi: 10.3390/cancers13040762

29. Fogg VC, Lanning NJ, MacKeigan JP. Mitochondria in Cancer: At the Crossroads of Life and Death. *Chin J Cancer* (2011) 30(8):526. doi: 10.5732/cjc.011.10018

30. Muller FL, Liu Y, Van Remmen H. Complex III Releases Superoxide to Both Sides of the Inner Mitochondrial Membrane. *J Biol Chem* (2004) 279 (47):49064–73. doi: 10.1074/jbc.M407715200

31. Lunt SY, Vander Heiden MG. Aerobic Glycolysis: Meeting the Metabolic Requirements of Cell Proliferation. *Annu Rev Cell Dev Biol* (2011) 27:441–61. doi: 10.1146/annurev-cellbio-092910-154237

32. Yu M, Chen S, Hong W, Gu Y, Huang B, Lin Y, et al. Prognostic Role of Glycolysis for Cancer Outcome: Evidence From 86 Studies. *J Cancer Res Clin Oncol* (2019) 145(4):967–99. doi: 10.1007/s00432-019-02847-w

33. Fedorova O, Petukhov A, Daks A, Shuvalov O, Leonova T, Vasileva E, et al. Orphan Receptor NR4A3 Is a Novel Target of P53 That Contributes to Apoptosis. *Oncogene* (2019) 38(12):2108–22. doi: 10.1038/s41388-018-0566-8

34. Shuvalov O, Kizenko A, Shakirova A, Fedorova O, Petukhov A, Aksenov N, et al. Nutlin Sensitizes Lung Carcinoma Cells to Interferon-Alpha Treatment in MDM2-Dependent But P53-Independent Manner. *Biochem Biophys Res Commun* (2018) 495(1):1233–9. doi: 10.1016/j.bbrc.2017.11.118

35. Warburg O. The Metabolism of Carcinoma Cells. *J Cancer Res* (1925) 9 (1):148–63. doi: 10.1158/jcr.1925.148

36. Ward PS, Thompson CB. Metabolic Reprogramming: A Cancer Hallmark Even Warburg did Not Anticipate. *Cancer Cell* (2012) 21(3):297–308. doi: 10.1016/j.ccr.2012.02.014

37. Fernandez-de-Cossio-Diaz J, Vazquez A. Limits of Aerobic Metabolism in Cancer Cells. *Sci Rep* (2017) 7(1):1–8. doi: 10.1038/s41598-017-14071-y

38. Liberti MV, Locasale JW. The Warburg Effect: How Does It Benefit Cancer Cells? *Trends Biochem Sci* (2016) 41(3):211–8. doi: 10.1016/j.tibs.2015.12.001

39. Vanhove K, Graulus G-J, Mesotten L, Thomeer M, Derveaux E, Noben J-P, et al. The Metabolic Landscape of Lung Cancer: New Insights in a Disturbed Glucose Metabolism. *Front Oncol* (2019) 9:1215. doi: 10.3389/fonc.2019.01215

40. Chen Z, Zeng H, Guo Y, Liu P, Pan H, Deng A, et al. miRNA-145 Inhibits Non-Small Cell Lung Cancer Cell Proliferation by Targeting C-Myc. *J Exp Clin Cancer Res* (2010) 29(1):1–10. doi: 10.1186/1756-9966-29-151

41. Shuvalov O, Petukhov A, Daks A, Fedorova O, Vasileva E, Barlev NA. One-Carbon Metabolism and Nucleotide Biosynthesis as Attractive Targets for Anticancer Therapy. *Oncotarget* (2017) 8(14):23955. doi: 10.18632/oncotarget.15053

42. Marin-Hernandez A, Gallardo-Perez JC, Ralph SJ, Rodriguez-Enriquez S, Moreno-Sanchez R. HIF-1α Modulates Energy Metabolism in Cancer Cells by Inducing Over-Expression of Specific Glycolytic Isoforms. *Mini Rev medicinal Chem* (2009) 9(9):1084–101. doi: 10.2174/138955709788922610

43. Liu J, Wu N, Ma L, Liu M, Liu G, Zhang Y, et al. Oleanolic Acid Suppresses Aerobic Glycolysis in Cancer Cells by Switching Pyruvate Kinase Type M Isoforms. *PloS One* (2014) 9(3):e91606. doi: 10.1371/journal.pone.0091606

44. Taniguchi K, Sugito N, Kumazaki M, Shinohara H, Yamada N, Matsuhashi N, et al. Positive Feedback of DDX6/c-Myc/PTB1 Regulated by miR-124 Contributes to Maintenance of the Warburg Effect in Colon Cancer Cells. *Biochim Biophys Acta (BBA)-Molecular Basis Dis* (2015) 1852(9):1971–80. doi: 10.1016/j.bbadis.2015.06.022

45. Chanvorachote P, Sriratanasak N, Nonpanya N. C-Myc Contributes to Malignancy of Lung Cancer: A Potential Anticancer Drug Target. *Anticancer Res* (2020) 40(2):609–18. doi: 10.21873/anticanres.13990

46. Stegeman H, Span PN, Peeters WJ, Verheijen MM, Grénman R, Meijer TW, et al. Interaction Between Hypoxia, AKT and HIF-1 Signaling in HNSCC and NSCLC: Implications for Future Treatment Strategies. *Future Sci OA* (2016) 2 (1):FSO84. doi: 10.4155/fso.15.84

47. Liu X, Chen Z, Xu C, Leng X, Cao H, Ouyang G, et al. Repression of Hypoxia-Inducible Factor α Signaling by Set7-Mediated Methylation. *Nucleic Acids Res* (2015) 43(10):5081–98. doi: 10.1093/nar/gkv379

48. Marbaniang C, Kma L. Dysregulation of Glucose Metabolism by Oncogenes and Tumor Suppressors in Cancer Cells. *Asian Pacific J Cancer prevention: APJCP* (2018) 19(9):2377. doi: 10.22034/APJCP.2018.19.9.2377

49. Lunt SY, Vander Heiden MG. Aerobic Glycolysis: Meeting the Metabolic Requirements of Cell Proliferation. *Annu Rev Cell Dev Biol* (2011) 27:441–64. doi: 10.1146/annurev-cellbio-092910-154237

50. Gründker C, Läsche M, Hellinger JW, Emons G. Mechanisms of Metastasis and Cell Mobility–The Role of Metabolism. *Geburtshilfe und Frauenheilkunde* (2019) 79(2):184. doi: 10.1055/a-0805-9113

51. Lincet H, Icard P. How do Glycolytic Enzymes Favour Cancer Cell Proliferation by Nonmetabolic Functions? *Oncogene* (2015) 34(29):3751–9. doi: 10.1038/onc.2014.320

52. Wei Q, Qian Y, Yu J, Wong CC. Metabolic Rewiring in the Promotion of Cancer Metastasis: Mechanisms and Therapeutic Implications. *Oncogene* (2020) 39(39):6139–56. doi: 10.1038/s41388-020-01432-7

53. Chen X, Chen S, Yu D. Metabolic Reprogramming of Chemoresistant Cancer Cells and the Potential Significance of Metabolic Regulation in the Reversal of Cancer Chemoresistance. *Metabolites* (2020) 10(7):289. doi: 10.3390/metabo10070289

54. Lin J, Xia L, Liang J, Han Y, Wang H, Oyang L, et al. The Roles of Glucose Metabolic Reprogramming in Chemo-and Radio-Resistance. *J Exp Clin Cancer Res* (2019) 38(1):1–13. doi: 10.1186/s13046-019-1214-z

55. Ma L, Zong X. Metabolic Symbiosis in Chemoresistance: Refocusing the Role of Aerobic Glycolysis. *Front Oncol* (2020) 10:5. doi: 10.3389/fonc.2020.00005

56. Song Y, Zhang J, Tian T, Fu X, Wang W, Li S, et al. SET7/9 Inhibits Oncogenic Activities Through Regulation of Gli-1 Expression in Breast Cancer. *Tumor Biol* (2016) 37(7):9311–22. doi: 10.1007/s13277-016-4822-7

57. Vasileva E, Shuvalov O, Petukhov A, Fedorova O, Daks A, Nader R, et al. KMT Set7/9 Is a New Regulator of Sam68 STAR-Protein. *Biochem Biophys Res Commun* (2020) 525(4):1018–24. doi: 10.1016/j.bbrc.2020.03.017

58. Daks A, Mamontova V, Fedorova O, Petukhov A, Shuvalov O, Parfenyev S, et al. Set7/9 Controls Proliferation and Genotoxic Drug Resistance of NSCLC Cells. *Biochem Biophys Res Commun* (2021) 572:41–8. doi: 10.1016/j.bbrc.2021.07.086

59. Kurash JK, Lei H, Shen Q, Marston WL, Granda BW, Fan H, et al. Methylation of P53 by Set7/9 Mediates P53 Acetylation and Activity *In Vivo*. *Mol Cell* (2008) 29(3):392–400. doi: 10.1016/j.molcel.2007.12.025

60. Liu X, Wang D, Zhao Y, Tu B, Zheng Z, Wang L, et al. Methyltransferase Set7/9 Regulates P53 Activity by Interacting With Sirtuin 1 (Sirt1). *Proc Natl Acad Sci* (2011) 108(5):1925–30. doi: 10.1073/pnas.1019619108

61. Oudhoff MJ, Braam MJ, Freeman SA, Wong D, Rattray DG, Wang J, et al. SETD7 Controls Intestinal Regeneration and Tumorigenesis by Regulating Wnt/β-Catenin and Hippo/YAP Signaling. *Dev Cell* (2016) 37(1):47–57. doi: 10.1016/j.devcel.2016.03.002

Aberrant Cholesterol Metabolism in Ovarian Cancer: Identification of Novel Therapeutic Targets

Jiangnan He[†], Michelle K.Y. Siu[†], Hextan Y. S. Ngan and Karen K. L. Chan[*]

Departments of Obstetrics and Gynaecology, Li Ka Shing (LKS) Faculty of Medicine, The University of Hong Kong, Pok Fu Lam, Hong Kong, SAR China

Cholesterol is an essential substance in mammalian cells, and cholesterol metabolism plays crucial roles in multiple biological functions. Dysregulated cholesterol metabolism is a metabolic hallmark in several cancers, beyond the Warburg effect. Reprogrammed cholesterol metabolism has been reported to enhance tumorigenesis, metastasis and chemoresistance in multiple cancer types, including ovarian cancer. Ovarian cancer is one of the most aggressive malignancies worldwide. Alterations in metabolic pathways are characteristic features of ovarian cancer; however, the specific role of cholesterol metabolism remains to be established. In this report, we provide an overview of the key proteins involved in cholesterol metabolism in ovarian cancer, including the rate-limiting enzymes in cholesterol biosynthesis, and the proteins involved in cholesterol uptake, storage and trafficking. Also, we review the roles of cholesterol and its derivatives in ovarian cancer and the tumor microenvironment, and discuss promising related therapeutic targets for ovarian cancer.

Keywords: cholesterol metabolism, tumor microenvironment, carcinogenesis, therapeutic targets, ovarian cancer

1 INTRODUCTION

Ovarian cancer is one of the most aggressive malignancies worldwide (1). Due to the lack of obvious symptoms of early-stage ovarian cancer, newly diagnosed patients often present in advanced stages of disease, leading to the designation "silent killer" (2). Epithelial ovarian cancer can be classified into type I and type II ovarian tumors mainly on the basis of their cellular morphology and genetic alterations (3). Type I tumors consist of low grade serous, endometrioid, clear cell, and mucinous carcinomas, which are genetically characterized by BRAF, Kras, PTEN, or PI3KCA mutations primarily affecting PI3K/AKT/mTOR signaling (4–7). However, type II tumors mainly include high grade serous and undifferentiated carcinomas, typically with TP53 mutation and BRCA1/2 mutation (3, 8).

Metabolism in ovarian cancer shows heterogeneity, because the viability of ovarian cancer cells is maintained in a manner dependent not solely on metabolism but on the outside environment. Accumulating evidence indicates not only the active expression of aerobic glycolysis or oxidative phosphorylation (OXPHOS) in ovarian cancer but also aberrant lipid metabolism, which is strongly associated with ovarian cancer progression (9–12).

Patients with late-stage disease commonly display tumor metastases with an accumulation of ascites. The tumor microenvironment (TME) in ovarian cancer is composed of non-malignant cells, mainly including cancer-associated fibroblasts (CAF), cancer-associated adipocytes (CAA), immune-related cells, malignant cells, and secreted cytokines or other soluble molecules in ascites, which facilitate immunosuppression through crosstalk interactions among one another (13). Given that the major site of metastasis is the omentum, the TME in ovarian cancer is different from that in other cancers and is characterized as an adipocyte- and lipid-rich milieu, which has been shown to contribute to tumorigenesis, tumor immune escape, chemoresistance, and cancer recurrence (13–15). Other typical features of the tumor microenvironment include an insufficient supply of glucose and oxygen, which are non-beneficial for survival of tumor cells. To overcome this limitation, tumor cells and tumor-associated cells act in concert to develop reprogrammed adaptive metabolism (16). Ovarian tumor cells in this lipid-rich environment also tend to predominantly utilize lipid-dominant and alternative metabolic pathways (17). In addition, studies using co-culture of adipocytes and ovarian tumor cells have indicated that adipocytes promote tumor growth and metastasis of ovarian tumors, on the basis of the stimulation of adipocytes by the altered lipid metabolism in ovarian cancer, thus resulting in upregulation of lipid uptake from adipocytes and lipolysis in ovarian cancer cells (14).

Fatty acids and cholesterol are two main types of lipids. Multiple fatty acids and enzymes involved in fatty acid metabolism, such as fatty acid-binding protein 4 (FABP4), CD36 and stearoyl-CoA desaturase 1 (SCD1), significantly enhance ovarian cancer proliferation, survival, drug resistance and metastasis, and even contribute to stemness maintenance (14, 18–21). Recently, considerable evidence supporting the importance of reprogrammed cholesterol metabolism in ovarian cancer has been reported. Highly expressed proteins and enzymes involved in cholesterol metabolism promote ovarian cancer progression; cholesterol and its derivatives also contribute to proliferation and chemoresistance in ovarian cancer and have roles in the immunosuppressive tumor microenvironment (22–25). Here, we have systematically summarized the most recent findings on cholesterol and its derivatives in ovarian cancer, with the aim of comprehensively understanding their specific functions to facilitate the identification of novel markers and therapeutic targets.

2 OVERVIEW OF CHOLESTEROL METABOLISM

Cholesterol is a fundamental metabolite of mammalian cells to maintain structural integrity and fluidity of the plasma membrane, and regulates cells or cell-to-cell interactions by mediating alterations in signaling involved in cell proliferation, immunity, and inflammation (26). Several routes of cholesterol metabolism within cells have been determined (**Figure 1**), including (i) *de novo* cholesterol synthesis, (ii) exogenous
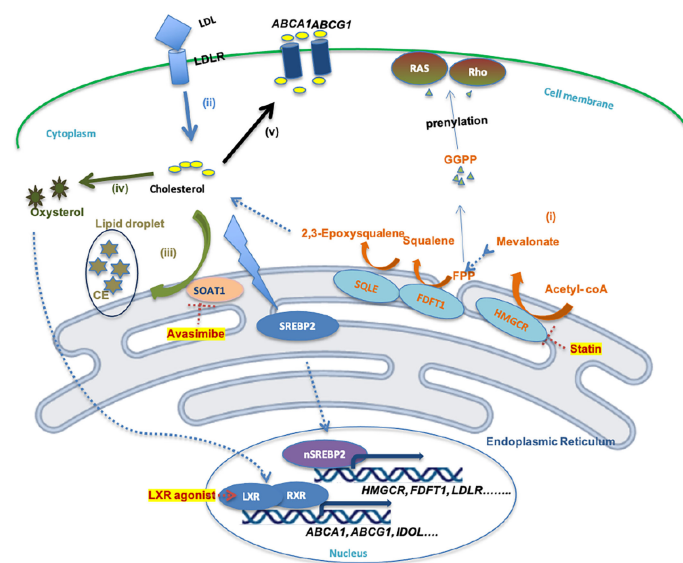
FIGURE 1 | Schematic illustration of cholesterol metabolism homeostasis and potential drugs. (i)Cholesterol bio synthesis. (ii) Cholesterol uptake. (iii) Cholesterol storage. (iv) Cholesterol conversion. (v) Cholesterol efflux. (i) *De novo* cholesterol synthesis involves nearly 30 enzymatic reactions, in which HMGR and SQLE are two key rate-limiting enzymes. FPP and GGPP, intermediates in this process, contribute to the prenylation of RAS and Rho proteins, which is necessary for RAS and Rho signaling activation. (ii) Cholesterol uptake is mediated by LDL-LDLR binding, which is followed by endocytosis of LDL by cells. However, high cholesterol accumulation leads to intracellular lipo-toxicity. High intracellular cholesterol levels suppress SREBP2 transcription factor activity, thereby restricting the expression of enzymes involved in cholesterol synthesis or cholesterol uptake. (iii) Excess cholesterol is converted into cholesterol ester by SOAT1 enzyme, then stored in lipid droplets. (iv) Excess cholesterol is converted to oxysterol through multiple enzymatic or non-enzymatic process. (v) Oxysterol activates LXR-RXR signaling and results in expression of ABCA1, ABCG1, and IDOL, which promote the cholesterol efflux pathway.

cholesterol uptake, (iii) cholesterol storage, (iv) cholesterol conversion, and (v) cholesterol trafficking (27).

(i) *De novo* cholesterol synthesis is initiated from acetyl-CoA *via* a complex enzymatic process. Within these reactions, 3-hydroxy-3-methylglutaryl-CoA (HMG-CoA) reductase (HMGCR), farnesyl-diphosphate farnesyltransferase 1 (FDFT1) and squalene epoxidase (SQLE) are key rate-limiting enzymes that convert HMG-CoA to mevalonate and squalene to 2,3-epoxysqualene (27). HMGCR, FDFT1 and SQLE are transcriptionally regulated by sterol regulatory element-binding protein 2 (SREBP2) (28). (ii) Mammalian cells take up exogenous cholesterol *via* low-density lipoprotein (LDL)-LDL receptor (LDLR) interactions, which internalizes cholesterol *via* endocytosis (12). However, free intracellular cholesterol levels require stringent control within the cytoplasm, because high levels lead to lipo-toxicity (26). An increased free cholesterol concentration >5% activates binding of SREBP cleavage-activating protein (SCAP) and Insig-1 on the endoplasmic reticulum (ER) membrane, leading to the retention of the SCAP-SREBP complex in the ER and preventing cholesterol/fatty acid synthesis and transportation, and thus lipid toxicity (29). (iii) Sterol O-acyltransferase (SOAT) is allosterically activated by elevated intracellular free cholesterol levels, promoting the conversion of cholesterols to cholesterol esters (CE), which is stored in lipid droplets (LD) (30). (iv) Oxysterol from excess cholesterol as a ligand directly activates the liver X receptor (LXR) transcription factor to regulate the (v) cholesterol efflux pathway by mediating the expression of the ATP-binding cassette (ABC) transporters, such as ABCA1 and ABCG1 (31). Excess cholesterol is exported outside the cell by ABC transporters at the cell surface, among which ABCA1 and ABCG1 are ubiquitously expressed in human cells (32). The cholesterol exported by ABCA1 is loaded onto lipid-free apolipoprotein A-I, thus producing nascent high-density lipoprotein (HDL), which in turn is converted into mature HDL by lecithin:cholesterol acyltransferase (LCAT) in the plasma (33). However, cholesterol exported by ABCG1 can directly become mature HDL (33), which can be ingested by liver cells or steroidogenic cells *via* binding to the HDL receptor, Scavenger receptor type B1 (SR-B1), thus resulting in selective CE uptake for subsequent synthesis of bile salts or steroid hormones (33, 34).

3 PROTEINS INVOLVED IN CHOLESTEROL METABOLISM IN OVARIAN CANCER

Several abnormally expressed proteins mediate cholesterol metabolism alterations to promote tumor cell viability, proliferation, migration, and invasion in ovarian cancer (**Table 1**). Therefore, the development of strategies targeting such proteins could lay the foundation for novel therapeutic treatment options.

3.1 Cholesterol Biosynthesis
3.1.1 HMG-CoA Reductase (HMGCR)
HMGCR, a glycoprotein located in the ER, is one of rate-limiting enzymes in the mevalonate pathway that catalyzes the generation of mevalonate from HMG-CoA with the consumption of two NAPDH molecules (26, 47). In addition to cholesterol generation to meet nutritional and membrane structure demands, intermediates of the mevalonate pathway are essential for the regulation of well-characterized oncogene-mediated signaling molecules, such as farnesyl pyrophosphate (FPP) and geranylgeranyl pyrophosphate (GGPP), which are essential for prenylation of the small GTPase proteins, Ras and Rho (48). Prenylation of Ras or Rho is critical for their membrane localization and activity (49). Oncogenic roles of HMGCR have been reported in various tumor types, including gastric, liver, and breast cancers (50–53).

The Keto and Wolf groups have reported higher HMGCR expression in cell lines and primary cultures from ovarian cancer than in normal ovarian epithelial cell lines and ovarian tissues (35, 54). Immunohistochemical expression was observed in the

TABLE 1 | The roles of enzymes and proteins involved in cholesterol metabolism in ovarian cancer.

Pathway of cholesterol metabolism	Involved enzyme or protein	Expression	Role in ovarian cancer	References
Cholesterol synthesis	HMGCR	Upregulated	Enhances ovarian cancer proliferation by activating Rho/Ras signaling	(35–37)
	FDFT1	Upregulated	Contributes to chemoresistance	(23)
	SQLE	Upregulated	High expression correlates with poor-progression-free survival and overall survival rates in patients with ovarian cancer	(38)
	SREBP2	Upregulated	Contributes to chemoresistance; enhances ovarian tumor progression *via* SIK2 and MIEF2-activated PI3K/AKT/mTOR signaling	(23, 39, 40)
Cholesterol uptake	LDLR	Upregulated	Enhances chemoresistance through the LDLR/LPC/FAM83B/FGFR axis	(23, 41)
Cholesterol storage	SOAT 1	Upregulated	Promotes ovarian tumor progression, SOAT1 inhibition impaired tumor cell proliferation, migration and increased chemosensitivity	(42)
Cholesterol trafficking	ABCA1	Upregulated	Promotes tumor cell proliferation, migration and invasion, chemoresistance and stemness maintenance	(43, 44)
	ABCG1	Upregulated	Upregulated in only high grade serous ovarian cancer; further research needed	(45)
	LXR	— — — —	Inhibition of ovarian tumor proliferation after LXR agonist treatment	(46)
	SR-B1	Upregulated	High expression positively associated with patient survival rates	(38)

HMGCR, 3-hydroxy-3-methylglutaryl-CoA (HMG-CoA) reductase; FDFT1, Farnesyl-Diphosphate Farnesyltransferase 1; SQLE, Squalene epoxidase; SREBP2, Sterol regulatory element-binding protein 2; LDLR, Low-density lipoprotein receptor; SOAT 1, Sterol O-acyltransferase; LXR, Liver X receptor (LXR); ABCA1, ABC subfamily A member 1; ABCG1, ABC subfamily G member 1; SR-B1, Scavenger receptor type B1.

majority of ovarian cancer tissues (55). Mechanistically, gain-of-function TP53 variants displayed ectopic expression in SKOV-3, while the lack of endogenous p53 expression or native TP53 mutations in OVCAR-3 resulted in elevated HMGCR mRNA levels and protein expression (36, 54). HMGCR inhibition with specific statin-like drugs has been found to inhibit monolayer and ovarian tumor spheroid cellular proliferation and tumor growth in xenograft mouse models, enhance autophagy, induce cellular arrest in G0/G1, promote extrinsic and mitochondrial (intrinsic) apoptosis with increased activity of caspase-3, 8, 9 and elevated Poly (ADP-ribose) polymerase (PARP) cleavage, and increase the sensitivity of ovarian cancer cells to carboplatin (35, 37, 56, 57). However, the addition of GGPP or mevalonate instead of cholesterol rescued the anti-proliferative effect mediated by statin and activated Ras/Rho signaling (35, 37).

3.1.2 Farnesyl-Diphosphate Farnesyltransferase 1 (FDFT1)

FDFT1, also known as squalene synthase, is located in the ER and acts downstream of HMGCR to synthesize squalene from FPP (58). The role of FDFT1 in cancer development is ambiguous at present. Reports to date suggest oncogenic effects of FDFT1, such as promoting proliferation, increasing anti-apoptotic protein levels, and preventing ferroptosis by increasing squalene levels in some cancer types, and conversely, plays an anti-oncogenic role in other cancers. For instance, overexpression of FDFT1 has been shown to induce the suppression of glycolysis through the blockage of AKT/mTOR/HIF-1α signaling in colorectal cancer (59).

FDFT1 is highly expressed in ovarian cancer. Zheng et al. showed a nearly 7-fold upregulation of FDFT1 in A2780 cisplatin-resistant ovarian cancer cells relative to sensitive cells (23). Interestingly, siRNA mediated FDFT1 inhibition in A2780 cells slightly augmented tumor cell proliferation, while its overexpression impaired migration and invasion of SKOV3 and 3AO cells (60). These findings may be attributed to squalene accumulation inducing cytotoxicity within cells (61).

3.1.3 Squalene Epoxidase (SQLE)

SQLE, also known as squalene monooxygenase, is located in the ER and is a rate-limiting enzyme in the mevalonate pathway that mediates the conversion of squalene into 2,3-epoxysqualene *via* usage of NADPH and a molecular oxygen (62). SQLE overexpression has been observed in multiple cancers, including breast cancer, liver and lung cancer, and is correlated with their aggressive behaviors and poorer prognosis (63–67). High expression and gain of the SQLE locus have been reported in ovarian cancer (63). Furthermore, the Kaplan-Meier analysis of ovarian cancer has shown that high SQLE expression is correlated with relatively poor progression-free survival and overall survival rates in patients with ovarian cancer (38). Therefore, further research on the potential involvement of SQLE in the pathogenesis of ovarian cancer should be considered.

3.1.4 Sterol Regulatory Element-Binding Protein 2 (SREBP2)

SREBP2 is a key transcription factor of enzymes involved in cholesterol synthesis and transport, including HMGCR, FDFT1,

SQLE and LDLR (28). Under conditions of cholesterol sufficiency, SREBP2 is located in the ER in an inactive state (28). Upon depletion of cholesterol, SREBP2 translocates to the Golgi apparatus and is cleaved by site 1 protease (S1P) and S2P to an active state. The active protein subsequently enters the nucleus to bind other regulatory factors at the promotor regions of target genes (68).

SREBP2 can enhance chemotherapeutic drug resistance in ovarian cancer cells *via* the upregulation of cholesterol synthesis (23). Zheng et al. (23) reported that the levels of SREBP2 and SREBP-targeted genes, such as HMGCR, FDFT1 and LDLR, in A2780 cells were proportionally correlated with cisplatin doses. Karashcuk and co-workers additionally reported that SREBP2 mediates ovarian cancer recurrence and escape from cell cycle arrest after paclitaxel treatment (69). The inhibition of SREBP2 with CRISPR technology in OVCAR-8 cell lines led to slower recovery rates of cell growth following paclitaxel treatment, compared to control cells (70). Thus, targeting of SREBP2 may improve drug sensitivity and lower the recurrence of ovarian cancer.

In addition to being regulated by the free intracellular cholesterol level, SREBP2 expression is also regulated by the PI3K/AKT/mTOR signaling pathway (71). In the cholesterol synthesis pathway, SREBP2 is upregulated by salt-inducible kinase 2 (SIK2), an AMPK-related kinase, and mitochondrial elongation factor 2 (MIEF2)-activated PI3K/AKT or ROS/AKT/mTOR signaling, thus, leading to the promotion of ovarian tumor growth (39, 40).

3.2 Cholesterol Uptake

3.2.1 Low-Density Lipoprotein Receptor (LDLR)

Binding of LDLR, a transmembrane glycoprotein located on the cell plasma membrane, to LDL facilitates cholesterol uptake *via* endocytosis (72). Based on TCGA data, high LDLR expression is significantly associated with poor overall survival rates of ovarian tumor patients (22). IHC findings have revealed a strong intensity of LDLR in endometrioid and clear cell types of ovarian cancer (41). Zheng et al. showed that LDLR was upregulated in an ovarian cancer cell line resistant to cisplatin (23). Silencing of LDLR improved the sensitivity of ovarian tumor cells to cisplatin treatment by mediating the LPC (lysophosophatidylcholine)/FAM83B (family with sequence similarity 83 member B)/FGFR (fibroblast growth factor receptor) axis (41). Therefore, LDLR may be recognized as a marker of cisplatin treatment response to ovarian tumors, and in particular, the endometrioid and clear-cell types.

3.3 Cholesterol Storage

3.3.1 Sterol O-Acyltransferase (SOAT)

Sterol O-acyltransferase (SOAT), also designated as acyl-coenzyme A cholesterol acyltransferase (ACAT), converts cholesterol and acyl-CoA to cholesterol esters (CE) in the ER, which are then stored in lipid droplets (33). SOAT exists as two isoforms, including SOAT1 and SOAT2. SOAT1 is generally detectable in all tissues, while SOAT2 is limited to the liver or intestinal tissue (73). SOAT1, but not SOAT2, is expressed highly in liver cancer, brain cancer, prostate cancer, and pancreatic cancer tissues and associated with their low overall survival rates

(74–77). These findings suggest an oncogenic role for SOAT1 and support its utility as a potential therapeutic target.

Ayyagari et al. (42) reported higher SOAT1 expression levels than SOAT2 expression levels, and elevated CE levels in ovarian cancer cell lines compared to normal cell lines. Mechanistically, SOAT1 inhibition by shRNA or Avasimibe suppressed proliferation, migration and invasion of SKOV3, OC-314, and IGROV-1 cell lines by promoting mitochondrial apoptosis; the cells showed decreased mitochondrial potential, high activity of caspase 3/7, and increased ROS and p53 expression, regardless of mutation status. Furthermore, knockdown of SOAT1 improved the cisplatin sensitivity of ovarian cancer cells (42).

Of note, SOAT1 deficiency in CD8+ T cells augments their tumor-killing ability *via* increasing the cholesterol content on the plasma membrane and subsequently promoting T-cell receptor (TCR) clustering and immunological synapse formation in CD8+ T cells (78). SOAT1 depletion in mesothelin-directed chimeric antigen receptor T cells (CART) can strengthen their anti-tumor response against pancreatic carcinoma *in vitro* or *in vivo* (79). Therefore, SOAT1 inhibition may mediate dual anti-tumor effects in cancer treatment in terms of tumor inhibition and immunity enhancement, and is likely to have value in combination with immunotherapy.

3.4 Cholesterol Trafficking
3.4.1 ABC Subfamily A Member 1 (ABCA1)
ATP-binding cassette (ABC) transporters in the cell membrane mainly consisting of ABC subfamily A member 1 (ABCA1) and ABC subfamily G members 1, 5 and 8 (ABCG1, ABCG5, ABCG8) contribute to cholesterol efflux (80). Unlike ABCG5 and ABCG8 that are restricted to hepatocytes and enterocytes, ABCA1 and ABCG1 are ubiquitously expressed throughout the body (81). Hedditch et al. reported that high ABCA1 expression in ovarian cancer tissue was significantly correlated with poor survival outcomes of patients. In terms of functional analyses, depletion of ABCA in A2780, 27/87 and SKOV3 ovarian cancer cell lines *via* siRNA attenuated colony formation, migration, and invasion (43). Moreover, ABCA1 promoted ovarian cancer drug resistance and tumorigenesis. Silencing of ABCA1 in MCP2 platinum-resistant cells led to improved cisplatin sensitivity (82). In addition, ABCA1 was upregulated in EPCAM+CD45+ tumor cells derived from ascites of patients with ovarian cancer with aggressive features (44). Chou et al. showed that hypermethylation of ABCA1 was correlated with a poorer prognosis of ovarian cancer patients (83). Specifically, *in vitro* treatment of MCP3 and HeyC2 cell lines with shABCA1, or an *in vivo* HeyC2 cell-based xenograft mouse model mimicking hypermethylation enhanced tumor cell growth (83). Thus, the roles of ABCA1 in ovarian cancer require further investigation.

3.4.2 ATP Binding Cassette Subfamily G Member 1 (ABCG1)
ABCG1, located at the cell membrane surface, mediates cholesterol export from cells by mature HDL. High expression of ABCG1 has been observed in pancreatic cancer, breast cancer, lung cancer, and colon cancer (84–87). ABCG1 promotes cell proliferation, migration, and invasion in lung cancer cells, and is associated

with expression of anti-apoptotic proteins (B-cell lymphoma 2 (BCL2) or Myeloid-cell leukemia 1 (MCL1)), stemness markers (CD133 and ALDH), and proliferative markers (such as c-Myc) (87). ABCG1 inhibition by knockdown suppresses tumor growth in a colon tumor mouse model by blocking extracellular vesicle (EV) lipid efflux, thereby leading to the accumulation of EVs, which mediate cellular toxicity (86). In addition, ABCG1 is associated with tumor immunity. ABCG1 contributes to the macrophage phenotype shift from M1 to M2 (88). Macrophages with ABCG1 deficiency have higher cytotoxicity with NF-κB activation (88). In addition, depletion of ABCG1 causes hyperproliferation of CD4+ T cells in the peripheral blood in mice (89). These findings illustrate that ABCG1 may be a promising anti-tumor target. However, the high expression of ABCG1 has been observed in only high grade serous ovarian carcinoma (HGSC) (45). Its detailed mechanisms in ovarian cancer should be further explored.

3.4.3 Liver X Receptor (LXR)
LXR, which belongs to the nuclear receptor family, plays an important role in maintaining intracellular cholesterol homeostasis (31). LXR is activated by LXR agonists and subsequently forms a heterodimer with retinoid X receptor (RXR). This LXR-RER heterodimer combined with co-activator binds LXR-responsive-elements (LXREs) in the nucleus and mediates the expression of cholesterol metabolism-related genes, such as ABCA1, ABCG1, and inducible degrader of LDLR (IDOL) (90). LXR activation mediates anti-tumor effects in multiple cancers (91). LXR activation induces expression of inducible degrader of LDLR (IDOL), which decreases the LDLR expression induced by EGFR/SREBP-1 signaling in glioblastoma tumor cells (92). Likewise, LXR activation by its agonists significantly suppresses ovarian tumor cell proliferation (46).

3.4.4 Scavenger Receptor Type B1 (SR-B1)
SR-B1 recognizes HDL and then selectively takes up CEs into cells without the apolipoprotein moiety. SR-BI is commonly expressed in the liver cells and steroidogenic cells. SR-BI is highly expressed in multiple cancer cell lines including ovarian cancer cells lines (93). High SR-BI expression has been observed in lung cancer and breast cancer, and it is associated with malignancy and poor prognosis (94, 95). SR-BI is recognized as a biomarker of melanoma progression in patients and has been associated with STAT5 expression in clinical samples (96). However, SR-B1 expression in patients with ovarian cancer patients is positively correlated with survival rate (38). To provide further clarification, its detailed mechanisms require further exploration.

4 ROLES OF CHOLESTEROL AND CHOLESTEROL DERIVATIVES IN OVARIAN CANCER AND TUMOR MICROENVIRONMENT

4.1 Cholesterol
Previous studies have shown high cholesterol levels in ascites fluid in ovarian tumors (97). Helzlsouer et al. initially reported that the

cholesterol concentration in blood was proportionally correlated with the risk of ovarian cancer (98). In addition, LDL, a main blood carrier of cholesterol, and large amounts of cholesterol are associated with aggressiveness and poor survival outcomes of ovarian cancer (99). In the murine ID8 model of ovarian cancer, mice subjected to a high cholesterol diet exhibited increased tumor growth compared to that observed in the control groups (24). Dysregulated cholesterol homeostasis has been reported to enhance platinum resistance in ovarian cancer (22). Besides, high cholesterol levels in aggressive ascites were shown to contribute to cisplatin resistance in ovarian tumor cells by activating an LXR α/β nuclear receptor, with sequential upregulation of multidrug resistance protein 1 (MDR1) (100). High cholesterol loading in mitochondria perturbs mitochondrial function, inhibiting mitochondrial membrane permeabilization and the release of cytochrome c, a pro-apoptotic signal, thus contributing to chemotherapy resistance in liver cancer cells (101). The effects of dysregulated cholesterol homeostasis in mitochondria on drug resistance in ovarian cancer requires further investigation.

Cholesterol also influences energetic metabolism, thus contributing to tumor progression. In breast cancer cells, exogenous cholesterol alters metabolic pathways and consequently enhances cell proliferation in an estrogen-related receptor alpha-dependent manner, thus increasing oxidative phosphorylation and the tricarboxylic acid cycle (TCA) cycle (102). Aerobic glycolysis has been found to be augmented by exogenous cholesterol in only triple-negative breast cancer cell lines (102). Furthermore, high mitochondrial cholesterol loading increases hexokinase translocation to the mitochondria and may contribute to aerobic glycolysis in cancer cells (103). However, the relationship between cholesterol and energetic metabolism is less clear in ovarian cancer and requires further study.

Other than its effects on tumor cells, cholesterol may contribute to the immunosuppressive TME. Evidence has shown that cholesterol influences tumor-associated macrophages (TAM) in the microenvironment. Peritoneal TAMs in the ovarian cancer mouse model were reported to show increased cholesterol efflux activated by high molecular weight hyaluronic acid secretion from ID8 ovarian tumor cells, in turn, augmenting IL-4/PI3K/Akt/STAT6 signaling. However, attenuation of the IFN-γ-induced gene signature in TAM contributes to immunosuppression and the energetic needs of tumors (25). Specific knockout of ABCA1 or ABCG1 with the inhibition of cholesterol efflux in TAM effectively reversed the pro-tumorigenic effect of TAM in ovarian cancer, which could be applied to develop a novel therapeutic strategy. In addition, a large amount of cholesterol secreted from tumor cells impairs the cytotoxicity of CD8+ effector T cells and induces exhausted CD8+ T cells. HMGCR knockdown or statin treatment in B16 melanoma cells significantly decreases the frequency of exhausted CD8+ T cells at tumor sites (104). Mechanistically, high cholesterol augments endoplasmic reticulum (ER) stress in CD8+ T cells and consequently results in XBP-1 activation, which elevates the expression of immune checkpoint proteins, such as T cell immunoglobulin and mucin domain-containing protein 3 (TIM-3), Programmed cell death protein 1 (PD-1),

Lymphocyte activation gene 3 protein (LAG-3), and 2B4 (CD244), in CD8+ T cells (104).

4.2 Oxysterol

Oxysterol, the hydroxylation product of cholesterol, participates in numerous cellular processes, such as cell signaling, membrane fluidity, and the activation of membrane proteins, similar to cholesterol (105). The 27-Hydroxycholesterol (27HC), a type of oxysterol, is catalyzed from cholesterol by Cytochrome P450 Family 27 Subfamily A Member 1 (CYP27A1) (106). High CYP27A1 expression is associated with poor prognosis at the early stages of disease and poorer progression-free survival but serves as a positive predictor in late-stage ovarian cancer (24). Functionally, exogenous 27HC treatment could abolish the proliferative capacity of ovarian cancer cell lines via LXR activation-induced cholesterol efflux in tumor cells. Intriguingly, however, CYP27A1 or exogenous 27HC treatment in the ovarian cancer mouse model has also been shown to augment peritoneal tumor spread and carboplatin resistance, consistent with Kaplan–Meier analyses of CYP27A1 in ovarian cancer patients (24). These data suggest that CYP27A1 and its product 27HC promote ovarian cancer progression by influencing the tumor microenvironment, rather than intrinsic effects on the tumor itself.

Reprogrammed macrophage patterns have been observed in ovarian tumors in the presence of exogenous 27HC, including increased concentrations of monocytic myeloid-derived suppressor cells (MDSC) and decreases in antigen-presenting macrophages (24). Genetic depletion of CYP27A1 could reverse the immunosuppressive effect of 27HC. In addition, a combination of the CYP27A1 inhibitor, GW273297X, and anti-PDL1 antibodies induced a significant decrease in ovarian tumor growth in mouse models compared to either treatment alone (24). In addition, the oxysterol secreted by tumor cells has been shown to impair the antigen presentation of dendritic cells (DC) by LXR-α signaling activation, thus mediating downregulation of the expression of C-C chemokine receptor type 7 (CCR7), a lymphoid homing marker of DC, on the DC cell surface (107). LXR-α activation in DCs compromises DC migration to lymph nodes, thus decreasing T cell priming (107). Treatment with Sulfotransferase 2B1b (SULT2B1b), an LXR ligand-inactive enzyme, relieves the CCR7 inhibition in DCs, and restores DC function and the anti-tumor response (107). LXR signaling activation suppresses the proliferation and expansion of T cells (108). However, Tavazoie et al. have shown that LXR activation suppressed the immunosuppressive effect of myeloid-derived suppressor cells (MDSC) by inducing Apolipoprotein E (ApoE) expression and consequently augmenting the T cell killing ability (109).

Another type of oxysterol, 25-hydroxycholesterol (25HC), is synthesized by cholesterol 25-hydroxylase (CH25H) (110). The specific role of 25-hydroxycholesterol (25HC) in ovarian cancer remains to be established. The 25HC is reported to stimulate the proliferation of BG-1 ovarian cancer cells in an estrogen receptor-α-activation-dependent manner (110). However, 25HC combined with statin reduced the viability of OVCAR-8 and SKOV3 cell lines via the suppression of SREBP2. SREBP2

suppression was greater following the combined treatment compared to that observed with statin treatment alone (111). Therefore, future studies should focus on the precise mechanisms of action of 25HC in ovarian cancer.

5 POTENTIAL THERAPEUTIC DRUGS IN OVARIAN CANCER

5.1 Statins

Statins are specific inhibitors of HMGCR that block the mevalonate pathway (112). Statins were originally used to lower the cholesterol level in blood and were found to be well-tolerated. Freed-Pastor et al. demonstrated that upregulation of the mevalonate pathway was mostly mediated by TP53 mutations, which is a dominant genetic mutation profile in ovarian cancer. Several reports have confirmed that lipophilic statins (**Table 2**), such as simvastatin and lovastatin, but not hydrophilic statins, significantly suppressed cell viability and proliferation, stemness, invasion and migration, and enhance mitochondrial apoptosis and chemotherapeutic sensitivity of ovarian cancer cell lines and primary ovarian cancer samples derived from patients or mouse models, without causing damage to normal cells (35, 37, 54, 56, 57). Statins exert pluripotent effects against cancer. Göbel and co-workers showed that lipophilic statins attenuated the expression of IL-6, IL-8, Vascular endothelial growth factor (VEGF), and Transforming growth factor beta (TGF-β), which contributed to ovarian tumor progression (115). Meanwhile, statin treatment of ovarian cancer cell lines activated c-Jun N-terminal kinase (JNK) signaling and induced the pro-apoptotic protein, Bim, reduced c-Myc phosphorylation, and blocked Ras/Rho signaling (37, 57, 113).

In addition to promoting resistance against tumor growth, statins are reported to enhance antigen presentation in dendritic cells (DC) and T cell cytotoxic functions in a B16 melanoma mouse model by attenuating Rab5 protein prenylation by GGPP or FPP, which are involved in the endosomal trafficking process;

thus, reducing antigen internalization and degradation at the cell surface (116). Notably, the combination of statin with anti-PD1 antibodies exerted a stronger synergistic anti-tumor effect comparison with the alone treatment (116). Therefore, statin-like drugs present potent therapeutic options for ovarian cancer.

Several clinical trials (NCT04457089 and NCT00585052) on ovarian cancer have been conducted. Statins, and in particular, lipophilic statins are clearly associated with a lower risk of ovarian cancer occurrence (117).

5.2 Avasimibe

Avasimibe, an inhibitor of SOAT and a cholesterol-lowering drug, can suppress CE generation. Accumulating preclinical studies have revealed the inhibitory effects of Avasimibe on tumor growth in various cancer types, including hepatocellular carcinoma, glioblastoma, pancreatic adenocarcinoma, and prostate cancer through the regulation of intracellular cholesterol metabolism (74–77). Ayyagari et al. (42) demonstrated the anti-tumor growth effect of Avasimibe in ovarian cancer cell lines.

In addition to its tumor suppression activity, Avasimibe is also an immunomodulatory agent. Avasimibe can augment the tumor-killing function of CD8+ T cells *via* the enhancement of T cell receptor (TCR) signaling and immunological synapse formation of CD8+ T cells by enhancing the cholesterol level of the plasma membrane (78). Consequently, many combined therapeutic strategies have been developed for Avasimibe and other immunotherapies, such as anti-PD1 antibodies, cancer stem cell-dendritic cell (CSC-DC) vaccines, and Kras peptide vaccines (78, 118, 119).

In earlier atherosclerosis clinical trials, Avasimibe exhibited a well-tolerated safety profile (120), and thus, should be strongly considered for ovarian cancer clinical trials.

5.3 LXR Agonist

Liver X receptor, a nuclear receptor, senses alterations in cholesterol metabolism (33). Natural ligands of this receptor include different

TABLE 2 | Potential drugs for targeting cholesterol metabolism in ovarian cancer.

Involved proteins	Drug	Function	Mechanism	Cell source	Clinical trial	References
HMGCR	Atorvastatin	Inhibit proliferation, stemness, migration, invasion; enhance apoptosis, cell cycle arrest and chemotherapy sensitivity	Decrease p-S6 and p-c-Myc	Hey, SKOV3.	NCT02201381, Phase 3 (Recruiting)	(57)
	Simvastatin		Block Ras/Rho signaling *via* reduction of FPP and GGPP, attenuate stemness by inactivating Hippo/YAP/TAZ/signaling	A2780, Hey8, primary ovarian cancer cells	NCT04457089, Early Phase 1 (Recruiting)	(35, 56)
	Lovastatin		Upregulate Bim (pro-apoptotic protein) expression, induce autophagy, anti- Ras/Rho signaling	Hey1B, SKOV3, OVCAR5, mouse model	NCT00585052, Phase 2 (Terminated)	(37, 113)
SOAT1	Avasimibe	Anti-proliferative effect	— — — — — —	OC314, SKOV3, IGROV-1	— — — —	(42)
Liver X receptor	GW3965	Induce apoptosis	Decrease LD accumulation induced by hypoxia	IGOVR-1, SKOV3	— — — —	(114)
	T0901317	Anti-tumor growth, induce cell cycle arrest	Upregulate p21, p27. expression in an FXR activation dependent manner	CaOV3, A2780, SKOV3	— — — —	(46)

types of oxysterol, such as 22-hydroxycholesterol (22HC), 20-hydroxycholesterol (20HC), and 27HC (121). The 27HC is known to exert anti-proliferative effects in ovarian tumors. GW3965 and T0901317 are synthetic LRX ligands (121) and Curtarello et al. showed that GW3965 could significantly promote apoptosis of SKOV3 and IGROV1 cell lines by reducing LD accumulation under hypoxic conditions to a similar degree as the anti-VEGF antibody, bevacizumab (114). Combination treatment with GW3965 and bevacizumab further promoted treatment efficiency. Additionally, T0901317 exerted a significant inhibitory effect on ovarian cancer cells in a dose- and time-dependent manner *via* interactions with farnesoid-X receptor (FXR), rather than *via* LXR activation (46). However, limited research has focused on the involvement of LXR, and further experiments are required to determine the role of LXR agonists in ovarian cancer.

6 CONCLUSIONS

Numerous studies have implicated essential enzymes or proteins involved in cholesterol metabolism in ovarian cancer, thus, supporting the theory that aberrant cholesterol metabolism contributes to disease progression. Cholesterol and oxysterol, its derivative, are not only intrinsic tumor-promoting factors but also extrinsic tumor-promoting factors *via* reprogramming the tumor microenvironment. Elevated levels of cholesterol and oxysterol also contribute to the immunosuppressive environment. High cholesterol level in TME contributes to the generation of exhausted CD8+T cells. Oxysterol can reprogramme the TAM pattern and influence the antigen presentation ability of DC in the tumor site. Thus, drugs targeting cholesterol metabolism may present potential treatments and even overcome the immunotherapy resistance, as a combined therapy with immune checkpoint blockades. Further studies are needed to clarify the specific roles and associated mechanisms of action of these proteins in the pathogenesis of ovarian cancer to facilitate the development of therapeutic clinical agents.

AUTHOR CONTRIBUTIONS

Writing the original draft preparation, JH. Writing—review and editing, MS and KC. Supervision, MS, HN, and KC. All authors contributed to the article and approved the submitted version.

FUNDING

REFERENCES

1. Torre LA, Trabert B, DeSantis CE, Miller KD, Samimi G, Runowicz CD, et al. Ovarian Cancer Statistics, 2018. *CA Cancer J Clin* (2018) 68(4):284–96. doi: 10.3322/caac.21456

2. Lengyel E. Ovarian Cancer Development and Metastasis. *Am J Pathol* (2010) 177(3):1053–64. doi: 10.2353/ajpath.2010.100105

3. Shih Ie M, Kurman RJ. Ovarian Tumorigenesis: A Proposed Model Based on Morphological and Molecular Genetic Analysis. *Am J Pathol* (2004) 164 (5):1511–8. doi: 10.1016/s0002-9440(10)63708-x

4. Kaldawy A, Segev Y, Lavie O, Auslender R, Sopik V, Narod SA. Low-Grade Serous Ovarian Cancer: A Review. *Gynecologic Oncol* (2016) 143(2):433–8. doi: 10.1016/j.ygyno.2016.08.320

5. Pierson WE, Peters PN, Chang MT, Chen LM, Quigley DA, Ashworth A, et al. An Integrated Molecular Profile of Endometrioid Ovarian Cancer. *Gynecologic Oncol* (2020) 157(1):55–61. doi: 10.1016/j.ygyno.2020.02.011

6. Gemignani ML, Schlaerth AC, Bogomolniy F, Barakat RR, Lin O, Soslow R, et al. Role of KRAS and BRAF Gene Mutations in Mucinous Ovarian Carcinoma. *Gynecologic Oncol* (2003) 90(2):378–81. doi: 10.1016/S0090-8258(03)00264-6

7. Wiegand KC, Shah SP, Al-Agha OM, Zhao Y, Tse K, Zeng T, et al. ARID1A Mutations in Endometriosis-Associated Ovarian Carcinomas. *New Engl J Med* (2010) 363(16):1532–43. doi: 10.1056/NEJMoa1008433

8. Kurman RJ, Shih Ie M. The Dualistic Model of Ovarian Carcinogenesis: Revisited, Revised, and Expanded. *Am J Pathol* (2016) 186(4):733–47. doi: 10.1016/j.ajpath.2015.11.011

9. Siu MKY, Jiang YX, Wang JJ, Leung THY, Han CY, Tsang BK, et al. Hexokinase 2 Regulates Ovarian Cancer Cell Migration, Invasion and Stemness *via* FAK/ERK1/2/MMP9/NANOG/SOX9 Signaling Cascades. *Cancers* (2019) 11(6):813. doi: 10.3390/cancers11060813

10. Siu MKY, Jiang Y-x, Wang J-j, Leung THY, Ngu SF, Cheung ANY, et al. PDK1 Promotes Ovarian Cancer Metastasis by Modulating Tumor-Mesothelial Adhesion, Invasion, and Angiogenesis *via* α5β1 Integrin and JNK/IL-8 Signaling. *Oncogenesis* (2020) 9(2):24. doi: 10.1038/s41389-020-0209-0

11. Shen L, Zhou L, Xia M, Lin N, Ma J, Dong D, et al. Pgc1α Regulates Mitochondrial Oxidative Phosphorylation Involved in Cisplatin Resistance in Ovarian Cancer Cells *via* Nucleo-Mitochondrial Transcriptional Feedback. *Exp Cell Res* (2021) 398(1):112369. doi: 10.1016/j.yexcr.2020.112369

12. Chen RR, Yung MMH, Xuan Y, Zhan S, Leung LL, Liang RR, et al. Targeting of Lipid Metabolism With a Metabolic Inhibitor Cocktail Eradicates Peritoneal Metastases in Ovarian Cancer Cells. *Commun Biol* (2019) 2:281. doi: 10.1038/s42003-019-0508-1

13. Worzfeld T, Pogge von Strandmann E, Huber M, Adhikary T, Wagner U, Reinartz S, et al. The Unique Molecular and Cellular Microenvironment of Ovarian Cancer. *Front Oncol* (2017) 7:24. doi: 10.3389/fonc.2017.00024

14. Nieman KM, Kenny HA, Penicka CV, Ladanyi A, Buell-Gutbrod R, Zillhardt MR, et al. Adipocytes Promote Ovarian Cancer Metastasis and Provide Energy for Rapid Tumor Growth. *Nat Med* (2011) 17(11):1498–503. doi: 10.1038/nm.2492

15. Khan SM, Funk HM, Thiolloy S, Lotan TL, Hickson J, Prins GS, et al. *In Vitro* Metastatic Colonization of Human Ovarian Cancer Cells to the Omentum. *Clin Exp Metastasis* (2010) 27(3):185–96. doi: 10.1007/s10585-010-9317-0

16. Riscal R, Skuli N, Simon MC. Even Cancer Cells Watch Their Cholesterol! *Mol Cell* (2019) 76(2):220–31. doi: 10.1016/j.molcel.2019.09.008

17. Ahmed N, Escalona R, Leung D, Chan E, Kannourakis G. Tumour Microenvironment and Metabolic Plasticity in Cancer and Cancer Stem Cells: Perspectives on Metabolic and Immune Regulatory Signatures in Chemoresistant Ovarian Cancer Stem Cells. *Semin Cancer Biol* (2018) 53:265–81. doi: 10.1016/j.semcancer.2018.10.002

18. Ji Z, Shen Y, Feng X, Kong Y, Shao Y, Meng J, et al. Deregulation of Lipid Metabolism: The Critical Factors in Ovarian Cancer. *Front Oncol* (2020) 10:593017. doi: 10.3389/fonc.2020.593017

19. Ladanyi A, Mukherjee A, Kenny HA, Johnson A, Mitra AK, Sundaresan S, et al. Adipocyte-Induced CD36 Expression Drives Ovarian Cancer Progression and Metastasis. *Oncogene* (2018) 37(17):2285–301. doi: 10.1038/s41388-017-0093-z

20. Tesfay L, Paul BT, Konstorum A, Deng Z, Cox AO, Lee J, et al. Stearoyl-CoA Desaturase 1 Protects Ovarian Cancer Cells From Ferroptotic Cell Death. *Cancer Res* (2019) 79(20):5355–66. doi: 10.1158/0008-5472.CAN-19-0369

21. Li J, Condello S, Thomes-Pepin J, Ma X, Xia Y, Hurley TD, et al. Lipid Desaturation Is a Metabolic Marker and Therapeutic Target of Ovarian Cancer Stem Cells. *Cell Stem Cell* (2017) 20(3):303–14.e5. doi: 10.1016/j.stem.2016.11.004

22. Criscuolo D, Avolio R, Calice G, Laezza C, Paladino S, Navarra G, et al. Cholesterol Homeostasis Modulates Platinum Sensitivity in Human Ovarian Cancer. *Cells* (2020) 9(4):828. doi: 10.3390/cells9040828

23. Zheng L, Li L, Lu Y, Jiang F, Yang XA. SREBP2 Contributes to Cisplatin Resistance in Ovarian Cancer Cells. *Exp Biol Med (Maywood NJ)* (2018) 243 (7):655–62. doi: 10.1177/1535370218760283

24. He S, Ma L, Baek AE, Vardanyan A, Vembar V, Chen JJ, et al. Host CYP27A1 Expression Is Essential for Ovarian Cancer Progression. *Endocrine-Related Cancer* (2019) 26(7):659–75. doi: 10.1530/ERC-18-0572

25. Goossens P, Rodriguez-Vita J, Etzerodt A, Masse M, Rastoin O, Gouirand V, et al. Membrane Cholesterol Efflux Drives Tumor-Associated Macrophage Reprogramming and Tumor Progression. *Cell Metab* (2019) 29(6):1376–89.e4. doi: 10.1016/j.cmet.2019.02.016

26. Luo J, Yang H, Song BL. Mechanisms and Regulation of Cholesterol Homeostasis. *Nat Rev Mol Cell Biol* (2020) 21(4):225–45. doi: 10.1038/s41580-019-0190-7

27. Xu H, Zhou S, Tang Q, Xia H, Bi F. Cholesterol Metabolism: New Functions and Therapeutic Approaches in Cancer. *Biochim Biophys Acta Rev Cancer* (2020) 1874(1):188394. doi: 10.1016/j.bbcan.2020.188394

28. Eberlé D, Hegarty B, Bossard P, Ferré P, Foufelle F. SREBP Transcription Factors: Master Regulators of Lipid Homeostasis. *Biochimie* (2004) 86 (11):839–48. doi: 10.1016/j.biochi.2004.09.018

29. Radhakrishnan A, Goldstein JL, McDonald JG, Brown MS. Switch-Like Control of SREBP-2 Transport Triggered by Small Changes in ER Cholesterol: A Delicate Balance. *Cell Metab* (2008) 8(6):512–21. doi: 10.1016/j.cmet.2008.10.008

30. Long T, Sun Y, Hassan A, Qi X, Li X. Structure of Nevanimibe-Bound Tetrameric Human ACAT1. *Nature* (2020) 581(7808):339–43. doi: 10.1038/s41586-020-2295-8

31. Wang B, Tontonoz P. Liver X Receptors in Lipid Signalling and Membrane Homeostasis. *Nat Rev Endocrinol* (2018) 14(8):452–63. doi: 10.1038/s41574-018-0037-x

32. Phillips MC. Molecular Mechanisms of Cellular Cholesterol Efflux. *J Biol Chem* (2014) 289(35):24020–9. doi: 10.1074/jbc.R114.583658

33. Chang TY, Chang CC, Ohgami N, Yamauchi Y. Cholesterol Sensing, Trafficking, and Esterification. *Annu Rev Cell Dev Biol* (2006) 22:129–57. doi: 10.1146/annurev.cellbio.22.010305.104656

34. Krieger M. Charting the Fate of the "Good Cholesterol": Identification and Characterization of the High-Density Lipoprotein Receptor SR-Bi. *Annu Rev Biochem* (1999) 68:523–58. doi: 10.1146/annurev.biochem.68.1.523

35. Kato S, Smalley S, Sadarangani A, Chen-Lin K, Oliva B, Brañes J, et al. Lipophilic But Not Hydrophilic Statins Selectively Induce Cell Death in Gynaecological Cancers Expressing High Levels of HMGCoA Reductase. *J Cell Mol Med* (2010) 14(5):1180–93. doi: 10.1111/j.1582-4934.2009.00771.x

36. Abdullah MI, Abed MN, Richardson A. The Interplay Between TP53 and Mevalonate Pathway in Ovarian Cancer. *Ann Oncol* (2017) 28:v6. doi: 10.1093/annonc/mdx361.020

37. Kobayashi Y, Kashima H, Wu RC, Jung JG, Kuan JC, Gu J, et al. Mevalonate Pathway Antagonist Suppresses Formation of Serous Tubal Intraepithelial Carcinoma and Ovarian Carcinoma in Mouse Models. *Clin Cancer Res* (2015) 21(20):4652–62. doi: 10.1158/1078-0432.CCR-14-3368

38. Gyorffy B, Lánczky A, Szállási Z. Implementing an Online Tool for Genome-Wide Validation of Survival-Associated Biomarkers in Ovarian-Cancer Using Microarray Data From 1287 Patients. *Endocrine-Related Cancer* (2012) 19(2):197–208. doi: 10.1530/ERC-11-0329

39. Zhao S, Cheng L, Shi Y, Li J, Yun Q, Yang H. MIEF2 Reprograms Lipid Metabolism to Drive Progression of Ovarian Cancer Through ROS/AKT/mTOR Signaling Pathway. *Cell Death Dis* (2021) 12(1):18. doi: 10.1038/s41419-020-03336-6

40. Zhao J, Zhang X, Gao T, Wang S, Hou Y, Yuan P, et al. SIK2 Enhances Synthesis of Fatty Acid and Cholesterol in Ovarian Cancer Cells and Tumor Growth Through PI3K/Akt Signaling Pathway. *Cell Death Dis* (2020) 11 (1):25. doi: 10.1038/s41419-019-2221-x

41. Chang WC, Wang HC, Cheng WC, Yang JC, Chung WM, Ho YP, et al. LDLR-Mediated Lipidome-Transcriptome Reprogramming in Cisplatin Insensitivity. *Endocrine-Related Cancer* (2020) 27(2):81–95. doi: 10.1530/ERC-19-0095

42. Ayyagari VN, Wang X, Diaz-Sylvester PL, Groesch K, Brard L. Assessment of Acyl-CoA Cholesterol Acyltransferase (ACAT-1) Role in Ovarian Cancer Progression-An *In Vitro* Study. *PloS One* (2020) 15(1):e0228024. doi: 10.1371/journal.pone.0228024

43. Hedditch EL, Gao B, Russell AJ, Lu Y, Emmanuel C, Beesley J, et al. ABCA Transporter Gene Expression and Poor Outcome in Epithelial Ovarian Cancer. *J Natl Cancer Institute* (2014) 106(7):dju149. doi: 10.1093/jnci/dju149

44. Akhter MZ, Sharawat SK, Kumar V, Kochat V, Equbal Z, Ramakrishnan M, et al. Aggressive Serous Epithelial Ovarian Cancer Is Potentially Propagated by EpCAM(+)CD45(+) Phenotype. *Oncogene* (2018) 37(16):2089–103. doi: 10.1038/s41388-017-0106-y

45. Elsnerova K, Mohelnikova-Duchonova B, Cerovska E, Ehrlichova M, Gut I, Rob L, et al. Gene Expression of Membrane Transporters: Importance for Prognosis and Progression of Ovarian Carcinoma. *Oncol Rep* (2016) 35 (4):2159–70. doi: 10.3892/or.2016.4599

46. Rough JJ, Monroy MA, Yerrum S, Daly JM. Anti-Proliferative Effect of LXR Agonist T0901317 in Ovarian Carcinoma Cells. *J Ovarian Res* (2010) 3:13. doi: 10.1186/1757-2215-3-13

47. Liscum L, Finer-Moore J, Stroud RM, Luskey KL, Brown MS, Goldstein JL. Domain Structure of 3-Hydroxy-3-Methylglutaryl Coenzyme A Reductase, a Glycoprotein of the Endoplasmic Reticulum. *J Biol Chem* (1985) 260(1):522–30. doi: 10.1016/S0021-9258(18)89764-2

48. Gruenbacher G, Thurnher M. Mevalonate Metabolism in Cancer. *Cancer Lett* (2015) 356(2 Pt A):192–6. doi: 10.1016/j.canlet.2014.01.013

49. Wang M, Casey PJ. Protein Prenylation: Unique Fats Make Their Mark on Biology. *Nat Rev Mol Cell Biol* (2016) 17(2):110–22. doi: 10.1038/nrm.2015.11

50. Chushi L, Wei W, Kangkang X, Yongzeng F, Ning X, Xiaolei C. HMGCR is Up-Regulated in Gastric Cancer and Promotes the Growth and Migration of the Cancer Cells. *Gene* (2016) 587(1):42–7. doi: 10.1016/j.gene.2016.04.029

51. Dong L, Xue L, Zhang C, Li H, Cai Z, Guo R. HSP90 Interacts With HMGCR and Promotes the Progression of Hepatocellular Carcinoma. *Mol Med Rep* (2019) 19(1):524–32. doi: 10.3892/mmr.2018.9667

52. Clendening JW, Pandyra A, Boutros PC, El Ghamrasni S, Khosravi F, Trentin GA, et al. Dysregulation of the Mevalonate Pathway Promotes Transformation. *Proc Natl Acad Sci USA* (2010) 107(34):15051–6. doi: 10.1073/pnas.0910258107

53. Göbel A, Breining D, Rauner M, Hofbauer LC, Rachner TD. Induction of 3-Hydroxy-3-Methylglutaryl-CoA Reductase Mediates Statin Resistance in Breast Cancer Cells. *Cell Death Dis* (2019) 10(2):91. doi: 10.1038/s41419-019-1322-x

54. de Wolf E, Abdullah MI, Jones SM, Menezes K, Moss DM, Drijfhout FP, et al. Dietary Geranylgeraniol can Limit the Activity of Pitavastatin as a Potential Treatment for Drug-Resistant Ovarian Cancer. *Sci Rep* (2017) 7 (1):5410. doi: 10.1038/s41598-017-05595-4

55. Brennan DJ, Brändstedt J, Rexhepaj E, Foley M, Pontén F, Uhlén M, et al. Tumour-Specific HMG-CoAR Is an Independent Predictor of Recurrence Free Survival in Epithelial Ovarian Cancer. *BMC Cancer* (2010) 10:125. doi: 10.1186/1471-2407-10-125

56. Kato S, Liberona MF, Cerda-Infante J, Sánchez M, Henríquez J, Bizama C, et al. Simvastatin Interferes With Cancer 'Stem-Cell' Plasticity Reducing Metastasis in Ovarian Cancer. *Endocrine-Related Cancer* (2018) 25(10):821–36. doi: 10.1530/ERC-18-0132

57. Jones HM, Fang Z, Sun W, Clark LH, Stine JE, Tran AQ, et al. Atorvastatin Exhibits Anti-Tumorigenic and Anti-Metastatic Effects in Ovarian Cancer *In Vitro*. *Am J Cancer Res* (2017) 7(12):2478–90.

58. Tansey TR, Shechter I. Squalene Synthase: Structure and Regulation. *Prog Nucleic Acid Res Mol Biol* (2001) 65:157–95. doi: 10.1016/S0079-6603(00)65005-5

59. Ha NT, Lee CH. Roles of Farnesyl-Diphosphate Farnesyltransferase 1 in Tumour and Tumour Microenvironments. *Cells* (2020) 9(11):2352. doi: 10.3390/cells9112352

60. Lu J, Zhou Y, Zheng X, Chen L, Tuo X, Chen H, et al. 20(S)-Rg3 Upregulates FDFT1 *via* Reducing miR-4425 to Inhibit Ovarian Cancer Progression. *Arch Biochem Biophysics* (2020) 693:108569. doi: 10.1016/j.abb.2020.108569

61. Mahoney CE, Pirman D, Chubukov V, Sleger T, Hayes S, Fan ZP, et al. A Chemical Biology Screen Identifies a Vulnerability of Neuroendocrine Cancer Cells to SQLE Inhibition. *Nat Commun* (2019) 10(1):96. doi: 10.1038/s41467-018-07959-4

62. Gill S, Stevenson J, Kristiana I, Brown AJ. Cholesterol-Dependent Degradation of Squalene Monooxygenase, a Control Point in Cholesterol Synthesis Beyond HMG-CoA Reductase. *Cell Metab* (2011) 13(3):260–73. doi: 10.1016/j.cmet.2011.01.015

63. Brown DN, Caffa I, Cirmena G, Piras D, Garuti A, Gallo M, et al. Squalene Epoxidase is a Bona Fide Oncogene by Amplification With Clinical Relevance in Breast Cancer. *Sci Rep* (2016) 6:19435. doi: 10.1038/srep19435

64. Helms MW, Kemming D, Pospisil H, Vogt U, Buerger H, Korsching E, et al. Squalene Epoxidase, Located on Chromosome 8q24.1, is Upregulated in 8q+ Breast Cancer and Indicates Poor Clinical Outcome in Stage I and II Disease. *Br J Cancer* (2008) 99(5):774–80. doi: 10.1038/sj.bjc.6604556

65. Liu D, Wong CC, Fu L, Chen H, Zhao L, Li C, et al. Squalene Epoxidase Drives NAFLD-Induced Hepatocellular Carcinoma and Is a Pharmaceutical Target. *Sci Trans Med* (2018) 10(437):eaap9840. doi: 10.1126/scitranslmed.aap9840

66. Sui Z, Zhou J, Cheng Z, Lu P. Squalene Epoxidase (SQLE) Promotes the Growth and Migration of the Hepatocellular Carcinoma Cells. *Tumour Biol: J Int Soc Oncodevelopmental Biol Med* (2015) 36(8):6173–9. doi: 10.1007/s13277-015-3301-x

67. Ge H, Zhao Y, Shi X, Tan Z, Chi X, He M, et al. Squalene Epoxidase Promotes the Proliferation and Metastasis of Lung Squamous Cell Carcinoma Cells Though Extracellular Signal-Regulated Kinase Signaling. *Thorac Cancer* (2019) 10(3):428–36. doi: 10.1111/1759-7714.12944

68. Brown MS, Radhakrishnan A, Goldstein JL. Retrospective on Cholesterol Homeostasis: The Central Role of Scap. *Annu Rev Biochem* (2018) 87:783–807. doi: 10.1146/annurev-biochem-062917-011852

69. Karashchuk G, Brodsky AS. Abstract A58: Transcription Factor SREBP2 Mediates Ovarian Cancer Drug Resistance and Recurrence. *Clinical Cancer Res* (2018) 24(15 Supplement):A58–A. doi: 10.1158/1557-3265.OVCA17-A58

70. Karashchuk G, Karashchuk N, Caksa S, Smith TS, Brodsky AS. Abstract 4409: Cholesterol Pathway Determines Ovarian Cancer Drug Resistance Through Transcription Factor SREBP2. *Cancer Res* (2017) 77(13 Supplement):4409–. doi: 10.1158/1538-7445.AM2017-4409

71. Düvel K, Yecies JL, Menon S, Raman P, Lipovsky AI, Souza AL, et al. Activation of a Metabolic Gene Regulatory Network Downstream of mTOR Complex 1. *Mol Cell* (2010) 39(2):171–83. doi: 10.1016/j.molcel.2010.06.022

72. Jeon H, Blacklow SC. Structure and Physiologic Function of the Low-Density Lipoprotein Receptor. *Annu Rev Biochem* (2005) 74:535–62. doi: 10.1146/annurev.biochem.74.082803.133354

73. Chang TY, Li BL, Chang CC, Urano Y. Acyl-Coenzyme A:cholesterol Acyltransferases. *Am J Physiol Endocrinol Metab* (2009) 297(1):E1–9. doi: 10.1152/ajpendo.90926.2008

74. Geng F, Cheng X, Wu X, Yoo JY, Cheng C, Guo JY, et al. Inhibition of SOAT1 Suppresses Glioblastoma Growth *via* Blocking SREBP-1-Mediated Lipogenesis. *Clin Cancer Res* (2016) 22(21):5337–48. doi: 10.1158/1078-0432.CCR-15-2973

75. Jiang Y, Sun A, Zhao Y, Ying W, Sun H, Yang X, et al. Proteomics Identifies New Therapeutic Targets of Early-Stage Hepatocellular Carcinoma. *Nature* (2019) 567(7747):257–61. doi: 10.1038/s41586-019-0987-8

76. Oni TE, Biffi G, Baker LA, Hao Y, Tonelli C, Somerville TDD, et al. SOAT1 Promotes Mevalonate Pathway Dependency in Pancreatic Cancer. *J Exp Med* (2020) 217(9):e20192389. doi: 10.1084/jem.20192389

77. Lee HJ, Li J, Vickman RE, Li J, Liu R, Durkes AC, et al. Cholesterol Esterification Inhibition Suppresses Prostate Cancer Metastasis by Impairing the Wnt/β-Catenin Pathway. *Mol Cancer Res* (2018) 16(6):974–85. doi: 10.1158/1541-7786.MCR-17-0665

78. Yang W, Bai Y, Xiong Y, Zhang J, Chen S, Zheng X, et al. Potentiating the Antitumour Response of CD8(+) T Cells by Modulating Cholesterol Metabolism. *Nature* (2016) 531(7596):651–5. doi: 10.1038/nature17412

79. Zhao L, Liu Y, Zhao F, Jin Y, Feng J, Geng R, et al. Inhibition of Cholesterol Esterification Enzyme Enhances the Potency of Human Chimeric Antigen Receptor T Cells Against Pancreatic Carcinoma. *Mol Ther Oncolytics* (2020) 16:262–71. doi: 10.1016/j.omto.2020.01.008

80. Rosenson RS, Brewer HBJr., Davidson WS, Fayad ZA, Fuster V, Goldstein J, et al. Cholesterol Efflux and Atheroprotection: Advancing the Concept of Reverse Cholesterol Transport. *Circulation* (2012) 125(15):1905–19. doi: 10.1161/CIRCULATIONAHA.111.066589

81. Graf GA, Yu L, Li WP, Gerard R, Tuma PL, Cohen JC, et al. ABCG5 and ABCG8 are Obligate Heterodimers for Protein Trafficking and Biliary Cholesterol Excretion. *J Biol Chem* (2003) 278(48):48275–82. doi: 10.1074/jbc.M310223200

82. Chou J-L, Chen L-Y, Su H-Y, Lin S-J, Huang Y-W, Deatherage DE, et al. Abstract 83: Hypomethylation of TGF-Beta Target Gene, ABCA1 in Ovarian Cancer and Cancer Initialing Cell and Is Associated With Poor Prognosis in Cancer Patients. *Cancer Res* (2011) 71(8 Supplement):83–. doi: 10.1158/1538-7445.AM2011-83

83. Chou JL, Huang RL, Shay J, Chen LY, Lin SJ, Yan PS, et al. Hypermethylation of the TGF-β Target, ABCA1 Is Associated With Poor Prognosis in Ovarian Cancer Patients. *Clin Epigenet* (2015) 7(1):1. doi: 10.1186/s13148-014-0036-2

84. Mohelnikova-Duchonova B, Brynychova V, Oliverius M, Honsova E, Kala Z, Muckova K, et al. Differences in Transcript Levels of ABC Transporters Between Pancreatic Adenocarcinoma and Nonneoplastic Tissues. *Pancreas* (2013) 42(4):707–16. doi: 10.1097/MPA.0b013e318279b861

85. Hlaváč V, Brynychová V, Václavíková R, Ehrlichová M, Vrána D, Pecha V, et al. The Expression Profile of ATP-Binding Cassette Transporter Genes in Breast Carcinoma. *Pharmacogenomics* (2013) 14(5):515–29. doi: 10.2217/pgs.13.26

86. Namba Y, Sogawa C, Okusha Y, Kawai H, Itagaki M, Ono K, et al. Depletion of Lipid Efflux Pump ABCG1 Triggers the Intracellular Accumulation of Extracellular Vesicles and Reduces Aggregation and Tumorigenesis of Metastatic Cancer Cells. *Front Oncol* (2018) 8:376. doi: 10.3389/fonc.2018.00376

87. Tian C, Huang D, Yu Y, Zhang J, Fang Q, Xie C. ABCG1 as a Potential Oncogene in Lung Cancer. *Exp Ther Med* (2017) 13(6):3189–94. doi: 10.3892/etm.2017.4393

88. Sag D, Cekic C, Wu R, Linden J, Hedrick CC. The Cholesterol Transporter ABCG1 Links Cholesterol Homeostasis and Tumour Immunity. *Nat Commun* (2015) 6(1):6354. doi: 10.1038/ncomms7354

89. Armstrong AJ, Gebre AK, Parks JS, Hedrick CC. ATP-Binding Cassette Transporter G1 Negatively Regulates Thymocyte and Peripheral Lymphocyte Proliferation. *J Immunol (Baltimore Md: 1950)* (2010) 184 (1):173–83. doi: 10.4049/jimmunol.0902372

90. Willy PJ, Umesono K, Ong ES, Evans RM, Heyman RA, Mangelsdorf DJ. LXR, a Nuclear Receptor That Defines a Distinct Retinoid Response Pathway. *Genes Dev* (1995) 9(9):1033–45. doi: 10.1101/gad.9.9.1033

91. Bilotta MT, Petillo S, Santoni A, Cippitelli M. Liver X Receptors: Regulators of Cholesterol Metabolism, Inflammation, Autoimmunity, and Cancer. *Front Immunol* (2020) 11:584303. doi: 10.3389/fimmu.2020.584303

92. Guo D, Reinitz F, Youssef M, Hong C, Nathanson D, Akhavan D, et al. An LXR Agonist Promotes Glioblastoma Cell Death Through Inhibition of an EGFR/AKT/SREBP-1/LDLR-Dependent Pathway. *Cancer Discov* (2011) 1 (5):442–56. doi: 10.1158/2159-8290.CD-11-0102

93. Shahzad MM, Mangala LS, Han HD, Lu C, Bottsford-Miller J, Nishimura M, et al. Targeted Delivery of Small Interfering RNA Using Reconstituted High-Density Lipoprotein Nanoparticles. *Neoplasia (New York NY)* (2011) 13 (4):309–19. doi: 10.1593/neo.101372

94. Yuan B, Wu C, Wang X, Wang D, Liu H, Guo L, et al. High Scavenger Receptor Class B Type I Expression is Related to Tumor Aggressiveness and Poor Prognosis in Breast Cancer. *Tumour Biol: J Int Soc Oncodevelopmental Biol Med* (2016) 37(3):3581–8. doi: 10.1007/s13277-015-4141-4

95. Feng H, Wang M, Wu C, Yu J, Wang D, Ma J, et al. High Scavenger Receptor Class B Type I Expression Is Related to Tumor Aggressiveness and Poor Prognosis in Lung Adenocarcinoma: A STROBE Compliant Article. *Medicine* (2018) 97(13):e0203. doi: 10.1097/MD.0000000000010203

96. Kinslechner K, Schörghofer D, Schütz B, Vallianou M, Wingelhofer B, Mikulits W, et al. Malignant Phenotypes in Metastatic Melanoma Are Governed by SR-BI and Its Association With Glycosylation and STAT5 Activation. *Mol Cancer Res* (2018) 16(1):135–46. doi: 10.1158/1541-7786.MCR-17-0292

97. Penet MF, Krishnamachary B, Wildes FB, Mironchik Y, Hung CF, Wu TC, et al. Ascites Volumes and the Ovarian Cancer Microenvironment. *Front Oncol* (2018) 8:595. doi: 10.3389/fonc.2018.00595

98. Helzlsouer KJ, Alberg AJ, Norkus EP, Morris JS, Hoffman SC, Comstock GW. Prospective Study of Serum Micronutrients and Ovarian Cancer. *J Natl Cancer Institute* (1996) 88(1):32–7. doi: 10.1093/jnci/88.1.32

99. Li AJ, Elmore RG, Chen IY, Karlan BY. Serum Low-Density Lipoprotein Levels Correlate With Survival in Advanced Stage Epithelial Ovarian Cancers. *Gynecologic Oncol* (2010) 116(1):78–81. doi: 10.1016/j.ygyno.2009.09.027

100. Kim S, Lee M, Dhanasekaran DN, Song YS. Activation of Lxrα/β by Cholesterol in Malignant Ascites Promotes Chemoresistance in Ovarian Cancer. *BMC Cancer* (2018) 18(1):1232. doi: 10.1186/s12885-018-5152-5

101. Montero J, Morales A, Llacuna L, Lluis JM, Terrones O, Basañez G, et al. Mitochondrial Cholesterol Contributes to Chemotherapy Resistance in Hepatocellular Carcinoma. *Cancer Res* (2008) 68(13):5246–56. doi: 10.1158/0008-5472.CAN-07-6161

102. Ghanbari F, Fortier A-M, Park M, Philip A. Cholesterol-Induced Metabolic Reprogramming in Breast Cancer Cells Is Mediated *via* the Errα Pathway. *Cancers (Basel)* (2021) 13(11):2605. doi: 10.3390/cancers13112605

103. Campbell AM, Chan SHP. Mitochondrial Membrane Cholesterol, the Voltage Dependent Anion Channel (VDAC), and the Warburg Effect. *J Bioenergetics Biomembranes* (2008) 40(3):193–7. doi: 10.1007/s10863-008-9138-x

104. Ma X, Bi E, Lu Y, Su P, Huang C, Liu L, et al. Cholesterol Induces CD8(+) T Cell Exhaustion in the Tumor Microenvironment. *Cell Metab* (2019) 30(1):143–56.e5. doi: 10.1016/j.cmet.2019.04.002

105. Kloudova A, Guengerich FP, Soucek P. The Role of Oxysterols in Human Cancer. *Trends Endocrinol Metabol: TEM* (2017) 28(7):485–96. doi: 10.1016/j.tem.2017.03.002

106. van Reyk DM, Brown AJ, Hult'en LM, Dean RT, Jessup W. Oxysterols in Biological Systems: Sources, Metabolism and Pathophysiological Relevance. *Redox Report: Commun Free Radical Res* (2006) 11(6):255–62. doi: 10.1179/135100006X155003

107. Villablanca EJ, Raccosta L, Zhou D, Fontana R, Maggioni D, Negro A, et al. Tumor-Mediated Liver X Receptor-Alpha Activation Inhibits CC Chemokine Receptor-7 Expression on Dendritic Cells and Dampens Antitumor Responses. *Nat Med* (2010) 16(1):98–105. doi: 10.1038/nm.2074

108. Bensinger SJ, Bradley MN, Joseph SB, Zelcer N, Janssen EM, Hausner MA, et al. LXR Signaling Couples Sterol Metabolism to Proliferation in the Acquired Immune Response. *Cell* (2008) 134(1):97–111. doi: 10.1016/j.cell.2008.04.052

109. Tavazoie MF, Pollack I, Tanqueco R, Ostendorf BN, Reis BS, Gonsalves FC, et al. LXR/ApoE Activation Restricts Innate Immune Suppression in Cancer. *Cell* (2018) 172(4):825–40.e18. doi: 10.1016/j.cell.2017.12.026

110. Lappano R, Recchia AG, De Francesco EM, Angelone T, Cerra MC, Picard D, et al. The Cholesterol Metabolite 25-Hydroxycholesterol Activates Estrogen Receptor α-Mediated Signaling in Cancer Cells and in Cardiomyocytes. *PloS One* (2011) 6(1):e16631. doi: 10.1371/journal.pone.0016631

111. Casella C, Miller DH, Lynch K, Brodsky AS. Oxysterols Synergize With Statins by Inhibiting SREBP-2 in Ovarian Cancer Cells. *Gynecologic Oncol* (2014) 135(2):333–41. doi: 10.1016/j.ygyno.2014.08.015

112. Istvan ES, Deisenhofer J. Structural Mechanism for Statin Inhibition of HMG-CoA Reductase. *Sci (New York NY)* (2001) 292(5519):1160–4. doi: 10.1126/science.1059344

113. Liu H, Liang SL, Kumar S, Weyman CM, Liu W, Zhou A. Statins Induce Apoptosis in Ovarian Cancer Cells Through Activation of JNK and Enhancement of Bim Expression. *Cancer Chemother Pharmacol* (2009) 63(6):997–1005. doi: 10.1007/s00280-008-0830-7

114. Curtarello M, Tognon M, Venturoli C, Silic-Benussi M, Grassi A, Verza M, et al. Rewiring of Lipid Metabolism and Storage in Ovarian Cancer Cells After Anti-VEGF Therapy. *Cells* (2019) 8(12):1601. doi: 10.3390/cells8121601

115. Göbel A, Zinna VM, Dell'Endice S, Jaschke N, Kuhlmann JD, Wimberger P, et al. Anti-Tumor Effects of Mevalonate Pathway Inhibition in Ovarian Cancer. *BMC Cancer* (2020) 20(1):703. doi: 10.1186/s12885-020-07164-x

116. Xia Y, Xie Y, Yu Z, Xiao H, Jiang G, Zhou X, et al. The Mevalonate Pathway Is a Druggable Target for Vaccine Adjuvant Discovery. *Cell* (2018) 175(4):1059–73.e21. doi: 10.1016/j.cell.2018.08.070

117. Akinwunmi B, Vitonis AF, Titus L, Terry KL, Cramer DW. Statin Therapy and Association With Ovarian Cancer Risk in the New England Case Control (NEC) Study. *Int J Cancer* (2019) 144(5):991–1000. doi: 10.1002/ijc.31758

118. Chen X, Song Q, Xia L, Xu X. Synergy of Dendritic Cell Vaccines and Avasimibe in Treatment of Head and Neck Cancer in Mice. *Med Sci Monitor: Int Med J Exp Clin Res* (2017) 23:4471–6. doi: 10.12659/MSM.905814

119. Pan J, Zhang Q, Palen K, Wang L, Qiao L, Johnson B, et al. Potentiation of Kras Peptide Cancer Vaccine by Avasimibe, a Cholesterol Modulator. *EBioMedicine* (2019) 49:72–81. doi: 10.1016/j.ebiom.2019.10.044

120. Pal P, Gandhi H, Giridhar R, Yadav MR. ACAT Inhibitors: The Search for Novel Cholesterol Lowering Agents. *Mini Rev Med Chem* (2013) 13(8):1195–219. doi: 10.2174/1389557511313080007

121. Komati R, Spadoni D, Zheng S, Sridhar J, Riley KE, Wang G. Ligands of Therapeutic Utility for the Liver X Receptors. *Mol (Basel Switzerland)* (2017) 22(1):88. doi: 10.3390/molecules22010088

Intracellular Water Lifetime as a Tumor Biomarker to Monitor Doxorubicin Treatment *via* FFC-Relaxometry in a Breast Cancer Model

Maria Rosaria Ruggiero[1], Simona Baroni[1], Valeria Bitonto[1], Roberto Ruiu[1], Smeralda Rapisarda[1], Silvio Aime[2] and Simonetta Geninatti Crich[1]*

[1] Department of Molecular Biotechnology and Health Sciences, University of Turin, Turin, Italy, [2] IRCCS SDN, Naples, Italy

This study aims to explore whether the water exchange rate constants in tumor cells can act as a hallmark of pathology status and a reporter of therapeutic outcomes. It has been shown, using 4T1 cell cultures and murine allografts, that an early assessment of the therapeutic effect of doxorubicin can be detected through changes in the cellular water efflux rate constant k_{io}. The latter has been estimated by analyzing the magnetization recovery curve in standard NMR T_1 measurements when there is a marked difference in the proton relaxation rate constants (R_1) between the intra- and the extra-cellular compartments. In cellular studies, T_1 measurements were carried out on a relaxometer working at 0.5 T, and the required difference in R_1 between the two compartments was achieved *via* the addition of a paramagnetic agent into the extracellular compartment. For *in-vivo* experiments, the large difference in the R_1 values of the two-compartments was achieved when the T_1 measurements were carried out at low magnetic field strengths. This task was accomplished using a Fast Field Cycling (FFC) relaxometer that was properly modified to host a mouse in its probe head. The decrease in k_{io} upon the administration of doxorubicin is the result of the decreased activity of Na^+/K^+-ATPase, as shown in an independent test on the cellular uptake of Rb ions. The results reported herein suggest that k_{io} can be considered a non-invasive, early and predictive biomarker for the identification of responsive patients immediately from the first doxorubicin treatment.

Keywords: NMR relaxometry, theranostics, doxorubicin, magnetic resonance imaging, cellular water efflux rate constant

INTRODUCTION

Diagnostic imaging tools play a key role in the characterization of complex, heterogeneous and multifactorial diseases such as cancer. They are often crucial for the selection of the most suitable therapy and for the evaluation of its outcome, i.e. to increase the chance of success and reduce the side effects (1). The currently available pharmacological options in the field of breast cancer, which

is the most common cancer in women, are under intense scrutiny to find means to obtain an early evaluation as to their efficacy. The World Health Organization (WHO) criteria and Response Evaluation Criteria in Solid Tumors (RECIST) are based on the assessment of tumor size in morphological images by Computer Tomography (CT) and Magnetic Resonance Imaging (MRI) (2, 3). However, volume changes are quite late events and their use in the evaluation of the undertaken therapy may be an issue when dealing with a disease for which time is a very important parameter. Therefore, there is a continuous search for methods that can report the early effects of therapy, in particular those that use biomarkers to report changes in tumor metabolic activity. Currently, metabolic assessments that are based on the use of positron emission tomography (PET) tracers are widely used as they reflect the viability of cancer cells and other functional changes in the response to anticancer treatments (4, 5). Moreover, the availability of advanced functional magnetic resonance imaging (fMRI) techniques has furnished new possibilities in the monitoring of therapeutic responses (6). There is a growing consensus that MRI protocols may provide powerful diagnostic tools in the field of oncology (7). Their diagnostic power arises primarily from disease-induced changes in the nuclear magnetic resonance (NMR) relaxation times of tissue, especially in the spin-lattice relaxation time T_1 (8, 9). However, these changes cannot be fully exploited at the magnetic field strengths of currently available MRI scanners, as changes in tissue T_1 do not appear to be sensitive enough at these field strengths to report on the response of the tumor cells to therapy. On the other hand, our group has recently demonstrated that measuring T_1 at lower magnetic field strengths can be very informative and report on the tumor metabolic status (10, 11). This is possible because tissue T_1 varies with applied magnetic field strength, with the differences between tissues being higher at lower magnetic field strengths (12–15). This behavior (often referred to as "T_1-dispersion", or simply relaxometry) is a marker of disease, but is invisible to conventional, fixed-field MRI scanners. Fast Field-Cycling (FFC)-NMR is the only practicable technique for measuring T_1-dispersion. It involves switching the magnetic field between different field strengths (from 0.2 to 200 mT, typically) during the measurement procedure (16). The proton relaxation rate constants ($R_1 = 1/T_1$) of tissues are dependent on the extra/intracellular water ratio and the water exchange rate between the two compartments (10). Both terms are affected by tumor-cell metabolism. The relative amount of water in the two compartments and their exchange across cellular membranes are significantly different in healthy and tumor tissues. Recent studies have shown that the osmosis- and metabolism-driven movement of free water molecules across membranes, which affect cell volume and shape, may be an intrinsic and extremely sensitive reporter of pathology and its energetic deregulation (17–20).

In our previous work (10, 11), we demonstrated that observing R_1 at low magnetic fields can clearly discriminate between healthy and tumor tissues as well as between different types of adenocarcinoma breast cancer. The differences in the observed relaxometric behavior can be accounted for in terms of

the cellular water efflux rate constant, k_{io}, that can be obtained from fitting the Magnetization decay acquired on the FFC-NMR relaxometer. This observation reports on the particular characteristics of the given tumor cell type. A smaller k_{io} indicates a slower water exchange rate across the transcytolemmal membrane, and this has been shown to be related to the overexpression/upregulation of the GLUT1 and Na^+/K^+-ATPase transporters.

On this basis, FFC-NMR is expected to provide relevant information about the metabolic mechanisms involved in disease progression and response to treatment. We hypothesize that k_{io} may be used as an early predictive biomarker of response to treatment. In this study, we have performed in-vitro and in-vivo experiments to evaluate how changes in k_{io} are related to treatment with doxorubicin, an anthracycline drug, that is routinely used in the treatment of several cancers including breast, lung, gastric, ovarian, thyroid, non-Hodgkin's and Hodgkin's lymphoma, multiple myeloma, sarcoma and pediatric cancers (21).

MATERIAL AND METHODS

Cell Cultures

The 4T1 (ATCC® CRL-2539™) cell line, initially derived from spontaneous breast tumor growth in a BALB/c, was purchased from American Type Culture Collection (ATCC, USA). 4T1-R was derived from 4T1 (ATCC® CRL-2539™). They were grown in RPMI 1640 medium supplemented with 10% fetal bovine serum (FBS), 100 U/mL Penicillin with 100 µg/ml Streptomycin, and 4 mM glutamine. Cells were cultured in 5% CO_2/95% air at 37°C in a humidified chamber and were split every 2 to 3 days. All cells tested negative for mycoplasma using the MycoAlert™ Mycoplasma Detection Kit. All materials were purchased from Lonza (Basel, Switzerland).

Drug-Resistant Cell Line (4T1-R)

4T1-R was derived from 4T1 (ATCC® CRL-2539™), which was treated for six months with an increased concentration of doxorubicin (Sigma Aldrich) (from 50 nM to 5 µM) (22–24). At the confluence of 80%, the cells were seeded for the next treatment cycle with a higher concentration of the drug. The acquisition of drug resistance was evaluated using an MTT assay, based on the reduction of tetrazolium salts to formazan by mitochondrial succinate dehydrogenase, and quantified spectrophotometrically. The cells were seeded in 96 multi-well plates at a density of 10000 cells/well. After 24 h, doxorubicin (Sigma Aldrich) (1 to 50 µM)) was added to the cell suspensions, which were then incubated for a further 24 h at 37°C and 5% CO_2. The medium was then removed and 100 µl of Thiazolyl Blue Tetrazolium Bromide (Sigma Aldrich) was added at a concentration of 0.45 mg/ml into each well and the plate was incubated for 4 h at 37°C and 5% CO_2. After the removal of the suspension medium, 150 µl of dimethyl sulfoxide (DMSO) was added to each well to solubilize the formazan salt crystals that

were produced by the metabolism of the live cells. After 30 minutes, the absorbance was read at 570 nm using an iMark microplate reader (Biorad). Cell vitality was reported as the percentage of dead cells relative to the control. The experiment was performed in quadruplicate and the data were graphically presented as mean ± SD.

Western Blot

Frozen cells, that had not previously been treated with trypsin for detachment, were incubated in RIPA lysis buffer (150 mM NaCl; 50 mM Tris-HCl, pH 8.0; sodium dodecyl sulphate (SDS) 0,1%; sodium deoxycholate 0,5%; Nonidet P-40 1%) supplemented with 1 mM PMSF, 1 mM NaVO$_4$, 1 mM NaF and protease-inhibitor cocktail (Sigma-Aldrich) for 40 min on ice. Cell lysates were centrifuged for 10 min at 14.000 g and the supernatant was harvested for quantification. The total protein concentration was quantified using the Pierce[TM] BCA Protein Assay Kit (Thermo-Fisher Scientific). After 30 min incubation at room temperature (when not otherwise specified) in β-mercaptoethanol-containing Laemmli Sample Buffer (Bio-Rad), equal amounts of protein lysates (ranging between 30 and 70 μg) were separated *via* electrophoresis in a 4-15% Mini-Protean TGX precast gel (Bio-Rad) and then transferred onto an Immobilion-P PVDF membrane (0.45 μm pore size, Merck Millipore). After blocking with either 5% non-fat dry milk (Santa Cruz Biotechnology) or 5% BSA (Sigma-Aldrich) in wash buffer (Tris Buffered Saline supplemented with 0.1% Tween-20 - T-TBS - from Sigma-Aldrich), the membranes were incubated overnight at 4°C with either rabbit anti-MDR1 (Cat#sc-9313, clone H-241 Santa Cruz Biotechnology, 1:250 in PBS, 1% BSA) or mouse anti-β-actin (Cat#sc-69879, Clone AC-15, Santa Cruz Biotechnology, 1:200 in T-TBS, 5% Milk) antibodies in blocking buffer. The membranes were then rinsed 3 times in T-TBS and incubated for 1 hour at room temperature with either HRP-conjugated anti-rabbit (Cat#A0545, Sigma-Aldrich, 1:2000 in T-TBS, 5% Milk) or anti-mouse (Cat#A4416, Sigma-Aldrich, 1:2000 in T-TBS, 5% Milk). β-actin was used as the loading control. The membranes were incubated with Pierce[®] ECL Western Blotting Substrate (Thermo-Fisher Scientific) and images were acquired using a ChemiDoc[TM] Touch Imaging System (Bio-Rad).

In-Vitro Determination of Cellular Membrane Water Exchange Rate Constants by a Relaxometric Procedure After Doxorubicin Treatment

The determination of cellular membrane water exchange rate constants was performed following the protocol described by Ruggiero et al. (10, 11). 4T1 and 4T1-R were seeded in a 175 cm^2 flask at a density of 6 million cells/flask. After 24 h, cells were incubated with 0, 0.1, 0.5, 1, 5 μM of doxorubicin for a further 24 h (25, 26). The cells were detached using 0.05% trypsin and 0.02% EDTA, washed once with Phosphate Buffer Saline (PBS) and re-suspended in the presence of 10 mM Gd-HPDO3A (Prohance, kindly provided by Bracco S.p.A. (Milan, Italy)) in PBS. The relaxometric measurements were carried out within 15 min, during which cells were transferred to 5 mm NMR tubes and centrifuged for 5 minutes at 0.1 rcf (4°C). The water proton T$_1$ values of the cellular pellets were measured at 0.5 T and 25°C on a Stelar SPINMASTER spectrometer (Stelar, Mede, Italy) using the inversion-recovery (IR) pulse sequence with 64 τ increments. The apparently biexponential recovery of the magnetization was observed. The water exchange rate constants (efflux, k$_{io}$ and influx, k$_{oi}$) across the cell membrane were determined by analyzing the IR data using the 2SX model (17, 18).

Determination of Rb Uptake

Seven thousand and fifty cells were plated in 10 cm Ø dishes. After 24 h, they are incubated with different concentrations of doxorubicin (from 0 to 5 μM) for a further 24 h. They were then incubated for 1 h with 0.12 mM RbCl in Earle's Balanced Salt Solution (EBSS) at 37°C and 5% CO$_2$. Following four washing steps with cold PBS to remove the extracellular RbCl, the cells were harvested. A Bradford assay was used to determine the protein concentration before acidic digestion. 200 μl of the cell suspension and 200 μl of HNO$_3$ (70%) were subjected to acidic mineralization to oxidize the organic matter, solubilize all metals and simplify the matrix. The microwave (ETHOS UP Milestone, Bergamo, Italy) heating program consisted of a ramp to 150°C in 6 minutes, followed by 8 min to 150°C. After mineralization, sample volumes were brought to 3 ml with doubly deionized water. The quantification of Rb was performed *via* ICP-MS (Element-2; Thermo-Finnigan, Rodano (MI), Italy) analysis. The calibration curve was obtained using absorption standard solutions (Sigma-Aldrich) in the range 0.2–0.005 μg/mL.

Flow Cytometry

Having performed enzymatic detachment and several washings, the cells were resuspended in Annexin V binding buffer (Annexin V Apoptosis Detection Kit APC, eBioscience[TM]) and incubated in flow cytometry tubes with the Annexin V-APC reagent, according to manufacturer's instructions. After 15 min incubation at room temperature, the cells were rinsed in Annexin V binding buffer, the tubes were centrifuged and the supernatant was discarded. DAPI (1 μg/mL; Sigma Aldrich) was added to the tubes before acquisition with a flow cytometer. The fluorescence intensity and distribution of the cells were measured using a BD FACSVerse[TM] flow cytometer (BD - *Becton*, *Dickinson*, and Company) and the data were analyzed using FlowJo (LLC) software. Doxorubicin incorporation was estimated based on the mean fluorescence intensity (MFI) that resulted from doxorubicin intrinsic fluorescence (λ$_{Ex}$ 470 nm, λ$_{Em}$ 585 nm), which can be excited with a blue laser (488 nm) and detected using a PE (586/42 nm) filter. Cells that displayed negative staining for both Annexin V-APC and DAPI were considered to be live cells, those that were staining positive for Annexin V-APC, but negative for DAPI were considered early apoptotic. Those that were staining double positive were considered late apoptotic, whereas those staining positive for DAPI only were considered dead, but not apoptotic. Appropriate negative and positive controls were used.

Animal Models

8-week-old female BALB/c mice were inoculated in their hind-limb muscle with 1 million 4T1 cells suspended in 100 μl of Phosphate Buffered Saline (PBS). BALB/c mice (Charles River Laboratories Italia S.r.l., Calco Italia) were maintained under specific pathogen-free conditions in the animal facility at the Molecular Biotechnology Center, University of Turin, and treated in accordance with EU (EU2010/63) and Italian (d.lgs 26/2014) regulations. Before undergoing imaging and nuclear magnetic resonance experiments, the mice were anesthetized with a mixture of tiletamine/zolazepam (Zoletil 100; Vibac, Milan, Italy) 20 mg/kg and xylazine (Rompun; Bayer, Milan, Italy) 5 mg/kg. The animal treatment protocol was approved by the Italian Ministry of Health (authorization number 807/2017-PR). When the tumor reached volumes of around 150-200 mm^3, the animals were treated three times at 1-day intervals (days 0, 2 and 4) intravenously *via* the tail vein at a dose of 5 mg/kg of doxorubicin (26–28).

Magnetic Resonance Imaging

T$_2$-weighted images were acquired at 1 T on an Aspect M2-High Performance MRI System (Aspect Magnet Technologies Ltd., Netanya, Israel) consisting of a NdFeB magnet, equipped with a 35 mm solenoid Tx/Tr coil with an inner diameter of 35 mm. This system is equipped with fast gradient coils (gradient strength, 450 mT m^{-1} at 60 A; ramp time, 250 μs at 160 V) with a field homogeneity of 0.2–0.5 G. MR images were acquired using a Fast Spin Echo sequence (FSE) (TR 3000 ms; TE 50 ms; number of slices 11; slice thickness 1 mm; FOV 50x50 mm; matrix 168 × 160, Flip angle 90°). Tumor volume was determined using ITK-SNAP software.

In-Vivo Nuclear Magnetic Resonance Dispersion Profiles (NMRD)

In-vivo NMRD profiles were acquired on the Stelar FFC-NMR relaxometer (Stelar S.n.c., Mede (PV), Italy), which is equipped with a 40 mm 0.5 T FC magnet and a dedicated 11 mm solenoid detection coil. The relaxometer operates under complete computer control with an absolute uncertainty in the 1/T$_1$ value of ±2%. The typical field sequences used were the Non-Polarized sequence (NP/S), between 16 and 7 MHz, and the Pre-Polarized sequence (PP/S), between 7 and 0.01 MHz. The observation field was set at 14.5 MHz, while the polarization field was set at 13 MHz. Acquisition was performed using 32 τ over a long-time range (2.8-4 s) in order to sample both the rapidly and slowly relaxing magnetization components. These profiles were acquired at seven different relaxation field strengths (0.01, 0.02, 0.037, 0.07, 0.15, 0.39, 1 MHz in terms of proton Larmor frequency). During acquisition, murine temperature was maintained at 25°C using a gel pad. Data were simultaneously analyzed using Origin software (OriginPro 8.5.0 SR1, OriginLab, Northampton, MA, Levenberg-Marquardt algorithm, RRID : SCR_014212), in accordance with the 2SX model (10, 17, 18), sharing the extracellular volume fraction, V$_{ex}$, and the extracellular water life time constant, τ$_{ex}$, parameters and maintaining the extracellular relaxation rate constant, R$_{1ex}$, fixed to the Matrigel values obtained in a separated experiment (10). The V$_{ex}$ value was allowed to vary within a reliable range as reported in the literature; 0.09-0.19 for healthy mouse hind limbs, and 0.15-0.5 for tumor mouse hind limbs (18–20, 29, 30).

Tunel Assay

Immediately after the NMRD profile was acquired (3 days after the first doxorubicin treatment), the mice were sacrificed and perfused, *via* the vascular system, with a 4% paraformaldehyde solution as a fixation procedure to obtain the best possible preservation of the tumor tissue for immunohistochemistry (31). PFA-fixed and paraffin-embedded Dewaxed 5 μm tumor sections were stained with the *in-situ* Apoptosis Detection Kit (Abcam), according to manufacturer's protocol.

RESULTS AND DISCUSSION

In-Vitro Experiments on Murine Adenocarcinoma Cells (4T1)

Murine adenocarcinoma 4T1 cells were treated with doxorubicin (0.1-5 μM) for 24 h. The quantitative determination of the cellular water efflux rate constant (k$_{io}$) was carried out by following a well-established relaxometry-based method at 0.5 T in the presence of a 10 mM solution of the paramagnetic Gd-HPDO3A complex in the extracellular space of the cellular suspension (10, 32–34). The extracellular distribution of the paramagnetic agent allows a marked difference in proton relaxation rates to be achieved between the extra- and the intra-cellular compartments. It follows that the recovery of the magnetization curve after its selective inversion is characterized by an apparently bi-exponential behavior, whose fitting yields estimated values for k$_{io}$.

In **Figure 1A**, the obtained k$_{io}$ values are plotted as a function of the doxorubicin concentrations. The observed variations were statistically significant at low doses of the drug (0.1 and 0.5 μM) with P-values of 0.0000499 and 0.000215, respectively. Moreover, at the same doxorubicin concentrations, the MTT test showed that the treated cells had high vitality, which is very similar to the results found in the control experiment (**Figure 1B**). This finding is taken as a good indicator to support the view that k$_{io}$ variations could be considered to be an early predictive biomarker of treatment response.

We surmise that the observed behavior, induced by the presence of increasing doses of the drug, can be accounted for in terms of the cellular system being subjected to a variety of different effects. In the experiments at low drug concentrations, the main biologically detectable phenomenon is a decrease in k$_{io}$, which is, in principle, associated with an alteration of the membrane transport system, which is likely due to a decrease in Na$^+$/K$^+$-ATPase activity, as previously reported (10). In the case of the experiments at higher concentrations of the drug, one has to deal with extensive transformations that eventually lead to cell death. In cancer cells, doxorubicin acts *via* two principal
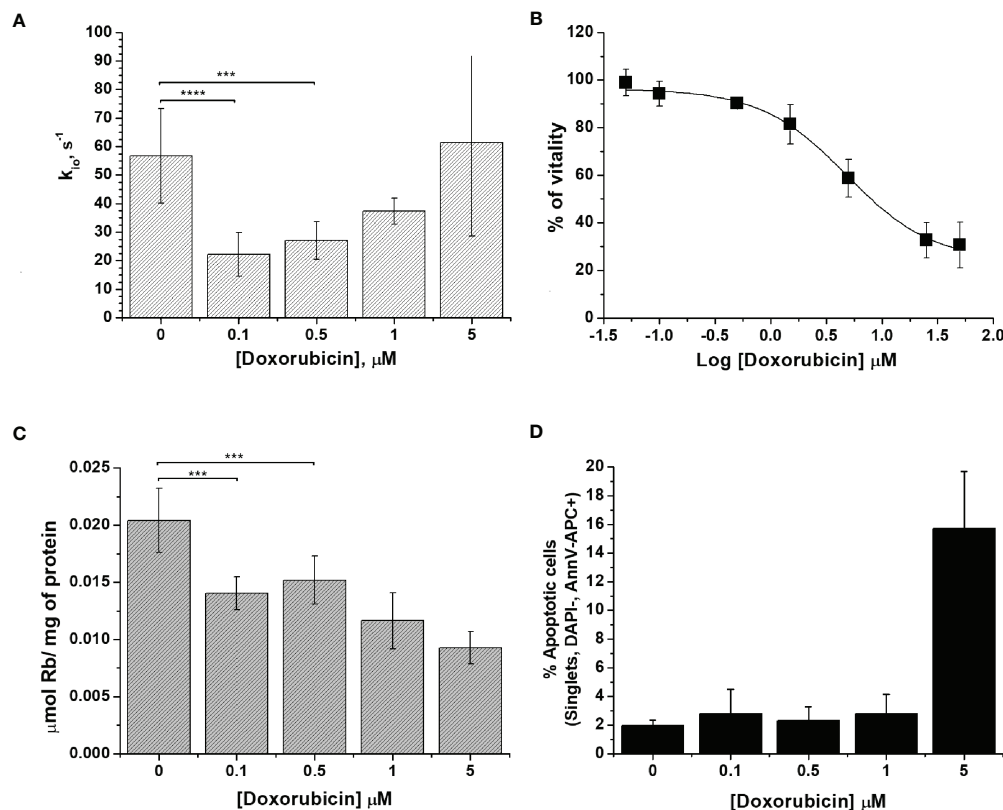
FIGURE 1 | The characterization of 4T1 cells. **(A)** The cellular water efflux rate constant, k_{io} (s^{-1}), as determined 24 h after doxorubicin treatment at different drug concentrations (0.1-5 µM). k_{io} was determined by measuring the water proton relaxation times of cell suspensions in the presence of 10 mM of Gd-HPDO3A at 25°C on a fixed frequency spectrometer operating at 0.5 T. Data are expressed as the mean ± SD with n ≥7. **(B)** Percentage of viable cells plotted vs. Log[Doxorubicin] after 24 h of treatment, obtained using the MTT test. Data are expressed as the mean ± SD of three independent experiments. **(C)** Cellular uptake of Rb (µmol of Rb/mg of protein) measured 24 h after doxorubicin treatment. The cells were suspended in a medium containing RbCl 0.12 mM for 1 h at 37°C and 5% of CO_2. Data are expressed as the mean ± SD of three independent experiments. **(D)** Determination of the % of apoptotic cells after doxorubicin treatment at different concentrations. The percentage of apoptotic cells was assessed using DAPI-, AnnV-APC+ staining with FACS analysis. Data are expressed as the mean ± SD of three independent experiments. (***p ≤ 0.001, ****p ≤ 0.0001).

mechanisms: i) intercalation into DNA and the disruption of topoisomerase-II-mediated DNA repair, with the consequent generation of free radicals, which damage lipids, DNA and proteins (21); and, ii) the inhibition of membrane-associated ion pumps, which is induced by the major metabolite of doxorubicin, doxorubicinol (21, 35–37). In principle, the two mechanisms can have opposite effects on k_{io}. The transport activity of Na^+/K^+-ATPase was assessed to provide more insight into the doxorubicin response. The method (38), relies on the ICP-MS quantification of the cellular uptake of the rubidium ion, Rb^+, which is an established congener for K^+ transport by Na^+/K^+-ATPase (38, 39). It is well established that this ICP-MS method provides great accuracy in monitoring metal-ion transporters in a wide range of cell types and conditions (40). After doxorubicin treatment, adherent cells were incubated in the presence of RbCl 0.12 mM for 1 h at 37°C and 5% of CO_2. The uptake of Rb, normalized to the amount of cell proteins, decreased significantly even in cells treated with the lowest doses of the drug (i.e. when the concentrations were 0.1 and 0.5

µM, respectively, with a P-value <0.01) (**Figure 1C**). The decrease in Rb uptake supports the view that the first effect induced in the treated cells is a reduced Na^+/K^+-ATPase efficiency, which, in turn, is responsible for the observed decrease in water exchange across the cellular membrane. For 4T1 cells, the amount of Rb per cell decreased by 30% and 54% upon changing from 0.1 to 5 µM doxorubicin treatment, respectively.

The response to doxorubicin in terms of cell deaths was assessed next. **Figure 1D** reports the percentages of apoptotic cells as a function of the applied doxorubicin concentrations. From these results, it is evident that apoptosis occurs only at higher drug concentrations, which corroborates our working hypothesis according to which k_{io} variations report early changes in cellular activity following doxorubicin treatment.

In Vitro Experiments on Doxorubicin-Resistant 4T1 Cells (4T1-R)

One of the major drawbacks of chemotherapy is drug resistance. To mimic the acquisition of drug resistance (25), the murine

mammary carcinoma 4T1 cells were treated with doxorubicin for several cycles with an increased concentration of doxorubicin (from 50 nM to 1 µM). After six months of treatment, the cells became resistant to doxorubicin as assessed by the results of the vitality test (i.e. MTT) (**Figure 2B**).

In a previous work, the acquisition of drug resistance was ascribed to the overexpression of ATP binding transporters, such as the MDR1/P-glycoprotein (Pgp, encoded by the *ABCB1* gene) (25, 41). We can confirm this notion as the western blot analysis of the MDR1/P-glycoprotein (**Figure S1**), using both cytoplasmic and nuclear extracts of 4T1 and 4T1-R cells, reported the overexpression of this glycoprotein in the resistant cell line.

The detection of doxorubicin fluorescence is a good reporter of the intracellular incorporation of the drug. **Figure S2** shows that the fluorescent response was concentration-dependent and significantly higher in 4T1 than in 4T1-R cells. Further support was gained by plotting the mean fluorescence intensity (MFI) as a function of doxorubicin concentration in the incubation medium. The results confirmed the increased doxorubicin uptake in wild type 4T1 cells compared to the resistant clone (**Figure S2**).

Subsequently, we investigated whether the administration of doxorubicin has an effect on the transport of water molecules across the membrane of 4T1-R cells (**Figure 2A**). The obtained k_{io} values showed a non-significant decrease and remained almost constant over the entire range of investigated doxorubicin concentrations. These results support the view that the k_{io} decrease in 4T1 cells observed at the low drug concentrations is due to the specific cytotoxic effect that is induced by doxorubicin, and not to an aspecific interaction between doxorubicin and the cell membrane that may potentially cause a change in cell-membrane permeability, which, most likely, would also have been present in the 4T1-R cells. The ICP-MS quantification of Rb confirmed that the transport activity of Na^+/K^+-ATPase in 4T1-R was not affected by the administration of doxorubicin. The uptake of Rb ions, normalized to the amount of cell proteins, was not significantly different in the cells treated with different concentrations (0.1 and 5 µM) of the drug, compared to control cells (**Figure 2C**).
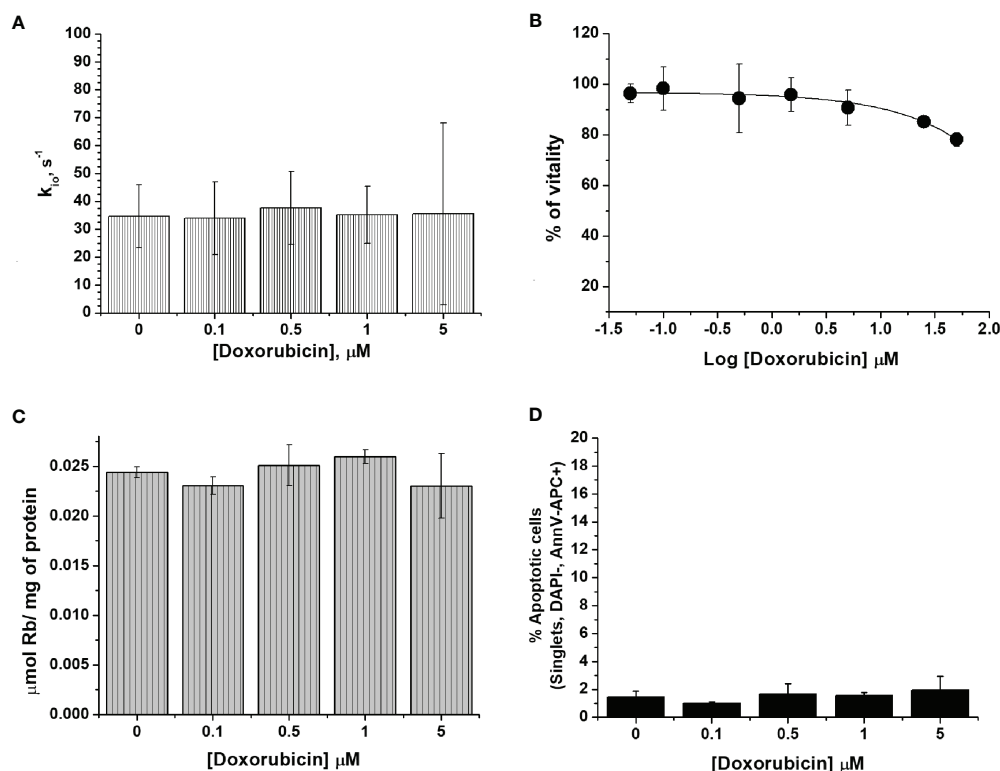

FIGURE 2 | The characterization of 4T1-R cells. **(A)** The cellular water efflux rate constant, k_{io} (s^{-1}), determined 24 h after doxorubicin treatment at different drug concentrations (0.1-5 µM). k_{io} values were determined by measuring the water proton relaxation times of cell suspensions in the presence of 10 mM of Gd-HPDO3A at 25°C on a fixed frequency spectrometer operating at 0.5 T. Data are expressed as the mean ± SD with n= 4. **(B)** Percentage of viable cells as determined using the MTT test and plotted vs Log[Doxorubicin] µM. Data are expressed as the mean ± SD of three independent experiments. **(C)** Cellular uptake of Rb (µmol of Rb/ mg of protein) measured 24 h after doxorubicin treatment. The cells were suspended in a medium containing RbCl 0.12 mM for 1 h at 37°C and 5% of CO_2. Data are expressed as the mean ± SD of three independent experiments. **(D)** Determination of the % of apoptotic cells after doxorubicin treatment at different concentrations. The percentage of apoptotic cells was assessed by DAPI-, AnnV-APC+ staining using FACS analysis. Data are expressed as the mean ± SD of three independent experiments.

The determination of the percentage of apoptotic cells by FACS analysis confirmed that the 4T1-R resistant cell line was not affected by the toxicity of the drug. (**Figure 2D**).

In-Vivo Experiments: Relaxometric Assessment of Doxorubicin Treatment in Balb/c Mice Bearing 4T1 Tumors

To verify the hypothesis that the assessment of k_{io} may be used as an early predictive biomarker of treatment response *in-vivo*, an experimental setup was designed for mammary-tumor-bearing mice (**Figure 3**). The determination of k_{io}, *via* the acquisition of the FFC-NMR profiles of the tumor region, was carried out before, during and after drug treatment.
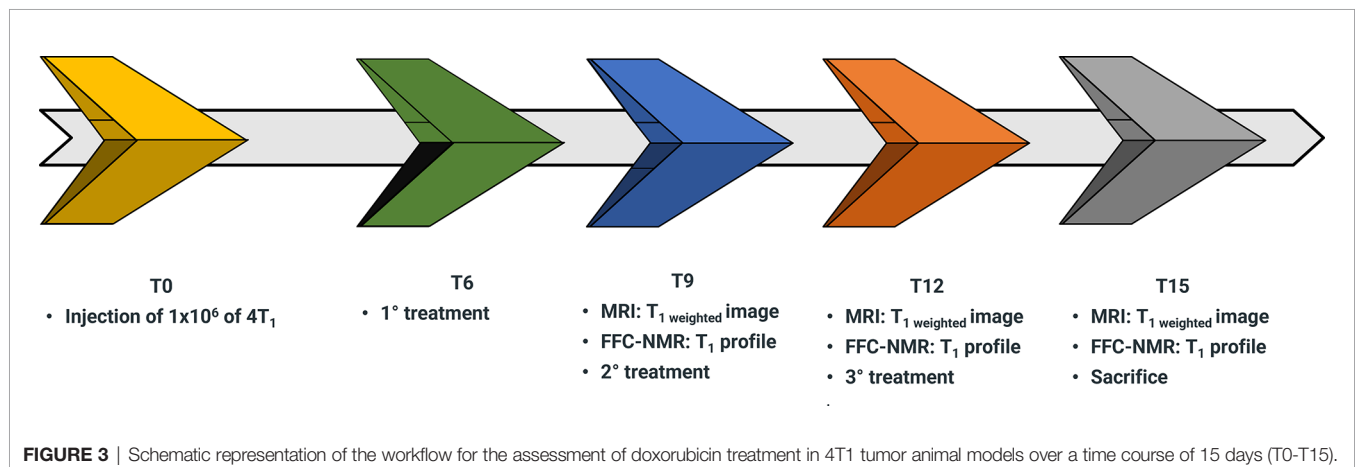
4T1 cells ($1x10^6$) were injected into the hind-limb muscle to obtain the corresponding tumor xenograft for the *in-vivo* acquisition of proton relaxation rates at low and variable magnetic fields. This was carried out using a FFC-relaxometer that was equipped with a wide bore magnet (40 mm diameter) that can host a small mouse. The position of the graft was dictated by the circular shape of the detection coil and its 11 mm diameter (10, 42). Due to the absence of spatial discrimination, the acquisitions were only carried out on mice bearing tumors with a volume > 60% of the total leg. Starting from the sixth day (T6 in the workflow sketch of **Figure 3**) from injection, mice (n= 7) were treated with 5 mg/kg of doxorubicin or with the vehicle (control mice n=7). The treatment was repeated twice more at three-day intervals. The relaxation profiles were acquired in the range 0.01-10 MHz three days after each treatment.
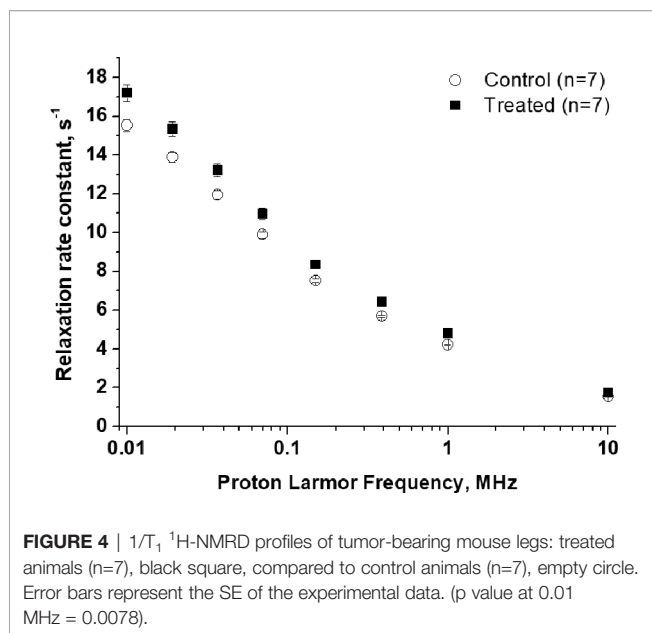
The acquisition of each $1/T_1$ ^{1}H-NMRD profile took about 20 minutes and the temperature of the mice was maintained using a gel pad heated at 37°C. **Figure 4** shows a comparison of the relaxation profiles acquired in control (untreated tumor) and doxorubicin-treated mice. Even after the first treatment, a significant increase in the relaxation rate constants was observed for the treated mice (P-value at 0.01 MHz = 0.00779). The larger R_1 values observed for the treated mice reflect the slower water exchange (corresponding to a smaller k_{io}) between the intra- and extracellular compartments, as seen in the *in-vitro* experiments reported above. Here again, treatment with

doxorubicin first resulted in a decrease of k_{io} (due to damage induced in the transporting system) that, in turn, leads to an increase in the measured R_1 values. The smaller R_1 value of the largest intra-cellular compartment dominates the observed R_1 in the presence of limited exchange between the two compartments. Interestingly, the effect of doxorubicin treatment was not detectable in T_2-weighted MR images acquired at 1 T, as the tumor volume was not significantly different in the treated animals and controls (P > 0.05) (**Figure 5A** and **Figure S3**). This observation indicates that morphological changes need longer time to be detected thus hampering an early assessment of the therapeutic outcome.
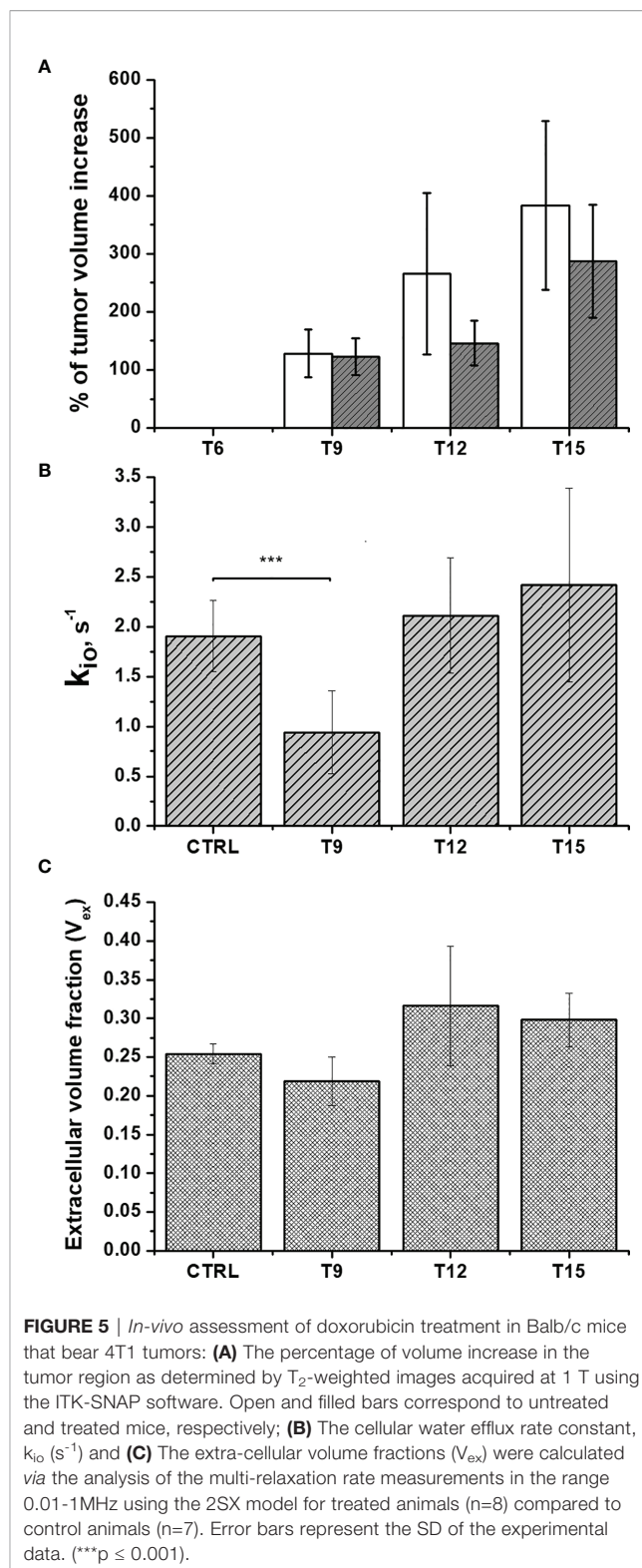
It follows that, as reported previously (10, 11, 32), the differences in relaxation rate constants, observed at low magnetic fields, are related to the occurrence of different water exchange regimes between the intra and extra-cellular compartments in the tumor tissue. During the time of an NMR experiment (or in image acquisition), water molecules explore both compartments and the observed R_1 results from a mixing of their relaxation rate constants (R_{1in} and R_{1ex}) weighted by their respective volume fractions (V_{in} and V_{ex}). Unlike with high-field measurements, the *in-vivo* acquisition of a relaxation dispersion profile between 0.01-1 MHz allows us to work with differences in the intra- and extra-cellular relaxation rate constants (R_{1in} and R_{1ex}, respectively) that are large enough to make the magnetization decay directly dependent on k_{io} (10, 32, 42). As demonstrated both in the cell suspensions and *in-vivo* experiments, k_{io} appears to be a good biomarker of tumor-cell status that can be exploited to non-invasively monitor the early effects of doxorubicin treatment. Therefore, k_{io} can be measured *in vivo* using multi-relaxation rate measurements in the range 0.01-1 MHz and the 2SX model [6,18], without the need to use paramagnetic contrast agents. **Figure 5B** shows that a significant decrease (P=0.000207) in k_{io} was observed 3 days after the first treatment, providing an early indication of the effect of doxorubicin on cell metabolism and vitality.

As previously reported and herein confirmed in the Rb-uptake experiment, one of the important cytotoxic effects of this antitumor drug is its hampering of Na^+/K^+-ATPase activity. After the second and the third treatment, k_{io} returns to the initial

T0
• Injection of $1x10^6$ of $4T_1$

T6
• 1° treatment

T9
• MRI: $T_{1\ weighted}$ image
• FFC-NMR: T_1 profile
• 2° treatment

T12
• MRI: $T_{1\ weighted}$ image
• FFC-NMR: T_1 profile
• 3° treatment

T15
• MRI: $T_{1\ weighted}$ image
• FFC-NMR: T_1 profile
• Sacrifice

FIGURE 3 | Schematic representation of the workflow for the assessment of doxorubicin treatment in 4T1 tumor animal models over a time course of 15 days (T0-T15).

FIGURE 4 | $1/T_1$ ^1H-NMRD profiles of tumor-bearing mouse legs: treated animals (n=7), black square, compared to control animals (n=7), empty circle. Error bars represent the SE of the experimental data. (p value at 0.01 MHz = 0.0078).

value. We think that this result reflects the massive death of tumor cells, which completely permeabilizes the cytosolic membrane to water. Accordingly, **Figure 5C** shows an initial decrease in V_{ex}, as a consequence of the decreased k_{io}, followed by an increase in V_{ex} after the 2nd and 3rd treatments. The observed increase in V_{ex} is, again, a direct consequence of the cell death caused by doxorubicin. Once the membrane of the dead cells becomes fully permeable to water, the corresponding volume occupied by these cells becomes part of the V_{ex} compartment. These results are in good agreement with the histological apoptosis evaluation on the slices of tumors, that were recovered 3 days after the first treatment, using the TUNEL (terminal deoxynucleotidyl transferase-mediated deoxyuridine triphosphate nick-end labeling) assay. **Figure 6** shows that there are more apoptotic cells in the treated sample than in the control, suggesting that both k_{io} and V_{ex} may act as biomarkers for the toxic effect of doxorubicin, significantly earlier than the macroscopic observation associated to the morphological changes related to slower tumor growth. Finally, it is important to notice that *in vivo* k_{io} magnitude is reduced by a factor of ~25, (**Figure 5B**) in respect to the *in vitro* values (**Figures 1** and **2**). There are many possible reasons to account for the observed behaviour. Cells within a tissue interact with neighbouring cells and with the extracellular matrix in a very different fashion in respect to what occurs in cellular pellets. This may result in significant modification of cell properties, size, morphology, elasticity, etc., i.e. properties that, in turn, may affect both passive and energetically driven components of water exchange across the cellular membrane. One may also expect that the high interstitial fluid pressure/flow and the low lymphatic drainage, in particular in the inner core of a solid tumor (43), may play a role in the translation from *in vivo* to *in vitro* studies. Likely the cells in culture take up more nutrients than in tissue and this would favour the view that the main determinant of the observed change relies on the increased

FIGURE 5 | *In-vivo* assessment of doxorubicin treatment in Balb/c mice that bear 4T1 tumors: **(A)** The percentage of volume increase in the tumor region as determined by T_2-weighted images acquired at 1 T using the ITK-SNAP software. Open and filled bars correspond to untreated and treated mice, respectively; **(B)** The cellular water efflux rate constant, k_{io} (s^{-1}) and **(C)** The extra-cellular volume fractions (V_{ex}) were calculated *via* the analysis of the multi-relaxation rate measurements in the range 0.01-1MHz using the 2SX model for treated animals (n=8) compared to control animals (n=7). Error bars represent the SD of the experimental data. (***p ≤ 0.001).

metabolic activity of the tumour cells. Interestingly, upon comparing cell lines, characterized by different metabolic activities, it was found that the differences in kio observed *in vivo* in tumour tissues are maintained *in vitro* (10). Analogously,
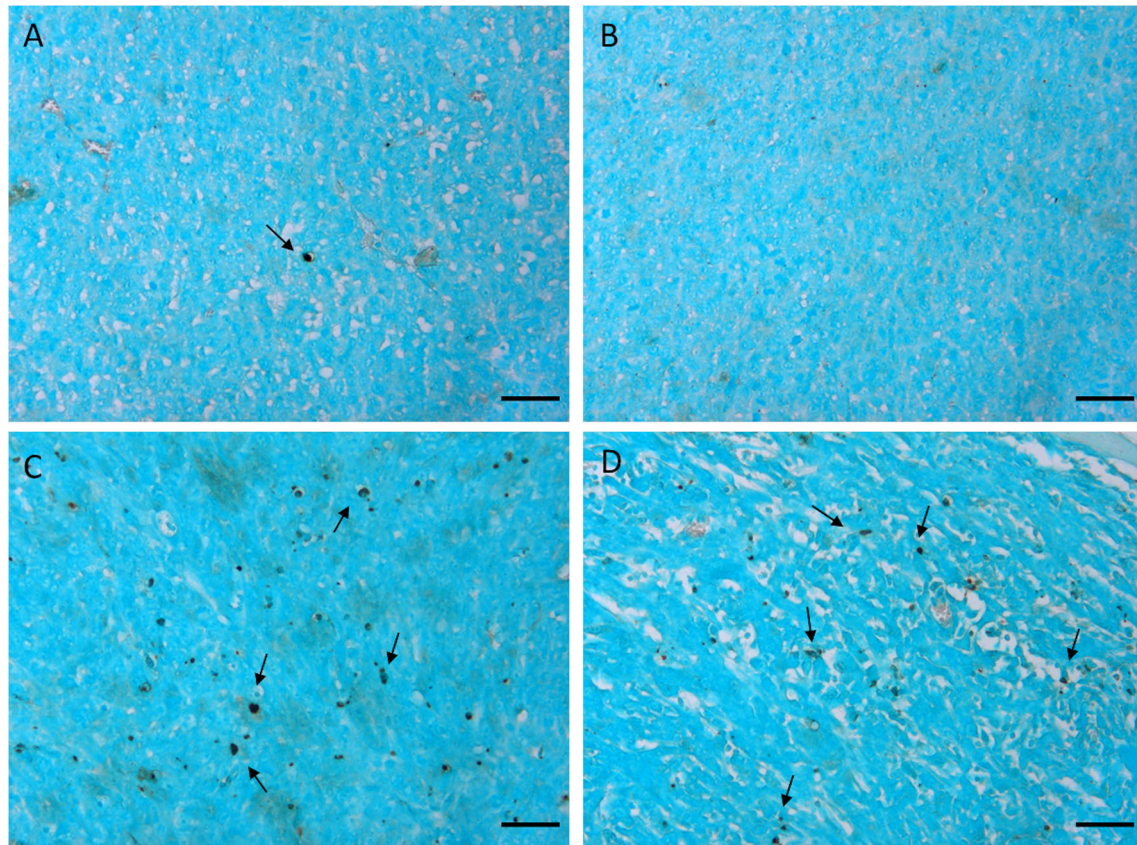
FIGURE 6 | TUNEL staining of 4T1 tumors excised 3 days after the first treatment. Representative images of tumors treated with the vehicle (0.9% saline solution) **(A, B)** and with doxorubicin 5 mg/kg **(C, D)**. Arrows indicate apoptotic nuclei. Cells were counterstained with methyl green. Scale bars= 50 µm".

in this study, it was observed that the effect of doxorubicin treatment *in vivo* is maintained in the *in vitro* experiment

CONCLUSION

In summary, the results reported herein show that relaxometric measurements using FFC-NMR on tumor specimens can provide an important diagnostic contribution for the early assessment of the therapeutic effects associated with the application of doxorubicin. This method is based on the exploitation of the changes in the MR proton water signal that are induced by water exchange rate across the cellular membrane, causing a variation in V_{ex}. It appears to act as a hallmark that can report on the status of the tumor and its response to treatment. The herein-reported results suggest that k_{io} can be considered an early and predictive biomarker for the identification of responsive patients after the first treatment with doxorubicin. Even though FFC-NMR instrumentation is not endowed with spatial resolution, the knowledge obtained in this study can facilitate new diagnostic opportunities for the determination of therapeutic outcomes that would be possible

with FFC MRI scanners. Two prototypes of human whole-body-sized FFC-MRI scanners have recently been built at Aberdeen University by Lurie and coworkers (44–46).

DATA AVAILABILITY STATEMENT

The original contributions presented in the study are included in the article/**Supplementary Material**. Further inquiries can be directed to the corresponding author.

ETHICS STATEMENT

The animal treatment protocol was approved by the Italian Ministry of Health (authorization number 807/2017-PR).

AUTHOR CONTRIBUTIONS

Conceptualization, MR, SB, VB, SA, and SGC. Methodology, MR and SGC. Validation, MR, SB, VB, and RR. Formal analysis, MR,

SUPPLEMENTARY MATERIAL

The Supplementary Material for this article can be found online at: https://www.frontiersin.org/articles/10.3389/fonc.2021.778823/full#supplementary-material

REFERENCES

1. Massoud TF, Gambhir SS. Molecular Imaging in Living Subjects: Seeing Fundamental Biological Processes in a New Light. *Genes Dev* (2003) 17:545–80. doi: 10.1101/gad.1047403
2. Kim JH. Comparison of the EORTC Criteria and PERCIST in Solid Tumors: A Pooled Analysis and Review. *Oncotarget* (2016) 7:58105–10. doi: 10.18632/oncotarget.11171
3. Aykan NF, Özatlı T. Objective Response Rate Assessment in Oncology: Current Situation and Future Expectations. *World J Clin Oncol* (2020) 11:53–73. doi: 10.5306/wjco.v11.i2.53
4. Challapalli A, Aboagye EO. Positron Emission Tomography Imaging of Tumor Cell Metabolism and Application to Therapy Response Monitoring. *Front Oncol* (2016) 6:44–50. doi: 10.3389/fonc.2016.00044
5. Barca C, Wiesmann M, Calahorra J, Wachsmuth L, Döring C, Foray C, et al. Impact of Hydroxytyrosol on Stroke: Tracking Therapy Response on Neuroinflammation and Cerebrovascular Parameters Using PET-MR Imaging and on Functional Outcomes. *Theranostics* (2021) 11:4030–49. doi: 10.7150/thno.48110
6. Mervin LH, Mitricheva E, Logothetis NK, Bifone A, Bender A, Noori HR. Neurochemical Underpinning of Hemodynamic Response to Neuropsychiatric Drugs: A Meta- and Cluster Analysis of Preclinical Studies. *J Cereb Blood Flow Metab* (2021) 41:874–85. doi: 10.1177/0271678X20916003
7. Ntziachristos V, Pleitez MA, Aime S, Brindle KM. Emerging Technologies to Image Tissue Metabolism. *Cell Metab* (2019) 29:518–38. doi: 10.1016/j.cmet.2018.09.004
8. Terreno E, Dastru W, Delli Castelli D, Gianolio E, Geninatti Crich S, Longo D, et al. Advances in Metal-Based Probes for MR Molecular Imaging Applications. *Curr Med Chem* (2010) 17:3684–700. doi: 10.2174/092986710793213823
9. Leithner D, Wengert GJ, Helbich TH, Thakur S, Ochoa-Albiztegui RE, Morris EA, et al. Clinical Role of Breast MRI Now and Going Forward. *Clin Radiol* (2018) 73:700–14. doi: 10.1016/j.crad.2017.10.021
10. Ruggiero MR, Baroni S, Pezzana S, Ferrante G, Geninatti Crich S, Aime S. Evidence for the Role of Intracellular Water Lifetime as a Tumour Biomarker Obtained by *In Vivo* Field-Cycling Relaxometry. *Angew Chemie - Int Ed* (2018) 57:7468–72. doi: 10.1002/anie.201713318
11. Ruggiero MR, Baroni S, Aime S, Crich SG. Relaxometric Investigations Addressing the Determination of Intracellular Water Lifetime: A Novel Tumour Biomarker of General Applicability. *Mol Phys* (2019) 117:968–74. doi: 10.1080/00268976.2018.1527045
12. Koenig SH. Molecular Basis of Magnetic Relaxation of Water Protons of Tissue. *Acad Radiol* (1996) 3:597–606. doi: 10.1016/S1076-6332(96)80225-X
13. Masiewicz E, Ashcroft GP, Boddie D, Dundas SR, Kruk D, Broche LM. Towards Applying NMR Relaxometry as a Diagnostic Tool for Bone and Soft Tissue Sarcomas: A Pilot Study. *Sci Rep* (2020) 10:14207. doi: 10.1038/s41598-020-71067-x
14. Diakova G, Korb J-P, Bryant RG. The Magnetic Field Dependence of Water T 1 in Tissues. *Magn Reson Med* (2012) 68:272–7. doi: 10.1002/mrm.23229
15. Araya YT, Martínez-Santiesteban F, Handler WB, Harris CT, Chronik BA, Scholl TJ. Nuclear Magnetic Relaxation Dispersion of Murine Tissue for Development of T 1 (R 1) Dispersion Contrast Imaging. *NMR BioMed* (2017) 30:e3789. doi: 10.1002/nbm.3789
16. Steele RM, Korb JP, Ferrante G, Bubici S. New Applications and Perspectives of Fast Field Cycling NMR Relaxometry. *Magn Reson Chem* (2016) 54:502–9. doi: 10.1002/mrc.4220
17. Springer CS, Li X, Tudorica LA, Oh KY, Roy N, Chui SY, et al. Intratumor Mapping of Intracellular Water Lifetime: Metabolic Images of Breast Cancer? *NMR BioMed* (2014) 27:760–73. doi: 10.1002/nbm.3111
18. Landis CS, Li X, Telang FW, Molina PE, Palyka I, Vetek G, et al. Equilibrium Transcytolemmal Water-Exchange Kinetics in Skeletal Muscle. *vivo Magn Reson Med* (1999) 42:467–78. doi: 10.1002/(SICI)1522-2594(199909)42:3<467::AID-MRM9>3.0.CO;2-0
19. Li X, Huang W, Morris EA, Tudorica LA, Seshan VE, Rooney WD, et al. Dynamic NMR Effects in Breast Cancer Dynamic-Contrast-Enhanced MRI. *Proc Natl Acad Sci* (2008) 105:17937–42. doi: 10.1073/pnas.0804224105
20. Li X, Mangia S, Lee J, Bai R, Springer CS. NMR Shutter-Speed Elucidates Apparent Population Inversion of 1 H 2 O Signals Due to Active Transmembrane Water Cycling. *Magn Reson Med* (2019) 82:411–24. doi: 10.1002/mrm.27725
21. Thorn CF, Oshiro C, Marsh S, Hernandez-Boussard T, McLeod H, Klein TE, et al. Doxorubicin Pathways. *Pharmacogenet Genomics* (2011) 21:440–6. doi: 10.1097/FPC.0b013e32833ffb56
22. Rong Y, Yuan CH, Qu Z, Zhou H, Guan Q, Yang N, et al. Doxorubicin Resistant Cancer Cells Activate Myeloid-Derived Suppressor Cells by Releasing PGE2. *Sci Rep* (2016) 6:1–11. doi: 10.1038/srep23824
23. Sloval ML, Dalton WS, Trent JM, Hoeltge GA. Pharmacological and Biological Evidence for Differing Mechanisms of Doxorubicin Resistance in Two Human Tumor Cell Lines. *Cancer Res* (1988) 48:2793–7.
24. Mechetner E, Kyshtoobayeva A, Zonis S, Kim H, Stroup R, Garcia R, et al. Levels of Multidrug Resistance (MDR1) P-Glycoprotein Expression by Human Breast Cancer Correlate With *In Vitro* Resistance to Taxol and Doxorubicin. *Clin Cancer Res* (1998) 4:389–98.
25. Bao L, Haque A, Jackson K, Hazari S, Moroz K, Jetly R, et al. Increased Expression of P-Glycoprotein Is Associated With Doxorubicin Chemoresistance in the Metastatic 4t1 Breast Cancer Model. *Am J Pathol* (2011) 178:838–52. doi: 10.1016/j.ajpath.2010.10.029
26. Di X, Gennings C, Bear HD, Graham LJ, Sheth CM, White KL, et al. Influence of the Phosphodiesterase-5 Inhibitor, Sildenafil, on Sensitivity to Chemotherapy in Breast Tumor Cells. *Breast Cancer Res Treat* (2010) 124:349–60. doi: 10.1007/s10549-010-0765-7

27. Akbaribazm M, Khazaei MR, Khazaei M. Trifolium Pratense L. (Red Clover) Extract and Doxorubicin Synergistically Inhibits Proliferation of 4T1 Breast Cancer in Tumor-Bearing BALB/c Mice Through Modulation of Apoptosis and Increase Antioxidant and Anti-Inflammatory Related Pathways. *Food Sci Nutr* (2020) 8:4276–90. doi: 10.1002/fsn3.1724

28. Hafizi M, Soleimani M, Noorian S, Kalanaky S, Fakharzadeh S, Saleh NT, et al. Effects of BCc1 Nanoparticle and its Mixture With Doxorubicin on Survival of Murine 4T1 Tumor Model. *Onco Targets Ther* (2019) 12:4691–701. doi: 10.2147/OTT.S200446

29. Barnes SL, Sorace AG, Loveless ME, Whisenant JG, Yankeelov TE. Correlation of Tumor Characteristics Derived From DCE-MRI and DW-MRI With Histology in Murine Models of Breast Cancer. *NMR BioMed* (2015) 28:1345–56. doi: 10.1002/nbm.3377

30. Panagiotaki E, Walker-Samuel S, Siow B, Johnson SP, Rajkumar V, Pedley RB, et al. Noninvasive Quantification of Solid Tumor Microstructure Using VERDICT MRI. *Cancer Res* (2014) 74:1902–12. doi: 10.1158/0008-5472.CAN-13-2511

31. Gage GJ, Kipke DR, Shain W. Whole Animal Perfusion Fixation for Rodents. *J Vis Exp* (2012) 65:3564. doi: 10.3791/3564

32. Baroni S, Ruggiero MR, Aime S, Geninatti Crich S. Exploring the Tumour Extracellular Matrix by *In Vivo* Fast Field Cycling Relaxometry After the Administration of a Gadolinium-Based MRI Contrast Agent. *Magn Reson Chem* (2019) 57:845–51. doi: 10.1002/mrc.4837

33. Springer CS. Using 1h2o MR to Measure and Map Sodium Pump Activity. *vivo J Magn Reson* (2018) 291:110–26. doi: 10.1016/j.jmr.2018.02.018

34. Bai R, Springer CS, Plenz D, Basser PJ. Fast, Na + /K + Pump Driven, Steady-State Transcytolemmal Water Exchange in Neuronal Tissue: A Study of Rat Brain Cortical Cultures. *Magn Reson Med* (2018) 79:3207–17. doi: 10.1002/mrm.26980

35. Pérez-Blanco JS, Santos-Buelga D, Fernández de Gatta M del M, Hernández-Rivas JM, Martín A, García MJ. Population Pharmacokinetics of Doxorubicin and Doxorubicinol in Patients Diagnosed With non-Hodgkin's Lymphoma. *Br J Clin Pharmacol* (2016) 82:1517–27. doi: 10.1111/bcp.13070

36. Speth PAJ, van Hoesel QGCM, Haanen C. Clinical Pharmacokinetics of Doxorubicin. *Clin Pharmacokinet* (1988) 15:15–31. doi: 10.2165/00003088-198815010-00002

37. Boucek RJ, Olson RD, Brenner DE, Ogunbunmi EM, Inui M, Fleischer S. The Major Metabolite of Doxorubicin is a Potent Inhibitor of Membrane-Associated Ion Pumps. A Correlative Study of Cardiac Muscle With Isolated Membrane Fractions. *J Biol Chem* (1987) 262:15851–6. doi: 10.1016/S0021-9258(18)47666-1

38. Figueroa JAL, Stiner CA, Radzyukevich TL, Heiny JA. Metal Ion Transport Quantified by ICP-MS in Intact Cells. *Sci Rep* (2016) 6:20551. doi: 10.1038/srep20551

39. Hakimjavadi H, Stiner C, Radzyukevich T, Lingrel J, Norman N, Landero Figueroa J, et al. K+ and Rb+ Affinities of the Na,K-ATPase α1 and α2 Isozymes: An Application of ICP-MS for Quantification of Na+ Pump Kinetics in Myofibers. *Int J Mol Sci* (2018) 19:2725. doi: 10.3390/ijms19092725

40. Pröfrock D, Prange A. Inductively Coupled Plasma–Mass Spectrometry (ICP-MS) for Quantitative Analysis in Environmental and Life Sciences: A Review of Challenges, Solutions, and Trends. *Appl Spectrosc* (2012) 66:843–68. doi: 10.1366/12-06681

41. Abolhoda A, Wilson AE, Ross H, DP V, Burt M, Scotto KW. Rapid Activation of MDR1 Gene Expression in Human Metastatic Sarcoma After *In Vivo* Exposure to Doxorubicin. *Clin Cancer Res an Off J Am Assoc Cancer Res* (1999) 5:3352–6.

42. Baroni S, Ruggiero MR, Bitonto V, Broche LM, Lurie DJ, Aime S, et al. *In Vivo* Assessment of Tumour Associated Macrophages in Murine Melanoma Obtained by Low-Field Relaxometry in the Presence of Iron Oxide Particles. *Biomaterials* (2020) 236:119805. doi: 10.1016/j.biomaterials.2020.119805

43. Liu LJ, Brown SL, Ewing JR, Ala BD, Schneider KM, Schlesinger M. Estimation of Tumor Interstitial Fluid Pressure (TIFP) Noninvasively. *PloS One* (2016) 11:e0140892. doi: 10.1371/JOURNAL.PONE.0140892

44. Broche LM, Ross PJ, Davies GR, MacLeod MJ, Lurie DJ. A Whole-Body Fast Field-Cycling Scanner for Clinical Molecular Imaging Studies. *Sci Rep* (2019) 9:1–11. doi: 10.1038/s41598-019-46648-0

45. Ross PJ, Broche LM, Lurie DJ. Rapid Field-Cycling MRI Using Fast Spin-Echo. *Magn Reson Med* (2015) 73:1120–4. doi: 10.1002/mrm.25233

46. Broche LM, Ashcroft GP, Lurie DJ. Detection of Osteoarthritis in Knee and Hip Joints by Fast Field-Cycling NMR. *Magn Reson Med* (2012) 68:358–62. doi: 10.1002/mrm.23266

Conflict of Interest: The authors declare that the research was conducted in the absence of any commercial or financial relationships that could be construed as a potential conflict of interest.

Publisher's Note: All claims expressed in this article are solely those of the authors and do not necessarily represent those of their affiliated organizations, or those of the publisher, the editors and the reviewers. Any product that may be evaluated in this article, or claim that may be made by its manufacturer, is not guaranteed or endorsed by the publisher.

Check for updates

Metabolic Pathways and Targets in Chondrosarcoma

Ida Micaily[1], Megan Roche[1], Mohammad Y. Ibrahim[2], Ubaldo Martinez-Outschoorn[1] and Atrayee Basu Mallick[1*]

[1] Department of Medical Oncology, Thomas Jefferson University, Philadelphia, PA, United States, [2] Saint Francis Medical Center, Seton Hall University, Trenton, NJ, United States

Chondrosarcomas are the second most common primary bone malignancy. Chondrosarcomas are characterized by the production of cartilaginous matrix and are generally resistant to radiation and chemotherapy and the outcomes are overall poor. Hence, there is strong interest in determining mechanisms of cancer aggressiveness and therapeutic resistance in chondrosarcomas. There are metabolic alterations in chondrosarcoma that are linked to the epigenetic state and tumor microenvironment that drive treatment resistance. This review focuses on metabolic changes in chondrosarcoma, and the relationship between signaling *via* isocitrate dehydrogenase 1 and 2 (IDH1 and IDH2), hedgehog, PI3K-mTOR-AKT, and SRC, as well as histone acetylation and angiogenesis. Also, potential treatment strategies targeting metabolism will be discussed including potential synergy with immunotherapies.

INTRODUCTION

Chondrosarcomas encompass a heterogeneous group of malignant cartilaginous matrix- producing tumors of the bone and are the second most common primary bone malignancy in humans, representing 25% of bone neoplasms (1). Histological grading and staging of chondrosarcomas are the most important factors to aid in prognostication. 85% of chondrosarcomas are histologically classified as conventional chondrosarcomas and can be subcategorized as central or peripherally located (1–3). The other 15% of chondrosarcoma histological subtypes include dedifferentiated, mesenchymal, clear cell and myxoid. Chondrosarcomas are graded from 1 to 3, or low, intermediate and high grade, based on cellularity, nuclear size, nuclear atypia, mitotic activity and matrix alterations (3). The majority of non-conventional chondrosarcomas include low and intermediate grade tumors that are slowly growing with low metastatic potential. However, 5-10% of chondrosarcomas are high-grade and this includes mesenchymal and dedifferentiated chondrosarcomas as well as a subset of conventional chondrosarcomas, which have a high metastatic potential and carry a poor prognosis (4).

The histological grade, stage, and tumor location determine treatment of chondrosarcomas. It is unclear if anticancer agents are active in chondrosarcomas emphasizing the need to understand drivers of cancer aggressiveness that may be the basis of novel therapeutics (2). Surgical management for

---

Abbreviations: IDH, Isocitrate dehydrogenase; LDH, Lactate dehydrogenase; PD-1, Programmed-Death Receptor-1; PDL-1, Programmed-Death Receptor Ligand 1.

localized disease is the mainstay of treatment but the specific surgical approach depends on the size, histological type and grade of chondrosarcoma. Small, atypical cartilaginous tumors/grade 1 chondrosarcoma are treated with intralesional curettage, and local high-grade chondrosarcoma are resected en-block (4). Conventional chondrosarcoma that is inoperable or widespread is routinely treated with chemotherapy due to its aggressive nature although it is unclear if any agents are active since there have been no high quality randomized controlled clinical trials in this disease. Chemotherapy was associated with improved overall survival for unresectable conventional chondrosarcoma in a retrospective study from the Rizzoli Institute in Bologna, Italy and Leiden University Medical Center in the Netherlands (3). Specifically, there was a survival advantage when being treated with chemotherapy at 3 years (OS of 26% with chemotherapy vs. 8% without chemotherapy, p<0.05) and the median overall survival was only 11 months for those patients that did not receive chemotherapy (3). However, it is unknown if selection bias contributed significantly to the differences in survival in this retrospective study. Another multi-institutional retrospective analysis with a 180 patients confirmed the poor outcomes for patients with unresectable chondrosarcoma with a median PFS of 4.7 months for first-line chemotherapy (4). The most commonly used chemotherapy regimens for chondrosarcoma are anthracycline-based regimens. However, there are no preferred regimens since there is a lack of positive randomized controlled trials and these tumors are generally chemo-resistant, with the exception of dedifferentiated and mesenchymal which may be partially chemo-sensitive (5).

Chondrosarcoma clinical research is focused on novel therapeutic approaches for inoperable, chemotherapy-refractory or metastatic chondrosarcomas. Although most cancer subtypes have multiple novel therapeutic options, chondrosarcoma lacks effective therapies with the exception of surgery and continues to be associated with poor clinical outcomes (4). Altered metabolism is a hallmark of cancers (6). A deeper understanding of chondrosarcoma metabolism, including glycolytic and TCA enzymes, metabolites, as well as signaling pathways, and tumor suppressor genes and oncogenes that modulate metabolism may identify vulnerabilities that could be exploited therapeutically (7). Genetic changes that affect mitochondrial metabolism are of particular interest in chondrosarcomas, since the most common mutations in these cancers are in the isocitrate dehydrogenase (IDH) gene, and the encoded mutant enzyme modulates mitochondrial metabolism (8). Specifically, mutations in IDH1 or IDH2 isoforms are identified in approximately 60% of chondrosarcomas (2). Also, glutaminolysis affects mitochondrial metabolism in a similar fashion to IDH mutations and is increased in chondrosarcoma (2, 6).

TARGETING ISOCITRATE DEHYDROGENASE (IDH) MUTATIONS IN CHONDROSARCOMA

IDH enzymes are the most commonly mutated genes in chondrosarcoma and the IDH1 isoform is more commonly mutated than IDH2 (8, 9). Mutant IDH-mediated epigenetic dysregulation leads to chondrocyte differentiation of mesenchymal stem cells and downregulation of osteogenic markers, which may explain the high and low prevalence of IDH mutations in chondrosarcoma and osteosarcoma respectively (10). Post-natal IDH1 R172Q mutations in chondrocytes in mice leads to enchondromas, which is a precursor lesion for chondrosarcoma (11). Knockout of both the mutated and wild type IDH1 *via* CRISPR–Cas9 from chondrosarcoma cell lines impaired anchorage-independent cell growth and migration with downregulation of integrins, which implicated mutant IDH1 in chondrosarcoma in the epithelial-to-mesenchymal transition with reduced growth rates *in vivo* and this phenotype was not rescued with restoration experiments with wild type IDH1 (12). Interestingly, mutations in IDH in high grade chondrosarcomas have been associated with CDKN2A/2B and TP53 alterations, prolonged relapse-free and metastasis-free survival (9). In contrast, a meta-analysis revealed that IDH mutations in chondrosarcoma are associated with poor outcomes (13).

IDH mutations are being targeted therapeutically in many cancer subtypes (8). IDH catalyzes the conversion of isocitrate to alpha-ketoglutarate (a-KG) and CO_2 in the Krebs or TCA cycle (8). Three isoforms of IDH exist: IDH1 (cytoplasmic), IDH2 (mitochondrial-TCA cycle) and IDH3 (mitochondrial-TCA cycle). IDH1 and IDH2 are NADP-dependent enzymes that are mutated in 38-70% of conventional and dedifferentiated chondrosarcoma cases and induce a neomorphic enzymatic activity (6–13). The mutant forms of IDH1 and IDH2 require a-KG in order to produce a novel metabolite, D-2-hydroxyglutarate (D-2-HG), which becomes a competitive inhibitor in a-KG dependent enzymes and an oncometabolite, which activates hypoxia inducible factor (HIF) (11). HIF-1α expression is highly expressed in the majority of chondrsarcomas and is associated with poor outcomes (14). Also, HIF-2α is upregulated in human high-grade chondrosarcoma biopsies compared to low grade samples and gene amplification is associated with poor prognosis in chondrosarcoma patients (15). HIF-2α promotes chondrosarcoma tumor growth, invasion and metastasis using xenograft models *in vivo* and pharmacological inhibition of HIF-2α induces apoptosis (15). HIF-1α and HIF-2α are degraded in the proteosome *via* von-Hippel Lindau (VHL) and VHL disease is due to inactivating mutations in the VHL gene (pVHL), which leads to HIF-1α and HIF-2α stabilization (16). Chondrosarcomas have been described in patients with VHL disease (17–19). Also, low VHL expression is associated with higher grade, higher stage and worse outcomes in chondrosarcoma (20). In sum, IDH and HIF signaling is frequently altered in chondrosarcoma.

IDH1 and IDH2 mutated chondrosarcomas have a distinct metabolomic profile with increased lactate, the TCA intermediates succinate, fumarate, and malate, amino acids broadly and acylcarnitines compared to non-mutated cancer cells based on patient derived xenografts (21). This metabolomic profile of IDH mutated chondrosarcoma is consistent with increased glycolysis, anaplerotic flux into the TCA cycle and fatty acid oxidation (21) and is consistent with other studies that have revealed that there is HIF activation, high rates of glutaminolysis and lipid metabolism in chondrosarcomas (7, 15, 22, 23). Chondrosarcomas with high

mRNA expression of glycolytic, TCA, glutamine catabolism and fatty acid oxidation genes were associated with poor outcomes in patients with chondrosarcoma (21).

Pharmacological inhibition of IDH1 reduced colony formation, migration, proliferation, and induced apoptosis in chondrosarcoma cells *in vitro* (24). However, a different group of investigators using other chondrosarcoma cell lines *in vitro* did not find that a mutant IDH1 inhibitor had an effect on proliferation and migration (25). IDH1 and 2 mutated chondrosarcoma cells have been shown to up-regulate glutaminolysis and glycolysis for the production of a-KG (25–27). High-grade chondrosarcomas have higher glutaminase expression although no significant differences were observed on the basis of IDH status (14). A subset of chondrosarcoma cell lines are sensitive to drugs targeting glutaminolysis and Bovee et al. studied the glutaminase inhibitor CB-839, the glutamate dehydrogenase inhibitor chloroquine as well as metformin and phenformin, which are inhibitors of mitochondrial oxidative phosphorylation (OXPHOS) and c-MYC and downstream of glutaminolysis (22). Interestingly, this study demonstrated that chloroquine increased apoptosis by increasing caspase 3/7 activity in three out of five cell lines (22). Metformin and phenformin reduced mTOR signaling in these chondrosarcoma cells by decreasing phosphorylated S6 (22) as has been previously demonstrated in other cancers (6). Metformin modulated autophagy with a decrease in LC3B-II levels. Metformin did not affect chondrosarcoma cell viability despite its known effects on mTOR signaling and mitochondrial respiration or OXPHOS. IDH2 mutations in chondrosarcoma cells are known to modulate mesenchymal differentiation through epigenetic dysregulation and treatment with the hypomethylating agent 5-azacytidine is a promising therapeutic strategy (15).

IDH1 inhibition in preclinical and clinical studies has had mixed results (12, 15, 16). A phase I multicenter clinical trial investigating the mutant IDH1 inhibitor ivosidenib (AG-120) in twenty-one patients with advanced chondrosarcoma demonstrated safety with minimal toxicity and a median progression free survival (PFS) of 5.6 months with a PFS rate of 39.5% at 6 months (28). 52% of the 21 patients had stable disease (28). There are ongoing phase I/II clinical trials of novel IDH inhibitors including AG-881 (NCT02481154) and AG-120 (NCT02073994). Aphase I/II clinical trial of metformin and chloroquine in IDH1/2-mutated solid tumors including three patients with chondrosarcoma (NCT02496741) did not find clinical activity (29). A clinical trial of the IDH-inhibitor AG-221 in chondrosarcoma is pending results (NCT02273739) (**Table 1**). In sum, mutant IDH causes metabolic reprogramming with production of D-2-HG that results in dysregulation of gene expression, differentiation status, DNA damage repair, inflammation, intracellular trafficking, ageing and cell death programs in cancer cells (8). Further research on mutant IDH inhibition is needed to determine its therapeutic value in chondrosarcoma.

TARGETING LIPID METABOLISM IN CHONDROSARCOMA

Lipids in cancer are thought to be protumorigenic due to their effects on epigenetic reprogramming, maintainance of redox balance by generating NADPH, reduction of ER stress/unfolded protein response, reduction of ferroptosis, effects as second messengers, pro-inflammatory effects, substrates for biomass production, and serving as catabolites to generate ATP (30). Also, increased amounts of cholesterol in the tumor microenvironment induce exhaustion in CD8+ T cells (31). Specifically, high levels of phospholipids and cholesterol are associated with aggressive cancer (32, 33). High cholesterol levels transform the lipid membrane and promote the activity of multidrug efflux pumps driving a multidrug resistant phenotype (33). Cholesterol acting as a second messenger activates mTOR and Hedgehog signaling (34). Conversely, mTOR activation induces denovo lipid and cholesterol synthesis (30, 35).

Inhibition of intracellular cholesterol biogenesis by deletion of sterol regulatory element–binding protein cleavage-activating protein (SCAP) reduces Hedgehog signaling and alters chondrocyte development (36). Statin drugs, which inhibit cholesterol synthesis, restore chondrocyte development and morphology (37, 38). There is upregulation of genes that are activated in cholesterol biosynthesis in IDH1 mutant chondrocytes (23). Consistent with increased biosynthesis, cholesterol levels are higher in IDH1 mutated chondrosarcomas (23). From a therapeutic standpoint, statins reduce cholesterol synthesis and administration of the statin lovastatin reduced chondrosarcoma progression *in vivo* with reduced proliferation and increased apoptosis rates (23). Hypoxia and starvation, as well as gene mutations in PI3K/AKT, RAS, and MYC have been implicated in upregulation of *de novo* lipogenesis, cholesterol synthesis and fatty acid desaturation (39). Autophagy is also related to lipid metabolism and there is upregulation in chondrosarcomas (40, 41).

The role of cholesterol and lipid homeostasis in chondrosarcoma is not elucidated. IDH1 mutations are known to cause metabolic reprogramming and regulate intracellular cholesterol biosynthesis.

TABLE 1 | Clinical trials utilizing IDH and Hh pathway inhibitors in Chondrosarcoma.

AGENTS	STUDY DESIGN/PHASE	# of PATIENTS	PRIMARY EFFICACY ENDPOINT	REFERENCE
CB-839 (Glutaminase inhibitor)	Phase I	n=41	Safety/Efficacy	NCT02071862
Metformin/Chloroquine	Phase IB/II	n=38	Rate of disease control = 50%	NCT02496741 (29)
GDC-0449 (Hedgehog inhibitor)	Phase II	n=45	6 month clinical benefit rate	NCT01267955
IPI-926	Phase II	n=105	PFS, OS, ORR	NCT01310816
AG-221 (IDH2 inhibitor)	Phase I/II	n=21	Safety/Dose escalation	NCT02273739
AG-120 (IDH1 inhibitor	Phase I	n=170	Safety/Dose escalation	NCT02073994 (16)

A mouse model utilizing IDH1 mutated chondrosarcoma cells identified an activation of cholesterol biosynthesis (21). IDH1/2 mutated chondrosarcoma cells treated with lovastatin reduced viability (42). These preclinical study suggests that targeting cholesterol metabolism may be promising in chondrosarcoma.

TARGETING GLUCOSE METABOLISM IN CHONDROSARCOMA

Metabolism of chondrocytes using cell lines has been studied (17, 18). One of the earliest studies of metabolism of UDP-sugar metabolism in chondrocytes utilized Swarm rat chondrosarcoma chondrocytes to better understand the role of glycosylation in cartilage glycosaminoglycan and proteoglycan synthesis. This model demonstrated that stimulation through insulin or fetal calf-serum could increase biosynthetic activity of chondrocytes that can increase the demand of UDP-sugars in cartilage synthesis (43).

Glucose catabolism to C02 and water in the mitochondria occurs in the majority of cells, however under anaerobic conditions catabolism of glucose occurs exclusively in the cytosol and the end product of glycolysis is lactate. Aerobic glycolysis occurs at high rates in cancer cells and has been termed the Warburg Effect. Also, there is a greater appreciation of other cells that are glycolytic within the tumor microenvironment. The Reverse Warburg Effect describes when glycolysis in the cancer-associated stroma metabolically supports adjacent cancer cells. This catabolite transfer, which induces stromal-cancer metabolic coupling, allows cancer cells to generate ATP, increase proliferation, and reduce cell death (44).

Studies have been performed with inhibition of glycolysis in order to treat disease and overcome resistance to other anticancer agents. Multiple nodes in glucose metabolism and reactive oxygen species have been targeted in conjunction with conventional cytotoxic chemotherapy including doxorubicin, cisplatin and paclitaxel (19–23). Expression of lactate dehydrogenase- A (LDHA), which is a key glycolytic enzyme, in cancer cells has been associated with chemotherapy and radiotherapy resistance (2). Additionally, glycolysis can be suppressed by utilizing LDHA inhibitors such as oxamate and FX11 (2). Early studies focused on targeting glycolysis as a mechanism to overcome drug resistance were focused on LDHA. *In vitro*, paclitaxel resistance was overcome by utilizing the LDHA inhibitor oxamate which induced apoptosis (45). Given the high activity of LDHA and glycolysis in chondrosarcoma cells, LDHA may be a therapeutic target in chondrosarcoma. A cell line exposed to the LDHA inhibitor oxamate can overcome doxorubicin-resistance in chondrosarcoma (46). Another study demonstrated that the addition of oxamate to cisplatin helped overcome chemo-resistance in a chondrosarcoma mouse model (47). Also, the LDHA inhibitor, 1-(phenylseleno)-4-(trifluouromethyl) benzene (PSTMB) has been studied in models of colon cancer, lung cancer, breast cancer, hepatocellular carcinoma and has shown anticancer activity (48). Glucose metabolism may be a future therapeutic target in chondrosarcoma; although to our knowledge, no clinical trials are testing this therapeutic strategy.

TARGETING THE HEDGEHOG PATHWAYS IN METABOLISM OF CHONDROSARCOMA

The hedgehog (Hh) protein regulatory pathway has been implicated in metabolic control, homeostasis and development (49, 50–52). The Hh pathway, which exerts potent metabolic effects, requires the appropriate control of Hh ligand production, processing, secretion and transport (49). A pathological role of the Hh pathway is associated with constitutive activation of transcriptional responses. Binding of Hh to the negative patched regulator (PTCH1) depressed positive smoothened regulator (SMO) in the cilia and phosphorylation and the cytoplasmic end, ultimately mediating downstream signal transduction (49). Glioma zinc finger transcription factors are activated by SMO, which translocate the transcription factors into the nucleus and bind to the promoters of several oncogenes. The disruption of this pathway drives tumorigenesis and glycolysis (49). Chondrosarcomas express high levels of hedgehog (Hh) proteins, and inhibition of the hedgehog pathway *in vitro* decreased proliferation of chondrosarcoma cells (49) and other solid tumors with down-regulation of P-glycoprotein (50). Additionally, the Indian Hedgehog (IHH)/parathyroid hormone related peptide pathway has been implicated in the pathogenesis of chondrosarcoma. IPI-926 (saridegib), a potent oral- Hh inhibitor, has been assessed in chondrosarcoma cell lines and has shown activity (51). Thereafter, another human chondrosarcoma cell line was also studied with Hh inhibition revealing decreased proliferation, invasion and migratory capacity (52, 53). IPI-926 was tested in a phase II study in chondrosarcoma that was stopped to accrual due to lack of efficacy (51). Another phase II, multicenter clinical trial was conducted on 45 patients with advanced, progressive chondrosarcoma utilizing the Hh pathway inhibitor GDC-0449 (vismodegib). The primary end point was a clinical benefit rate (CBR). The goal CBR was 40% at 6 months. However, the primary end point was not met, as the CBR at 6 months was 25.6% (95% CI 13-42%). Despite the negative results of this clinical trial, clinical benefit was observed in a subset of patients. A possible subpopulation of patients with grade 1 or 2 disease may benefit Hh pathway inhibition in combination with chemotherapy (**Table 1**). Previous studies have shown that the hedgehog pathway is dysregulated in chondrosarcoma and clinical trials evaluating Hh inhibition have shown that there could be a modest clinical benefit in chondrosarcoma (49–52).

PI3K-AKT- MTOR PATHWAY IN CHONDROSARCOMA

The mTOR pathway is a crucial regulator of cell metabolism, survival and proliferation (54). The growth factor regulated phosphoinositol 3-kinase (PI3K)-AKT signaling network has many direct and indirect downstream effects on cellular metabolism (6). Physiologically, PI3K-AKT pathway is activated in response to metabolic factors such as insulin, growth factors and cytokines to regulate glucose metabolism, biosynthesis of

macromolecules and redox balance (54). These processes support metabolic homeostasis and the growth and metabolism of individual cells (55–58). Pathologically, oncogenic activation of PI3K-AKT reprograms cellular metabolism to anabolism and to promote cancer growth (59). AKT promotes glycolysis and glucose dependency for survival. Protein synthesis is also induced downstream of AKT through mTOR signaling (59).

The mTOR/PI3K pathway as well as IGFR-1 have been studied as a therapeutic anticancer target and this work has served as a foundation for studies in chondrosarcoma (55, 56). Inhibitors of the mTOR pathway have been utilized as single agents or in combination with other agents in both solid and hematologic malignancies (54–58). Human chondrosarcoma-derived cell lines demonstrated phosphorylation of receptor tyrosine kinases (RTKs), particularly AKT, MEK and S6 kinase suggesting clinical relevance of the PI3K/ATK/mTOR pathway in chondrosarcoma (54–58). RTK inhibition in the mTOR/PI3K pathway was studied preclinically utilizing a dual inhibitor, BEZ235 (54). Dual PI3K/mTOR inhibition was studied in a chondrosarcoma xenograft model and demonstrated significant suppression of growth utilizing BEZ235 and GCD-041 with rapamycin (54). Baicalin, a flavonoid extract utilized in traditional Chinese medicine, was found to induce apoptosis in a human chondosarcoma cell line *via* targeting of PI3K, AKT and mTOR pathways (57). Similarly, the mTOR pathway was studied in a preclinical rat chondrosarcoma model by utilizing the mTOR inhibitor everolimus which blocked cell proliferation as well as GLUT1 and HIF1a expression *in vivo* (58). Activation of the HIF-1 pathway plays a central role in the adaptive response of tumor cells to hypoxia, and HIF-1 alpha expression is associated with high-grade chondrosarcomas and reduced disease free survival (60, 61). Everolimus reduced GLUT1 expression and HIF1a activity (60). However, single agent everolimus did not induce tumor regression in chondrosarcoma rat models (60). Additionally, doxorubicin was utilized in combination with everolimus and the combination had synergistic activity (61). One proposed mechanism for the synergy between everolimus and doxorubicin is by inhibiting both mTOR and AKT pathways simultaneously. The mTOR inhibitors sapanisertib and rapamycin have also been studied in chondrosarcoma cell lines and they induce decreased oxidative and glycolytic metabolism, independent of IDH status (7). Interestingly, chondrosarcoma cell lines treated with sapanisertib or rapamycin reduced cell viability with a decrease in glucose dependence and a shift towards glutaminolysis and fatty acid catabolism, and sapanisertib had the strongest response (57). Clinical studies of mTOR pathway inhibition in chondrosarcoma hold promise given the encouraging pre-clinical data.

TARGETING ANGIOGENESIS IN CHONDROSARCOMA

Tumors and require high rates of metabolite uptake from the vasculature to support their growth and have high vascularization (6). PI3K activation promotes vascular endothelial growth factor-A (VEGF-A) expression leading to angiogenesis, a key component of tumor growth and metastases (44, 62). Catabolites implicated in metabolic coupling include the monocarboxylates lactate, pyruvate, and ketone bodies. Monocarboxylate transporters (MCT) are critically necessary for release and uptake of these catabolites (63). MCT4 is involved in the release of monocarboxylates from cells, is regulated by catabolic transcription factors such as hypoxia inducible factor 1 alpha (HIF1A) and nuclear factor kappa-light-chain-enhancer of activated B cells (NF-κB), and is highly expressed in cancer cells as well as cancer-associated fibroblasts and has been shown to be highly expressed in sarcomas (63).

In chondrosarcoma human cell lines, angiogenesis is promoted by the fatty acid metabolic hormone adiponectin on VEGF-A (44). VEGF-A expression was induced by adiponectin through the utilization of the adiponectin receptor, PI3K, AKT, mTOR and HIF-1a pathways [7,59]. Pretreatment of chondrosarcoma cells with PI3K, AKT or mTOR inhibitors abolished the adiponectin effect on VEGF-A. As a previous study on chondrosarcoma cells demonstrated that adiponectin was linked to metastasis, this could be a possible treatment target in chondrosarcoma (62). The chemokine CCL5 has also been found to promote VEGF-A expression and angiogenesis in chondrosarcoma by activating the PI3K pathway (64). Inhibition of the PI3K pathway abolished the CCL5 effect on VEGF-A and angiogenesis (64). Targeting angiogenesis through multi-tyrosine kinase inhibitors was also studied in preclinical chondrosarcoma models (65). An inhibitor of VEFR2, PDGFR-B and FGFR1 through SU668 was used in a high-grade chondrosarcoma animal model (65).

Another mediator of angiogenesis, cyclooxygenase-2 (COX-2) and prostaglandin activity was studied in chondrosarcoma to determine if inhibiting its activity can improve chemotherapy and radiation sensitivity (42). Preclinical studies utilized agent celecoxib and NS-398 in four high-grade cell lines and although there was initial tumor regression, there was tumor relapse by 6 weeks (42).

A single-arm, multicenter phase 2 trial examining VEGF-inhibition by the oral tyrosine kinase inhibitor (TKI) pazopanib in metastatic or unresectable conventional chondrosarcoma was performed (66). Of the 47 enrolled patients, the primary endpoint of disease control rate (DCR) at 16 weeks was 43%, although this was not statistically significant (66). However, OS was 17.6 months and the median PFS was 7.9 months, which are promising time points in chondrosarcoma clinical trials. Grade 3 adverse events such as hypertension were observed, which are well-described with VEGF inhibitors (66).

As mentioned in **Table 1**, phase II studies investigating the safety and efficacy of multi-targeted tyrosine kinase inhibitors in various forms of chondrosarcomas are ongoing. These studies highlight the promise of targeting signaling pathways for the treatment of chondrosarcoma.

TARGETING THE SRC PATHWAY IN CHONDROSARCOMA

SRC proteins are cellular tyrosine kinases that have been studied in multiple solid tumor types and SRC modulates cell signaling,

survival, angiogenesis, proliferation and migration. Cytoplasmic-RSC (c-SRC) contributes to receptor signaling from a number of growth factor receptors (47). Redox regulation of platelet derived growth factor receptor (PDGFR) stimulation, protein kinase C, PI3K and NADPH oxidase activity contribute to complex SRC kinase activation (67). In chondrosarcoma, negative regulators of the intrinsic or mitochondrial apoptotic pathway such as BCL2, which has crosstalk with SRC, are upregulated and mediate chemo-resistance in cancer (67). The multifunctional tyrosine kinase inhibitor Dasatinib (BMS-354825), which inhibits SRC and down-regulates BCL2 was studied in chondrosarcoma cell lines (66, 67). In chondrosarcoma, it has been studied in combination with doxorubicin in TP53 mutant chondrosarcoma cell lines (68). In the 8 doxorubicin resistant chondrosarcoma cell lines utilized in this study, SRC inhibition was found to overcome doxorubicin resistance by inducing apoptosis and inhibiting migration (68).

Another receptor tyrosine kinase target in chondrosarcoma is the platelet derived growth factor receptor (PDGFR), as preclinical data suggests that it's signaling is induced in chondrosarcoma (67). Preclinical data has demonstrated that PDGFRa can mediate rapamycin-induced AKT phosphorylation in synovial sarcoma cell lines (67). As such, the PDGFR pathway was further studied in clinical trials utilizing single agent imatinib in chondrosarcoma without strong activity signals (see **Table 2**). The PDGFR pathway remains a promising therapeutic target in chondrosarcoma.

HISTONE DEACTYLASE INHIBITORS IN CHONDROSARCOMA

Histone dysregulation is a common future across multiple cancer subtypes. Histone acetylation helps alter the regulatory switch to disrupt homeostasis and cause tumor growth. Histone deacetylation and acetylation play key roles in chondrocyte differentiation. As such, histone deacetylase inhibitors (HDAC inhibitors) have been well studied as treatment for various cancers, particularly chondrosarcoma (69). In a preclinical model, HDAC inhibitors were found to have antitumor effects by causing differentiation, apoptosis and inducing cell arrest (43). Subsequently, IDH wild type and mutant chondrosarcoma cell lines were studied with the combination of the HDAC inhibitor romidepsin and the glutaminase inhibitor CB-839 (22, 66). Another HDAC inhibitor, depsipeptide demonstrated antitumor activity in both chondrosarcoma cell lines as well as rat models (65). The promising results of these preclinical studies

spurred further interest in clinical trials utilizing HDAC inhibitors, and we are awaiting results.

MITOCHONDRIAL METABOLISM IN CHONDROSARCOMA

The mitochondria are the main source of ATP and the main site of generation of reactive oxygen species (ROS) and its effects have been studied in the progression of various malignancies. ROS is a second messenger notably used in tumor stemness, cell cycle progression, cell proliferation, cell survival, energy metabolism, cell motility, and angiogenesis (70). There is an interest in targeting ROS to induce cell death through induction of mitochondrial ROS production or alternatively using antioxidant strategies. Critical nodes in ROS production or antioxidant activity utilize cofactors such as NADPH, glutathione and FADH. 38-79% of chondrosarcomas have IDH1/IDH2 mutations with an enzymatic neomorphic activity and they use NADPH or NADH as a cofactor. The wild-type enzymes help with conversion of isocitrate dehydrogenase to α-ketoglutarate in cytoplasm and mitochondria respectively and when mutated they drive 2-hydroxyglutarate production, which is a metabolite that drives HIF-1α signaling (60). Hence, there is interest in evaluating the role of mitochondrial metabolism and the redox state in the treatment of chondrosarcoma (22).

The effects of targeting mitochondrial metabolism and apoptosis have been studied in human chondrosarcoma cell lines including studying effects of drugs on BCL2, BAX, Bid, cytochrome c and caspase-3 (71). The fungal metabolite Trichodermin from *N psidii* demonstrated anti-tumor activity by inducing mitochondrial apoptosis in chondrosarcoma cell lines (53). Other derivatives such as benzimadazole, benzofuran and honokiol have also been studied as pro-apoptotic agents (71–73).

Alterations in mitochondrial metabolism have also been implicated in resistance to chemotherapeutic effect. Translocase of the outer mitochondrial membrane complex subunit 20 (TOMM20) is an important subunit that is responsible for recognizing and translocating mitochondrial proteins into the mitochondria from the cytoplasm (62). Cells with greater mitochondrial mass and activity have greater TOMM20 expression. TOMM20 has been studied in human chondrosarcoma cell lines and found to have higher expression in higher grade chondrosarcomas, indicating a role of increased mitochondrial metabolism, glucose and lactose utilization and oxygen consumption (74). *In vivo*, TOMM20 induced larger tumor size. Additionally, TOMM20 overexpression was found to induce resistance to cell cycle specific chemotherapy agents (74).

TABLE 2 | Clinical trials utilizing Tyrosine Kinase Inhibitors (TKIs) in Chondrosarcoma.

TKI	STUDY DESIGN/PHASE	# OF PATIENTS	PRIMARY EFFICACY ENDPOINT	REFERENCE
Dasatinib	Phase II	n=366	RR, 6 month PFS	NCT00464620
Imatinib	Interventional	n=35	Tumor response	NCT00928525
Pazopanib	Phase II	n=70	ORR	NCT02066285
Regorafinib	Phase II	n=132	PFS	NCT02389244
Depsipeptide (Romidepsin)	Phase II	n=40	OR, time to progression, toxicity	NCT00112463

IMMUNOTHERAPY IN CHONDROSARCOMA

The altered metabolic landscape of tumor microenvironment can influence the suppression of immune cells and anti-tumor immunity (63). Metabolic dysregulation in cancer cells can also effect cell surface expression of proteins related to immune surveillance (75, 76). Specifically, PI3K-AKT-mTOR, HIF-1α and other pathways are implicated in immunotherapy resistance (63). The TCGCA does not include chondrosarcoma but IDH1 mutations have been associated with suppressed immune response pathways based on bioinformatics analyses of TCGA transcriptomic datasets (77). Chondrosarcomas are known to escape immune surveillance through the expression of immune checkpoints and express PD-L1/PD-L2 (78). Dedifferentiated chondrosarcomas are known to have tumor lymphocyte infiltration that correlates with PD-L1 expression and HLA expression, which suggest that these tumors might be sensitive to anticancer immunotherapy (78). Clinical trials utilizing immune checkpoint inhibition are listed in **Table 3**, and trials are ongoing to investigate the addition of immune checkpoint inhibition in conjunction with other immunotherapy or other novel agents. Preclinical studies of chondrosarcomas with hypomethylating agents in combination with immunotherapy

with NY-ESO-1 and PRAME are promising (79). There is an ongoing phase I clinical trial utilizing this agent (see **Table 3**). Given the current ongoing research in sarcomas and immunotherapy (80), future directions for research may include incorporating metabolic agents in the treatment of chondrosarcoma with novel agents such as immunotherapy, T cell therapy and combination treatments.

TARGETING EXTRINSIC APOPTOSIS IN CHONDROSARCOMA

Apoptosis is the process of death and elimination of unwanted cells in the body as a normal part of growth and development. Cancer cells are known to evade apoptosis (76). Apoptosis can be mediated through the intrinsic pathway *via* BCL 2 or extrinsic pathway *via* pro-apoptotic receptors like death receptors (DR), such as DR4/DR5. INBRX-109 (a DR5 agonist) is one such pro-apoptotic receptor agonist drug that has been tested in chondrosarcoma with promising results (76, 81). Interim analysis of 12 patients with chondrosarcoma treated in the phase 1 expansion cohort with INBRX-109 showed a decrease in tumor burden by RECIST in 67% (8/12) of patients and disease control rate of 92% (11/12), and a phase 2 study is

TABLE 3 | Immunotherapy in Chondrosarcoma.

| AGENTS	STUDY DESIGN/PHASE	# of PATIENTS	PRIMARY EFFICACY ENDPOINT	REFERENCE
NY-ESO-1 specific T Cell Receptor (TCR) T Cell in Sarcoma	Phase I	n=20	Safety/Efficacy	NCT03462316
LN-145, aldesleukin	Phase II	n=80	To evaluate efficacy using ORR	NCT03449108
Pembrolizumab (anti PD-1)	Phase II	n=146	ORR	NCT02301039
Nivolumab plus Ipilimumab (anti PD-1 and anti CTLA4)	Phase II	n=40	CR and PR	NCT02982486
Toripalimab (anti PD-1)	Phase I	n=258	Safety/Efficacy	NCT0347640
Nivolumab plus ABI-009 (Nab-rapamycin)	Phase Ib	n=40	Safety, dose-escalation	NCT03190174
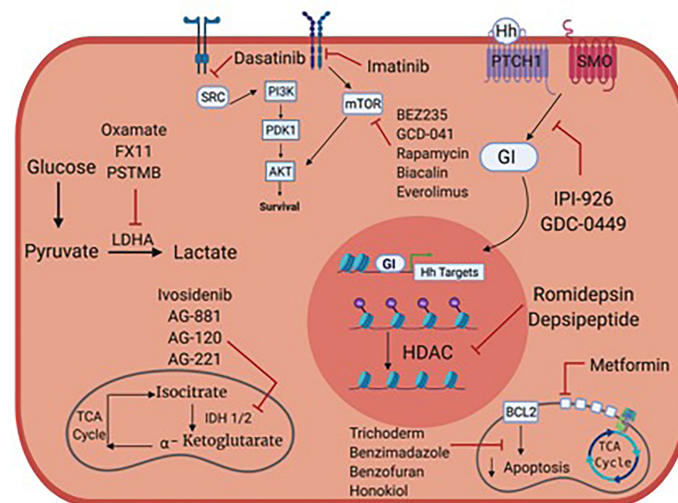
FIGURE 1 | Metabolic targets and potential therapies in chondrosarcoma.

planned. We await these results to elucidate the role of targeting apoptosis in chondrosarcoma therapy.

CONCLUSION

High grade, locally advanced and metastatic chondrosarcomas are frequently not amenable to surgery and are resistant to chemotherapy and radiation therapy. Preclinical studies focused on metabolism and/or oncogenic signaling pathways have led to clinical trials, but we still lack active anticancer agents in chondrosarcoma. **Figure 1** summarizes potential metabolic and therapeutic targets in chondrosarcoma. **Tables 1–3** list many relevant clinical therapeutic trials in chondrosarcoma. Targeting IDH mutations, lipid, glucose and mitochondrial metabolic targets, hedgehog, PI3K/Akt/MTOR, HIF and SRC pathways have yielded mixed results in clinical studies without clear therapeutic options in chondrosarcoma. While metabolic targets have been instrumental in understanding tumor development, the complex, heterogeneous roles of metabolism in chondrosarcoma likely renders mixed therapeutic results. As such, the therapy paradigm in chondrosarcoma aims to incorporate new approaches with anti-angiogenic agents and immunotherapy. Clinical trials will reveal the role of anti-angiogenic agents, immunotherapy and combination treatments and further research will be pivotal in illustrating their future therapeutic role with metabolic agents.

AUTHOR CONTRIBUTIONS

IM wrote, read and approved the final manuscript. MR edited and aided with images. MY aided in editing the manuscript and citations. UM-O wrote and edited the manuscript. AB wrote and edited the final manuscript. All authors contributed to the article and approved the submitted version.

REFERENCES

1. Dorfman HD, Czerniak B. Bone Cancers. *Cancer* (1995) 75:203–10. doi: 10.1002/1097-0142(19950101)75:1+<203::AID-CNCR2820751308>3.0.CO;2-V
2. Bovee JV, Cleton-Jansen AM, Taminiau AH, Hogendoorn PC. Emerging Pathways in the Development of Chondrosarcoma of Bone and Implications for Targeted Treatment. *Lancet Oncol* (2005) 6:599–607. doi: 10.1016/S1470-2045(05)70282-5
3. van Maldegem AM, Gelderblom H, Palmerini E, Dijkstra SD, Gambarotti M, Ruggieri P, et al. Outcome of Advanced, Unresectable Conventional Central Chondrosarcoma. *Cancer* (2014) 120:3159–64. doi: 10.1002/cncr.28845
4. Italiano A, Mir O, Cioffi A, Palmerini E, Piperno-Neumann S, Perrin C, et al. Advanced Chondrosarcomas: Role of Chemotherapy and Survival. *Ann Oncol* (2013) 24:2916–22. doi: 10.1093/annonc/mdt374
5. Biermann JS, Chow W, Reed DR, Lucas D, Adkins DR, Agulnik M, et al. NCCN Guidelines Insights: Bone Cancer, Version 2.2017. *J Natl Compr Canc Netw* (2017) 15:155–67. doi: 10.6004/jnccn.2017.0017
6. Martinez-Outschoorn UE, Peiris-Pages M, Pestell RG, Sotgia F, Lisanti MP. Cancer Metabolism: A Therapeutic Perspective. *Nat Rev Clin Oncol* (2017) 14:11–31. doi: 10.1038/nrclinonc.2016.60
7. Addie RD, de Jong Y, Alberti G, Kruisselbrink AB, Que I, Baelde H, et al. Exploration of the Chondrosarcoma Metabolome; the mTOR Pathway as an Important Pro-Survival Pathway. *J Bone Oncol* (2019) 15:100222. doi: 10.1016/j.jbo.2019.100222
8. Pirozzi CJ, Yan H. The Implications of IDH Mutations for Cancer Development and Therapy. *Nat Rev Clin Oncol* (2021) 18:645–61. doi: 10.1038/s41571-021-00521-0
9. Zhu GG, Nafa K, Agaram N, Zehir A, Benayed R, Sadowska J, et al. Genomic Profiling Identifies Association of IDH1/IDH2 Mutation With Longer Relapse-Free and Metastasis-Free Survival in High-Grade Chondrosarcoma. *Clin Cancer Res* (2020) 26:419–27. doi: 10.1158/1078-0432.CCR-18-4212
10. Jin Y, Elalaf H, Watanabe M, Tamaki S, Hineno S, Matsunaga K, et al. Mutant IDH1 Dysregulates the Differentiation of Mesenchymal Stem Cells in Association With Gene-Specific Histone Modifications to Cartilage- and Bone-Related Genes. *PloS One* (2015) 10:e0131998. doi: 10.1371/journal.pone.0131998
11. Hirata M, Sasaki M, Cairns RA, Inoue S, Puviindran V, Li WY, et al. Mutant IDH Is Sufficient to Initiate Enchondromatosis in Mice. *Proc Natl Acad Sci USA* (2015) 112:2829–34. doi: 10.1073/pnas.1424400112
12. Li L, Hu X, Eid JE, Rosenberg AE, Wilky BA, Ban Y, et al. Mutant IDH1 Depletion Downregulates Integrins and Impairs Chondrosarcoma Growth. *Cancers (Basel)* (2020) 12:141. doi: 10.3390/cancers12010141
13. Vuong HG, Ngo TNM, Dunn IF. Prognostic Importance of IDH Mutations in Chondrosarcoma: An Individual Patient Data Meta-Analysis. *Cancer Med* (2021) 10:4415–23. doi: 10.1002/cam4.4019
14. Chen C, Zhou H, Wei F, Jiang L, Liu X, Liu Z, et al. Increased Levels of Hypoxia-Inducible Factor-1alpha Are Associated With Bcl-xL Expression, Tumor Apoptosis, and Clinical Outcome in Chondrosarcoma. *J Orthop Res* (2011) 29:143–51. doi: 10.1002/jor.21193
15. Kim H, Cho Y, Kim HS, Kang D, Cheon D, Kim YJ, et al. A System-Level Approach Identifies HIF-2alpha as a Critical Regulator of Chondrosarcoma Progression. *Nat Commun* (2020) 11:5023. doi: 10.1038/s41467-020-18817-7
16. Tarade D, Ohh M. The HIF and Other Quandaries in VHL Disease. *Oncogene* (2018) 37:139–47. doi: 10.1038/onc.2017.338
17. Marinozzi A, Papapietro N, Barnaba SA, Di Martino A, Tonini G, Denaro V. Chondrosarcoma of the Iliac Wing in Von Hippel-Lindau Disease. *J Exp Clin Cancer Res* (2007) 26:599–601.
18. Song MJ, Won KY, Park S. Clear Cell Chondrosarcoma of the Talus in Von Hippel-Lindau Disease: A Rare Tumor in an Unusual Location and Uncommon Co-Presentation. *Int J Clin Exp Pathol* (2020) 13:266–71.
19. Dreijerink KMA, van Leeuwaarde RS, Hackeng WM, Giles RH, de Leng WWJ, Jutte PC, et al. Clear Cell Chondrosarcoma in Von Hippel-Lindau Disease. *Fam Cancer* (2020) 19:41–5. doi: 10.1007/s10689-019-00149-1
20. Chen C, Zhou H, Liu X, Liu Z, Ma Q. Reduced Expression of Von Hippel-Lindau Protein Correlates With Decreased Apoptosis and High Chondrosarcoma Grade. *J Bone Joint Surg Am* (2011) 93:1833–40. doi: 10.2106/JBJS.I.01553
21. Pathmanapan S, Ilkayeva O, Martin JT, Loe AKH, Zhang H, Zhang GF, et al. Mutant IDH and non-Mutant Chondrosarcomas Display Distinct Cellular Metabolomes. *Cancer Metab* (2021) 9:13. doi: 10.1186/s40170-021-00247-8
22. Peterse EFP, Niessen B, Addie RD, de Jong Y, Cleven AHG, Kruisselbrink AB, et al. Targeting Glutaminolysis in Chondrosarcoma in Context of the IDH1/2 Mutation. *Br J Cancer* (2018) 118:1074–83. doi: 10.1038/s41416-018-0050-9
23. Zhang H, Wei Q, Tsushima H, Puviindran V, Tang YJ, Pathmanapan S, et al. Intracellular Cholesterol Biosynthesis in Enchondroma and Chondrosarcoma. *JCI Insight* (2019) 5:e127232. doi: 10.1172/jci.insight.127232
24. Li L, Paz AC, Wilky BA, Johnson B, Galoian K, Rosenberg A, et al. Treatment With a Small Molecule Mutant IDH1 Inhibitor Suppresses Tumorigenic Activity and Decreases Production of the Oncometabolite 2-Hydroxyglutarate in Human Chondrosarcoma Cells. *PloS One* (2015) 10: e0133813. doi: 10.1371/journal.pone.0133813
25. Suijker J, Oosting J, Koornneef A, Struys EA, Salomons GS, Schaap FG, et al. Inhibition of Mutant IDH1 Decreases D-2-HG Levels Without Affecting Tumorigenic Properties of Chondrosarcoma Cell Lines. *Oncotarget* (2015) 6:12505–19. doi: 10.18632/oncotarget.3723
26. Xu W, Yang H, Liu Y, Yang Y, Wang P, Kim SH, et al. Oncometabolite 2-Hydroxyglutarate Is a Competitive Inhibitor of Alpha-Ketoglutarate-Dependent Dioxygenases. *Cancer Cell* (2011) 19:17–30. doi: 10.1016/j.ccr.2010.12.014

27. Grassian AR, Parker SJ, Davidson SM, Divakaruni AS, Green CR, Zhang X, et al. IDH1 Mutations Alter Citric Acid Cycle Metabolism and Increase Dependence on Oxidative Mitochondrial Metabolism. *Cancer Res* (2014) 74:3317–31. doi: 10.1158/0008-5472.CAN-14-0772-T

28. Tap WD, Villalobos VM, Cote GM, Burris H, Janku F, Mir O, et al. Phase I Study of the Mutant IDH1 Inhibitor Ivosidenib: Safety and Clinical Activity in Patients With Advanced Chondrosarcoma. *J Clin Oncol* (2020) 38:1693–701. doi: 10.1200/JCO.19.02492

29. Khurshed M, Molenaar RJ, van Linde ME, Mathot RA, Struys EA, van Wezel T, et al. A Phase Ib Clinical Trial of Metformin and Chloroquine in Patients With IDH1-Mutated Solid Tumors. *Cancers (Basel)* (2021) 13:2474. doi: 10.3390/cancers13102474

30. Snaebjornsson MT, Janaki-Raman S, Schulze A. Greasing the Wheels of the Cancer Machine: The Role of Lipid Metabolism in Cancer. *Cell Metab* (2020) 31:62–76. doi: 10.1016/j.cmet.2019.11.010

31. Ma X, Bi E, Lu Y, Su P, Huang C, Liu L, et al. Cholesterol Induces CD8(+) T Cell Exhaustion in the Tumor Microenvironment. *Cell Metab* (2019) 30:143–156 e5. doi: 10.1016/j.cmet.2019.04.002

32. Kuzu OF, Noory MA, Robertson GP. The Role of Cholesterol in Cancer. *Cancer Res* (2016) 76:2063–70. doi: 10.1158/0008-5472.CAN-15-2613

33. Kopecka J, Trouillas P, Gasparovic AC, Gazzano E, Assaraf YG, Riganti C. Phospholipids and Cholesterol: Inducers of Cancer Multidrug Resistance and Therapeutic Targets. *Drug Resist Updat* (2020) 49:100670. doi: 10.1016/j.drup.2019.100670

34. Ding X, Zhang W, Li S, Yang H. The Role of Cholesterol Metabolism in Cancer. *Am J Cancer Res* (2019) 9:219–27.

35. Porstmann T, Santos CR, Griffiths B, Cully M, Wu M, Leevers S, et al. SREBP Activity Is Regulated by Mtorc1 and Contributes to Akt-Dependent Cell Growth. *Cell Metab* (2008) 8:224–36. doi: 10.1016/j.cmet.2008.07.007

36. Tsushima H, Tang YJ, Puviindran V, Hsu SC, Nadesan P, Yu C, et al. Intracellular Biosynthesis of Lipids and Cholesterol by Scap and Insig in Mesenchymal Cells Regulates Long Bone Growth and Chondrocyte Homeostasis. *Development* (2018) 145:dev162396. doi: 10.1242/dev.162396

37. Yamashita A, Morioka M, Kishi H, Kimura T, Yahara Y, Okada M, et al. Statin Treatment Rescues FGFR3 Skeletal Dysplasia Phenotypes. *Nature* (2014) 513:507–11. doi: 10.1038/nature13775

38. Terabe K, Takahashi N, Cobb M, Askew EB, Knudson CB, Knudson W. Simvastatin Promotes Restoration of Chondrocyte Morphology and Phenotype. *Arch Biochem Biophys* (2019) 665:1–11. doi: 10.1016/j.abb.2019.01.038

39. Park JK, Coffey NJ, Limoges A, Le A. The Heterogeneity of Lipid Metabolism in Cancer. *Adv Exp Med Biol* (2021) 1311:39–56. doi: 10.1007/978-3-030-65768-0_3

40. Wilde L, Tanson K, Curry J, Martinez-Outschoorn U. Autophagy in Cancer: A Complex Relationship. *Biochem J* (2018) 475:1939–54. doi: 10.1042/BCJ20170847

41. Zeng W, Xiao T, Cai A, Cai W, Liu H, Liu J, et al. Inhibiting ROS-TFEB-Dependent Autophagy Enhances Salidroside-Induced Apoptosis in Human Chondrosarcoma Cells. *Cell Physiol Biochem* (2017) 43:1487–502. doi: 10.1159/000481971

42. Schrage YM, Machado I, Meijer D, Briaire-de Bruijn I, van den Akker BE, Taminiau AH, et al. COX-2 Expression in Chondrosarcoma: A Role for Celecoxib Treatment? *Eur J Cancer* (2010) 46:616–24. doi: 10.1016/j.ejca.2009.11.002

43. Sweeney C, Mackintosh D, Mason RM. UDP-Sugar Metabolism in Swarm Rat Chondrosarcoma Chondrocytes. *Biochem J* (1993) 290(Pt 2):563–70. doi: 10.1042/bj2900563

44. Lee HP, Lin CY, Shih JS, Fong YC, Wang SW, Li TM, et al. Adiponectin Promotes VEGF-A-Dependent Angiogenesis in Human Chondrosarcoma Through PI3K, Akt, mTOR, and HIF-Alpha Pathway. *Oncotarget* (2015) 6:36746–61. doi: 10.18632/oncotarget.5479

45. Zhang J, Zhou F, Wu X, Zhang X, Chen Y, Zha BS, et al. Cellular Pharmacokinetic Mechanisms of Adriamycin Resistance and its Modulation by 20(S)-Ginsenoside Rh2 in MCF-7/Adr Cells. *Br J Pharmacol* (2012) 165:120–34. doi: 10.1111/j.1476-5381.2011.01505.x

46. Hua G, Liu Y, Li X, Xu P, Luo Y. Targeting Glucose Metabolism in Chondrosarcoma Cells Enhances the Sensitivity to Doxorubicin Through the Inhibition of Lactate Dehydrogenase-A. *Oncol Rep* (2014) 31:2727–34. doi: 10.3892/or.2014.3156

47. Song YD, Zhang KF, Liu D, Guo YQ, Wang DY, Cui MY, et al. Inhibition of EGFR-Induced Glucose Metabolism Sensitizes Chondrosarcoma Cells to Cisplatin. *Tumour Biol* (2014) 35:7017–24. doi: 10.1007/s13277-014-1902-4

48. Kim EY, Chung TW, Han CW, Park SY, Park KH, Jang SB. And Ha KT. A Novel Lactate Dehydrogenase Inhibitor, 1-(Phenylseleno)-4-(Trifluoromethyl) Benzene, Suppresses Tumor Growth Through Apoptotic Cell Death. *Sci Rep* (2019) 9:3969. doi: 10.1038/s41598-019-40617-3

49. Tiet TD, Hopyan S, Nadesan P, Gokgoz N, Poon R, Lin AC, et al. Constitutive Hedgehog Signaling in Chondrosarcoma Up-Regulates Tumor Cell Proliferation. *Am J Pathol* (2006) 168:321–30. doi: 10.2353/ajpath.2006.050001

50. Chen YJ, Kuo CD, Chen SH, Chen WJ, Huang WC, Chao KS, et al. Small-Molecule Synthetic Compound Norcantharidin Reverses Multi-Drug Resistance by Regulating Sonic Hedgehog Signaling in Human Breast Cancer Cells. *PLoS One* (2012) 7:e37006. doi: 10.1371/journal.pone.0037006

51. Campbell VT, Nadesan P, Ali SA, Wang CY, Whetstone H, Poon R, et al. Hedgehog Pathway Inhibition in Chondrosarcoma Using the Smoothened Inhibitor IPI-926 Directly Inhibits Sarcoma Cell Growth. *Mol Cancer Ther* (2014) 13:1259–69. doi: 10.1158/1535-7163.MCT-13-0731

52. Xiang W, Jiang T, Guo F, Gong C, Yang K, Wu Y, et al. Hedgehog Pathway Inhibitor-4 Suppresses Malignant Properties of Chondrosarcoma Cells by Disturbing Tumor Ciliogenesis. *Oncol Rep* (2014) 32:1622–30. doi: 10.3892/or.2014.3372

53. Su CM, Wang SW, Lee TH, Tzeng WP, Hsiao CJ, Liu SC, et al. Trichodermin Induces Cell Apoptosis Through Mitochondrial Dysfunction and Endoplasmic Reticulum Stress in Human Chondrosarcoma Cells. *Toxicol Appl Pharmacol* (2013) 272:335–44. doi: 10.1016/j.taap.2013.06.010

54. Zhang YX, van Oosterwijk JG, Sicinska E, Moss S, Remillard SP, van Wezel T, et al. Functional Profiling of Receptor Tyrosine Kinases and Downstream Signaling in Human Chondrosarcomas Identifies Pathways for Rational Targeted Therapy. *Clin Cancer Res* (2013) 19:3796–807. doi: 10.1158/1078-0432.CCR-12-3647

55. Mazzoletti M, Bortolin F, Brunelli L, Pastorelli R, Di Giandomenico S, Erba E, et al. Combination of PI3K/mTOR Inhibitors: Antitumor Activity and Molecular Correlates. *Cancer Res* (2011) 71:4573–84. doi: 10.1158/0008-5472.CAN-10-4322

56. Quek R, Wang Q, Morgan JA, Shapiro GI, Butrynski JE, Ramaiya N, et al. Combination mTOR and IGF-1R Inhibition: Phase I Trial of Everolimus and Figitumumab in Patients With Advanced Sarcomas and Other Solid Tumors. *Clin Cancer Res* (2011) 17:871–9. doi: 10.1158/1078-0432.CCR-10-2621

57. Zhu M, Ying J, Lin C, Wang Y, Huang K, Zhou Y, et al. Baicalin Induces Apoptotic Death of Human Chondrosarcoma Cells Through Mitochondrial Dysfunction and Downregulation of the PI3K/Akt/mTOR Pathway. *Planta Med* (2019) 85:360–9. doi: 10.1055/a-0791-1049

58. Perez J, Decouvelaere AV, Pointecouteau T, Pissaloux D, Michot JP, Besse A, et al. Inhibition of Chondrosarcoma Growth by mTOR Inhibitor in an *In Vivo* Syngeneic Rat Model. *PLoS One* (2012) 7:e32458. doi: 10.1371/journal.pone.0032458

59. Hoxhaj G, Manning BD. The PI3K-AKT Network at the Interface of Oncogenic Signalling and Cancer Metabolism. *Nat Rev Cancer* (2020) 20:74–88. doi: 10.1038/s41568-019-0216-7

60. Kubo T, Sugita T, Shimose S, Matsuo T, Arihiro K, Ochi M. Expression of Hypoxia-Inducible Factor-1alpha and its Relationship to Tumour Angiogenesis and Cell Proliferation in Cartilage Tumours. *J Bone Joint Surg Br* (2008) 90:364–70. doi: 10.1302/0301-620X.90B3.19806

61. Boeuf S, Bovee JV, Lehner B, Hogendoorn PC, Richter W. Correlation of Hypoxic Signalling to Histological Grade and Outcome in Cartilage Tumours. *Histopathology* (2010) 56:641–51. doi: 10.1111/j.1365-2559.2010.03528.x

62. Chiu YC, Shieh DC, Tong KM, Chen CP, Huang KC, Chen PC, et al. Involvement of AdipoR Receptor in Adiponectin-Induced Motility and Alpha2beta1 Integrin Upregulation in Human Chondrosarcoma Cells. *Carcinogenesis* (2009) 30:1651–9. doi: 10.1093/carcin/bgp156

63. Wilde L, Roche M, Domingo-Vidal M, Tanson K, Philp N, Curry J, et al. Metabolic Coupling and the Reverse Warburg Effect in Cancer: Implications for Novel Biomarker and Anticancer Agent Development. *Semin Oncol* (2017) 44:198–203. doi: 10.1053/j.seminoncol.2017.10.004

64. Liu GT, Chen HT, Tsou HK, Tan TW, Fong YC, Chen PC, et al. CCL5 Promotes VEGF-Dependent Angiogenesis by Down-Regulating miR-200b

Through PI3K/Akt Signaling Pathway in Human Chondrosarcoma Cells. *Oncotarget* (2014) 5:10718–31. doi: 10.18632/oncotarget.2532

65. Sakimura R, Tanaka K, Yamamoto S, Matsunobu T, Li X, Hanada M, et al. The Effects of Histone Deacetylase Inhibitors on the Induction of Differentiation in Chondrosarcoma Cells. *Clin Cancer Res* (2007) 13:275–82. doi: 10.1158/1078-0432.CCR-06-1696

66. Chow W, Frankel P, Ruel C, Araujo DM, Milhem M, Okuno S, et al. Results of a Prospective Phase 2 Study of Pazopanib in Patients With Surgically Unresectable or Metastatic Chondrosarcoma. *Cancer* (2020) 126:105–11. doi: 10.1002/cncr.32515

67. van Oosterwijk JG, van Ruler MA, Briaire-de Bruijn IH, Herpers B, Gelderblom H, van de Water B, et al. Src Kinases in Chondrosarcoma Chemoresistance and Migration: Dasatinib Sensitises to Doxorubicin in TP53 Mutant Cells. *Br J Cancer* (2013) 109:1214–22. doi: 10.1038/bjc.2013.451

68. Chow WA. Chondrosarcoma: Biology, Genetics, and Epigenetics. *F1000Res* (2018) 7(F1000 Faculty Rev):1826. doi: 10.12688/f1000research.15953.1

69. Sheikh TN, Patwardhan PP, Cremers S, Schwartz GK. Targeted Inhibition of Glutaminase as a Potential New Approach for the Treatment of NF1 Associated Soft Tissue Malignancies. *Oncotarget* (2017) 8:94054–68. doi: 10.18632/oncotarget.21573

70. Liou GY, Storz P. Reactive Oxygen Species in Cancer. *Free Radic Res* (2010) 44:479–96. doi: 10.3109/10715761003667554

71. Su CM, Chen CY, Lu T, Sun Y, Li W, Huang YL, et al. A Novel Benzofuran Derivative, ACDB, Induces Apoptosis of Human Chondrosarcoma Cells Through Mitochondrial Dysfunction and Endoplasmic Reticulum Stress. *Oncotarget* (2016) 7:83530–43. doi: 10.18632/oncotarget.13171

72. Chen YJ, Wu CL, Liu JF, Fong YC, Hsu SF, Li TM, et al. Honokiol Induces Cell Apoptosis in Human Chondrosarcoma Cells Through Mitochondrial Dysfunction and Endoplasmic Reticulum Stress. *Cancer Lett* (2010) 291:20–30. doi: 10.1016/j.canlet.2009.08.032

73. Li TM, Lin TY, Hsu SF, Wu CM, Su YC, Kao ST, et al. The Novel Benzimidazole Derivative, MPTB, Induces Cell Apoptosis in Human Chondrosarcoma Cells. *Mol Carcinog* (2011) 50:791–803. doi: 10.1002/mc.20749

74. Roche ME, Lin Z, Whitaker-Menezes D, Zhan T, Szuhai K, Bovee J, et al. Translocase of the Outer Mitochondrial Membrane Complex Subunit 20 (TOMM20) Facilitates Cancer Aggressiveness and Therapeutic Resistance in Chondrosarcoma. *Biochim Biophys Acta Mol Basis Dis* (2020) 1866:165962. doi: 10.1016/j.bbadis.2020.165962

75. Ramapriyan R, Caetano MS, Barsoumian HB, Mafra ACP, Zambalde EP, Menon H, et al. Altered Cancer Metabolism in Mechanisms of Immunotherapy Resistance. *Pharmacol Ther* (2019) 195:162–71. doi: 10.1016/j.pharmthera.2018.11.004

76. Ashkenazi A. Directing Cancer Cells to Self-Destruct With Pro-Apoptotic Receptor Agonists. *Nat Rev Drug Discovery* (2008) 7:1001–12. doi: 10.1038/nrd2637

77. Unruh D, Zewde M, Buss A, Drumm MR, Tran AN, Scholtens DM, et al. Methylation and Transcription Patterns Are Distinct in IDH Mutant Gliomas Compared to Other IDH Mutant Cancers. *Sci Rep* (2019) 9:8946. doi: 10.1038/s41598-019-45346-1

78. Kostine M, Cleven AH, de Miranda NF, Italiano A, Cleton-Jansen AM, Bovee JV. Analysis of PD-L1, T-Cell Infiltrate and HLA Expression in Chondrosarcoma Indicates Potential for Response to Immunotherapy Specifically in the Dedifferentiated Subtype. *Mod Pathol* (2016) 29:1028–37. doi: 10.1038/modpathol.2016.108

79. Pollack SM, Li Y, Blaisdell MJ, Farrar EA, Chou J, Hoch BL, et al. NYESO-1/LAGE-1s and PRAME Are Targets for Antigen Specific T Cells in Chondrosarcoma Following Treatment With 5-Aza-2-Deoxycitabine. *PloS One* (2012) 7:e32165. doi: 10.1371/journal.pone.0032165

80. Heymann MF, Schiavone K, Heymann D. Bone Sarcomas in the Immunotherapy Era. *Br J Pharmacol* (2021) 178:1955–72. doi: 10.1111/bph.14999

81. Li B, Li G, Yan X, Zhu D, Lin PP, Wang Z, et al. Fresh Tissue Multi-Omics Profiling Reveals Immune Classification and Suggests Immunotherapy Candidates for Conventional Chondrosarcoma. *Clin Cancer Res* (2021) CCR-21-1893. doi: 10.1158/1078-0432.CCR-21-1893

frontiers | Frontiers in Oncology

Lactate Induces the Expressions of MCT1 and HCAR1 to Promote Tumor Growth and Progression in Glioblastoma

Lucia Longhitano[1][†], Nunzio Vicario[1][†], Daniele Tibullo[1*][†], Cesarina Giallongo[2],
Giuseppe Broggi[2], Rosario Caltabiano[2], Giuseppe Maria Vincenzo Barbagallo[3,4],
Roberto Altieri[3,4], Marta Baghini[5], Michelino Di Rosa[1], Rosalba Parenti[1],
Antonio Giordano[6], Maria Caterina Mione[5‡] and Giovanni Li Volti[1*‡]

[1] Department of Biomedical and Biotechnological Sciences, University of Catania, Catania, Italy, [2] Department of Medical and Surgical Sciences and Advanced Technologies "G.F. Ingrassia", Catania, Italy, [3] Department of Medical and Surgical Sciences and Advanced Technologies "G.F. Ingrassia" Neurological Surgery, Policlinico "G. Rodolico-San Marco" University Hospital, University of Catania, Catania, Italy, [4] Interdisciplinary Research Center on Brain Tumors Diagnosis and Treatment, University of Catania, Catania, Italy, [5] Department of Cellular, Computational and Integrative Biology (CIBIO), University of Trento, Trento, Italy, [6] Sbarro Institute for Cancer Research and Molecular Medicine and Center of Biotechnology, College of Science and Technology, Temple University, Philadelphia, PA, United States

The tumor microenvironment (TME) plays a pivotal role in establishing malignancy, and it is associated with high glycolytic metabolism and lactate release through monocarboxylate transporters (MCTs). Several lines of evidence suggest that lactate also serves as a signaling molecule through its receptor hydroxycarboxylic acid receptor 1 (HCAR1/GPR81), thus functioning as a paracrine and autocrine signaling molecule. The aim of the present study was to investigate the role of lactate in glioblastoma (GBM) progression and metabolic reprogramming in an *in vitro* and *in vivo* model. The cell proliferation, migration, and clonogenicity were tested *in vitro* in three different human GBM cell lines. The expressions of *MCT1*, *MCT4*, and *HCAR1* were evaluated both *in vitro* and in a zebrafish GBM model. The results were further validated in patient-derived GBM biopsies. Our results showed that lactate significantly increased the cell proliferation, migration, and colony formation capacity of GBM cells, both *in vitro* and *in vivo*. We also showed that lactate increased the expressions of *MCT1* and *HCAR1*. Moreover, lactate modulated the epithelial–mesenchymal transition protein markers E-cadherin and β-catenin. Interestingly, lactate induced mitochondrial mass and the *OXPHOS* gene, suggesting improved mitochondrial fitness. Similar effects were observed after treatment with 3,5-dihydroxybenzoic acid, a known agonist of *HCAR1*. Consistently, the GBM zebrafish model exhibited an altered metabolism and increased expressions of *MCT1* and *HCAR1*,

leading to high levels of extracellular lactate and, thus, supporting tumor cell proliferation. Our data from human GBM biopsies also showed that, in high proliferative GBM biopsies, Ki67-positive cells expressed significantly higher levels of *MCT1* compared to low proliferative GBM cells. In conclusion, our data suggest that lactate and its transporter and receptor play a major role in GBM proliferation and migration, thus representing a potential target for new therapeutic strategies to counteract tumor progression and recurrence.

INTRODUCTION

Glioblastoma (GBM) represents the most common primary brain tumor in the adult population and is classified by the WHO as grade IV glioma. Current therapeutic approaches for newly diagnosed GBM include surgical resection, radiotherapy, and chemotherapy (i.e., temozolomide) (1). However, despite aggressive therapeutic regimens, these tumors still have a dismal prognosis, with median overall survival of 12–15 months. Histologically, GBM is a highly cellular glioma composed of glial cells with significant pleomorphism and nuclear atypia (2). Such cellular features are coupled with microvascular proliferation and palisading necrosis characterized by regular areas of necrosis and dense accumulation of GBM cells (2). The characteristics of GBM are related to cell proliferation, usually assessed by evaluating Ki67-expressing cells classified into high proliferative index (HPI; Ki67-positive cells >30%) and low proliferative index (LPI; Ki67-positive cells <30%). Furthermore, the proliferation, migration, and invasiveness of GBM cells are closely related to the availability of blood-derived nutrients and oxygen. Indeed, two niches have been described in GBM in relation to the availability of oxygen: the so-called perivascular niche, in which GBM cells receive glucose and oxygen from the bloodstream and oxidative phosphorylation in these cells determines a highly efficient metabolism, and the GBM hypoxic niche at the tumor core, in which low oxygen levels shape the metabolism toward a glycolytic state, inducing lactate accumulation (3). Indeed, such tumors have a rapid rate of glucose consumption and convert large amounts of glucose into lactic acid, even in the presence of oxygen (4). This metabolic phenotype, known as the Warburg effect, contrasts sharply with that observed in normal tissues, in which glycolysis occurs mainly in hypoxic conditions (5).

To maintain an enhanced glycolytic flow, GBMs require the rapid outflow of lactic acid into the tumor microenvironment (TME), facilitated by a series of plasma membrane transporters called monocarboxylate transporters (MCTs) (6); among these, only four (MCT1–4) are known to play a role in lactic acid transport in mammalian tissues, including cancers (7), and *MCT1* and *MCT4* have been implicated in multiple aspects of GBM progression, including angiogenesis, cell proliferation, and immunity modulation (8). Glycolytic cancer cells are known to upregulate lactate export by increasing the expression of *MCT4* to better adapt to lactate accumulation. In contrast, tumor cells of oxidative tumors have been reported to upregulate the expression of *MCT1* to mediate the uptake of lactate from the extracellular environment in order to fuel metabolism (9). A recent report has suggested that this dynamic arrangement may create a metabolic symbiosis between the two GBM subpopulations, maintaining a favorable environment for both subtypes (8, 10).

Besides having a role as an end-product metabolite of glycolysis and being utilized by cellular metabolic programs to produce energy, lactate also acts as a signaling molecule through its receptor hydroxycarboxylic acid receptor 1 (*HCAR1*; also known as G-protein-coupled receptor GPR81) (11). Therefore, extracellular lactate is not a simple bystander causing milieu acidification; it also serves as a paracrine and autocrine signaling molecule in the TME (12). An elevated expression of *HCAR1* was found in carcinomas of the breast, pancreas, and cervix, despite negligible expression in the corresponding benign epithelium (12, 13). Several groups have identified autocrine roles for *HCAR1* in the TME, where lactate produced by tumor cells activates *HCAR1* and confers cancer-promoting phenotypes (14), including the upregulation of the transporters *MCT1* and *MCT4* and the secretion of factors that promote angiogenesis and tumor progression (15). The aim of the present study was to assess the role of lactate metabolism in cancer growth and progression in several GBM cell lines in pathological specimens and in an *in vivo* model.

MATERIALS AND METHODS

GBM Cell Lines

Human GBM cell lines (U87-MG, A172, and U251) were purchased from ATCC Company (Milan, Italy). Cells were suspended in Dulbecco's modified Eagle's medium (DMEM) (cat. no. 11965092) containing 10% fetal bovine serum (FBS) (cat. no. 10082147), 100 U/ml penicillin, and 100 U/ml streptomycin (cat. no. 15070063; all from Gibco, Waltham, MA, USA). At 80% confluency, cells were passaged using trypsin–EDTA solution (0.05% trypsin and 0.02% EDTA; cat. no. 25300054, Gibco, Waltham, MA, USA).

Sodium lactate and 3,5-dihydroxybenzoic acid (3,5-DHBA) (both from Sigma-Aldrich, Milan, Italy) were added into the cell culture of all experiments at final concentrations of 20 mM and 150 µM, respectively, for 24, 48, and 72 h.

Clonogenic Assay and Surviving Fraction

The clonogenic assay was performed with the Operetta High-Content Screening (HCS) System (PerkinElmer, Waltham, MA, USA) and the surviving fractions obtained as previously described (16, 17). Briefly, colony assays were performed by seeding cells in 6-well plates at a low density (2,000 cells/well) and allowing growth for 10 days. Colonies were fixed and incubated with 0.05% crystal violet diluted in 20% ethanol for 30 min at room temperature. They were then quantified with the Operetta HCS System (Perkin-Elmer) and the surviving fraction obtained normalizing the counted colonies over the total plated cells, which was expressed as the percentage of control assumed as 100%. Each experiment was performed in quadruplicate.

Real-Time Monitoring of Cell Proliferation

xCELLigence experiments were performed using the Real-Time Cell Analysis (RTCA) dual plate (DP) instrument according to the manufacturers' instructions (Roche Applied Science, Mannheim, Germany, and ACEA Biosciences, San Diego, CA, USA). The RTCA DP Instrument includes three main components: i) RTCA DP analyzer, which is placed inside a humidified incubator maintained at 37°C and 5% CO_2; ii) RTCA control unit with the preinstalled RTCA software; and iii) E-Plate 16 for the proliferation assay. Firstly, the optimal seeding number was determined by cell titration and growth experiments. After seeding the optimal cell number (3,000 cells/well), the cells were treated and automatically monitored every 15 min for 24 h. The optimal cell number was determined in a preliminary set of experiments (data not shown) to obtain a significant cell index value and a constant cell growth during the entire duration of the experiment.

Cell Migration

Cell migration was examined by employing the wound healing assay. Briefly, the cells were seeded in 24-well dishes and cultured until confluence. Then, they were treated with vehicle, lactate, or 3,5-DHBA, scraped with a 200-µl micropipette tip, and monitored at 0, 24, and 48 h. The uncovered wound area was measured and quantified at different intervals with ImageJ v1.37 (NIH, Bethesda, MD, USA).

Immunoblotting

Briefly, for Western blot analysis, 30 µg of protein was loaded onto a 12% polyacrylamide gel, MiniPROTEAN® TGXTM (Bio-Rad, Milan, Italy), followed by electrotransfer to a nitrocellulose membrane, TransBlot® TurboTM, using TransBlot® SE Semi-Dry Transfer Cell (both from Bio-Rad, Milan, Italy) (18). Subsequently, the membrane was blocked in Odyssey Blocking Buffer (Licor, Milan, Italy) for 1 h at room temperature. After blocking, the membrane was washed three times in phosphate-buffered saline (PBS) for 5 min and incubated with primary antibodies against MCT1 (1:1,000; AB90582), MCT4 (1:1,000; AB74109), β-catenin (1:500; AB16051), E-cadherin (1:500; AB76055, all from Abcam, Cambridge, UK), and β-actin (1:1,000; anti-mouse, cat. no. 4967S; Cell Signalling Technology, Milan, Italy) overnight at 4°C. The next day, the membranes were washed three times in PBS for 5 min and incubated with infrared anti-mouse IRDye800CW (1:5,000) and anti-rabbit IRDye700CW secondary antibodies (1:5,000) in PBS/0.5% Tween-20 for 1 h at room temperature. All antibodies were diluted in Odyssey Blocking Buffer. The blots were visualized using Odyssey Infrared Imaging Scanner (Licor, Milan, Italy), and the protein levels were quantified by densitometric analysis. Data were normalized to the expression of β-actin.

Real-Time RT-PCR for Gene Expression Analysis

RNA was extracted using Trizol® reagent (Invitrogen, Carlsbad, CA, USA) (19). First-strand complementary DNA (cDNA) was then synthesized with a reverse transcription reagent from Applied Biosystems (Foster City, CA, USA). Quantitative real-time PCR (qRT-PCR) was performed in StepOne Fast Real-Time PCR System (Applied Biosystems) using the SYBR Green PCR MasterMix (Life Technologies, Monza, Italy) (20). The specific PCR products were detected with SYBR Green fluorescence. The relative messenger RNA (mRNA) expression level was calculated by the threshold cycle (C_t) value of each PCR product and normalized with that of actin using a comparative $2^{-\Delta\Delta Ct}$ method. The sequences of the primers used are presented in **Table 1**.

TABLE 1 | Genes of interest.

Genes	Forward primer (5′⟶3′)	Reverse primer (5′⟶3′)
PGC1α	ATGAAGGGTACTTTTCTGCCCC	GGTCTTCACCAACCAGAGCA
SIRT1	AGGCCACGGATAGGTCCATA	GTGGAGGTATTGTTTCCGGC
TFAM	CCGAGGTGGTTTTCATCTGT	AGTCTTCAGCTTTTCCTGCG
ND4	CCAGTGGAATGCCTTGCCTA	TTGATCGCGGTGAGATTCCC
CyB	ACGAGCCACCGAAACAGAAT	ACGATTTTCGCCAGTCACCT
COX II	ACGACCTCGATGTTGGATCA	ATCATTTACGGGGGAAGGCG
COX IV	GCGGCAGAATGTTGGCTAC	AGACAGGTGCTTGACATGGG
ATP synthase	CCGCCTTCCGCGGGTATAATC	ATGTACGCGGGCAATACCAT
MCT1	TGTTGTTGCAAATGGAGTGT	AAGTCGATAATTGATGCCCATGCCAA
MCT4	TATCCAGATCTACCTCACCAC	GGCCTGGCAAAGATGTCGATGA
HCAR1	TTCGTATTTGGTGGCAGGCA	TTTCGAGGGGTCCAGGTACA
β-Actin	CCTTTGCCGATCCGCCG	AACATGATCTGGGTCATCTTCTCGC

Zebrafish Model

Adult zebrafish (*Danio rerio*) were housed in the Model Organism Facility—Center for Integrative Biology (CIBIO), University of Trento, and maintained under standard conditions (21). All zebrafish studies were performed according to European and Italian laws (D.Lgs. 26/2014, authorization 148/2018-PR to M.C. Mione). Fishes with somatic and germline expression of oncogenic HRAS were generated as described (22, 23). The following zebrafish transgenic lines were used in the course of this study: *Et(zic4: Gal4TA4, UAS:mCherry)$_{hzm5}$*, called zic:Gal4 (22), and *Tg(UAS: eGFP-HRAS_G12V)$_{io006}$*, called UAS : RAS (23). The characterization of the GBM model is described in detail in Mayrhofer et al. (22).

Gene Expression Analysis

Analysis of the expressions of the genes involved in glycolysis in zebrafish brain tumors was performed on previously generated data (GSE74754; https://www.ncbi.nlm.nih.gov/geo/query/acc. cgi?acc=GSE74754). A heatmap was generated using the web application Heatmapper (http://www.heatmapper.ca/).

For the gene expression analysis of further samples, total RNA was extracted from larval heads and brains/tumors with the TRIzol reagent (Invitrogen). Total RNA was cleaned up using the RNeasy Mini Kit (Qiagen, Hilden, Germany) following the manufacturer's instructions and treated twice with DNase I (1 U/μg RNA; Qiagen). The RNA concentration was quantified using NanoDrop 2000 (Thermo Fisher, Waltham, MA, USA), and VILO SuperScript Kit (Thermo Fisher) was used for first-strand cDNA synthesis performed according to the manufacturer's protocol. qRT-PCR analysis was performed using the qPCRBIO SyGreen Mix (Resnova–PCR Biosystem, Rome, Italy) following a standard amplification protocol. The primers used were as follows: for zebrafish *mct1*: forward 5′-GTC ACCATTGTGGAATGTGC-3′ and reverse 5′-TCATCATAG ATATCGTTGAGTCGTC-3′; for zebrafish *hcar1*: forward 5′-CATCGTCATCTACTGCTCCAC-3′ and reverse 5′-GCTAACACAAACCGCACA-3′; and for zebrafish *rps11* (housekeeping): forward 5′-ACAGAAATGCCCCTTCACTG-3′ and reverse: 5′-GCCTCTTCTCAAAACGGTTG-3′. RT-PCR was performed with a CFX96 Real-Time PCR Detection System (Bio-Rad) machine. Quantitative PCR analysis was performed with Microsoft Excel and GraphPad Prism. In all cases, each PCR was performed with triplicate samples and repeated with at least two independent samples.

Immunofluorescence in Zebrafish

Adult zebrafish resulting from crosses between zic:Gal4 and UAS: RAS, or from the somatic expression of UAS : RAS (22), were screened under a fluorescent stereomicroscope for the presence of GFP-HRAS[G12V] brain masses. Positive fish (over 90% of screened fish) were sacrificed by an overdose of MS222 and their brains removed, fixed, and sectioned as previously described (22).

The sections were then washed in PBS (pH 7.4) and incubated with primary antibodies diluted in PBS containing 5% normal goat serum and 0.1% Triton X-100 at 4°C overnight. The antibodies used and their dilutions were as follows: MCT1 (1:100), HCAR1 (1:100), and phospho-histone 3 (1:1,000; all from Abcam, Cambridge, UK). A secondary antibody conjugated with Alexa 546 (1:250; Abcam) was used for 2 h at room temperature, and the nuclei were counterstained with DAPI. Images were acquired using an inverted Leica TSP8 confocal microscope. For whole-mount immunofluorescence of 5-day post-fertilization (dpf) zebrafish, the larvae of the zic:Gal4 line (controls) or zic:Gal4 × UAS : RAS line (tumor) were treated with 20 mM lactate or 10 mM AZ3965 in 1% dimethyl sulfoxide (DMSO) in E3, or with 1% DMSO alone. Solutions with the drugs were changed every day starting at 1 dpf until 5 dpf, when the larvae were culled by anesthetic overdose, fixed in 4% paraformaldehyde (PFA) for 2–12 h at 4 C, their brains carefully removed under a stereomicroscope and processed with Ph3 antibody, and diluted 1:1,000 in 5% normal goat serum (NGS) and 0.5% Triton X100 in PBS overnight. A secondary antibody conjugated with Alexa 546 was used for 6 h at room temperature. Images were acquired using an inverted Leica TSP8 confocal microscope after equilibrating the brains in 100% glycerol.

Seahorse on Zebrafish

For Seahorse analysis, tumors from adult fish or control brains were dissociated with a pipette tip in the assay medium provided by the manufacturer, passed through a 40-mM sieve, and counted. A total of 50,000 cells were seeded on poly-D-lysin-coated Seahorse XFP plates and incubated for 20 min in the absence of CO_2 before adding medium up to a final volume of 180 μl. The XF Mito Stress Test kit including oligomycin, carbonyl cyanide *p*-trifluoromethoxyphenylhydrazone (FCCP), rotenone A, and UK5099 was obtained from Seahorse Bioscience, Inc. (Billerica, MA, USA). The XFp cell culture plates, sensor cartridges, and XF base medium were also purchased from Seahorse Bioscience, Inc. The Agilent Seahorse XFp Sensor Cartridge was hydrated in the Agilent Seahorse XF Calibrant at 28°C in a non-CO_2 incubator overnight. Zebrafish brain tumor cells were plated in the Agilent Seahorse XFp Cell Culture Miniplate at the desired density (50,000 per well) using the appropriate cell culture growth medium. We added 1× PBS to the chambers to prevent evaporation of the culture medium. Within 1 h from plating, the Agilent Seahorse XFp Cell Culture Miniplate was placed into a 28°C non-CO_2 incubator for 1 h prior to the assay (24).

For the Mito Stress test, the assay medium was prepared by supplementing the Agilent Seahorse XF base medium with 1 mM pyruvate, 2 mM glutamine, and 10 mM glucose, bringing the pH to 7.4 with 0.1 N NaOH. The cells were placed in a 28°C incubator without CO_2. Oligomycin (final concentration, 2.5 μM), FCCP (final concentration, 2 μM), and rotenone A (final concentration, 0.5 μM) were diluted in the assay medium following the user guide for the Agilent Seahorse XFp Mito

Stress test and then loaded into ports B, C, and D, respectively. In port A, we placed either the assay medium, lactate (final concentration, 20 mM), AZ3965 (final concentration, 10 µM), or UK5099 (final concentration, 2 µM). The machine was calibrated at 28°C, and the assay was performed using the acute Mito Stress test assay protocol as suggested by the manufacturer (Seahorse Bioscience, Inc., Billerica, MA, USA). The oxygen consumption rate (OCR) was measured under basal conditions and after injection of the assay medium (control), lactate, UK5099, or AZ3965, followed by the sequential addition of oligomycin, FCCP, and rotenone/antimycin A. All Seahorse data (at least 3 biological replicates) were normalized to the total number of cells and counted by nuclear DAPI staining following the assay. The XF reports of the Mito Stress data were analyzed with the freeware Wave and exported to Excel and Prism for further analysis and visualization.

Glioblastoma Biopsies

Formalin-fixed and paraffin-embedded (FFPE) tissue specimens from 10 patients affected by GBM were obtained from the surgical pathology files at the Anatomic Pathology, Department G.F. Ingrassia, University of Catania, Catania, Italy. Multiple sections (at least 5) were obtained from FFPE tissue specimens. Due to the retrospective nature of the study, no written informed consent was obtained from the patients. The study included 6 male and 4 female patients (mean age = 61 years, range = 41–81 years). The study was conducted according to the guidelines of the Declaration of Helsinki and approved by the Catania 1 Ethics Committee, Catania, Italy (protocol code: 166/2015/PO; 17/12/2015). According to the WHO criteria, the histological diagnosis of GBM was rendered in the presence of the following morphological criteria: i) high-grade glioma with astrocytic morphology; ii) diffuse growth pattern; and iii) foci of necrosis and/or microvascular proliferation.

Immunohistochemical Analysis

Sections were processed as previously described (25). Thereafter, they were incubated overnight at 4°C with rabbit polyclonal anti-MCT1 antibody (Sigma, Milan, Italy), ready-to-use PBS (Sigma, Milan, Italy), and MIB-1, a monoclonal antibody directed against the Ki67 antigen (M7240; Dako Corporation, Glostrup, Denmark), and diluted 1:75 in PBS. The secondary antibody, biotinylated anti-rabbit antibody, was applied for 30 min at room temperature, followed by the avidin–biotin–peroxidase complex (Vector Laboratories, Burlingame, CA, USA) for a further 30 min at room temperature. The immunoreaction was visualized by incubating the sections for 4 min in 0.1% 3,3′-diaminobenzidine (DAB) and 0.02% hydrogen peroxide solution (DAB substrate kit; Vector Laboratories, Burlingame, CA, USA). The sections were lightly counterstained with Mayer's hematoxylin (Histolab Products AB, Göteborg, Sweden) mounted in glycerol vinyl alcohol (GVA) mounting medium (Zymed Laboratories, San Francisco, CA, USA) and observed with a Zeiss Axioplan light microscope (Carl Zeiss, Oberkochen, Germany). MCT1 staining (both nuclear and cytoplasmic) was semi-quantitatively evaluated according to a 0 to 3 scale of intensity of staining

(IS) and to the percentage of positively stained cells [extent score (ES) on a five-tier system: <5%, 5%–30%, 31%–50%, 51%–75%, and >75%].

The immunohistochemical expression of MIB-1 was assessed as low if positive in less than 50% of neoplastic cells and as high if positive in more than 50% of neoplastic cells.

Human Gene Expression
Dataset Selection

The NCBI Gene Expression Omnibus (GEO) database (http://www.ncbi.nlm.nih.gov/geo/) (26) was used to select transcriptome datasets of interest. The mesh terms "human," "glioblastoma," and "tumor grade" were used to identify the datasets. We sorted the datasets by the number of samples (from high to low), age, and sex of the participants and by the clinical data made available by the authors. We selected the GSE108474 dataset (27) over the others available for the number of subjects recruited (541), for the availability of clinical data (tumor staging), and for the variety of tumors analyzed (GBM, oligodendrocytoma, astrocytoma, and normal subjects).

Data Processing, Experimental Design, and Statistics

For statistical analyses, a two-tailed unpaired Student's t-test was used for the comparison of two groups. For the comparison of three or more groups, one-way analysis of variance (ANOVA) followed by Bonferroni *post-hoc* test for multiple comparisons was used. Data are presented as the mean ± SEM of biological replicates. Data analysis was performed using GraphPad Prism software, version 5.00. A value of $p < 0.05$ was considered statistically significant (the symbols used to indicate statistical differences are described in the figure legends).

To process and identify significant differentially expressed genes (SDEGs) within the datasets, we used the MultiExperiment Viewer (MeV) software [The Institute for Genomic Research (TIGR), J. Craig Venter Institute, La Jolla, CA, USA]. In cases where multiple gene probes have insisted on the same NCBI GeneID, we used those with the highest variance. For GSE108474 (**Table 2**), we performed statistical analysis with GEO2R, applying the Benjamini and Hochberg procedure (false discovery rate) (28–30). **Table 2** presents the results of sample detection from the GSE dataset and the significant differences between groups assessed using ordinary one-way ANOVA; correction with Tukey's multiple comparison test was also performed to compare the data between all groups. Correlations were determined using Pearson's correlation. All tests were two-sided, and significance was determined at an

TABLE 2 | Samples selected from the GSE108474 dataset.

Disease type	Number	Grade
NT	28	Negative
Astrocytoma	148	G2 = 65; G3 = 58; Na = 25
Oligodendrocytoma	67	G2 = 30; G3 = 23; Na = 14
Glioblastoma	221	G4 = 130; Na = 91

G, tumor grade; Na, not assigned; NT, non-tumor

adjusted *p*-value of 0.05. The dataset selected was transformed for the analysis of *Z*-score intensity signal. The *Z*-scores were calculated by taking the ratio of the weighted mean difference to the combined standard deviation according to Box and Tiao (31). The application of a classical method of data normalization, *Z*-score transformation, provides a way of standardizing the data across a wide range of experiments and allows the comparison of microarray data independent of the original hybridization intensities. The *Z*-score is considered a reliable procedure for this type of analysis and can be considered a state-of-the-art method, as demonstrated by numerous research works (32–43). The efficiency of each biomarker across the different tumor grades was assessed by analysis of the receiver operating characteristic (ROC) curves (44–46). The ROC curves analyzed the brain biopsies of healthy subjects (non-tumor, NT) *vs*. GBM patients, astrocytoma *vs*. GBM, and oligodendroglioma *vs*. GBM. The area under the ROC curve (AUC) and its 95% confidence interval (95% CI) indicated diagnostic efficiency. The accuracy of the test with the percent errors were reported (47).

RESULTS

Lactate Induces Glioblastoma Cell Proliferation and Migration *via HCAR1* and *MCT1*

We first analyzed the effects of lactate on 3 human GBM cell lines (i.e., U-87 MG, A-172, and U-251 MG) by performing a clonogenic assay on lactate-exposed cells (**Supplementary Figure S1**). It was observed that lactate induced an increase of about 2-fold in both the number (78.3 ± 9.0 control vs. 151.0 ± 17.1 lactate) and area (123.2 ± 8.2 control vs. 215.0 ± 30.4 lactate) of colonies of U-87 MG cells (**Supplementary Figure S1**). Interestingly, analysis of clonogenicity on A-172 revealed that lactate reduced the total number of colonies (35.7 ± 0.3 control vs. 21.0 ± 1.2 lactate) (**Supplementary Figure S1**), but dramatically affected the area of colonies, which was increased more than 4-fold compared to control cultures (731.3 ± 0.5 control vs. 3470.8 ± 30.3 lactate) (**Supplementary Figure S1**). We also repeated our analysis on U-251 MG cells, which showed a similar response observed in U-87 MG cells, with a significant increase in the total number of colonies (26.5 ± 0.9 control vs. 38.0 ± 3.6 lactate) and mean colony area (700.0 ± 7.1 control vs. 1409.4 ± 28.0 lactate) (**Supplementary Figure S1**).

We then subsequently compared the effect of increased levels of extracellular lactate with the selective stimulation of the lactate receptor HCAR1 mediated by 3,5-DHBA. We observed in all tested cells a significant increase of the normalized cell index after lactate exposure (**Figures 1A–C**), confirmed by an increase of the total AUCs for U-87 MG (76.5 ± 0.4 lactate vs. 38.9 ± 0.2 control), A-172 (86.6 ± 0.8 lactate vs. 64.4 ± 0.4 control), and U-251 MG (78.1 ± 1.1 lactate vs. 40.5 ± 0.8 control) (**Figures 1A–C**, respectively). 3,5-DHBA stimulation was also able to induce similar effects on cell proliferation on the U-87 MG, A-172, and U-251 MG cell lines, showing increased normalized cell indices in all tested cell lines confirmed by an increase of the total AUCs

for U-87 MG (106.3 ± 2.4), A-172 (134.6 ± 1.1), and U-251 MG (122.9 ± 1.3) (**Figures 1A–C**, respectively). We then tested whether lactate affects the cell migration of GBM cells. Interestingly, we observed a reduced percentage of wideness in the scratch assay at 24 and 48 h in all tested cell lines (**Figures 1D–G**). We also confirmed the effects of HCAR1 stimulation through 3,5-DHBA on cell migration, finding a significantly reduced percentage of wideness in the scratch assay at 48 h in all tested cell lines (**Figures 1D–G**).

In order to verify whether lactate metabolism was involved in these effects on GBM cell proliferation and migration, we analyzed the effect of the MCT1 inhibitor (AZD3965, 10 μM) and the HCAR1 antagonist (3-OBA, 3 mM). Interestingly, our results showed that treatments of both AZD3965 and 3-OBA alone had no effect on cell proliferation, as indicated by the normalized cell index and AUC values compared to untreated control cells in all three tested cell lines (**Figures 2A–F**). Moreover, the U-87 MG cell line co-treated with lactate/AZD3965 showed significant decreases in the cell index (**Figure 2A**) and the AUC (73.14 ± 1.2 lactate/AZD3965 vs. 120.3 ± 8.6 untreated) (**Figure 2A**), while the A-172 and U-251 MG cell lines showed no significant effects (**Figures 2B, E**). However, the co-treatment of lactate/3-OBA showed decreased normalized cell indices for all three cell lines tested (**Figures 2B, D, F**), as confirmed by the decreased total AUCs of U-87 MG (65.1 ± 1.9 lactate/3-OBA vs. 120.3 ± 8.6 untreated), A-172 (137.0 ± 5.1 lactate/3-OBA vs. 181. ± 3.5 untreated), and U-251 MG (139.4 ± 3.9 lactate/3-OBA vs. 245.2 ± 4.8 untreated) (**Figures 2B, D, F**, respectively). We then evaluated whether MCT1 inhibition and HCAR1 antagonism affect the cell migration and surviving fraction (**Supplementary Figures S2, S3**). The results showed that both co-treatments (lactate/AZD3965 and lactate/3-OBA) resulted in a significant increase in the percentage of wideness in the scratch assay compared to the lactate and untreated control cells in the U-87 MG cell line (68.0 ± 2.1 lactate/AZD3965, 61.5 ± 4.5 lactate/3-OBA vs. 0.0 ± 0.0 lactate, vs. 25.75 ± 8.1 untreated) (**Supplementary Figures S2B, E**) and the A-172 cell line (47.3 ± 5.3 lactate/AZD3965, 87.1 ± 4.9 lactate/3-OBA vs. 0.0 ± 0.0 lactate, vs. 22.3 ± 2.3 untreated) (**Supplementary Figures S2A, C, F**) cell lines, as well as a significant increase in the percentage of wideness in the scratch assay compared to lactate in the U-251 MG cell line (58.7 ± 3.2 lactate/AZD3965, 64.7 ± 5.5 lactate/3-OBA vs. 26.5 ± 5.0 lactate) (**Supplementary Figures S2D, G**). The same results were obtained in the surviving fraction assay (**Supplementary Figure S3**).

HCAR1 Targeting Increases the Expression Levels of *MCT1* and *MCT4*

In an effort to link lactate, as a positive modulator of cell proliferation and migration, to the underlying molecular mechanisms activated in GBM cell lines, we performed Western blot analysis for the lactate transporters MCT1 and MCT4 and for β-catenin and E-cadherin on the control and lactate-treated U-87 MG, A-172, and U-251 MG cells.

We found that U-87 MG cells responded to increased levels of extracellular lactate by increasing the levels of the MCT1
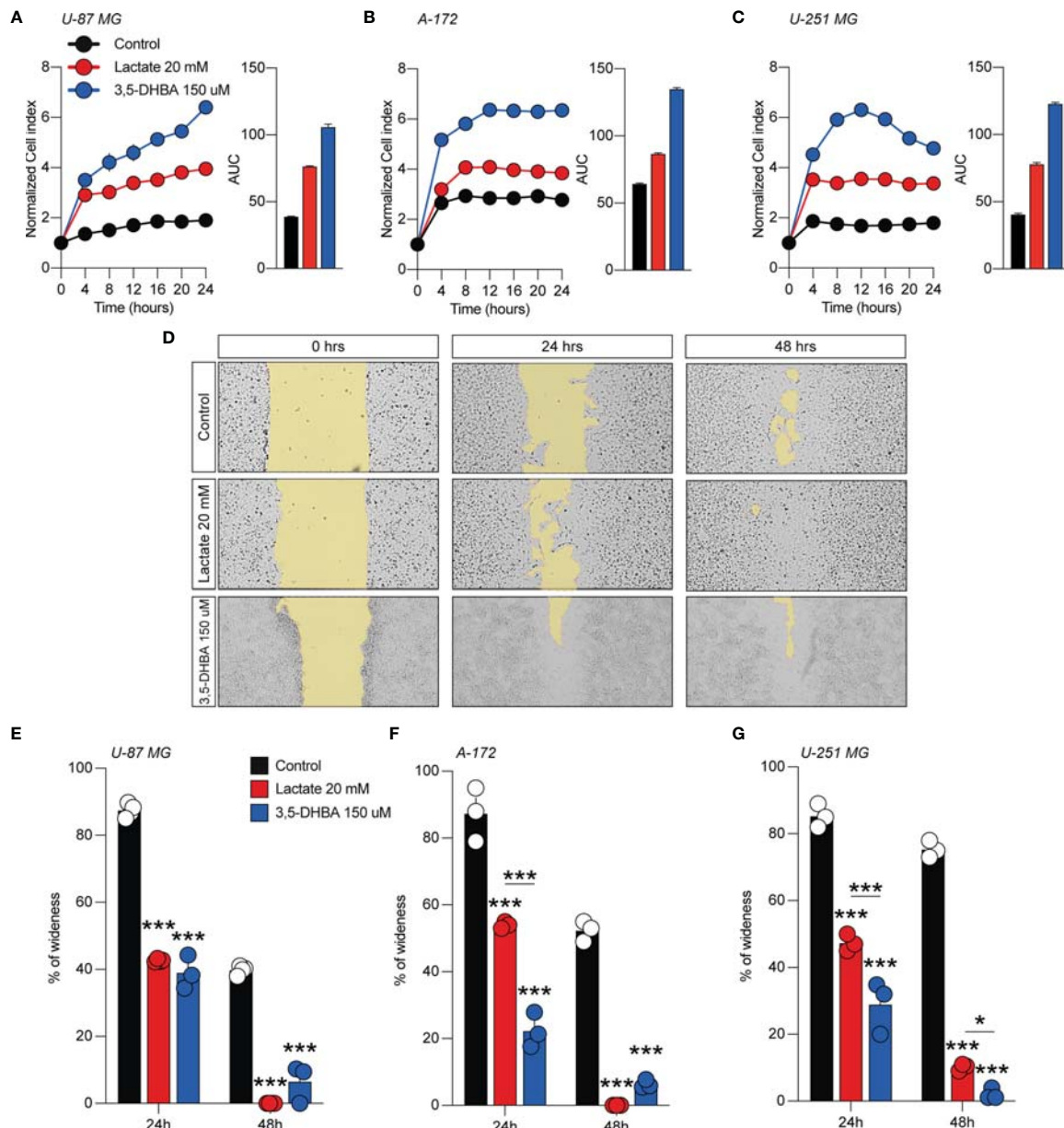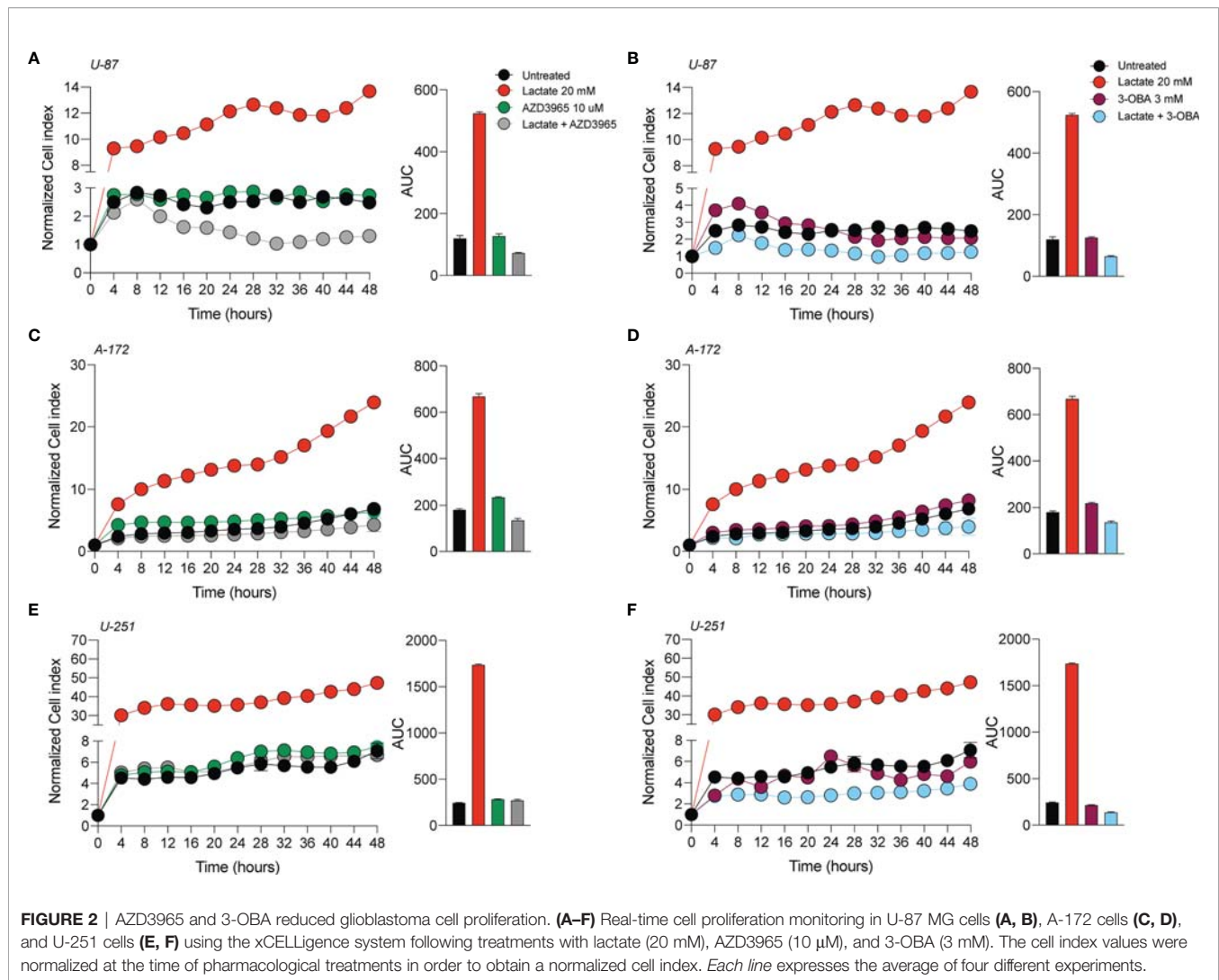
FIGURE 1 | Lactate and 3,5-dihydroxybenzoic acid (3,5-DHBA) promoted glioblastoma cell proliferation and migration. **(A–C)** Real-time cell proliferation monitoring in U-87 MG cells **(A)**, A-172 cells **(B)**, and U-251 cells **(C)** using the xCELLigence system following treatments with lactate (20 mM) and 3,5-DHBA (150 μM). The cell index values were normalized at the time of pharmacological treatments in order to obtain a normalized cell index. *Each line* expresses the average of four different experiments. **(E–G)** Analysis of human glioblastoma cell migration in U-87 MG cells **(E)**, A-172 cells **(D–F)**, and U-251 MG cells **(G)** with the wound healing assay following treatments with lactate (20 mM) and 3,5-DHBA (150 μM). The figures presented are representative of at least three independent experiments (mean ± SEM). *P*-values <0.05 were considered as statistically significant (*$p < 0.05$; ***$p < 0.001$).

transporter about 2.5-fold compared to control cultures and slightly, but significantly, reducing the expression level of MCT4 (**Figure 3A**).

Importantly, the protein levels of β-catenin were found to be significantly increase about 6-fold in lactate-exposed U-87 MG cells, and such a modulation was coupled with reduced expression levels of E-cadherin (**Figure 3A**). Notably, analysis

of A-172 and U-251 MG cells exposed to increased extracellular lactate levels revealed some differences in the cellular responses compared to U-87 MG cells. Indeed, it was confirmed that exposure to lactate increased the expression levels of MCT1 and β-catenin in both A-172 (**Figure 3B**) and U-251 MG (**Figure 3C**) cells, but showed that the response of both cell lines to lactate also induced significantly higher MCT4, an

FIGURE 2 | AZD3965 and 3-OBA reduced glioblastoma cell proliferation. **(A–F)** Real-time cell proliferation monitoring in U-87 MG cells **(A, B)**, A-172 cells **(C, D)**, and U-251 cells **(E, F)** using the xCELLigence system following treatments with lactate (20 mM), AZD3965 (10 μM), and 3-OBA (3 mM). The cell index values were normalized at the time of pharmacological treatments in order to obtain a normalized cell index. *Each line* expresses the average of four different experiments.

increase of about 1.2-fold in both, and E-cadherin expression levels (**Figures 3B, C**).

Given the evidence on cellular modulation exerted by increased extracellular levels of lactate, we sought to link the molecular mechanisms underlying these phenomena with the activation of the lactate receptor HCAR1. We first investigated the mRNA expression levels of HCAR1 on the U-87 MG, A-172, and U-251 MG cell lines after exposure to lactate, which revealed a significant increase of the mRNA levels of HCAR1 in all tested cells at 24 h (**Figure 3D**). We then evaluated the effects of 3,5-DHBA, confirming a significant increase of the mRNA levels of HCAR1 in all tested cell lines 24 h after 3,5-DHBA incubation (**Figure 3E**).

To determine whether selective stimulation of HCAR1 was able to increase the expressions of the lactate transporters MCT1 and MCT4, we also checked the mRNA expression levels of these transporters, finding that 3,5-DHBA stimulation was able to significantly increase MCT1 expression about 25-, 5-, and 13-fold in U-87 MG, A-172, and U-251 MG cells, respectively

(**Figure 3F**). Such pieces of evidence were coupled with contrasting data on the other tested transporter, MCT4. Indeed, we observed that U-87 MG cells responded to 3,5-DHBA stimulation by increasing the mRNA expression of MCT4 about 2-fold (**Figure 3G**), but A-172 cells showed no significant changes in MCT4 expression, while U-251 MG cells showed a significant reduction of MCT4 expression upon treatment with 3,5-DHBA compared to untreated cells (**Figure 3G**).

Lactate Stimulation on Glioblastoma Cell Lines Increases Mitochondrial Fitness and Energy Metabolism *via* HCAR1

To further expand our evidence on the molecular mechanisms induced by the increase of extracellular lactate, we analyzed a panel of mRNAs of the genes involved in mitochondrial activity and energy metabolism. Our data showed that U-87 MG cells significantly increased about 4-fold the relative mRNA levels of transcription factor A, mitochondrial (TFAM), PPARG coactivator 1 alpha (PGC1a), and sirtuin 1 (SIRT1)
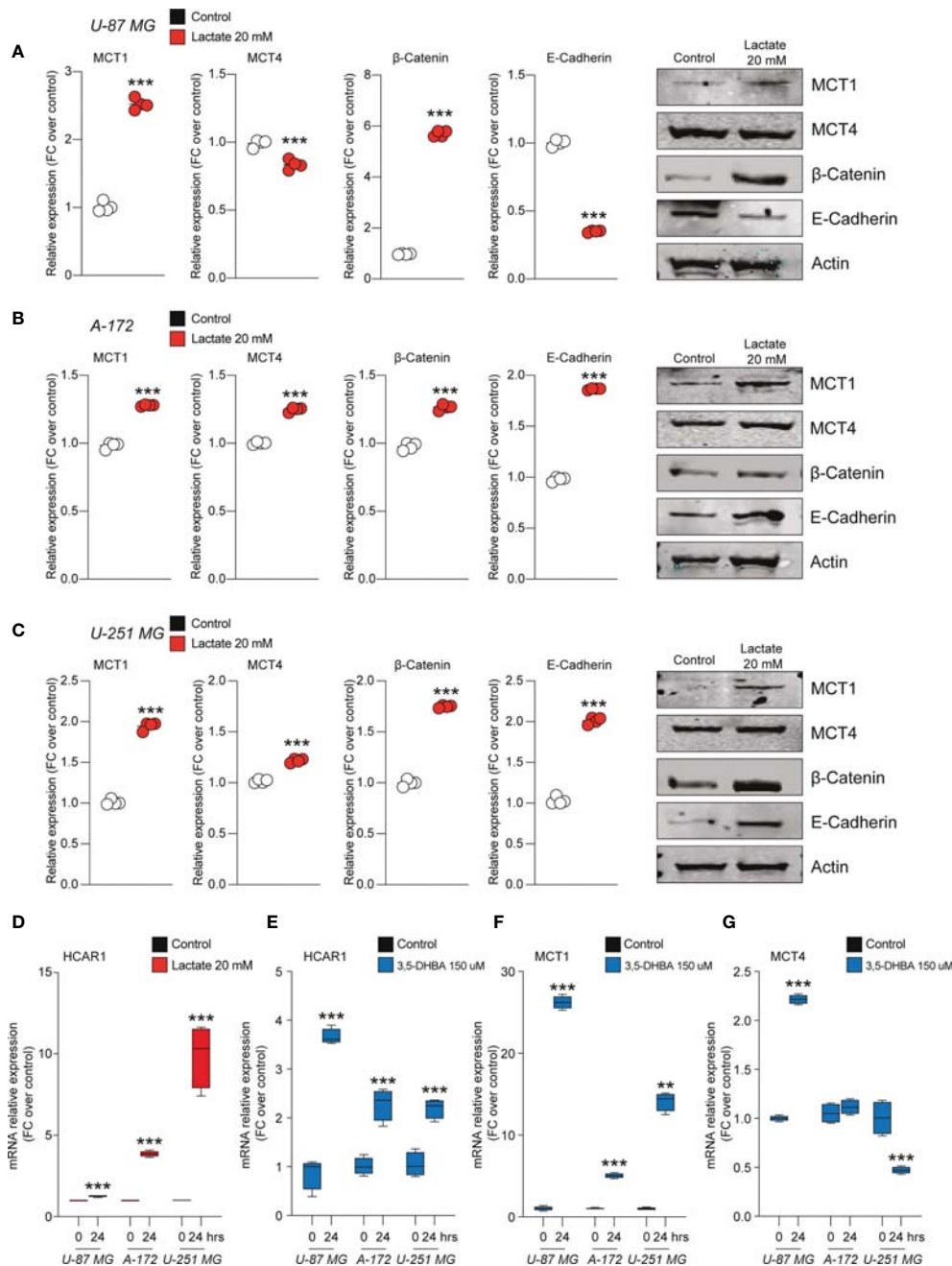
FIGURE 3 | Lactate regulated the expression of monocarboxylate transporters (MCTs) and epithelial–mesenchymal transition (EMT) markers in glioblastoma cells. **(A–C)** Protein expressions of MCT1, MCT4, β-catenin, and E-cadherin in U-87 MG cells **(A)**, A-172 cells **(B)**, and U-251 MG cells **(C)** following 72 h of lactate (20 mM) treatment. The figures presented are representative of at least four independent experiments, and values represent the mean ± SEM of experiments performed in quadruplicate. **(D)** HCAR1 gene expression in U-87 MG, A-172, and U-251 MG cells following 24 h of lactate (20 mM) treatment. **(E–G)** Gene expressions of HCAR1 **(E)**, MCT1 **(F)**, and MCT4 **(G)** in U-87 MG, A172, and U-251 MG cells following 24 h of 3,5-dihydroxybenzoic acid (3,5-DHBA, 150 μM) treatment. Values represent the mean ± SEM of experiments performed in quadruplicate. P-values <0.05 were considered as statistically significant (**$p < 0.01$; ***$p < 0.001$ vs. untreated).

(**Figures 4A, B**), coupled with an overall increase of ATP synthase (ATP syn), cytochrome c oxidase subunit 4 (COX IV) and COX II, mitochondrial cytochrome b (CYTB), and mitochondrial NADH-ubiquinone oxidoreductase chain 4

(ND4) (**Figure 4A**), when exposed to lactate for 24 or 48 h compared with untreated cells (**Figures 4A, B**). These observations were confirmed in the A-172 (**Figures 4C, D**) and U-251 MG (**Figures 4E, F**) cell lines. Specifically, we
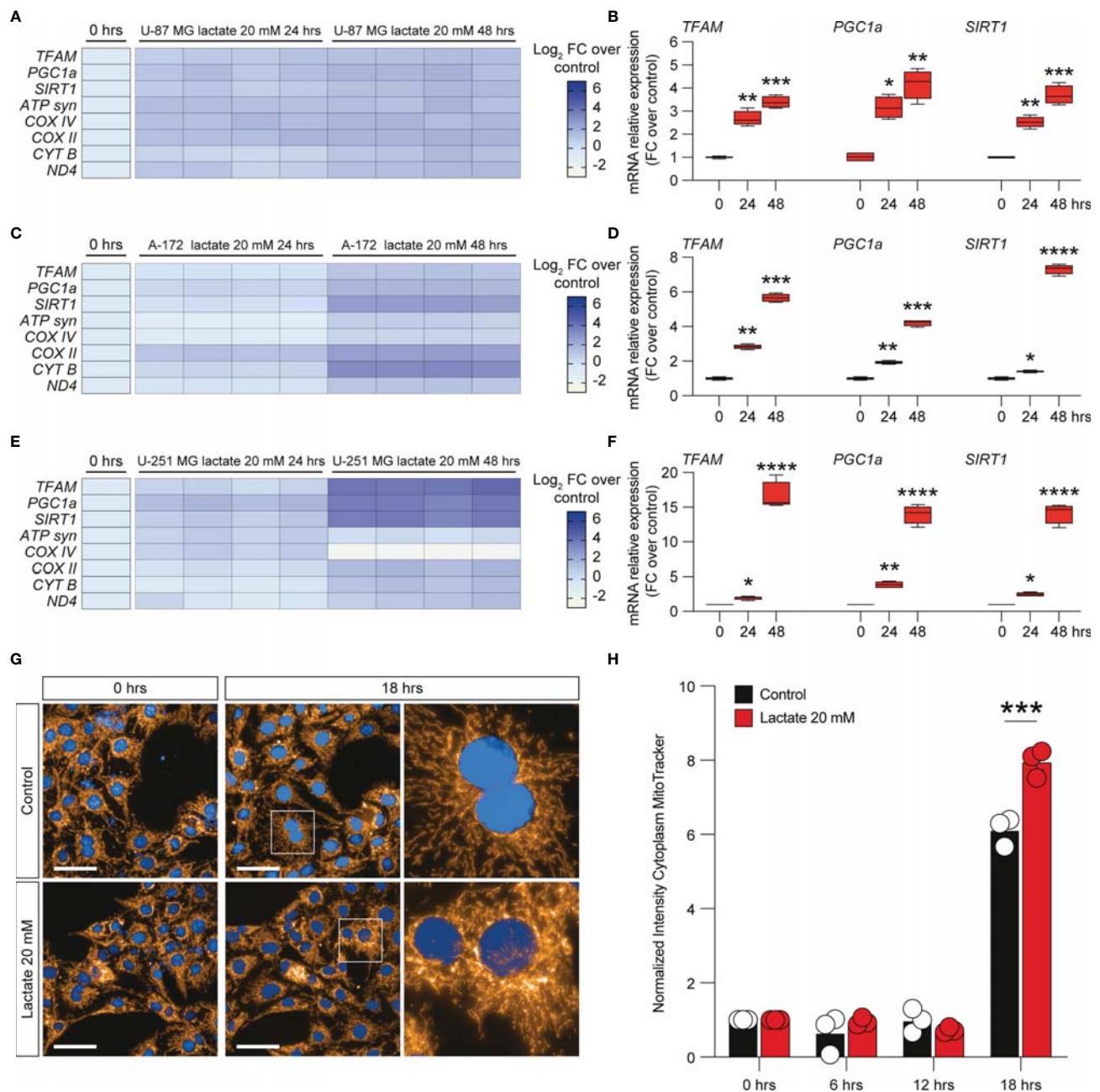
FIGURE 4 | Lactate promoted the upregulation of mitochondrial activity gene expressions in glioblastoma cells. **(A–F)** Effect of lactate (20 mM) on mitochondrial biogenesis and *OXPHOS* gene expression in U-87 MG cells **(A, B)**, A-172 cells **(C, D)**, and U-251 MG cells **(E, F)** following 24 and 48 h of treatment. **(G, H)** Computerized analysis of the MitoTracker fluorescence intensity in the control *versus* lactate 18 h after treatment. The figures presented are representative of at least three independent experiments. Values represent the mean ± SEM of experiments performed in quadruplicate. *P*-values <0.05 were considered as statistically significant (*p < 0.05; **p < 0.01; ***p < 0.001 ; ****p < 0.0001 *vs*. untreated).

observed superimposable effects on A-172 compared to U-87 MG cells, where U-251 MG showed an increase of about 15-fold of TFAM, PGC1a, and SIRT1 at 48 h compared to untreated cells (**Figure 4F**), coupled with a slight reduction of COX IV mRNA at the same time point [−1.87 ± 0.1 $\log_2$ fold change (FC) over the

control] (**Figure 4E**). We also performed a computer-assisted analysis of the MitoTracker fluorescence intensity on control versus lactate-treated cells, finding that lactate was able to significantly increase the cytoplasmic MitoTracker intensity 18 h post-treatment (**Figure 4G, H**).
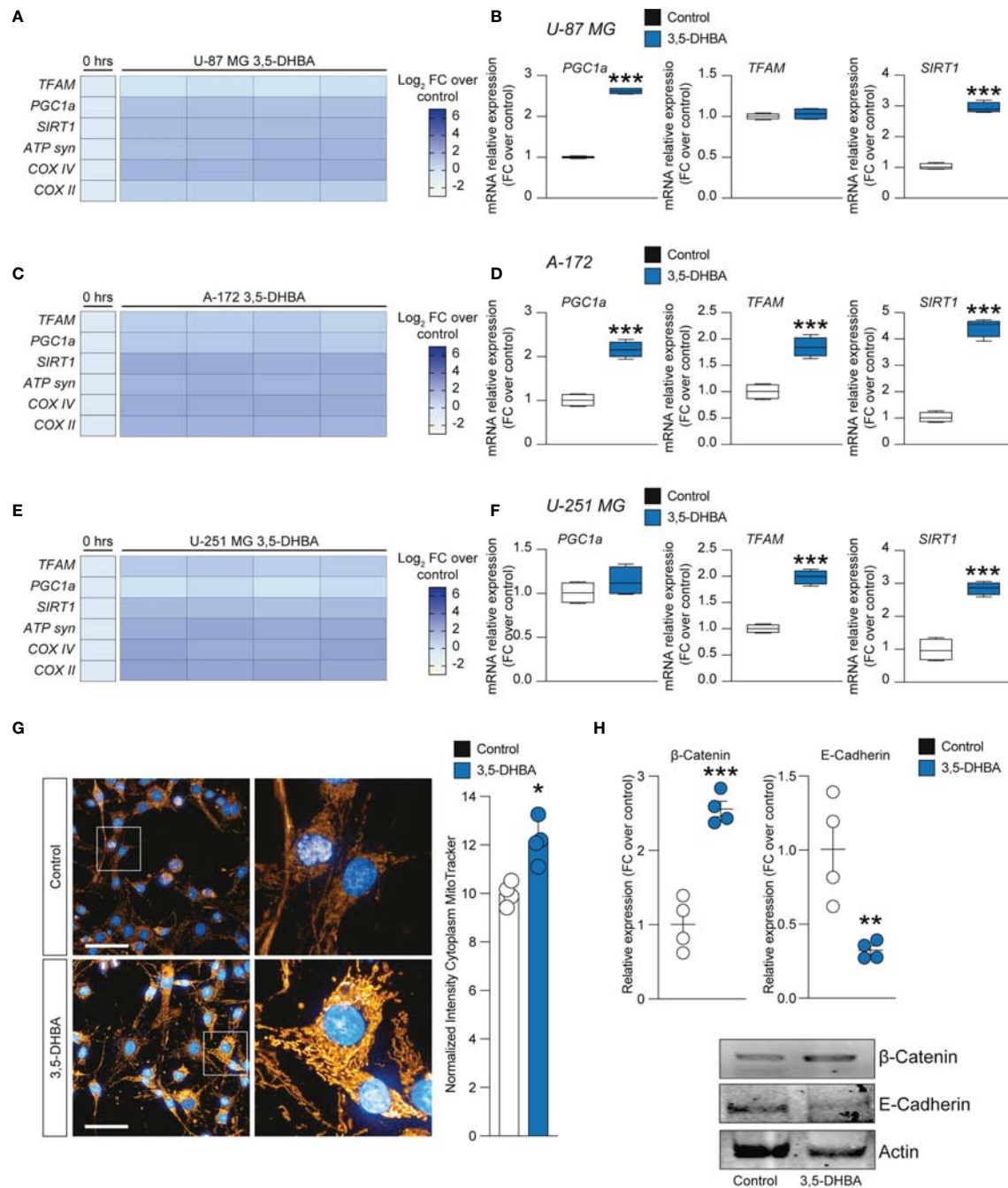
FIGURE 5 | *HCAR1* selective stimulation promoted the upregulation of mitochondrial activity gene expressions and regulated the protein expressions of the epithelial–mesenchymal transition (EMT) markers in glioblastoma cells. **(A–F)** Effect of 3,5-dihydroxybenzoic acid (3,5-DHBA, 150 μM) on mitochondrial biogenesis and *OXPHOS* gene expression in U-87 MG cells **(A, B)**, A-172 cells **(C, D)**, and U-251 MG cells **(E, F)** following 24 h of treatment. **(G)** Computerized analysis of the MitoTracker fluorescence intensity on the control *versus* lactate 18 h after treatment. The figures presented are representative of at least three independent experiments. **(H)** Protein expressions of β-catenin and E-cadherin in A-172 cells following 72 h of *HCAR1* stimulation. The figures presented are representative of at least four independent experiments, and values represent the mean ± SEM of experiments performed in quadruplicate. *P*-values <0.05 were considered as statistically significant (**p* < 0.05; ***p* < 0.01; ****p* < 0.001 *vs.* untreated).

To link the intracellular mediators of mitochondrial fitness with HCAR1 stimulation, we performed an analysis of the mRNA expression levels of PGC1a, TFAM, SIRT1, ATP syn, COX II, and COX IV on 3,5-DHBA-stimulated cells. Our analysis revealed that U-87 MG cells exposed to 3,5-DHBA recapitulated the molecular mRNA activation observed with lactate (**Figures 5A, B**). Indeed, all tested genes, except for TFAM, were significantly increased in cultures exposed to HCAR1 stimulation (**Figure 5B**). These data were confirmed in A-172 cells, which showed increased levels of all tested genes upon 3,5-DHBA stimulation (**Figures 5C, D**). Finally, U-251 MG showed very similar mRNA expression profiles, but we observed that HCAR1 stimulation through 3,5-DHBA did not modulate the expression of PGC1a at the tested time point in this cell line (**Figures 5E, F**).

To finally link HCAR1 stimulation with the effects on the mitochondria observed in GBM cell lines exposed to increased extracellular lactate levels, we performed a MitoTracker analysis, which demonstrated a significant increase of normalized intensity in 3,5-DHBA-stimulated cells compared to control cultures (**Figure 5G**).

Given the capability of extracellular lactate to modulate the expression levels of β-catenin and E-cadherin, we performed Western blot analysis on 3,5-DHBA-stimulated A-172 cells. Our analysis revealed that HCAR1 activation induced a significant increase in the protein expression levels of β-catenin compared to control cultures, and this phenomenon was coupled with a significant reduction of E-cadherin (**Figure 5H**), revealing that lactate may also act via additional mechanisms to induce E-cadherin not related to HCAR1 activation.

Lactate Stimulation Modulates Metabolism and *MCT1* in the Zebrafish Model of Glioblastoma

To investigate whether lactate accumulation, resulting from increased glycolysis, may have similar effects *in vivo*, we used the zebrafish model of GBM (22) (**Figure 6A**) and analyzed the metabolic phenotypes of these tumors. Comparison of the expression levels of 29 genes encoding for enzymes and transporters involved in the glycolytic pathway acquired through RNA sequencing (GSE74754; https://www.ncbi.nlm.nih.gov/geo/query/acc.cgi?acc=GSE74754) revealed the increased expressions ($\log_2$ FC > 1.2, p < 0.001, or adjusted p < 0.05) of 26 out of 29 genes, with aldh1a3, hk2, and hcar1-3 being the most upregulated in tumors (**Figure 6B**). We then performed a Mito Stress test on freshly dissociated zebrafish tumor brains using the Seahorse XFp apparatus and acute injection of lactate (20 mM), UK5099 [an inhibitor of the mitochondrial pyruvate carrier (MPC), 2 μM], or AZ3695 (10 μM, to inhibit MCT1). This test confirmed that acute injection of lactate (upper panel in **Figure 6C**) had little effect on the OCR of zebrafish brain tumor cells, whereas, upon blockage of the MPC (UK5099) (middle panel in **Figure 6C**), the response of the cells at maximal respiration (after FCCP injection) was partly inhibited and,

upon blockage of the MCT1 transporter (AZ3695) (lower panel in **Figure 6C**), the energy production through mitochondrial respiration was blocked, suggesting that blocking the transport of lactate has profound consequences on the ability of zebrafish GBM cells to oxidize substrates for energy production (**Figure 6C**). Staining for MCT1 and HCAR1 in sections of zebrafish brain tumors revealed an increase in the number of both MCT1+ and HCAR1+ cells (**Figure 6D**), whereas qPCR analysis of the mRNA expressions of mct1 and hcar1 revealed a significant increase in the expression for mct1 in adult tumors compared to the control brain and a significant increase in the expression of hcar1 in both adult brain tumors and in 5-dpf larvae expressing oncogenic RAS (**Figure 6E**).

Subsequently, we evaluated the effects of exposing zebrafish brain tumor cells to lactate or to the MCT1 inhibitor, AZD3965, on the proliferation rate of control brains and brains expressing oncogenic RAS using immunostaining for a mitotic marker (phosphoserine 10 on histone 3, PH3). Incubation of developing larvae from 1 to 5 dpf with 20 μM lactate induced a significant increase in proliferation in brains expressing oncogenic RAS, but not in control brains, while treatment with 10 μM AZD3965 did not affect the proliferation rate in either control or RAS-expressing brains (**Figure 6F**).

HCAR1 and *MCT1* Positively Correlated With Human Glioma Aggressiveness

The *MCT1* gene expression analysis obtained from the GSE108474 dataset showed that there were significant differences when the expression levels obtained from brain biopsies of GBM patients were compared to other brain tumor stages (**Figure 7**). Specifically, patients with GBM expressed significantly higher levels of the *MCT1* messenger in the brain than did patients with oligodendrocytoma (p < 0.0001) and astrocytoma (p < 0.0001) or healthy subjects (p < 0.0001) (**Figure 6A**). This finding was confirmed by the significantly positive correlation between the expression levels of *MCT1* and tumor grade (r = 0.4026, p = 0.0223) (**Figure 6B**). According to these results, we investigated the prognostic potential of *MCT1* expression in the progression of main brain tumors. Currently, analysis of the expression of isocitrate dehydrogenase [NADP (+)] 1 (*IDH1*) and the identification of its main mutations (e.g., R132H) were used for glioma diagnosis and prognosis (48). By carrying out Pearson's correlation analysis between the expression levels of *MCT1* and *IDH1* in brain tumors, we highlighted that, in GBM patients, the expression levels of these two genes were significantly closely inversely correlated (r = −0.4163, p < 0.0001) (**Figure 7C**). Furthermore, in order to evaluate the potential diagnostic ability of *MCT1* gene expression to discriminate against the brain tumor stages, we performed an ROC analysis. We confirmed the diagnostic ability of *MCT1* to discriminate GBM patients from healthy subjects (AUC = 0.7558, p < 0.0001) (**Figure 7D**) or from patients affected by astrocytoma (AUC = 0.7775, p < 0.0001) (**Figure 6E**) or oligodendrocytoma (AUC = 0.8104, p < 0.0001) (**Figure 7F**).
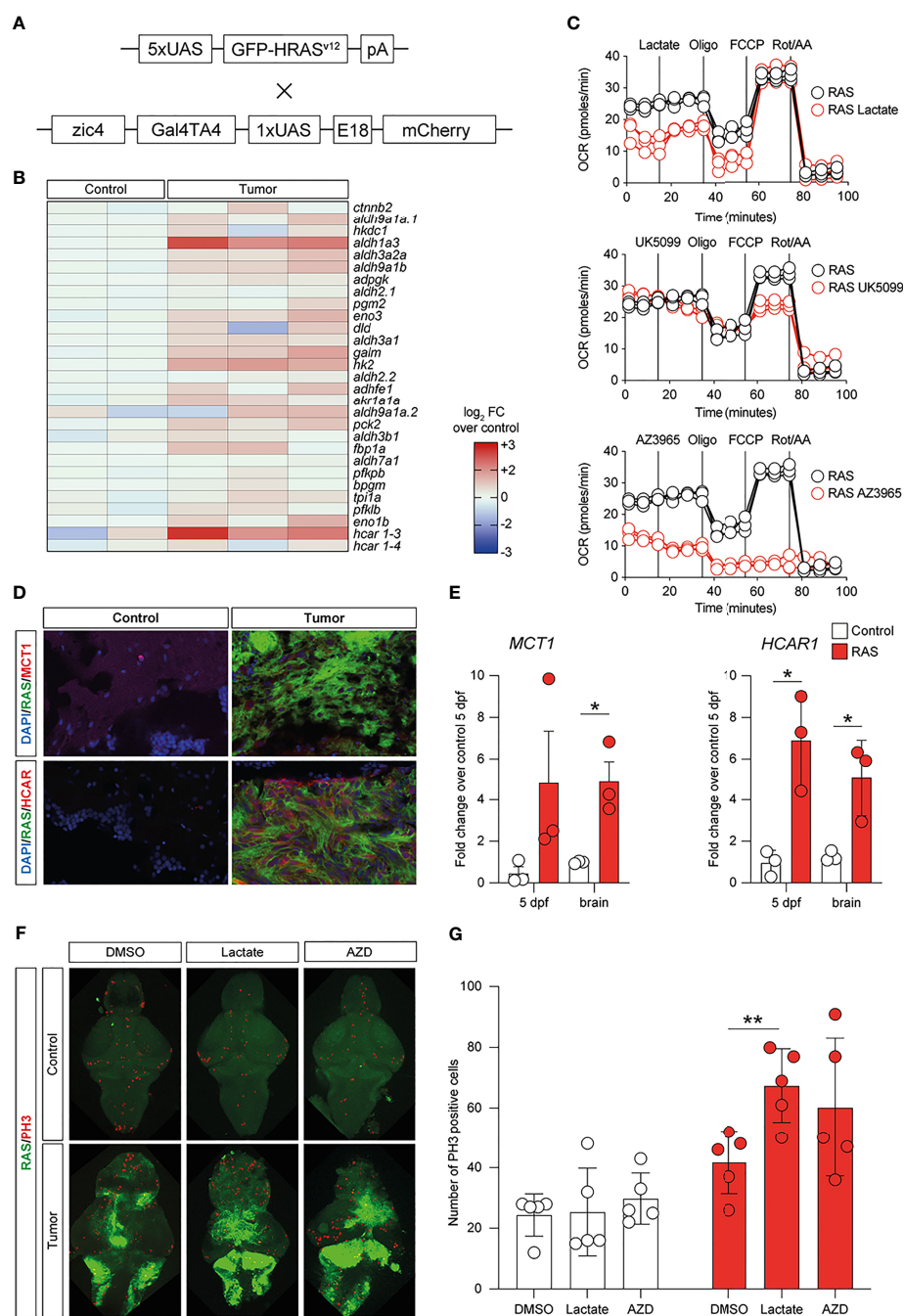
FIGURE 6 | Metabolic changes in a zebrafish model of glioblastoma (GBM) led to increased glycolysis and lactate transport and sensing. **(A)** Schematic representation of the genetic components of the zebrafish GBM model (Mayrhofer et al., 2017). **(B)** Increased expression of several members of the glycolytic pathway in GBM. Heatmap representing 29 glycolysis genes and their relative expression levels. **(C)** Analysis of mitochondrial metabolism (acute Mito Stress test) of tumor cells with the Seahorse XP technology. Each experiment was performed in triplicate and normalized to the number of cells. **(D)** Increased levels of *HCAR1* in tumors *vs.* control as visualized by immunofluorescence. Staining as detailed in the figures, which are representative of at least three different experiments. **(E)** Gene expression analysis through quantitative PCR (qPCR) expressed as fold changes compared to controls, at 5 days post-fertilization and in adult tumors. Values represent the mean ± SEM of experiments performed in triplicate. *P*-values <0.05 were considered as statistically significant (**p* < 0.05 *vs*. controls). **(F)** Whole-mount immunofluorescence of Ph3 proliferating cells in controls and in HRAS-overexpressing larvae treated or not with 20 mM lactate. Green fluorescence represents tumoral cells expressing eGFP-HRASG12V. **(G)** Number of proliferating cells in the brains treated as indicated.
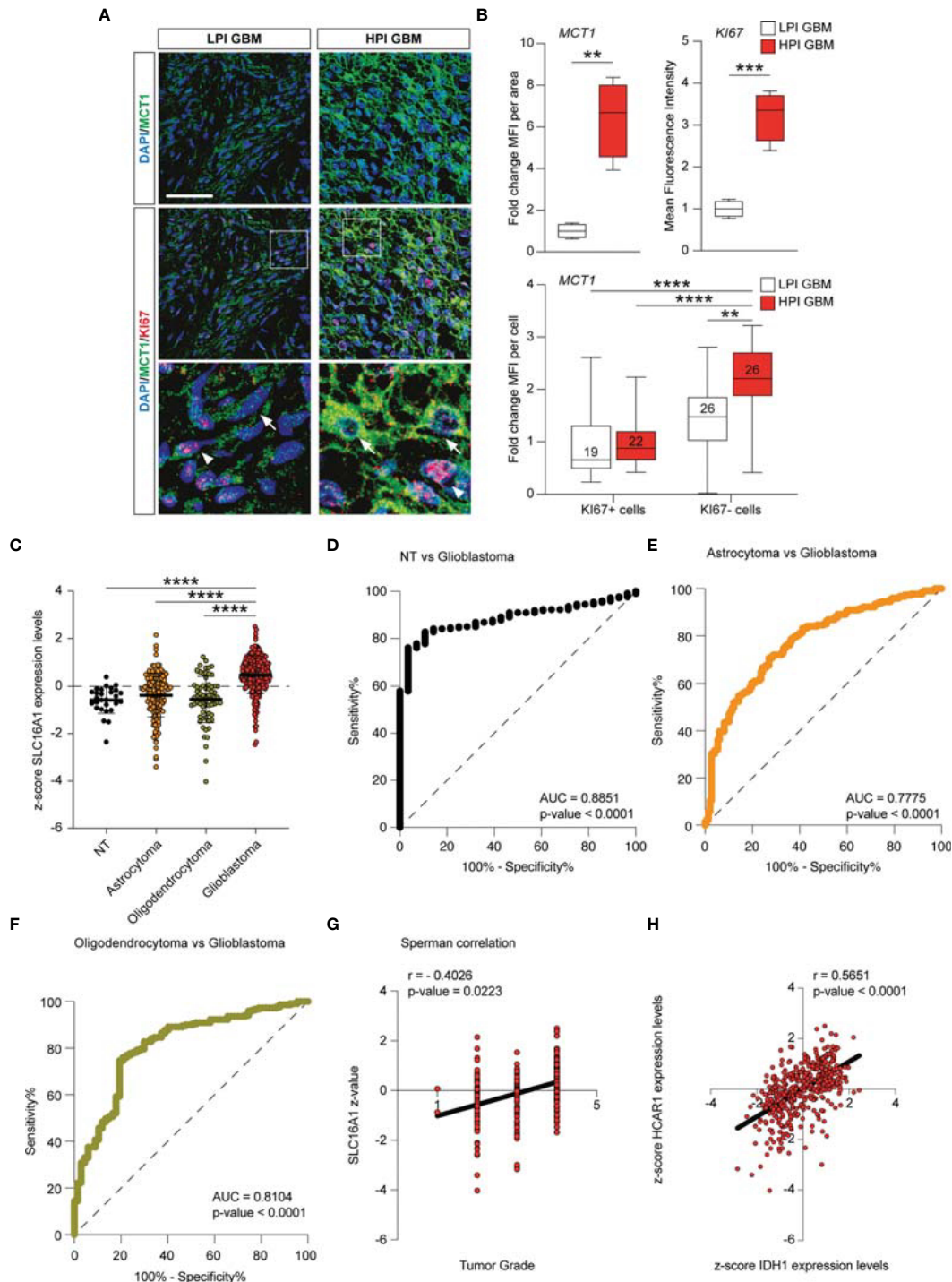
FIGURE 7 | *MCT1* expression analysis from the human brain tumor GSE108474 dataset. (**A**) Analysis of the MCT1 gene expression in brain biopsies of patients with astrocytoma, oligodendrocytoma, and glioblastoma (GBM) and in healthy subjects. (**B**) Pearson's correlation analysis between the expression levels of MCT1 and the tumor grade of brain biopsies obtained from patients affected by main brain tumors. (**C**) Pearson's correlation between the expression levels of MCT1 and IDH1 in brain biopsies of patients with GBM. (**D–F**) Receiver operating characteristic (ROC) analysis between the expression levels of MCT1 in the brain in healthy subjects vs. GBM patients (**D**), between GBM patients vs. astrocytoma patients (**E**), and between GMB patients vs. oligodendrocytoma patients (**F**). (**G**) Sperman correlation of SLC16A1 z-value and tumor grade. (**H**) Correlation between HCAR1 and IDH1 expression levels. Data are expressed as the mean ± SD of at least four independent experiments (**p < 0.005; ***p < 0.001; ****p < 0.0001)..

DISCUSSION

Cell metabolism and its related intercellular signaling have been shown to be of great importance in a number of physiological and pathological processes (49). In the present study, we first evaluated the effects of lactate on three human GBM cell lines, finding that it increased both cell migration and proliferation. Such a phenomenon was linked to lactate-dependent *HCAR1* activation, as suggested by the effects of 3,5-DHBA, a selective *HCAR1* agonist.

Several authors showed that stimulation of *HCAR1* leads to the activation of cell survival signals, promoting cell proliferation *via* the inhibition of apoptosis and stimulating the secretion of several angiogenic factors in a PI3K/Akt-CREB signaling pathway-dependent manner (50). Interestingly, the role of *HCAR1* in brain cell proliferation was also reported in the repair process that follows neonatal brain injury. Lauritz et al. demonstrated, using the neurosphere assay, that brain cells lacking *HCAR1* had reduced proliferation and repair abilities (51). Moreover, *MCT1* is mainly used by oxidative cells for extracellular lactate intake, and *MCT4* is mainly used to release accumulated lactate into the extracellular milieu, in many cases by hypoxic and/or highly glycolytic cells (52–54). Our data supported the hypothesis that lactate leads GBM cells to increase the levels of *HCAR1* and *MCT1* in order to mediate lactate sensing (*HCAR1*) and lactate intake (*MCT1*) from the extracellular milieu. This phenomenon is coupled with increased mitochondrial content and fitness, thus prompting GBM cells toward oxidative metabolism. It is worth noting that this mechanism is not related to the increased lactate level itself, but is dependent on the interaction with the *HCAR1* receptor. Indeed, we were able to reproduce this metabolic reshaping using the selective *HCAR1* agonist 3,5-DHBA. Consistently, a study performed in *HCAR1*-silenced pancreatic cancer cells led to reduced mitochondrial activity and survival in several cancer cell (55). In particular, several cancer cell types, including colon, breast, lung, cervical, and pancreatic cancer cells, showed an increase in the expression of *HCAR1*, and functional studies indicated that this increase is important for lactate regulation of the genes involved in lactate uptake and metabolism. Moreover, *HCAR1* is critical for cancer cell survival only when glucose is absent and in the presence of lactate (56).

Interestingly, we observed major differences in the cell response to *HCAR1* activation when analyzing the levels of *MCT4*. Indeed, we observed that 24 h of lactate exposure mediated a reduction in the protein levels of *MCT4* in U-87 MG, whether we found a significant *MCT4* increase in both U-251 MG and A-172. It is noteworthy that the quantification of the main mitochondrial genes revealed that U-87 MG cells underwent a rapid increase of mitochondrial content, although less pronounced *versus* the basal levels, compared to that of A-172 and U-251 MG. Our data suggest that U-87 MG cells have different responses compared to the other cell lines in terms of timing to repurpose their transporters and metabolism. Indeed, upon 3,5-DHBA stimulation of *HCAR1*, we observed a significant increase of *MCT4* in U-87 MG, whereas we

obtained contrasting results for A-172 and U-251 MG. Such a differential response of U-87 MG, characterized by a concomitant increase of *MCT1* and *MCT4*, may represent the molecular substrate leading to the heterogeneous response to *HCAR1* targeting in terms of E-cadherin activation among the tested cells. Further studies addressing the role of *MCT4* in epithelial–mesenchymal transition (EMT) and heterogeneity in the time–response to *HCAR1* activation between cell lines are needed.

This set of experiments suggests that the activation *HCAR1* induced the increase in *MCT1*, thus mediating lactate intake in stimulated cells. It is therefore conceivable that intercellular metabolism and mitochondrial content are closely related to the activation of *HCAR1* by several pathways. In this regard, Zaho et al. showed that increasing the lactate concentration in the liver TME could activate the *HCAR1* receptor and facilitate the *MCT1*-mediated uptake of lactate, leading to increased ATP production and decreased AMP/ATP ratio in the intracellular compartment (57). Tumor cells stimulate mitochondrial biogenesis not only for proliferation but also for promoting malignant transformation in the migration and invasiveness and during tumor adaptation to hypoxia (58, 59). As previously mentioned, we observed an increase of mitochondrial biogenesis in GBM cells treated with lactate or the *HCAR1* inducer. This phenomenon could be due to the increase of lactate uptake after *MCT1* overproduction. Moreover, we also showed that the increase of mitochondrial mass also induced an increase in *OXPHOS* gene expression. Exogenous treatment of lactate in various tumor cell lines induced an increase in ROS levels. We hypothesized that this latter increase in oxidative state enhanced mitochondrial biogenesis, similar to the increase in the expressions of *PGC1a* and *SIRT1* and oxidative genes.

Interestingly, our results also indicate that the activation of *HCAR1* promoted the modulation of β-catenin and E-cadherin expressions, suggesting that lactate participates in EMT in GBM. Several studies have been conducted to investigate the metabolic changes during EMT in breast, lung, and ovarian cancers, following an increased recognition of metabolic reprogramming as a hallmark of tumor development (60–62).

The lactate produced and exported by tumor cells can also be used by adjacent tumor cells in the TME, including endothelial cells and stromal cancer-associated fibroblasts, reprogramming their functions and contributing to tumor progression (63). Consequently, several authors hypothesized that lactate might also modulate the same epigenetic mechanisms in adjacent normal cells, including EMT processes (64, 65).

Given the insights from *in vitro* experiments on relevant human GBM cell lines, we employed a HRAS-overexpressing zebrafish model of GBM to examine whether similar metabolic changes are taking place in this model. Our data confirmed a widespread upregulation of glycolytic enzymes with the upregulation of *HCAR1*, thus indicating a prominent role in lactate signaling. In tumor cells, blockage of the MPC induced a reduction of the oxygen consumption in stress conditions and a massive reduction of the energy production through oxidative

phosphorylation when lactate transport is inhibited, suggesting that lactate is an important source of energy in these cells. The increased expressions of the lactate transporter (*mct1*) and sensor (*hcar1*) were already present at 5 dpf, when tumors started to grow. Lactate exposure determined a significant increase in proliferating PH3-positive cells in RAS-overexpressing zebrafish brains, but not in control brains, and this was reverted by the selective inhibition of *MCT1*. This evidence suggests that lactate intake supports cell proliferation in cancer and that metabolic reshaping is a critical stimulus in the GBM microenvironment.

Thus, both cell culture and *in vivo* studies, using different approaches and different genes, converged toward the same conclusion, i.e., that glycolysis is prominent in GBM and leads to a massive production of lactate, which shapes the microenvironment toward an aggressive phenotype, providing energy substrates and representing a valid therapeutic target.

Our data from human GBM biopsies were also consistent with the preclinical evidence provided herein. We observed that, in high proliferative GBM biopsies, Ki67-negative cells expressed significantly higher levels of *MCT1* compared to proliferative cells and low proliferative GBM cells. This indicates that the response of GBM cells to lactate, besides sustaining metabolic reshaping and response, favored the proliferation of neighboring cells by cooperating with their glycolytic metabolism, sensing and removing extracellular lactate. Our data are consistent with those of other studies in patients with advanced cancer showing that *MCT1* inhibition may have a significant effect on cancer growth and progression and may represent a druggable target for the development of new therapeutic strategies [ClinicalTrials.gov identifier (NCT number): NCT01791595].

Further confirmation of our study results was obtained by analyzing the human GSE108474 dataset. The analysis allowed us to highlight that *MCT1* is significantly modulated during the progression of the disease. In particular, significant expression changes were highlighted with the increase in the degree of malignancy. Furthermore, our results showed that the expression of *MCT1* can potentially be used in order to discriminate patients with GBM *versus* those with astrocytoma and oligodendrocytoma. These data are in agreement with the current research study, which considers *MCT1* a new prognostic biomarker and a potential target in human GBM (66). Interestingly, the correlation analysis between the expression levels of *MCT1* and *IDH1* in GBM patients was inversely proportional, further confirming recently obtained data in which mutant *IDH1* expression was associated with the downregulation of monocarboxylate transporters (67).

CONCLUSIONS

In conclusion, we showed that lactate is involved in various mechanisms favoring tumor development and progression. In particular, lactate has a dual role, being involved in the metabolic changes of tumor cells and acting as a molecule promoting cellular signaling through its membrane receptors. The ability of GBM cells to metabolically shift from glycolytic to oxidative metabolism, and *vice versa*, is likely to confer an advantage in survival, progression, and drug resistance. Firstly, glycolytic metabolism (the Warburg effect) supports fast cancer growth and provides an advantage for tumor proliferation. The lactate thus produced accumulates in the TME, which, on the one hand, favors the immune escape mechanisms and, on the other hand, modifies the metabolism of the adjacent tumor cells, also making them more resistant to antiblastic therapies. Therefore, lactate metabolism may be considered as a therapeutic target to develop novel pharmacological strategies for GBM therapy and to improve the outcome and quality of life of GBM patients.

DATA AVAILABILITY STATEMENT

The raw data supporting the conclusions of this article will be made available by the authors, without undue reservation.

ETHICS STATEMENT

The studies involving human participants were reviewed and approved by the University of Catania. The patients/participants provided written informed consent to participate in this study. The animal study was reviewed and approved by the University of Trento.

AUTHOR CONTRIBUTIONS

NV, DT, GVB, AG, MM, and GV: conceptualization. LL, NV, DT, CG, AG, MM, and GV: project administration. LL, NV, DT, GB, MB, MR, RP, MM, and GV: methodology. LL, NV, DT, CG, GB, MB, and MR: investigation. LL, NV, DT, RC, GVB, MR, RP, AG, MM, and GV: formal analysis. DT, RC, RP, MM, and GV: resources. LL, NV, DT, RP, AG, MM, and GV: supervision. LL, NV, DT, MM, and GV: writing—original draft. LL, NV, DT, CG, GVB, MR, RP, AG, MM, and GV: writing–reviewing and editing. All authors contributed to the article and approved the submitted version.

FUNDING

ACKNOWLEDGMENTS

SUPPLEMENTARY MATERIAL

The Supplementary Material for this article can be found online at: https://www.frontiersin.org/articles/10.3389/fonc.2022.871798/full#supplementary-material

REFERENCES

1. Stupp R, Hegi ME, Mason WP, van den Bent MJ, Taphoorn MJ, Janzer RC, et al. Effects of Radiotherapy With Concomitant and Adjuvant Temozolomide Versus Radiotherapy Alone on Survival in Glioblastoma in a Randomised Phase Iii Study: 5-Year Analysis of the Eortc-Ncic Trial. *Lancet Oncol* (2009) 10(5):459–66. doi: 10.1016/S1470-2045(09)70025-7

2. Torrisi F, Vicario N, Spitale FM, Cammarata FP, Minafra L, Salvatorelli L, et al. The Role of Hypoxia and Src Tyrosine Kinase in Glioblastoma Invasiveness and Radioresistance. *Cancers (Basel)* (2020) 12(10):2860. doi: 10.3390/cancers12102860

3. Charles N, Holland EC. The Perivascular Niche Microenvironment in Brain Tumor Progression. *Cell Cycle* (2010) 9(15):3012–21. doi: 10.4161/cc.9.15.12710

4. Liberti MV, Locasale JW. The Warburg Effect: How Does It Benefit Cancer Cells? *Trends Biochem Sci* (2016) 41(3):211–8. doi: 10.1016/j.tibs.2015.12.001

5. Vander Heiden MG, Cantley LC, Thompson CB. Understanding the Warburg Effect: The Metabolic Requirements of Cell Proliferation. *Science* (2009) 324 (5930):1029–33. doi: 10.1126/science.1160809

6. Miranda-Goncalves V, Bezerra F, Costa-Almeida R, Freitas-Cunha M, Soares R, Martinho O, et al. Monocarboxylate Transporter 1 Is a Key Player in Glioma-Endothelial Cell Crosstalk. *Mol Carcinog* (2017) 56(12):2630–42. doi: 10.1002/mc.22707

7. Kobayashi M, Narumi K, Furugen A, Iseki K. Transport Function, Regulation, and Biology of Human Monocarboxylate Transporter 1 (Hmct1) and 4 (Hmct4). *Pharmacol Ther* (2021) 226:107862. doi: 10.1016/j.pharmthera.2021.107862

8. Park SJ, Smith CP, Wilbur RR, Cain CP, Kallu SR, Valasapalli S, et al. An Overview of Mct1 and Mct4 in Gbm: Small Molecule Transporters With Large Implications. *Am J Cancer Res* (2018) 8(10):1967–76.

9. Payen VL, Hsu MY, Radecke KS, Wyart E, Vazeille T, Bouzin C, et al. Monocarboxylate Transporter Mct1 Promotes Tumor Metastasis Independently of Its Activity as a Lactate Transporter. *Cancer Res* (2017) 77(20):5591–601. doi: 10.1158/0008-5472.CAN-17-0764

10. Garnier D, Renoult O, Alves-Guerra MC, Paris F, Pecqueur C. Glioblastoma Stem-Like Cells, Metabolic Strategy to Kill a Challenging Target. *Front Oncol* (2019) 9:118. doi: 10.3389/fonc.2019.00118

11. Hoque R, Farooq A, Ghani A, Gorelick F, Mehal WZ. Lactate Reduces Liver and Pancreatic Injury in Toll-Like Receptor- and Inflammasome-Mediated Inflammation Via Gpr81-Mediated Suppression of Innate Immunity. *Gastroenterology* (2014) 146(7):1763–74. doi: 10.1053/j.gastro.2014.03.014

12. Brown TP, Ganapathy V. Lactate/Gpr81 Signaling and Proton Motive Force in Cancer: Role in Angiogenesis, Immune Escape, Nutrition, and Warburg Phenomenon. *Pharmacol Ther* (2020) 206:107451. doi: 10.1016/j.pharmthera.2019.107451

13. Ristic B, Bhutia YD, Ganapathy V. Cell-Surface G-Protein-Coupled Receptors for Tumor-Associated Metabolites: A Direct Link to Mitochondrial Dysfunction in Cancer. *Biochim Biophys Acta Rev Cancer* (2017) 1868 (1):246–57. doi: 10.1016/j.bbcan.2017.05.003

14. Ahmed K, Tunaru S, Tang C, Muller M, Gille A, Sassmann A, et al. An Autocrine Lactate Loop Mediates Insulin-Dependent Inhibition of Lipolysis Through Gpr81. *Cell Metab* (2010) 11(4):311–9. doi: 10.1016/j.cmet.2010.02.012

15. Roland CL, Arumugam T, Deng D, Liu SH, Philip B, Gomez S, et al. Cell Surface Lactate Receptor Gpr81 Is Crucial for Cancer Cell Survival. *Cancer Res* (2014) 74(18):5301–10. doi: 10.1158/0008-5472.CAN-14-0319

16. Longhitano L, Forte S, Orlando L, Grasso S, Barbato A, Vicario N, et al. The Crosstalk Between Gpr81/Igfbp6 Promotes Breast Cancer Progression by Modulating Lactate Metabolism and Oxidative Stress. *Antioxid (Basel)* (2022) 11(2):275. doi: 10.3390/antiox11020275

17. Torrisi F, Minafra L, Cammarata FP, Savoca G, Calvaruso M, Vicario N, et al. Src Tyrosine Kinase Inhibitor and X-Rays Combined Effect on Glioblastoma Cell Lines. *Int J Mol Sci* (2020) 21(11):3917. doi: 10.3390/ijms21113917

18. Salomone F, Li Volti G, Vitaglione P, Morisco F, Fogliano V, Zappala A, et al. Coffee Enhances the Expression of Chaperones and Antioxidant Proteins in Rats With Nonalcoholic Fatty Liver Disease. *Transl Res* (2014) 163(6):593–602. doi: 10.1016/j.trsl.2013.12.001

19. Sacerdoti D, Colombrita C, Ghattas MH, Ismaeil EF, Scapagnini G, Bolognesi M, et al. Heme Oxygenase-1 Transduction in Endothelial Cells Causes Downregulation of Monocyte Chemoattractant Protein-1 and of Genes Involved in Inflammation and Growth. *Cell Mol Biol (Noisy-le-grand)* (2005) 51(4):363–70.

20. Tibullo D, Barbagallo I, Giallongo C, Vanella L, Conticello C, Romano A, et al. Heme Oxygenase-1 Nuclear Translocation Regulates Bortezomibinduced Cytotoxicity and Mediates Genomic Instability in Myeloma Cells. *Oncotarget* (2016) 7(20):28868–80. doi: 10.18632/oncotarget.7563

21. Detrich HW,M, Zon LI. *Essential Zebrafish Methods: Cell and Developmental Biology*. 1 ed. HW, M Detrich, LI Zon, editors. Elsevier (2009).

22. Mayrhofer M, Gourain V, Reischl M, Affaticati P, Jenett A, Joly JS, et al. A Novel Brain Tumour Model in Zebrafish Reveals the Role of Yap Activation in Mapk- and Pi3k-Induced Malignant Growth. *Dis Model Mech* (2017) 10 (1):15–28. doi: 10.1242/dmm.026500

23. Santoriello C, Gennaro E, Anelli V, Distel M, Kelly A, Koster RW, et al. Kita Driven Expression of Oncogenic Hras Leads to Early Onset and Highly Penetrant Melanoma in Zebrafish. *PloS One* (2010) 5(12):e15170. doi: 10.1371/journal.pone.0015170

24. Idilli AI, Pagani F, Kerschbamer E, Berardinelli F, Bernabe M, Cayuela ML, et al. Changes in the Expression of Pre-Replicative Complex Genes in Htert and Alt Pediatric Brain Tumors. *Cancers (Basel)* (2020) 12(4):180158. doi: 10.3390/cancers12041028

25. Broggi G, Salvatorelli L, Barbagallo D, Certo F, Altieri R, Tirro E, et al. Diagnostic Utility of the Immunohistochemical Expression of Serine and Arginine Rich Splicing Factor 1 (Srsf1) in the Differential Diagnosis of Adult Gliomas. *Cancers (Basel)* (2021) 13(9):2873-81. doi: 10.3390/cancers13092086

26. Clough E, Barrett T. The Gene Expression Omnibus Database. *Methods Mol Biol* (2016) 1418:93–110. doi: 10.1007/978-1-4939-3578-9_5

27. Gusev Y, Bhuvaneshwar K, Song L, Zenklusen JC, Fine H, Madhavan S. The Rembrandt Study, a Large Collection of Genomic Data From Brain Cancer Patients. *Sci Data* (2018) 5:180158. doi: 10.1038/sdata.2018.158

28. Xiao J, Cao H, Chen J. False Discovery Rate Control Incorporating Phylogenetic Tree Increases Detection Power in Microbiome-Wide Multiple Testing. *Bioinformatics* (2017) 33(18):2873–81. doi: 10.1093/bioinformatics/btx311

29. Smyth GK. Linear Models and Empirical Bayes Methods for Assessing Differential Expression in Microarray Experiments. *Stat Appl Genet Mol Biol* (2004) 3:Article3. doi: 10.2202/1544-6115.1027

30. Davis S, Meltzer PS. Geoquery: A Bridge Between the Gene Expression Omnibus (Geo) and Bioconductor. *Bioinformatics* (2007) 23(14):1846–7. doi: 10.1093/bioinformatics/btm254

31. Box GT GC. *Bayesan Interference in Statistical Analysis*. GC Box GT, editor. New York: Wiley Online Library (1992).

32. Cheadle C, Vawter MP, Freed WJ, Becker KG. Analysis of Microarray Data Using Z Score Transformation. *J Mol Diagn* (2003) 5(2):73–81. doi: 10.1016/S1525-1578(10)60455-2

33. Scarpino M, Pinzone MR, Di Rosa M, Madeddu G, Foca E, Martellotta F, et al. Kidney Disease in Hiv-Infected Patients. *Eur Rev Med Pharmacol Sci* (2013) 17(19):2660–7.

34. Care MA, Barrans S, Worrillow L, Jack A, Westhead DR, Tooze RM. A Microarray Platform-Independent Classification Tool for Cell of Origin Class

Allows Comparative Analysis of Gene Expression in Diffuse Large B-Cell Lymphoma. *PloS One* (2013) 8(2):e55895. doi: 10.1371/journal.pone.0055895

35. Wang J, Coombes KR, Highsmith WE, Keating MJ, Abruzzo LV. Differences in Gene Expression Between B-Cell Chronic Lymphocytic Leukemia and Normal B Cells: A Meta-Analysis of Three Microarray Studies. *Bioinformatics* (2004) 20(17):3166–78. doi: 10.1093/bioinformatics/bth381

36. Reddy TB, Riley R, Wymore F, Montgomery P, DeCaprio D, Engels R, et al. Tb Database: An Integrated Platform for Tuberculosis Research. *Nucleic Acids Res* (2009) 37(Database issue):D499–508. doi: 10.1093/nar/gkn652

37. Le Cao KA, Rohart F, McHugh L, Korn O, Wells CA. Yugene: A Simple Approach to Scale Gene Expression Data Derived From Different Platforms for Integrated Analyses. *Genomics* (2014) 103(4):239–51. doi: 10.1016/j.ygeno.2014.03.001

38. Chen QR, Song YK, Wei JS, Bilke S, Asgharzadeh S, Seeger RC, et al. An Integrated Cross-Platform Prognosis Study on Neuroblastoma Patients. *Genomics* (2008) 92(4):195–203. doi: 10.1016/j.ygeno.2008.05.014

39. Mehmood R, El-Ashram S, Bie R, Dawood H, Kos A. Clustering by Fast Search and Merge of Local Density Peaks for Gene Expression Microarray Data. *Sci Rep* (2017) 7:45602. doi: 10.1038/srep45602

40. Yasrebi H, Sperisen P, Praz V, Bucher P. Can Survival Prediction Be Improved by Merging Gene Expression Data Sets? *PloS One* (2009) 4(10):e7431. doi: 10.1371/journal.pone.0007431

41. Cheadle C, Cho-Chung YS, Becker KG, Vawter MP. Application of Z-Score Transformation to Affymetrix Data. *Appl Bioinf* (2003) 2(4):209–17.

42. Feng C, Wu J, Yang F, Qiu M, Hu S, Guo S, et al. Expression of Bcl-2 Is a Favorable Prognostic Biomarker in Lung Squamous Cell Carcinoma. *Oncol Lett* (2018) 15(5):6925–30. doi: 10.3892/ol.2018.8198

43. Kang C, Huo Y, Xin L, Tian B, Yu B. Feature Selection and Tumor Classification for Microarray Data Using Relaxed Lasso and Generalized Multi-Class Support Vector Machine. *J Theor Biol* (2019) 463:77–91. doi: 10.1016/j.jtbi.2018.12.010

44. Lusted LB. Signal Detectability and Medical Decision-Making. *Science* (1971) 171(3977):1217–9. doi: 10.1126/science.171.3977.1217

45. Castrogiovanni P, Sanfilippo C, Imbesi R, Maugeri G, Lo Furno D, Tibullo D, et al. Brain Chid1 Expression Correlates With Nrgn and Calb1 in Healthy Subjects and Ad Patients. *Cells* (2021) 10(4)1580-9. doi: 10.3390/cells10040882

46. Catrogiovanni P, Musumeci G, Giunta S, Imbesi R, Di Rosa M. The Expression Levels of Chi3l1 and Il15ralpha Correlate With Tgm2 in Duodenum Biopsies of Patients With Celiac Disease. *Inflammation Res* (2020) 69(9):925–35. doi: 10.1007/s00011-020-01371-9

47. Zetterberg H, Bozzetta E, Favole A, Corona C, Cavarretta MC, Ingravalle F, et al. Neurofilaments in Blood Is a New Promising Preclinical Biomarker for the Screening of Natural Scrapie in Sheep. *PloS One* (2019) 14(12):e0226697. doi: 10.1371/journal.pone.0226697

48. Han S, Liu Y, Cai SJ, Qian M, Ding J, Larion M, et al. Idh Mutation in Glioma: Molecular Mechanisms and Potential Therapeutic Targets. *Br J Cancer* (2020) 122(11):1580–9. doi: 10.1038/s41416-020-0814-x

49. Neagu M, Constantin C, Popescu ID, Zipeto D, Tzanakakis G, Nikitovic D, et al. Inflammation and Metabolism in Cancer Cell-Mitochondria Key Player. *Front Oncol* (2019) 9:348. doi: 10.3389/fonc.2019.00348

50. Lee YJ, Shin KJ, Park SA, Park KS, Park S, Heo K, et al. G-Protein-Coupled Receptor 81 Promotes a Malignant Phenotype in Breast Cancer Through Angiogenic Factor Secretion. *Oncotarget* (2016) 7(43):70898–911. doi: 10.18632/oncotarget.12286

51. Kennedy LG, ER, Palibrk V, Pannone M, Wang W, Ali HJ, et al. Lactate Receptor Hcar1 Regulates Neurogenesis and Microglia Activation After Neonatal Hypoxia-Ischemia. *biorxiv* (2020). doi: 10.1101/2020.12.02.408070

52. Kennedy KM, Dewhirst MW. Tumor Metabolism of Lactate: The Influence and Therapeutic Potential for Mct and Cd147 Regulation. *Future Oncol* (2010) 6(1):127–48. doi: 10.2217/fon.09.145

53. Sun X, Wang M, Wang M, Yao L, Li X, Dong H, et al. Role of Proton-Coupled Monocarboxylate Transporters in Cancer: From Metabolic Crosstalk to Therapeutic Potential. *Front Cell Dev Biol* (2020) 8:651. doi: 10.3389/fcell.2020.00651

54. Merezhinskaya N, Fishbein WN. Monocarboxylate Transporters: Past, Present, and Future. *Histol Histopathol* (2009) 24(2):243–64. doi: 10.14670/HH-24.243

55. Hanahan D, Weinberg RA. Hallmarks of Cancer: The Next Generation. *Cell* (2011) 144(5):646–74. doi: 10.1016/j.cell.2011.02.013

56. Wagner W, Kania KD, Blauz A, Ciszewski WM. The Lactate Receptor (Hcar1/Gpr81) Contributes to Doxorubicin Chemoresistance *Via* Abcb1 Transporter Up-Regulation in Human Cervical Cancer Hela Cells. *J Physiol Pharmacol* (2017) 68(4):555–64.

57. Zhao Y, Li M, Yao X, Fei Y, Lin Z, Li Z, et al. Hcar1/Mct1 Regulates Tumor Ferroptosis Through the Lactate-Mediated Ampk-Scd1 Activity and Its Therapeutic Implications. *Cell Rep* (2020) 33(10):108487. doi: 10.1016/j.celrep.2020.108487

58. Cormio A, Guerra F, Cormio G, Pesce V, Fracasso F, Loizzi V, et al. Mitochondrial DNA Content and Mass Increase in Progression From Normal to Hyperplastic to Cancer Endometrium. *BMC Res Notes* (2012) 5:279. doi: 10.1186/1756-0500-5-279

59. LeBleu VS, O'Connell JT, Gonzalez Herrera KN, Wikman H, Pantel K, Haigis MC, et al. Pgc-1alpha Mediates Mitochondrial Biogenesis and Oxidative Phosphorylation in Cancer Cells to Promote Metastasis. *Nat Cell Biol* (2014) 16(10):992–1003, 1-15. doi: 10.1038/ncb3039

60. Li W, Wei Z, Liu Y, Li H, Ren R, Tang Y. Increased 18f-Fdg Uptake and Expression of Glut1 in the Emt Transformed Breast Cancer Cells Induced by Tgf-Beta. *Neoplasma* (2010) 57(3):234–40. doi: 10.4149/neo_2010_03_234

61. Li J, Dong L, Wei D, Wang X, Zhang S, Li H. Fatty Acid Synthase Mediates the Epithelial-Mesenchymal Transition of Breast Cancer Cells. *Int J Biol Sci* (2014) 10(2):171–80. doi: 10.7150/ijbs.7357

62. Jiang L, Xiao L, Sugiura H, Huang X, Ali A, Kuro-o M, et al. Metabolic Reprogramming During Tgfbeta1-Induced Epithelial-To-Mesenchymal Transition. *Oncogene* (2015) 34(30):3908–16. doi: 10.1038/onc.2014.321

63. Rattigan YI, Patel BB, Ackerstaff E, Sukenick G, Koutcher JA, Glod JW, et al. Lactate Is a Mediator of Metabolic Cooperation Between Stromal Carcinoma Associated Fibroblasts and Glycolytic Tumor Cells in the Tumor Microenvironment. *Exp Cell Res* (2012) 318(4):326–35. doi: 10.1016/j.yexcr.2011.11.014

64. Hanieh H, Ahmed EA, Vishnubalaji R, Alajez NM. Sox4: Epigenetic Regulation and Role in Tumorigenesis. *Semin Cancer Biol* (2020) 67(Pt 1):91–104. doi: 10.1016/j.semcancer.2019.06.022

65. Bhagat TD, Von Ahrens D, Dawlaty M, Zou Y, Baddour J, Achreja A, et al. Lactate-Mediated Epigenetic Reprogramming Regulates Formation of Human Pancreatic Cancer-Associated Fibroblasts. *Elife* (2019) 8: e50663. doi: 10.7554/eLife.50663

66. Miranda-Goncalves V, Goncalves CS, Granja S, Vieira de Castro J, Reis RM, Costa BM, et al. Mct1 Is a New Prognostic Biomarker and Its Therapeutic Inhibition Boosts Response to Temozolomide in Human Glioblastoma. *Cancers (Basel)* (2021) 13(14):3468. doi: 10.3390/cancers13143468

67. Viswanath P, Najac C, Izquierdo-Garcia JL, Pankov A, Hong C, Eriksson P, et al. Mutant Idh1 Expression Is Associated With Down-Regulation of Monocarboxylate Transporters. *Oncotarget* (2016) 7(23):34942–55. doi: 10.18632/oncotarget.9006

Check for updates

Understanding the Potential and Risk of Bacterial Siderophores in Cancer

Valentina Pita-Grisanti [1,2,3], Kaylin Chasser [2,3], Trevor Sobol [2,3] and Zobeida Cruz-Monserrate [2,3*]

[1] The Ohio State University Interdisciplinary Nutrition Program, The Ohio State University, Columbus, OH, United States, [2] Division of Gastroenterology, Hepatology, and Nutrition, Division of Internal Medicine, The Ohio State University Wexner Medical Center, Columbus, OH, United States, [3] The Comprehensive Cancer Center–Arthur G. James Cancer Hospital and Richard J. Solove Research Institute, The Ohio State University, Columbus, OH, United States

Siderophores are iron chelating molecules produced by nearly all organisms, most notably by bacteria, to efficiently sequester the limited iron that is available in the environment. Siderophores are an essential component of mammalian iron homeostasis and the ongoing interspecies competition for iron. Bacteria produce a broad repertoire of siderophores with a canonical role in iron chelation and the capacity to perform versatile functions such as interacting with other microbes and the host immune system. Siderophores are a vast area of untapped potential in the field of cancer research because cancer cells demand increased iron concentrations to sustain rapid proliferation. Studies investigating siderophores as therapeutics in cancer generally focused on the role of a few siderophores as iron chelators; however, these studies are limited and some show conflicting results. Moreover, siderophores are biologically conserved, structurally diverse molecules that perform additional functions related to iron chelation. Siderophores also have a role in inflammation due to their iron acquisition and chelation properties. These diverse functions may contribute to both risks and benefits as therapeutic agents in cancer. The potential of siderophore-mediated iron and bacterial modulation to be used in the treatment of cancer warrants further investigation. This review discusses the wide range of bacterial siderophore functions and their utilization in cancer treatment to further expand their functional relevance in cancer detection and treatment.

Keywords: microbiome, bacteria, siderophores, enterobactin, deferoxamine, cancer, tumor, iron

1 INTRODUCTION

Siderophores are iron chelating molecules produced by nearly all organisms to enhance iron acquisition from the environment (1–3). Iron is an essential micronutrient for biological and metabolic cellular functions, but has limited availability in the environment (2, 3). Iron can accept and donate electrons and primarily exists in two states in biological systems, ferric (Fe^{3+}) and ferrous (Fe^{2+}), which allows iron to bind different ligands. Ferrous iron (Fe^{2+}) can generate reactive oxygen species (ROS) through the Fenton and Haber-Weiss reactions (4, 5). At physiological pH, ferrous (Fe^{2+}) iron is oxidized to the low solubility ferric (Fe^{3+}) state (6). Iron levels are tightly

regulated through the production of various binding molecules and transporters such as transferrin, ferritin and ferroportin, which decrease the potential of ferrous iron to generate ROS (4, 7) (**Figure 1A**). This regulation results in an ongoing battle for iron between mammalian hosts and their microbial inhabitants (8–11). Bacteria evolved to improve their odds in this battle by producing an extensive repertoire of siderophores that bind ferric (Fe^{3+}) iron (2, 12). These siderophores are recognized for their diverse functionality beyond iron binding, including roles in signaling, virulence, protection against oxidative stress, metal acquisition, and competition with other microbes and their hosts (13–15).

Siderophores and iron have become relevant in carcinogenesis because cancer cells demand increased iron concentrations to sustain rapid proliferation, which increases the activity of many iron-binding molecules [transferrin, the transferrin receptor, ferritin and lipocalin 2 (Lcn2)] while decreasing the activity of the cell iron exporter ferroportin (**Figure 1B**) (11, 16–18). Bacterial dysbiosis is also common during cancer (19–22), which could affect siderophore secretion in this disease (**Figure 1B**). Iron accumulation is usually observed in tumors, which has been linked to worse cancer prognosis and increased invasion and metastasis (11, 23) (**Figure 2A**). There is extensive evidence that iron supports various steps of cancer progression, and modulating iron levels has been considered as a promising alternative cancer therapy. Bacterial and synthetic siderophores have been used as iron chelating agents to reduce iron levels in tumors (24) but the function and potential of siderophores in cancer continues to be severely underexplored. Published preclinical data and some clinical studies using siderophores in cancer reported both beneficial and inconsistent results (**Figure 2B**; **Tables 1**, **2**) (35, 46, 68–70), suggesting that their role in cancer warrants further investigation.

Siderophore interactions with the immune system contribute to the ongoing struggle for iron homeostasis. Immune cells enhance the production of siderophore-binding proteins and proinflammatory cytokines (71–73). In response, bacteria upregulate siderophore production and synthesize stealth siderophores to evade host immune defenses which will be described in detail below (3, 72). These siderophore-mediated adjustments in iron availability suggest a link between the immune response and iron accumulation in cancer cells. Insight into the balance between iron, siderophores, and immune function could contribute to a more comprehensive understanding of the role of siderophores in cancer.

This review focuses on the current research investigating the role and therapeutic potential of bacterial siderophores in cancer, highlighting their functions and interactions with the microbiome and the immune system that could be relevant in cancer research. While we provide brief summaries on siderophore functionality and the relationship between iron and cancer, we would like to direct the readers to the following reviews for a deeper understanding of these topics (4, 13, 14, 23).
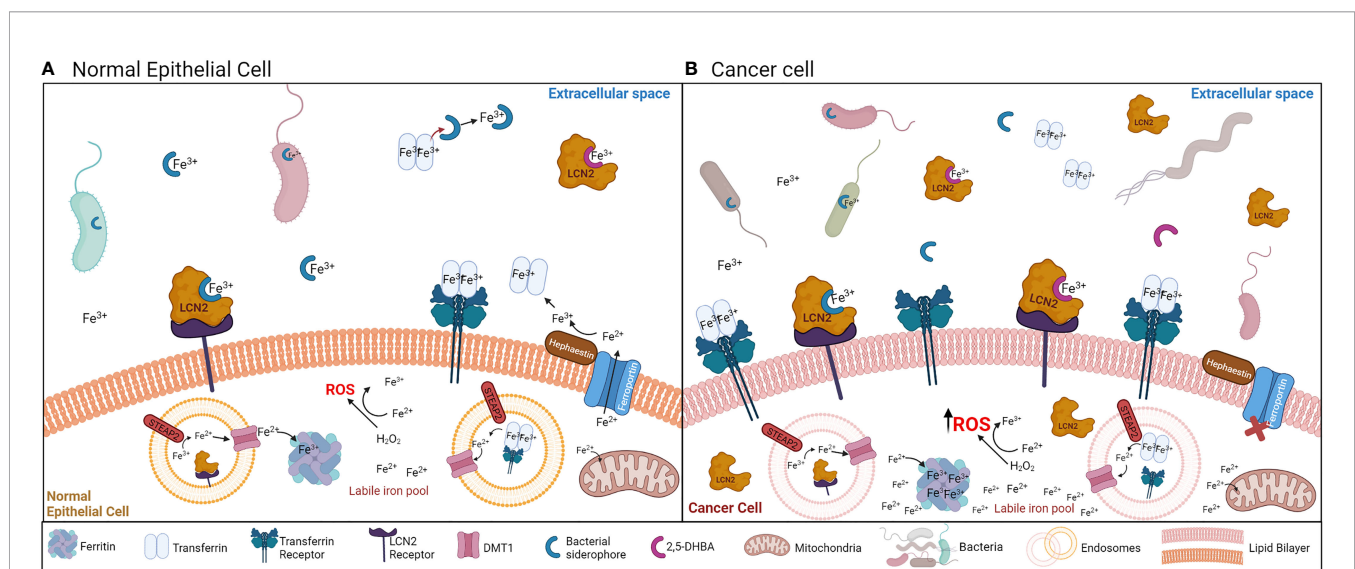

FIGURE 1 | **(A)** Mechanisms of iron acquisition between bacteria and normal epithelial cells. Bacteria-secreted siderophores and mammalian siderophores (2,5-DHBA) acquire ferric iron (Fe^{3+}) for bacteria or host uptake. Siderophores can also chelate iron away from transferrin. LCN2 can bind the bacteria-secreted siderophores to sequester ferric iron (Fe^{3+}) away from bacteria. Transferrin and LCN2 bind ferric iron in the extracellular space, and by binding the transferrin receptor or the LCN2 receptor (respectively) in the cell surface, the transferrin/LCN2-iron complex enters the cell through endocytosis. Once iron is in the cytoplasm, it is converted to the ferrous form (Fe^{2+}) by the STEAP2 enzyme, and exits the endosome through the DMT1 transporter. In the cytosol, iron can be stored in ferritin back in the ferric form (Fe^{3+}). Iron can exit the cell *via* ferroportin, which is regulated by hephaestin. This process is tightly regulated to avoid the generation of ROS from the labile iron pool (free ferrous iron (Fe^{2+}) in the cytoplasm). **(B)** Mechanisms of iron acquisition between bacteria and cancer cells. Many cancers are characterized by increased bacterial growth and dysbiosis. Iron uptake is increased in cancer cells, which is accomplished by increasing the function of transferrin, the transferrin receptor, ferritin iron storage, and decreasing the function of ferroportin. LCN2 and its receptor are also increased during cancer. Increased ferrous iron (Fe^{2+}) accumulation in the cytosol generates ROS.
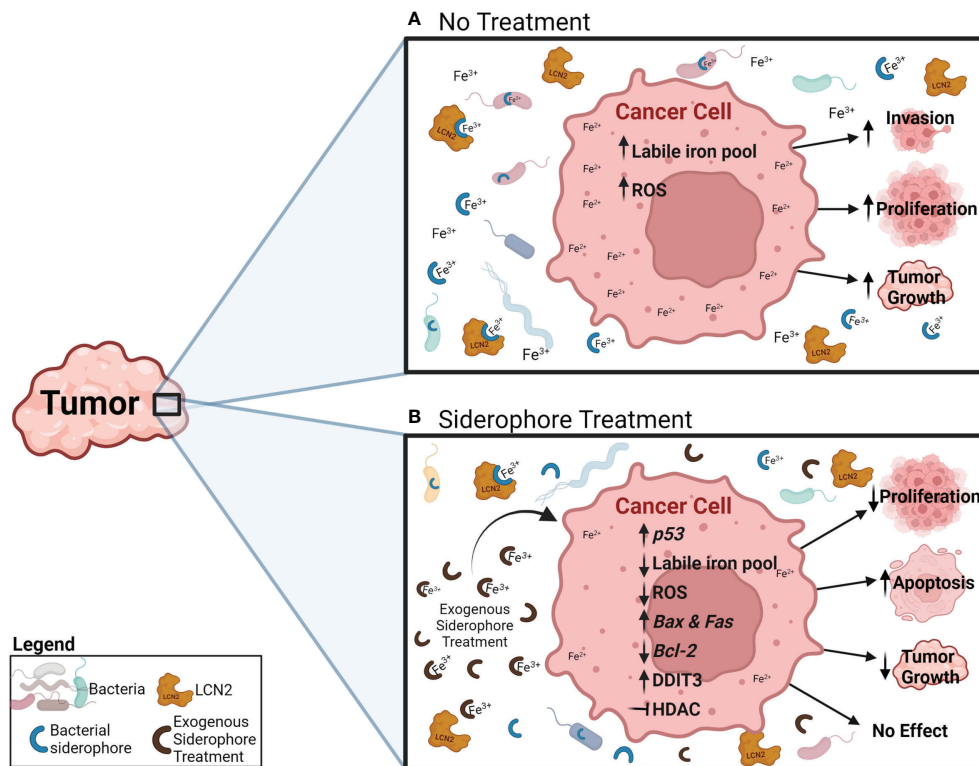
FIGURE 2 | Potential effects and mechanisms of an exogenous siderophore treatment in cancer cells. **(A)** Under normal conditions, cancer cells increase their iron uptake, which increases the iron labile pool (Fe^{2+}) and ROS generation, and has been related to increased invasion, proliferation and tumor growth. **(B)** During exogenous siderophore treatment, siderophores bind ferric iron (Fe^{3+}) and decrease the levels of free iron available for bacteria, LCN2 and cancer cells. As a result, cancer cells display reduced proliferation and tumor growth, and induction of apoptosis. Proposed mechanisms include: reduction of ferric iron (Fe^{3+}) availability, the intracellular iron pool (Fe^{2+}), ROS generation and expression of the anti-apoptotic gene *Bcl-2*, increasing expression of *p53* and the pro-apoptotic genes *Bax* and *Fas*, activating the pro-apoptotic pathway through *DDIT3*, and inhibiting HDAC.

This review also lists the clinical trials that use siderophores and analogs as interventions in cancer. We compare and discuss their settings and regimens to provide a broader perspective of how siderophores are administered to patients, and what factors need to be taken into consideration in cancer. We searched the following databases: clinicaltrials.gov, the European Society of Medical Oncology (ESMO), and the World Health Organization. We used the following search terms: "siderophores" OR "deferoxamine" OR "deferasirox" OR "enterobactin" OR "desferrithiocin" OR "ferrichrome" OR "deferiprone" OR "2,3-dihydroxybenzoic acid" AND "cancer". By highlighting the role of these siderophore interactions and how they are used in preclinical cancer models, we aim to promote novel research that leverages these connections in cancer detection and treatment.
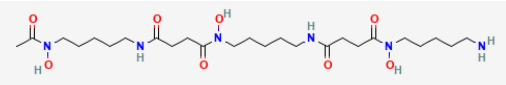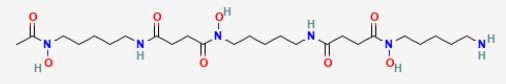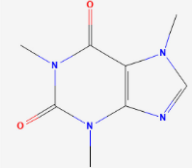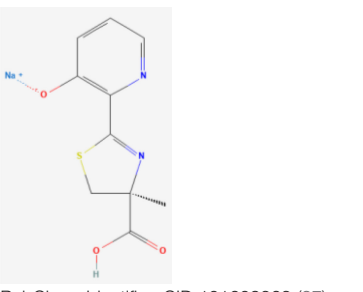
2 SIDEROPHORES AS IRON CHELATORS
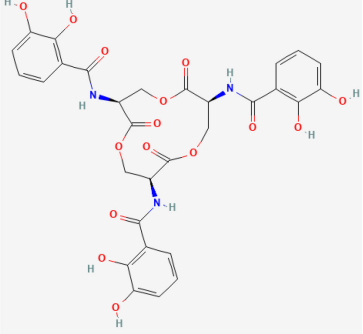
Iron is an essential element for nearly all life forms, with critical roles in various biological and metabolic processes for cell survival. Iron availability within aerobic environments is severely limited due to low ferric (Fe^{3+}) iron solubility and low ferrous (Fe^{2+}) iron availability (2, 3). Essentially all microorganisms, bacteria, fungi, plants, and animals produce siderophores to sequester iron from the environment. Siderophores are high-affinity iron chelators that bind iron to maintain iron levels required for survival (1, 3, 8, 12, 14). Siderophores are small molecules, around 500–1500 Daltons in molecular weight that bind primarily to ferric iron (Fe^{3+}) (2) and exhibit high structural diversity (hundreds have been structurally characterized and described) (2, 74). Thus, siderophores are biologically important and have the potential to selectively compete in cellular processes, which makes them an interesting target in cancer research. Understanding their functions and interactions in the microbiome and with the host will be needed to explore their role and potential in cancer.

2.1 Mammalian Siderophores
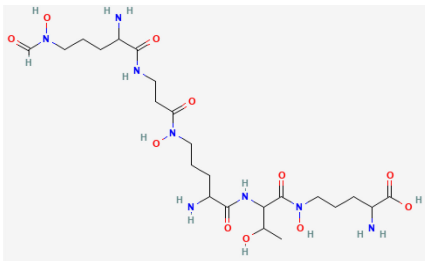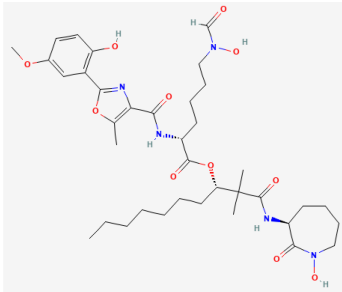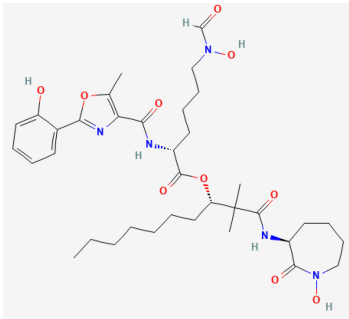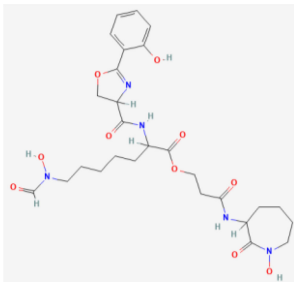
Free ferric iron (Fe^{3+}) is tightly regulated in human hosts; most iron is bound to transferrin in serum, or to lactoferrin primarily in secretory fluids, thereby limiting iron availability for bacterial acquisition (8–10). Mammals produce a limited number of siderophores, including 2,5-dihydroxybenzoic acid (2,5-DHBA) (8, 75) and catechols (76, 77), which enable iron acquisition from transferrin, lactoferrin, and the environment **Figure 1A** (71, 77, 78).

TABLE 1 | Bacterial siderophores used in cancer research.

Siderophore	Structure 2D	Secreted by	Cancer Type Studied
Deferoxamine (DFO)	 PubChem Identifier: CID 2973 (25)	*Streptomyces* spp	Macrophage (34), leukemia (34, 35), breast cancer (34, 36, 37), hepatocellular carcinoma (34, 38–40), gastric cancer (41), neuroblastoma (42, 43), ovarian (36), epidermoid carcinoma (36).
DFCAF (DFO complex)	 PubChem Identifier: CID 2973 (25) PubChem Identifier: CID 2519 (26)	*Streptomyces* spp	Cancer stem cells (44).
Desferrithiocin (DFT)	 PubChem Identifier: CID 101609363 (27)	*Streptomyces antibioticus* DSM	Hepatocellular carcinoma (45).
Enterobactin	 PubChem Identifier: CID 34231 (28)	*E. coli, Salmonella enterica, Shigella dysenteriae and Klebsiella pneumoniae*	Monocyte-derived cancer cells (46).
Ferrichrome	 PubChem Identifier: CID 644246 (29)	*Lactobacillus casei*	Gastric (47) and colon cancer (48, 49).

(Continued)

TABLE 1 | Continued

Siderophore	Structure 2D	Secreted by	Cancer Type Studied
Exochelin-MS	PubChem Identifier: CID 139583168 (30)	*Mycobacterium smegmatis*	Macrophage, liver cancer, leukemia, breast cancer (34).
Mycobactin S	PubChem Identifier: CID 3083702 (31)	*Mycobacterium smegmatis*	Macrophage, liver cancer, leukemia, breast cancer (34).
Amamistatin A	PubChem Identifier: CID 135430484 Amamistatin A (32)	*Nocardia asteroids*	Leukemia, breast, lung, and stomach cancer (50).
Amamistatin B	PubChem Identifier: CID 135438025 Amamistatin B (33)	*Nocardia asteroids*	Leukemia, breast, lung, and stomach cancer (50).

Synthesis of the mammalian siderophore 2,5-DHBA is catalyzed by the enzyme 3-hydroxybutyrate dehydrogenase-2 (Bdh2) (8). During the innate immune response to lipopolysaccharide exposure, toll-like receptor 4 (TLR4) suppresses Bdh2 through the transcriptional repressor B lymphocyte–induced maturation protein (Blimp-1) (8, 79). This reduces the circulating 2,5-DHBA levels during bacterial infection and limits the host-derived iron complexes available for pathogens to sequester (76, 77, 79). Embedded in the role of iron binding and transport, 2,5-DHBA is involved in intracellular iron homeostasis, erythrocyte maturation, and mitochondrial iron uptake (8, 80, 81). Decreased 2,5-DHBA through reduction of Bdh2 can lead to anemia, cytoplasmic iron accumulation, mitochondrial dysfunction, and potential apoptosis (8, 80, 81). A group of siderophore-binding proteins called lipocalins or siderocalins bind mammalian and bacterial siderophores with specificity for nearly all catecholate

siderophores and some carboxylate siderophores (71, 72). Thus, mammalian siderophores, alongside lipocalins and transferrin, have a critical role in mammalian iron homeostasis through intracellular iron balance and mitochondrial function (8, 71, 77, 78, 80). Future work might uncover new siderophores and functionalities within the mammalian iron chelator protein family that could be used to alter iron availability within cancer cells.

2.2 Bacterial Siderophores

Bacteria produce siderophores to obtain iron from their hosts or environment and to outcompete other microbes within their environment (3, 14, 82). The ferric uptake regulator (Fur) is a bacterial transcription factor that upregulates siderophore production based on low intracellular iron availability to rapidly acquire iron for metabolic processes and virulence (9, 83, 84). When iron availability is high, Fur suppresses iron acquisition and transport genes, including TonB, thereby preventing iron toxicity and intracellular oxidative stress (83–85). Siderophores enable bacteria to bind ferric iron (Fe^{3+}) from their hosts or environment when under low iron availability, and then selectively import iron *via* specific cognate receptors. The specificity of siderophores and siderophore receptors enable microbes to support their own proliferation while competing with other microbial populations for limited iron resources (12, 14). However, there is evidence of both cooperation and competition among bacterial populations for iron, and bacteria can modulate siderophore production in specific hosts or environments (14, 86, 87). Cooperation in bacterial iron uptake involves the production of siderophores that can be taken up by bacterial species other than the initial producer, although there is a correlation between bacterial relatedness and cooperation. Competition in bacterial iron uptake occurs when bacteria that do not produce specific siderophores express receptors that enable siderophore uptake, thereby exploiting the siderophore production of other bacteria. Competition also happens when bacteria secrete specific siderophores for which other bacteria lack the matching receptors for uptake or when the secreted siderophores have higher affinity for iron. Therefore, the bacteria that secreted the specific siderophore (or higher affinity siderophores) decreases the iron available to other species (14, 88). Cooperation and competition has been extensively studied in *Pseudomonas aeruginosa* and its siderophore pyoverdine (PVD) (14, 15, 88–91).

Bacteria can synthesize multiple siderophores with varying iron affinities and minor structural variations, which can enhance iron uptake, reduce the frequency of competitive theft, and improve the competitive advantage over other microbes (3, 12, 82). Several microbes produce stealth siderophores, which are essential in evading the mammalian host innate immune molecule, siderophore binding Lcn2 (3, 72). For example, *E. coli* and *Salmonella* spp. can modify the siderophore enterobactin, which can be neutralized by Lcn2, to form salmochelin, a stealth siderophore that cannot be bound by Lcn2, thereby enhancing their survival when the acute phase response of infection and inflammation has been triggered (2, 3). Enterobactin from *E. coli* is usually associated with a negative impact on iron homeostasis and host health.

Mice deficient in Lcn2 have increased susceptibility to *E. coli*-induced septicemia (73). At the same time, enterobactin increases the host iron pool and promotes mitochondrial iron uptake by binding to the ATP synthase α subunit in mammalian cells and *C. elegans* (92). This positive relationship between enterobactin and the host could explain why the host continues to tolerate enterobactin-producing bacteria in their microbiome.

To further showcase the multifunctionality of siderophores, PVD, a siderophore produced by *P. aeruginosa*, can enter *C. elegans* and induce death by acting as a toxin. PVD and *P. aeruginosa* can also disrupt *C. elegans'* mitochondrial homeostasis inducing mitophagy, which is accomplished by the host as a mechanism to resist damages by PVD or *P. aeruginosa* (93). Exogenous iron chelators attenuate *P. aeruginosa*-mediated *C. elegans* killing by limiting bacterial growth. Interestingly, the same iron chelators reduce mitochondrial mass and induce mitochondrial fragmentation in *C. elegans*, and induce mitochondrial turnover and degradation in mammalian cells (93). This same group found that the siderophore PVD (but not pyochelin) was required for *P. aeruginosa* to induce cell death in *C. elegans*, which occurs through hypoxia induction. Similarly, exogenous iron chelators at higher concentrations also trigger a hypoxic response and death in *C. elegans* (94). The flexibility and diversity of bacterial siderophore production indicates that these molecules have important and complex roles in iron acquisition that should be taken into consideration in the context of cancer.

2.3 Other Siderophores

Both plants and fungi produce hundreds of unique siderophores. Plant siderophores (phytosiderophores) are most notably secreted by gramineous plants to obtain ferric iron (Fe^{3+}), and likely zinc and copper, from soils that are deficient in these metals (95). Fungi utilize siderophores for iron import and can even upregulate bacterial siderophore transporters to compete for iron in the environment (2, 96–98). The focus of this review is bacterial siderophores and their role in cancer; however, the interactions among fungal, bacterial, and host iron acquisition systems may be disrupted in cancer and should be considered.

3 VERSATILE FUNCTIONS OF SIDEROPHORES

Siderophores perform a multitude of functions in addition to iron acquisition. These include roles in signaling, protection against oxidative stress, sequestration of other metals, and siderophore moieties as antibiotics (13). Although iron chelation is the most important and well-characterized role of siderophores, these additional functionalities indicate their biological significance and structural diversity (12). Understanding whether these functions can be applied or studied in the context of cancer will elucidate the potential of siderophores as cancer research targets.

TABLE 2 | Clinical trials that investigated siderophores and siderophore analogs as cancer therapeutics.

Study title	Age years	Status	Enrollment	Condition	Intervention	Primary Outcome	Intervention Regime	Clinical Trial Number	Source	Refs.
Pilot Study to Assess Hematologic Response in Patients with Acute Myeloid Leukemia or High Risk Myelodysplastic Syndromes Undergoing Monotherapy With Exjade (Deferasirox)	≥18	Completed	25 (estimated)	High risk myelodysplastic syndromes or acute myeloid leukemia	Deferasirox (Exjade, ICL670)	Number of adverse events (time frame: 2 years)	Oral administration	NCT02233504	clinicaltrial. gov	
Deferasirox in Treating Iron Overload Caused by Blood Transfusions in Patients with Hematologic Malignancies	≥18	Completed	16	Leukemia, lymphoma, and 133 more	Deferasirox (Exjade, ICL670)	Changes in mean neutrophil values (measured by lab) for Arm 1 (time frame: baseline up to 6 months)	Once daily, orally, for up to 6 months or until blood counts recover in the absence of disease progression or unacceptable toxicity	NCT01273766	clinicaltrial. gov	
Combination Study of Deferasirox and Erythropoietin in Patients with Low- and Int-1-risk Myelodysplastic Syndrome	≥18	Completed	28	Low and Int 1-risk myelodysplastic syndrome	Deferasirox, erythropoietin alpha	Difference in percentage of patients achieving erythroid response within 12 Weeks, by treatment group (time frame: baseline up to 12 weeks)	Deferasirox dispersible tablet 10 mg/kg/day or deferasirox film-coated tablet (FCT) 7 mg/kg/day in combination with erythropoietin 40,000 units/week (or erythropoietin alone)	NCT01868477	clinicaltrial. gov	
Myelodysplastic syndromes (MDS) Event Free Survival with Iron Chelation Therapy Study	≥18	Completed	225	Myelodysplastic syndromes	Deferasirox	Event free survival (time frame: Day 1 to end of treatment period, approx. 7 years)	10 mg/kg/day (once daily) for the first 2 weeks of treatment, followed by 20 mg/kg/day (once daily) from Week 2 to end of treatment	NCT00940602	clinicaltrial. gov	(51)
This Study Will Evaluate Efficacy and Safety of Deferasirox in Patients with Myelodysplastic Syndromes (MDS), Thalassemia and Rare Anemia Types Having Transfusion-Induced Iron Overload	≥2	Completed	111	Myelodysplastic syndrome, thalassemia	Deferasirox, ICL670	Changes in ferritin level compared to baseline in patients with transfusion-induced iron overload treated with exjade (time frame: baseline assessment is followed by monthly assessments for up to 1 year)	NA	NCT01250951	clinicaltrial. gov	(52)
Efficacy and Safety of Deferasirox in Patients with Myelodysplastic Syndrome and Transfusion-dependent Iron Overload	≥18	Completed	63	Myelodysplastic syndromes, transfusion-dependent iron overload	ICL670/ Deferasirox	To assess iron chelation by comparing serum ferritin values at baseline vs. 52 weeks of treatment with deferasirox (time frame: 52 weeks)	NA	NCT00481143	clinicaltrial. gov	(53)
Evaluating the Efficacy of Deferasirox in Transfusion Dependent Chronic Anaemias (Myelodysplastic Syndrome, Beta-thalassaemia Patients) with Chronic Iron Overload	18–80	Completed	309 (estimated)	Myelodysplastic syndromes, beta-thalassemia	Deferasirox	This study will evaluate the safety and efficacy of deferasirox in transfusion dependent myelodysplastic syndrome, beta-thalassemia major patients with chronic iron overload [time frame: monthly during the therapy and at the end of the treatment (after 9 months therapy)]	NA	NCT00564941	clinicaltrial. gov	
Safety, Tolerability, and Efficacy of Deferasirox in MDS	18–80	Completed	158	Myelodysplastic syndromes, hemosiderosis	Deferasirox	To evaluate the tolerability and safety profile of deferasirox in patients with MDS with post-transfusional hemosiderosis (time frame: baseline assessment and then monthly thereafter)	NA	NCT00469560	clinicaltrial. gov	(54–56)

(Continued)

TABLE 2 | Continued

Study title	Age years	Status	Enrollment	Condition	Intervention	Primary Outcome	Intervention Regime	Clinical Trial Number	Source	Refs.
Study of Deferasirox in Iron Overload from Beta-thalassemia Unable to be Treated with Deferoxamine or Chronic Anemias	≥2	Completed	175	Beta-thalassemia, myelodysplastic syndromes, Fanconi syndrome, Diamond-Blackfan anemia, aplastic anemia	Deferasirox	To evaluate the effects of treatment on the liver iron content	NA	NCT00061763	clinicaltrial.gov	
Magnetic Resonance Imaging (MRI) Assessments of the Heart and Liver Iron Load in Patients with Transfusion Induced Iron Overload	≥18	Completed	118	Hemoglobinopathies, myelodysplastic syndromes, other inherited or acquired anemia, MPD syndrome, Diamond-Blackfan anemia, other rare anemias, transfusional iron overload	Deferasirox	Change in cardiac iron load and cardiac ejection fraction by MRI recorded at baseline and after 53 weeks (time frame: 12 months)	Deferasirox up to 40 mg/kg/day, per os (PO) (orally), dispersible tablets, taken once daily	NCT00673608	clinicaltrial.gov	(57)
Study for the Treatment of Transfusional Iron Overload in Myelodysplastic Patients	≥18	Completed	24	Myelodysplastic syndromes, iron overload	Deferasirox	Number of participants with adverse events and serious adverse events (time frame: up to Week 52)	Deferasirox 20 mg/kg/day OD for 12 months; deferasirox was taken every morning 30 minutes before breakfast	NCT00117507	clinicaltrial.gov	(58)
Evaluation the Effect of Exjade on Oxidative Stress in Low Risk Myelodysplastic Syndrome Patients with Iron Overload	≥18	Completed	21	Myelodysplastic syndrome	Deferasirox (Exjade)	To evaluate the antioxidative effect of Exjade therapy in MDS patients (time frame: one year)	NA	NCT00452660	clinicaltrial.gov	(59)
Effect of Deferiprone on Oxidative-Stress and Iron-Overload in Low Risk Transfusion Dependent MDS Patients	≥18	Completed	19	Myelodysplastic syndrome, iron overload due to repeated red blood cell transfusion	Deferiprone	To evaluate the effect of deferiprone on oxidative stress parameter ROS in iron overloaded and blood dependent patients with MDS (time frame: 4 months)	NA	NCT02477631	clinicaltrial.gov	
A Phase 2 Study of the Efficacy and Safety of Deferasirox Administered at Early Iron Loading in Patients with Transfusion-Dependent Myelodysplastic Syndromes	≥18	Completed	13	Myelodysplastic syndromes	Deferasirox (Exjade)	Primary outcome is time to mean serum ferritin > 1500 µg/l, as measured from the time of initiation using the mean serum ferritin value of 2 consecutive measurements of ferritin, where the first level is >1500 µg/l and CRP is <3 times baseline measurement	Dispersible tablet administered orally, 10 mg/kg/day	2011-004559-38 ISRCTN62162141	EU Clinical Trials Register	
The Efficacy of Deferoxamine in Preventing Nephrotoxicity of Anthracyclins in Pediatric Cancer Patients	2–18	Completed	60	Nephropathy in pediatric cancer patients	Deferoxamine	Blood urea nitrogen, microalbuminuria (urine albumin-to-creatinine ratio), nephropathy sign, serum creatinine, urine creatinine, urine N-acetyl beta glucosaminidase, urine protein	Deferoxamine 10-20,g/kg or 50 mg/kg, once per day via IV over 8 hours with or without anthracyclin infusion	IRCT2016021915666N3	World Health Organization	
Deferoxamine for Patients with Advanced Pancreatic Cancer: Pilot Study	≥20	Completed/ terminated	10	Pancreatic cancer	Deferoxamine	Safety	NA	JPRN-UMIN000009054	World Health Organization	
The Safety and Efficacy of Deferoxamine for Treating Unresectable Hepatocellular Carcinoma	≥18	Recruiting	100 (estimated)	Unresectable hepatocellular carcinoma	Deferoxamine	Progression free survival in participants with unresectable hepatocellular cancer [time frame: first dose to date of progressive disease or death due to any cause, every 3 cycles up to 36 months (1 cycle=2 weeks)]	Intervention combined with conventional transarterial chemoembolization	NCT03652467	clinicaltrial.gov	

(Continued)

TABLE 2 | Continued

Study title	Age years	Status	Enrollment	Condition	Intervention	Primary Outcome	Intervention Regime	Clinical Trial Number	Source	Refs.
Evaluating Low-Dose Deferasirox (DFX) in Patients with Low-Risk MDS Resistant or Relapsing After ESA Agents	18–100	Recruiting	39	Myelodysplasia	Deferasirox (Exjade)	Percentage of patients without transfusion-dependence at 12 months (time frame: 12 months)	Deferasirox at 3.5 mg/kg/day, orally	NCT03387475	clinicaltrial.gov	
Phase II Study to Evaluate Overall Response in Patients with Higher Risk Myelodysplastic Syndromes (MDS) Treated with Azacitidine with or without Deferasirox	18–80	Terminated	1	High risk myelodysplasia	Azacitidine, azacitidine plus deferasirox	Overall response rate per IWG 2006 criteria (time frame: 1 year)	Azacitidine 75 mg/m^2, 7 days/28 day cycle SC or IV, deferasirox 10 mg/kg/day	NCT02159040	clinicaltrial.gov	
A Phase II Pilot Study to Assess the Presence of Molecular Factors Predictive for Hematologic Response in Myelodysplastic Syndrome Patients Receiving DeferasiroxTherapy	≥18	Terminated	1	Myelodysplastic syndrome	Bone marrow aspirate, and deferasirox	Fold increase/decrease in gene transcription from baseline bone marrow aspirate of responders versus nonresponders (time frame: 18 months)	Deferasirox; patients are already on commercial deferasirox before entering the study	NCT02663752	clinicaltrial.gov	
Myelodysplastic Syndrome (MDS) Gastrointestinal (GI) Tolerability Study	≥18	Terminated (low enrollment)	12	Myelodysplastic syndrome, transfusional iron overload	Deferasirox (ICL670)	Difference in the frequency of overall newly occurring GI adverse events in the two treatment arms (time frame: 3 months)	Deferasirox 20 mg/kg/day taken in the morning, 30 minutes before food OR deferasirox 20 mg/kg/day taken in the evening, no less than 2 hours after the last food intake or at least 30 minutes before the evening meal	NCT01326845	clinicaltrial.gov	
Azacitidine Plus Deferasirox (ICL670) in Higher Risk Myelodysplastic Syndromes (MDS)	≥18	Terminated (accrual too slow)	1	Myelodysplastic syndromes	Deferasirox (Exjade, ICL670) plus azacitidine	Difference in proportion of patients with hematologic improvement as defined by the IWG criteria[30] with the addition of deferasirox to azacitidine compared with azacitidine alone in higher risk non-responding MDS patients after 6 cycles of azacitidine (time frame: 6 months)	Azacitidine 75 mg/m^2 sc daily for 7 days every 28 days for 6 cycles plus deferasirox 10–30 mg/kg/day depending on transfusion needs	NCT02038816	clinicaltrial.gov	
Deferoxamine for Iron Overload before Allogeneic Stem Cell Transplantation	≥18	Terminated (slow patient accrual)	5	Acute myeloid leukemia, acute lymphoblastic leukemia, myelodysplastic syndrome	Deferoxamine	Safety of deferoxamine therapy determined by the number of participants with Grade 3 or higher toxicities (time frame: baseline, 6 months, 1 year)	50 mg/kg/day of deferoxamine as chelation therapy for at least 2 weeks prior to receiving myeloablative transplant, intravenously or subcutaneously	NCT00658411	clinicaltrial.gov	(60)
Deferasirox in Treating Patients with Iron Overload after Undergoing a Donor Stem Cell Transplant	≥18	Terminated(slow accrual of patients)	4	Breast cancer, iron overload, leukemia, lymphoma, multiple myeloma and plasma cell neoplasm, myelodysplastic syndromes, neuroblastoma, ovarian cancer	Deferasirox (Exjade)	Number of patients not completing treatment (time frame: 6 months)	20 mg/kg once daily orally for 6 months	NCT00602446	clinicaltrial.gov	
Treatment of Iron Overload with Deferasirox (Exjade) in Hereditary Hemochromatosis and Myelodysplastic Syndrome	18–80	Terminated (failure to recruit patients with hemochromatosis	50	Hemochromatosis, myelodysplastic syndromes	Deferasirox (Exjade) and Venesection	Changes from baseline in liver iron concentration and heart iron concentration determined by MRI, and in bone marrow iron content determined by microscopy after treatment with	Deferasirox tablet (250 mg or 500 mg) dispersed in a drinkable solution, 10 mg/kg/day, once daily for 12 months OR once daily for 2 weeks and thereafter 20 mg/kg/day for 11.5 months, treated with venesection every 8–10 days for 12 months,	NCT01892644	clinicaltrial.gov	(61–65)

(Continued)

TABLE 2 | Continued

Study title	Age years	Status	Enrollment	Condition	Intervention	Primary Outcome	Intervention Regime	Clinical Trial Number	Source	Refs.
		to the deferasirox arm)				deferasirox (time frame: 0, 6, and 12 months)	or until serum-ferritin has been reduced to 50 µg/L			
Deferasirox for Treating Patients Who Have Undergone Allogeneic Stem Cell Transplant and Have Iron Overload	≥18	Terminated (low enrollment)	1	Leukemia, lymphoma, and 133 more	Deferasirox (Exjade, ICL670)	Number of patients with elevated labile plasma iron above threshold (0.5 Umol/L) (time frame: at baseline)	Patients receive oral deferasirox once daily for up to 6 months in the absence of unacceptable toxicity, low dose deferasirox on labile plasma iron is also examined	NCT01159067	clinicaltrial.gov	
Deferasirox, Cholecalciferol, and Azacitidine in the Treatment of Newly Diagnosed AML Patients Over 65	65-89	Terminated (low patient accrual)	4	Acute Myeloid Leukemia	Deferasirox (Exjade), cholecalciferol and azacitidine	Complete remission rate (time frame: up to 5 years)	Deferasirox (20 mg/kg/day) on days 1–7 of protocol, repeated every four weeks for 8 cycles given PO; cholecalciferol (4,000 units/day), on days 1–7 of protocol, repeated every four weeks for 8 cycles given PO; azacitidine (75 mg/m² SC or IV administration) on days 1–7 of protocol, repeated every four weeks for 8 cycles	NCT02341495	clinicaltrial.gov	
Deferasirox in Treating Patients with Very Low, Low, or Intermediate-Risk Red Blood Cell Transfusion Dependent Anemia or Myelodysplastic Syndrome	≥18	Terminated (low accrual)	2	Anemia, myelodysplastic syndrome	Deferasirox (Exjade)	Proportion of patients that achieve erythroid hematologic improvement	PO QD; treatment continues for up to 52 weeks in the absence of disease progression or unacceptable toxicity	NCT02943668	clinicaltrial.gov	
The Effect of Deferasirox on Response Rate of Acute Leukemia Patients Not Treated by Standard Chemotherapy Regimens	≥15	Unknown	40	Acute myeloid leukemia, acute lymphoid leukemia	Cytarabine (cytosar) and deferasirox (osveral)	Complete remission (time frame: first month)	Oral deferasirox at 20 mg/kg per day with cytarabine at 20 mg/m², SC, two times a day for 10 days every 30 days for 1 cycle (or cytarabine alone)	NCT02413021	clinicaltrial.gov	(66, 67)
Study of the Outcome of Patients with Acute Myeloblastic Leukemia and Myelodysplastic Syndrome Receiving Iron Chelation Therapy after Allogeneic Hematopoietic Stem Cell Transplantation	≥18	Unknown	150 (estimated)	Myeloid leukemia, myelodysplastic syndromes	Exjade (deferasirox)	Impact of iron chelation on relapse-free survival rate (time frame: at 2 years)	Exjade at 10 mg/kg per day if the ferritin level reached 1000 ng/ml at 6 months after allograft, for a minimum duration of three months and up to 6 months	NCT03659084	clinicaltrial.gov	

3.1 Siderophores as Virulence Factors

Siderophores have been rigorously linked to pathogen virulence (99–104). As mentioned earlier, *Pseudomonas aeruginosa* produces PVD, a siderophore that stimulates its own production along with the virulence factors exotoxin A and lysyl endoprotease through a transmembrane signaling pathway described by Lamont et al. (99, 105). *Klebsiella pneumoniae* strain CG43 carries the virulence plasmid pLVPK, which expresses genes involved in iron acquisition, pathogenicity, capsular polysaccharide synthesis, and genes that confer resistance to lead and tellurite (106). *K. pneumoniae* genes for the siderophores enterobactin, aerobactin, and salmochelin are encoded in the chromosome, the plasmid, or both; aerobactin and salmochelin are associated with hypervirulence (104). Siderophore synthesis promotes iron acquisition in an iron-limited environment, which enhances microbial proliferation and pathogenic virulence during invasion and colonization of the host.

3.2 Siderophores as Signaling Molecules

Microbes can use siderophores as intraspecies signaling molecules that are responsive to their environment and modify their own iron acquisition capabilities, and as interspecies signaling molecules between microbial populations across the environment (13). The siderophore PVD from *P. aeruginosa* is produced through a complex signaling pathway, described by Lamont et al. and Beare et al., that also initiates transcriptional activation of the endotoxin A (*toxA*) gene (99, 107, 108). Another signaling mechanism of *P. aeruginosa* involves siderophore-induced upregulation of the TonB-dependent receptors FoxA and FiuA in response to the heterologous siderophores ferrioxamine B and ferrichrome (109). This confers a competitive advantage to *P. aeruginosa* by enhancing iron sequestration from the environment. The *E. coli* TonB-dependent receptor FecA is activated by binding to ferric citrate, and then initiates the transcription of ferric citrate transport proteins to facilitate transport of citrate-bound iron (ferric citrate) into the cytoplasm (110, 111). Some microbial siderophores act as signaling molecules that regulate the production of their own virulence factors, stimulate iron transport, and communicate within and between microbial communities, an important consideration when factoring in disrupted iron homeostasis in hosts with cancer.

3.3 Siderophores in Oxidative Stress

ROS are a lethal threat to microbes, and are often synthesized by mammalian polymorphonuclear lymphocytes that utilize iron as part of the innate immune response (112, 113). Siderophores have been implicated in reducing the levels of ROS produced by the host and minimizing oxidative stress through multiple mechanisms (7, 114, 115). For example, the siderophore yersiniabactin, which is produced by some *Yersinia* spp. and other Enterobacteriaceae, inhibits ROS production in human and mouse white blood cells by binding iron more effectively than mammalian lactoferrin and transferrin (7). This subsequently blocks the innate immune system by blocking iron acquisition for the production of ROS, which ultimately reduces oxidative stress in the presence of yersiniabactin (7). *E. coli* produces the enterobactin siderophore, which protects against oxidative stress (116). Enterobactin is internalized and hydrolyzed in the bacteria cytoplasm to relieve oxidative stress by scavenging radicals (116, 117). The role of siderophores in oxidative stress will be discussed in greater detail later.

3.4 Metal Sequestration by Siderophores

Siderophores primarily bind iron, but they also can bind other metals based on their major structural group (118). *P. aeruginosa* produces two major siderophores, PVD and pyochelin, which form complexes with Fe^{3+}, Ag^+, Al^{3+}, Cd^{2+}, Co^{2+}, Cr^{2+}, Cu^{2+}, Eu^{3+}, Ga^{3+}, Hg^{2+}, Mn^{2+}, Ni^{2+}, Pb^{2+}, Sn^{2+}, Tb^{3+}, Tl^+, and Zn^{2+}, although many of these metals are not efficiently transported into the cell (119, 120). The ability of siderophores to bind and selectively transport specific metals into cells allows these metals to act as cofactors for biological processes (119, 120). However, toxic metals may remain bound to siderophores with limited uptake into cells, while potentially triggering the production of additional siderophores (120–122). Toxic metals that are transported into the microbial cytoplasm can be expelled *via* efflux pumps, thereby enhancing microbial survival in environments containing toxic metals (119, 121–123). This is seen during *E. coli* infections, where *E. coli* secretes the siderophore yersiniabactin as a protective mechanism against copper toxicity (124). Yersiniabactin was found to be a favorable copper (II) ligand that prevents copper (II) reduction to copper (I) and helps *E. coli* resist toxicity during infections (7, 124).

With a different purpose, gallium (Ga^{3+}) can replace ferric iron (Fe^{3+}) already bound to siderophores (125). Gallium and iron share similar chemical properties, which allows gallium to also bind iron-binding molecules like transferrin and ferritin, and to be taken up by cells through the transferrin receptor (126–129). Gallium and iron differ in their pharmacokinetics and cellular functions, iron is eliminated at a faster rate than gallium and they cannot be interchanged in essential iron-catalyzed reactions (130). The ability of siderophores to bind other metals and interfere with iron metabolism suggests a therapeutic potential for gallium to control and treat bacterial infections (see section titled "*Antibiotic Activity of Siderophores*"). The mechanisms explored here could potentially be applied for siderophores in cancer research. Gallium treatment is already used as a cancer treatment in pre-clinical models, which we describe in the section titled "*Siderophores as Iron Chelating Anticancer Agents*".

3.5 Antibiotic Activity of Siderophores

Targeting siderophore-mediated iron acquisition has become an attractive approach to treat bacteria, as they become more resistant to drug antibiotics. For example, gallium was found to reduce microbial iron uptake and hamper bacterial growth. By binding endogenous siderophores like PVD and pyochelin, gallium can be taken up instead of iron by *P. aeruginosa*, which disrupts iron metabolism and inhibits bacterial growth (131–134). Gallium coupled with the siderophore deferrioxamine is a successful bactericidal therapy against *P.*

aeruginosa infection (135). Importantly, the antibacterial activity of gallium on *P. aeruginosa* is greatly influenced by the siderophore ligand type and the bacterial carbon source, which is important to consider when using this mechanism to develop medical therapies (136). Therefore, siderophores may have antibacterial effects by starving pathogens for iron. Similarly, pathogens can control the growth of bacteria by limiting iron acquisition through competition, discussed in the "*Bacterial Siderophores*" section (14). Additionally, siderophores exert antimicrobial activity against competing microbes through the formation of sideromycins (2, 13). Sideromycins are generated by linking a siderophore to an antibiotic component, although naturally occurring sideromycins are limited (2, 13, 137). A number of sideromycins have been synthesized to use as therapeutics against bacterial infections due to their targeted antimicrobial activity (10, 118, 137). *Burkholderia thailandensis* produces the natural sideromycin malleonitrone (138), which exhibits antibiotic activity against Gram-negative bacteria and inhibits *P. aeruginosa* (138). *Streptomyces* spp. produce the sideromycin albomycin, which inhibits protein synthesis and exerts a broad range of antibiotic and antimicrobial activities (2, 13, 137). Nonetheless, pathogenic bacteria can still develop resistance to sideromycins. This is seen in many bacteria mainly through the loss of siderophore receptors (139, 140), and therefore understanding the mechanisms of resistance is vital to develop more effective and targeted treatments. Salmycins, ferromycins, and microcins are sideromycins that exhibit more limited antimicrobial effects, typically against Gram-positive bacteria (13). The antibiotic and antimicrobial activities of sideromycins suggest that the extensive variety of siderophores produced by microbes has biological relevance beyond the acquisition of iron.

3.6 Siderophore Interactions With the Immune System

Iron has a key role in immune competency (13). As previously discussed, iron availability within hosts is limited and results in pathogen upregulation of siderophores to confer a survival advantage (83, 141). Iron availability and acquisition are critical for bacterial pathogenesis (103, 142, 143). Increased iron availability in normal and once-immunized mice was associated with lethal infection regardless of *Salmonella typhimurium* virulence, and the observed reduction in mortality of twice-immunized mice was associated with timing of the iron injection in relation to infection (142). Although excess siderophores in normal mice increased mortality, the injection of siderophores into immune mice did not enhance the lethality of infection (142). Siderophores enhance microbial iron acquisition and may induce competition that alters the balance of the microbiome and iron homeostasis in the host (10, 14, 144).

Iron availability within hosts potentiates pathogen infection/proliferation and cancer, so bound iron is essential for immunity. Iron regulation is more tightly controlled during host disease states as a form of nonspecific immunity used to mitigate the proliferation of pathogens or cancer (77, 145, 146). As previously mentioned, Lcn2 represents a method of iron regulation during immune stimulation as part of the acute phase response (72, 77, 147), and can be synthesized by a variety of cells, including neutrophils and epithelial cells (147–149). Mouse Lcn2 was upregulated in macrophages (*in vitro*) and in serum (*in vivo*) *via* TLR4 receptor signaling when stimulated or injected, respectively, with lipopolysaccharide (73). Lcn2 transcription was increased in blood cells, hepatocytes, macrophages, fibroblasts, and endothelial cells of mice infected with *E. coli* H9049, further implicating its role in innate immune function (73). Lcn2 has been extensively reviewed in the literature regarding its relation to cancer (150–155), whereas interactions between siderophores and the immune system have not been as comprehensively studied.

Some siderophores interact directly with the immune system by interfering with host defense mechanisms. For example, the enterobactin siderophore produced by *E. coli* impeded the defensive functionality of neutrophils by inhibiting ROS that prevented the formation of neutrophil extracellular traps (156). Enterobactin also inhibited myeloperoxidase activity by binding directly to the enzyme, thereby preventing an oxidative burst (157). Lcn2 can bind enterobactin and counterbalance its immune-inhibiting activity in ROS production, neutrophil extracellular trap formation, and myeloperoxidase activity (156–158). By binding siderophores, Lcn2 aids in limiting microbial iron acquisition while simultaneously enhancing the innate immune system (157, 158). However, this competition triggers the production of stealth siderophores that cannot be bound by Lcn2 (2, 157), perpetuating the battle for iron and forcing the host to utilize additional defenses. The host defense peptide LL-37 is produced ubiquitously at epithelial surfaces and binds stealth siderophores such as aerobactin and rhizoferrin to defend against pathogenic microbes (159). Siderophores and Lcn2 also have roles in stimulating the immune response (71, 160, 161). Enterobactin enhanced the secretion of Lcn2 and triggered the release of the inflammatory cytokine IL-6 (161). Siderophores and siderophore-Lcn2 complexes also increase IL-8 expression (160, 161). The Lcn2-induced secretion of proinflammatory cytokines IL-6, IL-8, and CCL20 was enhanced through superfluous siderophore iron chelation (161). Immune cells are sensitive to the levels of iron and other metals that modulate signaling, cytokine production, and antimicrobial functionality (162). Siderophores can initiate the innate immune response and modulate the immune response system through various mechanisms related to iron homeostasis. The ability of hosts to respond to siderophores and control iron homeostasis could be crucial for controlling iron availability in cancer.

The potential of siderophores as therapeutics for cancer warrants further investigation, but the complex interactions between siderophores and the immune system could complicate any beneficial effects. Therefore, it is necessary to understand the role of siderophores in iron chelation and immune response mechanisms before developing innovative cancer therapeutics.

4 SIDEROPHORES AND CANCER

4.1 Iron and Cancer

There is a complex relationship between iron and cancer, as different cancers display distinct and altered iron regulation and metabolism (11). Health status and associated diseases have an important role in determining the fate of iron in the body and during carcinogenesis. Most solid tumors accumulate iron within the cancer site (11). Tissue-specific transcriptomic analyses showed that excess ferrous iron (Fe^{2+}) and H_2O_2 undergo Fenton reactions in the cytosol and mitochondria of 14 different cancers (163). This study predicted that cytosolic Fenton reactions increase intracellular pH by producing OH^-, thereby increasing glycolytic ATP and nucleotide synthesis, which are key mediators of rapid cancer proliferation (23, 164). The Fenton reaction also generates hydroxyl radicals (•OH), which promotes inflammation and metabolic rewiring, dysregulates cell signals, damages lipids in the cell membrane, and can ultimately induce iron-dependent ferroptotic cell death (23).

The relationship between iron and cancer is clear in hereditary hemochromatosis, a genetic disorder that causes increased iron absorption. Hemochromatosis is a known risk factor for hepatocellular carcinoma (HCC) (165, 166), and previous studies investigated the mechanisms underlying hemochromatosis-mediated excess iron accumulation and tumor development (167). Reducing iron levels *in vitro* and *in vivo* suppresses HCC cell growth (168), and iron chelation therapy is advised for patients with hemochromatosis. The evidence suggests that excess iron can induce p53 mutations (169), which are the primary causes for increased risk of HCC along with increased oxidative stress (170).

One of the most widely accepted hypotheses for the increased iron levels in tumors is the need for increased iron to support and sustain the rapid growth and proliferation of cancer cells compared to non-neoplastic cells. Consistent with this proposal, many cancer cells display upregulation of the iron import protein transferrin, its receptor, and the iron storage protein ferritin **Figure 1B** (16, 18, 171, 172). HCC, breast cancer, ovarian cancer, and colorectal cancer (CRC) display increased levels of transferrin receptor and aberrant expression of other iron transport–related proteins such as ferroportin (iron export transmembrane protein) and the divalent metal transporter (DMT1), required for iron uptake into enterocytes and transport across the endosomal membrane once iron is taken up by the cell (173) **Figure 1B** (174–176). Suppression of the transferrin receptor or reduction of intracellular iron levels in breast and ovarian cancers reduces cancer cell proliferation *in vitro*, inhibits tumor growth *in vivo*, and decreases metastases (175, 176). Conversely, increased cellular iron accumulation from iron loading is associated with increased proliferation in CRC cells and decreased mRNA and protein expression of E-cadherin (174). CRC cells can increase motility and invasiveness by reducing E-cadherin expression, suggesting a role for iron in promoting invasion (174). The Carotene and Retinol Efficacy Trial revealed a trend relating higher iron intake with increased risk of clinically aggressive prostate cancer (177). Although there

was no significant association between iron intake and overall risk for prostate cancer in this study, it proposes that iron intake could have a prominent role in prostate cancer (177). Iron dysregulation and excess have been implicated in other cancers, including pancreas (178), lung (179), and bladder cancer (180), melanoma (36), and hematological malignancies (181, 182). These studies support the role of iron in increasing cancer risk by promoting cancer cell proliferation, invasion, tumor growth, and inhibiting apoptosis **Figure 2A**.

Dietary iron supplementation can modulate iron availability in the host, thereby increasing iron availability to cancer cells, promoting microbial siderophore-mediated iron acquisition, changing the intestinal microbiome, and potentially increasing inflammation (183–186). In particular, iron fortification increases the growth of enterobacteria over bifidobacteria or lactobacilli, and increases pathogenic *E. coli* in the microbiome of children (187). Most bifidobacteria and lactobacilli do not secrete siderophores and provide a barrier against pathogenic invasion (188, 189), whereas enterobacteria usually secrete siderophores for iron uptake. This demonstrates a powerful role of dietary iron and siderophores in bacterial growth, and the potential for these changes to influence cancer development.

There is extensive evidence, reviewed here (4, 23), that iron supports cancer progression, and that modulating iron levels can be considered a promising cancer therapy. Iron chelators have been tested as an anticancer treatment to reduce iron levels (190). These chelators consist of bidentate, tridentate, and hexadentate ligands that form octahedral complexes with ferric iron (Fe^{3+}) (24). Siderophores secreted by bacteria are considered iron chelators, and siderophore-like molecules have been synthesized to mimic the iron chelation activity of bacterial siderophores and tested in preclinical models (**Table 1**) and patients (**Table 2**). Reducing iron levels through iron chelation has successfully reduced proliferation, tumor growth, and metastasis in preclinical models of pancreatic (191), liver (34, 38), gastric (41), breast (37, 192), prostate (193), esophageal (69), and melanoma (36) cancers (**Table 1**; **Figure 2B**); however, the results from the few patient interventions have had conflicting outcomes (**Table 2**). The following sections evaluate cases and studies where siderophores were involved in cancer.

4.2 Siderophore Detection in Cancer

There is scarce evidence on whether siderophores can be detected in tumors or in the microbiome of subjects with cancer. A small pilot study in 2017 evaluated the potential of the sputum microbiome for diagnosing lung cancer status and stage (194). The study included 10 patients referred with possible lung cancer; four were diagnosed with lung cancer after one year, and the other six remained cancer free (194). The study investigated differences in the bacterial species present in patients that developed lung cancer and those that did not. Seven bacterial species were found in both cohorts, and from those, five species were more abundant in the patients that developed lung cancer than those that did not, but only the average percentage abundance of *Streptococcus viridans* was significantly higher. The abundances of *Granulicatella adiacens*, *Streptococcus intermedius*, *Mycobacterium tuberculosis*, *Streptococcus viridans*, and *Mycobacterium bovis* were significantly

higher in patients that developed lung cancer than those that did not. Of note, *Mycobacterium tuberculosis* and *Mycobacterium bovis* secrete mycobactin siderophores for iron uptake (143, 195). The researchers used metagenomics sequencing and functional alignment analyses to determine that iron siderophore receptors were higher in patients that developed lung cancer than those that did not (194). Since excess iron has been implicated in lung carcinogenesis (179), understanding the reason for sputum microbiome upregulation of iron siderophore receptors in lung cancer is relevant to understand disease progression. This was the only study that identified resident siderophores or their receptors in cancer. Future studies should characterize these molecules to further understand tumor-microbiome interactions.

4.3 Siderophores in Cancer Treatment

Natural and synthetic siderophores have been extensively studied as potential therapies and therapy vehicles for different cancers due to their iron chelating capabilities (**Table 1**; **Figure 2B**). These approaches are discussed in the following sections.

4.3.1 Siderophores as Iron Chelating Anticancer Agents

One of the most popular bacterial siderophores in cancer therapy research is deferoxamine (Desferal, desferrioxamine, desferrioxamine-B, or DFO), which is a water-soluble trihydroxamate hexadentate siderophore secreted by many *Streptomyces* species (196, 197). DFO is commercially available and has been used to treat iron overload diseases (70, 198–200). In leukemia, DFO promotes apoptosis *in vitro* by upregulating the tumor suppressor gene *p53* and the pro-apoptotic genes *Bax* and *Fas*, and reducing the expression of the anti-apoptotic gene *Bcl-2* (35). DFO alone and in combination with doxorubicin chemotherapy inhibited breast tumor growth in xenograft mouse models (37). When combined with doxorubicin, DFO inhibited the cardiotoxic side effects that commonly occur in doxorubicin therapy without compromising the treatment efficacy, suggesting that siderophores have a beneficial role as an adjunct treatment with chemotherapy (37). DFO administration during the initial stages of tumor formation in a subcutaneous xenograft mouse model of HCC regressed or slowed tumor growth due to a decrease in intracellular iron concentration (**Figure 2B**; **Table 1**) (39).

Most preclinical studies demonstrated the antitumor effects of DFO. By contrast, studies in cancer patients had conflicting outcomes, with many clinical trials terminating due to difficulties in patient enrollment (**Table 2**). An early clinical study of ten children with recurrent neuroblastoma (NB) after 1–3 treatment regimens administered continuous IV DFO infusion at 150 mg/kg/day for five consecutive days every other week (42). Within one month from the initiation of therapy, nine patients had progressive disease, and one patient had stable disease. This study concluded that the selected dosage and interval of DFO was ineffective as a single therapy for NB patients. Higher DFO doses such as 240 mg/kg/day have serious adverse effects and are not recommended for use (42). Another clinical trial of ten children with unresectable NB administered

DFO at 150 mg/kg/day followed by preoperative chemotherapy, surgery and postoperative chemotherapy (43). There were three complete responses, six partial responses, and one minor response. Nine out of ten patients underwent complete remission following surgery, and the tenth patient underwent complete remission after postoperative chemotherapy. The authors concluded that the DFO regimen used was effective in achieving complete tumor resection (43). A more recent study of ten adult patients with advanced HCC, who did not have a response to hepatic arterial infusion chemotherapy, were administered 10–80 mg/kg of DFO during 24 hours on alternate days an average of 27 times (40). The overall response rate and the 1-year cumulative survival for these patients was 20% (40), indicating that DFO treatment was not successful in the majority of cases. Only four of the clinical trials registered, that used siderophores and iron chelation therapy in cancer, used DFO for the intervention (**Table 2**). One of these studies focused on patients with leukemia and myelodysplastic syndrome and reported low accrual (*n*=5) due to the need for home administration of deferoxamine (50 mg/kg/day) and the considerable intervention window (60). All patients enrolled had iron overload and were scheduled to undergo myeloablative allogeneic hematopoietic stem cell transplantation (60). No serious adverse side effects were reported and serum ferritin decreased after the treatments, but liver iron content remained unchanged. The estimated progression-free survival after transplantation was 100% (60), but the authors are not able to draw any reliable conclusions due to the low number of patients enrolled. The other three clinical trials are in pediatric cancers with nephropathy, HCC patients, or pancreatic cancer patients. The HCC trial is currently recruiting while the pancreatic cancer trial was completed/terminated and did not provide the DFO dosage or preliminary results. Conclusions from the clinical studies described here are limited and should be taken with caution due to the low enrollment, lack of standardized dose, and absence of appropriate control groups.

DFO is a hydrophilic molecule that presents many disadvantages including poor membrane permeability, poor oral viability, and a short plasma half-life of ~12 minutes (201, 202). This requires that DFO is continuously administered subcutaneously or intravenously (68, 203) according to a rigorous infusion regime 8–12 hours/day 3–7 days/week (204, 205). As expected, this administration method has a compliance of <50% (206). The inconsistent success of DFO as an antitumor agent has encouraged the design of more effective iron chelators, with particular focus on chelator lipophilicity, membrane permeability, and selective antitumor activity.

To improve the efficacy of DFO as a cancer therapy, researchers analyzed the effects of a synthesized DFO variation bound to caffeine called desferrioxamine-caffeine dimer (DFCAF), which has greater cell permeability than DFO alone (44). DFCAF cytotoxicity was tested against cancer stem cells (CSCs, the source of biological variability within a tumor), which often determine neoplasm resistance to traditional therapies. CSCs give rise to diverse tumor cell populations and can initiate metastasis, and therefore demand a high intake of nutrients such as iron (44). DFCAF conferred greater ability to

sequester iron within breast CSCs, which was measured as the concentration of an intracellular iron storage protein remaining after treatment. The CSCs also had reduced viability, reversed epithelial-to-mesenchymal transition, and increased clearance after DFCAF treatment *in vitro*.

Another bacterial siderophore that has been studied is desferrithiocin (DFT) (**Table 1**). DFT is a tridentate natural siderophore from *Streptomyces antibioticus* DSM (207), which displays antineoplastic activity in HCCs *in vitro* and has high oral effectiveness (45). However, it also confers severe nephrotoxicity, which makes it unsuitable for chelation therapy.

Enterobactin is produced by Gram-negative Enterobacteriaceae (208) (*E. coli*, *Salmonella enterica*, *Shigella dysenteriae*, and *Klebsiella pneumoniae*) and is reported to have anticancer properties (**Table 1**). This siderophore does not have polar properties and is permeable across the cell membrane. Although there is a lack of evidence relating this siderophore to cancer, enterobactin displays anticancer properties by disrupting the generation of ROS and disturbing the homeostasis of the labile iron (redox-active iron that can be chelated) pool *in vitro*. (**Figure 2B**) (46) Enterobactin showed efficacy in selectively chelating iron in monocyte-derived cancer cell lines and refraining from sequestering iron pools in bone marrow–derived macrophages (46). Iron-bound enterobactin exhibits cytotoxic capabilities in rapidly dividing cell lines, whereas unbound enterobactin does not display cytotoxic effects. The observed increase in intracellular Lcn2 concentrations in noncancerous cells could reflect the reduced tendency of enterobactin-induced cytotoxicity in these cells, whereas the lower Lcn2 levels in cancerous cells may allow the increased free enterobactin to exhibit its anticancer properties (46). Lcn2 levels are usually higher in many types of cancers (152) (not the case in this study), which might prevent these results from being translated to other tumor types.

Ferrichrome is another bacterial siderophore with anticancer properties (**Table 1**). Ferrichrome originates from the common probiotic strain *Lactobacillus casei* (47), and was studied for potential cytotoxic effects on gastric and colon cancer cell lines and xenograft mouse models (47, 48). Unbound ferrichrome has antitumor activity through activation of the pro-apoptotic pathway c-Jun N-terminal (JNK)-DNA damage–inducible transcript 3 (DDIT3) (**Figure 2B**). In this study, iron-bound ferrichrome did not display the same antitumor suppression activity. The authors suggested that the mechanism of antitumor activity in ferrichrome is likely located in the iron-chelation site (47). Another study used a xenograft model of CRC and reported similar results for the tumor suppression activity of unbound ferrichrome through upregulated DDIT3 (49). Ferrichrome treatment did not alter serum iron levels in mice, suggesting that it does not necessarily reduce systemic iron levels (49).

A recent study investigated the effects of three bacterial siderophores on the proliferation of malignant and non-malignant mouse and human cell lines: exochelin-MS (Exo-MS), mycobactin S (MBS), and deferoxamine B (DFO) (34). Exo-MS and MBS are water-soluble and lipid-soluble siderophores, respectively, and both are produced by *Mycobacterium smegmatis*. DFO is a water-soluble siderophore. Exo-MS inhibited the growth of mouse cancer cell lines, but not human cancer cell lines (34). DFO inhibited the growth of mouse cancer cells and human breast and leukemia cancer cells (34). MBS decreased the survival of human liver cancer cells, which was not observed with DFO or Exo-MS. The authors suggested that conjugating water-soluble siderophores with lipid molecules could increase their effectiveness against tumor cells (34).

The antitumor effects of siderophore-like molecules derived from bacteria have also been investigated. Amamistatin A and B were isolated from the actinomycete *Nocardia asteroids*, and have similar structures as mycobacterial siderophores. Amamistatin A displayed antiproliferative effects against the human tumor cell lines MCF-7 breast, A549 lung, and MKN45 stomach. Amamistatin A and B displayed cytotoxicity against mouse lymphocytic leukemia cells (50). The authors suggested that the antitumor activity of amamistatins could be explained by their iron chelating properties, similar to the bacterial siderophores. Amamistatins might act as histone deacetylase (HDAC) inhibitors through their N-formyl hydroxylamine or retrohydroxamate moiety. HDAC inhibition prevents tumor growth (209), and the retrohydroxamate ligand has been utilized in small molecule HDAC inhibitors (210), suggesting that amamistatins may be useful in cancer therapy and warrant further investigation.

Since siderophores are also able to bind gallium, which prevents the growth of pathogenic bacteria, research has expanded to understand this interaction in cancer. Gallium can be taken up by tumors exhibiting antineoplastic activity (211, 212). In human lymphoma cells, gallium induced cell death by activating pro-apoptotic Bax and inducing mitochondria-generated ROS (168). Gallium nitrate is approved by the FDA and is being studied in clinical trials to treat cancers like Non-Hodgkin's Lymphoma, where it had favorable results (213). Cancer patients treated with gallium have a disrupted iron metabolism (214) which indicates that the antitumor function of gallium might be due to iron-related effects. However, the mechanism of action in cancer is still not clear, and patients treated with gallium are at higher risk of iron deficiency and complications like anemia. Continuous treatment with gallium nitrate promotes the development of resistance, which is accompanied by changes in iron trafficking and metabolism (134). Interestingly, other types of gallium, like gallium maltolate, can still inhibit the growth of lymphoma cells that become resistant to gallium nitrate (215). Since some bacteria can become resistant to sideromycins, it will be important to assess whether bacterial and synthetic siderophores could generate resistance in cancer cells.

Recent research focus has shifted to the development of synthetic iron chelators with superior pharmacological properties and similar preclinical results (211, 212), that avoid the adverse effects of siderophores in humans. Optimal iron chelators for cancer treatment must be readily absorbable, with a long-half life in the blood and higher affinity for iron over other metals, although we have reported the benefits of siderophores being able to bind other metals. Selectivity for or against cancer cells is also an important characteristic that should be investigated to avoid systemic iron

deprivation when it is not needed (212, 216). The synthetic iron chelator thiosemicarbazone-24 (TSC24) suppressed human HCC tumor growth by disrupting iron homeostasis, reducing available iron, and triggering cell cycle arrest and apoptosis without any apparent host toxicity (168). Other synthetic iron chelators currently in preclinical studies as anticancer agents include deferiprone (193) and deferasirox (191, 192, 217), which are also in clinical trials to treat cancers related to iron overload (**Table 2**).

All clinical trials using iron chelation as a cancer therapy are summarized in **Table 2**. A number of bacterial siderophores and siderophore analogs are studied in preclinical studies; however, only DFO, deferasirox (synthetic), and deferiprone (synthetic) are undergoing clinical trials. Deferasirox is more commonly used than DFO, probably due to its more convenient oral administration. None of these clinical trials are investigating the effects of chelators/siderophores in solid tumors (other than one HCC and one pancreatic cancer study without results), whereas most of the research in preclinical studies is focused on tumors. All conditions and diseases studied in the clinical trials involve systemic iron overload, including beta-thalassemia, leukemia, and myelodysplastic syndrome (which requires increased blood transfusions). The clinical studies are not reflective of the preclinical data generated in mouse models and *in vitro* cell cultures, where siderophores are studied for tumor treatment regardless of systemic iron overload. A potential reason for this is that these chelators act systemically and do not specifically target the tumor. Therefore, other tissues could be damaged and anemia could be developed by a drastic reduction in iron levels. Future studies should address chelator targeting for non-systemic reduction in tumor iron levels and obtain further evidence to increase the translation of these studies to the clinic.

4.3.2 Siderophores as Mediators of Drug Delivery

Siderophores and their analogs are also used for iron transport–mediated drug delivery through sideromycins (Trojan horse antibiotics). Microbes can develop antibiotic resistance by altering permeability barriers, altering the drug target binding sites, synthesizing enzymes that destroy antibiotics, and developing mechanisms to transport antibiotics out of the cell before they induce damage (218). Siderophores can evade membrane-associated drug resistance because microbes require nutrient uptake from the environment for survival, which enables a route and target of drug delivery. Siderophores were investigated as a drug transport agent to overcome antibiotic resistance and target pathogenic bacteria. Successful results in targeting antibiotic-resistant bacteria suggested that this mechanism could be used to target cancer cells. This seems to be a promising proposition, as siderophore-iron complexes can bind Lcn2 and travel in circulation (219), and iron-loaded Lcn2 can be taken up by cancer cells where Lcn2 is commonly upregulated (220), creating a pathway for the implementation of a modified "Trojan horse" drug delivery.

A recent study conjugated the siderophore PVD from *P. aeruginosa*, a mixed-type siderophore with hydroxamate and catecholate groups, to synthesize superparamagnetic iron oxide nanoparticles (SPION) (221). The PVD-iron complex has strong binding and high stability, which protects it from hydrolysis and enzymatic degradation. PVD-SPION was covalently conjugated to a mucine 1 aptamer ($MUC1_{Apt}$) and loaded with doxorubicin, which is used in chemotherapy. $MUC1_{Apt}$ is one of the most studied aptamers as it specifically recognizes the mucin 1 (MUC1) protein that is strongly upregulated in most cancer cell surfaces, which makes it a great target in cancer (222). The investigators showed that the $PVD-SPION-MUC1_{Apt}$ complex was successfully taken up by cancer cells, and conferred tumor inhibitory growth effects and improved survival in mice bearing C26 colon carcinoma (221). This complex also served as a diagnostic agent that improved contrast at the tumor site in magnetic resonance images (221). This study is one of the first to show the potential of siderophores as chemotherapy delivery agents and diagnostic tools in cancer.

4.3.3 Risks of Siderophore Treatment

While siderophore treatment in cancer has shown some beneficial results in pre-clinical models, and some siderophores and analogs have been used in clinical trials, additional studies are needed to determine side effects or potential risks of these interventions. Understanding siderophore functions in mammalian cells will help assess the risk of siderophore implementation in cancer. We previously mentioned that iron chelation reduces mitochondrial mass and induces mitochondrial fragmentation in *C. elegans*, and that it promotes mitochondrial degradation in mammalian cells (93) In addition, iron chelation induces *C. elegans'* death through hypoxia (94). Iron chelation therapy is commonly used to lower systemic iron levels in iron overload diseases (202), and data from the literature suggest that chelation therapy could also enhance iron absorption, which might be undesirable in the context of cancer (223). Therefore, investigating the effects of siderophore therapy on the microbiome, the mitochondria (in not only cancer cells, but also other cells of the body) and systemic and cellular iron levels, will be vital when evaluating the feasibility of these interventions.

Another factor to consider is whether cancer cells can become resistant to siderophore treatment, as bacteria are known to become resistant to sideromycins by losing their siderophore receptors (139, 140), and to gallium nitrate treatment (134). Moreover, it is supported that cancer cells employ Lcn2 to collect extracellular iron to support cancer growth in renal cell carcinoma (220) and leptomeningeal metastasis (224). Thus, understanding the function of Lcn2 as a result of a siderophore treatment will further elucidate additional risks related to these treatments.

5 CONCLUSIONS

Siderophores are secreted by many organisms including bacteria, to sequester essential iron from the environment to sustain their growth. This function has gained interest in cancer research because excess iron availability is linked to increased cancer risk, and cancer cells require higher iron levels to sustain their rapid proliferation and growth **Figure 1** (71, 225). Therefore, bacterial siderophores and siderophore analogs are being utilized to chelate iron and prevent it from being taken up by cancer cells, which inhibits the proliferation and growth of many different cancers in preclinical studies **Figure 2**.

Siderophores also function as signaling molecules that can lead to the production of virulence factors and the regulation of siderophore synthesis. Siderophores can interact with the immune system, mitigate oxidative stress, protect microbes from ROS and bind other metals in addition to ferric iron (Fe^{3+}). Finally, siderophores can form sideromycins and have antimicrobial effects against other microbes in the environment. Each of these described siderophore functions does not fully consider the interactions between microbes in a competitive environment, and how these functions may be enhanced or suppressed through these interactions.

There is still much to learn about the effects and interactions of siderophores in cancer. Most of the preclinical and clinical studies use inconsistent dosages, conditions, and safety and outcome measures, which reduce their translational value for additional studies in patients. Data regarding endogenous siderophores in cancer and related changes to the microbiome are also lacking. Additional studies are needed in these areas to assess the potential efficacy of siderophores in cancer detection and therapeutics. This review discussed bacterial siderophores and analogs that have potential benefits for cancer therapy, but even less is known about mammalian or fungal siderophores in cancer and immunity. It will be crucial to map the relationships between siderophores, iron, immune function, and cancer to develop stable, effective, and targeted therapeutics. These efforts should leverage the functions of siderophores and translate the outcomes to the clinical setting.

AUTHOR CONTRIBUTIONS

VP-G: study concept and design, development of methodology, drafting of initial manuscript, writing, review, and/or revision of the manuscript, administrative, technical, or material support, and final approval of the version to be submitted. KC: study concept and design, development of methodology, drafting of initial manuscript, writing, review, and/or revision of the manuscript, administrative, technical, or material support, and final approval of the version to be submitted. TS: drafting of initial manuscript and writing, review, and/or revision of the manuscript. ZC-M: study concept and design, development of methodology, drafting of initial manuscript, writing, review, and/or revision of the manuscript, administrative, technical, or material support, final approval of the version to be submitted, and study supervision.

FUNDING

ACKNOWLEDGMENTS

REFERENCES

1. Neilands JB. Microbial Iron Compounds. *Annu Rev Biochem* (1981) 50:715–31. doi: 10.1146/annurev.bi.50.070181.003435

2. Hider RC, Kong X. Chemistry and Biology of Siderophores. *Nat Prod Rep* (2010) 27(5):637–57. doi: 10.1039/b906679a

3. Wilson BR, Bogdan AR, Miyazawa M, Hashimoto K, Tsuji Y. Siderophores in Iron Metabolism: From Mechanism to Therapy Potential. *Trends Mol Med* (2016) 22(12):1077–90. doi: 10.1016/j.molmed.2016.10.005

4. Torti SV, Manz DH, Paul BT, Blanchette-Farra N, Torti FM. Iron and Cancer. *Annu Rev Nutr* (2018) 38:97–125. doi: 10.1146/annurev-nutr-082117-051732

5. Fenton HJH. LXXIII—Oxidation of Tartaric Acid in Presence of Iron. *J Chem Soc Trans* (1894) 65:899–910. doi: 10.1039/CT8946500899

6. Ems T, St Lucia K, Huecker MR. *Biochemistry, Iron Absorption*. Treasure Island, FL: StatPearls (2022).

7. Paauw A, Leverstein-van Hall MA, van Kessel KP, Verhoef J, Fluit AC. Yersiniabactin Reduces the Respiratory Oxidative Stress Response of Innate Immune Cells. *PloS One* (2009) 4(12):e8240. doi: 10.1371/journal.pone.0008240

8. Devireddy LR, Hart DO, Goetz DH, Green MR. A Mammalian Siderophore Synthesized by an Enzyme With a Bacterial Homolog Involved in Enterobactin Production. *Cell* (2010) 141(6):1006–17. doi: 10.1016/j.cell.2010.04.040

9. Raymond KN, Dertz EA, Kim SS. Enterobactin: An Archetype for Microbial Iron Transport. *Proc Natl Acad Sci USA* (2003) 100(7):3584–8. doi: 10.1073/pnas.0630018100

10. Page MGP. The Role of Iron and Siderophores in Infection, and the Development of Siderophore Antibiotics. *Clin Infect Dis* (2019) 69(Suppl 7):S529–S37. doi: 10.1093/cid/ciz825

11. Torti SV, Torti FM. Iron and Cancer: More Ore to be Mined. *Nat Rev Cancer* (2013) 13(5):342–55. doi: 10.1038/nrc3495

12. McRose DL, Seyedsayamdost MR, Morel FMM. Multiple Siderophores: Bug or Feature? *J Biol Inorg Chem* (2018) 23(7):983–93. doi: 10.1007/s00775-018-1617-x

13. Johnstone TC, Nolan EM. Beyond Iron: Non-Classical Biological Functions of Bacterial Siderophores. *Dalton Trans* (2015) 44(14):6320–39. doi: 10.1039/C4DT03559C

14. Kramer J, Özkaya Ö, Kümmerli R. Bacterial Siderophores in Community and Host Interactions. *Nat Rev Microbiol* (2020) 18(3):152–63. doi: 10.1038/s41579-019-0284-4

15. Kümmerli R, Jiricny N, Clarke LS, West SA, Griffin AS. Phenotypic Plasticity of a Cooperative Behaviour in Bacteria. *J Evol Biol* (2009) 22(3):589–98. doi: 10.1111/j.1420-9101.2008.01666.x

16. Kew MC, Torrance JD, Derman D, Simon M, Macnab GM, Charlton RW, et al. Serum and Tumour Ferritins in Primary Liver Cancer. *Gut* (1978) 19(4):294–9. doi: 10.1136/gut.19.4.294

17. Marcus DM, Zinberg N. Isolation of Ferritin From Human Mammary and Pancreatic Carcinomas by Means of Antibody Immunoadsorbents. *Arch Biochem Biophys* (1974) 162(2):493–501. doi: 10.1016/0003-9861(74)90209-4

18. Weinstein RE, Bond BH, Silberberg BK. Tissue Ferritin Concentration in Carcinoma of the Breast. *Cancer* (1982) 50(11):2406–9. doi: 10.1002/1097-0142(19821201)50:11<2406::AID-CNCR2820501127>3.0.CO;2-S

19. Mendez R, Kesh K, Arora N, Di Martino L, McAllister F, Merchant N, et al. Microbial Dysbiosis and Polyamine Metabolism as Predictive Markers for Early Detection of Pancreatic Cancer. *Carcinogenesis* (2020) 41(5):561–70. doi: 10.1093/carcin/bgz116

20. Riquelme E, Zhang Y, Zhang L, Montiel M, Zoltan M, Dong W, et al. Tumor Microbiome Diversity and Composition Influence Pancreatic Cancer Outcomes. *Cell* (2019) 178(4):795–806.e12. doi: 10.1016/j.cell.2019.07.008

21. Koliarakis I, Messaritakis I, Nikolouzakis TK, Hamilos G, Souglakos J, Tsiaoussis J. Oral Bacteria and Intestinal Dysbiosis in Colorectal Cancer. *Int J Mol Sci* (2019) 20(17):4146. doi: 10.3390/ijms20174146

22. Gopalakrishnan V, Helmink BA, Spencer CN, Reuben A, Wargo JA. The Influence of the Gut Microbiome on Cancer, Immunity, and Cancer Immunotherapy. *Cancer Cell* (2018) 33(4):570–80. doi: 10.1016/j.ccell.2018.03.015

23. Brown RAM, Richardson KL, Kabir TD, Trinder D, Ganss R, Leedman PJ. Altered Iron Metabolism and Impact in Cancer Biology, Metastasis, and Immunology. *Front Oncol* (2020) 10:476. doi: 10.3389/fonc.2020.00476

24. Zhou T, Ma Y, Kong X, Hider RC. Design of Iron Chelators With Therapeutic Application. *Dalton Trans* (2012) 41(21):6371–89. doi: 10.1039/c2dt12159j

25. National Center for Biotechnology Information (2022). PubChem Compound Summary for CID 2973, Deferoxamine. Retrieved May 24, 2022 from https://pubchem.ncbi.nlm.nih.gov/compound/Deferoxamine.

26. National Center for Biotechnology Information (2022). PubChem Compound Summary for CID 2519, Caffeine. Retrieved May 24, 2022 from https://pubchem.ncbi.nlm.nih.gov/compound/Caffeine.

27. National Center for Biotechnology Information (2022). PubChem Compound Summary for CID 101609363. Retrieved May 24, 2022 from https://pubchem.ncbi.nlm.nih.gov/compound/101609363.

28. National Center for Biotechnology Information (2022). PubChem Compound Summary for CID 34231, Enterobactin. Retrieved May 24, 2022 from https://pubchem.ncbi.nlm.nih.gov/compound/Enterobactin.

29. National Center for Biotechnology Information (2022). PubChem Compound Summary for CID 644246, [55Fe] Ferrichrome. Retrieved May 24, 2022 from https://pubchem.ncbi.nlm.nih.gov/compound/55Fe_-Ferrichrome.

30. National Center for Biotechnology Information (2022). PubChem Compound Summary for CID 139583168, Exochelin MS. Retrieved May 24, 2022 from https://pubchem.ncbi.nlm.nih.gov/compound/Exochelin-MS.

31. National Center for Biotechnology Information (2022). PubChem Compound Summary for CID 3083702, Mycobactin. Retrieved May 24, 2022 from https://pubchem.ncbi.nlm.nih.gov/compound/Mycobactin.

32. National Center for Biotechnology Information. (2022). PubChemCompound Summary for CID 13543048, Amamistatin A. Retrieved May 24. Available at: https://pubchem.ncbi.nlm.nih.gov/compound/amamistatin_a..

33. National Center for Biotechnology Information. (2022). PubChemCompound Summary for CID 135438025, Amamistatin B. Retrieved May 24, Available at: https://pubchem.ncbi.nlm.nih.gov/compound/amamistatin_b.

34. Gokarn K, Sarangdhar V, Pal RB. Effect of Microbial Siderophores on Mammalian Non-Malignant and Malignant Cell Lines. *BMC Complement Altern Med* (2017) 17(1):145. doi: 10.1186/s12906-017-1657-8

35. Yang Y, Xu Y, Su A, Yang D, Zhang X. Effects of Deferoxamine on Leukemia *In Vitro* and Its Related Mechanism. *Med Sci Monit* (2018) 24:6735–41. doi: 10.12659/MSM.910325

36. Whitnall M, Howard J, Ponka P, Richardson DR. A Class of Iron Chelators With a Wide Spectrum of Potent Antitumor Activity That Overcomes Resistance to Chemotherapeutics. *Proc Natl Acad Sci USA* (2006) 103(40):14901–6. doi: 10.1073/pnas.0604979103

37. Hoke EM, Maylock CA, Shacter E. Desferal Inhibits Breast Tumor Growth and Does Not Interfere With the Tumoricidal Activity of Doxorubicin. *Free Radic Biol Med* (2005) 39(3):403–11. doi: 10.1016/j.freeradbiomed.2005.03.029

38. Saeki I, Yamamoto N, Yamasaki T, Takami T, Maeda M, Fujisawa K, et al. Effects of an Oral Iron Chelator, Deferasirox, on Advanced Hepatocellular Carcinoma. *World J Gastroenterol* (2016) 22(40):8967–77. doi: 10.3748/wjg.v22.i40.8967

39. Hann HW, Stahlhut MW, Rubin R, Maddrey WC. Antitumor Effect of Deferoxamine on Human Hepatocellular Carcinoma Growing in Athymic Nude Mice. *Cancer* (1992) 70(8):2051–6. doi: 10.1002/1097-0142(19921015)70:8<2051::AID-CNCR2820700806>3.0.CO;2-1

40. Yamasaki T, Terai S, Sakaida I. Deferoxamine for Advanced Hepatocellular Carcinoma. *N Engl J Med* (2011) 365(6):576–8. doi: 10.1056/NEJMc1105726

41. Kim JL, Lee DH, Na YJ, Kim BR, Jeong YA, Lee SI, et al. Iron Chelator-Induced Apoptosis *via* the ER Stress Pathway in Gastric Cancer Cells. *Tumour Biol* (2016) 37(7):9709–19. doi: 10.1007/s13277-016-4878-4

42. Blatt J. Deferoxamine in Children With Recurrent Neuroblastoma. *Anticancer Res* (1994) 14(5B):2109–12.

43. Donfrancesco A, Deb G, Dominici C, De Sio L, Inserra A, Boglino C, et al. D-CECaT as Preoperative Chemotherapy for Unresectable Neuroblastoma in Children Over One Year of Age. *Anticancer Res* (1995) 15(5B):2347–50.

44. Li B, Esposito BP, Wang S, Zhang J, Xu M, Zhang S, et al. Desferrioxamine-Caffeine Shows Improved Efficacy in Chelating Iron and Depleting Cancer Stem Cells. *J Trace Elem Med Biol* (2019) 52:232–8. doi: 10.1016/j.jtemb.2019.01.004

45. Bergeron RJ, Wiegand J, Dionis JB, Egli-Karmakka M, Frei J, Huxley-Tencer A, et al. Evaluation of Desferrithiocin and its Synthetic Analogues as Orally Effective Iron Chelators. *J Med Chem* (1991) 34(7):2072–8. doi: 10.1021/jm00111a023

46. Saha P, Yeoh BS, Xiao X, Golonka RM, Kumarasamy S, Vijay-Kumar M. Enterobactin, an Iron Chelating Bacterial Siderophore, Arrests Cancer Cell Proliferation. *Biochem Pharmacol* (2019) 168:71–81. doi: 10.1016/j.bcp.2019.06.017

47. Ijiri M, Fujiya M, Konishi H, Tanaka H, Ueno N, Kashima S, et al. Ferrichrome Identified From Lactobacillus Casei ATCC334 Induces Apoptosis Through its Iron-Binding Site in Gastric Cancer Cells. *Tumour Biol* (2017) 39(6):1010428317711311. doi: 10.1177/1010428317711311

48. Konishi H, Fujiya M, Tanaka H, Ueno N, Moriichi K, Sasajima J, et al. Probiotic-Derived Ferrichrome Inhibits Colon Cancer Progression *via* JNK-Mediated Apoptosis. *Nat Commun* (2016) 7:12365. doi: 10.1038/ncomms12365

49. Iwama T, Fujiya M, Konishi H, Tanaka H, Murakami Y, Kunogi T, et al. Bacteria-Derived Ferrichrome Inhibits Tumor Progression in Sporadic Colorectal Neoplasms and Colitis-Associated Cancer. *Cancer Cell Int* (2021) 21(1):21. doi: 10.1186/s12935-020-01723-9

50. Fennell KA, Mollmann U, Miller MJ. Syntheses and Biological Activity of Amamistatin B and Analogs. *J Org Chem* (2008) 73(3):1018–24. doi: 10.1021/jo7020532

51. Angelucci E, Li J, Greenberg P, Wu D, Hou M, Montano Figueroa EH, et al. Iron Chelation in Transfusion-Dependent Patients With Low- to Intermediate-1-Risk Myelodysplastic Syndromes: A Randomized Trial. *Ann Intern Med* (2020) 172(8):513–22. doi: 10.7326/M19-0916

52. Cappellini MD, Porter J, El-Beshlawy A, Li CK, Seymour JF, Elalfy M, et al. Tailoring Iron Chelation by Iron Intake and Serum Ferritin: The Prospective EPIC Study of Deferasirox in 1744 Patients With Transfusion-Dependent Anemias. *Haematologica* (2010) 95(4):557–66. doi: 10.3324/haematol.2009.014696

53. Nolte F, Hochsmann B, Giagounidis A, Lubbert M, Platzbecker U, Haase D, et al. Results From a 1-Year, Open-Label, Single Arm, Multi-Center Trial Evaluating the Efficacy and Safety of Oral Deferasirox in Patients Diagnosed With Low and Int-1 Risk Myelodysplastic Syndrome (MDS) and Transfusion-Dependent Iron Overload. *Ann Hematol* (2013) 92(2):191–8. doi: 10.1007/s00277-012-1594-z

54. Borgna-Pignatti C, Franchini M, Gandini G, Vassanelli A, De Gironcoli M, Aprili G. Subcutaneous Bolus Injection of Deferoxamine in Adult Patients Affected by Onco-Hematologic Diseases and Iron Overload. *Haematologica* (1998) 83(9):788–90.

55. Galanello R. Evaluation of ICL670, a Once-Daily Oral Iron Chelator in a Phase III Clinical Trial of Beta-Thalassemia Patients With Transfusional Iron Overload. *Ann N Y Acad Sci* (2005) 1054:183–5. doi: 10.1196/annals.1345.021

56. Efficace F, Santini V, La Nasa G, Cottone F, Finelli C, Borin L, et al. Health-Related Quality of Life in Transfusion-Dependent Patients With Myelodysplastic Syndromes: A Prospective Study to Assess the Impact of Iron Chelation Therapy. *BMJ Support Palliat Care* (2016) 6(1):80–8. doi: 10.1136/bmjspcare-2014-000726

57. Ho PJ, Tay L, Teo J, Marlton P, Grigg A, St Pierre T, et al. Cardiac Iron Load and Function in Transfused Patients Treated With Deferasirox (the MILE Study). *Eur J Haematol* (2017) 98(2):97–105. doi: 10.1111/ejh.12793

58. Greenberg PL, Koller CA, Cabantchik ZI, Warsi G, Glynos T, Paley C, et al. Prospective Assessment of Effects on Iron-Overload Parameters of Deferasirox Therapy in Patients With Myelodysplastic Syndromes. *Leuk Res* (2010) 34(12):1560–5. doi: 10.1016/j.leukres.2010.06.013

59. Ghoti H, Fibach E, Merkel D, Perez-Avraham G, Grisariu S, Rachmilewitz EA. Changes in Parameters of Oxidative Stress and Free Iron Biomarkers During Treatment With Deferasirox in Iron-Overloaded Patients With Myelodysplastic Syndromes. *Haematologica* (2010) 95(8):1433–4. doi: 10.3324/haematol.2010.024992

60. Armand P, Sainvil MM, Kim HT, Rhodes J, Cutler C, Ho VT, et al. Pre-Transplantation Iron Chelation in Patients With MDS or Acute Leukemia and Iron Overload Undergoing Myeloablative Allo-SCT. *Bone Marrow Transplant* (2013) 48(1):146–7. doi: 10.1038/bmt.2012.94

61. Messa E, Carturan S, Maffe C, Pautasso M, Bracco E, Roetto A, et al. Deferasirox Is a Powerful NF-kappaB Inhibitor in Myelodysplastic Cells and in Leukemia Cell Lines Acting Independently From Cell Iron Deprivation by Chelation and Reactive Oxygen Species Scavenging. *Haematologica* (2010) 95(8):1308–16. doi: 10.3324/haematol.2009.016824

62. Brissot P, Ball S, Rofail D, Cannon H, Jin VW. Hereditary Hemochromatosis: Patient Experiences of the Disease and Phlebotomy Treatment. *Transfusion* (2011) 51(6):1331–8. doi: 10.1111/j.1537-2995.2010.02997.x

63. Phatak P, Brissot P, Wurster M, Adams PC, Bonkovsky HL, Gross J, et al. A Phase 1/2, Dose-Escalation Trial of Deferasirox for the Treatment of Iron Overload in HFE-Related Hereditary Hemochromatosis. *Hepatology* (2010) 52(5):1671–779. doi: 10.1002/hep.23879

64. Barany E, Bergdahl IA, Bratteby LE, Lundh T, Samuelson G, Skerfving S, et al. Iron Status Influences Trace Element Levels in Human Blood and Serum. *Environ Res* (2005) 98(2):215–23. doi: 10.1016/j.envres.2004.09.010

65. Hori A, Mizoue T, Kasai H, Kawai K, Matsushita Y, Nanri A, et al. Body Iron Store as a Predictor of Oxidative DNA Damage in Healthy Men and Women. *Cancer Sci* (2010) 101(2):517–22. doi: 10.1111/j.1349-7006.2009.01394.x

66. Fukushima T, Kawabata H, Nakamura T, Iwao H, Nakajima A, Miki M, et al. Iron Chelation Therapy With Deferasirox Induced Complete Remission in a Patient With Chemotherapy-Resistant Acute Monocytic Leukemia. *Anticancer Res* (2011) 31(5):1741–4.

67. Paubelle E, Zylbersztejn F, Alkhaeir S, Suarez F, Callens C, Dussiot M, et al. Deferasirox and Vitamin D Improves Overall Survival in Elderly Patients With Acute Myeloid Leukemia After Demethylating Agents Failure. *PloS One* (2013) 8(6):e65998. doi: 10.1371/journal.pone.0065998

68. Donfrancesco A, Deb G, De Sio L, Cozza R, Castellano A. Role of Deferoxamine in Tumor Therapy. *Acta Haematol* (1996) 95(1):66–9. doi: 10.1159/000203951

69. Ford SJ, Obeidy P, Lovejoy DB, Bedford M, Nichols L, Chadwick C, et al. Deferasirox (ICL670A) Effectively Inhibits Oesophageal Cancer Growth *In Vitro* and *In Vivo*. *Br J Pharmacol* (2013) 168(6):1316–28. doi: 10.1111/bph.12045

70. Gattermann N. Overview of Guidelines on Iron Chelation Therapy in Patients With Myelodysplastic Syndromes and Transfusional Iron Overload. *Int J Hematol* (2008) 88(1):24–9. doi: 10.1007/s12185-008-0118-z

71. Golonka R, Yeoh BS, Vijay-Kumar M. The Iron Tug-Of-War Between Bacterial Siderophores and Innate Immunity. *J Innate Immun* (2019) 11(3):249–62. doi: 10.1159/000494627

72. Xiao X, Yeoh BS, Vijay-Kumar M. Lipocalin 2: An Emerging Player in Iron Homeostasis and Inflammation. *Annu Rev Nutr* (2017) 37:103–30. doi: 10.1146/annurev-nutr-071816-064559

73. Flo TH, Smith KD, Sato S, Rodriguez DJ, Holmes MA, Strong RK, et al. Lipocalin 2 Mediates an Innate Immune Response to Bacterial Infection by Sequestrating Iron. *Nature* (2004) 432(7019):917–21. doi: 10.1038/nature03104

74. Saha M, Sarkar S, Sarkar B, Sharma BK, Bhattacharjee S, Tribedi P. Microbial Siderophores and Their Potential Applications: A Review. *Environ Sci Pollut Res Int* (2016) 23(5):3984–99. doi: 10.1007/s11356-015-4294-0

75. Liu Z, Lanford R, Mueller S, Gerhard GS, Luscieti S, Sanchez M, et al. Siderophore-Mediated Iron Trafficking in Humans Is Regulated by Iron. *J Mol Med (Berl)* (2012) 90(10):1209–21. doi: 10.1007/s00109-012-0899-7

76. Caza M, Kronstad JW. Shared and Distinct Mechanisms of Iron Acquisition by Bacterial and Fungal Pathogens of Humans. *Front Cell Infect Microbiol* (2013) 3:80. doi: 10.3389/fcimb.2013.00080

77. Correnti C, Strong RK. Mammalian Siderophores, Siderophore-Binding Lipocalins, and the Labile Iron Pool. *J Biol Chem* (2012) 287(17):13524–31. doi: 10.1074/jbc.R111.311829

78. Khan A, Singh P, Srivastava A. Synthesis, Nature and Utility of Universal Iron Chelator - Siderophore: A Review. *Microbiol Res* (2018) 212-213:103–11. doi: 10.1016/j.micres.2017.10.012

79. Liu Z, Reba S, Chen WD, Porwal SK, Boom WH, Petersen RB, et al. Regulation of Mammalian Siderophore 2,5-DHBA in the Innate Immune Response to Infection. *J Exp Med* (2014) 211(6):1197–213. doi: 10.1084/jem.20132629

80. Liu Z, Ciocea A, Devireddy L. Endogenous Siderophore 2,5-Dihydroxybenzoic Acid Deficiency Promotes Anemia and Splenic Iron Overload in Mice. *Mol Cell Biol* (2014) 34(13):2533–46. doi: 10.1128/MCB.00231-14

81. Davuluri G, Song P, Liu Z, Wald D, Sakaguchi TF, Green MR, et al. Inactivation of 3-Hydroxybutyrate Dehydrogenase 2 Delays Zebrafish Erythroid Maturation by Conferring Premature Mitophagy. *Proc Natl Acad Sci USA* (2016) 113(11):E1460–9. doi: 10.1073/pnas.1600077113

82. Holden VI, Bachman MA. Diverging Roles of Bacterial Siderophores During Infection. *Metallomics* (2015) 7(6):986–95. doi: 10.1039/C4MT00333K

83. Santos R, Batista BB, da Silva Neto JF. Ferric Uptake Regulator Fur Coordinates Siderophore Production and Defense Against Iron Toxicity and Oxidative Stress and Contributes to Virulence in Chromobacterium Violaceum. *Appl Environ Microbiol* (2020) 86(21):e01620–20. doi: 10.1128/AEM.01620-20

84. Fillat MF, The FUR. (Ferric Uptake Regulator) Superfamily: Diversity and Versatility of Key Transcriptional Regulators. *Arch Biochem Biophys* (2014) 546:41–52. doi: 10.1016/j.abb.2014.01.029

85. da Silva Neto JF, Braz VS, Italiani VC, Marques MV. Fur Controls Iron Homeostasis and Oxidative Stress Defense in the Oligotrophic Alpha-Proteobacterium Caulobacter Crescentus. *Nucleic Acids Res* (2009) 37(14):4812–25. doi: 10.1093/nar/gkp509

86. West SA, Buckling A. Cooperation, Virulence and Siderophore Production in Bacterial Parasites. *Proc Biol Sci* (2003) 270(1510):37–44. doi: 10.1098/rspb.2002.2209

87. Niehus R, Picot A, Oliveira NM, Mitri S, Foster KR. The Evolution of Siderophore Production as a Competitive Trait. *Evolution* (2017) 71(6):1443–55. doi: 10.1111/evo.13230

88. Stilwell P, Lowe C, Buckling A. The Effect of Cheats on Siderophore Diversity in Pseudomonas Aeruginosa. *J Evol Biol* (2018) 31(9):1330–9. doi: 10.1111/jeb.13307

89. Buckling A, Harrison F, Vos M, Brockhurst MA, Gardner A, West SA, et al. Siderophore-Mediated Cooperation and Virulence in Pseudomonas Aeruginosa. *FEMS Microbiol Ecol* (2007) 62(2):135–41. doi: 10.1111/j.1574-6941.2007.00388.x

90. Butaitè E, Baumgartner M, Wyder S, Kümmerli R. Siderophore Cheating and Cheating Resistance Shape Competition for Iron in Soil and Freshwater Pseudomonas Communities. *Nat Commun* (2017) 8(1):414. doi: 10.1038/s41467-017-00509-4

91. Harrison F, Paul J, Massey RC, Buckling A. Interspecific Competition and Siderophore-Mediated Cooperation in Pseudomonas Aeruginosa. *Isme J* (2008) 2(1):49–55. doi: 10.1038/ismej.2007.96

92. Qi B, Han M. Microbial Siderophore Enterobactin Promotes Mitochondrial Iron Uptake and Development of the Host *via* Interaction With ATP Synthase. *Cell* (2018) 175(2):571–82.e11. doi: 10.1016/j.cell.2018.07.032

93. Kirienko NV, Ausubel FM, Ruvkun G. Mitophagy Confers Resistance to Siderophore-Mediated Killing by Pseudomonas Aeruginosa. *Proc Natl Acad Sci USA* (2015) 112(6):1821–6. doi: 10.1073/pnas.1424954112

94. Kirienko NV, Kirienko DR, Larkins-Ford J, Wahlby C, Ruvkun G, Ausubel FM. Pseudomonas Aeruginosa Disrupts Caenorhabditis Elegans Iron Homeostasis, Causing a Hypoxic Response and Death. *Cell Host Microbe* (2013) 13(4):406–16. doi: 10.1016/j.chom.2013.03.003

95. Kratena N, Gökler T, Maltrovsky L, Oburger E, Stanetty C. A Unified Approach to Phytosiderophore Natural Products. *Chemistry* (2021) 27(2):577–80. doi: 10.1002/chem.202004004

96. Martínez-Pastor MT, Puig S. Adaptation to Iron Deficiency in Human Pathogenic Fungi. *Biochim Biophys Acta Mol Cell Res* (2020) 1867(10):118797. doi: 10.1016/j.bbamcr.2020.118797

97. Misslinger M, Hortschansky P, Brakhage AA, Haas H. Fungal Iron Homeostasis With a Focus on Aspergillus Fumigatus. *Biochim Biophys*

Acta Mol Cell Res (2021) 1868(1):118885. doi: 10.1016/j.bbamcr.2020.118885

98. Ipcho S, Sundelin T, Erbs G, Kistler HC, Newman MA, Olsson S. Fungal Innate Immunity Induced by Bacterial Microbe-Associated Molecular Patterns (MAMPs). *G3 (Bethesda)* (2016) 6(6):1585–95. doi: 10.1534/g3.116.027987

99. Lamont IL, Beare PA, Ochsner U, Vasil AI, Vasil ML. Siderophore-Mediated Signaling Regulates Virulence Factor Production in Pseudomonasaeruginosa. *Proc Natl Acad Sci USA* (2002) 99(10):7072–7. doi: 10.1073/pnas.092016999

100. Naves P, del Prado G, Huelves L, Gracia M, Ruiz V, Blanco J, et al. Correlation Between Virulence Factors and *In Vitro* Biofilm Formation by Escherichia Coli Strains. *Microb Pathog* (2008) 45(2):86–91. doi: 10.1016/j.micpath.2008.03.003

101. Kang D, Kirienko NV. Interdependence Between Iron Acquisition and Biofilm Formation in Pseudomonas Aeruginosa. *J Microbiol* (2018) 56(7):449–57. doi: 10.1007/s12275-018-8114-3

102. Dietl AM, Binder U, Bauer I, Shadkchan Y, Osherov N, Haas H. Arginine Auxotrophy Affects Siderophore Biosynthesis and Attenuates Virulence of Aspergillus Fumigatus. *Genes (Basel)* (2020) 11(4):423. doi: 10.3390/genes11040423

103. Batista BB, Santos R, Ricci-Azevedo R, da Silva Neto JF. Production and Uptake of Distinct Endogenous Catecholate-Type Siderophores Are Required for Iron Acquisition and Virulence in Chromobacterium Violaceum. *Infect Immun* (2019) 87(12):e00577–19. doi: 10.1128/IAI.00577-19

104. Lam MMC, Wyres KL, Judd LM, Wick RR, Jenney A, Brisse S, et al. Tracking Key Virulence Loci Encoding Aerobactin and Salmochelin Siderophore Synthesis in Klebsiella Pneumoniae. *Genome Med* (2018) 10(1):77. doi: 10.1186/s13073-018-0587-5

105. Wilderman PJ, Vasil AI, Johnson Z, Wilson MJ, Cunliffe HE, Lamont IL, et al. Characterization of an Endoprotease (PrpL) Encoded by a PvdS-Regulated Gene in Pseudomonas Aeruginosa. *Infect Immun* (2001) 69(9):5385–94. doi: 10.1128/IAI.69.9.5385-5394.2001

106. Chen YT, Chang HY, Lai YC, Pan CC, Tsai SF, Peng HL. Sequencing and Analysis of the Large Virulence Plasmid pLVPK of Klebsiella Pneumoniae CG43. *Gene* (2004) 337:189–98. doi: 10.1016/j.gene.2004.05.008

107. Shirley M, Lamont IL. Role of TonB1 in Pyoverdine-Mediated Signaling in Pseudomonas Aeruginosa. *J Bacteriol* (2009) 191(18):5634–40. doi: 10.1128/JB.00742-09

108. Beare PA, For RJ, Martin LW, Lamont IL. Siderophore-Mediated Cell Signalling in Pseudomonas Aeruginosa: Divergent Pathways Regulate Virulence Factor Production and Siderophore Receptor Synthesis. *Mol Microbiol* (2003) 47(1):195–207. doi: 10.1046/j.1365-2958.2003.03288.x

109. Llamas MA, Sparrius M, Kloet R, Jiménez CR, Vandenbroucke-Grauls C, Bitter W. The Heterologous Siderophores Ferrioxamine B and Ferrichrome Activate Signaling Pathways in Pseudomonas Aeruginosa. *J Bacteriol* (2006) 188(5):1882–91. doi: 10.1128/JB.188.5.1882-1891.2006

110. Welz D, Braun V. Ferric Citrate Transport of Escherichia Coli: Functional Regions of the FecR Transmembrane Regulatory Protein. *J Bacteriol* (1998) 180(9):2387–94. doi: 10.1128/JB.180.9.2387-2394.1998

111. Braun V, Braun M. Iron Transport and Signaling in Escherichia Coli. *FEBS Lett* (2002) 529(1):78–85. doi: 10.1016/S0014-5793(02)03185-X

112. Levay PF, Viljoen M. Lactoferrin: A General Review. *Haematologica* (1995) 80(3):252–67.

113. Rosa L, Cutone A, Lepanto MS, Paesano R, Valenti P. Lactoferrin: A Natural Glycoprotein Involved in Iron and Inflammatory Homeostasis. *Int J Mol Sci* (2017) 18(9):1985. doi: 10.3390/ijms18091985

114. Adler C, Corbalan NS, Peralta DR, Pomares MF, de Cristóbal RE, Vincent PA. The Alternative Role of Enterobactin as an Oxidative Stress Protector Allows Escherichia Coli Colony Development. *PloS One* (2014) 9(1):e84734. doi: 10.1371/journal.pone.0084734

115. Zhang W, Zhang Y, Wang X, Ding F, Fu Y, Zhao J, et al. Siderophores in Clinical Isolates of Klebsiella Pneumoniae Promote Ciprofloxacin Resistance by Inhibiting the Oxidative Stress. *Biochem Biophys Res Commun* (2017) 491(3):855–61. doi: 10.1016/j.bbrc.2017.04.108

116. Peralta DR, Adler C, Corbalán NS, Paz García EC, Pomares MF, Vincent PA. Enterobactin as Part of the Oxidative Stress Response Repertoire. *PloS One* (2016) 11(6):e0157799. doi: 10.1371/journal.pone.0157799

117. Adler C, Corbalán NS, Seyedsayamdost MR, Pomares MF, de Cristóbal RE, Clardy J, et al. Catecholate Siderophores Protect Bacteria From Pyochelin Toxicity. *PloS One* (2012) 7(10):e46754. doi: 10.1371/journal.pone.0046754

118. Swayambhu G, Bruno M, Gulick AM, Pfeifer BA. Siderophore Natural Products as Pharmaceutical Agents. *Curr Opin Biotechnol* (2021) 69:242–51. doi: 10.1016/j.copbio.2021.01.021

119. Braud A, Hannauer M, Mislin GL, Schalk IJ. The Pseudomonas Aeruginosa Pyochelin-Iron Uptake Pathway and its Metal Specificity. *J Bacteriol* (2009) 191(11):3517–25. doi: 10.1128/JB.00010-09

120. Braud A, Hoegy F, Jezequel K, Lebeau T, Schalk IJ. New Insights Into the Metal Specificity of the Pseudomonas Aeruginosa Pyoverdine-Iron Uptake Pathway. *Environ Microbiol* (2009) 11(5):1079–91. doi: 10.1111/j.1462-2920.2008.01838.x

121. Wichard T, Bellenger JP, Loison A, Kraepiel AM. Catechol Siderophores Control Tungsten Uptake and Toxicity in the Nitrogen-Fixing Bacterium Azotobacter Vinelandii. *Environ Sci Technol* (2008) 42(7):2408–13. doi: 10.1021/es702651f

122. Teitzel GM, Geddie A, De Long SK, Kirisits MJ, Whiteley M, Parsek MR. Survival and Growth in the Presence of Elevated Copper: Transcriptional Profiling of Copper-Stressed Pseudomonas Aeruginosa. *J Bacteriol* (2006) 188(20):7242–56. doi: 10.1128/JB.00837-06

123. McRose DL, Baars O, Morel FMM, Kraepiel AML. Siderophore Production in Azotobacter Vinelandii in Response to Fe-, Mo- and V-Limitation. *Environ Microbiol* (2017) 19(9):3595–605. doi: 10.1111/1462-2920.13857

124. Chaturvedi KS, Hung CS, Crowley JR, Stapleton AE, Henderson JP. The Siderophore Yersiniabactin Binds Copper to Protect Pathogens During Infection. *Nat Chem Biol* (2012) 8(8):731–6. doi: 10.1038/nchembio.1020

125. Emery T. Exchange of Iron by Gallium in Siderophores. *Biochemistry* (1986) 25(16):4629–33. doi: 10.1021/bi00364a026

126. Harris AW, Sephton RG. Transferrin Promotion of 67Ga and 59Fe Uptake by Cultured Mouse Myeloma Cells. *Cancer Res* (1977) 37(10):3634–8.

127. Bernstein LR. Mechanisms of Therapeutic Activity for Gallium. *Pharmacol Rev* (1998) 50(4):665–82.

128. Weiner RE, Schreiber GJ, Hoffer PB. *In Vitro* Transfer of Ga-67 From Transferrin to Ferritin. *J Nucl Med* (1983) 24(7):608–14.

129. Sephton RG, Kraft N. 67Ga and 59Fe Uptakes by Cultured Human Lymphoblasts and Lymphocytes. *Cancer Res* (1978) 38(5):1213–6.

130. Logan KJ, Ng PK, Turner CJ, Schmidt RP, Terner UK, Scott JR, et al. Comparative Pharmacokinetics of Ga-67 and Fe-59 in Humans. *Int J Nucl Med Biol* (1981) 8(4):271–6. doi: 10.1016/0047-0740(81)90033-4

131. Frangipani E, Bonchi C, Minandri F, Imperi F, Visca P. Pyochelin Potentiates the Inhibitory Activity of Gallium on Pseudomonas Aeruginosa. *Antimicrob Agents Chemother* (2014) 58(9):5572–5. doi: 10.1128/AAC.03154-14

132. Olakanmi O, Britigan BE, Schlesinger LS. Gallium Disrupts Iron Metabolism of Mycobacteria Residing Within Human Macrophages. *Infect Immun* (2000) 68(10):5619–27. doi: 10.1128/IAI.68.10.5619-5627.2000

133. Kaneko Y, Thoendel M, Olakanmi O, Britigan BE, Singh PK. The Transition Metal Gallium Disrupts Pseudomonas Aeruginosa Iron Metabolism and has Antimicrobial and Antibiofilm Activity. *J Clin Invest* (2007) 117(4):877–88. doi: 10.1172/JCI30783

134. Davies NP, Suryo Rahmanto Y, Chitambar CR, Richardson DR. Resistance to the Antineoplastic Agent Gallium Nitrate Results in Marked Alterations in Intracellular Iron and Gallium Trafficking: Identification of Novel Intermediates. *J Pharmacol Exp Ther* (2006) 317(1):153–62. doi: 10.1124/jpet.105.099044

135. Banin E, Lozinski A, Brady KM, Berenshtein E, Butterfield PW, Moshe M, et al. The Potential of Desferrioxamine-Gallium as an Anti-Pseudomonas Therapeutic Agent. *Proc Natl Acad Sci USA* (2008) 105(43):16761–6. doi: 10.1073/pnas.0808608105

136. Rzhepishevska O, Ekstrand-Hammarstrom B, Popp M, Bjorn E, Bucht A, Sjostedt A, et al. The Antibacterial Activity of Ga3+ Is Influenced by Ligand Complexation as Well as the Bacterial Carbon Source. *Antimicrob Agents Chemother* (2011) 55(12):5568–80. doi: 10.1128/AAC.00386-11

137. Braun V, Pramanik A, Gwinner T, Köberle M, Bohn E. Sideromycins: Tools and Antibiotics. *Biometals* (2009) 22(1):3–13. doi: 10.1007/s10534-008-9199-7

138. Trottmann F, Franke J, Ishida K, García-Altares M, Hertweck C. A Pair of Bacterial Siderophores Releases and Traps an Intercellular Signal Molecule: An Unusual Case of Natural Nitrone Bioconjugation. *Angew Chem Int Ed Engl* (2019) 58(1):200–4. doi: 10.1002/anie.201811131

139. Tomaras AP, Crandon JL, McPherson CJ, Banevicius MA, Finegan SM, Irvine RL, et al. Adaptation-Based Resistance to Siderophore-Conjugated Antibacterial Agents by Pseudomonas Aeruginosa. *Antimicrob Agents Chemother* (2013) 57(9):4197–207. doi: 10.1128/AAC.00629-13

140. Kim A, Kutschke A, Ehmann DE, Patey SA, Crandon JL, Gorseth E, et al. Pharmacodynamic Profiling of a Siderophore-Conjugated Monocarbam in Pseudomonas Aeruginosa: Assessing the Risk for Resistance and Attenuated Efficacy. *Antimicrob Agents Chemother* (2015) 59(12):7743–52. doi: 10.1128/AAC.00831-15

141. Zughaier SM, Kandler JL, Shafer WM. Neisseria Gonorrhoeae Modulates Iron-Limiting Innate Immune Defenses in Macrophages. *PloS One* (2014) 9(1):e87688. doi: 10.1371/journal.pone.0087688

142. Kochan I, Wasynczuk J, McCabe MA. Effects of Injected Iron and Siderophores on Infections in Normal and Immune Mice. *Infect Immun* (1978) 22(2):560–7. doi: 10.1128/iai.22.2.560-567.1978

143. Chao A, Sieminski PJ, Owens CP, Goulding CW. Iron Acquisition in Mycobacterium Tuberculosis. *Chem Rev* (2019) 119(2):1193–220. doi: 10.1021/acs.chemrev.8b00285

144. Ellermann M, Arthur JC. Siderophore-Mediated Iron Acquisition and Modulation of Host-Bacterial Interactions. *Free Radic Biol Med* (2017) 105:68–78. doi: 10.1016/j.freeradbiomed.2016.10.489

145. Jurado RL. Iron, Infections, and Anemia of Inflammation. *Clin Infect Dis* (1997) 25(4):888–95. doi: 10.1086/515549

146. Pieracci FM, Barie PS. Iron and the Risk of Infection. *Surg Infect (Larchmt)* (2005) 6 Suppl 1:S41–6. doi: 10.1089/sur.2005.6.s1-41

147. Goetz DH, Holmes MA, Borregaard N, Bluhm ME, Raymond KN, Strong RK. The Neutrophil Lipocalin NGAL Is a Bacteriostatic Agent That Interferes With Siderophore-Mediated Iron Acquisition. *Mol Cell* (2002) 10(5):1033–43. doi: 10.1016/S1097-2765(02)00708-6

148. Bachman MA, Miller VL, Weiser JN. Mucosal Lipocalin 2 has Pro-Inflammatory and Iron-Sequestering Effects in Response to Bacterial Enterobactin. *PloS Pathog* (2009) 5(10):e1000622. doi: 10.1371/journal.ppat.1000622

149. Borregaard N, Cowland JB. Neutrophil Gelatinase-Associated Lipocalin, a Siderophore-Binding Eukaryotic Protein. *Biometals* (2006) 19(2):211–5. doi: 10.1007/s10534-005-3251-7

150. Jaberi SA, Cohen A, D'Souza C, Abdulrazzaq YM, Ojha S, Bastaki S, et al. Lipocalin-2: Structure, Function, Distribution and Role in Metabolic Disorders. *BioMed Pharmacother* (2021) 142:112002. doi: 10.1016/j.biopha.2021.112002

151. Krizanac M, Mass Sanchez PB, Weiskirchen R, Asimakopoulos A. A Scoping Review on Lipocalin-2 and Its Role in Non-Alcoholic Steatohepatitis and Hepatocellular Carcinoma. *Int J Mol Sci* (2021) 22(6). doi: 10.3390/ijms22062865

152. Santiago-Sanchez GS, Pita-Grisanti V, Quinones-Diaz B, Gumpper K, Cruz-Monserrate Z, Vivas-Mejia PE. Biological Functions and Therapeutic Potential of Lipocalin 2 in Cancer. *Int J Mol Sci* (2020) 21(12). doi: 10.3390/ijms21124365

153. Rahimi S, Roushandeh AM, Ahmadzadeh E, Jahanian-Najafabadi A, Roudkenar MH. Implication and Role of Neutrophil Gelatinase-Associated Lipocalin in Cancer: Lipocalin-2 as a Potential Novel Emerging Comprehensive Therapeutic Target for a Variety of Cancer Types. *Mol Biol Rep* (2020) 47(3):2327–46. doi: 10.1007/s11033-020-05261-5

154. Gumpper K, Dangel AW, Pita-Grisanti V, Krishna SG, Lara LF, Mace T, et al. Lipocalin-2 Expression and Function in Pancreatic Diseases. *Pancreatology* (2020) 20(3):419–24. doi: 10.1016/j.pan.2020.01.002

155. Jung M, Mertens C, Tomat E, Brune B. Iron as a Central Player and Promising Target in Cancer Progression. *Int J Mol Sci* (2019) 20(2). doi: 10.3390/ijms20020273

156. Saha P, Yeoh BS, Olvera RA, Xiao X, Singh V, Awasthi D, et al. Bacterial Siderophores Hijack Neutrophil Functions. *J Immunol* (2017) 198(11):4293–303. doi: 10.4049/jimmunol.1700261

157. Singh V, Yeoh BS, Xiao X, Kumar M, Bachman M, Borregaard N, et al. Interplay Between Enterobactin, Myeloperoxidase and Lipocalin 2 Regulates E. Coli Survival in the Inflamed Gut. *Nat Commun* (2015) 6:7113. doi: 10.1038/ncomms8113

158. Clifton MC, Corrent C, Strong RK. Siderocalins: Siderophore-Binding Proteins of the Innate Immune System. *Biometals* (2009) 22(4):557–64. doi: 10.1007/s10534-009-9207-6

159. Zsila F, Beke-Somfai T. Human Host-Defense Peptide LL-37 Targets Stealth Siderophores. *Biochem Biophys Res Commun* (2020) 526(3):780–5. doi: 10.1016/j.bbrc.2020.03.162

160. Choi EY, Kim EC, Oh HM, Kim S, Lee HJ, Cho EY, et al. Iron Chelator Triggers Inflammatory Signals in Human Intestinal Epithelial Cells: Involvement of P38 and Extracellular Signal-Regulated Kinase Signaling Pathways. *J Immunol* (2004) 172(11):7069–77. doi: 10.4049/jimmunol.172.11.7069

161. Holden VI, Lenio S, Kuick R, Ramakrishnan SK, Shah YM, Bachman MA. Bacterial Siderophores That Evade or Overwhelm Lipocalin 2 Induce Hypoxia Inducible Factor 1α and Proinflammatory Cytokine Secretion in Cultured Respiratory Epithelial Cells. *Infect Immun* (2014) 82(9):3826–36. doi: 10.1128/IAI.01849-14

162. Monteith AJ, Skaar EP. The Impact of Metal Availability on Immune Function During Infection. *Trends Endocrinol Metab* (2021) 32(11):916–28. doi: 10.1016/j.tem.2021.08.004

163. Sun H, Zhang C, Cao S, Sheng T, Dong N, Xu Y. Fenton Reactions Drive Nucleotide and ATP Syntheses in Cancer. *J Mol Cell Biol* (2018) 10(5):448–59. doi: 10.1093/jmcb/mjy039

164. Vander Heiden MG, DeBerardinis RJ. Understanding the Intersections Between Metabolism and Cancer Biology. *Cell* (2017) 168(4):657–69. doi: 10.1016/j.cell.2016.12.039

165. El-Serag HB. Hepatocellular Carcinoma. *N Engl J Med* (2011) 365(12):1118–27. doi: 10.1056/NEJMra1001683

166. Ko C, Siddaiah N, Berger J, Gish R, Brandhagen D, Sterling RK, et al. Prevalence of Hepatic Iron Overload and Association With Hepatocellular Cancer in End-Stage Liver Disease: Results From the National Hemochromatosis Transplant Registry. *Liver Int* (2007) 27(10):1394–401. doi: 10.1111/j.1478-3231.2007.01596.x

167. Muto Y, Moroishi T, Ichihara K, Nishiyama M, Shimizu H, Eguchi H, et al. Disruption of FBXL5-Mediated Cellular Iron Homeostasis Promotes Liver Carcinogenesis. *J Exp Med* (2019) 216(4):950–65. doi: 10.1084/jem.20180900

168. Ba Q, Hao M, Huang H, Hou J, Ge S, Zhang Z, et al. Iron Deprivation Suppresses Hepatocellular Carcinoma Growth in Experimental Studies. *Clin Cancer Res* (2011) 17(24):7625–33. doi: 10.1158/1078-0432.CCR-10-3099

169. Hussain SP, Raja K, Amstad PA, Sawyer M, Trudel LJ, Wogan GN, et al. Increased P53 Mutation Load in Nontumorous Human Liver of Wilson Disease and Hemochromatosis: Oxyradical Overload Diseases. *Proc Natl Acad Sci USA* (2000) 97(23):12770–5. doi: 10.1073/pnas.220416097

170. Marrogi AJ, Khan MA, van Gijssel HE, Welsh JA, Rahim H, Demetris AJ, et al. Oxidative Stress and P53 Mutations in the Carcinogenesis of Iron Overload-Associated Hepatocellular Carcinoma. *J Natl Cancer Inst* (2001) 93(21):1652–5. doi: 10.1093/jnci/93.21.1652

171. Shen Y, Li X, Dong D, Zhang B, Xue Y, Shang P. Transferrin Receptor 1 in Cancer: A New Sight for Cancer Therapy. *Am J Cancer Res* (2018) 8(6):916–31.

172. Weinstein RE, Bond BH, Silberberg BK, Vaughn CB, Subbaiah P, Pieper DR. Tissue Ferritin Concentration and Prognosis in Carcinoma of the Breast. *Breast Cancer Res Treat* (1989) 14(3):349–53. doi: 10.1007/BF01806307

173. Canonne-Hergaux F, Zhang AS, Ponka P, Gros P. Characterization of the Iron Transporter DMT1 (NRAMP2/DCT1) in Red Blood Cells of Normal and Anemic Mk/Mk Mice. *Blood* (2001) 98(13):3823–30. doi: 10.1182/blood.V98.13.3823

174. Brookes MJ, Hughes S, Turner FE, Reynolds G, Sharma N, Ismail T, et al. Modulation of Iron Transport Proteins in Human Colorectal Carcinogenesis. *Gut* (2006) 55(10):1449–60. doi: 10.1136/gut.2006.094060

175. Basuli D, Tesfay L, Deng Z, Paul B, Yamamoto Y, Ning G, et al. Iron Addiction: A Novel Therapeutic Target in Ovarian Cancer. *Oncogene* (2017) 36(29):4089–99. doi: 10.1038/onc.2017.11

176. Jiang XP, Elliott RL, Head JF. Manipulation of Iron Transporter Genes Results in the Suppression of Human and Mouse Mammary Adenocarcinomas. *Anticancer Res* (2010) 30(3):759–65.

177. Choi JY, Neuhouser ML, Barnett MJ, Hong CC, Kristal AR, Thornquist MD, et al. Iron Intake, Oxidative Stress-Related Genes (MnSOD and MPO) and Prostate Cancer Risk in CARET Cohort. *Carcinogenesis* (2008) 29(5):964–70. doi: 10.1093/carcin/bgn056

178. Richardson A, Kovacevic Z, Richardson DR. Iron Chelation: Inhibition of Key Signaling Pathways in the Induction of the Epithelial Mesenchymal Transition in Pancreatic Cancer and Other Tumors. *Crit Rev Oncog* (2013) 18(5):409–34. doi: 10.1615/CritRevOncog.2013007921

179. Xiong W, Wang L, Yu F. Regulation of Cellular Iron Metabolism and its Implications in Lung Cancer Progression. *Med Oncol* (2014) 31(7):28. doi: 10.1007/s12032-014-0028-2

180. Torti SV, Torti FM, Whitman SP, Brechbiel MW, Park G, Planalp RP. Tumor Cell Cytotoxicity of a Novel Metal Chelator. *Blood* (1998) 92 (4):1384–9. doi: 10.1182/blood.V92.4.1384

181. Song S, Christova T, Perusini S, Alizadeh S, Bao RY, Miller BW, et al. Wnt Inhibitor Screen Reveals Iron Dependence of Beta-Catenin Signaling in Cancers. *Cancer Res* (2011) 71(24):7628–39. doi: 10.1158/0008-5472.CAN-11-2745

182. Franke GN, Kubasch AS, Cross M, Vucinic V, Platzbecker U. Iron Overload and its Impact on Outcome of Patients With Hematological Diseases. *Mol Aspects Med* (2020) 75:100868. doi: 10.1016/j.mam.2020.100868

183. Krebs NF, Sherlock LG, Westcott J, Culbertson D, Hambidge KM, Feazel LM, et al. Effects of Different Complementary Feeding Regimens on Iron Status and Enteric Microbiota in Breastfed Infants. *J Pediatr* (2013) 163 (2):416–23. doi: 10.1016/j.jpeds.2013.01.024

184. Seril DN, Liao J, Ho KL, Warsi A, Yang CS, Yang GY. Dietary Iron Supplementation Enhances DSS-Induced Colitis and Associated Colorectal Carcinoma Development in Mice. *Dig Dis Sci* (2002) 47(6):1266–78. doi: 10.1023/A:1015362228659

185. Carrier JC, Aghdassi E, Jeejeebhoy K, Allard JP. Exacerbation of Dextran Sulfate Sodium-Induced Colitis by Dietary Iron Supplementation: Role of NF-Kappab. *Int J Colorectal Dis* (2006) 21(4):381–7. doi: 10.1007/s00384-005-0011-7

186. Lee T, Clavel T, Smirnov K, Schmidt A, Lagkouvardos I, Walker A, et al. Oral Versus Intravenous Iron Replacement Therapy Distinctly Alters the Gut Microbiota and Metabolome in Patients With IBD. *Gut* (2017) 66(5):863–71. doi: 10.1136/gutjnl-2015-309940

187. Jaeggi T, Kortman GA, Moretti D, Chassard C, Holding P, Dostal A, et al. Iron Fortification Adversely Affects the Gut Microbiome, Increases Pathogen Abundance and Induces Intestinal Inflammation in Kenyan Infants. *Gut* (2015) 64(5):731–42. doi: 10.1136/gutjnl-2014-307720

188. Lievin V, Peiffer I, Hudault S, Rochat F, Brassart D, Neeser JR, et al. Bifidobacterium Strains From Resident Infant Human Gastrointestinal Microflora Exert Antimicrobial Activity. *Gut* (2000) 47(5):646–52. doi: 10.1136/gut.47.5.646

189. Coconnier MH, Lievin V, Bernet-Camard MF, Hudault S, Servin AL. Antibacterial Effect of the Adhering Human Lactobacillus Acidophilus Strain LB. *Antimicrob Agents Chemother* (1997) 41(5):1046–52. doi: 10.1128/AAC.41.5.1046

190. Ibrahim O, O'Sullivan J. Iron Chelators in Cancer Therapy. *Biometals* (2020) 33(4-5):201–15. doi: 10.1007/s10534-020-00243-3

191. Harima H, Kaino S, Takami T, Shinoda S, Matsumoto T, Fujisawa K, et al. Deferasirox, a Novel Oral Iron Chelator, Shows Antiproliferative Activity Against Pancreatic Cancer *In Vitro* and *In Vivo*. *BMC Cancer* (2016) 16:702. doi: 10.1186/s12885-016-2744-9

192. Tury S, Assayag F, Bonin F, Chateau-Joubert S, Servely JL, Vacher S, et al. The Iron Chelator Deferasirox Synergises With Chemotherapy to Treat Triple-Negative Breast Cancers. *J Pathol* (2018) 246(1):103–14. doi: 10.1002/path.5104

193. Leftin A, Zhao H, Turkekul M, de Stanchina E, Manova K, Koutcher JA. Iron Deposition is Associated With Differential Macrophage Infiltration and Therapeutic Response to Iron Chelation in Prostate Cancer. *Sci Rep* (2017) 7(1):11632. doi: 10.1038/s41598-017-11899-2

194. Cameron SJS, Lewis KE, Huws SA, Hegarty MJ, Lewis PD, Pachebat JA, et al. A Pilot Study Using Metagenomic Sequencing of the Sputum Microbiome Suggests Potential Bacterial Biomarkers for Lung Cancer. *PloS One* (2017) 12 (5):e0177062. doi: 10.1371/journal.pone.0177062

195. Gobin J, Wong DK, Gibson BW, Horwitz MA. Characterization of Exochelins of the Mycobacterium Bovis Type Strain and BCG Substrains. *Infect Immun* (1999) 67(4):2035–9. doi: 10.1128/IAI.67.4.2035-2039.1999

196. Schupp T, Toupet C, Divers M. Cloning and Expression of Two Genes of Streptomyces Pilosus Involved in the Biosynthesis of the Siderophore Desferrioxamine B. *Gene* (1988) 64(2):179–88. doi: 10.1016/0378-1119(88)90333-2

197. Blondeau R, Imbert M, Béchet M. Comparison of the Main Siderophores Produced by Some Species of Streptomyces. *Curr Microbiol* (1995) 31:129–33. doi: 10.1007/BF00294289

198. Maggio A. Light and Shadows in the Iron Chelation Treatment of Haematological Diseases. *Br J Haematol* (2007) 138(4):407–21. doi: 10.1111/j.1365-2141.2007.06666.x

199. Leitch HA. Improving Clinical Outcome in Patients With Myelodysplastic Syndrome and Iron Overload Using Iron Chelation Therapy. *Leuk Res* (2007) 31 Suppl 3:S7–9. doi: 10.1016/S0145-2126(07)70460-5

200. Lee KH, Choi E, Chun YS, Kim MS, Park JW. Differential Responses of Two Degradation Domains of HIF-1alpha to Hypoxia and Iron Deficiency. *Biochimie* (2006) 88(2):163–9. doi: 10.1016/j.biochi.2005.07.011

201. Richardson D, Ponka P, Baker E. The Effect of the Iron(III) Chelator, Desferrioxamine, on Iron and Transferrin Uptake by the Human Malignant Melanoma Cell. *Cancer Res* (1994) 54(3):685–9.

202. Kalinowski DS, Richardson DR. The Evolution of Iron Chelators for the Treatment of Iron Overload Disease and Cancer. *Pharmacol Rev* (2005) 57 (4):547–83. doi: 10.1124/pr.57.4.2

203. Keberle H. The Biochemistry of Desferrioxamine and Its Relation to Iron Metabolism. *Ann N Y Acad Sci* (1964) 119:758–68. doi: 10.1111/j.1749-6632.1965.tb54077.x

204. Hershko C, Hershkov A, Konijn A, Breuer W, Cabantchik I Z, Pootrakul P, et al. Objectives and Methods of Iron Chelation Therapy. *Bioinorg Chem Appl* (2003). 1(2):151–68. doi: 10.1155/S1565363303000128

205. Olivieri NF, Brittenham GM. Iron-Chelating Therapy and the Treatment of Thalassemia. *Blood* (1997) 89(3):739–61. doi: 10.1182/blood.V89.3.739

206. Kontoghiorghes GJ. Comparative Efficacy and Toxicity of Desferrioxamine, Deferiprone and Other Iron and Aluminium Chelating Drugs. *Toxicol Lett* (1995) 80(1-3):1–18. doi: 10.1016/0378-4274(95)03415-H

207. Naegeli H-U ZH. Metabolites of Microorganisms. *Helv Chim Acta* (1980) 63:1400–6.

208. Fischbach MA, Lin H, Liu DR, Walsh CT. How Pathogenic Bacteria Evade Mammalian Sabotage in the Battle for Iron. *Nat Chem Biol* (2006) 2(3):132–8. doi: 10.1038/nchembio771

209. McClure JJ, Li X, Chou CJ. Advances and Challenges of HDAC Inhibitors in Cancer Therapeutics. *Adv Cancer Res* (2018) 138:183–211. doi: 10.1016/bs.acr.2018.02.006

210. Nishino N, Yoshikawa D, Watanabe LA, Kato T, Jose B, Komatsu Y, et al. Synthesis and Histone Deacetylase Inhibitory Activity of Cyclic Tetrapeptides Containing a Retrohydroxamate as Zinc Ligand. *Bioorg Med Chem Lett* (2004) 14(10):2427–31. doi: 10.1016/j.bmcl.2004.03.018

211. Yu Y, Wong J, Lovejoy DB, Kalinowski DS, Richardson DR. Chelators at the Cancer Coalface: Desferrioxamine to Triapine and Beyond. *Clin Cancer Res* (2006) 12(23):6876–83. doi: 10.1158/1078-0432.CCR-06-1954

212. Hatcher HC, Singh RN, Torti FM, Torti SV. Synthetic and Natural Iron Chelators: Therapeutic Potential and Clinical Use. *Future Med Chem* (2009) 1(9):1643–70. doi: 10.4155/fmc.09.121

213. Chitambar CR. Gallium Nitrate for the Treatment of non-Hodgkin's Lymphoma. *Expert Opin Investig Drugs* (2004) 13(5):531–41. doi: 10.1517/13543784.13.5.531

214. Seligman PA, Moran PL, Schleicher RB, Crawford ED. Treatment With Gallium Nitrate: Evidence for Interference With Iron Metabolism *In Vivo*. *Am J Hematol* (1992) 41(4):232–40. doi: 10.1002/ajh.2830410403

215. Chitambar CR, Purpi DP, Woodliff J, Yang M, Wereley JP. Development of Gallium Compounds for Treatment of Lymphoma: Gallium Maltolate, a Novel Hydroxypyrone Gallium Compound, Induces Apoptosis and Circumvents Lymphoma Cell Resistance to Gallium Nitrate. *J Pharmacol Exp Ther* (2007) 322(3):1228–36. doi: 10.1124/jpet.107.126342

216. Cunningham MJ, Nathan DG. New Developments in Iron Chelators. *Curr Opin Hematol* (2005) 12(2):129–34. doi: 10.1097/01.moh.0000152631.63469.07

217. Lui GY, Obeidy P, Ford SJ, Tselepis C, Sharp DM, Jansson PJ, et al. The Iron Chelator, Deferasirox, as a Novel Strategy for Cancer Treatment: Oral Activity Against Human Lung Tumor Xenografts and Molecular Mechanism of Action. *Mol Pharmacol* (2013) 83(1):179–90. doi: 10.1124/mol.112.081893

218. Miller MJ, Zhu H, Xu Y, Wu C, Walz A, Vergne A, et al. Utilization of Microbial Iron Assimilation Processes for the Development of New Antibiotics and Inspiration for the Design of New Anticancer Agents. *Biometals: Int J Role Metal Ions Biol Biochem Med* (2009) 22(1):61–75. doi: 10.1007/s10534-008-9185-0

219. Bao G, Clifton M, Hoette TM, Mori K, Deng SX, Qiu A, et al. Iron Traffics in Circulation Bound to a Siderocalin (Ngal)-Catechol Complex. *Nat Chem Biol* (2010) 6(8):602–9. doi: 10.1038/nchembio.402

220. Rehwald C, Schnetz M, Urbschat A, Mertens C, Meier JK, Bauer R, et al. The Iron Load of Lipocalin-2 (LCN-2) Defines Its Pro-Tumour Function in Clear-Cell Renal Cell Carcinoma. *Br J Cancer* (2020) 122(3):421–33. doi: 10.1038/s41416-019-0655-7

221. Nosrati R, Abnous K, Alibolandi M, Mosafer J, Dehghani S, Taghdisi SM, et al. Targeted SPION Siderophore Conjugate Loaded With Doxorubicin as a Theranostic Agent for Imaging and Treatment of Colon Carcinoma. *Sci Rep* (2021) 11(1):13065. doi: 10.1038/s41598-021-92391-w

222. Horm TM, Schroeder JA. MUC1 and Metastatic Cancer: Expression, Function and Therapeutic Targeting. *Cell Adh Migr* (2013) 7(2):187–98. doi: 10.4161/cam.23131

223. Feng X, Jiang S, Zhang F, Wang R, Zhao Y, Zeng M. Siderophore (From Synechococcus Sp. PCC 7002)-Chelated Iron Promotes Iron Uptake in Caco-2 Cells and Ameliorates Iron Deficiency in Rats. *Mar Drugs* (2019) 17(12). doi: 10.3390/md17120709

224. Chi Y, Remsik J, Kiseliovas V, Derderian C, Sener U, Alghader M, et al. Cancer Cells Deploy Lipocalin-2 to Collect Limiting Iron in Leptomeningeal Metastasis. *Science* (2020) 369(6501):276–82. doi: 10.1126/science.aaz2193

225. Huang X. Iron Overload and Its Association With Cancer Risk in Humans: Evidence for Iron as a Carcinogenic Metal. *Mutat Res* (2003) 533(1-2):153–71. doi: 10.1016/j.mrfmmm.2003.08.023

Check for updates

From Transcriptomics, Metabolomics to Functional Studies: Extracellular ATP Induces TGF-β-Like Epithelial Mesenchymal Transition in Lung Cancer Cells

Maria Evers [1,2‡], *Jingwen Song* [3,4,5‡], *Pratik Shriwas* [3,5†], *Harrison S. Greenbaum* [2] *and Xiaozhuo Chen* [3,4,5,6*]

[1] Honors Tutorial College, Ohio University, Athens, OH, United States, [2] The Ben May Department for Cancer Research, University of Chicago, Chicago, IL, United States, [3] Department of Biological Sciences, Ohio University, Athens, OH, United States, [4] The Molecular and Cellular Biology Program, Ohio University, Athens, OH, United States, [5] The Edison Biotechnology Institute, Ohio University, Athens, OH, United States, [6] Department of Biomedical Sciences, The Heritage College of Osteopathic Medicine, Ohio University, Athens, OH, United States

We and others previously showed that extracellular ATP (eATP) is implicated in epithelial mesenchymal transition (EMT). However, the mechanisms by which eATP induces EMT and ATP's relationship to TGF-β, a well-known EMT inducer, are largely unclear. Also, eATP-induced EMT has never been studied at transcriptomic and metabolomics levels. Based on our previous studies, we hypothesized that eATP acts as a specific inducer and regulator of EMT at all levels in cancer cells. RNAseq and metabolomics analyses were performed on human non-small cell lung cancer (NSCLC) A549 cells treated with either eATP or TGF-β. Bio-functional assays, such as invasion, intracellular ATP, cell proliferation, cytoskeleton remodeling, and others were conducted in NSCLC A549 and H1299 cells to validate changes observed from RNAseq and metabolomics studies. In the RNAseq study, eATP significantly enriched expressions of genes involved in EMT similarly to TGF-β after 2 and 6 hours of treatment. Samples treated with eATP for 2 hours share 131 upregulated EMT genes with those of TGF-β treated samples, and 42 genes at 6 hours treatment. Eleven genes, with known or unknown functions in EMT, are significantly upregulated by both inducers at both time points, have been identified. *BLOC1S6*, one of the 11 genes, was selected for further study. eATP induced numerous EMT-related changes in metabolic pathways, including cytoskeleton rearrangement, glycolysis, glutaminolysis, ROS, and individual metabolic changes similar to those induced by TGF-β. Functional bioassays verified the findings from RNAseq and metabolomics that eATP EMT-like changes in A549 and H1299 cells similarly to TGF-β. *BLOC1S6* was found to be implicated in EMT. In these studies, eATP-induced EMT, at all levels examined, is similar but non-identical to that induced by TGF-β, and functions in such a way that

exogenous addition of TGF-β is unnecessary for the induction. The study of *BLOC1S6* further verified its potential roles in EMT and the RNAseq analysis results. All these strongly indicate that eATP is a multi-functional and multi-locational inducer and regulator of EMT, changing our thinking on how EMT is induced and regulated and pointing to new directions for inhibiting EMT in cancer.

Keywords: EMT, invasion, RNA sequencing, cancer metabolism, ROS, cytoskeleton remodeling, heatmap, TCA cycle

INTRODUCTION

Metastasis is associated with up to 90% of all cancer-related death (1) but is also one of the least understood processes in cancer. Metastasis starts with a process known as epithelial to mesenchymal transition (EMT), in which a group of epithelial (E) related genes in cancer cells are downregulated and phenotypes suppressed while some mesenchymal (M) genes are upregulated and M phenotypes are expressed (2, 3), in preparation for subsequent invasion and metastasis. EMT also occurs in normal processes such as early embryonic development when cell migration and cell differentiation are required (3). EMT in cancer cells appear to be a process that mimics EMT in normal cells to achieve their own purpose of increased migration and survival.

EMT itself is a complicated and partially understood process that involves various sub-steps with each corresponding change in cell signaling, gene expression, metabolism, cytoskeleton remodeling, motility, and cell functions (4, 5). In addition, cells of different cancer types have been shown to respond to various kinds of tumor microenvironmental (TME) stimuli and express somewhat different sets of genes to reach a general state termed partial EMT (6–8). In a partial EMT state, which happens in all cancer cells examined upon EMT induction, cancer cells of different cancer types upregulate an incomplete and somewhat different set of mesenchymal genes and downregulate an incomplete and different set of epithelial genes depending upon cancer types, induction conditions, and TME cues (6–8). All of these indicate the plasticity and heterogeneity of EMT in cancer (3). Exactly how EMT is induced and regulated in cancer is far from fully understood, but TGF-β has long been recognized as a major EMT inducer and regulator (9, 10). TGF-β binds and activates cell membrane-associated TGF-β receptors. The activation of TGF-β receptors results in cascades of intracellular signaling, leading to EMT-related gene expression, metabolic reprograming, and phenotypic changes (11, 12). One of the TGF-β signaling pathways and induced processes described in cancer cells is the exocytosis of cytosolic ATP-containing vesicles, releasing ATP to the extracellular environment and creating an autocrine/paracrine signaling loop through extracellular binding and activating of purinergic receptors (PR) located on plasma membrane of cancer cells (13, 14). PR signaling by ATP is vitally important for inducing EMT (15). However, ATP-PR signaling is only one of the several signaling pathways induced by TGF-β, and it remained unclear if extracellular ATP alone is sufficient to induce EMT at levels from transcription, metabolism, to other functionalities.

Ample evidence strongly suggests that extracellular ATP (eATP) plays very important roles in EMT and metastasis. First, intratumoral eATP (ieATP) in TME has been found to be in a concentration range of 10^3 to 10^4 times higher than those in normal tissues (16–19), between ~200-600 μM. Previously, we reported that eATP, at the reported intratumoral concentrations, was internalized by macropinocytosis, a special form of endocytosis (20–22), both *in vitro* and *in vivo* in cancer cells of various cancer types (23–26). We also reported that internalized ATP greatly elevates intracellular ATP levels, which in turn increases the cancer cell proliferation rate and resistance to anticancer drugs, including those target drugs that compete with ATP for the ATP binding site of the protein targets (27, 28). More recently, we have reported the observation of a wide variety of eATP-induced EMT related phenotypic changes, including cell detachment, cell migration and invasion, morphologic and motility changes including loss of cell polarity, cytoskeleton remodeling, and protein expression alterations in human NSCLC A549 cells (29). All these changes cover almost entire spectrum of distinctive EMT features characterized *in vitro* (3), indicating that eATP induces EMT. In addition, ATP is a transcription cofactor involved in various steps of the transcription process (30–34). Extracellular ATP is also a danger signal in both bacteria (35) and animal cells (36), including cancer cells, informing cells to leave its present location for a safer place; it functions as a warning signal for migration, invasion, and metastasis in cancer.

However, if/how much eATP induces corresponding changes at either the gene expression or metabolic level during EMT process have never been systematically investigated, let alone investigated together. In addition, the similarities and differences between eATP and TGF-β in EMT induction at these levels were never compared.

In this study, we hypothesized that eATP functions as key master inducer and regulator for EMT similar to TGF-β, at all biological levels in cancer cells. Thus, we combined RNA sequencing (37, 38) with metabolomics analyses to test this hypothesis primarily in A549 cells and verified these results with various functional studies including studies of a novel gene identified from the RNAseq study. These studies were included

---

because EMT is characterized by the expression of specific genes with subsequent metabolic reprogramming in cancer cells (3). These metabolites are the end products of EMT induction and correspond to the phenotypic changes associated with EMT. We then performed various bio-functional assays to characterize cellular and functional changes for supporting, confirming, and validating eATP-induced and -regulated the onset EMT revealed by RNAseq and metabolomics analyses. These assays demonstrate that EMT-related gene expression leads to EMT-related phenotypic changes. We used TGF-β as a known EMT inducer and TGF-β treated NSCLC cell lines as cell controls for comparison. In addition, we evaluated the importance and contribution of eATP-enhanced intracellular ATP concentrations in eATP-induced EMT. As a final step, we selected a gene identified from the RNAseq analysis, and studied its potential roles in EMT. The results of these studies show significant and independent contributions of eATP to EMT, and possibly the entire metastatic process.

MATERIALS AND METHODS

Chemicals, Proteins, and Antibodies

Cell culture reagents were purchased from VWR. ATP was purchased from Sigma-Aldrich. TGF- β1 protein was from Cell Signaling. Pan-neutralizing antibody against TGF-β ligands was from Cell Signaling.

Cell Lines and Cell Culture

Human non-small cell lung cancer (NSCLC) cell lines A549 and H1299 were purchased from ATCC. A549 and H1299 cells were cultured in Dulbecco's Modified Eagle Medium (DMEM) as previously described (25–29).

We chose human lung cancer A549 and H1299 cells for the study because lung cancer has been our lab's major cancer target and these two NSCLC cell lines have been used in our and other labs frequently before (24–27).

RNA Sequencing
Sample Preparation
A549 cells were treated by ATP or TGF-β for 2 or 6 hrs because we were primarily interested in focusing on and catching early phase gene expression which is responsible for the induction of EMT. The timing was also based on the previous study, which revealed that EMT-related phenotypic changes occur around 2-6 hours post-induction (29). In addition, preliminary data showed a pattern of several EMT-TF levels peaking 6 hours post treatment (unpublished observation). After treatment, RNA was isolated from cells using an RNA Isolation kit (Thermo Fisher) following manufacturer's instructions. Genomic DNA was removed from the samples using a genomic DNA removal kit (Thermo Fisher). RNA samples were eluted in DEPC treated water (Thermo Fisher). RNA Integrity number values were measured by the Ohio University Genomics Facility to ensure quality of the RNA before samples were shipped to LC Sciences in Houston, TX, for a total polyA RNA sequencing.

RNA Sequencing Data Analysis
A complete transcriptome was assembled after the sequencing and the primary analysis of the transcriptome provided by the company were further analyzed to identify gene expression changes associated with EMT induction. Analyses were performed to identify gene sets that were enriched in ATP and TGF-β treated cells, and gene sets were considered significantly enriched if their false discovery rate (FDR) q value was < 0.10, which is 15% less than the value recommended by the GSEA user guide (< 0.25). Heat map genes were identified from GSEA enrichments (39–41). Identified genes expression levels were averaged between samples, gene names were converted from ensemble transcript ID to universal gene symbol using the DAVID database (42, 43), and top hits were visualized utilizing Morpheus heatmapping software form the Broad Institute (https://software.broadinstitute.org/morpheus).

Metabolomics Analysis
Sample preparation: Treatment times of 2, 6, and 12 hours were chosen for the reasons of matching with the RNAseq conditions (2 and 6 hr) and including a condition for later phase of EMT (12hr). A549 cells were treated as follows: no treatment/control,.5 mM eATP, and 10 ng/mL TGF-β. Cell culture metabolism was stopped by briefly incubating in ddH$_2$O, metabolites were extracted by 80% ice cold methanol, and samples were sonicated and centrifuged at 4°C. Metabolites are present in the supernatant, which was removed and freeze dried (44). Samples were stored in -80°C and analyzed at the Ohio State University Campus chemical instrumentation center (CCIC).

Metabolomics data analysis: Metabolomics study was completed by quantitative untargeted LC-MS utilizing Q-TOF 6545 mass spectrometer connected to an Agilent 1290 UHPLC system with a Poroshell 120 SB-C18 (2 × 100 mm, 2.7-µm particle size) column. Metabolomics data was generated and received from CCIC. Masshunter software (Agilent Technology) was used for acquiring data and peaks were integrated using Progenesis (Agilent Technology). Compounds were identified with XCMS as well as Metaboanalyst 5.0 software. Peak areas were normalized using internal standards and were subjected to relative quantification analyses with control (no treatment).

Invasion Assays
Cancer cell invasion assays, which are based on cancer cells penetrating a porous filter covered with a layer of Matrigel in an inner well (the well in another outer well) Transwell system, were performed as previously described with more extensive dose-dependent studies (29). The invading cancer cells have to "eat through" the Matrigel layer to reach the other side of the filter to be stained and then counted. The cells were incubated under different conditions (treatments applied to both the upper and lower chambers. After 20 hours incubation at 37°C, invaded cells to the bottom (opposite side) of the polycarbonate membrane of the upper insert were fixed with 4% paraformaldehyde and stained with crystal violet, and visually counted from six representative visual fields per well in experimental triplicate using compound light microscopy (200X magnification), and

then averaged. The TGF-β concentrations used in these assays were the commonly reported ones in the literature.

Fluorescence Microscopy of eATP Treated Cancer Cells

To observe morphological changes of filopodia-like protrusions, fluorescence microscopy was performed as previously described with an extensive time-dependent study (29). Briefly, F-actin (filamentous-actin) of cells were stained with Fluorescent Phalloxins. A549 or H1299 cells were seeded overnight on glass coverslips placed in 24-well plates, then treated with or without ATP or TGF-β for various time periods (2, 6, and 12 hours). Stained cells were examined and photographed using a Fluor Motorized DIC Polarization Phase Contrast Microscope (Zeiss AXIO Observer) at 200× magnification.

ATP Assay

ATP assays, which are based on measurement of light intensity generated from a biochemical reaction that uses ATP in cell lysates as energy source, were performed as previously described (25, 26, 29).

Cell Proliferation/Viability Assay

Cell viability was measured using a Resazurin Assay. A549 cells were treated as follows: no treatment/control,.25 µg/ml TGF-β antibody,.50 µg/ml TGF-β antibody,.75 µg/ml TGF-β antibody,.25 µg/ml TGF-β antibody +.5 mM ATP,.50 µg/ml

TGF-β antibody +.5 mM ATP,.75 µg/ml TGF-β antibody +.5 mM ATP, and.5 mM ATP for 24 hours. Media was aspirated from cells and replaced with fresh media containing 0.0045% of resazurin dye. Cells were incubated at 37°C for 10 minutes and the plate was read with a fluorescence microplate reader (Citation 3, BioTek) with excitation at 570 nm and emission at 590 nm.

Western Blot Analysis

Proteins were isolated from cells treated with no treatment,.5 mM ATP for hours or 6 hours, or 10 ng/ml TGF-β for 2 hours or 6 hours. Proteins were analyzed with western blots using appropriate primary rabbit anti-human antibodies all purchased from Cell signaling Technologies: E-cadherin (# 3195), Snail (#3879), Vimentin (# 5741), MMP-1 (#54376), MMP-3 (# 14351), MMP-9 (# 2270), Claudin-2 (# 48120), and NF-κBp65 (# 4764). Secondary antibody staining was completed with anti-rabbit IgG, HRP-linked antibody (Goat, 1:1000, CST, #7074). Cofilin (D3F9) XP® Rabbit mAb (#5175) was used as a protein loading control. The signals were detected with Super Signal West Pico Chemiluminescent substrate (Thermo Fisher Scientific) and was developed using (Odyssey Fc 2800, LI-COR Biosciences). Intensities of protein bands were quantified by the corresponding Odyssey Fc software used to develop blots.

Study of Gene BLOC1S6 and Its Functions

To test the functional relevance of consistently upregulated genes identified from RNAseq analysis, we selected *BLOC1S6* as a study

TABLE 1 | Comparison of common genes significantly up- and down-regulated by eATP and TGF-β.

Upregulated Conserved Genes

Gene Symbol	Gene Name	log2(FC) values			
		2 hr ATP	6 hr ATP	2 hr TGF-β	6 hr TGF-β
SOX8	SRY-Box Transcription Factor 8	2.01	2. 94	2.72	2.91
STC1	Stanniocalcin-1	3.41	1.29	1.48	1.39
BMP6	Bore morphogenetic protein 6	1.70	1.27	1.17	1.77
GJB3	Gap Junction Protein Beta 3	2.12	1. 73	1.64	1.40
MMP10	Matrix Metallopeptidase 10	1.36	1. 87	1.10	2.51
BLOC1S6	Biogenesis Of Lysosomal Organelles Complex 1 Subunit 6	1.40	1.27	1.51	1.39
ATP6V1G2-DDX39B	ATP6V1G2-DDX39B readthrough	1.57	2. 31	2.04	2.43
ILIA	Interleukin 1 Alpha	1.39	1. 06	3.06	3.95
LRRC38	Leucine Rich Repeat Containing 38	1.78	1.20	2.59	2.49
PLXNA4	Plexin A4	1.61	1. 10	3.40	3.61
SYTL3	Synaptotagmin Like 3	1.23	1. 04	1.03	1.12

Downregulated Conserved Genes

Gene Symbol	Gene Name	logZ(FC) values			
		2 hr ATP	6 hr ATP	2 hr TGF-β	6 hr TGF-β
FOS	c-Fos	-4 .20	-1. 05	-3.21	-3.32
VAV3	Vav Guanine Nucleotide Exchange Factor 3	-1.07	-1. 11	-1.50	-1.94
ANKS4B	Ankyrin Repeat And Sterile Alpha Motif Domain Containing 4B	-1.61	-1.03	-1.55	-2.26
LINC00488	Long Intergenic Non-Protein Coding RNA 488	-1.21	-1.08	-2.02	-2.32
LINCD1783	Long Intergenic Non-Protein Coding RNA 1783	-1.92	-1.44	-1.91	-1.71
DAG1	Dystroglycan 1	-1.74	-1. 74	-2.40	-1.90
AGPAT3	l-Acylglycerol-3-Phosphate 0-Acyltransf erase 3	-1.23	-1. 31	-1.24	-1.20

Gene expression values are expressed in Log2 fold changes (Log2fc).
All those values shown in **Table 1** *are statistically significantly different from those of the untreated controls (Log2fc = 0). Positive and negative values represent gene upregulations and gene downregulations, respectively.*

target for the following reasons. It is a gene relatively unknown for its functions, particularly totally unknown in EMT. In addition, it is a gene that its mRNA expression levels are inversely proportional to the survival of lung cancer patients with a large survival margin between low and high *BLOC1S6* expressors (45). This comparison of tumor samples from close to one thousand human lung cancer patients strongly implies that *BLOC1S6* expression levels significantly affect the survival of lung cancer patients.

The reasons for focusing on *BLOC1S6* also include (a) *BLOC1S6* is one of the eleven genes that were found to be consistently upregulated by both eATP and TGF-β at both detecting times (**Table 1**). Thus, BLOC1S6 is likely to play important roles in EMT. (b). *BLOC1S6* is one of several genes among the 11 genes that has not been studied in the fields of cancer and EMT. Thus, studying *BLOC1S6* would be more impactful than studying other well-known genes on the list such as *Sox8*, *BMP6*, and *MMP10* (**Table 1**). (c) In addition, earlier studies by others suggested that the protein BLOC1S6 is involved in intracellular vesicle trafficking (46), a process similar to macropinocytosis which is heavily used in eATP internalization as we observed (20–22, 25–29). This further links BLOC1S6 with eATP functions and EMT.

An siRNA study was conducted to knockdown (KD) the expression of BLOC1S6. Sequences of *BLOC1S6* siRNA is 5'-ATACGAGGTTTCATTGTTTAA -3'.

The transfection of the siRNA into A549 cells was performed as previously described (29). Functional assays such as cell proliferation, invasion drug resistance, and soft agar anchor-independent colony formation assay (47), were conducted to assess the potential roles of BLOC1S6 in EMT.

Data Analysis

Each experimental condition will be performed in at least triplicates and repeated at least once. Results were reported as mean ± standard deviation. The statistical difference, or difference between control and treatment groups, was analyzed using Student's t-test or one-way ANOVA. P<0.05 was considered statistically significant.

RESULTS

RNA Sequencing Reveals That eATP Induces Gene Expression Similar but Not Identical to Those Induced by TGF-β

First, we wanted to determine if and how eATP induces changes at the gene expression level as compared with TGF-β. Such a study was never done at the transcriptome level. To that end, RNA sequencing (RNAseq) analysis was performed (**Figure 1A**).

At 2 hours of treatment, TGF-β significantly upregulated a total of 613 genes while eATP upregulated 394 genes (**Figure 1B** left). In addition, among these genes, 131 were common between both treatments at 2 hours (**Figure 1B** left and **1C** left). At 6 hours, TGF-β induced 648 genes whereas eATP induced 135 genes. Between 2 hours and 6 hours, TGF-β significantly induced

roughly the same number of genes while eATP significantly induced only about 1/3 of the genes at 6 hours compared with those of 2 hours. At 6 hours, 42 genes were significantly upregulated by both inducers (**Figure 1B** left and **1C** left). These large changes over time in the eATP-induced gene expressions correlate with the invasion and morphology changes induced by eATP (**Figures 3**, **4**).

In comparison, at 2 hours, TGF-β significantly downregulated 229 genes while eATP downregulated 177 genes (**Figure 1B** right). At 6 hours, TGF-β significantly downregulated 612 genes. In contrast, eATP significantly downregulated 146 genes, a small decrease compared with its 2-hour counterpart (**Figure 1B** right).

Similarly, eATP and TGF-β also downregulated numerous genes, primarily epithelial genes (**Figure S1A, B**).

All these data shown above supports the notion that the state induced by eATP, similar to the one induced by TGF-β, is a partial EMT.

In the gene set enrichment analysis (GSEA) plots for the "Hallmark - Epithelial mesenchymal transition" signature, EMT is more enriched at 2 hours (**Figure 1D**) and at 6 hours (**Figure 1E**) for both eATP and TGF-β treatments compared to the untreated controls. Comparisons between 2 and 6 hours of the same treatment show that EMT is more enriched at 2 hours than 6 hours for ATP (**Figure 1F**), while EMT is more enriched for TGF-β at 6 hours than two hours (**Figure 1G**), suggesting that EMT enrichment/progress induced by ATP is earlier/faster than that for TGF-β. From the gene set enrichment analysis, we found the top 20 most enriched genes in common between ATP and TGF-β at both 2 hours and 6 hours (**Figures 1G, H**). The results from the top 20 enriched genes are consistent with ATP appearing to induce EMT earlier than TGF-β. EMT related genes were more enriched by ATP induction at 2 hours (**Figure 1H**) while TGF-β induced genes were more enriched than ATP at 6 hours (**Figure 1I**). Thus, the heatmap results are consistent with the enrichment analyses (**Figures 1F, G**), again confirming that ATP appears to induce EMT enrichment earlier than TGF-β. In addition, enrichment analysis showed that TGF-β had significantly more genes enriched for EMT in comparison to ATP at 6 hours (**Figure S1C**, right), but not at 2 hours (**Figure S1D**, left).

Eleven Genes Were Upregulated and Conserved in Inductions by Both eATP and TGF-β

Both eATP and TGF-β induced significant upregulation of a common set of 11 genes at both 2 and 6 hours of treatment (**Table 1**, top half). Among these 11 genes, several are well-known to be involved in EMT, such as *Sox8*, *BMP6*, *MMP10*, and others. Several other genes, however, are less well known or not currently known to be associated with EMT. These include *STC1*, *GJB3*, and *BLOC1S6*. Intriguingly, ATP6V1G2-DDX39B, a long non-translated fusion RNA (LncRNA), was also conserved in this group. This readthrough transcript contains an ATPase gene and the *DDX39B*, an RNA splicing gene, raising questions as how this RNA participates in the induction and regulation of EMT.

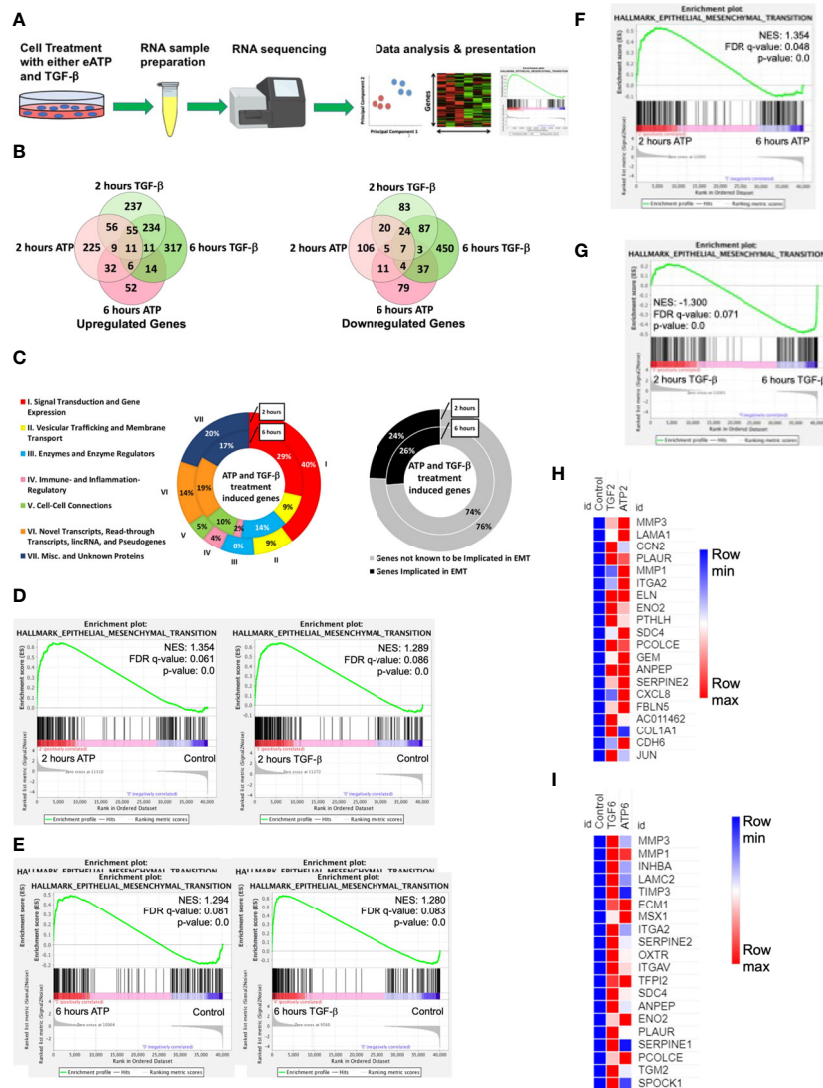RNAseq analysis also identified 7 genes that were conserved and significantly downregulated by both eATP and TGF-β at

FIGURE 1 | RNAseq study. A549 cells were treated with either 0.5 mM ATP or 10 ng/mL TGF-β for 2 or 6 hours with three replicates per treatment condition. After the treatment, polyA-containing RNA was isolated and then sent to a commercial service company for RNAseq analysis as described in detail in the Materials and Methods. The general RNAseq results are presented in Venn diagrams, pie graphs, GSEA plots, and heatmaps. NES: normalized enrichment score. **(A)** Workflow for RNA-sequencing study. **(B)** Venn Diagram of genes significantly upregulated (left) or downregulated (right) by either ATP or TGF-β at 2 or 6 hours. **(C)** pie graph that shows the 131 EMT related genes upregulated by both eATP and TGF-β at 2 hours and 42 genes at 6 hours (left), and percentage of known EMT genes at both times (right). **(D)** Gene set enrichment analysis (GSEA) plots for the "Hallmark - Epithelial mesenchymal transition" signature, 2 hours ATP compared to control (left) and 2 hours TGF-β compared to control (right). **(E–G):** GSEA plots for the "Hallmark - Epithelial mesenchymal transition" signature. **(E)** 6 hours ATP compared to control (left) and 6 hours TGF-β compared to control (right). **(F)** 2 hours ATP compared to 6 hours ATP. **(G)** 2 hours TGF-β compared to 6 hours TGF-β. **(H, I):** Heatmap showing top 20 enriched genes from the "Hallmark - Epithelial mesenchymal transition" signature in **(H)** 2 hours ATP and 2 hours TGF-β and **(I)** 6 hours ATP and 6 hours TGF-β. For heatmaps **(H)** and **(I)**, FPKM values for all three replicates of each gene are shown in the **Supplemental Tables 2**, **3**.

both times (**Table 1**, bottom half). Some of these genes or LncRNAs are also unknown for their functions in EMT.

A closer examination of the RNAseq results revealed that 6 other EMT related genes were also upregulated but not significantly at both times (**Table 2**). One gene is an exception in this category: HGF, which was significantly downregulated by both eATP and TGF-β at 6 hours.

Another category of EMT related genes were also identified (**Table 3**). These genes were either upregulated or downregulated by TGF-β significantly. In comparison, they were regulated in the same directions by eATP but not significantly (**Table 3**).

Four known epithelial genes were also identified to be downregulated by both eATP and TGF-β, but not to a similar degree (**Supplemental Table 1**)

All these RNAseq results indicate that eATP induces and regulates EMT at the gene expression level similarly but also differently to TGF-β.

Metabolomics Analyses of eATP Treated A549 Cells Show Changes Associated With EMT

Metabolic profiles of eATP- or TGF-β-treated cancer cells induced at various times are "snapshots" of cancer cells' total sum of metabolic changes and reflections of metabolic and phenotypic changes during EMT induction at those time points. For these reasons, the metabolomics study was conducted (**Figure 2A**). Partial least-square discriminant analysis (PLS-DA) was performed on the data collected by performing negative ion mode LC-MS/MS. The PLS-DA analysis showed that control treated A549 cancer cells could be separated (based on their metabolite abundances) from ATP- and TGF-β-treated cells after 2, 6 and 12 hours of treatment

(**Figure 2B**). Similarly, PLS-DA analysis was performed on data collected by positive ion mode (**Figure S2**)

Metabolic pathway enrichment analyses show that, among the 25 most enriched pathways in each treatment, about half of those pathways are either identical or similar between control vs 2hr ATP and control vs 2hr TGF- β treated A549 cells (**Figures 2C, D**). Those identical metabolic pathways are concentrated in the glucose metabolism area, including glycolysis/gluconeogenesis, TCA cycle, glutamine, pyruvate, and purine. TGF-β induces these for EMT ([11], [12]). These pathways are known to be inducers of EMT and thus this shows similarity in EMT-like alterations induced by ATP and TGF- β in A549 cell metabolism.

eATP Induced Similar Cell Invasion to TGF-β in Two Human Lung Cancer Cell Lines Tested

Transwell assays showed that the invasion rates were eATP dose-dependent in both A549 cells (**Figure S3A**) and H1299 cells
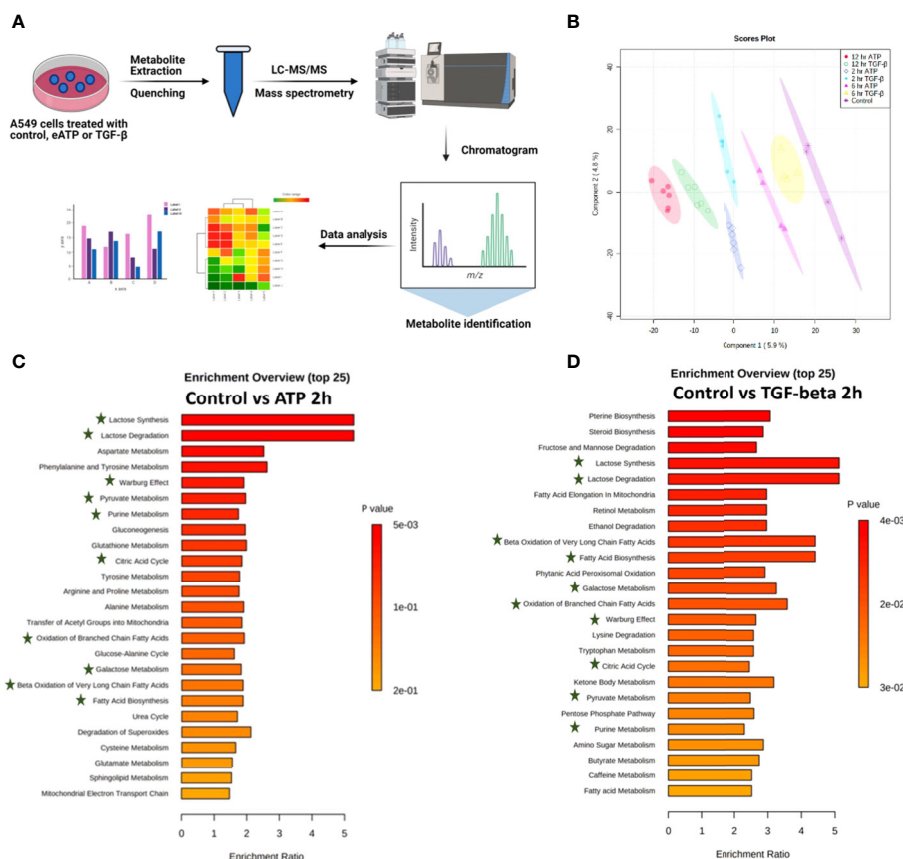

FIGURE 2 | Metabolomics analysis of metabolic changes induced by Eatp. A549 cells were treated with either ATP or TGF-β for 0 (control), 2, 6 and 12 hours. Specially prepared cell lysates were subjected to a metabolomics analysis as described in Materials and Methods. The metabolomics data were presented in different ways to show their EMT-related features, similarities between ATP and TGF-β, and differences from the control. **(A)** Schematic presentation of the design of the metabolomics study. **(B)** PLS-DA plot for eATP or TGF-β treated samples at different treatment times as compared to the untreated control. **(C, D)** Metabolic pathway enrichment analysis of ATP treatment at 2 hr **(C)**, and enrichment by TGF-β at 2 hr **(D)**. Shared metabolic pathways enriched in both conditions are highlighted with asterisks.
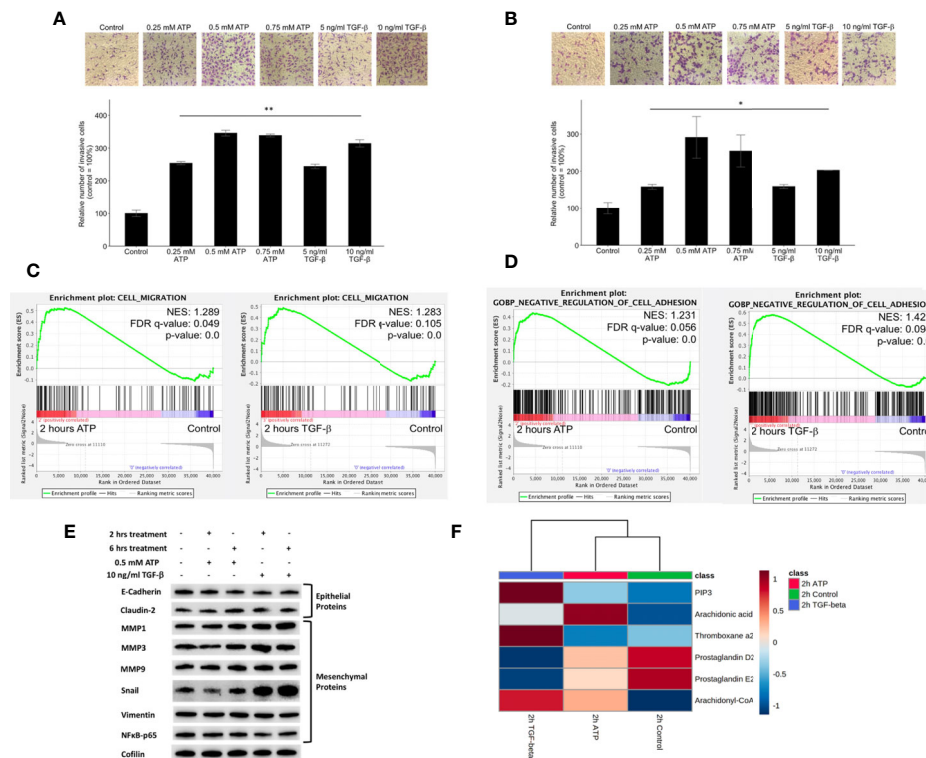
FIGURE 3 | Extracellular ATP induces dose-dependent invasion faster than TGF-β. Human NSCLC A549 and H1299 cells were grown in Transwells with collagen Matrigel coated membranes for 20 hours (invasion assay) in the presence or absence of ATP or TGF-β at various concentrations. After the treatment, invaded cells were fixed, stained, and visually counted and averaged. RNAseq analysis was used to identify corresponding gene expression changes. GSEA plots for the "cell migration" and "negative regulation of cell adhesion" signatures were performed to match/verify the observed phenotypic changes. NES: normalized enrichment score. *$P < 0.05$, **$P < 0.01$. **(A, B)** eATP and TGF-β induce cell invasion in A549 cells **(A)** and in H1299 cells **(B, C)** GSEA plots, 2 hours ATP compared to control (left) and 2 hours TGF-β compared to control (right). **(D)** GSEA plots for the "Negative regulation of cell adhesion" signature, 2 hours ATP compared to control (top) and 2 hours TGF-β compared to control (bottom). **(E)** Western blot analysis of selected proteins related to EMT. Cofilin served as a loading control. The quantification of these proteins can be found in the **Supplemental Figure S3**. **(F)** Metabolomics heatmap for 6 metabolites involved in cell migration in differently treated cells.

(**Figure S3B**). Transwell invasion assays show that eATP induced dose-dependent invasions similar to TGF-β in NSCLC cell lines A549 (**Figure 3A**) and H1299 cells (**Figure 3B**). Gene set enrichment analysis (GSEA) reveals that genes involved in cell migration (**Figure 3C**) and in negative cell adhesion regulation (**Figure 3D**) were significantly enriched by eATP and TGF-β, supporting the increased invasion, compared with the untreated controls, induced by both molecules is likely through similar mechanisms.

Western blot analysis indicated that selected E-type proteins were in general downregulated while M-type proteins were upregulated by eATP, and eATP induced changes are in general in the same direction as TGF-β (**Figure 3E**) and its quantification of (**Figure S3C**), further supporting the role of eATP in EMT induction.

Finally, the increased invasion was confirmed by the metabolomics analysis of invasion/migration-related metabolites, whose abundances were altered in a similar way in both 2hr ATP- and 2hr TGF-β induced samples (**Figure 3F**). These results also indicate that invasion as an EMT-required

phenotypes could be induced by eATP in the range of eATP concentrations found in TME (15–18).

eATP Induced Formation of Filopodia-Like Protrusions Earlier Than TGF-β in Two Human Lung Cancer Cell Lines

Filopodia are "feet-like" cell structures necessary for loss of cell polarity and cytoskeleton remodeling, and cell migration and invasion and are a cellular morphology feature induced in EMT. We previously demonstrated eATP-induced formation of filopodia-like protrusions in A549 cells (29). But we did not know when the protrusions were induced or if the timing of protrusion formation induced by eATP or TGF-β differ from each other. The time course study revealed that the protrusions were formed as early as 2 hours in A549 cells treated with eATP and these protrusions persist for at least 12 hours (**Figure 4A**). Similar changes were also observed in H1299 cells (**Figure 4B**) with the difference of some protrusions being formed even without eATP or TGF-β treatment. The pre-existing
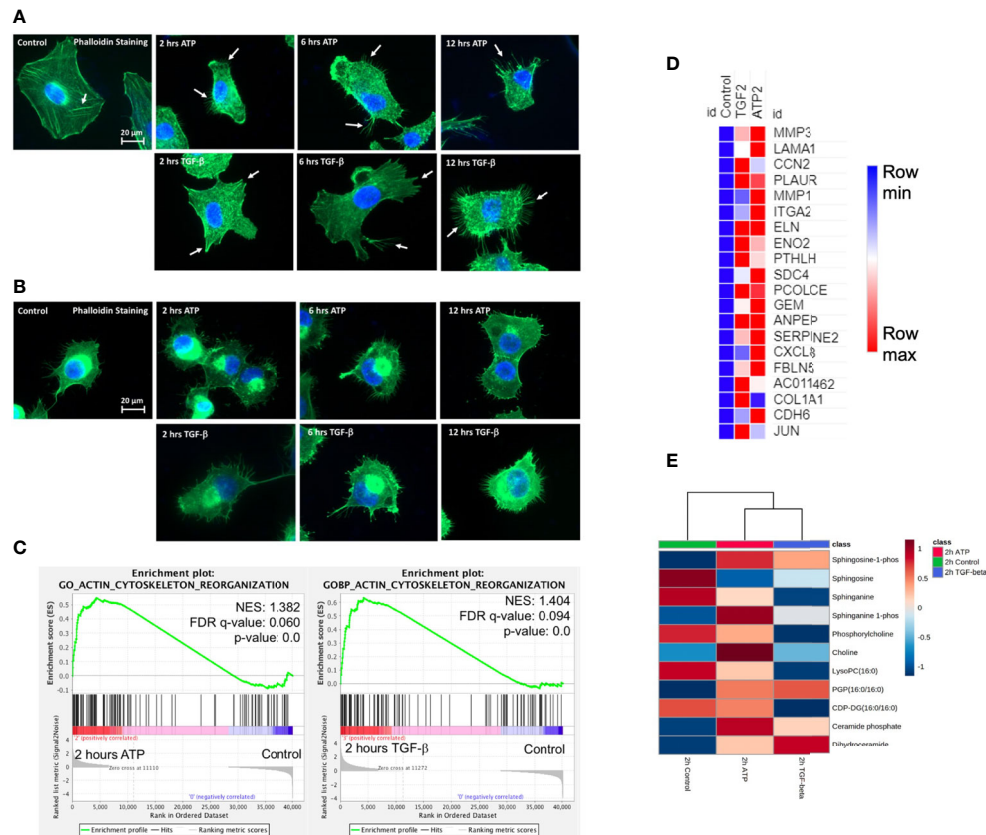
FIGURE 4 | Extracellular ATP induces time-dependent formation of filopodia similar to TGF-β confirmed by transcriptomics and metabolomics analyses. Human NSCLC A549 and H1299 cells were grown on coverslips in cell culture plates were treated with either eATP or TGF-β for various hours. After treatment, fluorescence microscopy was used to visualize time-dependent formation of filopodia-like protrusions in eATP- or TGF-β-treated A549 and H1299 cells. NES: normalized enrichment score. **(A, B)** Fluorescence microscopy of time-dependent formation of filopodia-like protrusion formation in eATP-treated A549 cells **(A)** and H1299 cells **(B)**. Untreated and TGF-β treated cells served as negative and positive controls. Arrows point to distinctive protrusions of the cells. The quantification of the filopodia formation can be found in the **Supplemental Figure S4**. **(C)** Transcriptomics GSEA plots for the "GO Actin Cytoskeleton Reorganization" signature derived from RNAseq data, 2 hours ATP compared to control (top) and 2 hours TGF-β compared to control (bottom). **(D)** Heat mal of the top 20 enriched genes in common between ATP and TGF-β for actin cytoskeleton reorganization. The FPKM values of three replicates of each gene are shown in **Supplemental Table 4**. **(E)** Heatmap of metabolomics analysis showing metabolites involved in actin cytoskeletal rearrangement altered by ATP and TGF-β in A549 cancer cells after 2 hours of treatment.

protrusions in H1299 cells were previously documented (48). TGF-β concentrations used in these assays were most commonly reported in the literature. This assay provides a piece of visual evidence for the first time that eATP induces time-dependent EMT-related and EMT-required cellular morphology changes, and the induced filopodia formation is similar to those induced by TGF-β in timing and degree (**Figure S1H**).

RNAseq GSEA analysis shows that actin-cytoskeleton reorganization related genes are enriched 2 hours after ATP or TGF-β treatment (**Figure 4C**). The top 20 enriched genes in common between ATP and TGF-β for actin cytoskeleton reorganization show similar changes (**Figure 4D**). Metabolomics analysis on cell actin-cytoskeleton rearrangement showed that, among 12 metabolites in this group, 11 metabolites show concentration changes induced by eATP, either increased or decreased, in the same direction compared with TGF-β induction relative to the control at 2 hours (**Figure 4E**). These metabolites are known to be changed in EMT. Thus, these results

indicate that actin-cytoskeleton rearrangement has occurred in these cells treated with either molecule as a result of EMT.

ATP and TGF-βShow Additive Effects on Cell Invasion at Lower Concentrations but Not at Higher Concentrations

At concentrations significantly lower than their respective optimal concentrations for EMT induction, the combined treatment of eATP and TGF- β produced more invasion than the individual treatment alone (**Figure 5A**). However, this additive effect disappeared when regular concentrations were used (**Figure 5B**), suggesting that eATP and TGF-β are very likely to act by using, at least in part, the same pathways for inducing invasion. These same pathways include eATP activated purinergic receptor signaling (13–15). Both eATP and TGF-β are known to use purinergic receptor signaling for their EMT induction (12–14). The concentrations of eATP and TGF-β used in this study were selected for the following reasons. Intratumoral eATP concentrations have been reported to be in the

TABLE 2 | EMT genes significantly changed by both the ATP and TGF- β treatments (but may not be changed significantly at all time points).

Gene Symbol	Gene Name	log2(FC) values			
		2 hr ATP	6 hr ATP	2 hrTGF-Beta	6 hrTGF-Beta
BMP2	Bone morphogenic protein 2	**1.66**	0.61	**1.51**	**1.66**
HGF	hepatocyte growth factor	0.07	**-1.28**	-0.24	**-2.70**
IL6	interlukin 6	**2.10**	0.60	0.99	**2.08**
MMP1	Matrix Metalloproteinases 1	**3.43**	**3.30**	0.93	**3.72**
MMP3	Matrix Metalloproteinases 3	**2.54**	**2.68**	1.18	**4.36**
MMP10	Matrix Metalloproteinases 10	**1.86**	**1.87**	1.10	**2.51**
NFKB1	Nuclear Factor Kappa B Subunit 1	**1.49**	0.05	**1.13**	0.97

Those values shown in bold face are statistically significantly different from the untreated controls.

range of 0.2 – 0.6 mM (16–19). Thus, 0.5 mM is the eATP concentration found in real tumors. 0.5 mM has been the eATP concentration we used in our previous studies (25–29). This concentration has been chosen by us and accepted by the field. These concentrations are also consistent with the concentrations used in the RNAseq and Metabolomics analysis in this study.

eATP Restored Invasiveness of A549 Cells Reduced by Antibodies Against TGF-β

To further characterize the functional relationship between eATP and TGF-β in invasion, a cell viability assay was conducted. This assay result revealed that normal cell viability/proliferation was not stopped in A549 cells by the addition of TGF-β neutralizing antibodies, but the cell viability was further increased by the addition of eATP (**Figure 5C**). In comparison, cell invasiveness was reduced by TGF-β neutralizing antibody treatment but the reduced invasiveness was partially restored by the addition of ATP (**Figure 5D**). However, this restoration was reduced by the increasing amount of the antibodies. These results indicate that eATP could rescue A549 cells, at least in partial, from the invasion-inhibitory activities exerted by TGF-β neutralizing antibodies. This also strongly suggests that eATP's invasion inducing

activity is partially dependent upon TGF-β signaling. These results are consistent with those found in invasion studies (**Figure 3**), cell morphology studies (**Figure 4**), and the additive effect study (**Figures 5A, B**).

RNAseq analysis revealed that, after 2 hours of treatment, a set of genes involved in EMT were enriched by TGF-β but not by eATP, while another set of EMT genes were enriched by eATP but not by TGF-β (**Figure 5G**). These results, in combination with **Figures 1G, H**, show that ATP and TGF-β use some identical and some different genes to induce EMT, providing an explanation for the additive effect observed at low doses and ATP's ability to rescue invasion when TGF-β signaling is not present.

Extracellular ATP Induces Dose-Dependent Elevation of Intracellular ATP Concentrations While TGF-β Does Not

To compare the similarities and differences between eATP and TGF-β in their respective mechanisms in EMT induction, the treatment followed by intracellular ATP (iATP) measurements were performed. The assay showed that eATP induced dose-dependent elevation of iATP concentrations in A549 cells

TABLE 3 | EMT genes significantly changed by TGF- β treatment only (but may not be changed at both time points).

Gene Symbol	Gene Name	log2(FC) values			
		2 hr ATP	6 hr ATP	2 hr TGF-Beta	6 hr TGF-Beta
NOTCH3	Notch 3	-0.03	-0.24	-0.15	**-1.42**
PDGFA	Platelet-derived growth factor A	-0.13	0.49	**1. 03**	1.28
PDGFB	Platelet-derived growth factor B	0.44	0.00	**3.59**	**4.06**
SERPINE1	serpin family E member 1	0.27	0.44	**2.48**	**3.50**
SHH	Sonic Hedgehog	-0.29	-0.76	**1.51**	0.38
SMAD7	SMAD family member 7	-0.82	-0.13	**1. 11**	**1.58**
SNAI1	Snail	0.21	0.50	**2.85**	**3.13**
SNAI2	Slug	0.58	0.58	**2.62**	**2.97**
TNF	Tumor necrosis factor	0.47	0.30	**1.46**	**1.29**
VEGFA	Vascular endothelial growth factor A	0.02	0.32	**1.29**	**2.39**
VEGFC	Vascular endothelial growth factor C	0.47	0.23	-0.52	**-1.08**
VIM	Vimentin	-0.10	0.18	0.36	**1. 06**
WNT3	Wnt family member 3	0.25	-0.40	**1. 11**	0.63
WNT5A	Wnt Family Member 5A	-0.38	-0.17	-0.71	**-1.11**
WNT7A	Wnt family member 7A	-0.55	**1.51**	**2.64**	**4.78**
WNT9A	Wnt family member 9A	0.59	0.92	**1.87**	**1.79**

Those values shown in bold face are statistically significantly different from the untreated controls.
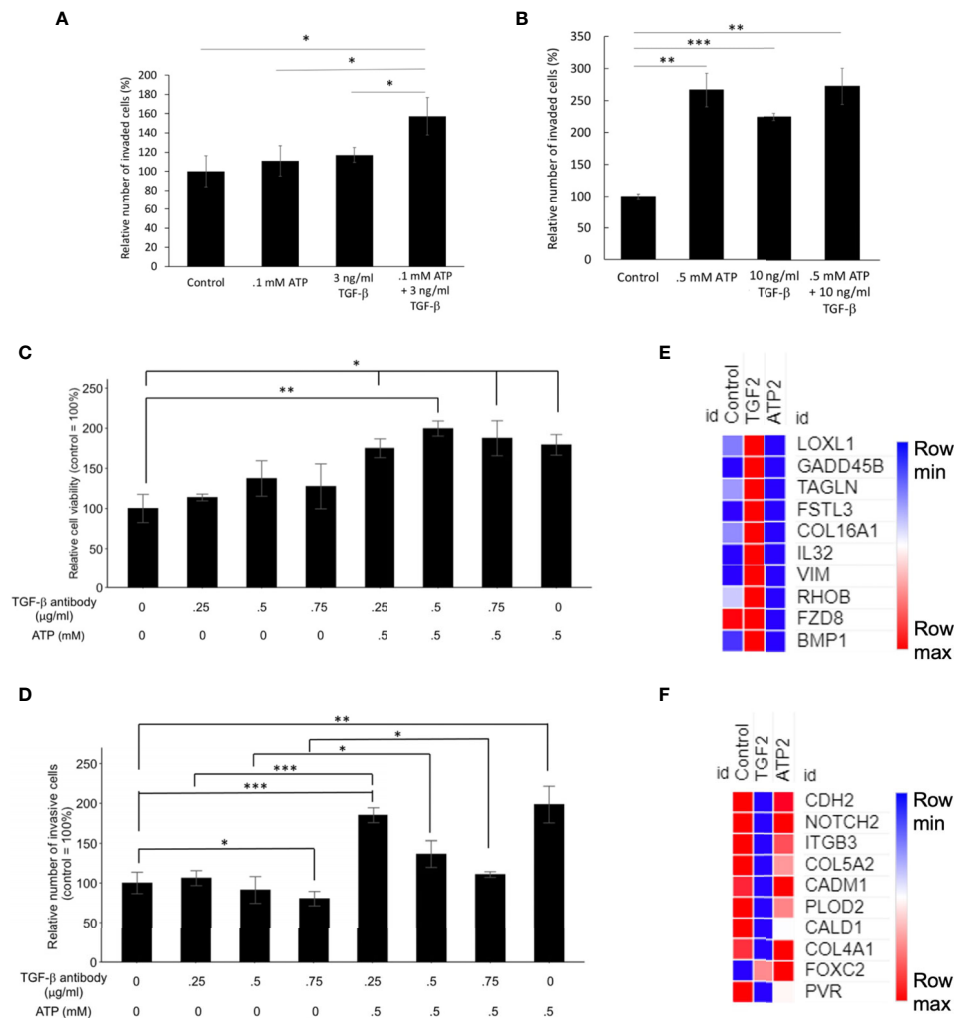
FIGURE 5 | Mechanism study I: Similarities and differences in EMT induced by eATP or TGF-β. Human NSCLC A549 and/or H1299 cells grown in either regular cell culture plates or transwell plates were treated with either ATP, TGF-β, or both at various concentrations and measured for their respective intracellular ATP levels or additive effect in the invasion assay. In a different study, A549 cells were treated with anti-TGF-β neutralizing antibody at various concentrations in the presence or absence of different concentrations of eATP. 24 hours after the treatment, treated cells were assayed for their intracellular ATP levels or their cell viability by resazurin assay. *P < 0.05, **P < 0.01. ***P <.001. **(A, B)** eATP and TGF-β show an additive effect in inducing invasion at lower concentrations **(A)** while eATP and TGF-β do not show an additive effect in inducing invasion at higher concentrations **(B)**. **(C, D)** Extracellular ATP increased cell viability of cells treated with TGF-β neutralizing antibody **(C)**. Extracellular ATP restored the invasiveness of A549 cells treated with TGF-β antibody **(D)** in A549 cells. **(E, F)** Heatmaps of EMT-related genes upregulated by TGF-β at 2 hours **(E)**, and EMT-related genes upregulated by ATP at 2 hours **(F)**. The FPKM values of three replicates of each gene are shown in **Supplemental Tables 5**, **6**, respectively.

(**Figure 6A**) while TGF-β treatment did not change iATP level (**Figure 6B**). The same result was observed in H1299 cells (**Figures S4A, B**). These results suggest that, although eATP induces EMT by possibly using similar mechanisms used by TGF-β, eATP actions are aided by increased iATP concentration. In contrast, TGF-β's EMT-inducing mechanisms do not involve iATP level elevation. Therefore, the differences in iATP levels may account for the differences observed in the invasion and filopodia formation induced by the two molecules (**Figures 3**, **4**), since iATP can function as either an energy source for cell movement, a phosphate donor, a signal amplifier in signal transduction, and even a transcription cofactor.

eATP Induced Transcriptomics and Metabolomics Changes in ROS Pathways and Corresponding Metabolites

Glycolysis, glutaminolysis, and TCA cycle are known to be altered during EMT (11). Most of the metabolites in glycolysis and glutaminolysis changed their concentrations in the same direction 2 hours after the treatment by either ATP or TGF-β (**Figure 6C**). Larger differences can be found in the TCA cycle metabolism (**Figure 6D**). This may be due to the fact that one key function of the TCA cycle is for mitochondrial ATP synthesis but this synthesis is largely unnecessary for the eATP-treated cells because of the macropinocytosis mediated eATP
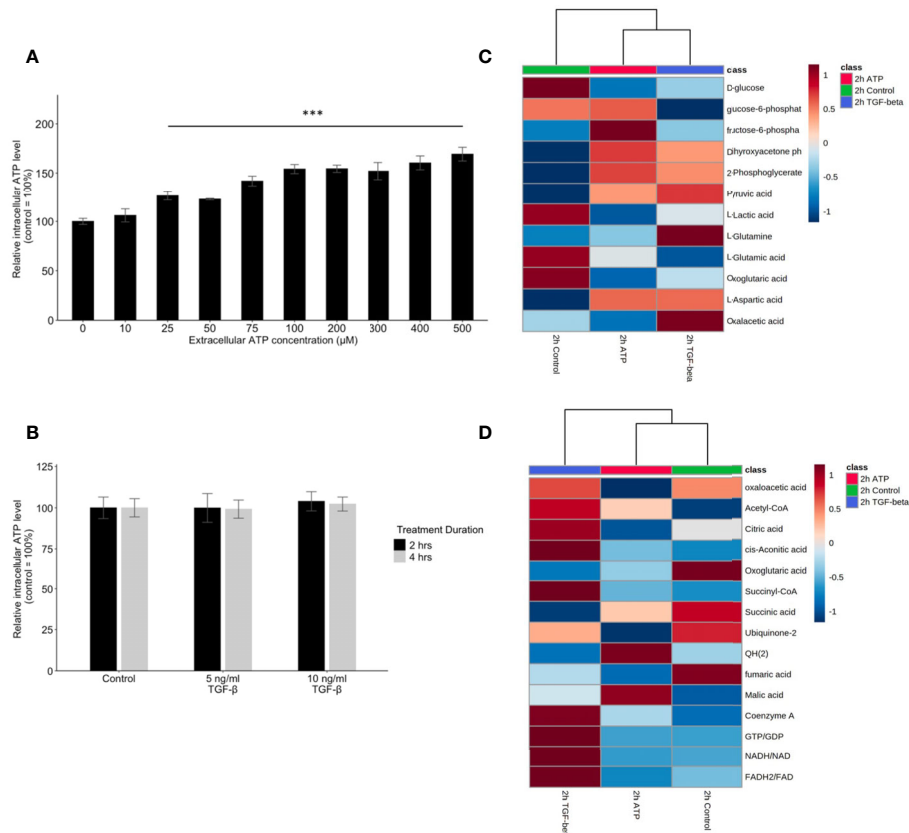
FIGURE 6 | Mechanism study II: similarity and difference between eATP and TGF-β in intracellular ATP and in ATP synthesis-related metabolites. A549 cells were treated with either various concentrations of ATP or TGF-β. 24 hours after the treatment, cells were lysed and measured for their intracellular ATP concentrations. A549 cells were also treated by ATP and TGF-b for 2 hours and then their specific metabolites analyzed. ***P <.001. **(A, B)** Intracellular ATP levels of cells treated by various concentrations of ATP **(A)** and TGF-β **(B)**. **(C, D)** Heatmaps of concentrations of metabolites involved in glycolysis **(C)** or TCA cycle **(D)** in cells treated with ATP or TGF-β for 2 hours compared with the untreated control.

internalization. Thus, it is not surprising that control and eATP treated samples were clustered together much more than TGF-β-treated samples.

ROS is well known to be involved in EMT (11). Metabolomics analysis reveals that concentrations of major metabolites in the ROS pathway changed to the same direction in both ATP- and TGF-β-treated samples after 2 hours of treatment (**Figure 7A**), indicating an increasing ROS status.

GSEA of RNAseq data also show that response to oxidative stress, cellular response to ROS, and superoxide metabolic processes are enriched (**Figures 7B–D**), matching and supporting the metabolic finding.

This indicates that, regarding the ROS and oxidative stress status, eATP-induced and TGF-β-induced cells were in very similar metabolic state, presumably an EMT state.

As a first step for assessing the functions of BLOC1S6 in EMT and CSC, we knocked down *BLOC1S6* gene (**Figure 8B**). *BLOC1S6* is a gene with its functions basically unknown but its expression levels found to be inversely proportional in lung cancer patients' survival (**Figure 8A**) (45). We also used eATP

to treat A549 cells and found that the treatment led to increased BLOC1S6 protein (**Figure 8C**), confirming the validity of our RNAseq data (**Table 1**). The KD of *BLOC1S6* also resulted in reduced cell proliferation (**Figure 8D**), Drug resistance to FDA approved target drug sunitinib (**Figure 8E**) (27), invasion (**Figure 8F**), and the capability of forming colonies (**Figure 8G**). All these strongly suggest that BLOC1S6 is involved in and contributes to EMT and CSC formations.

Based on all these new findings and our previous findings, we propose a new hypothetical model to explain the mechanisms used by eATP to induce EMT (**Figure 8H**).

DISCUSSION

In our previous study, we showed that eATP induced all the *in vitro* key features of EMT (29) as defined by the consensus of the field (3). These key features include cell detachment, loss of apical-basal polarity and cytoskeleton remodeling, cell migration and invasion, upregulation of some M protein markers and
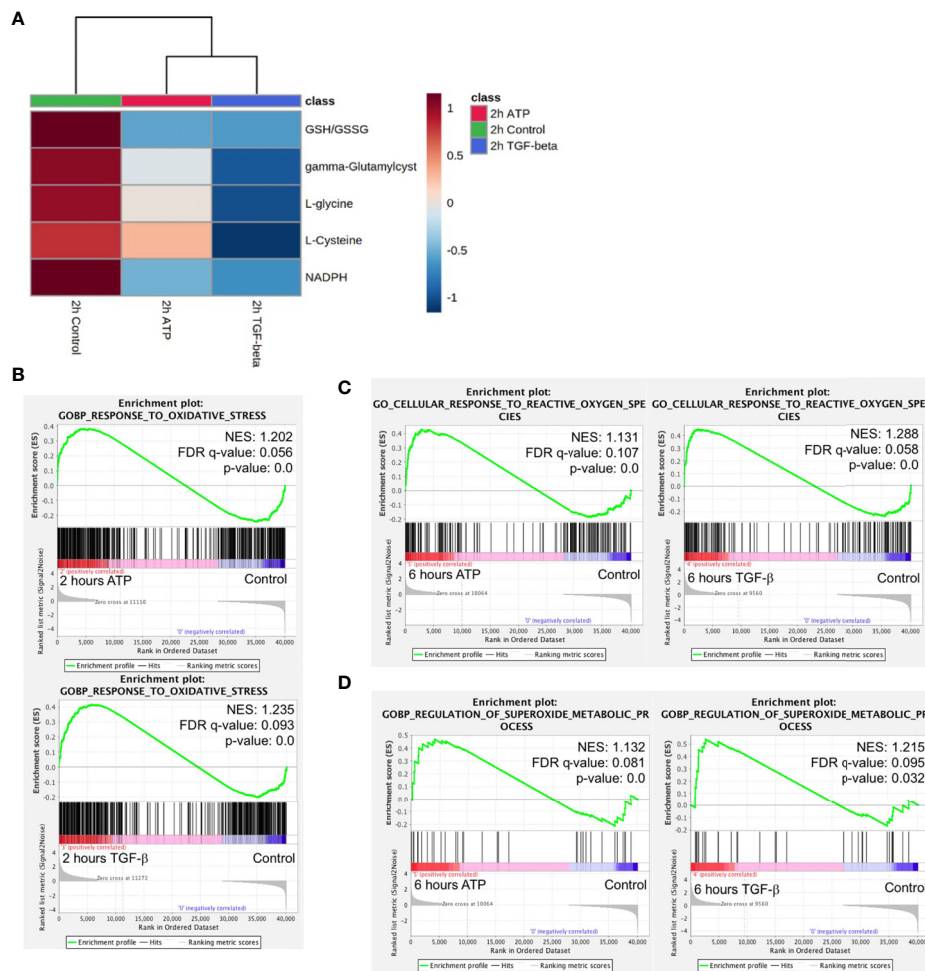
FIGURE 7 | Mechanism study III: similarity and difference between eATP and TGF-β in ROS-related metabolites and genes. A549 cells were treated with either ATP or TGF-β for 2 hours. Then analyzed for their respective transcriptome and metabolome profiles. **(A)** Heatmap of major metabolites involved in the ROS pathway and GSH/GSSG ratio (a marker for redox homeostasis in cancer cells). **(B–D)** GSEA of RNAseq data for the enrichment of oxidative stress **(B)**, cellular response to ROS **(C)**, and superoxide metabolism **(D)**.

reduction of some E markers (29). However, we did not show these changes at gene expression and metabolic levels. In this study, we continue and further expand the eATP study into transcriptomics and metabolomics, and to establish eATP as an inducer and regulator of EMT on a firmer basis.

As described in the Introduction, several unique features of eATP and macropinocytosed eATP support them as being a potential inducer and regulator of EMT. First, ATP is an extracellular messenger, secreted downstream of either a TGF-β-dependent pathway (13, 14), or independent pathways (15), for activating purinergic receptor (PR) mediated signaling, which has been implicated in EMT (49). The PR signaling provides a major part of action specificity for ATP-triggered signaling and actions. ATP is also a versatile transcription cofactor, participating in a wide variety of transcriptional activities such as DNA unwinding, transcription initiation, elongation, and termination (30–34), providing a second mechanism for action

specificity of ATP. Third, ATP is a protein phosphorylation donor involved in a large portion of intracellular signaling pathways. This way, in PR signaling, eATP not only triggers PR activation, but also enhances PR signaling by increasing phosphorylation of proteins/enzymes involved in PR signaling when eATP is internalized by macropinocytosis to elevate intracellular ATP concentrations. We previously demonstrated this activity in other cell growth signaling pathways (27). Furthermore, ATP is also a cofactor in energy-required enzymatic reactions, accelerating reaction rates of those ATP requiring enzymatic reactions. These properties make ATP stand out as a candidate for functioning as an inducer and regulator for EMT, a process that relies on well-regulated changes in signal transduction, gene expression (transcription), translation, and metabolism. More directly related to cell motility and metastasis, ATP is a well-known danger signal for bacteria and cancer cells (46, 47). Elevated ATP concentrations in the environment
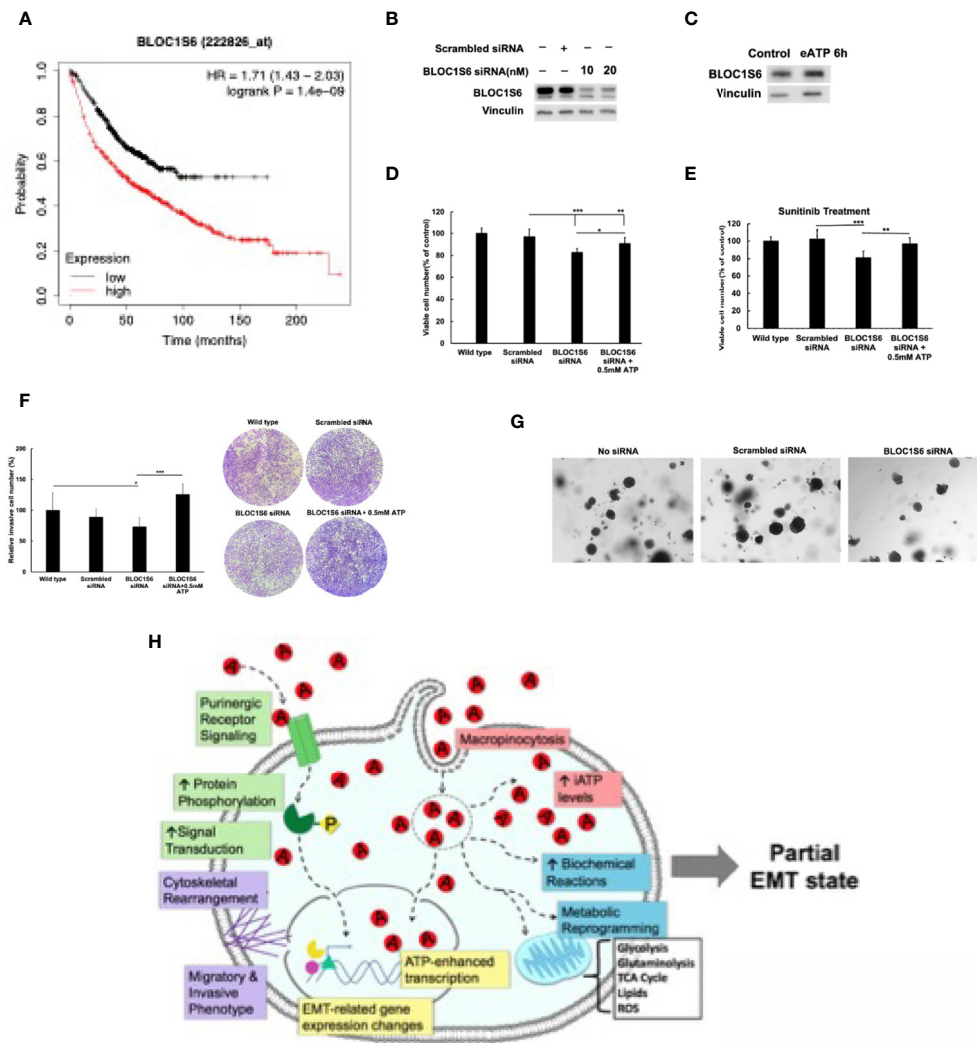
FIGURE 8 | *BLOC1S6* gene is involved in the eATP induced proliferation, drug resistance invasion and colony formation in A549 cells. *BLOC1S6* gene was knocked down or overexpressed in A549 cells. BLOC1S6 protein levels in these cells were measured by western blots. The KD A549 cells were tested in various assays to assess its potential roles in EMT and CSC formation compared with regular A549 cells. **(A)** The inverse proportional relationship between BLOC1S6 mRNA level and survival of lung cancer patients. Kaplan-Meier plots online tool (https://kmplot.com/analysis/) was used to analyze the relationship between Bloc1s6 genes and the overall survival rate of lung cancer. **(B)** Protein expression levels of BLOC1S6 under different siRNA treatment conditions. **(C)** Protein expression levels of BLOC1S6 with or without 0.5mM ATP treatment. **(D)** Cell viability/proliferation assay of KD cells with or without eATP treatment. **(E)** Cell viability/proliferation assay of KD cells treated with anticancer drug Sunitinib at 20 mM in the presence or absence of eATP. *P < 0.05, **P < 0.01,***P <.001. **(F)** Invasion assay of KD cells with or without eATP treatment. **(G)** Soft agar anchor-independent colony assay for testing KD cells' colony formation capability in KD and non-KD cells. Quantification of the assay can be found in **Supplemental Figure S6**. **(H)** A hypothetical model for the mechanisms used by eATP to induce EMT. Detailed explanation for the model can be found in Discussion.

functions as a warning signal to bacteria and animal cells for the incoming danger and informing them to flee for a safer environment. It can be envisioned that this conserved activity is hijacked and utilized by cancer cells to signal imminent danger of their original sites within tumors when the conditions is deteriorating due to hypoxia and shortage of nutritional supply. These deteriorations results in cell lysis and ATP release, sending departure signals leading to invasion and metastasis. Some major remaining questions we tried to

address include: how much, at what time and levels, and in what relationship to TGF-β, eATP contributes to EMT? Our current study was one of the first steps towards answering these key questions for better understanding of the eATP-mediated EMT induction process by using a combinatorial study strategy of RNAseq, metabolomics, and functional assays.

The RNAseq analysis show that, like TGF-β, eATP upregulated and downregulated many genes. Most of these genes are regulated similarly by eATP and TGF-β (**Tables 1**–

3), strongly suggesting that eATP induced and regulated the same process as TGF-β, namely early phase of EMT at 2 and 6 hours. In addition, like TGF-β, eATP exhibited time-dependent gene expressions. The 6-hour treatment led to significantly altered expression of some new genes that did not show up at the 2-hour treatment and downregulation of some other genes. These expression pattern changes suggest that eATP not only induces the onset of EMT, but also temporally regulates EMT, orchestrating the progress by expressing the right genes at the right times and at right levels, just like TGF-β. It is interesting to find out that the percentage of shared upregulated EMT genes by eATP and TGF-β was about 24% or 26% (**Figure 1C** right), or 23% for the downregulated EMT genes (**Figure S1B**). These values are very similar to those reported by others with large numbers of single cell samples and time courses: 22% (50).

On the first look, eATP induced fewer significant changes in upregulated and downregulated genes compared with TGF-β. A closer examination of the RNAseq data reveals that eATP induced changes of expression in about as many genes as TGF-β, but just not to the level of statistical significance determined by the RNAseq software (unpublished observations). Similar phenomenon was also observed in metabolomics data (**Figure 4E** and **5D**). The multi-functionality and multi-locality of ATP and macropinocytosis-internalized eATP might be behind these differences. It is possible that the elevated iATP concentrations (**Figure 5D**) lead to more protein phosphorylation in signal transduction and accelerated biochemical reactions while maintaining the expression of the enzyme genes and metabolites involved in these reactions at levels lower than those found in TGF-β-treated cells (**Table 1**, and **Figure 4E** and **5D**), as these changes make higher gene expression levels unnecessary.

In addition, for some of those M-type genes significantly altered by both eATP and TGF-β, eATP-induced genes tend to show higher Log2fc values at 2 hr than those induced by TGF-β, while genes induced by TGF-β tend to have higher Log2fc values at 6 hr than eATP-induced genes (**Table 1**). This pattern of gene expression suggests that eATP induces gene expression changes earlier and possibly faster than TGF-β, consistent with the observation that eATP induced faster morphological changes than TGF-β [**Figure 3** and (29)]. This phenomenon may also be due to the same multi-locational and multi-functional property of ATP.

Unlike the RNAseq profiles at 2 and 6 hours after the inductions, which reflected the changes in early and later stages of gene expression during EMT, the metabolomics profile represents changes at the metabolic and therefore phenotypic levels associated with EMT (48, 49). The metabolomics data provides evidence, in addition to the RNAseq gene expression data, that eATP induced a metabolic profile similar to that induced by TGF-β (**Figure 2**). The specific altered pathways and metabolite levels, compared with TGF-β, are clear indications that the metabolic state induced by eATP is similar to that induced by TGF-β, and is indeed a state corresponding to EMT. These findings have never been reported before.

We recently reported the observation that eATP induced both migration and invasion (29), two key features of EMT. Our current invasion assays further expand the study by showing dose-dependent comparison between eATP and TGF-β in not only A549 cells, but also in a second lung cancer cell line H1299 (**Figure 3A, B**). The new result shows that this is a multi-cell line and a potentially multi-cancer type phenomenon. The doses of eATP used in this study were the same as the concentration range of eATP found in TME (16–19), implying its roles in real tumors. Our subsequent fluorescent microscopy study revealed that the eATP treatment led to an earlier formation of filopodia-like protrusions, in A549 and H1299 cells in a time-dependent manner (**Figure 4A, B**) than TGF-β. This result provides a first piece of visual evidence for early phase EMT-related morphological changes, loss of apical-basal polarity and cytoskeleton remodeling, induced by eATP.

Eleven genes, which were significantly upregulated and completely conserved in eATP and TGF-β treated cells at both 2 and 6 hours, were identified (**Table 1**). Several genes in this group, including *Sox8*, *BMP6*, *MMP10*, and *IL-1A*, are known to play roles in EMT. Other genes such as *BLOC1S6*, are not known to be involved in EMT. It is particularly interesting to find that *ATP6V1G2-DDX39B*, a long noncoding transcript (LncRNA), containing untranslated ATPase and RNA splicing genes, is also included in this group eATP and TGF-β share some functional similarities and differences to each other (**Figure 5**). First, both eATP and TGF-β promote invasion. They enhance invasion induced by the other molecule when added together at low concentrations (**Figure 5A**), but not at higher concentrations. (**Figure 5B**), suggesting potential overlap of the invasion-inducing activities of the two molecules. When TGF-β neutralizing antibodies were added, cell viability/proliferation increases (**Figure 5C**), indicating that TGF-β itself is cell proliferation-inhibitory under the experimental conditions in A549 cells, different from eATP. In addition, the antibodies reduce invasion induced by TGF-β or by eATP (**Figure 5D**). The former activity indicates that TGF-β is invasion-promoting, the same as eATP. The latter activity indicates TGF-β signaling is important for invasion, and the invasion induced eATP also partially relies on TGF-β signaling, although no TGF-β needed to be added to the system.

The faster EMT induction by eATP than TGF-β may be related to macropinocytosis-mediated ATP internalization, which results in a large elevation of intracellular ATP (iATP) levels. The ATP assay confirmed this speculation in that eATP induced large dose-dependent iATP elevations in both A549 and H1299 cells, while TGF-β did not (**Figure 6A, B**). It is conceivable that the highly elevated iATP enhanced protein phosphorylation in signal transduction, accelerated biochemical reactions and cell morphology changes, and increased cell motility. We previously demonstrated that some of these activities were blocked when macropinocytosis, a primary hallmark of cancer metabolism (51), was inhibited (29). A549 and H1299 cells are known to exhibit macropinocytosis (52, 53). In addition, iATP directly participates in induction and regulation of gene expressions in

cancer cells as a transcriptional cofactor. All these combined together may account for the greater invasion rates compared with TGF-β (**Figure 3A, B**).

Our KD study with *BLOC1S6* indicates that this gene is very likely to be involved in EMT and CSCs, validating our RNAseq study and our selection of the gene as a candidate for EMT/CSC study. Very large differences between BLOC1S6 expression levels and lung patient survival times (**Figure 8A**) (45) also implies its importance in tumorigenesis. Much more detailed studies such as KO studies *in vitro* and *in vivo* are needed for elucidating the working mechanism(s) of the gene in EMT and CSCs. Nevertheless, this study provides initial evidence and justifies for further investigation.

Based on all the previous studies related to ATP-induced EMT (13, 29) and this study, here we propose a significantly updated hypothetical model for how eATP induces and regulates EMT spatially and temporally in human lung cancer cells (**Figure 8G**). First, eATP, at the concentration range found in TME (16–19), functions extracellularly by binding and activating various purinergic receptors (PR) located on plasma membrane of A549 cells (54–56), leading to PR-mediated specific signaling for EMT induction (49, 57, 58). Exactly which PR(s) are activated depend on the specific eATP concentration, as different PRs have different affinities for ATP. This part of eATP activity is similar or identical to the mechanism of TGF-β mediated PR signaling as TGF-β induces ATP exocytosis and subsequent ATP-PR binding/activating (12, 13) with the exception that eATP levels in the TME may be higher than those achieved by TGF-β -mediated ATP exocytosis, as our recently reported data implies (29). This is because eATP in the TME is from multiple sources (58, 59) in addition to TGF-β-induced exocytosis (12, 13). Simultaneously with the PR signaling, eATP is also internalized by macropinocytosis (19–21, 24–26, 29), greatly enhancing the level of intracellular ATP (iATP) by at least 30-50% within 2-3 hours (25–27, 29). The elevated iATP, in turn, accelerates all biochemical/enzymatic reactions inside the cell partly driven by ATP, including both ATP hydrolysis in metabolic reactions and protein phosphorylation in signal transduction (26, 27, 29). Furthermore, ATP is a versatile transcriptional cofactor, directly participating in and augmenting gene expression by ways of double strand DNA unwinding, transcription initiation, elongation, and other steps in transcription (30–34). All these processes working concurrently at different subcellular locations and at various levels of biological reactions result in induction and spatial and temporary regulation of EMT. While the specificity of the gene expression induced by eATP is likely to be originated from the PR signaling, the intensity of the gene expression is likely to be regulated by the other intracellular functions of eATP and potential negative feedback loops between gene transcription rates and enhanced enzymatic activities induced by augmented protein phosphorylation and/or faster enzymatic reactions (and therefore altered metabolite levels) driven by higher iATP levels. Thus, this model not only explains how eATP induces TGF-β-like EMT, but also explains why eATP induces EMT somewhat differently, due to both extracellular and intracellular actions of ATP, from TGF-β-induced EMT at the levels of transcription and biochemical reactions, resulting in earlier morphological/ functional changes. Additional studies are needed for the final validation of this hypothetical model.

CONCLUSIONS

eATP is abundantly present in the TME, is an evolutionarily conserved and selected but previously under-recognized molecule that has been emerging as a powerful inducer and regulator of EMT. Its roles in EMT induction are "amplified" by its internalization through macropinocytosis and subsequent drastic elevation of intracellular ATP levels. Results of this study not only demonstrate the multi-functional and multi-locational nature of eATP, but also exhibit the flexibility of cancer cells, which are able to use either TGF-β or eATP or both, whichever is present in the TME at appropriate concentrations or in various ratios to induce the onset of EMT. The RNAseq and metabolomics analyses not only reveal the eATP induces EMT from expression of specific genes to representative metabolite changes similar to those induced by TGF-β. The functional assays further validate the results from transcriptomics and metabolomics. New findings documented in this study will compel us to rethink exactly how EMT is induced and regulated in tumors, and how it will enable us to develop novel and effective anticancer and anti-metastasis strategies by targeting eATP (60) or its induced genes.

DATA AVAILABILITY STATEMENT

The original contributions presented in the study are publicly available. The RNAseq data is stored at NCBI GEO (Gene Expression Omnibus) with accession number: GSE160671.

AUTHOR CONTRIBUTIONS

ME: Design and execution of most experiments related to functional assays and data analysis of RNAseq, figure generation, manuscript writing and editing. JS: Performance of BLOC1S6 study, some supplementary assays, RNAseq related experiments and uploading RNAseq data to GEO database, writing and submission of manuscript. HSG: RNAseq enrichment analysis. XC: Conceptualization and Design of the study, supervision and coordination of the study, participation in writing and submission of the manuscript, and major funding support of the study. All authors contributed to the article and approved the submitted version.

FUNDING

ACKNOWLEDGMENTS

SUPPLEMENTARY MATERIAL

The Supplementary Material for this article can be found online at: https://www.frontiersin.org/articles/10.3389/fonc.2022.912065/full#supplementary-material

Supplementary Figure 1 | GSEA plots of gene enrichment in cells treated with either eATP or TGF-β. GSEA plots were made the same way as and . **(A)** Downregulated genes. **(B)** Downregulated genes involved in or not known to be involved in EMT. **(C)** Gene enrichment at 2 hours. **(D)** Gene enrichment at 6 hours.

Supplementary Figure 2 | PLS-DA analysis was performed on data collected by positive ion mode as in comparison with the negative ion mode.

Supplementary Figure 3 | Invasion and EMT studies.These studies were done the same way as described for . **(A)** Invasion rate study in A549 cells. **(B)** Invasion rate study in H1299 cells. **(C)** Quantification of the western blot analysis.

Supplementary Figure 4 | Quantification of filopodia induced by either eATP or TGF-β at different induction times. A549 and H1299 human NSCLC cells were treated by either eATP or TGF-β for 2, 6, and 12 hours. The formation of filopodia were photographed by fluorescence microscopy and counted from >10 randomly chosen views for each condition (average 100-200 cells per condition). Filopodia growing on the cells were arbitrarily categorized as none, early, mid, and late stages, based on their size, shape and number, and were separately counted by four individuals and then averaged. **(A)** A549 cells. **(B)** H1299 cells. These results indicate that eATP induced time-dependent filopodia formation similarly to TGF-β.

Supplementary Figure 5 | Intracellular ATP measurement study. This study was done the same way as described for but on H1299 cells. **(A)** iATP levels of H1299 cells treated with different concentrations of eATP. **(B)** iATP levels of H1299 cells treated with different concentrations of TGF-β. Untreated cells were used as negative control.

Supplementary Figure 6 | Quantification of the soft-agar colony formation assay. This quantification is for the assay shown in Figure 8G.

Supplementary Table 1 | Epithelial genes significantly changed by either ATP or TGF-β treatment.

Supplementary Table 2 | FPKM values of three replicate samples for each gene for heatmap in **Figure 1G.**

Supplementary Table 3 | FPKM values of three replicate samples for each gene for heatmap in **Figure 1H.**

Supplementary Table 4 | FPKM values of three replicate samples for each gene for heatmap of **Figure 4D.**

Supplementary Table 5 | FPKM values of three replicate samples for each gene for heatmap of **Figure 5E.**

Supplementary Table 6 | FPKM values of three replicate samples for each gene for heatmap of **Figure 5F.**

REFERENCES

1. Lambert AW, Pattabiraman DR, Weinberg RA. Emerging Biological Principles of Metastasis. *Cell* (2017) 168(4):670–91. doi: 10.1016/j.cell.2016.11.037

2. Nieto MA, Huang RY, Jackson RA, Thiery JP. EMT: 2016. *Cell* (2016) 166(1):21–45. doi: 10.1016/j.cell.2016.06.028

3. Yang J, Antin P, Berx G, Blanpain C, Brabletz T, Bronner M, et al. Guidelines and Definitions for Research on Epithelial–Mesenchymal Transition. *Nat Rev Mol Cell Biol* (2020) 21:341–52. doi: 10.1038/s41580-020-0237-9

4. Lamouille S, Xu J, Derynck R. Molecular Mechanisms of Epithelial-Mesenchymal Transition. *Nat Rev Mol Cell Biol* (2014) 15(3):178–96. doi: 10.1038/nrm3758

5. Lai X, Li Q, Wu F, Lin J, Chen J, Zheng H, et al. Epithelial-Mesenchymal Transition and Metabolic Switching in Cancer: Lessons From Somatic Cell Reprogramming. *Front Cell Dev Biol* (2020) 8:760. doi: 10.3389/fcell.2020.00760

6. Dongre A, Weinberg RA. New Insights Into the Mechanisms of Epithelial-Mesenchymal Transition and Implications for Cancer. *Nat Rev Mol Cell Biol* (2019) 20(2):69–84. doi: 10.1038/s41580-018-0080-4

7. Saitoh M. Involvement of Partial EMT in Cancer Progression. *J Biochem* (2018) 164(4):257–64. doi: 10.1093/jb/mvy047

8. Aiello NM, Maddipati R, Norgard RJ, Balli D, Li J, Yuan S, et al. EMT Subtype Influences Epithelial Plasticity and Mode of Cell Migration. *Dev Cell* (2018) 45(6):681–695.e4. doi: 10.1016/j.devcel.2018.05.027

9. Hao Y, Baker D, Ten Dijke P. TGF-β-Mediated Epithelial-Mesenchymal Transition and Cancer Metastasis. *Int J Mol Sci* (2019) 20(11):2767. doi: 10.3390/ijms20112767

10. Xu J, Lamouille S, Derynck R. TGF-Beta-Induced Epithelial to Mesenchymal Transition. *Cell Res* (2009) 19(2):156–72. doi: 10.1038/cr.2009.5

11. Hua W, Ten Dijke P, Kostidis S, Giera M, Hornsveld M. TGFβ-Induced Metabolic Reprogramming During Epithelial-to-Mesenchymal Transition in Cancer. *Cell Mol Life Sci* (2020) 77:2103–23. doi: 10.1007/s00018-019-03398-6

12. Ferrarelli L. Revisiting TGF-β and EMT. *Science* (2019) 363:941–3. doi: 10.1126/science.363.6430.941-s

13. Martínez-Ramírez AS, Díaz-Muñoz M, Butanda-Ochoa A, Vázquez-Cuevas FG. Nucleotides and Nucleoside Signaling in the Regulation of the Epithelium to Mesenchymal Transition (EMT). *Purinergic Signal* (2017) 13(1):1–12. doi: 10.1007/s11302-016-9550-3

14. Yang H, Geng YH, Wang P, Zhou YT, Yang H, Huo YF, et al. Extracellular ATP Promotes Breast Cancer Invasion and Epithelial-Mesenchymal Transition *via* Hypoxia-Inducible Factor 2α Signaling. *Cancer Sci* (2019) 110(8):2456–70. doi: 10.1111/cas.14086

15. Takai E, Tsukimoto M, Harada H, Kojima S. Autocrine Signaling *via* Release of ATP and Activation of P2X7 Receptor Influences Motile Activity of Human Lung Cancer Cells. *Purinergic Signal* (2014) 10(3):487–97. doi: 10.1007/s11302-014-9411-x

16. Pellegatti P, Raffaghello L, Bianchi G, Piccardi F, Pistoia V, Di Virgilio F. Increased Level of Extracellular ATP at Tumor Sites: *In Vivo* Imaging With

Plasma Membrane Luciferase. *PloS One* (2008) 3(7):e2599. doi: 10.1371/journal.pone.0002599

17. Wilhelm K, Ganesan J, Müller T, Dürr C, Grimm M, Beilhack A, et al. Graft-Versus-Host Disease is Enhanced by Extracellular ATP Activating P2X7R. *Nat Med* (2010) 16(12):1434–8. doi: 10.1038/nm.2242

18. Michaud M, Martins I, Sukkurwala AQ, Adjemian S, Ma Y, Pellegatti P, et al. Autophagy-Dependent Anticancer Immune Responses Induced by Chemotherapeutic Agents in Mice. *Science* (2011) 334(6062):1573–7. doi: 10.1126/science.1208347

19. Di Virgilio F, Adinolfi E. Extracellular Purines, Purinergic Receptors and Tumor Growth. *Oncogene* (2017) 36:293–303. doi: 10.1038/onc.2016.206

20. Commisso C, Davidson SM, Soydaner-Azeloglu RG, Parker SJ, Kamphorst JJ, Hackett S, et al. Macropinocytosis of Protein is an Amino Acid Supply Route in Ras-Transformed Cells. *Nature* (2013) 497(7451):633–7. doi: 10.1038/nature12138

21. Commisso C. The Pervasiveness of Macropinocytosis in Oncological Malignancies. *Philos Trans R Soc Lond B Biol Sci* (2019) 374(1765):20180153. doi: 10.1098/rstb.2018.0153

22. Swanson JA, King JS. The Breadth of Macropinocytosis Research. *Philos Trans R Soc Lond B Biol Sci* (2019) 374(1765):20180146. doi: 10.1098/rstb.2018.0146

23. Liu Y, Zhang W, Cao Y, Liu Y, Bergmeier S, Chen X. Small Compound Inhibitors of Basal Glucose Transport Inhibit Cell Proliferation and Induce Apoptosis in Cancer Cells *via* Glucose-Deprivation-Like Mechanisms. *Cancer Lett* (2010) 298(2):176–85. doi: 10.1016/j.canlet.2010.07.002

24. Liu Y, Cao Y, Zhang W, Bergmeier S, Qian Y, Akbar H, et al. A Small-Molecule Inhibitor of Glucose Transporter 1 Downregulates Glycolysis, Induces Cell-Cycle Arrest, and Inhibits Cancer Cell Growth *In Vitro* and *In Vivo*. *Mol Cancer Ther* (2012) 11(8):1672–82. doi: 10.1158/1535-7163.MCT-12-0131

25. Qian Y, Wang X, Liu Y, Li Y, Colvin RA, Tong L, et al. Extracellular ATP is Internalized by Macropinocytosis and Induces Intracellular ATP Increase and Drug Resistance in Cancer Cells. *Cancer Lett* (2014) 351(2):242–51. doi: 10.1016/j.canlet.2014.06.008

26. Qian Y, Wang X, Li Y, Cao Y, Chen X. Extracellular ATP a New Player in Cancer Metabolism: NSCLC Cells Internalize ATP *In Vitro* and *In Vivo* Using Multiple Endocytic Mechanisms. *Mol Cancer Res* (2016) 14(11):1087–96. doi: 10.1158/1541-7786.MCR-16-0118

27. Wang X, Li Y, Qian Y, Cao Y, Shriwas P, Zhang H, et al. Extracellular ATP, as an Energy and Phosphorylating Molecule, Induces Different Types of Drug Resistances in Cancer Cells Through ATP Internalization and Intracellular ATP Level Increase. *Oncotarget* (2017) 8(50):87860–77. doi: 10.18632/oncotarget.21231

28. Wang X, Zhang H, Chen X. Drug Resistance and Combating Drug Resistance in Cancer. *Cancer Drug Resistance* (2019) 2(2):141-160. doi: 10.20517/cdr.2019.10

29. Cao Y, Wang X, Li Y, Evers M, Zhang H, Chen X. Extracellular and Macropinocytosis Internalized ATP Work Together to Induce Epithelial-Mesenchymal Transition and Other Early Metastatic Activities in Lung Cancer. *Cancer Cell Int* (2019) 19:254. doi: 10.1186/s12935-019-0973-0

30. Dvir A, Garrett KP, Chalut C, Egly JM, Conaway JW, Conaway RC. A Role for ATP and TFIIH in Activation of the RNA Polymerase II Preinitiation Complex Prior to Transcription Initiation. *J Biol Chem* (1996) 271(13):7245–8. doi: 10.1074/jbc.271.13.7245

31. Conaway RC, Conaway JW. ATP Activates Transcription Initiation From Promoters by RNA Polymerase II in a Reversible Step Prior to RNA Synthesis. *J Biol Chem* (1988) 263(6):2962–8. doi: 10.1016/S0021-9258(18)69162-8

32. Porrua O, Libri D. Transcription Termination and the Control of the Transcriptome: Why, Where and How to Stop. *Nat Rev Mol Cell Biol* (2015) 16(3):190–202. doi: 10.1038/nrm3943

33. Fishburn J, Galburt E, Hahn S. Transcription Start Site Scanning and the Requirement for ATP During Transcription Initiation by RNA Polymerase Ii. *J Biol Chem* (2016) 291(25):13040–7. doi: 10.1074/jbc.M116.724583

34. Wang W, Carey M, Gralla JD. Polymerase II Promoter Activation: Closed Complex Formation and ATP-Driven Start Site Opening. *Science* (1992) 255(5043):450–3. doi: 10.1126/science.1310361

35. Ding Q, Tan KS. The Danger Signal Extracellular ATP Is an Inducer of *Fusobacterium Nucleatum* Biofilm Dispersal. *Front Cell Infect Microbiol* (2016) 6:155. doi: 10.3389/fcimb.2016.00155

36. Di Virgilio F, Pinton P, Falzoni S. Assessing Extracellular ATP as Danger Signal *In Vivo*: The Pmeluc System. *Methods Mol Biol* (2016) 1417:115–29. doi: 10.1007/978-1-4939-3566-6_7

37. Ashburner M, Ball CA, Blake JA, Botstein D, Butler H, Cherry JM, et al. Gene Ontology: Tool for the Unification of Biology. *Gene Ontology Consortium Nat Genet* (2000) 25(1):25–9. doi: 10.1038/75556

38. The Gene Ontology Consortium. The Gene Ontology Resource: Enriching a GOld Mine. *Nucleic Acids Res* (2021) 49(D1):D325–34. doi: 10.1093/nar/gkaa1113

39. Subramanian A, Tamayo P, Mootha VK, Mukherjee S, Ebert BL, Gillette MA, et al. Gene Set Enrichment Analysis: A Knowledge-Based Approach for Interpreting Genome-Wide Expression Profiles. *Proc Natl Acad Sci U S A.* (2005) 102(43):15545–50. doi: 10.1073/pnas.0506580102

40. Mootha VK, Lindgren CM, Eriksson KF, Subramanian A, Sihag S, Lehar J, et al. PGC-1α-Responsive Genes Involved in Oxidative Phosphorylation are Coordinately Downregulated in Human Diabetes. *Nat Genet* (2003) 34:267–73. doi: 10.1038/ng1180

41. Liberzon A, Subramanian A, Pinchback R, Thorvaldsdóttir H, Tamayo P, Mesirov JP. Molecular Signatures Database (MSigDB) 3.0. *Bioinformatics* (2011) 27(12):1739–40. doi: 10.1093/bioinformatics/btr260

42. Huang DW, Sherman BT, Lempicki RA. Systematic and Integrative Analysis of Large Gene Lists Using DAVID Bioinformatics Resources. *Nat Protoc* (2009) 4(1):44–57. doi: 10.1038/nprot.2008.211

43. Huang DW, Sherman BT, Lempicki RA. Bioinformatics Enrichment Tools: Paths Toward the Comprehensive Functional Analysis of Large Gene Lists. *Nucleic Acids Res* (2009) 37(1):1–13. doi: 10.1093/nar/gkn923

44. Shriwas P, Roberts D, Li Y, Wang L, Qian Y, Bergmeier S, et al. A Small-Molecule Pan-Class I Glucose Transporter Inhibitor Reduces Cancer Cell Proliferation In Vitro and Tumor Growth *In Vivo* by Targeting Glucose-Based Metabolism. *Cancer Metab* (2021) 9:14. doi: 10.1186/s40170-021-00248-7

45. Lanczky A, Gyorffy B. Web-Based Survival Analysis Tool Tailored for Medical Research (KMplot): Development and Implementation. *J Med Internet Res* (2021) 23(7):e27633. doi: 10.2196/27633

46. Huang L, Kuo YM, Gitschier J. The Pallid Gene Encodes a Novel, Syntaxin 13-Interacting Protein Involved in Platelet Storage Pool Deficiency. *Nat Genet* (1999) 23(3):329–32. doi: 10.1038/15507

47. Reya T, Morrison SJ, Clarke MF, Weissman IL. Stem Cells, Cancer, and Cancer Stem Cells. *Nature* (2001) 414(6859):105–11. doi: 10.1038/35102167

48. Yamada H, Takeda T, Michiue H, Abe T, Takei K. Actin Bundling by Dynamin 2 and Cortactin is Implicated in Cell Migration by Stabilizing Filopodia in Human non-Small Cell Lung Carcinoma Cells. *Int J Oncol* (2016) 49(3):877–86. doi: 10.3892/ijo.2016.3592

49. Di Virgilio F, Sarti AC, Falzoni S, De Marchi E, Adinolfi E. Extracellular ATP and P2 Purinergic Signalling in the Tumour Microenvironment. *Nat Rev Cancer.* (2018) 18(10):601–18. doi: 10.1038/s41568-018-0037-0

50. Cook DP, Vanderhyden BC. Context Specificity of the EMT Transcriptional Response. *Nat Commun* (2020) 11(1):2142. doi: 10.1038/s41467-020-16066-2

51. Pavlova NN, Thompson CB. The Emerging Hallmarks of Cancer Metabolism. *Cell Metab* (2016) 23(1):27–47. doi: 10.1016/j.cmet.2015.12.006

52. Yumoto R, Suzuka S, Oda K, Nagai J, Takano M. Endocytic Uptake of FITC-Albumin by Human Alveolar Epithelial Cell Line A549. *Drug Metab Pharmacokinet* (2012) 27(3):336–43. doi: 10.2133/dmpk.dmpk-11-rg-127

53. Hodakoski C, Hopkins BD, Zhang G, Su T, Cheng Z, Morris R, et al. Rac-Mediated Macropinocytosis of Extracellular Protein Promotes Glucose Independence in Non-Small Cell Lung Cancer. *Cancers (Basel).* (2019) 11(1):37. doi: 10.3390/cancers11010037

54. Taylor AL, Schwiebert LM, Smith JJ, King C, Jones JR, Sorscher EJ, et al. Epithelial P2X Purinergic Receptor Channel Expression and Function. *J Clin Invest* (1999) 104(7):875–84. doi: 10.1172/JCI7270

55. Belete HA, Hubmayr RD, Wang S, Singh RD. The Role of Purinergic Signaling on Deformation Induced Injury and Repair Responses of Alveolar Epithelial Cells. *PloS One* (2011) 6(11):e27469. doi: 10.1371/journal.pone.0027469

56. Leyva-Grado VH, Ermler ME, Schotsaert M, Gonzalez MG, Gillespie V, Lim JK, et al. Contribution of the Purinergic Receptor P2X7 to Development of Lung Immunopathology During Influenza Virus Infection. *mBio* (2017) 8(2):e00229–17. doi: 10.1128/mBio.00229-17

57. Burnstock G, Di Virgilio F. Purinergic Signalling and Cancer. *Purinergic Signal* (2013) 9(4):491–540. doi: 10.1007/s11302-013-9372-5

58. Di Virgilio F, Dal Ben D, Sarti AC, Giuliani AL, Falzoni S. The P2X7 Receptor in Infection and Inflammation. *Immunity* (2017) 47(1):15–31. doi: 10.1016/j.immuni.2017.06.020

59. Kroemer G, Galluzzi L, Kepp O, Zitvogel L. Immunogenic Cell Death in Cancer Therapy. *Annu Rev Immunol* (2013) 31:51–72. doi: 10.1146/annurev-immunol-032712-100008

60. Vultaggio-Poma V, Sarti AC, Di Virgilio F. Extracellular ATP: A Feasible Target for Cancer Therapy. *Cells* (2020) 9:2496. doi: 10.3390/cells9112496

Conflict of Interest: The authors declare that the research was conducted in the absence of any commercial or financial relationships that could be construed as a potential conflict of interest.

17-β Estradiol up-regulates energy metabolic pathways, cellular proliferation and tumor invasiveness in ER+ breast cancer spheroids

Silvia Cecilia Pacheco-Velázquez[1]*,
Ingrid Itzayanna Ortega-Mejía[1], Jorge Luis Vargas-Navarro[1],
Joaquín Alberto Padilla-Flores[1],
Diana Xochiquetzal Robledo-Cadena[1],
Gabriela Tapia-Martínez[1], Ignacio Peñalosa-Castro[2],
José Luis Aguilar-Ponce[3], Juan Carlos Granados-Rivas[4],
Rafael Moreno-Sánchez[2] and Sara Rodríguez-Enríquez[1,4]*

[1]Departamento de Bioquímica, Instituto Nacional de Cardiología, Ciudad de México, Mexico,
[2]Laboratorio de Control Metabólico, Carrera de Biología, Facultad de Estudios Superiores Iztacala,
Universidad Nacional Autónoma de México, Los Reyes Ixtacala, Hab, Tlalnepantla, Mexico, [3]Hospital
Médica Sur, Area de Oncología, Ciudad de México, Mexico, [4]Laboratorio de Control Metabólico,
Carrera de Medicina, Facultad de Estudios Superiores Iztacala, Universidad Nacional Autónoma de
México, Los Reyes Ixtacala, Hab, Tlalnepantla, Mexico

Several biological processes related to cancer malignancy are regulated by 17-
β estradiol (E2) in ER+-breast cancer. To establish the role of E2 on the atypical
cancer energy metabolism, a systematic study analyzing transcription factors,
proteins, and fluxes associated with energy metabolism was undertaken in
multicellular tumor spheroids (MCTS) from human ER+ MCF-7 breast cancer
cells. At E2 physiological concentrations (10 and 100 nM for 24 h), both ERα and
ERβ receptors, and their protein target pS2, increased by 0.6-3.5 times *vs.* non-
treated MCTS, revealing an activated E2/ER axis. E2 also increased by 30-470%
the content of several transcription factors associated to mitochondrial
biogenesis and oxidative phosphorylation (OxPhos) (p53, PGC1-α) and
glycolytic pathways (HIF1-α, c-MYC). Several OxPhos and glycolytic proteins
(36-257%) as well as pathway fluxes (48-156%) significantly increased being
OxPhos the principal ATP cellular supplier (>75%). As result of energy
metabolism stimulation by E2, cancer cell migration and invasion processes
and related proteins (SNAIL, FN, MM-9) contents augmented by 24-189% *vs.*
non-treated MCTS. Celecoxib at 10 nM blocked OxPhos (60%) as well as MCTS
growth, cell migration and invasiveness (>40%); whereas the glycolytic inhibitor
iodoacetate (0.5 μM) and doxorubicin (70 nM) were innocuous. Our results

show for the first time using a more physiological tridimensional cancer model, resembling the initial stages of solid tumors, that anti-mitochondrial therapy may be useful to deter hormone-dependent breast carcinomas.

Introduction

The estrogen positive (ER+) breast cancer is one of the most frequently diagnosed human cancers, becoming the main cause of death in women of reproductive age worldwide (1). Malignancy of ER+ breast cancer is associated to estrogen receptors (ERs) overexpression (2). The ERs (ERα and Erβ) belong to a steroid/nuclear receptor superfamily activated by 17β-estradiol (E2) (3) and by other ligands (estriol, estrone) but with lower affinity (4). ER/ligand complex promotes a monomer-to-dimer self-transition and nuclear localization (3). In consequence, ERs bind to DNA transcriptional regulatory regions called estrogen response elements (EREs) located in their target genes, increasing gene expression in response to E2.

The ER/E2 complex triggers several intracellular events linked to the overexpression of proteins associated to ER+ breast cancer cell proliferation (cyclin D1, p53, BRCA-1) and angiogenesis (VEGF-R2) (5–7). Recently, the role of ER/E2 complex has also emerged as a lipid metabolism regulator. In breast MCF-7 and T47D cancer cells, ER/E2 increases the mRNA level (4-times) of proteins associated with monounsaturated fatty acids biosynthesis like the stearoyl-CoA desaturase (8, 9), indicating its role as anabolic inducer. E2 also augments the mRNA level (3-times) of OCTN2, a carnitine associated-carrier protein located in plasma membrane to

supplying carnitine for mitochondrial β-oxidation (8, 9), which suggests a role for E2 as catabolic key primary regulator.

Scarce information is available regarding the role of E2 on cancer energy metabolism. In this regard, transcriptomic analysis reveals that E2 increases by 2-7 times the mRNA level of some glycolytic (HK-I and -II, PFK-2 and LDH-A) and mitochondrial (ND1 and COX-IV) enzymes in MCF-7 and T47D ER+-breast cancer cells (10, 11). E2 also increases the mRNA level of the mitochondrial biogenesis transcription factors PGC1-α and TFAM in breast MCF-7 and lung H1793 carcinoma cells (12). Unfortunately, transcriptomic results were not accompanied by experimental analysis of enzyme activities and fluxes of energy metabolism pathways, which should have allowed for elucidating whether E2 actually regulates energy metabolism function in cancer cells. In this last regard, it should be considered that there does not always exist a tight relationship between the mRNA/protein levels with enzyme/transporter activity and metabolic pathway fluxes or biological function (13); the regulatory mechanisms operating at the different levels of biological complexity should also be taken into account for more accurate data interpretation, avoiding unsubstantiated extrapolations.

In the present study, the effect of E2 was systematically analyzed on energy metabolism of breast ER+ cancer cells. Thus. (i) the levels of energy-metabolism associated transcription factors (ERα and β, HIF-1α, c-MYC, p53, PPAR-γ and PGC1-α); (ii) the protein levels and fluxes of glycolysis and oxidative phosphorylation (OxPhos); and (iii) metastatic ATP-dependent processes such as cell invasiveness and migration were determined by using the multicellular tumor spheroids (MCTS) model, a tridimensional cancer cell model (14). MCTS mimic the behavior and structure of cancer cells in their own physiological microenvironment, resembling the solid and non-vascularized initial stages of solid tumors by establishing metabolite gradients including carbon sources, oxygen, H+, added drugs, between peripheral well-oxygenated cell layers, inner poorly oxygenated cells layers and a central necrotic/apoptotic core.

Once the main ATP supplier can be identified in E2-stimulated MCTS, strategies using anti-OxPhos or anti-glycolytic inhibitors could be tested in order to block MCTS growth. This last goal is clinically relevant because the

commonly used chemo-therapies (tamoxifen, fulvestran, anti-estrogen analogues, aromatase inhibitors) against ER+ breast cancer do not always provide positive outcomes and such therapies are frequently associated with the development of severe side effects (15–17). This study shall provide the basis for designing improved treatments targeting the principal energy metabolism pathway in hormone-dependent cancers, looking for no adverse side-effects on non-cancer cells functions.

Materials and methods

Chemicals

17β-estradiol (E2, Sigma, MO, USA) was dissolved in a mix of ethanol 70%/dimethyl sulfoxide (DMSO) 30%. The maximal amount of ethanol/DMSO used was less than 10% of the final volume in the well, which did not affect the proliferation rate and cellular viability (>95%).

Cancer cell culture

Human ER+ breast MCF-7 cancer cells (American Type Culture Collection, Rockville, MD, USA) were cultured in Petri dishes in 20 mL of Dulbecco's Modified Eagle's Medium (DMEM, Sigma, MO, USA) supplemented with 10% fetal bovine serum (Biowest, Mexico) and 10 000 U penicillin/streptomycin (Sigma-Aldrich, MO, USA). The genotyping (INMEGEN, México) of MCF-7 revealed that the cell line shared 13 from 14 of the canonic allelic markers with the ATCC original clone. For growth and maintenance, cells were incubated in 5% CO_2/95% air at 37°C and kept until 80-90% of confluence was reached. Then, cells were harvested and use for further experiments (18).

Multi-cellular tumor spheroid cultures

For MCTS growth, MCF-7 (1×10^5 cells/ml) were seeded in 2% (w/v) agarose-coated culture dishes in 5 mL DMEM. After 5 days, old medium was replaced with fresh DMEM in the presence of different E2 (0.1, 1, 10 and 100 nM) concentrations and spheroids were placed under slow orbital shaking (20–50 rpm) at 37°C and 95% air/5% CO_2. To discard incompletely formed spheroids, fresh DMEM was replaced every three days. The spheroid growth was determined at different culture days by measuring diameters using a calibrated reticule (1/10 mm) in an inverted phase contrast microscope (Zeiss, Thornwood, NY) (14). The growth of each MCTS was followed for 25 days and analyzed by fitting data to the exponential growth curve equation using the Origin 8 software (Northampton MA, USA) (19).

Western blot

Once maximal size was reached (day 23 of culture), MCTS were recollected and re-suspended in Krebs-Ringer (KR, 125 mM NaCl, 5 mM KCl, 25 mM HEPES, 1 mM KH_2PO_4, 1 mM $MgCl_2$, 1.4 mM $CaCl_2$, pH 7.4) buffer. Samples were centrifuged at 2500 rpm for 3 min, and the pellets were dissolved in RIPA lysis buffer (phosphate buffer saline 1 X pH 7.2, 1% IGEPAL NP40, 0.1% SDS and 0.05% sodium deoxycholate) *plus* 1 mM phenyl methanesulfonyl fluoride (PMSF) and 1 protease inhibitors cocktail tablet (Roche, Mannheimm, Germany). Once the protein concentration was determined by the Lowry method (20), the supernatants were kept at -20°C until use. Samples (50 μg protein) were re-suspended in loading buffer *plus* 5% β-mercaptoethanol, loaded onto 10 or 12.5% polyacrylamide gels and separated under reducing conditions by 10-12% SDS-polyacrylamide gel electrophoresis (21). The proteins were blotted to PVDF membranes (BioRad, Hercules, CA, USA) and Western blot analysis was performed by immunoblotting with the following antibodies. From Novus Biologicals (Littleton, CO, USA), anti-GA (NBPZ-29940). From FineTest (Barcelona, Spain), PGC1-α (NFab06351). From Abcam (Waltham, MA, USA), PYK (ab150377) and PPAR-γ (ab70405). From Santa Cruz Biotechnology (Cambridge, MA, USA) α-tubulin (sc-5286), HIF-1α (sc-13515), ERα (sc-71094), ERβ (sc-53494), c-MYC (sc-40), p53 (sc-101762), GLUT-1 (sc-1603), GLUT-3 (sc-74399), HK-I (sc-46695), HK-II (sc-130358), PFK-1 (sc-31711), LDH-A (sc-130327), PDH (sc-65242), IDH3G (sc-365489), 2-OGDH (sc-49589), ND1 (sc-65237), COX-IV (sc-376731), ATPS (sc-58619) and ANT (sc-11433). All antibodies were used at final dilutions of 1:1000−1:2000. The hybridization bands were revealed with the corresponding secondary antibodies conjugated with horseradish peroxidase (Santa Cruz, MA, USA) and the ECL-plus detection system (Amersham, Buckinghamshire, U.K.). Densitometry analysis was performed using the Scion Image Software (Scion Corp., Frederic, MD, USA) and normalized against α-tubulin, which corresponded to 100% intensity.

OxPhos and glycolysis fluxes

For assessment of energy metabolism fluxes, MCF-7 spheroids from day 23 of culture were incubated in KR buffer plus trypsin/EDTA (0.25%) for 50 min; afterwards, MCTS were gently and mechanically disaggregated. Cells derived from disaggregated MCTS maintained viability up to 95%.

For glycolysis flux, disaggregated cells (2 mg protein/mL) were incubated in KR buffer. Glycolysis was started by adding 5 mM external glucose (Sigma-Aldrich, MO, USA), and cellular samples were collected after 0 and 10 min of incubation at 37°C under smooth orbital shaking. At the indicated times, the cells were

rapidly mixed with 3% (w/v) cold perchloric acid and centrifuged. The supernatants were neutralized with 1N KOH/100 mM Tris. To rule out lactate production by glutaminolysis, cells were also incubated with 2-deoxyglucose (2-DG, 10 mM) (Sigma-Aldrich, MO, USA) (22). Lactate was determined by a standard method with lactate dehydrogenase (Roche, Mannheim, Germany) following the NADH formation at 340 nm (23).

For OxPhos flux, cells (2-5 mg protein/mL) were incubated at 37°C in an air saturated RK medium plus 5 mM glucose. To distinguish between the oxygen consumption by mitochondria (i.e., net OxPhos flux) (22, 24) and non-mitochondrial sources (25, 26), cells were incubated with 5 µM oligomycin (Sigma-Aldrich, MO, USA), a potent, specific, and permeable inhibitor of the mitochondrial ATP synthase (ATPS). The net OxPhos rate was determined by using a Clark type electrode, as previously described (27) and by using a high-resolution respirometer (Oroboros Instruments, Innsbruck, Austria) (22) at 37°C. The contribution of OxPhos and glycolysis to the cellular ATP supply was determined, respectively, from the net OxPhos rate multiplied by the ATP/O or P»/O_2 ratio that corresponds to 2.5 (28) or 5 (22, 24), and from the rate of lactate production, assuming a stoichiometry of 1 mol of ATP produced per 1 mol of lactate produced (22).

Cell migration and invasiveness

For cell migration, mature MCF-7 spheroids were disaggregated as described in the previous section. Afterwards, cells were grown in complete DMEM medium in petri dishes (5×10^6 cells/well) at 37°C and 95% air/5% CO_2. After reaching 80-90% confluence, cell culture was wounded by using a plastic tip (wound healing assay). Then, culture was washed twice with 37°C PBS (155 mM NaCl, 1.5 mM KH_2PO_4, 2.7 mM NaH_2PO4, pH 7.2) and further incubated with fresh non-serum DMEM. Images of the cellular migration were taken at 0 and 24 h with an inverted microscope (Zeiss, Thornwood, NY, USA). For each experiment, the cellular migration distance from the border to the center of the petri dish was measured with a graduated reticule (Zeiss, Thornwood, NY, USA) (18).

For invasiveness assays, cells from disaggregated MCTS were incubated in free-serum DMEM for 24 h at 37°C and 95% air/5% CO_2. Afterwards, the cells were washed, re-suspended in free-serum DMEM medium, and placed in the upper compartment of 96-multiwell Boyden chambers (Merck Millipore, MA, USA) at a final concentration of 5×104 cells/well; the Boyden chamber lower compartment was filled with free-serum DMEM. Then, the Boyden chamber was incubated at 37°C and 95% air/5% CO_2 for 24 h. To detect invasive cells in the lower chamber compartment, cells were incubated with 60 nM calcein-AM for 1 h at 37°C and calcein-fluorescence was detected at 485 nm

excitation and 520 nm emission by using a microplate reader (Nunclon, Roskilde, Denmark) (18).

Determination of drug IC$_{50}$ (concentration required to reach 50% inhibition) values in MCF-7 MCTS

For evaluation of drug effect on MCTS growth, MCF-7 (1×10^5 cells/mL) were seeded in 2% (w/v) agarose-coated culture dishes in 5 mL DMEM. After 5 days, old medium was replaced with fresh DMEM in the presence of E2 (0, 10 and 100 nM) and either canonical anti-cancer (DOXO, doxorubicin), anti-glycolytic (IOA, iodoacetate) or anti-mitochondrial (CXB, celecoxib) drugs at 1, 10, 100, 250 and 500 nM concentrations (29). Afterwards, MCTS were placed under slow orbital shaking (20-50 rpm) at 37°C and 95% air/5% CO_2. The MCTS growth in the presence of each inhibitor was determined at different culture days by measuring diameters using a calibrated reticule (1/10 mm) in an inverted phase contrast microscope (Zeiss, Thornwood, NY) (14). The IC$_{50}$ inhibitor value for MCTS growth was determined at day 23 of culture corresponding to the time in which the MCTS maximal size was reached.

Data analysis

Experiments were performed with at least three independent cell preparations (n) (30). The data shown represent mean ± standard deviation (S.D.). Student's *t* test and ANOVA/*post hoc* Scheffe (31, 32) analyses with P values < 0.05 or lower were used to determine statistical significance.

Results

The results presented in this study were performed in the human ER+-breast MCF-7, the most common cancer cell line used as experimental model of ER-positive breast cancer, because these cells closely resemble several characteristics (*i.e.*, cellular phenotype, *in vivo* morphology, drug-resistance) found in patients with ER-positive breast tumors (33, 34).

Effect of 17β- estradiol (E2) on MCF-7 MCTS growth

Human ER+-breast MCF-7 MCTS reached a maximal spheroid diameter of 580 ± 20 nm at day 23 of culture (Figure 1) as it was previously reported (35). The presence of E2 at physiological concentrations of 10 and 100 nM (34) increased MCTS diameter
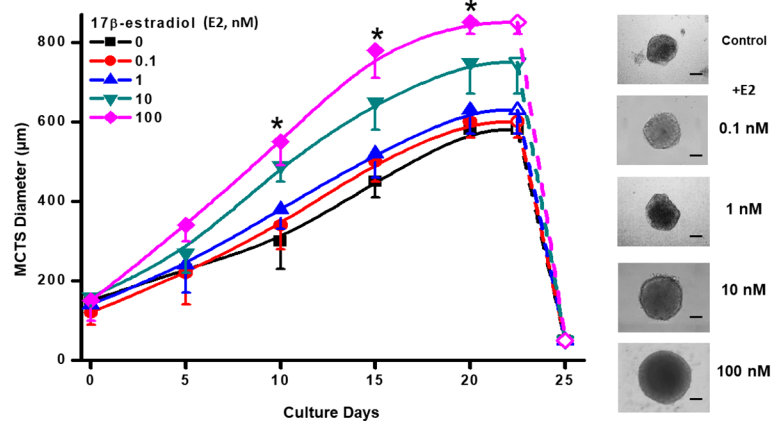
FIGURE 1
Effect of E2 on MCF-7 MCTS growth. The right panel shows contrast phase microscope images taken at day 20, which display the typical different MCTS sizes in the presence of exogenous E2. Scale Bar= 200 µm. Data shown represent the mean ± S.D. of at least 3 different independent preparations, n=30-40 spheroids. *P <0.05 vs. 10 and 100 nM of E2. E2, 17β-estradiol.

by 29% (750 ± 80, n= 30 spheroids) and 46% (850 ± 50, n= 30 spheroids), respectively at day 23 (Figure 1). Non-physiological and lower E2 concentrations (0.1 or 1 nM) were not able to promote MCTS growth throughout the culture time assessed (Figure 1). Morphology and maximal diameter of MCF-7 MCTS treated with 10 or 100 nM E2 was like that reported for other large-size tumor spheroids (14). After day 23 of culture, MCF-7 MCTS become unstable and spontaneously disaggregate (19). Although E2 stimulated MCTS growth, it was not able to prevent spontaneous and fast MCTS disaggregation after day 24 of culture (Figure 1). Because MCF-7 MCTS growth was stimulated with 10 and 100 nM

E2, subsequent experimentation was conducted by using these hormone concentrations.

Estrogen receptors (ER) and ER-target protein levels in MCF-7 MCTS exposed to 17β-estradiol

MCF-7 MCTS incubation with 10 or 100 nM E2 promoted a significant increment in the level of E2 receptors ERα (1.6-2.4 times) and ERβ (3.1-4.5 times) vs. non-hormone incubated MCTS (Figure 2). Change in ERα and ERβ contents correlated
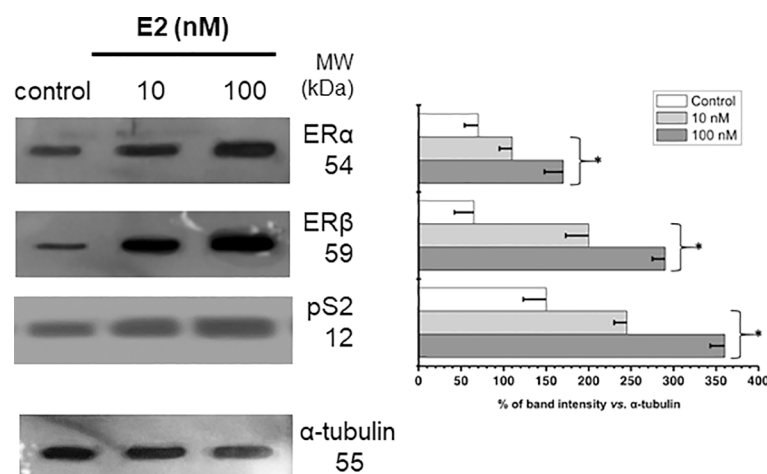

FIGURE 2
Effect of E2 on the contents of ERs and PS2 in MCF-7 MCTS. Histograms represent a double normalization against α-tubulin. Data shown represent the mean ± S.D. of at least three different preparations. * P <0.05 vs. control (non-treated cells).

with an elevation by 60-140% in the well-known E2-target pS2, a polypeptide with growth factor presumed function (3, 36, 37), supporting functional status for both α and β E2 receptors (Figure 2).

Energy associated-transcription factors and energy metabolism proteins levels in MCF-7 MCTS exposed to 17β-estradiol (E2)

The increased ERα and ERβ levels induced by E2 correlated with significant increments in the glycolytic transcriptional modulators HIF1-α (3.4-5.7 times) and c-MYC (1.4-2 times) vs. non-hormone treated MCTS (Figure 3A). Because of the elevated

HIF1-α and c-MYC levels, their glycolytic targets GLUT-1, GLUT-3, HK-I, and HK-II were also increased by 1.8-3.4 times vs. non-treated cells (Figure 3A). The levels of other glycolytic proteins like PFK-1, PYK and LDH-A remained without change.

The mitochondrial biogenesis-associated transcription regulator PGC1-α level was also increased 1.4-1.8 times by E2 (Figure 3B). No effect was observed on the level of PPAR-γ, which is involved in fatty acid storage and glucose metabolism (38). In addition, E2 increased the level of some respiratory chain proteins like ND1 (complex I) and COX-IV (complex IV) by 1.4-3.6 times vs. non-treated MCTS. Increments in PDH (1.4 times) and GA (2.1 times) levels were observed at E2 100 nM. Hormone did not affect the content of 2-OGDH, ATPS or ANT, but promoted a significant diminution (40%) in the Krebs cycle IDH3G level (Figure 3B).
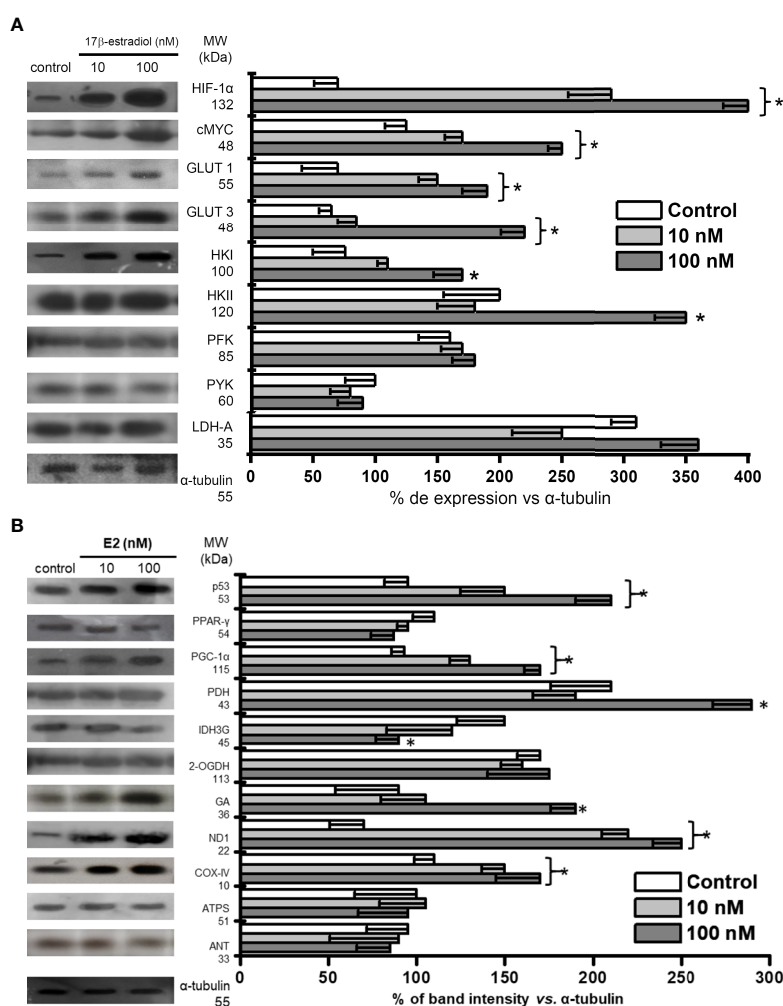
FIGURE 3
Effect of E2 on the contents of (A) transcription regulators and protein contents involved in glycolysis pathway; (B) transcription regulators and protein contents involved in OxPhos pathway of MCF-7 MCTS. Histograms represent a double normalization against α-tubulin. Data shown represent the mean ± S.D. of at least three different preparations. * P <0.05 vs. control (non-treated cells). The numerical values on the left y-axis indicate the respective molecular weights.

Effect of 17β- estradiol (E2) on MCF-7 MCTS energy metabolism fluxes

Both glycolysis (61-156%) and OxPhos (48-83%) fluxes were stimulated by 10 and 100 nM E2 (Figure 4A) correlating with a rise of several mitochondrial and glycolytic protein levels (Figures 3A, B). Glutamine oxidation (i.e., glutaminolysis) also increased by 60% further supporting E2-induced OxPhos up-regulation.

In the absence of E2, MCF-7 MCTS showed OxPhos as the predominant ATP supplier. Although both energy pathways were stimulated by E2 (Figure 4A), OxPhos remained as the principal energy provider (>75%) to sustain cancer cell processes (Figure 4B) (18).

Effect of 17β-estradiol (E2) on MCF7 MCTS cancer EMT, migration and invasiveness

Tridimensional architecture of MCTS favors the development of metastatic phenotype (21, 35). Thus, epithelial mesenchymal transition (EMT) marker proteins (SNAIL, fibronectin, E-cadherin, MMP-1, MMP-9 and vimentin) as well as cancer cell migration and invasiveness processes were analyzed in the presence of E2.

The stimulation of both metastatic processes (migration and invasiveness) by E2 correlated with a significant increase in several proteins related with (i) epithelial-mesenchymal transition (EMT) like SNAIL (7-10 times) and VEGF (2.7-4 times); (ii) extracellular matrix degradation proteins like MMP-1 (8-16%) and MMP-9 (34-60%); and (iii) motility associated proteins like vimentin (30-40%) and fibronectin (24-40%) (Figure 5A). In addition, the cell adhesion protein E-cadherin decreased by 19-45% (Figure 5A).

The cells from disaggregated MCF-7 MCTS maintained a high migratory capacity vs. their parental MCF-7 monolayer cells (Figure 5B). E2 (10 and 100 nM) increased cell migration by 30 and 78%, respectively (Figure 5B).

Other ATP-dependent process like cellular invasion was also analyzed in the presence of E2 (Figure 5C). The well-known highly invasive breast cancer MDA-MB-231 cell line was used as reference control to assess the relative invasiveness capacities of MCF-7 MCTS cells exposed to E2. As expected, bi-dimensional MCF-7 cells showed negligible invasiveness capacity (<10% vs. MDA-MB-231) confirming their low metastatic phenotype (39) (Figure 5C). In contrast, MCF-7 cells derived from disaggregated MCF-7 MCTS developed invasion capacity (35), which was significantly stimulated (50-95%) by E2.

Dependence of cell invasion and migration on OxPhos ATP supply in 17β-estradiol (E2) stimulated MCF-7 MCTS

The stimulation of MCF-7 MCTS energy pathways by E2 (10 or 100 nM) prompted that the intracellular ATP supplied by OxPhos remaining at prominent level (Figure 4B). It has been suggested that several biological functions in cancer cells mostly depend on the ATP provided by energy metabolism pathways (40, 41); but this assumption has not been experimentally demonstrated as yet. Therefore, to establish the dependence of cancer cell invasion and migration on net OxPhos ATP supply (Figure 6) or net cellular (OxPhos + glycolysis) ATP supply (Figure S1), the ATP supply derived from OxPhos or from the sum of both energy pathways was plotted vs. cellular migration and invasiveness.

As the rate of ATP synthesis increases as result of E2-OxPhos pathway stimulation, a proportional increase in both
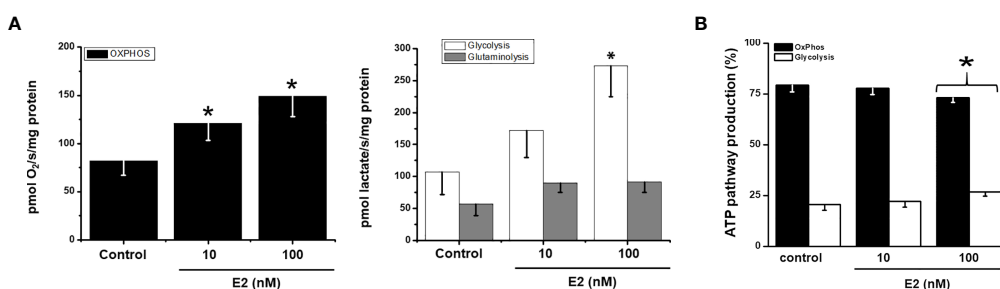
FIGURE 4
Effect of E2 on **(A)** energy metabolism fluxes and **(B)** ATP supply from glycolysis and OxPhos in MCF7 MCTS For OxPhos, flux represents the rate of oligomycin-sensitive oxygen consumption; for glycolysis, flux represents the rate of 2DG-sensitive lactate production; for glutaminolysis, flux represents the rate of 2DG-resistant lactate production. For ATP supply from OxPhos an ATP/O ratio of 2.5 (28), or P»/O2 ratio of 5 (22, 24), was used; for ATP supply from glycolysis it was assumed a stoichiometry of 1 mol of ATP produced per 1 mol of lactate formed. Data shown represent the mean ± S.D. of at least three different preparations. * P <0.05 vs. control (non-treated cells).

FIGURE 5
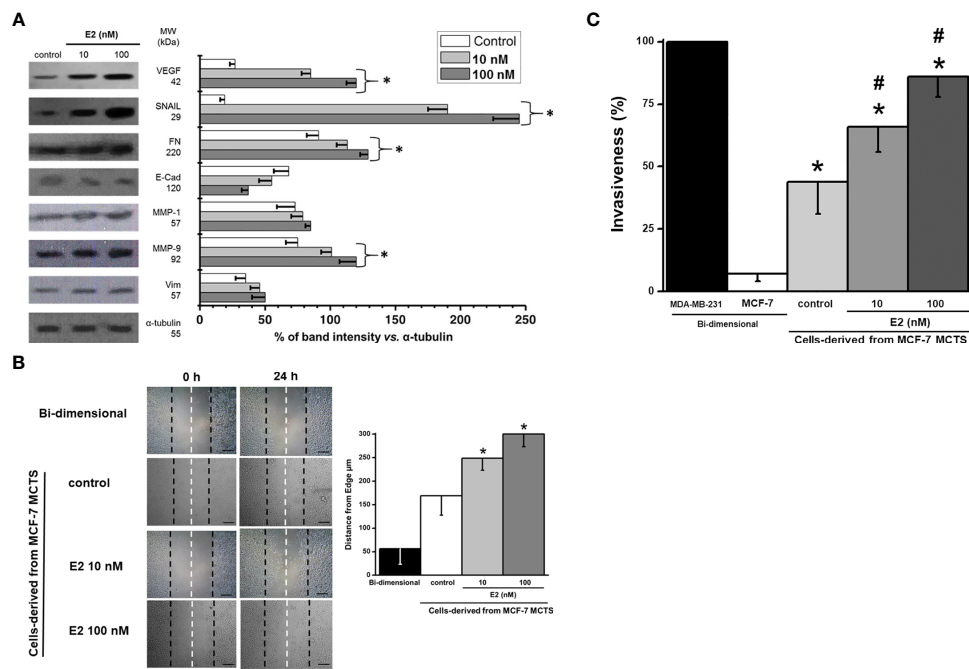Effect of E2 on **(A)** levels of EMT proteins of MCF-7 MCTS; **(B)** migration; and **(C)** invasion of cells derived from MCF-7 MCTS. For cell migration, contrast phase microscope images were taken at the beginning (t=0) and after 24 h E2 exposure, scale bar= 200 µm; right panel represents the distance traveled and calculated from the edge to the center of cell dish. Invasiveness was assessed by using multiwell Boyden chambers as it was indicated in the Material and Methods section. Data shown represent the mean $\pm$ S.D. of at least three different preparations. * P <0.05 vs. control (non-treated cells).

migration and invasiveness was observed, demonstrating a strict relationship between metastatic processes and the ATP supply derived from E2-stimulated OxPhos. Similar relationships were found when metastatic processes were plotted vs. total cytosolic + mitochondrial ATP supply. Under these conditions and applying metabolic control analysis (42, 43), the flux control coefficients were calculated from the initial slope of the plots shown in Figure 6, starting at the 100% reference control point,
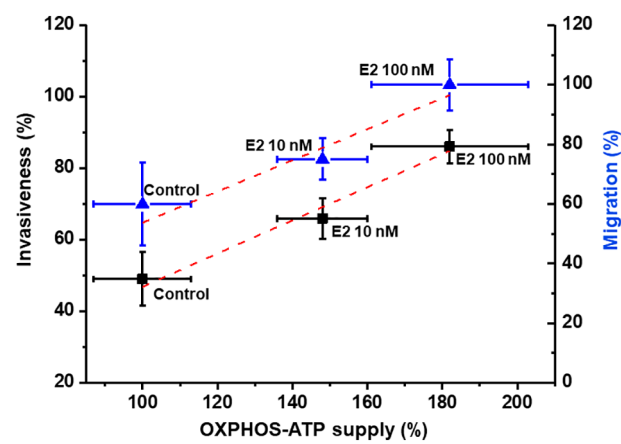
FIGURE 6
Dependence of invasion and migration on OxPhos ATP supply of cells derived from MCF-7 MCTS. Net OxPhos flux and metastasis processes were determined in the presence of E2 as described in the Material and Methods section. For cell invasion and migration, the 100 % value for net OxPhos flux without E2 was 408 $\pm$ 55 pmol O2/s/mg cell protein for cells derived from MCF-7 MCTS. For cell migration, the 100 % value was 290 $\pm$ 20 µm displacement for cells derived from MCF-7 MCTS after 24 h. Data represents the mean $\pm$ error standard of at least three different preparations.

which corresponds to non-added E2 (control condition). Thus, it was established that OxPhos pathway exerted high control of about 0.5 on both cancer cell migration and invasiveness after E2 treatment, i.e., the metastatic processes depended 50% on OxPhos (Figure 6). Total ATP supply (glycolysis + OxPhos) exerted a similar control on the metastasic processes (Figure S1).

Effect of OxPhos inhibition on growth and ATP dependent-processes in 17β-estradiol (E2) stimulated MCF-7 MCTS

OxPhos dependence of cellular migration and invasiveness were also analyzed in complete and intact MCF-7 MCTS. Celecoxib (CXB) is a repurposed NSAID, which displays strong inhibitory effect on OxPhos and growth of several metastatic cancer cell lines (29, 44). CXB at nanomolar doses decreased the growth of MCF-7 MCTS (IC50 = 5 nM); same CXB doses blocked the E2-stimulated OxPhos by 60% in cells derived from MCF-7 MCTS (data not shown). Likewise, CXB blocked E2-stimulated MCF-7 MCTS growth at low nanomolar concentrations (Table 1). CXB at IC50 concentrations for decreasing MCTS growth, potently inhibited both invasiveness

(46 ± 7.5%) and migration (41 ± 5%) (Figure 7). On the contrary, glycolytic inhibitors such as (iodoacetate) at concentrations at which glycolysis is inhibited by 65% or canonical anticancer drugs like doxorubicin required higher drug concentrations (50-500 nM) to slightly affect E2-stimulated MCF-7 MCTS growth and metastasis (Table 1; Figure 7).

Discussion

The substantial majority of studies showing the effect of E2 on cancer cell proliferation (45, 46), survival, angiogenesis (47), migration, invasion (48) or metastasis (17) have been performed in bi-dimensional cell cultures. Although bi-dimensional models have been helpful for understanding the biochemistry and physiology of cancer cells, such information has been difficult to translate into treatment and early detection or biomarker identification of actual tumors, because bi-dimensional cultures does not reflect the physiological behavior of tumor cells *in situ*. Therefore, the use of multicellular tumor spheroids (MCTS) emerges as a valuable tool for the identification of metabolic changes in solid tumors exposed to several factors (i.e., sexual hormones, chemotherapies). The different micro-regions found in

TABLE 1 IC$_{50}$ values (nM) of metabolic and canonical drugs for MCF-7 MCTS growth.

	Control	E2 (nM)	
		10	100
DOXO	38 ± 8	47 ± 10	72 ± 9
IOA	71 ± 9	178 ± 10	>500
CXB	5 ± 0.7	8 ± 0.6	10 ± 1

Drugs were added at the beginning of MCTS formation as it was indicated in the Material and Methods section. Data shown represent the mean ± S.D. of at least 3 different preparations; n=30-40 spheroids. Control, non E2 added. DOXO, doxorubicin; IOA, iodoacetate; CXB, celecoxib.
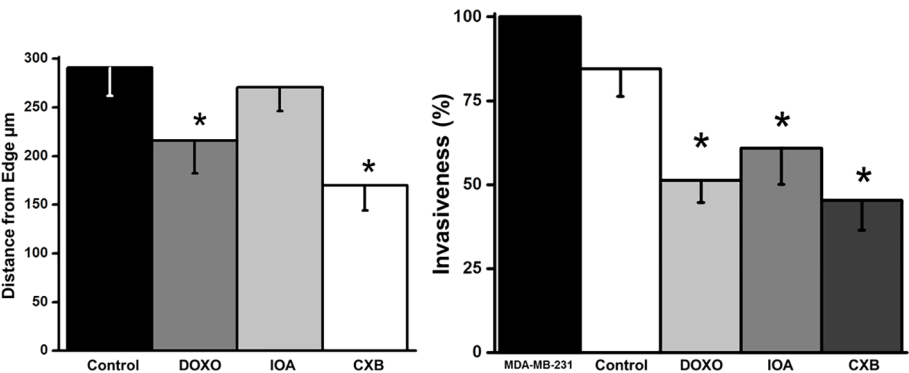

FIGURE 7
Effect of celecoxib (CXB), doxorubicin (DOXO) and iodoacetate (IOA) on migration and invasiveness of cells derived from MCF-7 MCTS. Drugs were added as it was indicated in the Material and Methods section at IC50 concentrations reported in Table 1. Data shown represent the mean ± S.D. of at least three different preparations. *P <0.05 vs. control (non-treated cells).

large, mature MCTS lead to the development of cells with different phenotypes, as occurs in solid tumors, located at different distances from the blood nourishing capillaries (49, 50). Thus, more closely realistic responses to E2 may be found in MCTS compared to bi-dimensional culture cells, which may allow envisioning better strategies for the treatment of Her2+-breast tumors.

17β-estradiol (E2) decreased the Erα/Erβ ratio in ER+ breast cancer MCTS

MCF-7 cells in tridimensional culture displayed high sensitivity to E2 for growth and ERα, ERβ and PS2 protein levels. Both ERs were increased by E2, with the levels of ERβ being higher than those of ERα. In this regard, there are some reports indicating that imbalance of these two estrogen receptors may lead to the occurrence of aggressive breast cancers. For example, it has been documented that ERβ downregulation prevents breast cancer cell migration through tyrosine kinase receptor [epidermal growth factor receptor (EGFR)/insulin-like growth factor-I receptor (IGF-IR)] and Janus kinase/signal transducer and activator of transcription (JAK/STAT) signaling pathways [reviewed by (51)].

17β-estradiol (E2) enhances ER+ breast MCTS growth

Physiological E2 concentrations stimulated by 29-46% the growth of MCF-7 MCTS. Similar effects of E2 have been observed in other studies using MELN (cells derived from MCF-7 cells) spheroids (52). E2 also stimulated MCF-7 cell proliferation in bi-dimensional cultures (46). The increase in cyclin D1 mRNA content via c-Jun/AF-2 signaling pathway (45); the suppression of p53/p21; and the up-regulation of PCNA and Ki-67 (46) are molecular mechanisms proposed to explain how estradiol may stimulate MCF-7 cell growth in bi-dimensional cultures. On the contrary, in non-cancer cells E2 blocks proliferation acting as a potent suppressor of Janus kinase pathway/cytokine signaling-2 protein involved in growth hormone activation (53); as well as inducing the release of E2-regulated autocrine growth factors, which antagonize and block the growth factor receptors [reviewed by (54)], thus limiting cellular proliferation.

Scarce information is available concerning E2 -dependent regulation of the cell cycle machinery in tridimensional models that resemble solid tumor physiology. Truchet et al. (52), showed in MELN (cells derived from MCF-7 cells) spheroids that E2 (1 nM, from 4 to 23 days incubation) induced a proliferation proteins gradient from MCTS periphery (higher content of Ki67- and cyclinD1- positive cells) to the center (low content of Ki67- and cyclin D1-positive cells), which may help explaining why E2 stimulates cell cycle in cancer spheroids. In the present study, the up regulation of energy metabolism pathways by E2 for ATP supply

was demonstrated and it is proposed as an essential molecular mechanism, which together with the well-known effect of E2 on cell cycle, modulates solid tumor growth.

17β-estradiol (E2) stimulates glycolytic metabolism in MCF-7 MCTS

The tridimensional arrangement of tumor spheroids leads to the development of several cell layers with important, marked metabolic differences (14). The inner center core of large spheroids becomes hypoxic and necrotic, promoting HIF-1α stabilization and glycolysis activation (c.f. Figure 3A) (14, 55). In MCTS, the level of HIF-1α was significantly increased (>3 times) by E2, as a consequence of estrogen-response elements in the HIF-1α gene (56); and direct interaction of ERα with HIF-1α (57).

Derived from HIF-1α stabilization, several HIF1α-induced glycolytic proteins are overexpressed (55) like the flux-controlling steps (58) GLUT-1, GLUT-3, HK-I and HK-II (c.f. Figure 3A) detected in E2-exposed MCF-7 MCTS vs. non-treated MCTS. Indeed, this last result correlates with some observations found in bi-dimensional culture cancer (hepatocellular carcinoma HepG2, MCF-7, T47D) cells incubated with E2 (1-100 nM). In these last models, E2 promotes (i) mRNA increase of glycolytic genes (GLUT-2, PFK-1) (10, 59); (ii) overexpression of glycolytic pathway genes through E2-induced PI3K/AKT activation (60); (iii) increased levels of the main PFK-1 co-activator Fru2,6BP (10); and (iv) increased activity of mitochondrial bound-HK (61).

Other observations showing up-regulation of glycolysis by estradiol include the stimulation of glucose uptake in bi-dimensional breast T47D and MCF-7, and cervix HeLa and SiHa cancer cells (10, 61, 62). E2 (10 and 100 nM) increased the glycolytic flux >45% in MCF-7 MCTS vs. non treated cells. This increment in glycolysis resembled the elevated lactate release to the extracellular milieu reported in MCF-7, T47D, HeLa and SiHa cells exposed to E2 (10 nM/24 h or 1 week) (61–63).

In a human biopsy study including 88 human breast Her2+ (luminal A and luminal B) cancer samples, it was found that the ERβ but not ERα isoform predominates in the stem cell phenotype. ERβ stimulation with diarylproprionitrile, its selective ligand, increased mammosphere growth as well as glycolytic metabolism, increasing the mRNA level of several genes related with glucose metabolism (HIF-1α, n-MYC, GLUT-1, PFK/FBP-4, glycogen branching enzyme GBE1), and glycolytic flux (64).

17β-estradiol (E2) stimulates OxPhos pathway in MCF-7 MCTS

The lipophilic property of E2 allows for passive diffusion into mitochondrial membranes from the external culture medium.

Moreover, E2 may be rapidly delivery into mitochondria *via* receptor-mediated endocytosis in hepatocarcinoma HepG2 cells (65).

In MCF-7 cells, a substantial fraction (approximately 20%) of total cellular ER is localized within the mitochondrial matrix (66). In addition, it has been documented that ERα and ERβ interactions with E2 improves mitochondrial function acting at different levels. These actions include (a) favoring a large and clear mitochondrial morphology (67); (b) activating transcription factors containing E2-response elements such as the Nuclear Respiratory Factor 1 (NRF1) (12) involved in the overexpression of mitochondrial metabolism (i.e. COX, ND1, SDH, bc-1complex, ATPS) enzymes (68), and biogenesis (12) genes, some of them correlating with elevated protein level (COX-IV) (12, 69); (c) activating TFAM, a NRF-1 target, which binds and promote mtDNA transcription of genes encoding for mitochondrial respiratory complex proteins (70).

Unfortunately, in all above-mentioned studies where E2 has shown an up-regulation effect on OxPhos, solely the transcript levels have been evaluated but proper mitochondrial functions have not been analyzed. This takes relevance because not always the transcript levels correlate with the related protein content and activity. Moreover, not often mRNA levels correlate with changes in metabolite intermediaries and pathway fluxes, or biological function, since robust regulation mechanisms are in place at the distinct levels of biological complexity (13).

Other studies have revealed contrasting results to those described above. For instance, Sastre-Serra et al. (71), found that E2 (1 nM, 48 h) diminished the TFAM and COX-IV levels and the activities of mitochondrial enzymes like CS, COX and ATP synthase in bi-dimensional culture MCF-7 cells. It was argued that low mitochondrial functionality of MCF-7 cells in the presence of E2 was linked to the presence of a high ERα/ERβ ratio (71). Hence, the tridimensional architecture of MCF-7 promoting a low ERα/ERβ ratio (c.f. Figure 2) could then favors mitochondrial metabolism.

In MCTS, the content of several mitochondrial proteins (COX-IV) significantly increased in the presence of E2 like reported for bi-dimensional MCF-7 cells (12, 69). However, the content of other OxPhos related proteins in 2-D cultured cancer cells, except for the study by Sastre-Serra et al. (71), has not been analyzed, and thus for comparative purposes, information is not available. In non-cancer cells (rat liver, brain, heart), E2 clearly promotes significant lowering in the content of OxPhos proteins (complex I, II, III, IV, and ATPS) (72, 73). Regarding OxPhos pathway flux, scarce (bi-dimensional cultures) or null (spheroids/mammospheres) information about E2 effects is available for Her2+ breast cancer cells. Radde et al. (74), observed negligible activation (less 5%) in the ATP-linked oxygen consumption of MCF-7 cells exposed to E2 (24 h, 1 nM, 10 nM). However, under serum starvation, the ATP-linked oxygen consumption and the maximal respiratory capacity of MCF-7 cells was stimulated (40-70%) by E2.

This last observation concurred with the strong OxPhos stimulation by E2 observed in MCF-7 MCTS (c.f. Figure 3A), further suggesting that serum components with limited availability due to the tridimensional architecture of spheroids were also involved in the OxPhos activation by E2. In addition, it is noted that data from bi-dimensional ER+ cancer cells [10, 59-63, 67-70], including results from the present study, support the conclusion that estradiol also potently promotes glycolytic and OxPhos activation in 3D-rearregment cancer cell models.

17β-estradiol (E2) enhances metastatic phenotype in MCF-7 MCTS

The epithelial–mesenchymal transition (EMT) promotes stationary cancer cells to migrate and invade. Indeed, E2 induced that MCF-7 MCTS-derived cells overexpressed several EMT proteins like SNAIL, FN, MMP-9 and Vim and decreased E-cadherin level (c.f. Figure 5A). In these cells, E2 (5 nM/72h) also induced loss of epithelial cell polarity, separation into individual cells, subsequent dispersion after the acquisition of cell motility, and loss of E-cadherin, indicating the development of mesenchymal cell-like characteristics. Tamoxifen prevented EMT process (75), suggesting that the E2/ER axis is involved in EMT activation.

MCF-7 MCTS showed an increased migration and invasiveness capacity induced by E2 (c.f. Figures 5B, C). Similarly, several studies in bi-dimensional breast and glioma cancer cells show that E2 (1-100 nM/24 h) stimulates cell migration. This is accomplished by inducing (i) the activation of signaling proteins (c-Src, FAK, paxillin, ERK and protein kinase B phosphorylation) related with cell migration (76); (ii) binding to a G protein coupled to ER (GPR30); this GPR30/E2 complex triggers a protein kinase (PRKACB) to phosphorylate and inactivate the aquaporin AQP2, which is involved in cancer cell migration (77). On the other hand, the strong HIF-1α stabilization observed in E2-stimulated MCF-7 MCTS may up-regulate angiogenic and migratory target genes such as that encoding for VEGF (57).

Furthermore, E2 (10-100 nM) in MCF-7 bi-dimensional cultures promotes cell-cell adhesion (78) and favors tumor formation in nude mouse (79, 80). This last result seems in consonance with our observation that E2 promotes spheroids formation (c.f. Figure 1). However, there are not reports indicating that cancer cells derived from spheroids develop mechanisms to increase their ability to invade. E2 enhances the phosphorylation and activation of ezrin, a protein related with the activation of PI3K/Akt/ROCK-2 signaling cascade, which promotes horizontal T47-D cell migration and invasion in three-dimensional matrices (81).

OxPhos inhibition for blocking 17β-estradiol-dependent aggressive tumors

The present study demonstrates for the first time that estradiol preserves that MCF-7 MCTS be predominantly oxidative. Both energy metabolism pathway fluxes in MCF-7 MCTS were rigorously assessed by correcting lactate production (glycolysis, 2DG-sensitive lactate production) derived from glutaminolysis, as well as total cellular oxygen consumption (OxPhos, oligomycin-sensitive respiration) derived from extramitochondrial sources and passive H+ leak across the inner mitochondrial membrane (22). Although in other studies, glycolysis and/or oxygen consumption fluxes were analyzed in the presence of E2, the contribution to ATP supply from each energy pathway was not determined.

Metabolic therapy targeting cancer mitochondria can be a promising alternative treatment. Our results (c.f. Figure 4B) clearly indicated that the principal ATP supplier in cancer cells was OxPhos pathway. In addition, cellular migration and invasiveness depended on ATP-derived from OxPhos with flux control coefficients of about 0.5, but not on glycolysis (c.f. Figures 6, S1) (18). Thus, both metastatic processes were further titrated with the alternative OxPhos inhibitor celecoxib (CXB), a repurposed NSAID, and its effect was compared with the glycolytic inhibitor iodoacetate, and with doxorubicin, a canonical anti-cancer drug. Up to 10 μM CXB has several targets including cyclooxygenase-2 inhibition (82); and apoptosis activation (83). Recently, it was demonstrated that at low doses CXB blocked OxPhos flux affecting mitochondrial membrane potential (18, 44) and consequently, cancer cell growth was severely impaired (44). For doxorubicin and iodoacetate, high doses were required to affect MCTS growth. Therefore, CXB may be considered as a suitable and promising therapeutic drug for the inhibition of estradiol dependent cancer growth.

Conclusion

The data of the present study show for the first time that E2 promotes marked increase in growth, energy metabolism and metastatic processes of MCTS. The data also showed a strong dependence of metastatic processes (i.e., invasiveness and migration) on the ATP derived from OxPhos. Therefore, the application of cancer chemotherapies based on OxPhos targeting by using repurposed drugs like celecoxib may help in the clinical setting against hormone-dependent tumors. The present results provide support for modifying and perhaps improving clinical strategies by using re-purposed drugs such as NSAIDs as adjuvant therapy. For cervical cancer cells, CXB has showed significant efficacy in combination with canonical chemotherapy drugs such as cisplatin, paclitaxel or doxorubicin (29). These drug combinations might be useful for the specific treatment of estradiol-dependent cancers.

Data availability statement

The raw data supporting the conclusions of this article will be made available by the authors, without undue reservation.

Author contributions

SR-E, SP-V: study conception and supervision, experimental design, manuscript writing, manuscript proofreading, manuscript revision. SP-V, IO-M, JV-N, JP-F, DR-C, GT-M, JG-R: methodology, data acquisition. SP-V, RM-S, SR-E: data analysis. SP-V, statistical analysis. IP-C, JA-P, RM-S, SR-E: manuscript proofreading and revision. All authors contributed to the article and approved the submitted version.

Funding

Conflict of interest

The authors declare that the research was conducted in the absence of any commercial or financial relationships that could be construed as a potential conflict of interest.

Publisher's note

All claims expressed in this article are solely those of the authors and do not necessarily represent those of their affiliated organizations, or those of the publisher, the editors and the reviewers. Any product that may be evaluated in this article, or claim that may be made by its manufacturer, is not guaranteed or endorsed by the publisher.

Supplementary material

The Supplementary Material for this article can be found online at: https://www.frontiersin.org/articles/10.3389/fonc.2022.1018137/full#supplementary-material

References

1. Howlader NR, Rahman MM, Hossain MA, Sultana R, Hossain SM, Mazid MA, et al. Genetic polymorphisms in DNA repair genes XRCC1 and 3 are associated with increased risk of breast cancer in Bangladeshi population. *Breast Cancer Res Treat* (2020) 182(3):739–50. doi: 10.1007/s10549-020-05738-8

2. Lari SA, Kuerer HM. Biological markers in DCIS and risk of breast recurrence: A systematic review. *J Cancer* (2011) 2:232–6. doi: 10.7150/jca.2.232

3. Yaşar P, Ayaz G, User SD, Güpür G, Muyan M. Molecular mechanism of estrogen-estrogen receptor signaling. *Reprod Med Biol* (2016) 16(1):4–20. doi: 10.1002/rmb2.12006

4. Zhu BT, Han GZ, Shim JY, Wen Y, Jiang XR. Quantitative structure-activity relationship of various endogenous estrogen metabolites for human estrogen receptor alpha and beta subtypes: Insights into the structural determinants favoring a differential subtype binding. *Endocrinology* (2006) 147(9):4132–50. doi: 10.1210/en.2006-0113

5. Ciocca DR, Fanelli MA. Estrogen receptors and cell proliferation in breast cancer. *Trends Endocrinol Metab* (1997) 8(8):313–21. doi: 10.1016/s1043-2760(97)00122-7

6. Elkin M, Orgel A, Kleinman HK. An angiogenic switch in breast cancer involves estrogen and soluble vascular endothelial growth factor receptor 1. *J Natl Cancer Inst* (2004) 96(11):875–78. doi: 10.1093/jnci/djh140

7. Higgins KJ, Liu S, Abdelrahim M, Yoon K, Vanderlaag K, Porter W, et al. Vascular endothelial growth factor receptor-2 expression is induced by 17beta-estradiol in ZR-75 breast cancer cells by estrogen receptor alpha/Sp proteins. *Endocrinology* (2006) 147(7):3285–95. doi: 10.1210/en.2006-0081

8. Wang F, Vihma V, Badeau M, Savolainen-Peltonen H, Leidenius M, Mikkola T, et al. Fatty acyl esterification and deesterification of 17β-estradiol in human breast subcutaneous adipose tissue. *J Clin Endocrinol Metab* (2012) 97(9):3349–56. doi: 10.1210/jc.2012-1762

9. Belkaid A, Duguay SR, Ouellette RJ, Surette ME. 17β-estradiol induces stearoyl-CoA desaturase-1 expression in estrogen receptor-positive breast cancer cells. *BMC Cancer* (2015) 15:440. doi: 10.1186/s12885-015-1452-1

10. Imbert-Fernandez Y, Clem BF, O'Neal J, Kerr DA, Spaulding R, Lanceta L, et al. Estradiol stimulates glucose metabolism *via* 6-phosphofructo-2-kinase (PFKFB3). *J Biol Chem* (2014) 289(13):9440–48. doi: 10.1074/jbc.M113.529990

11. Liao TL, Tzeng CR, Yu CL, Wang YP, Kao SH. Estrogen receptor-β in mitochondria: implications for mitochondrial bioenergetics and tumorigenesis. *Ann N Y Acad Sci* (2015) 1350:52–60. doi: 10.1111/nyas.12872

12. Mattingly KA, Ivanova MM, Riggs KA, Wickramasinghe NS, Barch MJ, Klinge CM. Estradiol stimulates transcription of nuclear respiratory factor-1 and increases mitochondrial biogenesis. *Mol Endocrinol* (2008) 22(3):609–22. doi: 10.1210/me.2007-0029

13. Moreno-Sánchez R, Saavedra E, Gallardo-Pérez JC, Rumjanek FD, Rodríguez-Enríquez S. Understanding the cancer cell phenotype beyond the limitations of current omics analyses. *FEBS J* (2016) 283:54–73. doi: 10.1111/febs.13535

14. Rodríguez-Enríquez S, Gallardo-Pérez JC, Avilés-Salas A, Marín-Hernández A, Carreño-Fuentes L, Maldonado-Lagunas V, et al. Energy metabolism transition in multi-cellular human tumor spheroids. *J Cell Physiol* (2008) 216(1):189–97. doi: 10.1002/jcp.21392

15. Fisher B, Costantino JP, Wickerham DL, Redmond CK, Kavanah M, Cronin WM, et al. Tamoxifen for prevention of breast cancer: report of the national surgical adjuvant breast and bowel project p-1 study. *J Natl Cancer Inst* (1998) 90 (18):1371–88. doi: 10.1093/jnci/90.18.1371

16. Cluze C, Rey D, Huiart L, BenDiane MK, Bouhnik AD, Berenger C, et al. Adjuvant endocrine therapy with tamoxifen in young women with breast cancer: determinants of interruptions vary over time. *Ann Oncol* (2012) 23(4):882–90. doi: 10.1093/annonc/mdr330

17. Yang X, Belosay A, Du M, Fan TM, Turner RT, Iwaniec UT, et al. Estradiol increases ER-negative breast cancer metastasis in an experimental model. *Clin Exp Metastasis* (2013) 30(6):711–21. doi: 10.1007/s10585-012-9559-0

18. Pacheco-Velázquez SC, Robledo-Cadena DX, Hernández-Reséndiz I, Gallardo-Pérez JC, Moreno-Sánchez R, Rodríguez-Enríquez S. Energy metabolism drugs block triple negative breast metastatic cancer cell phenotype. *Mol Pharm* (2018) 15(6):2151–64. doi: 10.1021/acs.molpharmaceut.8b00015

19. Mandujano-Tinoco EA, Gallardo-Pérez JC, Marín-Hernández A, Moreno-Sánchez R, Rodríguez-Enríquez S. Anti-mitochondrial therapy in human breast cancer multi-cellular spheroids. *Biochim Biophys Acta* (2013) 1833(3):541–51. doi: 10.1016/j.bbamcr.2012.11.013

20. Lowry OH, Rosebrough NJ, Farr AL, Randall RJ. Protein measurement with the folin phenol reagent. *J Biol Chem* (1951) 193(1):265–75. doi: 10.1016/S0021-9258(19)52451-6

21. Gallardo-Pérez JC, Adán-Ladrón de Guevara A, Marín-Hernández A, Moreno-Sánchez R, Rodríguez-Enríquez S. HPI/AMF inhibition halts the development of the aggressive phenotype of breast cancer stem cells. *Biochim Biophys Acta Mol Cell Res* (2017) 1864(10):1679–90. doi: 10.1016/j.bbamcr.2017.06.015

22. Moreno-Sánchez R, Robledo-Cadena DX, Pacheco-Velazquez SC, Rodríguez-Enríquez S. *Estimation of energy pathway fluxes in cancer cells-beyond the warburg effect.* (2022).

23. Vanderlinde RE. Measurement of total lactate dehydrogenase activity. *Ann Clin Lab Sci* (1985) 15(1):13–31.

24. Gnaiger E. Mitochondrial pathways and respiratory control. an introduction to OXPHOS analysis. *Bioenerg Commun* (2020) 2:1–145. doi: 10.26124/bec:2020-0002

25. Murphy BJ, Laderoute KR, Vreman HJ, Grant TD, Gill NS, Stevenson DK, et al. Enhancement of heme oxygenase expression and activity in A431 squamous carcinoma multicellular tumor spheroids. *Cancer Res* (1993) 53(12):2700–3.

26. Wu FJ, Friend JR, Remmel RP, Cerra FB, Hu WS. Enhanced cytochrome P450 IA1 activity of self-assembled rat hepatocyte spheroids. *Cell Transplant* (1999) 8(3):233–46. doi: 10.1177/096368979900800304

27. Rodríguez-Enríquez S, Torres-Márquez ME, Moreno-Sánchez R. Substrate oxidation and ATP supply in AS-30D hepatoma cells. *Arch Biochem Biophys* (2000) 375(1):21–30. doi: 10.1006/abbi.1999.1582

28. Nakashima RA, Paggi MG, Pedersen PL. Contributions of glycolysis and oxidative phosphorylation to adenosine 5'-triphosphate production in AS-30D hepatoma cells. *Cancer Res* (1984) 44(12 Pt 1):5702–6.

29. Robledo-Cadena DX, Gallardo-Pérez JC, Dávila-Borja V, Pacheco-Velázquez SC, Belmont-Díaz JA, Ralph SJ, et al. Non-steroidal anti-inflammatory drugs increase cisplatin, paclitaxel, and doxorubicin efficacy against human cervix cancer cells. *Pharm (Basel)* (2020) 13(12):463. doi: 10.3390/ph13120463

30. Rubinowitz H, Vogel S. The manual of scientific style: A guide for authors. *USA: Acad Press* (2008), 788 p. doi: 10.1016/B978-012373980-3.50027-7

31. Klockars AJ, Hancock GR. Scheffe's more powerful f-protected *Post hoc* procedure. *J Educ Behav Stat* (2000) 25:13–9. doi: 10.2307/1165310

32. Krzywinski M, Altman N. Points of significance: Analysis of variance and blocking. *Nat Methods* (2014) 11(7):699–700. doi: 10.1038/nmeth.3005

33. Comșa Ș, Cîmpean AM, Raica M. The story of MCF-7 breast cancer cell line: 40 years of experience in research. *Anticancer Res* (2015) 35(6):3147–54.

34. Sweeney EE, McDaniel RE, Maximov PY, Fan P, Jordan VC. Models and mechanisms of acquired antihormone resistance in breast cancer: Significant clinical progress despite limitations. *Horm Mol Biol Clin Investig* (2012) 9 (2):143–63. doi: 10.1515/hmbci-2011-0004

35. Gallardo-Pérez JC, Rivero-Segura NA, Marín-Hernández A, Moreno-Sánchez R, Rodríguez-Enríquez S. GPI/AMF inhibition blocks the development of the metastatic phenotype of mature multi-cellular tumor spheroids. *Biochim Biophys Acta* (2014) 1843(6):1043–53. doi: 10.1016/j.bbamcr.2014.01.013

36. Carmina E, Lobo RA. Evaluation of hormonal status. In: Strauss JF, Barbieri RL, editors. *Yen & jaffe´s reproductive endocrinology*. Philadelphia: W.B: Saunders (2009). p. 801–23.

37. Nunez AM, Jakowlev S, Briand JP, Gaire M, Krust A, Rio MC, et al. Characterization of the estrogen induced pS2 protein secreted by the human breast cancer cell line MCF-7. *Endocrinology* (1987) 121(5):1759–65. doi: 10.1210/endo-121-5-1759

38. Ahmadian M, Suh JM, Hah N, Liddle C, Atkins AR, Downes M, et al. PPARγ signaling and metabolism: the good, the bad and the future. *Nat Med* (2013) 19(5):557–66. doi: 10.1038/nm.3159

39. Espinoza-Sánchez NA, Vadillo E, Balandrán JC, Monroy-García A, Pelayo R, Fuentes-Pananá EM. Evidence of lateral transmission of aggressive features between different types of breast cancer cells. *Int J Oncol* (2017) 51(5):1482–96. doi: 10.3892/ijo.2017.4128

40. Vander-Heiden MG, Cantley LC, Thompson CB. Understanding the warburg effect: The metabolic requirements of cell proliferation. *Science* (2009) 324:1029–33. doi: 10.1126/science.1160809

41. Shahruzaman SH, Fakurazi F, Maniam S. Targeting energy metabolism to eliminate cancer cells. *Cancer Manag Res* (2018) 10:2325–35. doi: 10.2147/CMAR.S167424

42. Fell D. Understanding the control of metabolism. *London: Plenum Press* (1997) 1–301.

43. Moreno-Sánchez R, Saavedra E, Rodríguez-Enríquez S, Olín-Sandoval V. Metabolic control analysis: a tool for designing strategies to manipulate metabolic pathways. *J BioMed Biotechnol* (2008) 2008:597913. doi: 10.1155/2008/597913

44. Pritchard R, Rodríguez-Enríquez S, Pacheco-Velázquez SC, Bortnik V, Moreno-Sánchez R, Ralph S. Celecoxib inhibits mitochondrial O2 consumption, promoting ROS dependent death of murine and human metastatic cancer cells *via* the apoptotic signalling pathway. *Biochem Pharmacol* (2018) 154:318–34. doi: 10.1016/j.bcp.2018.05.013

45. Sabbah M, Courilleau D, Mester J, Redeuilh G. Estrogen induction of the cyclin D1 promoter: involvement of a cAMP response-like element. *Proc Natl Acad Sci USA* (1999) 96(20):11217–22. doi: 10.1073/pnas.96.20.11217

46. Liao XH, Lu DL, Wang N, Liu LY, Wang Y, Li YQ, et al. Estrogen receptor α mediates proliferation of breast cancer MCF-7 cells *via* a p21/PCNA/E2F1-dependent pathway. *FEBS J* (2014) 281(3):927–42. doi: 10.1111/febs.12658

47. Zhuo Y, Li X, Zheng Q, Fan X, Ma W, Chen J, et al. Estrogen enhances tumor growth and angiogenesis indirectly *via* mediation of bone marrow derived cells as well as directly through stimulation of tumor and endothelial cells. *Oncol Rep* (2018) 40(4):2147–56. doi: 10.3892/or.2018.6631

48. Sun Q, Liang Y, Zhang T, Wang K, Yang X. ER-α36 mediates estrogen-stimulated MAPK/ERK activation and regulates migration, invasion, proliferation in cervical cancer cells. *Biochem Biophys Res Commun* (2017) 487(3):625–32. doi: 10.1016/j.bbrc.2017.04.105

49. Sutherland RM. Cell and environment interactions in tumor microregions: the multicell spheroid model. *Science* (1988) 240(4849):177–84. doi: 10.1126/science.2451290

50. Kunz-Schughart LA, Freyer JP, Hofstaedter F, Ebner R. The use of 3-d cultures for high-throughput screening: the multicellular spheroid model. *J Biomol Screen* (2004) 9(4):273–85. doi: 10.1177/1087057104265040

51. Zhou Y, Liu X. The role of estrogen receptor beta in breast cancer. *biomark Res* (2020) 8:39. doi: 10.1186/s40364-020-00223-2

52. Truchet I, Jozan S, Baron S, Frongia C, Balaguer P, Richard-Foy H, et al. Estrogen and antiestrogen-dependent regulation of breast cancer cell proliferation in multicellular spheroids: Influence of cell microenvironment. *Int J Oncol* (2008) 32(5):1033–39. doi: 10.3892/ijo.32.5.1033

53. Leung KC, Johannsson G, Leong GM, Ho KKY. Estrogen regulation of growth hormone action. *Endocr Rev* (2004) 25(5):693–721. doi: 10.1210/er.2003-0035

54. Philips A, Chalbos D, Rochefort H. Estradiol increases and anti-estrogens antagonize the growth factor-induced activator protein-1 activity in MCF7 breast cancer cells without affecting c-fos and c-jun synthesis. *J Biol Chem* (1993) 268 (19):14103–8. doi: 10.1016/S0021-9258(19)85214-6

55. Robey IF, Lien AD, Welsh SJ, Baggett BK, Gillies RJ. Hypoxia-inducible factor-1alpha and the glycolytic phenotype in tumors. *Neoplasia* (2005) 7(4):324–30. doi: 10.1593/neo.04430

56. Yang J, AlTahan A, Jones DT, Buffa FM, Bridges E, Interiano RB, et al. Estrogen receptor-α directly regulates the hypoxia-inducible factor 1 pathway associated with antiestrogen response in breast cancer. *Proc Natl Acad Sci USA* (2015) 112(49):15172–7. doi: 10.1073/pnas.1422015112

57. Semenza GL. Defining the role of hypoxia-inducible factor 1 in cancer biology and therapeutics. *Oncogene* (2010) 29(5):625–34. doi: 10.1038/onc.2009.441

58. Marín-Hernández A, Rodríguez-Enríquez S, Vital-González PA, Flores-Rodríguez FL, Macías-Silva M, Sosa-Garrocho M, et al. Determining and understanding the control of glycolysis in fast-growth tumor cells. flux control by an over-expressed but strongly product-inhibited hexokinase. *FEBS J* (2006) 273 (9):1975–88. doi: 10.1111/j.1742-4658.2006.05214.x

59. Shen M, Xu M, Zhong F, Crist MC, Prior AB, Yang K, et al. A multi-omics study revealing the metabolic effects of estrogen in liver cancer cells HepG2. *Cells* (2021) 10(2):455. doi: 10.3390/cells10020455

60. Elstrom RL, Bauer DE, Buzzai M, Karnauskas R, Harris MH, Plas DR, et al. AKT stimulates aerobic glycolysis in cancer cells. *Cancer Res* (2004) 64:3892–99. doi: 10.1158/0008-5472.CAN-03-2904

61. Ko BH, Paik JY, Jung KH, Lee KH. 17beta-estradiol augments 18F-FDG uptake and glycolysis of T47D breast cancer cells *via* membrane-initiated rapid PI3K-akt activation. *J Nucl Med* (2010) 51(11):1740–7. doi: 10.2967/jnumed.110.074708

62. Riera-Leal A, Ortiz-Lazareno PC, Jave-Suárez LF, Ramírez De Arellano A, Aguilar-Lemarroy A, Ortiz-García YM, et al. 17β estradiol induced mitochondrial dysfunction and warburg effect in cervical cancer cells allow cell survival under metabolic stress. *Int J Oncol* (2020) 56(1):33–46. doi: 10.3892/ijo.2019.4912

63. O'Mahony F, Razandi M, Pedram A, Harvey BJ, Levin ER. Estrogen modulates metabolic pathway adaptation to available glucose in breast cancer cells. *Mol Endocrinol* (2012) 26(12):2058–70. doi: 10.1210/me.2012-1191

64. Ma R, Karthik GM, Lövrot J, Haglund F, Rosin G, Katchy A, et al. Estrogen receptor β as a therapeutic target in breast cancer stem cells. *J Natl Cancer Inst* (2017) 109(3):1–14. doi: 10.1093/jnci/djw236

65. Moats RK, Ramirez VD. Electron microscopic visualization of membrane-mediated uptake and translocation of estrogen-BSA:colloidal gold by hep G2 cells. *J Endocrinol* (2000) 166:631–47. doi: 10.1677/joe.0.1660631

66. Chen JQ, Yager JD. Estrogen's effects on mitochondrial gene expression: Mechanisms and potential contributions to estrogen carcinogenesis. *Ann N Y Acad Sci* (2004) 1028:258–72. doi: 10.1196/annals.1322.030

67. Vic P, Vignon F, Derocq D, Rochefort H. Effect of estradiol on the ultrastructure of the MCF7 human breast cancer cells in culture. *Cancer Res* (1982) 42:667–73.

68. Rodríguez-Enríquez S, Marín-Hernández Á, Gallardo-Pérez JC, Pacheco-Velázquez SC, Belmont-Díaz JA, Robledo-Cadena DX, et al. Transcriptional regulation of energy metabolism in cancer cells. *Cells* (2019) 8(10):1225. doi: 10.3390/cells8101225

69. Chen JQ, Yager JD, Russo J. Regulation of mitochondrial respiratory chain structure and function by estrogens/estrogen receptors and potential physiological/pathophysiological implications. *Biochim Biophys Acta* (2005) 1746(1):1–17. doi: 10.1016/j.bbamcr.2005.08.001

70. Klinge CM. Estrogenic control of mitochondrial function. *Redox Biol* (2020) 31:101435. doi: 10.1016/j.redox.2020.101435

71. Sastre-Serra J, Nadal-Serrano M, Pons DG, Valle A, Oliver J, Roca P. The effects of 17β-estradiol on mitochondrial biogenesis and function in breast cancer cell lines are dependent on the ERα/ERβ ratio. *Cell Physiol Biochem* (2012) 29(1-2):261–68. doi: 10.1159/000337607

72. Garcia MV, Cabezas JA, Perez-Gonzalez MN. Effects of estradiol, testosterone and medroxyprogesterone on subcellular fraction marker enzyme activities from rat liver and brain. *Comp Biochem Physiol B* (1985) 80:347–54. doi: 10.1016/0305-0491(85)90217-2

73. Kipp JL, Ramirez VD. Effect of estradiol, diethylstilbestrol, and resveratrol on F0F1-ATPase activity from mitochondrial preparations of rat heart, liver, and brain. *Endocrine* (2001) 15:165–75. doi: 10.1385/ENDO:15:2:165

74. Radde BN, Ivanova MM, Mai HX, Salabei JK, Hill BG, Klinge CM. Bioenergetic differences between MCF-7 and T47D breast cancer cells and their regulation by oestradiol and tamoxifen. *Biochem J* (2015) 465(1):49–61. doi: 10.1042/BJ20131608

75. Planas-Silva MD, Waltz PK. Estrogen promotes reversible epithelial-to-mesenchymal-like transition and collective motility in MCF-7 breast cancer cells. *J Steroid Biochem Mol Biol* (2007) 104(1-2):11–21. doi: 10.1016/j.jsbmb.2006.09.039

76. Li Y, Wang JP, Santen RJ, Kim TH, Park H, Fan P, et al. Estrogen stimulation of cell migration involves multiple signaling pathway interactions. *Endocrinology* (2010) 151(11):5146–56. doi: 10.1210/en.2009-1506

77. Wan S, Jiang J, Zheng C, Wang N, Zhai X, Fei X, et al. Estrogen nuclear receptors affect cell migration by altering sublocalization of AQP2 in glioma cell lines. *Cell Death Discovery* (2018) 4:49. doi: 10.1038/s41420-018-0113-y

78. Maynadier M, Nirdé P, Ramirez JM, Cathiard AM, Platet N, Chambon M, et al. Role of estrogens and their receptors in adhesion and invasiveness of breast cancer cells. *Adv Exp Med Biol* (2008) 617:485–91. doi: 10.1007/978-0-387-69080-3_48

79. Soule HD, McGrath CM. Estrogen responsive proliferation of clonal human breast carcinoma cells in athymic mice. *Cancer Lett* (1980) 10:177–89. doi: 10.1016/0304-3835(80)90042-7

80. Osborne CK, Hobbs K, Clark GM. Effect of estrogens and antiestrogens on growth of human breast cancer cells in athymic nude mice. *Cancer Res* (1985) 45:584–90.

81. Zheng S, Huang J, Zhou K, Zhang C, Xiang Q, Tan Z, et al. 17β-estradiol enhances breast cancer cell motility and invasion *via* extra-nuclear activation of actin-binding protein ezrin. *PloS One* (2011) 6(7):e22439. doi: 10.1371/journal.pone.0022439

82. Gierse JK, Koboldt CM, Walker MC, Seibert K, Isakson PC. Kinetic basis for selective inhibition of cyclo-oxygenase. *Biochem J* (1999) 339:607–14. doi: 10.1042/bj3390607

83. Ralph SJ, Pritchard R, Rodríguez-Enríquez S, Moreno-Sánchez R, Ralph RK. Hitting the bull's-eye in metastatic cancers-NSAIDs elevate ROS in mitochondria, inducing malignant cell death. *Pharm (Basel)* (2015) 8:62–106. doi: 10.3390/ph8010062

Frontiers in
Oncology

Advances knowledge of carcinogenesis and tumor progression for better treatment and management

The third most-cited oncology journal, which highlights research in carcinogenesis and tumor progression, bridging the gap between basic research and applications to imrpove diagnosis, therapeutics and management strategies.

Discover the latest Research Topics

See more →

frontiers | Research Topics